

テーマ1 細胞機能を人工的に制御するためのケミカルツールの創成

(1) 概要

テーマ1では、化学系研究者の合成技術や分子レベルでの種々の分析技術を用いて、細胞に狙い通りの摂動を与えるように精緻にデザインされた革新的ケミカルツール(高分子, 超分子, 分子集合体, ペプチド, 金属錯体, 触媒など)の合成を試みた。また、これらの物質群に基礎をおく創薬や治療法の開発などの応用について、生物学・医学・薬学などの境界領域の研究者との学際的な共同研究によって実現し、真に革新的かつ世界をリードするケミカルツールの開発を試みた。

(2) 構成員

テーマ責任者:北岸宏亮

学内(同志社大学)研究員:北岸宏亮, 小寺政人, 人見 穰, 浦野泰臣, 東 信行, 古賀智之

学外研究員:根木 滋(同志社女子大), 浜地 格(京都大), 林 高史(大阪大), 青野重利(自然科学研究機構・岡崎統合バイオ), 神戸大朋(京都大)

(3) 成果報告

「細胞機能を人工的に制御するためのケミカルツール創製」を主幹テーマとしており、①細胞内での遺伝子編集やタンパク質修飾などを行うケミカルツールの開発、②細胞内シグナル物質を捕捉や可視化するケミカルツールの開発、③細胞機能を外部から制御するためのケミカルツールの開発の3つの小テーマについて、検討した。

テーマ 1 では、5 年間のプロジェクトにおいてこれまでに、計 149 報の査読付き学術論文誌に掲載されており、今後も順次論文投稿を継続する。下記に、主要メンバーによる主だった成果(学術論文 24 編)についての概要を示す。

①細胞内での遺伝子編集やタンパク質修飾などを行うケミカルツールの開発について、小寺らは、癌細胞の DNA に特異的に作用する金属錯体を合成し、DNA に対する高い加水分解活性を示す触媒の開発に成功した(文献 1,2)。またベンゼンをフェノールに酸化する高い活性を示す有用な触媒開発にも成功した(文献 3)。根木らは、細胞内に侵入して遺伝子編集を行うための Zn フィンガードメインの研究を展開した(文献 4,5)。

②細胞内シグナル物質を捕捉や可視化するケミカルツールの開発について、北岸らは、林らと協力し、細胞内におけるヘムタンパク質集合体の構築に成功した(文献 6)。また細胞内における一酸化炭素の生理機能探索をおこなうケミカルツールの開発に成功し、その機能の有用性を確か

めた(文献7-10)。人見らは、細胞内に侵入するポルフィリン誘導体(文献11), DNA を加水分解する触媒(文献12), 細胞内にてNOを発生するケミカルツールの開発(文献13)に成功した。浦野らは、細胞内コレステロールの代謝および機能に着目し、ヒドロキシコレステロール誘導体による細胞死に関する新たな知見をもたらす研究を行った(文献14-17)。

③細胞機能を外部から制御するためのケミカルツールの開発について、東および古賀らは、細胞の足場材料を開発するために、光応答性ポリマーの利用(文献18,19), ナノ粒子の利用(文献20), 熱応答性機能性ポリマーの開発(文献21), またそれらのポリマーに関する物性評価に関する基礎研究(文献22-24)を行った。

上記以外に、学外研究者により多数の学術論文が発表された。また上記の研究により、一酸化炭素を検出する手法(特願2020-010710)および一酸化炭素を細胞に届けるケミカルツール(特願2019-040610)についての特許出願を行った。さらに、細胞内過酸化水素を検出するプローブが市販される予定である。24S-hydroxycholesterol エステル体の合成法および測定法について、特許出願(ヒドロキシコレステロール脂肪酸エステルの検出方法;特願2015-186371)を行った。タンパク質ラベル化剤が2つ市販された。

本報告書の末尾に、上に示した研究概要に関する図と、下記リストに挙げた主要論文を添付する。

(4) 参考文献

1. “Oxidative DNA Cleavage, Formation of μ -1,1-Hydroperoxo Species, and Cytotoxicity of Dicopper(II) Complex Supported by a p-Cresol-Derived Amide-Tether Ligand”
Y. Kadoya, K. Fukui, M. Hata, R. Miyano, Y. Hitomi, S. Yanagisawa, M. Kubo, M. Kodera, *Inorg. Chem.*, **58**, 14294-14298 (2019).
2. “Acceleration of Hydrolytic DNA Cleavage by Dicopper(II) Complexes with p-Cresol-Derived Dinucleating Ligands at Slightly Acidic pH and the Mechanistic Insights”
M. Kodera, Y. Kadoya, K. Aso, K. Fukui, A. Nomura, Y. Hitomi, H. Kitagishi
Bull. Chem. Soc. Jpn. (Selected Paper), **92**, 739-747 (2019).
3. “Specific Enhancement of Catalytic Activity by a Dicopper Core: Selective Hydroxylation of Benzene to Phenol with Hydrogen Peroxide”
T. Tsuji, A. A. Zaoputra, Y. Hitomi, K. Mieda, T. Ogura, Y. Shiota, K. Yoshizawa, H. Sato, M. Kodera, *Angew. Chem. Int. Ed.*, **56**, 7779-7782, (2017).
4. “Efficient cleavage of DNA oligonucleotides by a non-FokI-type zinc finger nuclease containing one His₄-type finger domain derived from the first finger domain of Sp1”
S. Negi, M. Yoshioka, H. Mima, M. Mastumoto, M. Suzuki, M. Yokoyama, K. Kano, Y. Sugiura, *Bioorg. Medicinal Chem. Letter*. **25**, 4074-4077 (2015).
5. “Intrinsic cell permeability of the GAGA zinc finger protein into HeLa cells”
S. Negi, Y. Terada, M. Suzuyama, M. Matsumoto, A. Honbo, Y. Amagase, Y. Mizukawa, A. Kiriyama, K. Iga, T. Urushidani, Y. Sugiura, *Biochem. Biophys. Res. Commun.* **464**, 1034-1039 (2015).
6. “Multivalent Effect for Cellular Uptake of a Hemoprotein Assembly”
K. Oohora, R. Kajihara, M. Jiromaru, H. Kitagishi, T. Hayashi, *Chem. Lett.*, **48**, 295–298 (2019).
7. “Supramolecular Complexation in Biological Media. NMR Study on Inclusion of an Anionic Tetraarylporphyrin into a Heptakis(2,3,6-tri-O-methyl)- β -cyclodextrin Cavity in Serum, Blood, and Urine”
H. Kitagishi, M. Saito, Q. Mao, A. Kiriyama, S. Negi, K. Kano, *Chem. Asian J.*, **14**, 3320–3328 (2019).
8. “Circadian Clock Disruption by Selective Removal of Endogenous Carbon Monoxide”
S. Minegishi, I. Sagami, S. Negi, K. Kano, H. Kitagishi, *Sci. Rep.*, **8**, 11996 (2018).
9. “Detection and Removal of Endogenous Carbon Monoxide by Selective and Cell-permeable

Hemoprotein-model Complexes”

S. Minegishi, A. Yumura, H. Miyoshi, S. Negi, S. Taketani, R. Motterlini, R. Foresti, K. Kano, H. Kitagishi, *J. Am. Chem. Soc.*, **139**, 5984–5991 (2017).

10. “Feedback Response to Selective Depletion of Endogenous Carbon Monoxide in the Blood”
H. Kitagishi, S. Minegishi, A. Yumura, S. Negi, S. Taketani, Y. Amagase, Y. Mizukawa, T. Urushidani, Y. Sugiura, K. Kano, *J. Am. Chem. Soc.*, **138**, 5417–5425 (2016).
11. “Structurally Simple Cell-permeable Porphyrins: Efficient Cellular Uptake and Photo-toxicity of Porphyrins with Four Peripheral Primary-amine-terminated Oligo(ethylene oxide) Chains”
N. Ohashi, A. Nomura, M. Kodera, Y. Hitomi, *Chem. Lett.*, **46**, 1754–1756 (2017).
12. “DNA Cleavage through Reductive Dioxygen Activation by Iron-Bleomycin Mimics with Carboxamido Ligation: Correlation between DNA Cleavage Efficacy and Redox Potential”
A. Nomura, Y. Iwamoto, K. Arakawa, A. Kashida, M. Kodera, Y. Hitomi, *Chem. Lett.*, **46**, 1109–1111 (2017).
13. “Uncaging a Catalytic Hydrogen Peroxide Generator through the Photo-Induced Release of Nitric Oxide from a {MnNO}⁶ Complex”
Y. Iwamoto, M. Kodera, Y. Hitomi, *Chem. Commun.*, **51**, 9539–9542 (2015).
14. “Curcumin Derivative GT863 Inhibits Amyloid-Beta Production via Inhibition of Protein N-Glycosylation.”
Y. Urano, M. Takahachi, R. Higashiura, H. Fujiwara, S. Funamoto, S. Imai, E. Futai, M. Okuda, H. Sugimoto, N. Noguchi, *Cells*, **9**, E349 (2020).
15. “24(S)-Hydroxycholesterol induces ER dysfunction-mediated unconventional cell death.”
Y. Urano, D. K. Ho Vo, H. Araki, N. Noguchi, *Cell Death Discov.*, **5**, E113 (2019).
16. “6-Hydroxydopamine induces secretion of PARK7/DJ-1 via autophagy-based unconventional secretory pathway.”
Y. Urano, C. Mori, A. Fuji, K. Konno, T. Yamamoto, S. Yashirogi, M. Ando, Y. Saito, N. Noguchi, *Autophagy*, **14**, 1943–1958 (2018).
17. “Esterification of 24S-OHC Induces Formation of Atypical Lipid Droplet-like Structures, Leading to Neuronal Cell Death”
W. Takabe, Y. Urano, D. H. Vo, K. Shibuya, M. Tanno, H. Kitagishi, T. Fujimoto, N. Noguchi, *J. Lipid Res.*, **57**, 2005–2014 (2016).
18. “Photo-responsive Azobenzene Interactions Promote Hierarchical Self-assembly of Collagen

Triple-Helical Peptides to Various Higher-order Structures”

N. Higashi, R. Yoshikawa, T. Koga, *RSC Adv.* **10**, 15947-15954 (2020).

19. “Photocleavable Peptide-Poly(2-hydroxyethyl methacrylate) Hybrid Graft Copolymer via Post-polymerization Modification by Click Chemistry to Modulate the Cell Affinities of 2D and 3D-Materials”

S. Nishimura, N. Hokazono, Y. Taki, H. Motoda, Y. Morita, K. Yamamoto, N. Higashi, T. Koga, *ACS Appl. Mater. Interfaces*, **11**, 24577-24587 (2019).

20. “Spontaneous Formation of Nanoparticles from Peptide-Vinyl Polymer Diblock Hybrids Prepared by RAFT Polymerization and Their Interactions with Cells”

N. Higashi, K. Narimatsu, M. Okumura, S. Nishimura, T. Koga, *ACS Omega*, **4**, 8104-8111 (2019).

21. “A Novel Thermo-responsive Multiblock Architecture Composed of a Sequential Peptide and an Amino Acid-derived Vinyl Polymer: Toward Protein-mimicking Single-chain Folding” ***10,11**

S. Nishimura, N. Higashi, T. Koga, *Chem. Commun.*, **55**, 1498-1501 (2019).

22. “Photocleavable and Polymerizable Peptide for Micropatterning of Bioactive Segments in Polymer Soft Materials”

S. Nishimura, A. Hirata, Y. Taki, Y. Morita, N. Higashi, T. Koga, *Chem. Lett.*, **47**, 555-558 (2018).

23. “Facile Synthesis of Multiblock Copolymers Containing Sequence-controlled Peptides and Well-defined Vinyl Polymers by Nitroxide-mediated Polymerization”

S. Nishimura, N. Higashi, T. Koga, *Chem. Eur. J.*, **23**, 15050-15058 (2017). (*Frontispiece in this issue.*)

24. “Thermo-responsive Amino Acid-based Vinyl Polymers Showing Widely Tunable LCST/USCT Behavior in Water”

N. Higashi, R. Sonoda, T. Koga, *RSC Advances*, **5**, 67652-67657 (2015).

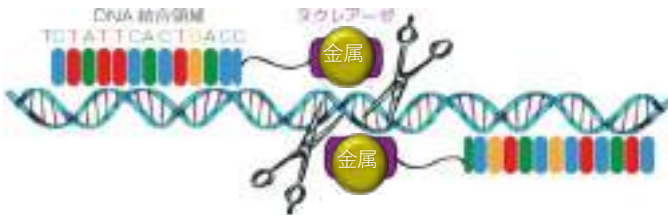
細胞自在操作のための分子化学技術の開発拠点形成

テーマ番号①：細胞機能を人工的に制御するためのケミカルツールの創製

研究者	専門分野
小寺 政人	金属錯体化学
東 信行	高分子化学
人見 穰	ケミカルバイオロジー
古賀 智之	ペプチド工学
北岸 宏亮	超分子化学
浦野 泰臣	分子生物学
根木 滋	遺伝子工学
神戸 大朋	細胞内金属イオン動態
青野 重利	タンパク質化学
林 高史	タンパク質工学
浜地 格	ケミカルバイオロジー

テーマ① 細胞機能を人工的に制御するためのケミカルツールの創製

(1) 遺伝子編集ツールの開発



少量で迅速にDNAを分解する触媒
ターゲット遺伝子を特異的に攻撃
外部環境に応じた活性ON/OFF調整

新規抗がん剤や遺伝子治療薬

(2) シグナル伝達系の人工制御ツール



細胞内小分子の**選択的捕捉**による可視化や擬ロックダウン

遺伝子工学では研究が困難なシグナル伝達系の探索

(3) 細胞足場材料（細胞外マトリクス）の開発



機能性ポリマー、ハイドロゲルによる細胞外マトリクス材料

再生医療のための細胞工学の基盤となる技術を提供

Dicopper complexes with amide ligands as anti-cancer drugs

同志社大学 小寺 政人

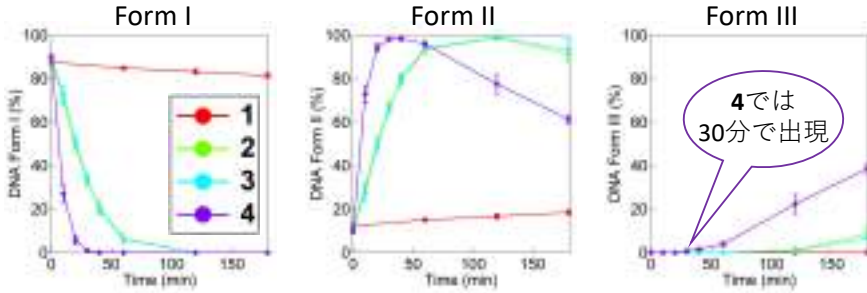
Cancer cell
がん細胞の特異的な環境

- low pH
- **high H₂O₂ concentration**
- low nutrition

がん細胞の特異的な環境下でのみDNAを切断するような金属錯体の開発

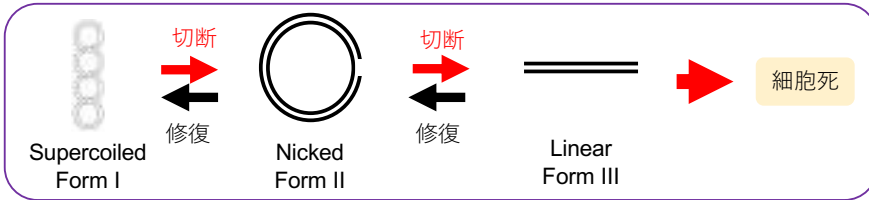
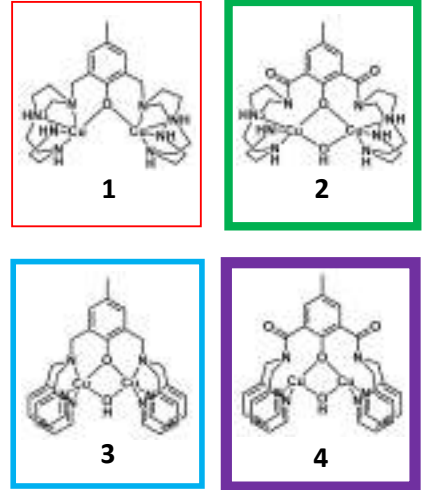
➡ 副作用のない抗がん剤への応用

Kato, Y. et al. *Cancer Cell International* **2013**, 13:89.
Zhou, D. et al. *Adv. Cancer Res.* **2014**, 122, 1–67.
Weidemann, A.; Johnson RS. *Cell Death and Differentiation* **2008**, 15, 621–627.



Oxidative cleavage of pUC19 DNA by 1-4. Experimental conditions: [NaCl] = 10 mM, [buffer] = 10 mM (pH 6.0 (MES)), [pUC19 DNA] = 0.05 mM bp, [complex] = 50 μM, [H₂O₂] = 500 μM for 180 min at 37° C.

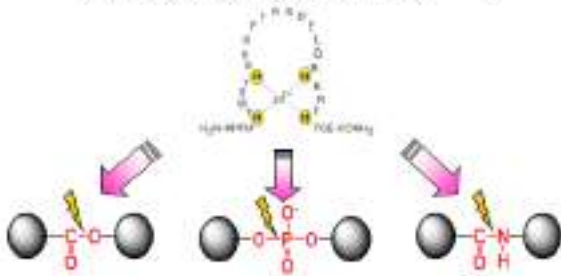
Large acceleration with amide ligand



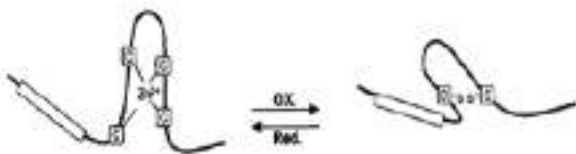
亜鉛フィンガータンパク質をフレームワークとする人工細胞透過性機能タンパク質の創製およびそれを用いた細胞マニピュレーション

同志社女子大学 根木 滋

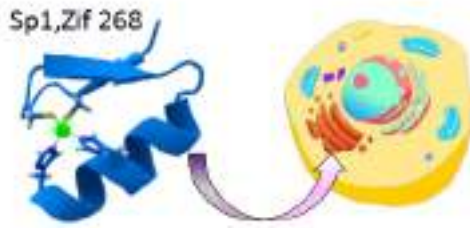
金属置換型フィンガータンパク質:
構造・機能解明、人工ヌクレアーゼ



亜鉛フィンガーのレドックスセンサーとしての機能:
金属コファクターの重要性

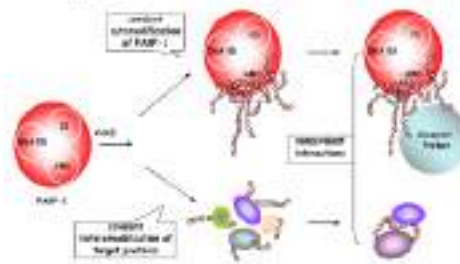


亜鉛フィンガーの細胞膜透過能:
2, 3次構造、カチオンクラスターの重要性



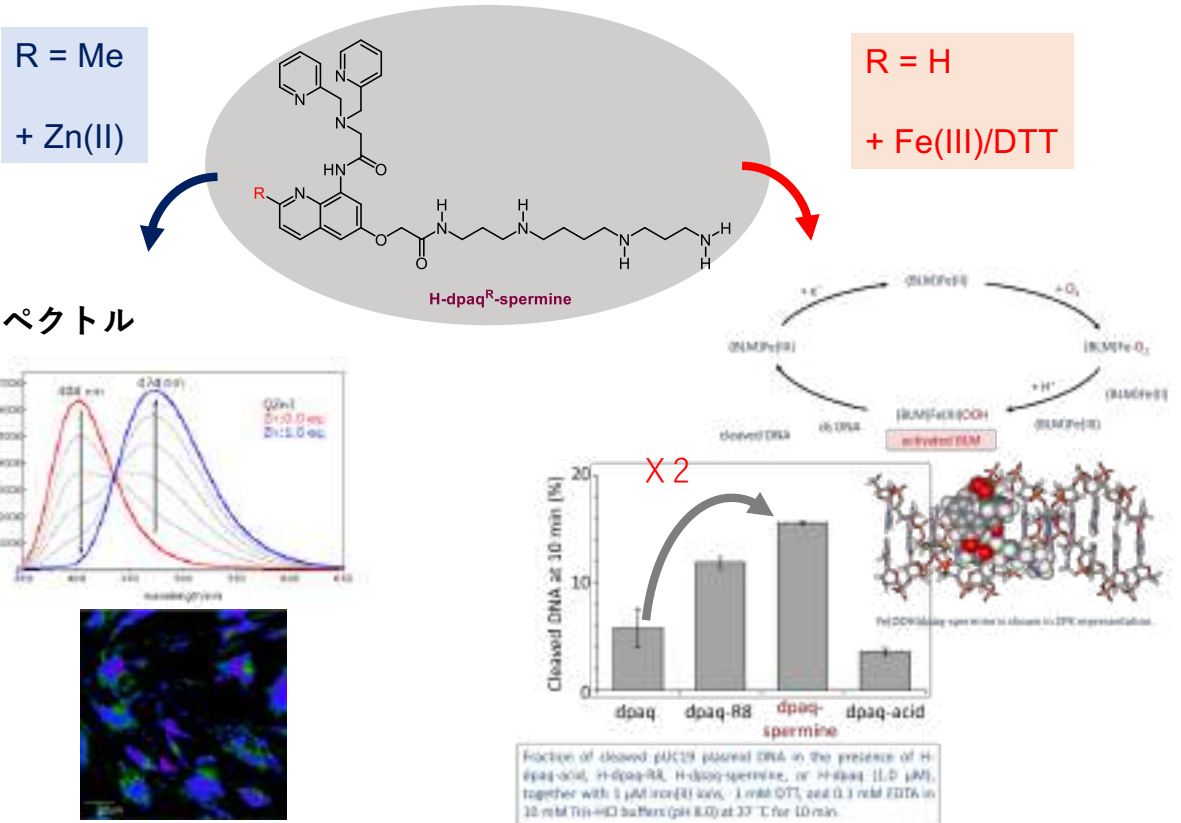
2015 BBRC

非古典的亜鉛フィンガー:
DNA修復タンパク質 PARPファミリー



金属イオンとの錯形成により機能発現する有機配位子の開発

同志社大学 人見 穰



亜鉛イオン選択的なレシオ型蛍光プローブ

1 microMの低濃度でDNAを酸化的に切断

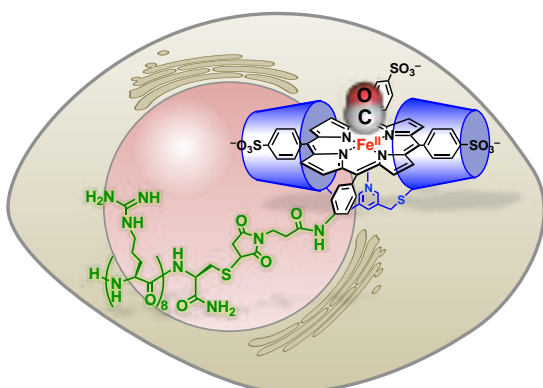
細胞内でシグナルメディエーターを捕捉する分子認識素子の開発

同志社大学理工学部
北岸 宏亮



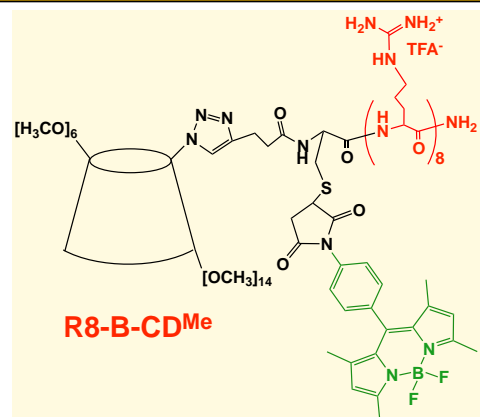
H. Kitagishi, K. Kano et al. *Angew Chem Int Ed* 2010

細胞内COの選択的捕捉による生理機能解明



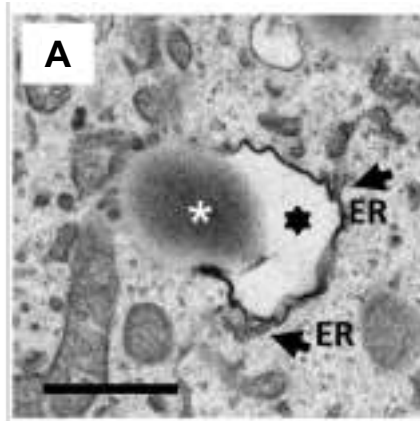
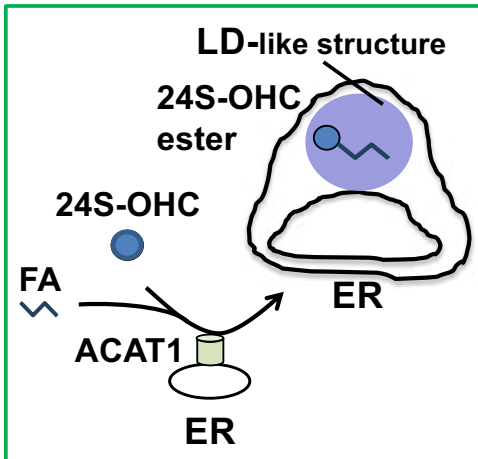
J. Am. Chem. Soc. 2017, 139, 5984.
Chem. Pharm. Bull. 2017, 65, 336.

細胞内で活躍する膜透過性CDの開発

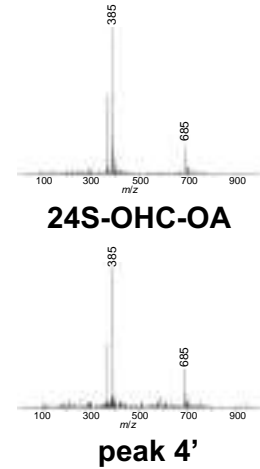


脳特異的オキシステロール24S-hydroxycholesterolによる神経細胞死誘導機構の解析

生命医科学部 浦野泰臣



電子顕微鏡による観察



DART-MSによる
24S-OHCエステルの同定

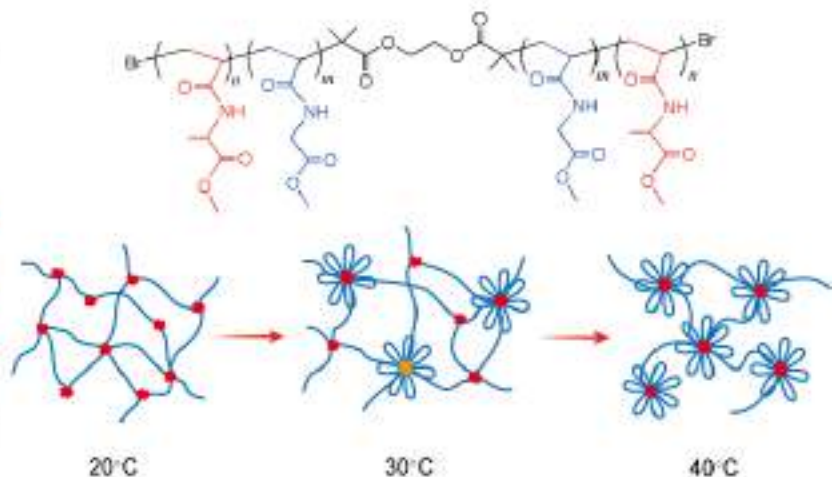
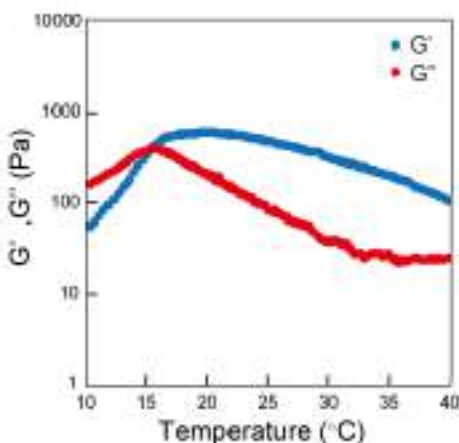
24S-hydroxycholesterol (24S-OHC)により誘導される細胞死では、24S-OHCのエステル化による脂肪滴様構造の形成が重要であることを示した。

Takabe W et al, J Lipid Res. (2016) 50:2005-2014
Shibuya K et al, Bioorg. Med. Chem. (2016) 24: 2559-2566
「ヒドロキシコレステロール脂肪酸エステルの検出方法」特開2017-62135

細胞足場材としてのアミノ酸由来ビニルポリマーからなるスマートインジェクタブル・ハイドロゲル

同志社大学 理工学部 東 信行

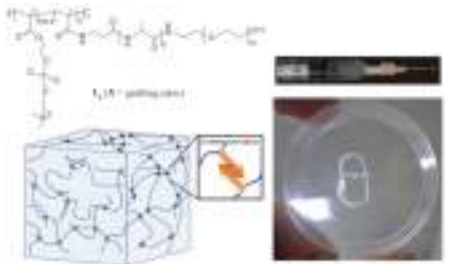
Thermo-responsive Hydrogels *via* Flower-like Micelle from Amino Acid-Based Triblock polymer



ペプチド-合成高分子・ハイブリッドを基盤とするスマート細胞足場材料の開発

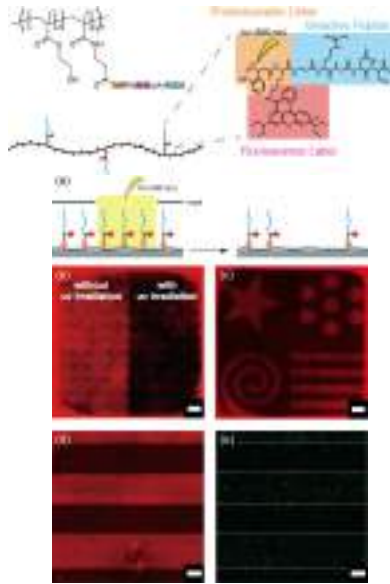
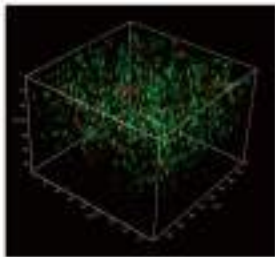
同志社大学 理工学部 古賀 智之

グラフト型ハイブリッド



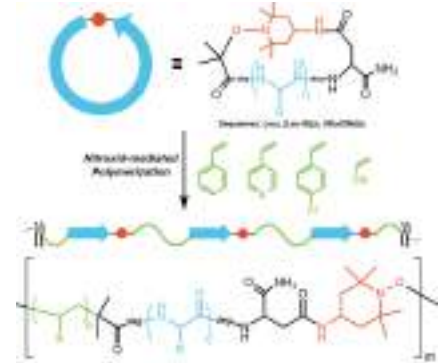
自己組織性ペプチドと生体適合性ポリマーからなるインジェクタブル・ハイドロゲルの開発

軟骨細胞の三次元足場材料としての応用 (緑:生細胞, 赤:死細胞)



光による細胞接着性ペプチドの二次元パターン化 (赤:RGDSペプチド, 緑:生細胞)

マルチブロック型ハイブリッド



配列制御ペプチドとビニルポリマーからなるマルチブロック型高分子の新しい精密合成法の開発

(環状ペプチド開始剤を利用したニトロキソド介在重合(NMP)による一段階マルチブロック化)

外部環境に応答した細胞内シグナル伝達反応の分子機構解明

青野 重利
(岡崎統合バイオ)

[酸素センサータンパク質HemAT, COセンサータンパク質CooAおよびヘムセンシング能を有するHmuTの物性評価](#)

特定タンパク質の選択的修飾による生細胞機能制御法の開発

浜地 格
(京都大学)

[細胞内の特定タンパク質を選択的に修飾する手法を開発](#)

[化学遺伝学的\(遺伝子工学と小分子の組み合わせ\)方法論による細胞機能の制御](#)

生体内バイオケミカル・バイオメタル制御機構の解明と先導的技術への応用展開

神戸 大朋
(京都大学)

[細胞内の金属輸送体の分子作用機序 生体内での金属要求性酵素の新たな制御機構を明らかにした](#)

細胞内外で機能を発現する人工ヘムタンパク質の創製

林 高史
(大阪大学)

[細胞内に侵入し, 光補修などの機能を発する人工ヘムタンパク質およびその集合体の構築を行った](#)

Oxidative DNA Cleavage, Formation of μ -1,1-Hydroperoxo Species, and Cytotoxicity of Dicopper(II) Complex Supported by a *p*-Cresol-Derived Amide-Tether Ligand

Yuki Kadoya,[†] Katsuki Fukui,[†] Machi Hata,[†] Risa Miyano,[†] Yutaka Hitomi,^{†,‡} Sachiko Yanagisawa,[‡] Minoru Kubo,[‡] and Masahito Kodera^{*,†,‡}

[†]Department of Molecular Chemistry and Biochemistry, Doshisha University, Kyotanabe Kyoto 610-0321, Japan

[‡]Department of Life Science, University of Hyogo, Kouto 2-1, Ako Kamigori Hyogo 678-1297, Japan

Supporting Information

ABSTRACT: Metal complexes to promote oxidative DNA cleavage by H₂O₂ are desirable as anticancer drugs. A dicopper(II) complex of known *p*-cresol-derived methylene-tether ligand Hbcc [Cu₂(bcc)]³⁺ did not promote DNA cleavage by H₂O₂. Here, we synthesized a new *p*-cresol-derived amide-tether one, 2,6-bis(1,4,7,10-tetraazacyclododecyl-1-carboxamide)-*p*-cresol (Hbcamide). A dicopper(II) complex of the new ligand [Cu₂(μ -OH)(bcamide)]²⁺ was structurally characterized. This complex promoted the oxidative cleavage of supercoiled plasmid pUC19 DNA (Form I) with H₂O₂ at pH 6.0–8.2 to give Forms II and III. The reaction was largely accelerated in a high pH region. A μ -1,1-hydroperoxo species was formed as the active species and spectroscopically identified. The amide-tether complex is more effective in cytotoxicity against HeLa cells than the methylene-tether one.

Various metal complexes have been developed as anticancer drugs that block DNA replication through binding and/or cutting DNA.¹ In particular, platinum(II) complexes, for example, cisplatin² and its derivatives, such as oxaliplatin,³ lobaplatin,⁴ and nedaplatin,⁵ are capable of strongly binding DNA to block the replication and are clinically used as anticancer drugs.⁶ However, dosing of this type of anticancer drugs is accompanied by heavy side-effects and platinum-resistance problems.⁷ As one of the other types of anticancer drugs clinically used, bleomycin is known to cleave double-strand DNA (ds-DNA).⁸ It has a metal binding site as a pentadentate donor including an amide donor. The iron complex of bleomycin reacts with dioxygen molecules and/or hydrogen peroxide to form the activated bleomycin, proposed as a hydroperoxoiron(III) complex, to oxidatively cleave ds-DNA.⁹ This, however, causes the problem of side-effects in the lungs with the long-time use.¹⁰

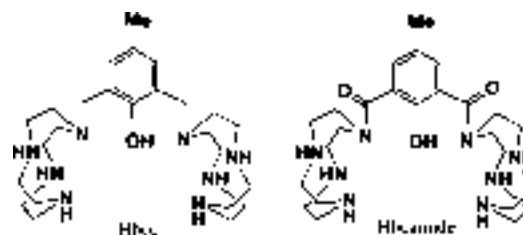
It is well-known that the microenvironment in the cancer cells is significantly different from that in normal cells.¹¹ As one of the key features of cancer cells, the concentration of reactive oxygen species (ROS) including H₂O₂ is relatively higher in cancer cells than in normal cells.¹² This is mainly caused by mitochondrial malfunction and increased metabolic activity of cancer cells.¹³ Thus, the overproduction of H₂O₂ in cancer

cells can be used to reduce the side-effect of anticancer drugs if we develop metal complexes capable of specifically activating H₂O₂ in cancer cells. So far, many complexes of copper,^{1a,14} iron,¹⁵ and various metals^{1d,16} have been reported to accelerate the oxidative DNA cleavage, but in most of them, large excess amounts of reducing reagents, such as 3-mercaptopropionic acid,^{14d} glutathione,^{14d,e} dithiothreitol,^{15b,d} and ascorbic acid,^{14a–c,15a} are essential. Amounts of reducing agents, however, are lower in cancer cells than in normal cells. Therefore, metal complexes capable of accelerating the oxidative DNA cleavage by H₂O₂ without reductants are desirable as anticancer drugs.

Previously, we reported that a dicopper(II) complex with *p*-cresol-derived methylene-tether ligand [Cu₂(bcc)](ClO₄)₃ (**1**) and related complexes accelerate hydrolytic DNA cleavage at pH 5–6,¹⁷ but **1** did not accelerate the DNA cleavage with H₂O₂. In this study, we synthesized a new *p*-cresol-derived amide-tether ligand 2,6-bis(1,4,7,10-tetraazacyclododecyl-1-carboxamide)-*p*-cresol (Hbcamide) and found that its dicopper(II) complex [Cu₂(μ -OH)(bcamide)](ClO₄)₂ (**2**) largely accelerates the oxidative DNA cleavage by H₂O₂ without reductants.

The methylene- and amide-tether ligands, Hbcc and Hbcamide, used in this study have two tetraazacyclododecane (cyclen) pendant groups tethered at 2,6-positions of *p*-cresol by –CH₂– and –CO– groups, respectively (Scheme 1). Hbcc and [Cu₂(bcc)](ClO₄)₂ (**1**) were prepared as previously reported.¹⁷ Hbcamide and [Cu₂(μ -OH)(bcamide)](ClO₄)₂ (**2**) are new compounds, and the synthetic details are shown

Scheme 1. Chemical Structures of Hbcc and Hbcamide



Received: July 13, 2019

Published: October 10, 2019

in the Supporting Information. **Caution!** Perchlorate salts are potentially explosive and should be handled with great caution.

The amide-tether complex **2** was structurally characterized by X-ray analysis (see Table S1 for the crystallographic data and Table S2 for the selected bond distances and angles). The crystal structure of **1** was previously reported.¹⁷ ORTEP views of **1** and **2** are shown in Figure 1A and B, respectively. In **2**,

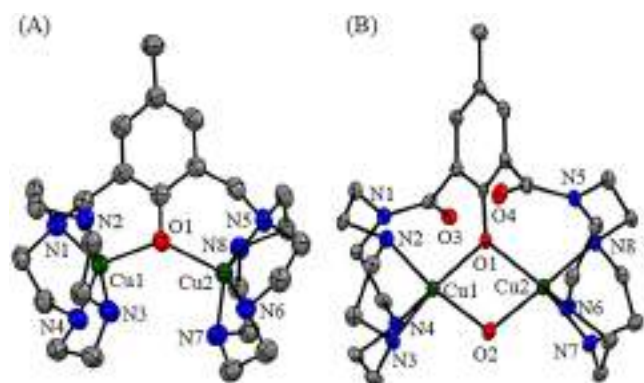


Figure 1. ORTEP diagrams of each cationic part of **1** (A) and **2** (B). Hydrogen atoms are omitted for clarity.

two Cu(II) ions are incorporated into a bcamide ligand and bridged by the endogenous μ -PhO and the exogenous μ -OH groups, where each Cu ion takes square pyramidal geometry with three N atoms of a pendant cyclen and two O atoms of the μ -OPh- μ -OH bridge. As previously reported, however, there is no μ -OH bridge in **1** where a Cu ion is coordinated by four N-atoms of pendant cyclen and the O-atom of the μ -PhO bridge. The Cu...Cu distance 3.047(11) Å of **2** is shorter than the 3.878(1) Å of **1**, due to the μ -PhO- μ -OH double bridge in **2**. The tether groups make these distinct differences in the Cu coordination structures between **1** and **2**.

The structure of **2** in an aqueous solution was examined by the spectroscopic studies. The ESI-MS spectrum of **2** in an aqueous solution is shown in Figure S1. The major peak appeared at m/z 745 corresponding to [bcamide + 2Cu(II) + OH + ClO₄]⁺. This shows that the μ -OPh- μ -OH bridge of **2** is kept in an aqueous solution. In the electronic absorption spectrum of **2** (Figure S2), two distinct bands appear at 326 and 390 nm assignable to HO⁻ and PhO⁻ to Cu(II) LMCT bands. These are similar to the LMCT bands at 340–400 nm reported for the related μ -OPh- μ -OH double bridged dicopper(II) complexes.^{17,18}

The reactivities of **1** and **2** in the DNA cleavage were examined using supercoiled plasmid pUC19 DNA (form I) as a substrate in the absence and presence of H₂O₂ under physiological pH 6.0–8.2 at 37 °C. Forms I, II, and III of DNA denote supercoiled close-circular, nicked circular, and linear double-strand DNA, respectively. Form I is converted to Forms II and III in the DNA cleavage. The amounts of Forms I, II, and III were analyzed by agarose gel electrophoresis. The gel patterns and time courses are shown in Figures S3–S12 and Tables S3–S7. The decreases of percent of Form I versus time in the reactions using **1** and **2** at pH 6.0 in the presence of H₂O₂ (0.5 mM) are shown in Figure 2. The decreased rate of Form I in the reaction of the methylene-tether complex **1** in the presence of H₂O₂ is exactly the same as that in the absence of H₂O₂. Thus, **1** did not accelerate the oxidative DNA cleavage with H₂O₂ at all. The decrease of percent of Form I in

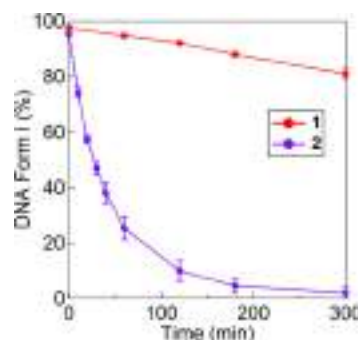


Figure 2. Time courses for the decrease of percent of Form I upon reaction of pUC19 DNA (50 μ M bp) with **1** (red) or **2** (purple; 50 μ M) in the presence of H₂O₂ (0.5 mM) at pH 6.0 (10 mM MES, 10 mM NaCl) at 37 °C.

the reaction of **1** is caused by hydrolytic DNA cleavage as previously reported.¹⁷ On the other hand, in the presence of H₂O₂, the amide-tether complex **2** significantly accelerated the decrease of percent of Form I as shown in Figure 2. The hydrolytic DNA cleavage activity of **2** was almost the same as that of **1** (see Figure S8). The oxidative DNA cleavage is confirmed by the fact that Form III produced in the reaction is not converted to form II by treatment with T4 DNA ligase (Figure S20). Thus, **2** specifically promoted oxidative DNA cleavage with H₂O₂, where **2** activates H₂O₂ for the oxidative DNA cleavage because H₂O₂ did not cleave DNA by itself in the absence of **2**. Moreover, the oxidative DNA cleavage rate increased with an increase of concentrations of both **2** and H₂O₂ as shown in Figures S9 and S10 and Tables S6. These results suggest that the reaction proceeds via formation of the active species from **2** and H₂O₂. The active species was spectroscopically identified as described below.

The pH dependence of the oxidative DNA cleavage was further examined by using the amide-tether complex **2** in detail. A decrease of percent of Form I and increase of percent of Form III in the reactions at pH 6.0, 7.4, and 8.2 in the presence of H₂O₂ (0.3 mM) are shown in Figure S4. As shown in Figure S4A, the decrease of percent of Form I is accelerated at higher pH. Moreover, it was found that the formation rate of Form III is drastically enhanced at higher pH as shown in Figure S4B. At pH 8.2, 50% of form I was converted to Form III in 5 h, but an almost negligible amount of Form III was detected at pH 6.0. This suggested that the formation of the active species is accelerated at high pH. Form III is a linear DNA formed by the cleavage of two phosphate-ester main chains at the near positions of ds-DNA. Actually, **2** showed relatively high oxidative DNA cleavage activity in the presence of H₂O₂ as compared with a tricopper complex reported before.¹⁴ Thus, the active species has a strong oxidation ability capable of cleaving ds-DNA, and this is similar to the activated bleomycin.

The oxidative DNA cleavage studies in the presence of various inhibitors, NaN₃ (singlet oxygen scavenger), DMSO (hydroxy radical scavenger), and KI (superoxide scavenger), were also carried out to identify the active species that may be formed in the reaction of **2** with H₂O₂. The results are shown in Figures S11 and S12 and Tables S7. The addition of NaN₃ (0.5 mM) and DMSO (0.5 mM) to the reaction of **2** slightly enhanced the DNA cleavage but did not inhibit at all, suggesting that both a singlet oxygen and a diffusible hydroxy radical are not the active species in the DNA cleavage. The

reaction was only slightly inhibited when KI (0.5 mM) was added to the reaction of **2**. In this case, KI acts as a reductant, and thus, H_2O_2 by itself and a Cu-bonded peroxide complex are possible candidates as the active species in the DNA cleavage. The former is not the active species because the DNA cleavage did not occur when only H_2O_2 was used. Both **2** and H_2O_2 are essential for DNA cleavage.

To detect the active species, the reactions of complexes, **1** and **2**, with H_2O_2 were monitored on the electronic absorption spectra. Upon the addition of H_2O_2 to a solution of the methylene-tether complex **1**, any spectral change did not occur (Figure S13), showing that **1** does not bind H_2O_2 . This is consistent with no reactivity of **1** in the oxidative DNA cleavage with H_2O_2 . On the other hand, the amide-tether complex **2** reacted with H_2O_2 to give clear bands at 340 ($\epsilon = 5600 \text{ M}^{-1} \text{ cm}^{-1}$) and 398 ($\epsilon = 4800 \text{ M}^{-1} \text{ cm}^{-1}$) nm (Figure S13). The band at 398 nm is similar to HO_2^- to Cu(II) LMCT bands around 390–400 nm reported for various μ -1,1-hydroperoxodicopper(II) complexes,¹⁹ indicating that a μ -1,1-hydroperoxodicopper(II) species $[\text{Cu}_2(\text{O}_2\text{H})(\text{bcamide})]^{2+}$ (**3**) may be formed in the reaction of **2** with H_2O_2 . Formation of **3** was not affected by Et_3N , small phosphate anions, and N_3^- ion as shown in Figure S14B–E. The formation of **3** is shown by CSI MS spectra, having two major peaks at m/z 331 and 761 corresponding to $[\text{bcamide} + 2\text{Cu}(\text{II}) + \text{O}_2\text{H}]^{2+}$ and $[\text{bcamide} + 2\text{Cu}(\text{II}) + \text{O}_2\text{H} + \text{ClO}_4]^{+}$, respectively (Figure S15). When ^{18}O -labeled $\text{H}_2^{18}\text{O}_2$ was used instead of $\text{H}_2^{16}\text{O}_2$, these shifted to m/z 333 and 765, demonstrating that two O atoms of **3** come from H_2O_2 (Figure S16). The CSI MS spectrum measured upon the reaction of **2** with H_2O_2 in H_2O gave two major peaks at m/z 331 and 761 (Figure S21), showing that **3** is formed in the oxidative DNA cleavage in H_2O . Moreover, the formation of **3** in H_2O was also observed on the electronic absorption spectrum (Figure S22).

The resonance Raman spectra of **3** are shown in Figure 3. A clear band appeared at 897 cm^{-1} upon reaction of **2** with

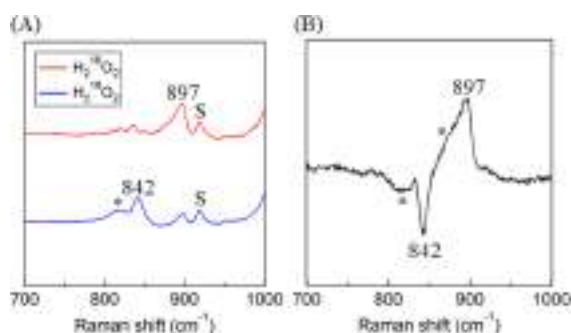


Figure 3. (A) Resonance Raman spectra of **3** prepared from **2** and excess amounts of $\text{H}_2^{16}\text{O}_2$ (red) or $\text{H}_2^{18}\text{O}_2$ (blue) in MeOH at -30°C with excitation at 405 nm. (B) A difference spectrum of A. S and * mean solvent and H_2O_2 .

$\text{H}_2^{16}\text{O}_2$. By using $\text{H}_2^{18}\text{O}_2$ instead of $\text{H}_2^{16}\text{O}_2$, this band shifted to 842 cm^{-1} due to the isotope shift (55 cm^{-1}). These data are similar to the $\nu_{\text{O-O}}$ band at 892 cm^{-1} and an isotope shift of 52 cm^{-1} of μ -1,1-hydroperoxodicopper(II) complex with the *p*-cresol derived ligand.²⁰ Thus, **3** is proposed as a μ -1,1-hydroperoxodicopper(II) complex shown in Figure 4.

The reaction of **3** (0.25 mM) with guaiacol (7.5 mM) was monitored by the electronic absorption spectral change (Figure S17), where **3** readily oxidized guaiacol to give corresponding

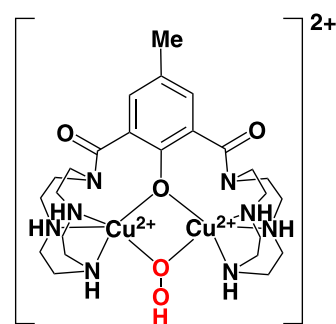


Figure 4. A proposed chemical structure of the μ -1,1-hydroperoxodicopper(II) complex **3**.

tetraguaiacol as an oxidized product, and the typical absorption bands appeared at 412 and 470 nm.²¹ The concentration of tetraguaiacol obtained was estimated as 0.05 mM from absorbance at 470 nm ($\epsilon = 26.6 \text{ mM}^{-1} \text{ cm}^{-1}$;^{21a,22} Figure S17B) where 0.2 mM of **3** was used to form tetraguaiacol because 4 equiv of **3** is consumed to convert guaiacol to tetraguaiacol. Thus, the yield of the tetraguaiacol was ca. 80% on the basis of **3** used. These results clearly show **3** is the active species in the reaction. The increase of tetraguaiacol was monitored at 500 nm, and the reaction rate was estimated as $2.93 \times 10^{-2} \text{ min}^{-1}$ (Figure S17C). Guaiacol was not oxidized only by H_2O_2 . These results indicate that **3** is the direct oxidant in the oxidative DNA cleavage.

Finally, we examined cytotoxicity of the methylene-tether complex **1** and the amide tether complex **2** against HeLa cells. HeLa is a human cell line derived from cervical cancer cells taken from Henrietta Lacks, a patient who died of cancer. The cytotoxicity was determined by means of MTT assay.²³ The details are described in the Supporting Information. The IC_{50} values (Table S8 and Figure S20) clearly show that **2** is more effective in the cytotoxicity than **1**. This is proportional to the high DNA cleavage ability of **2**.

In this study, we synthesized a new amide-tether ligand and its dicopper(II) complex $[\text{Cu}_2(\mu\text{-OH})(\text{bcamide})](\text{ClO}_4)_2$ (**2**) and found that the amide-tether complex **2** largely accelerated the oxidative DNA cleavage with H_2O_2 . Moreover, **2** reacts with H_2O_2 to form the active species, which was spectroscopically identified as a μ -1,1-hydroperoxodicopper(II) complex **3**. These results may shed light on the development of new anticancer drugs to reduce the heavy side-effect.

■ ASSOCIATED CONTENT

Supporting Information

The Supporting Information is available free of charge on the ACS Publications website at DOI: 10.1021/acs.inorgchem.9b02093.

Detailed experimental procedures, syntheses of ligands and complexes, Figures S1–S22, Tables S1–S8, and Schemes S1 and S2 (PDF)

Accession Codes

CCDC 1937747 contains the supplementary crystallographic data for this paper. These data can be obtained free of charge via www.ccdc.cam.ac.uk/data_request/cif, or by emailing data_request@ccdc.cam.ac.uk, or by contacting The Cambridge Crystallographic Data Centre, 12 Union Road, Cambridge CB2 1EZ, UK; fax: +44 1223 336033.

AUTHOR INFORMATION

Corresponding Author

*E-mail: mkodera@mail.doshisha.ac.jp.

ORCID

Yutaka Hitomi: 0000-0002-2448-296X

Masahito Kodera: 0000-0001-9979-1743

Notes

The authors declare no competing financial interest.

ACKNOWLEDGMENTS

This work was supported by MEXT-Supported Program of the Strategic Research Foundation at Private University, 2015–2019.

REFERENCES

- (1) (a) Santini, C.; Pellei, M.; Gandin, V.; Porchia, M.; Tisato, F.; Marzano, C. Advances in Copper Complexes as Anticancer Agents. *Chem. Rev.* **2014**, *114*, 815–862. (b) Kettenmann, S. D.; Louka, F. R.; Marine, E.; Fischer, R. C.; Mautner, F. A.; Kulak, N.; Massoud, S. S. Efficient Artificial Nucleases for Mediating DNA Cleavage Based on Tuning the Steric Effect in the Pyridyl Derivatives of Tripod Tetraamine-Cobalt(II) Complexes. *Eur. J. Inorg. Chem.* **2018**, *2018*, 2322–2338. (c) Dasari, S.; Bernard Tchounwou, P. Cisplatin in cancer therapy: Molecular mechanism of action. *Eur. J. Pharmacol.* **2014**, *740*, 364–378. (d) Copeland, K. D.; Fitzsimons, M. P.; Houser, R. P.; Barton, J. K. DNA Hydrolysis and Oxidative Cleavage by Metal-Binding Peptides Tethered to Rhodium Intercalators. *Biochemistry* **2002**, *41*, 343–356.
- (2) (a) Johnstone, T. C.; Suntharalingam, K.; Lippard, S. J. The Next Generation of Platinum Drugs: Targeted Pt(II) Agents, Nanoparticle Delivery, and Pt(IV) Prodrugs. *Chem. Rev.* **2016**, *116*, 3436–3486. (b) Rosenberg, B. Fundamental Studies With Cisplatin. *Cancer* **1985**, *55*, 2303–2316.
- (3) Kidani, Y.; Inagaki, K.; Iigo, M.; Hoshi, A.; Kuretani, K. Antitumor activity of 1,2-diaminocyclohexaneplatinum complexes against Sarcoma-180 ascites form. *J. Med. Chem.* **1978**, *21*, 1315–1318.
- (4) McKeage, M. J. Lobaplatin: a new antitumor platinum drug. *Expert Opin. Invest. Drugs* **2001**, *10*, 119–128.
- (5) Shimada, M.; Itamochi, H.; Kigawa, J. Nedaplatin: a cisplatin derivative in cancer chemotherapy. *Cancer Manage. Res.* **2013**, *5*, 67–76.
- (6) Jamieson, E. R.; Lippard, S. J. Structure, Recognition, and Processing of Cisplatin-DNA Adducts. *Chem. Rev.* **1999**, *99*, 2467–2498.
- (7) Florea, A.-M.; Büsselberg, D. Cisplatin as an Anti-Tumor Drug: Cellular Mechanisms of Activity, Drug Resistance and Induces Side Effects. *Cancers* **2011**, *3*, 1351–1371.
- (8) (a) Burger, R. M. Cleavage of Nucleic Acids by Bleomycin. *Chem. Rev.* **1998**, *98*, 1153–1169. (b) Abraham, A. T.; Zhou, X.; Hecht, S. M. DNA Cleavage by Fe(II)•Bleomycin Conjugated to a Solid Support. *J. Am. Chem. Soc.* **1999**, *121*, 1982–1983. (c) Huang, S.-X.; Feng, Z.; Wang, L.; Galm, U.; Wendt-Pienkowski, E.; Yang, D.; Tao, M.; Coughlin, J. M.; Duan, Y.; Shen, B. A Designer Bleomycin with Significantly Improved DNA Cleavage Activity. *J. Am. Chem. Soc.* **2012**, *134*, 13501–13509.
- (9) (a) Decker, A.; Chow, M. S.; Kemsley, J. N.; Lehnert, N.; Solomon, E. I. Direct Hydrogen-Atom Abstraction by Activated Bleomycin: An Experimental and Computational Study. *J. Am. Chem. Soc.* **2006**, *128*, 4719–4733. (b) Liu, L. V.; Bell, C. B., III; Wong, S. D.; Wilson, S. A.; Kwak, Y.; Chow, M. S.; Zhao, J.; Hodgson, K. O.; Hedman, B.; Solomon, E. I. Definition of the intermediates and mechanism of the anticancer drug bleomycin using nuclear resonance vibrational spectroscopy and related methods. *Proc. Natl. Acad. Sci. U. S. A.* **2010**, *107*, 22419–22424.
- (10) Adamson, I. Y. R. Pulmonary toxicity of bleomycin. *Environ. Health Perspect.* **1976**, *16*, 119–126.
- (11) Zhou, D.; Shao, L.; Spitz, D. R. Reactive Oxygen Species in Normal and Tumor Stem Cells. *Adv. Cancer Res.* **2014**, *122*, 1–67.
- (12) (a) Nogueira, V.; Hay, N. Molecular Pathways: Reactive Oxygen Species Homeostasis in Cancer Cells and Implications for Cancer Therapy. *Clin. Cancer Res.* **2013**, *19*, 4309–4314. (b) Szatrowski, T. P.; Nathan, C. F. Production of Large Amounts of hydrogen peroxide by Human Tumor Cells. *Cancer Res.* **1991**, *51*, 794–798.
- (13) (a) Aykin-Burns, N.; Ahmad, I. M.; Zhu, Y.; Oberley, L. W.; Spitz, D. R. Increased levels of superoxide and H₂O₂ mediate the differential susceptibility of cancer cells versus normal cells to glucose deprivation. *Biochem. J.* **2009**, *418*, 29–37. (b) Ishii, N.; Fujii, M.; Hartman, P. S.; Tsuda, M.; Yasuda, K.; Senoo-Matsuda, N.; Yanase, S.; Ayusawa, D.; Suzuki, K. A mutation in succinate dehydrogenase cytochrome *b* causes oxidative stress and ageing in nematodes. *Nature* **1998**, *394*, 694–697.
- (14) (a) Tu, C.; Shao, Y.; Gan, N.; Xu, Q.; Guo, Z. Oxidative DNA Strand Scission Induced by a Trinuclear Copper(II) Complex. *Inorg. Chem.* **2004**, *43*, 4761–4766. (b) González-Alvarez, M.; Alzuet, G.; Borrás, J.; Macías, B.; Castiñeiras, A. Oxidative Cleavage of DNA by a New Ferromagnetic Linear Trinuclear Copper(II) Complex in the Presence of H₂O₂/Sodium Ascorbate. *Inorg. Chem.* **2003**, *42*, 2992–2998. (c) Santra, B. K.; Reddy, P. A. N.; Neelakanta, G.; Mahadevan, S.; Nethaji, M.; Chakravarty, A. R. Oxidative cleavage of DNA by a dipyridoquinoxaline copper(II) complex in the presence of ascorbic acid. *J. Inorg. Biochem.* **2002**, *89*, 191–196. (d) Borrás, J.; Alzuet, G.; Gonzalez-Alvarez, M.; Garcia-Gimenez, J. L.; Macias, B.; Liu-Gonzalez, M. Efficient DNA Cleavage Induced by Copper(II) Complexes of Hydrolysis Derivatives of 2,4,6-Tris(2-pyridyl)-1,3,5-triazine in the Presence of Reducing Agents. *Eur. J. Inorg. Chem.* **2007**, *2007*, 822–834. (e) Vaidyanathan, V. G.; Nair, B. U. Oxidative cleavage of DNA by tridentate copper (II) complex. *J. Inorg. Biochem.* **2003**, *93*, 271–276.
- (15) (a) El Amrani, F. B. A.; Perello, L.; Real, J. A.; Gonzalez-Alvarez, M.; Alzuet, G.; Borrás, J.; Garcia-Granda, S.; Montejo-Bernardo, J. Oxidative DNA cleavage induced by an iron(III) flavonoid complex: Synthesis, crystal structure and characterization of chlorobis(flavonolate)(methanol) iron(III) complex. *J. Inorg. Biochem.* **2006**, *100*, 1208–1218. (b) Li, Q.; van den Berg, T. A.; Feringa, B. L.; Roelfes, G. Mononuclear Fe(II)-N4Py complexes in oxidative DNA cleavage: structure, activity and mechanism. *Dalton Trans* **2010**, *39*, 8012–8021. (c) Roelfes, G.; Branum, M. E.; Wang, L.; Que, L., Jr.; Feringa, B. L. Efficient DNA Cleavage with an Iron Complex without Added Reductant. *J. Am. Chem. Soc.* **2000**, *122*, 11517–11518. (d) van den Berg, T. A.; Feringa, B. L.; Roelfes, G. Double strand DNA cleavage with a binuclear iron complex. *Chem. Commun.* **2007**, *2*, 180–182.
- (16) (a) Satharaj, G.; Kiruthika, M.; Weyhermuller, T.; Unni Nair, B. Oxidative Cleavage of DNA Ruthenium(II) Complexes Containing a Ferrocene/Non-Ferrocene Conjugated Imidazole Phenol Ligand. *Organometallics* **2012**, *31*, 6980–6987. (b) Mack, D. P.; Dervan, P. B. Nickel-mediated sequence-specific oxidative cleavage of DNA by a designed metalloprotein. *J. Am. Chem. Soc.* **1990**, *112*, 4604–4606.
- (17) Kodera, M.; Kadoya, Y.; Aso, K.; Fukui, K.; Nomura, A.; Hitomi, Y.; Kitagishi, H. Acceleration of Hydrolytic DNA Cleavage by Dicopper(II) Complexes with *p*-Cresol-Derived Dinucleating Ligands at Slightly Acidic pH and Mechanistic Insights. *Bull. Chem. Soc. Jpn.* **2019**, *92*, 739–747.
- (18) (a) Rey, N. A.; Neves, A.; Bortoluzzi, A. J.; Pich, C. T.; Terenzi, H. Catalytic Promiscuity in Biomimetic Systems: Catecholase-like Activity, Phosphatase-like Activity, and Hydrolytic DNA Cleavage Promoted by a New Dicopper(II) Hydroxo-Bridged Complex. *Inorg. Chem.* **2007**, *46*, 348–350. (b) Amudha, P.; Kandaswamy, M.; Govindasamy, L.; Velmurugan, D. Synthesis and Characterization of New Symmetrical Binucleating Ligands and Their μ -Phenoxo-Bridged Bicuopper(II) Complexes: Structural, Electrochemical, and Magnetic Studies. *Inorg. Chem.* **1998**, *37*, 4486–4492.

- (19) (a) Root, D. E.; Mahroof-Tahir, M.; Karlin, K. D.; Solomon, E. I. Effect of Protonation on Peroxo-Copper Bonding: Spectroscopic and Electronic Structure Study of $[\text{Cu}_2(\text{UN-O})(\text{OOH})]^{2+}$. *Inorg. Chem.* **1998**, *37*, 4838–4848. (b) Kindermann, N.; Dechert, S.; Demeshko, S.; Meyer, F. Proton-Induced, Reversible Interconversion of a μ -1,2-Peroxo and a μ -1,1-Hydroperoxo Dicopper(II) Complex. *J. Am. Chem. Soc.* **2015**, *137*, 8002–8005. (c) Battaini, G.; Monzani, E.; Perotti, A.; Para, C.; Casella, L.; Santagostini, L.; Gullotti, M.; Dillinger, R.; Näther, C.; Tuczek, F. A Double Arene Hydroxylation Mediated by Dicopper-Hydroperoxide Species. *J. Am. Chem. Soc.* **2003**, *125*, 4185–4198.
- (20) (a) Li, L.; Narducci Sarjeant, A. A.; Vance, M. A.; Zakharov, L. N.; Rheingold, A. L.; Solomon, E. I.; Karlin, K. D. Exogenous Nitrile Substrate Hydroxylation by a New Dicopper-Hydroperoxide Complex. *J. Am. Chem. Soc.* **2005**, *127*, 15360–15361.
- (21) (a) Hong, J.; Wang, W.; Huang, K.; Yang, W.-Y.; Zhao, Y.-X.; Xiao, B.-L.; Gao, Y.-F.; Moosavi-Movahedi, Z.; Ahmadian, S.; Bohlooli, M.; Saboury, A. A.; Ghourchian, H.; Sheibani, N.; Moosavi-Movahedi, A. A. A self-assembled nano-cluster complex based on cytochrome *c* and nafion: An efficient nanostructured peroxidase. *Biochem. Eng. J.* **2012**, *65*, 16–22. (b) Hwang, S.; Lee, C.-H.; Ahn, I.-S. Product identification of guaiacol oxidation catalyzed by manganese peroxidase. *J. Ind. Eng. Chem.* **2008**, *14*, 487–492.
- (22) Lopes, L. C.; Brandao, I. V.; Sanchez, O. C.; Franceschi, E.; Borges, G.; Dariva, C.; Fricks, A. T. Horseradish peroxidase biocatalytic reaction monitoring using Near-Infrared (NIR) Spectroscopy. *Process Biochem.* **2018**, *71*, 127–133.
- (23) Mosmann, T. Rapid colorimetric assay for cellular growth and survival: Application to proliferation and cytotoxicity assays. *J. Immunol. Methods* **1983**, *65*, 55–63.

Acceleration of Hydrolytic DNA Cleavage by Dicopper(II) Complexes with *p*-Cresol-Derived Dinucleating Ligands at Slightly Acidic pH and Mechanistic Insights

Masahito Kodera,* Yuki Kadoya, Kenta Aso, Katsuki Fukui, Akiko Nomura, Yutaka Hitomi, and Hiroaki Kitagishi

Department of Molecular Chemistry and Biochemistry, Doshisha University, Kyotanabe, Kyoto 610-0321, Japan

E-mail: mkodera@mail.doshisha.ac.jp

Received: November 17, 2018; Accepted: December 26, 2018; Web Released: January 22, 2019



Masahito Kodera

Masahito Kodera is a Professor at the Department of Molecular Chemistry and Biochemistry, Graduate School of Science and Engineering, Doshisha University. He received his Ph.D. at the Engineering Graduate School, Kyoto University in 1987. He started his career as an Assistant Professor at the Institute for Molecular Science in 1987, and moved to Kyushu University. He was an Assistant Professor at Kyushu University from 1988 to 1993, and moved to Doshisha University. He was Lecturer at Doshisha University from 1993 to 1994, Associate Professor from 1994 to 2001, and has been Professor from 2001 until now.

Abstract

Four dicopper(II) complexes, $[\text{Cu}_2(\mu\text{-X})(\text{bcmp})](\text{ClO}_4)_2$ [$\text{X} = \text{OH}$ (**1a**) and $\text{X} = \text{Cl}$ (**1b**)], $[\text{Cu}_2(\mu\text{-OH})(\text{Me}_4\text{bcmp})](\text{ClO}_4)_2$ (**2**), and $[\text{Cu}_2(\text{bcc})](\text{ClO}_4)_3$ (**3**), were synthesized with three *p*-cresol-derived ligands, 2,6-bis(1,4,7-triazacyclononylmethyl)-4-methylphenol (Hbcmp), 2,6-bis(1,4,7-triaza-4,7-dimethylcyclononylmethyl)-4-methylphenol (HMe₄bcmp), and 2,6-bis(1,4,7,10-tetrazacyclododecylmethyl)-4-methylphenol (Hbcc) to study hydrolytic DNA cleavage. Crystal structures of **1a**, **1b**, **2**, and **3** were determined by X-ray analysis. The pH titrations and spectroscopic studies in the complexations of the ligands with copper(II) perchlorate revealed that the dicopper core structures of **1a**, **2**, and **3** in the solid state are kept at pH 5–9 in an aqueous solution. DNA binding abilities of **1a**, **2**, and **3** were examined by isothermal titration calorimetry (ITC). DNA cleavage studies were carried out by using supercoiled plasmid pUC19 DNA. **1a** largely accelerated hydrolytic DNA cleavage at pH 5–6 but not at pH 7–8. This is the first example of pH-dependent DNA cleavage by a dicopper complex. Inhibition studies with specific DNA binders, 4',6-diamidino-2-phenylindole and methyl green, suggested that **1a** accelerates the DNA cleavage via GC-specific binding. The mechanistic insights into the pH-dependent DNA cleavage are proposed on the basis of the crystal structures, structures in aqueous solutions, DNA binding modes, and DNA cleavage activities of **1a**, **1b**, **2**, and **3**.

Keywords: Dicopper(II) complex | DNA cleavage | Mechanism

1. Introduction

Recently, there have been considerable interests in the development of metal complexes for medical purposes by blocking DNA replication through binding and/or cutting DNA.¹ Various platinum(II) complexes, cisplatin² and its derivatives, such as oxaliplatin,³ lobaplatin,⁴ and nedaplatin,⁵ are used as anticancer drugs. Since these anticancer drugs are accompanied with heavy side-effects and resistance problems, metal complexes that bind and/or cut DNA of cancer cells selectively are required to solve these problems.

It is well known that the microenvironment in cancer cells is significantly different from that in normal cells.⁶ As one of the key features of cancer cells, tumor extracellular pH is often acidic.⁷ This is mainly caused by aerobic glycolysis. On the other hand, intracellular pH of tumors is neutral to alkaline.⁷ Various dinuclear metal complexes capable of promoting hydrolytic DNA cleavage have been synthesized for the purpose of developing a new type of anticancer drugs.^{1a–1c,8} Montagner reported that a dicopper(II) complex with Hbcmp $[\text{Cu}_2(\mu\text{-OH})(\text{bcmp})](\text{NO}_3)_2$ (**1c**) hydrolytically cleaved supercoiled plasmid pUC19 DNA (SC-DNA) at pH 8.2, and showed high cytotoxic activity to cancer cells, causing apoptosis.⁹ The pH-dependent hydrolytic DNA cleavage by **1c**, however, has not been reported. The selective apoptosis of cancer cells by using pH-dependent DNA cleavage of metal complexes is desirable for the development of anticancer drugs that are less toxic, target specific, and with reduced side effects. Even if hydrolytic cleavage is reversible as repair enzymes repair DNA damage in cancer cells, pH-dependent hydrolytic DNA cleav-

age may provide a new concept for a DNA cleavage study as well as the development of anti-cancer drugs.

In this study, we synthesized four dicopper(II) complexes [Cu₂(μ-OH)(bcmp)](ClO₄)₂ (**1a**), [Cu₂(μ-Cl)(bcmp)](ClO₄)₂ (**1b**), [Cu₂(μ-OH)(Me₄bcmp)](ClO₄)₂ (**2**), and [Cu₂(bcc)](ClO₄)₂ (**3**) to study the pH-dependence of hydrolytic DNA cleavage by the dicopper complexes, and found that **1a** largely accelerated the hydrolytic cleavage of supercoiled plasmid pUC19 DNA at pH 5.0–6.0, but did not at pH 7.0–8.0. Since usually hydrolytic cleavage of DNA is accelerated under basic conditions, the large acceleration at pH 5–6 is quite an unusual example. For example, purple acid phosphatases specifically accelerate the hydrolysis of phosphate ester at acidic pH. Here, we propose mechanistic insights into the pH-dependent activity control in the hydrolytic DNA cleavage of **1a**.

2. Experimental

Materials. All ordinary reagents were purchased and used as received unless otherwise noted. A supercoiled plasmid pUC19 DNA was purchased from Nippon Gene CO., LTD. A 33 mer oligo DNA 5'-d(GAC TCC ACA GTG CAT ACG TGG GCT CCA ACA GGT)-3' and the complementary strand were purchased from Thermo Fisher Scientific, from which a 33 mer double-strand DNA was prepared. Two *p*-cresol-derived ligands, 2,6-bis(1,4,7-triazacyclononylmethyl)-4-methylphenol (Hbcmp) and 2,6-bis(1,4,7,10-tetrazacyclododecylmethyl)-4-methylphenol (Hbcc) were prepared according to literature.¹⁰

Measurements. Elemental analyses (C, H, and N) were carried out on a Perkin-Elmer Elemental Analyzer 2400 II. UV-vis absorption spectra were recorded on an Agilent 8454 UV spectroscopy system. The pH measurement was carried out on a Horiba Laqua electrode. Electrospray ionization mass spectra (ESI MS) were recorded on a JEOL JMS-T100CS spectrometer. Infrared (IR) spectra were recorded on a Shimadzu Single Reflection HATR IR Affinity-1 MIRacle 10. ¹H NMR spectra were recorded on a JEOL ECA-500RX spectrometer using Me₄Si or TSP as an internal standard.

1-Tosyl-1,4,7-triazacyclononane. 1,4,7-Tritosyl-1,4,7-triazacyclononane (7.84 g, 13.2 mmol) and phenol (9.43 g, 100 mmol) were dissolved in 30% HBr solution in AcOH (110 mL). The solution was stirred for several hours at 30 °C until evolution of HBr ceased and then heated at 90 °C for 2 days. The HBr salt of the product generated was collected by filtration and washed with Et₂O. The solid was dissolved in 1.5 M aqueous NaOH (100 mL) and extracted with CHCl₃ (4 × 15 mL). The combined organic layer was dried over Na₂SO₄. After filtration and concentration, the product was obtained as white solid. Yield: 2.70 g (72%). ¹H NMR (500 MHz, CDCl₃); δ/ppm: 7.69 (d, *J* = 8.0 Hz, 2H, Ph), 7.31 (d, *J* = 8.0 Hz, 2H, Ph), 3.16–3.21 (m, 4H, CH₂), 3.05–3.11 (m, 4H, CH₂), 2.89 (s, 4H, CH₂), 2.43 (s, 3H, CH₃).

1,4-Dimethyl-7-tosyl-1,4,7-triazacyclononane. Formic acid (10 mL) and formaldehyde (10 mL) were added dropwise to a solution of 1-tosyl-1,4,7-triazacyclononane (2.62 g, 9.25 mmol) in H₂O (3 mL) at 0 °C. The mixture was stirred for 30 min, and refluxed at 110 °C for 15 h. To the resultant mixture was added 12 M HCl (6 mL), and concentrated to dryness. To the residue was added 1.5 M aqueous NaOH (20 mL) and extracted with CHCl₃ (4 × 20 mL). The extracts were com-

bined and dried over Na₂SO₄. After filtration and concentration, the product was obtained as yellow solid. Yield: 2.83 g (98%). ¹H NMR (500 MHz, CDCl₃); δ/ppm: 7.67 (d, *J* = 8.0 Hz, 2H, Ph), 7.30 (d, *J* = 8.0 Hz, 2H, Ph), 3.21–3.29 (m, 4H, CH₂), 2.87–2.94 (m, 4H, CH₂), 2.69 (s, 4H, CH₂), 2.42 (s, 3H, CH₃), 2.40 (s, 6H, CH₃).

1,4-Dimethyl-1,4,7-triazacyclononane. 1,4-Dimethyl-7-tosyl-1,4,7-triazacyclononane (3.24 g, 10.4 mmol) was added to conc. H₂SO₄ (15 mL) and heated at 120 °C for 36 h under N₂. The mixture was cooled to room temperature, and 12 M aqueous NaOH was slowly added until pH became 10. Generated Na₂SO₄ was filtered off, and extracted with CHCl₃ (5 × 40 mL). The product was obtained from the extracts as yellow oil. Yield: 0.933 g (57%). ¹H NMR (500 MHz, CDCl₃); δ/ppm: 2.65–2.71 (m, 4H, CH₂), 2.50–2.57 (m, 8H, CH₂), 2.41 (s, 6H, CH₃).

2,6-Bis(*N,N'*-4,7-dimethyl-1,4,7-triazacyclonon-1-ylmethyl)-4-methylphenol Pentahydrochloride (HMe₄bcmp·5HCl). 1,4-Dimethyl-1,4,7-triazacyclononane (0.365 g, 2.32 mmol) and 2,6-bis(chloromethyl)-4-methylphenol (0.215 g, 1.05 mmol) were dissolved in MeCN (40 mL) and Et₃N (0.34 mL, 2.44 mmol) was added. The solution was refluxed for 12 h under N₂. After concentration, the remainder was purified by column chromatography (alumina, CHCl₃/MeOH) to give 2,6-bis(*N,N'*-4,7-dimethyl-1,4,7-triazacyclonon-1-ylmethyl)-4-methylphenol as yellow oil. Yield: 0.330 g (70%). ¹H NMR (500 MHz, CDCl₃); δ/ppm: 6.87 (s, 2H, Ph), 3.72 (s, 4H, CH₂), 2.84–2.89 (m, 8H, CH₂), 2.63–2.69 (m, 16H, CH₂), 2.35 (s, 12H, CH₃), 2.23 (s, 3H, CH₃). The yellow oil product (1.19 g, 2.66 mmol) was dissolved in EtOH (27 mL) and 12 M HCl (9 mL) was added. The mixture was concentrated to dryness. After filtration and washing with EtOAc, the product was obtained as white solid. Yield: 1.41 g (2.24 mmol, 84%). Anal. calcd for HMe₄bcmp·5HCl·5H₂O: C, 41.76; H, 8.55; N, 11.69. Found: C, 41.69; H, 8.83; N, 12.22. ¹H NMR (500 MHz, D₂O); δ/ppm: 7.39 (s, 2H, Ph), 4.21 (s, 4H, CH₂), 3.10–3.79 (m, 24H, CH₂), 2.94 (s, 12H, CH₃), 2.34 (s, 3H, CH₃).

Dicopper Complexes 1a, 1b, 2, and 3. To a solution of Hbcmp (0.149 mmol) in H₂O (10 mL) was added a solution of Cu(ClO₄)₂·6H₂O (126.6 mg, 0.342 mmol) in H₂O (4 mL). The solution was neutralized with 1.0 M aqueous NaOH under N₂. After concentration, [Cu₂(μ-OH)(bcmp)](ClO₄)₂ (**1a**) was obtained as green solid and recrystallized from Et₂O/MeCN to give green crystals suitable for the X-ray analysis. Yield: 34.8 mg (44.5 μmol, 30%). Anal. calcd for [Cu₂(μ-OH)bcmp](ClO₄)₂·MeCN·0.5H₂O: C, 35.30; H, 5.41; N, 12.53. Found: C, 35.48; H, 5.50; N, 12.21. ESI MS (H₂O/MeCN *m/z*); [**1a** – ClO₄]⁺: 632.93. IR (KBr); $\tilde{\nu}/\text{cm}^{-1}$: 3586–2864, 1613, 1479, 1458, 1375, 1082. [Cu₂(μ-Cl)(bcmp)](ClO₄)₂ (**1b**) was obtained from Hbcmp·6HCl. Yield: 11.9 mg (31%). Anal. calcd for [Cu₂(μ-Cl)bcmp](ClO₄)₂·MeCN: C, 34.88; H, 5.09; N, 12.38. Found: C, 35.00; H, 5.14; N, 12.20. ESI MS (H₂O/MeCN *m/z*); [**1b** – ClO₄]⁺: 650.89. $\tilde{\nu}/\text{cm}^{-1}$: 3620–2872, 1614, 1476, 1446, 1354, 1103. [Cu₂(μ-OH)(Me₄bcmp)](ClO₄)₂ (**2**) was obtained from HMe₄bcmp. Yield: 94.3 mg (52%). Anal. calcd for [Cu₂(μ-OH)Me₄bcmp](ClO₄)₂·MeCN·2H₂O: C, 37.46; H, 6.17; N, 11.33. Found: C, 37.72; H, 6.26; N, 11.08. ESI-MS (H₂O/MeCN *m/z*); [**2** – ClO₄]⁺: 689.04. $\tilde{\nu}/\text{cm}^{-1}$: 3613–2868, 1614, 1481, 1472, 1431, 1366, 1082. [Cu₂(bcc)](ClO₄)₃ (**3**) was obtained from Hbcc and recrystal-

lized from Et₂O/MeCN/MeOH. Yield: 0.119 g (50%). Anal. calcd for [Cu₂bcc](ClO₄)₃·MeOH·1.5H₂O: C, 32.52; H, 5.67; N, 11.67. Found: C, 32.46; H, 5.41; N, 11.81. ESI MS (H₂O/MeCN *m/z*); [3 - ClO₄]⁺: 801.12, [3 - 2ClO₄]²⁺: 351.08. $\tilde{\nu}$ /cm⁻¹: 3620–293, 1616, 1470, 1441, 1381–1306, 1099.

Structure Determination of Single Crystals. The crystal structures of **1a**, **1b**, **2** and **3** were determined on a Rigaku R-AXIS RAPID diffractometer using multi-layer mirror monochromated Cu-K α radiation. The data were collected at a temperature of -160 ± 1 °C or -180 ± 1 °C to a maximum 2θ value of 136.5° . The linear absorption coefficient, μ , for Cu-K α radiation is 31.825, 38.394, 39.633, or 44.927 cm⁻¹. An empirical absorption correction was applied. The data were corrected for Lorentz and polarization effects. Crystallographic data of the complexes are shown in Table S1. Crystallographic data reported in this manuscript have been deposited with Cambridge Crystallographic Data Centre as supplementary publication no. CCDC-000000. Copies of the data can be obtained free of charge via CCDC Website.

pH Change and Spectral Studies in Complexation of Hbcmp, HMe₄bcmp, and Hbcc. A solution of each ligand (0.5 mM) and Cu(ClO₄)₂·6H₂O (1.0 mM) in H₂O (2.0 mL) was placed in a cuvette, and titrated with an aqueous NaOH (0.05 M) at 25 °C. The pH change was monitored on a pH meter. The electronic absorption and ESI MS spectra were measured using the same solution after measuring pH.

Isothermal Titration Calorimetry (ITC). ITC measurements were performed at 37 °C on a Malvern MacroCal VP-ITC. The solution of the 33 mer oligo ds-DNA (25 μ M) in a buffered aqueous solution (MES, 10 mM) containing NaCl (10 mM) was prepared in the cell. The solution of **1a**, **2**, or **3** (1.0 mM) in a buffered aqueous solution (MES, 10 mM) containing NaCl (10 mM) was prepared in the syringe. The 25 aliquots (10 μ L each) of the solution of **1a**, **2**, or **3** were added into the DNA solution to measure the heat of complexation. The raw data was corrected by subtracting the heat of dilution, and the titration curve thus obtained was analyzed using ORIGIN software. Each ITC data was collected by two independent measurers and the reproducible data was employed.

DNA Cleavage Study. DNA cleavage activity of **1a**, **1b**, **2**, and **3** were evaluated by using pUC19 DNA and followed by agarose gel electrophoresis. pUC19 DNA (0.50 μ g/ μ L) was incubated with the dicopper complex (10 μ M) in an aqueous buffer solution (10 mM, pH 5.0, 5.5, 5.9, 6.0 (MES), 7.4 (Tris-HCl), and 8.2 (TAPS)) containing NaCl (10 mM) at 37 °C in the dark. An aliquot was taken from the solution at 0, 1, 2, 5, and 10 h, and the reaction was quenched upon addition of loading buffer (0.025% bromophenol blue, 0.025% xylene cyanol FF, 1.0 mM EDTA and 30% glycerol). Each sample was loaded onto a 1% agarose gel in TAE (Tris/acetate/EDTA) buffer. The gels were subjected to electrophoresis for 1 h at 100 V, followed by staining with ethidium bromide (0.5 μ g/mL) for 1 h. Gel bands were visualized using UV transilluminator and photographed using a Vilber Lourmat ECX-20-M, and were quantified using a correction factor of 1.06 for the reduced stain uptake of Form I. All data for the conversion of Form I to Form II are shown in Figure S5–S13 and Table S4–S12.

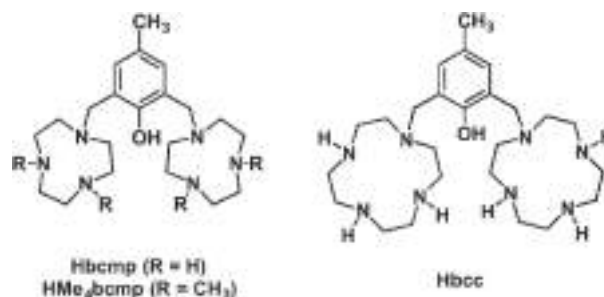
Inhibition of the DNA Cleavage of 1a. pUC19 DNA (0.50 μ g/ μ L) was dissolved in an aqueous buffer solution (10 mM,

pH 5.0 and 5.5 (MES)) containing NaCl (10 mM) in the presence of DAPI or methyl green (5, 10, 50 μ M), and **1a** (10 μ M) was added and incubated at 37 °C for 1 h in the dark. Progress of the reaction was evaluated as shown in the DNA cleavage study.

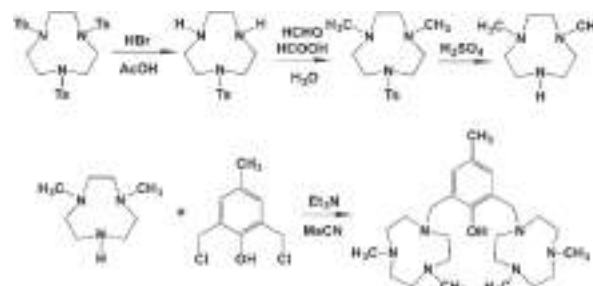
3. Results and Discussion

Syntheses and Structures of Dicopper Complexes. The chemical structures of 2,6-bis(1,4,7-triazacyclononylmethyl)-4-methylphenol (Hbcmp), 2,6-bis(1,4,7-triaza-4,7-dimethylcyclononylmethyl)-4-methylphenol (HMe₄bcmp), and 2,6-bis-(1,4,7,10-tetraazacyclododecylmethyl)-4-methylphenol (Hbcc) are shown in Scheme 1. Hbcmp and Hbcc have triazacyclononane (tacn) and tetraazacyclododecane (cyclen) as pendant groups at 2,6-positions of the *p*-cresol moiety, respectively, and prepared according to the literature.¹⁰ HMe₄bcmp is a new ligand where four macrocyclic NH groups of Hbcmp are fully methylated. The synthetic route of HMe₄bcmp is shown in Scheme 2. These ligands form dicopper(II) complexes [Cu₂(μ -X)(bcmp)](ClO₄)₂ [X = OH (**1a**) and X = Cl (**1b**)], [Cu₂(μ -OH)(Me₄bcmp)](ClO₄)₂ (**2**), and [Cu₂(bcc)](ClO₄)₃ (**3**). The complexes were structurally characterized by X-ray analysis, and characterized by elemental analysis and various spectroscopic measurements. As described below, the ligands stabilize the dinuclear structures at pH 5–9 in an aqueous solution.

ORTEP views of **1a**, **1b**, **2**, and **3** are shown in Figure 1. The crystallographic data are shown in Table S1, and the selected bond distances and angles are shown in Table S2. In **1a**, two Cu(II) ions are incorporated into a bcmp ligand with the μ -OPH- μ -OH double bridge, where each Cu ion takes distorted square pyramidal geometry with three *N*-atoms of a pendant tacn and two *O*-atoms of the μ -OPH- μ -OH bridge. **1b** is structurally almost the same as **1a** but μ -OH of **1a** is replaced by μ -Cl. In **2**, two Cu(II) ions are incorporated into a Me₄bcmp ligand with the μ -PhO- μ -OH double bridge. The overall structures of **1a** and **2** are almost the same except for NCH₃



Scheme 1. Chemical structures of supporting ligands.



Scheme 2. Synthetic scheme of H₂Mebcmp.

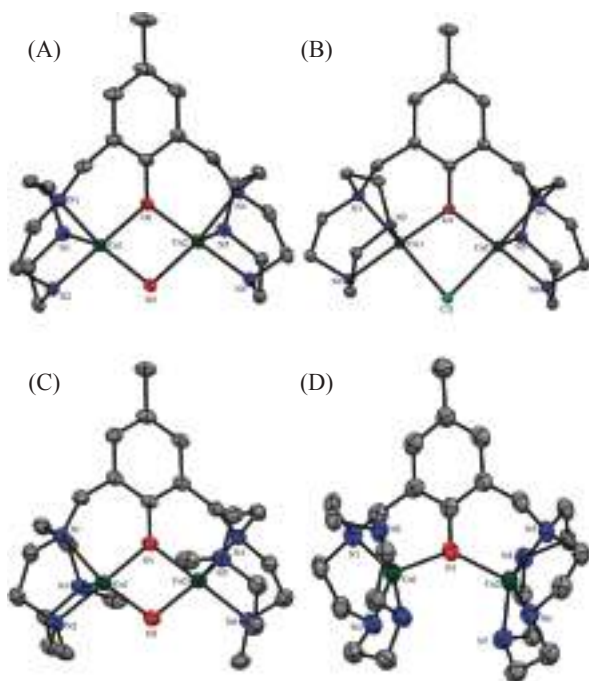


Figure 1. ORTEP diagrams of the cationic parts of (A) **1a**, (B) **1b**, (C) **2**, and (D) **3** (ORTEP plot; unlabeled open ellipsoids represent carbon atoms).

groups in **2**. In **3**, two Cu(II) ions are incorporated into a bcc ligand with the μ -PhO bridge, and each Cu takes square pyramidal geometry with four *N*-atoms of a pendant cyclen and a *O*-atom of the μ -OPh bridge. The Cu...Cu distances of **1a** and **2** are 2.9985(7) and 3.033(1) Å, close to each other, but shorter than 3.878(1) Å of **3**. This may reflect differences of the bridging structures where the μ -PhO- μ -OH doubly bridged structures of **1a** and **2** shorten the Cu...Cu distances as compared with the μ -PhO singly bridged one of **3**. The coordination geometry is examined by the τ -values that vary from 0, for an idealized square pyramidal, to 1, for an idealized trigonal bipyramidal.¹¹ The τ -values, $\tau_{\text{Cu}(1)} = 0.243$ and $\tau_{\text{Cu}(2)} = 0.228$ for **1a**, $\tau_{\text{Cu}(1)} = 0.217$ and $\tau_{\text{Cu}(2)} = 0.206$ for **2**, and $\tau_{\text{Cu}(1)} = 0.038$ and $\tau_{\text{Cu}(2)} = 0.066$ for **3**, show that **1a** and **2** are distorted square pyramidal similar to each other and **3** is regular square pyramidal.

In spite of the similar bridging structures of **1a** and **2**, the accessibility to the μ -OH group is significantly different. The *O*-atom of μ -OH in **1a** protrudes by 0.842 Å from the mean plane defined by four *N*-atoms of macrocyclic NH groups (Figure S1), clearly showing that the μ -OH group is easy to access from outside. On the other hand, the *O*-atom of μ -OH in **2** is surrounded by the NCH₃ groups that sterically hinder the access to the μ -OH group, where the deviation of the *O*-atom of μ -OH from the mean plane defined by four *C*-atoms of NCH₃ groups is 0.001 Å (Figure S1). Moreover, the Cu-O μ -OH bond distances 1.971(2) and 1.980(3) Å of **1a** are significantly longer than 1.930(3) and 1.925(4) Å of **2**. These data indicate that the μ -OH bridge of **1a** weakly bonds to two Cu(II) ions. These structural features suggest that the μ -OH bridge of **1a** is more reactive in the nucleophilic attack to an external substrate such as a phosphate moiety of DNA than that of **2**.

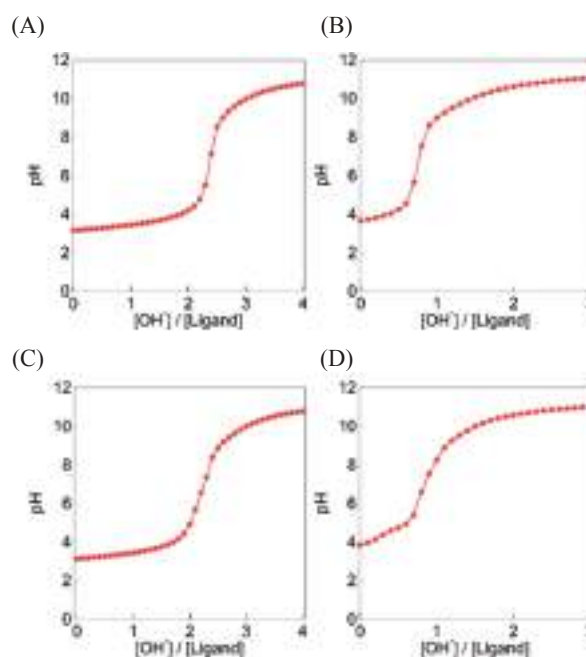


Figure 2. pH change of an aqueous solution containing each ligand (0.5 mM), (A) **Hbcmp**, (C) **HMe₄bcmp**, or (D) **Hbcc**, and Cu(ClO₄)₂·6H₂O (1.0 mM) upon titration with an aqueous NaOH solution (0.05 M) at 25 °C. In the case of (B), **1b** was used instead of the ligand, and the pH change was monitored in the same way.

Dicopper Core Structures at pH 5–9 in an Aqueous Solution. To examine dicopper core structures at pH 5–9 in an aqueous solution, complexations of the ligands were monitored by pH and spectroscopic measurements. To an aqueous solution of a 1:2 mixture of each ligand and Cu(ClO₄)₂·6H₂O was added standardized aqueous NaOH, and the pH change was monitored on a pH meter and the electronic absorption and electrospray ionization mass (ESI MS) spectra were measured. The plots of the pH change vs molar equivalent of NaOH added are shown in Figure 2. The electronic absorption and ESI MS spectra at various pH are shown in Figures S2 and S3, respectively.

In the complexations of **Hbcmp** and **HMe₄bcmp**, 2 eq of OH[−] was consumed by pH 5.0 as shown in Figure 2(A) and (C). This can be assigned to the release of two protons belonging to the phenol of each ligand and to a H₂O bonded to dicopper(II) core to form μ -OPh- μ -OH bridge. This is consistent with p*K*_a value of the H₂O bonded to the dicopper(II) core, 4.69, reported for **1c**.⁹ The electronic absorption spectra in complexation of **Hbcmp** and **HMe₄bcmp** at pH 5–9 are almost the same as those of **1a** and **2** in an aqueous solution, respectively (Figure S2). The spectra of **1a** and **2** exhibit two bands at around 340–380 nm assignable to phenoxo-Cu(II) and hydroxo-Cu(II) LMCT (ligand-to-metal charge transfer) bands, taking account of the reported data that the LMCT bands appear at 350–400 nm in related dicopper(II) complexes.¹² Moreover, the bridging structures of **1a** and **2** are confirmed by the ESI MS spectra shown in Figure S3. The ESI MS spectra of **1a** and **2** at pH 5–9 in aqueous solutions show the major peaks at *m/z* 632 and 689 corresponding to [bcmp + 2Cu(II) + OH + ClO₄]⁺

and $[\text{Me}_4\text{bcmp} + 2\text{Cu(II)} + \text{OH} + \text{ClO}_4]^+$, respectively. These results show that the $\mu\text{-OPh-}\mu\text{-OH}$ bridges of **1a** and **2** are kept at pH 5–9. Upon addition of aqueous NaOH to **1b** in an aqueous solution, 1 eq of OH^- was consumed by pH 5.0, (Figure 2(B)), showing that $\mu\text{-Cl}$ of **1b** was replaced by $\mu\text{-OH}$, and thus, **1b** is converted to **1a** in an aqueous solution.

In the complexation of Hbcc, 1 eq of OH^- was consumed by pH 5.0 (Figure 2(D)). The electronic absorption spectra in the complexation of Hbcc at pH 5–9 are the same as that of **3** in an aqueous solution (Figure S2), which exhibits a weak band at 410 nm assignable to the phenoxo-Cu(II) LMCT.¹³ The ESI MS spectra of **3** at pH 5–9 in an aqueous solution show the major peak at m/z 801 corresponding to $[\text{bcc} + 2\text{Cu(II)} + 2\text{ClO}_4]^+$ (Figure S3). These results show that the $\mu\text{-OPh}$ bridged structure of **3** is kept at pH 5–9 in an aqueous solution.

Thus, the $\mu\text{-OPh-}\mu\text{-OH}$ bridges of **1a** and **2** and the $\mu\text{-OPh}$ bridge of **3** are kept intact at pH 5–9 in H_2O . It was reported that the $\mu\text{-OPh-}\mu\text{-OH}$ bridge is kept intact at pH 5–12 in dicopper(II) complex with 2,6-bis(dipyridylmethylamino-methyl)-4-methyl-phenol, a *p*-cresol-derived heptadentate dinucleating ligand.^{14a} Thus, the $\mu\text{-OPh-}\mu\text{-OH}$ bridging structures are common in the dicopper(II) complexes with the *p*-cresol-derived heptadentate ligands in the wide range of pH. On the other hand, the $\mu\text{-OPh}$ singly bridged structure of **3** is kept with the bcc ligand under the same conditions.

DNA Binding of Dicopper(II) Complexes. The pH and structural effect on the DNA binding ability of **1a**, **2**, and **3** were explored by isothermal titration calorimetry (ITC). By the ITC measurement, the binding enthalpy (ΔH°) is directly obtained, and the entropy (ΔS°) and the binding constant (K) are derived from curve fitting and free energy relationship. A linear 33 mer oligo double-stranded DNA was used for the measurement of the DNA binding constant where the hydrolytic DNA cleavage by the dicopper complexes can be eliminated because of the low reactivity of linear DNA. The isothermal calorimetric titration curves were recorded for the titration of **1a** into the 33 mer oligo double-stranded DNA solution in 10 mM of MES buffer at pH 5.0, 5.5, and 6.0 in the presence of NaCl (10 mM) to keep a constant ionic strength. Moreover, the titration curves for DNA binding of **2** and **3** were obtained at pH 6.0 under the same conditions. The thermodynamic parameters, ΔH° , ΔS° , and K , are shown in Table S3. Negative ΔH° and positive ΔS° were obtained in all measurements, showing that DNA binding of **1a**, **2**, and **3** are enthalpically and entropically favorable. The ITC profiles and the corresponding molar ratio plots are shown in Figure 3.

The DNA binding constants of **1a** determined at pH 5.0, 5.5, and 6.0 are $1.81 \pm 0.84 \times 10^5$, $1.23 \pm 0.43 \times 10^5$, and $1.05 \pm 0.20 \times 10^5 \text{ M}^{-1}$, respectively (Table S3), and slightly increasing with lowering pH, indicating that a binding complex of **1a** with DNA is stabilized by the protonation. Since the structure of **1a** is kept intact at pH 5.0–9.0 in an aqueous solution, **1a** is not protonated in the pH domain. Thus, the protonation occurs in the binding complex of **1a** with DNA. The ΔH° and ΔS° values obtained at pH 5.0, 5.5, and 6.0 are -0.57 ± 0.08 , -1.08 ± 0.24 , and $-1.39 \pm 0.19 \text{ (kcal}\cdot\text{mol}^{-1})$ and 22.2, 19.8, and $18.5 \text{ (cal}\cdot\text{mol}^{-1}\cdot\text{K}^{-1})$, respectively (Table S3). Both ΔH° and ΔS° values increased with lowering pH, suggesting that the protonation may occur at the phosphate moiety of the DNA

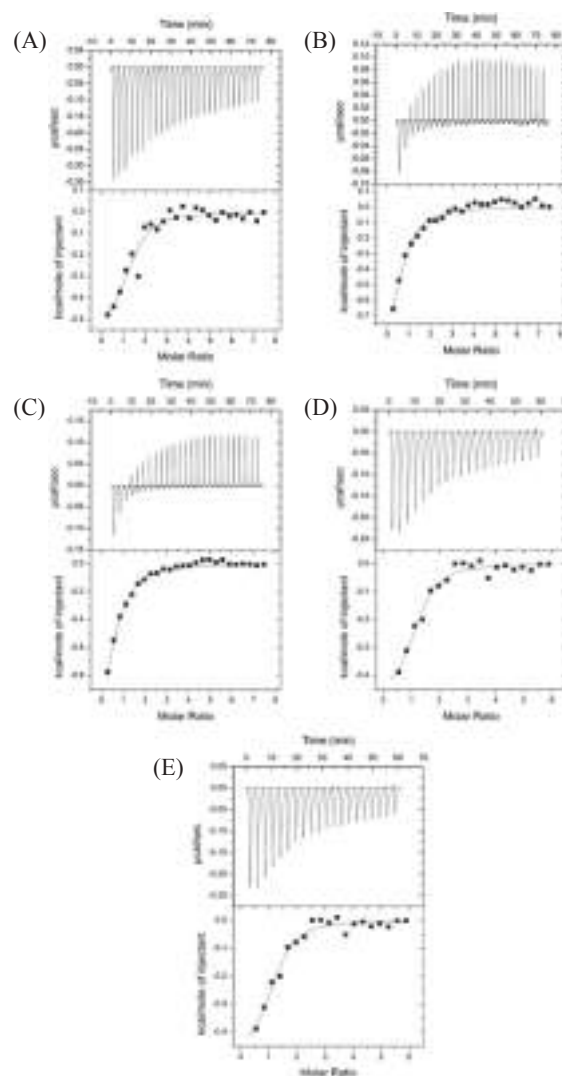


Figure 3. Isothermal calorimetric titration curves: **1a** at pH 5.0 (A), 5.5 (B), 6.0 (C), **2** at pH 6.0 (D), and **3** at pH 6.0 (E). Experimental conditions: A solution of **1a** (1 μM) in a syringe was added, in an equal interval 25 times, to a solution of the linear 33 mer ds-DNA (25 μM) in the cell in the presence of NaCl (10 mM) in an aqueous buffer solution at pH 5.0, 5.5, and 6.0 (MES, 10 mM) at 37 $^\circ\text{C}$. In the case of **2** and **3**, titrations were conducted in the same manner at pH 6.0 (MES, 10 mM).

main chain in the binding complex to induce dehydration. Thus, the increase in the binding constant of **1a** with DNA at low pH is entropy-driven.

Moreover, the DNA binding abilities of **2** and **3** may be explained from both hydrophobic and electrostatic interactions with DNA. The DNA binding constants of **2** and **3** determined at pH 6.0 are $2.64 \pm 0.97 \times 10^5$, and $2.63 \pm 0.53 \times 10^5 \text{ M}^{-1}$, respectively (Table S3). These values are almost the same. Interestingly, however, the ΔH° and ΔS° values, $-0.48 \pm 0.06 \text{ (kcal}\cdot\text{mol}^{-1})$ and $23.2 \text{ (cal}\cdot\text{mol}^{-1}\cdot\text{K}^{-1})$ for **2**, and $-2.26 \pm 0.11 \text{ (kcal}\cdot\text{mol}^{-1})$ and $17.5 \text{ (cal}\cdot\text{mol}^{-1}\cdot\text{K}^{-1})$ for **3**, are largely different between **2** and **3**. The increase of entropy shows the increase of degree of freedom in the system. Therefore, the largest ΔS° value 23.2 indicates that hydrophobic interaction of

2 with DNA plays a key contribution in the complexation where dehydration from **2** and DNA causes the ΔS° value. The hydrophobic interaction is important because **2** is the most hydrophobic in **1a**, **1b**, **2**, and **3**. The negative enthalpy shows the formation of some new bonds including H-bond and electrostatic interaction. In this case, the least exothermic ΔH° value -0.48 in the complexation of **2** with DNA indicates that the bonding interactions are not so important. This is reasonable because **2** does not have NH groups capable of forming H-bonds. On the basis of the same consideration, ΔH° and ΔS° values -2.26 and 17.5 in complexation of **3** with DNA clearly show that H-bond and electrostatic interaction largely contribute, and the hydrophobic interaction is not so important. This is reasonable because **3** has six NH groups with net charge $3+$, and thus, the most hydrophilic. The ΔH° values of **1a**, **2**, and **3** at pH 6 are -1.39 , -0.48 , and -2.26 , respectively. **1a** and **3** are more exothermic than **2**. This shows that the H-bonding interactions of the NH groups play a key role in the DNA binding. Thus, the chemical understandings of the DNA binding abilities are deduced from thermodynamic parameters ΔH° and ΔS° . Moreover, these results show that the interaction of **1a**, **2**, and **3** with DNA is controlled with chemical modifications of the pendant macrocyclic groups.

Acceleration of Hydrolytic Cleavage of Supercoiled Plasmid pUC19 DNA with Dicopper(II) Complexes in Slightly Acidic pH. Montagner et al. reported that **1c** promoted hydrolytic cleavage of supercoiled plasmid pUC19 DNA (SC-DNA, Form I) in an aqueous buffer solution at pH 8.2 at 37°C ,⁹ and that the reaction was dependent on concentration of **1c** where at $50\ \mu\text{M}$ of **1c**, almost complete nicking of Form I to Form II was observed in 3 h, but at $5\ \mu\text{M}$ of **1c**, Form II was not observed. In our study, the reaction of SC-DNA with **1a** ($10\ \mu\text{M}$) was examined at 37°C in aqueous solutions at pH 5.0, 5.5, 5.9, 6.0, 7.4, and 8.2. In the absence of the dicopper(II) complex, the DNA cleavage was not observed at all as shown in Figure 4(A) of the blank experiment. Time courses of the decrease of Form I in the reaction of **1a** at pH 5.0–8.2 are shown in Figure 4(B). The DNA cleavage was largely accelerated at pH 5.0–6.0. By using such a small amount, $10\ \mu\text{M}$, of **1a**, 80% conversion of Form I to Form II was attained at pH 5.0 for 5 h. Interestingly, however, no DNA cleavage activity was observed at pH 7.4 and 8.2. Tris buffer used at pH 7.4 is known to coordinate Cu(II) ion,^{14b} but in our case, gave no influence because the electronic spectra of **1a** in aqueous solutions using MES, Tris-HCl, and TAPS as buffer were completely the same each other. As shown in Figure 4(C), **1b** shows exactly the same activity as **1a**. This is because **1b** is rapidly converted to **1a** at pH 5–9 in an aqueous solution.

To examine the possibility of oxidative DNA cleavage by **1a**, the reaction was carried out in the presence of H_2O_2 (100 – $500\ \mu\text{M}$), but no acceleration occurred (Figure S4). Moreover, it was examined in the presence of NaN_3 and dimethyl sulfide that are known to inhibit oxidative DNA cleavage by singlet oxygen and hydroxyl radical, respectively, but the DNA cleavage of **1a** was not inhibited (Figure S4). Thus, it is demonstrated that the reaction of **1a** is not the oxidative DNA cleavage.

This is the first example of pH-dependent acceleration of hydrolytic DNA cleavage by synthetic metal complex. As

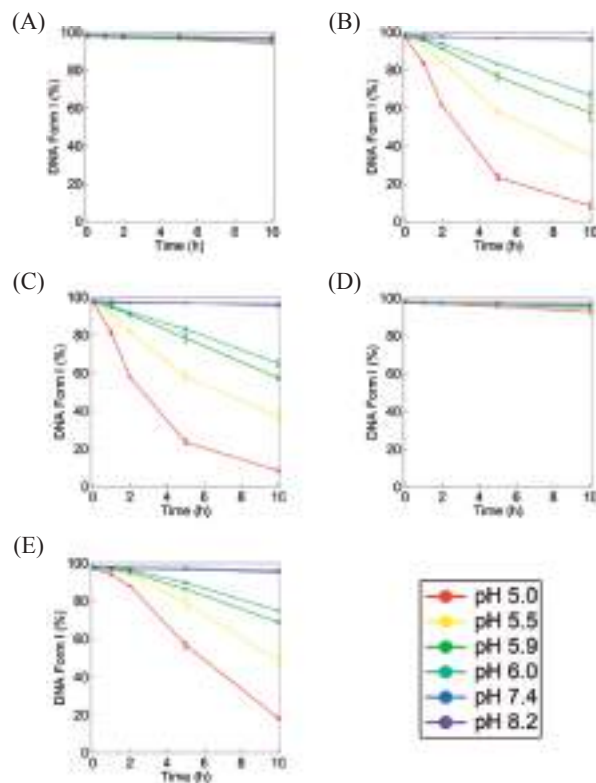


Figure 4. pH-dependent profile for DNA cleavage promoted by (A) Blank, (B) **1a**, (C) **1b**, (D) **2**, and (E) **3**, respectively. Experimental conditions: $[\text{NaCl}] = 10\ \text{mM}$, $[\text{buffer}] = 10\ \text{mM}$ (pH 5.0, 5.5, 5.9, 6.0 (MES), 7.4 (Tris-HCl), and 8.2 (TAPS)), $[\text{pUC19 DNA}] = 50\ \mu\text{M}$, $[\text{complex}] = 10\ \mu\text{M}$ at 37°C for 0, 1, 2, 5, and 10 h. Experiments were carried out at least three times.

one of the distinctive natures of cancer cells, it is known that $\text{pH}^{7\text{a}-7\text{c}}$ and concentrations of reactive oxygen species (ROS)¹⁵ in cancer cells are significantly different from those in normal cells. If we could control DNA cleavage activity of metal complexes depending on pH and ROS concentrations, it may serve to develop new types of anti-cancer drugs that selectively kill cancer cells but not normal cells. Therefore, pH-dependent acceleration of the hydrolytic DNA cleavage by **1a** may provide some insight into the development of a new type of anti-cancer drugs to reduce side-effects. It is necessary to investigate the cytotoxicity of **1a** to cancer cells in our future study.

Inhibition of DNA Cleavage with Specific DNA Binders. As estimated from the DNA binding constant of **1a**, ca 80–90% of the total amount of **1a** used bonds to DNA under the reaction conditions. Thus, it may be reasonable that the large acceleration of the hydrolytic DNA cleavage by **1a** is attained via the specific binding to DNA.

There are mainly four modes in non-covalent binding of metal complexes to ds-DNA, an intercalation, an electrostatic interaction with the DNA main chain, and a minor or a major groove binding. It is known that metal complexes having about a thousand molecular weight are suitable for the minor groove binding because of groove size.¹⁶ Generally, the minor groove binders have crescent-shape structures with cationic centers at

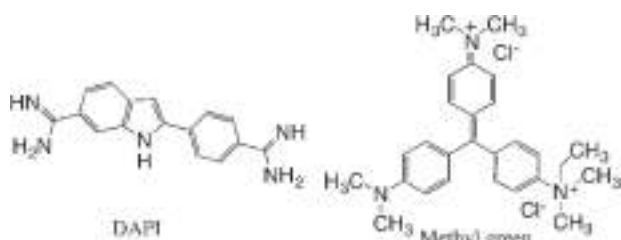


Figure 5. Chemical structures of 4',6-diamidino-2-phenylindole (DAPI) and methyl green.

the both ends of compounds. These structural features match the overall structure of **1a**. The major groove binding may be possible but not so important because the molecular size of **1a** is much smaller than the space of the major groove. To clarify a DNA binding mode of **1a**, we carried out inhibition experiments using 4',6-diamidino-2-phenylindole (DAPI),¹⁷ a minor groove binder, and methyl green,¹⁸ a major groove binder. The chemical structures of DAPI and methyl green are shown in Figure 5.

Time courses in the DNA cleavage of **1a** (10 μM) in the presence of DAPI (5.0–50 μM) at pH 5.0 are shown in Figure 6(A). The inhibition rates at 10 h are estimated from these data as 19, 50, and 87% in the presence of 10, 20, and 50 μM of DAPI, respectively, and increases with increase of the concentration of DAPI. Thus, the DNA cleavage of **1a** is inhibited by DAPI. The inhibition rates, however, are too small, considering from DNA binding constants, $4.7 \pm 0.3 \times 10^6 \text{ M}^{-1}$ reported for DAPI with ct-DNA in pH 5.0 acetate buffer at 25 $^\circ\text{C}$ ¹⁹ and $1.81 \pm 0.84 \times 10^5 \text{ M}^{-1}$ determined in this study for **1a** with a linear 33 mer oligo ds-DNA in pH 5.0 MES buffer at 37 $^\circ\text{C}$. The binding constant of DAPI is nearly 25-fold larger than that of **1a**. This means that the DNA cleavage of **1a** may be almost completely inhibited in the presence of the same concentration of DAPI. The inhibition rate, however, was only 19% at the same concentration of DAPI. It is known that DAPI strongly bonds to DNA at the AT-rich site as a minor groove binder but weakly at the GC-rich site as an intercalator.²⁰ The binding constant of DAPI with GC-DNA was reported to be $1.2 \times 10^5 \text{ M}^{-1}$,²⁰ slightly smaller than $1.81 \times 10^5 \text{ M}^{-1}$ of **1a**. The low inhibition rate of DAPI can be explained from these binding constants, and thus, DAPI blocks the DNA binding of **1a** at GC-site. Therefore, acceleration of the DNA cleavage by **1a** may be attained through intercalation to the GC-site.

The results of inhibition experiments using a major groove binder, methyl green, are shown in Figure 6(B). The inhibition rates at 10 h are 12, 26, and 64% in the presence of 10, 20, and 50 μM of methyl green, and slightly lower than 19, 50, and 87% by DAPI. Thus, DAPI is a stronger inhibitor than methyl green. Methyl green is a major groove binder,^{17b} and reported to retard DNA cleavage of deoxyribonuclease I, a minor groove binder.^{17b} Thus, methyl green inhibits DNA binding of **1a** at the major groove, and also retards DNA cleavage of **1a** at the minor groove. This may be the reason for the relatively weak inhibition of methyl green compared with DAPI.

It may be reasonable that a cresol moiety of **1a** acts as an intercalator. The cresol ring of **1a**, however, is smaller than the aromatic ring of DAPI. From the DNA binding studies, it was

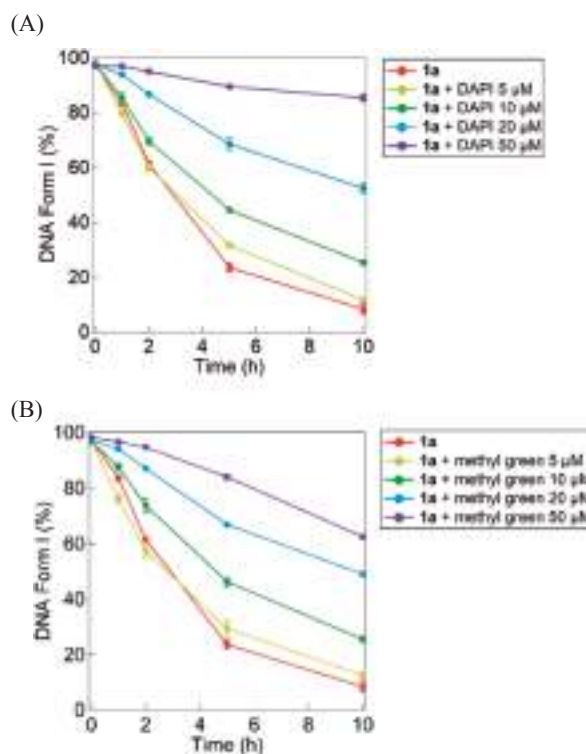


Figure 6. DNA cleavage by **1a** in the presence of (A) DAPI and (B) methyl green at pH 5.0. Experimental conditions: $[\text{NaCl}] = 10 \text{ mM}$, $[\text{buffer}] = 10 \text{ mM}$ (MES), $[\text{pUC19 DNA}] = 50 \mu\text{M}$ bp, $[\mathbf{1a}] = 10 \mu\text{M}$, and $[\text{DAPI}] = [\text{methyl green}] = 5, 10, 20, \text{ and } 50 \mu\text{M}$ at 37 $^\circ\text{C}$ for 0, 1, 2, 5, and 10 h. Experiments were carried out at least three times.

shown that the NH groups of **1a** form H-bonds with a phosphate moiety of the DNA main chain. Thus, the DNA binding ability of **1a** is enhanced by not only the intercalation of a cresol moiety but also the H-bonds of the NH groups.

Mechanistic Insights into the pH-Dependent Activity Control in Hydrolytic DNA Cleavage of **1a.** Purple acid phosphatases are widely distributed enzymes in biological systems, and catalyze hydrolytic cleavage of phosphate ester at slightly acidic pH.²¹ This has a $\mu\text{-OH}$ bridged dimetal active center where the $\mu\text{-OH}$ bridge directly attacks phosphate ester as a nucleophile to accelerate hydrolysis.²² Thus, it is likely that the $\mu\text{-OH}$ bridge is a key structure responsible for the large acceleration of hydrolytic DNA cleavage of **1a**. So, we examined the DNA cleavage of **2**, having a $\mu\text{-OH}$ bridge similar to **1a**, under the same reaction conditions to gain some insight into the mechanism of the acceleration in the hydrolytic DNA cleavage. As shown by time courses of decrease of Form I (Figure 4(D)), however, **2** showed no activity in the DNA cleavage at pH 5–8. The hydrolytic DNA cleavage activities of **1a** and **2** are totally different from each other in spite of similar bridging structures. This drastic difference may be explained by nucleophilicity of the $\mu\text{-OH}$ bridge and neighboring-group participation of the NH groups in **1a**. As shown by the crystal structures of **1a** and **2**, the $\mu\text{-OH}$ bridge of **1a** protrudes from the mean plane defined by four N-atoms of the NH groups by 0.842 \AA , and thus, can easily access the phosphate ester in DNA. On the other hand, the $\mu\text{-OH}$ bridge of **2** is difficult to

access due to the steric hinderance of the NCH_3 groups. The nucleophilicity of the $\mu\text{-OH}$ bridge may be responsible for the difference of the DNA cleavage activity between **1a** and **2**. Thus, it is proposed that the DNA cleavage of **1a** proceeds through the nucleophilic attack of the $\mu\text{-OH}$ bridge.

Neighboring-group participation by the macrocyclic NH groups of **1a** may play a key role in the DNA cleavage. This is reasonable because they enforce the DNA binding of **1a** through the H-bonds as described in the DNA binding studies. Moreover, it is well-known that NH groups located near the metal center can accelerate the metal complex-based hydrolytic cleavage of phosphate esters.²³ In this situation, in order to clarify the role of the macrocyclic NH groups, **3** that has six NH groups was used for the DNA cleavage. Time courses in the reactions of **3** at pH 5.0–8.2 are shown in Figure 4(E). In the comparison of the time courses shown in Figure 4(B) and (E), **1a** is more reactive than **3**. The relatively low reactivity of **3** may be due to the absence of the $\mu\text{-OH}$ bridge. This further supports that the $\mu\text{-OH}$ bridge is responsible for the DNA cleavage. Interestingly, however, **3** accelerated the DNA cleavage without a $\mu\text{-OH}$ bridge, where the NH groups can activate a phosphate ester of the DNA main chain by the H-bonds and hydrolytic DNA cleavage may be attained by nucleophilic attack of H_2O molecule. On the other hand, in **2**, the NCH_3 groups do not form the H-bond to the phosphate ester, resulting in almost no activity of **2** in the DNA cleavage. In the comparison of DNA cleavage activity among **1a**, **2**, and **3**, it is proposed that both the $\mu\text{-OH}$ bridge and the NH groups are the key structures for the hydrolytic DNA cleavage.

One of the mechanistic insights deduced from the DNA binding studies is that the dehydration occurs by the protonation to the phosphate moiety in the DNA binding complex of **1a**. Another mechanistic insight is the H-bonding interaction of the NH groups in **1a** to the phosphate diester in the DNA main chain to potentially activate it for the DNA cleavage. The mechanism proposed on the basis of these features is shown in Figure 7. In the first step of the hydrolytic DNA cleavage, **1a** binds to the GC-site as an intercalator to form the DNA binding complex. The DNA binding complex is stabilized by H-bonds of the NH groups with a phosphate moiety in the DNA main chain. In this stage, the binding complex is weakly protonated and entropically stabilized by dehydration, and the phosphate diester is activated by the protonation for hydrolytic cleavage. The protonation may decrease the transition energy in the nucleophilic attack of the $\mu\text{-OH}$ bridge to the phosphate ester. Here, the large acceleration of the hydrolytic DNA cleavage of **1a** at pH 5–6 is also explained from the pK_a values of phosphate monoester. The pK_{a1} and pK_{a2} values of deoxyribose-phosphate monoester are reported to be 1–2 and 5–6, respectively.²⁴ The pK_{a2} value, 5–6, is exactly the same as the pH value at which the hydrolytic DNA cleavage of **1a** is accelerated. Thus, stabilization of the product monoester is the driving force of the large acceleration of the DNA cleavage by **1a** at pH 5–6. Finally, the dicopper complex is released from the product monoester. Thus, it is proposed that hydrolytic DNA cleavage of **1a** proceeds through the three steps as follows, (1) the DNA binding, (2) the stabilization of the transition state by protonation to give the phosphate monoester, and (3) the release of **1a**.

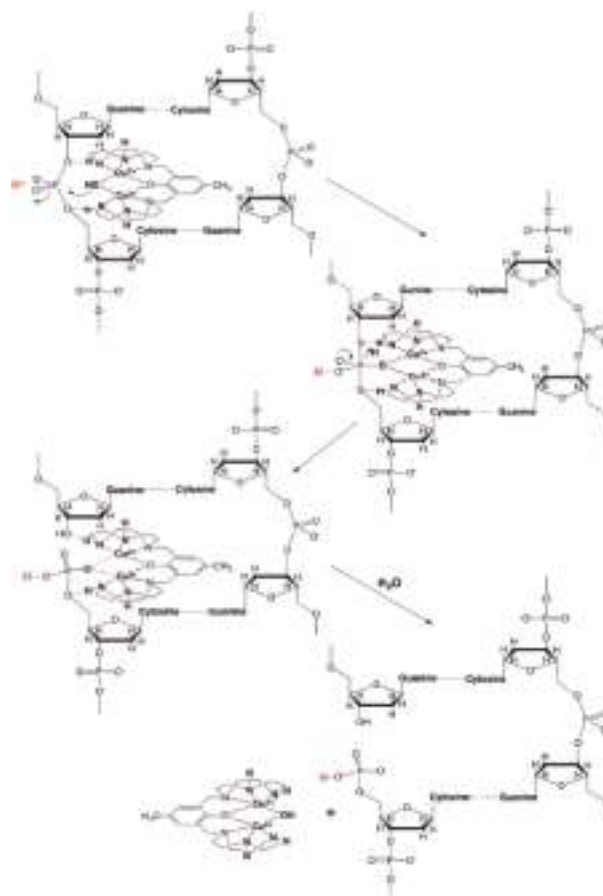


Figure 7. Proposed mechanism of the hydrolytic DNA cleavage by **1a**.

4. Conclusion

In this study, we synthesized dicopper complexes, **1a**, **1b**, **2**, and **3** with three *p*-cresol-derived ligands. The crystal structures revealed that overall structures of **1a** and **2** are similar but the accessibility to the $\mu\text{-OH}$ bridge is different. The dicopper core structures in the crystals are kept at pH 5–9 in an aqueous solution as shown by pH titrations and spectroscopic measurements in the complexations of the ligands with Cu(II) ions upon addition of a standardized aqueous NaOH. DNA binding mode of **1a** was examined by ITC measurements and inhibition experiments with specific DNA binders DAPI and methyl green, showing that **1a** bonds to DNA at the GC-site as an intercalator with assistance of the H-bond of the NH groups to a phosphate moiety in the DNA main chain. Moreover, the thermodynamic parameters, ΔH° , ΔS° , and K , indicated that the DNA binding is entropically and enthalpically favorable and the binding ability of **1a** is slightly enhanced by the protonation at pH 5–6. **1a** accelerated cleavage of supercoiled plasmid pUC19 DNA from Form I to Form II at pH 5–6. This is the first example of large acceleration of hydrolytic DNA cleavage by synthetic metal complexes at pH 5–6, though purple acid phosphatases accelerate hydrolysis of phosphate ester at acidic conditions. The comparison of the DNA cleavage activity among **1a**, **2**, and **3** revealed that the $\mu\text{-OH}$ bridge accelerates the DNA cleavage as a nucleophile and the NH

group is essential for the hydrolytic DNA cleavage. The transition state in the DNA cleavage by **1a** is stabilized by DNA binding and protonation to the DNA binding complex. Mechanistic insights are proposed on the basis of these studies. The pH dependent activity control in the DNA cleavage of **1a** may provide some insights into the development of new cancer drugs to reduce the side effects.

This work was supported by MEXT-Supported Program of the Strategic Research Foundation at Private University, 2015–2019.

Supporting Information

X-ray structural data for the dicopper complexes, distances of O-atom of μ -OH bridge from the mean planes of **1a** and **2**, electronic absorption and ESI MS spectra in the complexation of ligands, DNA cleavage by **1a** in the presence of H₂O₂, NaN₃, or dmsO, agarose gel electrophoresis profiles for all DNA cleavage studies, bond distances and angles for the dicopper complexes, data for the fractions of Form I, Form II, and Form III formed. This material is available on <https://doi.org/10.1246/bcsj.20180353>.

References

- 1 a) S. D. Kettenmann, F. R. Louka, E. Marine, R. C. Fischer, F. A. Mautner, N. Kulak, S. S. Massoud, *Eur. J. Inorg. Chem.* **2018**, 2322. b) T. J. P. McGivern, S. Afsharpour, C. J. Marmion, *Inorg. Chim. Acta* **2018**, 472, 12. c) C. Santini, M. Pellei, V. Gandin, M. Porchia, F. Tisato, C. Cristina Marzano, *Chem. Rev.* **2014**, 114, 815. d) S. Dasari, P. B. Tchounwou, *Eur. J. Pharmacol.* **2014**, 740, 364. e) J. Qian, W. Gu, H. Liu, F. Gao, L. Feng, S. Yan, D. Liao, P. Cheng, *Dalton Trans.* **2007**, 1060. f) K. D. Copeland, M. P. Fitzsimons, R. P. Houser, J. K. Barton, *Biochemistry* **2002**, 41, 343.
- 2 a) T. C. Johnstone, K. Suntharalingam, S. J. Lippard, *Chem. Rev.* **2016**, 116, 3436. b) B. Rosenberg, *Cancer* **1985**, 55, 2303.
- 3 Y. Kidani, K. Inagaki, M. Iigo, A. Hoshi, K. Kuretani, *J. Med. Chem.* **1978**, 21, 1315.
- 4 M. J. McKeage, *Expert Opin. Investig. Drugs* **2001**, 10, 119.
- 5 M. Shimada, H. Itamochi, J. Kigawa, *Cancer Manag. Res.* **2013**, 5, 67.
- 6 a) D. Zhou, L. Shao, D. R. Spitz, *Adv. Cancer Res.* **2014**, 122, 1. b) A. Weidemann, R. S. Johnson, *Cell Death Differ.* **2008**, 15, 621. c) Y. Kato, S. Ozawa, C. Miyamoto, Y. Maehata, A. Suzuki, T. Maeda, Y. Baba, *Cancer Cell Int.* **2013**, 13, 89.
- 7 a) R. J. Gillies, N. Raghunand, G. S. Karczmar, Z. M. Bhujwalla, *J. Magn. Reson. Imaging* **2002**, 16, 430. b) A. Kondo, S. Yamamoto, R. Nakaki, T. Shimamura, T. Hamakubo, J. Sakai, T. Kodama, T. Yoshida, H. Aburatani, T. Osawa, *Cell Reports* **2017**, 18, 2228. c) H. Lin, P. Herman, J. R. Lakowicz, *Cytometry* **2003**, 52A, 77.
- 8 a) S. S. Massoud, C. C. Ledet, T. Junk, S. Bosch, P. Comba, R. Herchel, J. Hošek, Z. Trávníček, R. C. Fischer, F. A. Mautner, *Dalton Trans.* **2016**, 45, 12933. b) L. J. K. Boerner, J. M. Zaleski, *Curr. Opin. Chem. Biol.* **2005**, 9, 135.
- 9 D. Montagner, V. Gandin, C. Marzano, A. Erxleben, *J. Inorg. Biochem.* **2015**, 145, 101.
- 10 a) C. A. Barta, S. R. Bayly, P. W. Read, B. O. Patrick, R. C. Thompson, C. Orvlg, *Inorg. Chem.* **2008**, 47, 2280. b) A. C. Benniston, P. Gunning, R. D. Peacock, *J. Org. Chem.* **2005**, 70, 115. c) S. Goswami, A. K. Das, A. K. Maity, A. Manna, K. Aich, S. Maity, P. Saha, T. K. Mandal, *Dalton Trans.* **2014**, 43, 231. d) P. Chirakul, P. D. Hampton, Z. Bencze, *J. Org. Chem.* **2000**, 65, 8297. e) D. A. Valyaev, S. Clair, L. Patrone, M. Abel, L. Porte, O. Chuzel, J.-L. Parrain, *Chem. Sci.* **2013**, 4, 2815. f) J. M. Wilson, F. Giordani, L. J. Farrugia, M. P. Barrett, D. J. Robins, A. Sutherland, *Org. Biomol. Chem.* **2007**, 5, 3651. g) E. Kimura, S. Aoki, T. Koike, M. Shiro, *J. Am. Chem. Soc.* **1997**, 119, 3068.
- 11 A. W. Addison, T. N. Rao, J. Reedijk, J. v. Rijn, G. C. Verschoor, *J. Chem. Soc., Dalton Trans.* **1984**, 1349.
- 12 a) N. A. Rey, A. Neves, A. J. Bortoluzzi, C. T. Pich, H. Terenzi, *Inorg. Chem.* **2007**, 46, 348. b) T. M. Rajendiran, R. Mahalakshmy, R. Kannappan, J. Rajeswari, R. Venkatesan, P. Rao, *Trans. Met. Chem.* **2003**, 28, 280. c) P. Amudha, M. Kandaswamy, L. Govindasamy, D. Velmurugan, *Inorg. Chem.* **1998**, 37, 4486.
- 13 a) C. R. Choudhury, S. K. Dey, R. Karmakar, C.-D. Wu, C.-Z. Lu, M. S. E. Fallah, S. Mitra, *New J. Chem.* **2003**, 27, 1360. b) S. J. Smith, C. J. Noble, R. C. Palmer, G. R. Hanson, G. Schenk, L. R. Gahan, M. J. Riley, *J. Biol. Inorg. Chem.* **2008**, 13, 499.
- 14 a) S. Torelli, C. Belle, I. Gautier-Luneau, J. L. Pierre, E. Sain-Aman, J. M. Latour, L. L. Pape, L. D. Luneau, *Inorg. Chem.* **2000**, 39, 3526. b) J. Nagaj, K. Stokowa-Sołtys, E. Kurowska, T. Frączyk, M. Jeżowska-Bojczuk, W. Bal, *Inorg. Chem.* **2013**, 52, 13927.
- 15 a) T. P. Szatrowski, C. F. Nathan, *Cancer Res.* **1991**, 51, 794. b) V. Nogueira, N. Hay, *Clin. Cancer Res.* **2013**, 19, 4309. c) G.-Y. Liou, P. Storz, *Free Radic. Res.* **2010**, 44, 479.
- 16 a) E. Tuite, P. Lincoln, B. Nordén, *J. Am. Chem. Soc.* **1997**, 119, 239. b) M. Eriksson, M. Leijon, C. Hiort, B. Nordén, A. Gräslund, *J. Am. Chem. Soc.* **1992**, 114, 4933.
- 17 a) G. Manzini, M. L. Barcellona, M. Avitabile, F. Quadrifoglio, *Nucleic Acids Res.* **1983**, 11, 8861. b) E. Tuite, U. Sehlstedt, P. Hagmar, B. Nordén, M. Takahashi, *Eur. J. Biochem.* **1997**, 243, 482. c) P. Wittung, P. Nielsen, B. Nordén, *J. Am. Chem. Soc.* **1996**, 118, 7049.
- 18 S. K. Kim, B. Nordén, *FEBS Lett.* **1993**, 315, 61.
- 19 A. K. Williams, S. C. Dasilva, A. Bhatta, B. Rawal, M. Liu, E. A. Korobkova, *Anal. Biochem.* **2012**, 422, 66.
- 20 W. D. Wilson, F. A. Tanious, H. J. Barton, L. Streckowski, D. W. Boykin, *J. Am. Chem. Soc.* **1989**, 111, 5008.
- 21 a) B. C. Antanaitis, P. Aisen, *Adv. Inorg. Biochem.* **1983**, 5, 111. b) D. C. Schlosnagle, F. W. Bazer, J. C. Tsibris, R. M. Roberts, *J. Biol. Chem.* **1974**, 249, 7574.
- 22 G. Schenk, N. Mitić, G. R. Hanson, P. Comba, *Coord. Chem. Rev.* **2013**, 257, 473.
- 23 G. Feng, D. Natale, R. Prabakaran, J. C. Mareque-Rivas, N. H. Williams, *Angew. Chem., Int. Ed.* **2006**, 45, 7056.
- 24 P. Thaplyal, P. C. Bevilacqua, *Methods Enzymol.* **2014**, 549, 189.

Oxidation

International Edition: DOI: 10.1002/anie.201702291
German Edition: DOI: 10.1002/ange.201702291

Specific Enhancement of Catalytic Activity by a Dicopper Core: Selective Hydroxylation of Benzene to Phenol with Hydrogen Peroxide

Tomokazu Tsuji, Antonius Andre Zaoputra, Yutaka Hitomi, Kaoru Mieda, Takashi Ogura, Yoshihito Shiota, Kazunari Yoshizawa, Hiroyasu Sato, and Masahito Koder*^a

Abstract: A dicopper(II) complex, stabilized by the bis(*tpa*) ligand 1,2-bis[2-[bis(2-pyridylmethyl)aminomethyl]-6-pyridyl]ethane (6-hpa), $[\text{Cu}_2(\mu\text{-OH})(6\text{-hpa})]^{3+}$, was synthesized and structurally characterized. This complex catalyzed selective hydroxylation of benzene to phenol using H_2O_2 , thus attaining large turnover numbers (TONs) and high H_2O_2 efficiency. The TON after 40 hours for the phenol production exceeded 12000 in MeCN at 50°C under N_2 , the highest value reported for benzene hydroxylation with H_2O_2 catalyzed by homogeneous complexes. At 22% benzene conversion, phenol (95.2%) and *p*-benzoquinone (4.8%) were produced. The mechanism of H_2O_2 activation and benzene hydroxylation is proposed.

Phenol is one of the most important chemical intermediates used to manufacture various industrial chemicals.^[1] However, industrial phenol production is dominated by inefficient three-step cumene methods where overall the yield of phenol from benzene is 5%, using O_2 as oxidant.^[2] Development of efficient catalysts for selective hydroxylation of benzene to phenol with a cheap oxidant, such as O_2 or H_2O_2 , has been one of the most important targets for industry.^[3]

Recently, great progress has been made in direct oxidation of benzene to phenol with H_2O_2 when catalyzed by heterogeneous systems.^[4] However, such reactions have not been mechanistically clarified because of the difficulty in spectroscopic observation of solid-surface reactions. More recently, monometal complexes have been developed as homogeneous catalysts for benzene hydroxylation using H_2O_2 , and mechanistically clarified. The turnover number (TON) of $[\text{Ni}(\text{tepa})]^{2+}$ [tepa = tris(2-pyridyl)ethylamine] was reported to be 749 after 216 hours in MeCN at 60°C,^[5] and that of $[\text{Cu}(\text{tmpa})]^{2+}$ [tmpa = tris(2-pyridyl)methylamine], incorpo-

rated into a mesoporous material, was reported as 4320 after 112 hours in acetone at 30°C where a hydroperoxyl radical (O_2H) was detected as the active oxidant.^[6]

Dicopper biosites are known to catalyze oxidations of various hydrocarbons, such as aromatic compounds and alkanes.^[7] Various dicopper complexes have been developed for O_2 binding,^[8] but are less studied as catalysts for the oxidation of methane and benzene.^[9] Herein, it was found that a dicopper complex with the dinucleating ligand 1,2-bis[2-[bis(2-pyridylmethyl)aminomethyl]-6-pyridyl]ethane^[10] (6-hpa), $[\text{Cu}_2(\mu\text{-OH})(6\text{-hpa})](\text{ClO}_4)_3$ (**1**), exhibits high catalytic activity in selective hydroxylation of benzene with H_2O_2 .

The complex **1** was synthesized and structurally characterized. The ORTEP view (Figure 1) of **1** shows that the dicopper(II) core with a $\mu\text{-OH}$ bridge is encapsulated by the 6-hpa ligand. The dicopper core of **1** is stable in a solution as shown by the ESI MS spectrum (see Figure S1 in the Supporting Information).

Both **1** and $[\text{Cu}(\text{MeCN})(\text{tmpa})](\text{ClO}_4)_2$ (**2**) were used to compare their catalytic activities for the benzene hydroxylation. In a typical reaction, 10 mL of 30% aqueous H_2O_2 (120 mmol) was added to an MeCN (20 mL) solution of 60 mmol of benzene, 1 μmol of **1**, and 5 μmol of Et_3N , with vigorous stirring under N_2 at 50°C. For the reaction of **2**, 2 μmol of **2** and 10 μmol of Et_3N were used under the same reaction conditions. The reaction products were analyzed using GC, GC-MS, and ^1H NMR spectroscopy. Small amounts of phenol were produced in the absence of catalyst, but less than 1% of the amount formed in the presence of **1**.

Time courses of phenol production catalyzed by **1** and **2** are shown in Figure 2. **1** showed a turnover frequency (TOF)

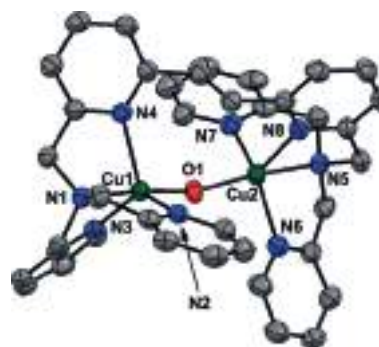


Figure 1. ORTEP view (ellipsoids shown at 50% probability) of the cationic portion of **1**.^[18] Selected bond distances [Å] and angle [°]: Cu1...Cu2 3.799, Cu1–O1 1.922(3), Cu1–N1 2.029(4), Cu1–N2 2.071(4), Cu1–N3 2.056(4), Cu1–N4 2.225(4), Cu2–O1 1.941(3), Cu2–N5 2.028(4), Cu2–N6 2.051(4), Cu2–N7 2.054(4), Cu2–N8 2.238(4); Cu1–O1–Cu2 158.18(19).

^[*] T. Tsuji, A. A. Zaoputra, Prof. Dr. Y. Hitomi, Prof. Dr. M. Koder*
Department of Molecular Chemistry and Biochemistry
Doshisha University, Kyotanabe Kyoto 610-0321 (Japan)
E-mail: mkoder*@mail.doshisha.ac.jp

K. Mieda, Prof. Dr. T. Ogura
Department of Life Science, University of Hyogo
Kouto, 2-1, Ako-gun, Kamigori-cho, Hyogo 678-1297 (Japan)

Dr. Y. Shiota, Prof. Dr. K. Yoshizawa
Institute for Materials Chemistry and Engineering
Kyushu University, Fukuoka 819-0395 (Japan)

Dr. H. Sato
Application Laboratory, Rigaku Corporation
Akishima Tokyo 196-8666 (Japan)

Supporting information and the ORCID identification number(s) for the author(s) of this article can be found under:
<https://doi.org/10.1002/anie.201702291>.

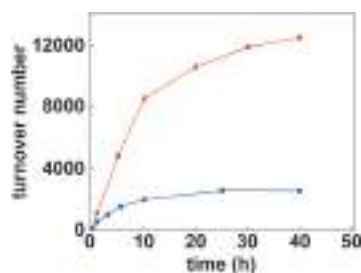


Figure 2. Time courses of phenol production through the oxidation of benzene (60 mmol) with H_2O_2 (10 mL of 30% aqueous H_2O_2 , 120 mmol) catalyzed by **1** (1 μmol ; red) and **2** (2 μmol ; blue) in the presence of Et_3N (5 μmol for **1** and 10 μmol for **2**) in MeCN (20 mL) at 50°C.

[mol phenol (mol catalyst) $^{-1}$ h $^{-1}$] of 1010 and an overall TON of 12000 after 40 hours. These are the largest values yet reported for benzene hydroxylation with H_2O_2 by homogeneous catalysis.^[5,6] After 40 hours, 22% of benzene was converted into phenol (95.2%) and *p*-benzoquinone (4.8%), and H_2O_2 efficiency [(mol phenol + mol *p*-benzoquinone \times 2) (mol H_2O_2 consumed) $^{-1}$] was 45%.^[11] The molar ratio of phenol and *p*-benzoquinone was determined by ^1H NMR spectroscopy (see Figure S2). After completion of the reaction, 1.10 grams (11.7 mmol) of phenol were isolated from the reaction mixture. In comparison, **2** showed a TOF of 444 and an overall TON of 2260 after 40 hours, and 8% of benzene was converted into phenol (91.3%) and *p*-benzoquinone (8.7%), and the H_2O_2 efficiency was 6%.^[11] The overall TON of **1** after 40 hours is 5.3-fold larger than that of **2**. This demonstrates the superiority of the catalyst **1** over **2**, and may be due to the dinuclear structure of **1** enhancing the catalytic activity, selectivity, and H_2O_2 efficiency.

Isotope-labeling experiments using $\text{H}_2^{18}\text{O}_2$ were carried out, showing that ^{18}O -incorporation into phenol is $95 \pm 2\%$ and $91 \pm 4\%$, when catalyzed by **1** and **2**, respectively. This result demonstrated that the O atom of H_2O_2 was incorporated into the phenol. Using a 1:1 mixture of C_6H_6 and C_6D_6 as substrates, kinetic isotope effects (KIE) were estimated as 1.04 and 1.40 for **1** and **2**, respectively, from peak intensity ratios [($\text{C}_6\text{H}_5\text{OH}$) ($\text{C}_6\text{D}_5\text{OH}$) $^{-1}$] using the GC-MS data (see Figure S3). This data showed that C–H bond cleavage of benzene is not involved in the rate-limiting step, and that the active species in the reaction of **1** is not a hydroxyl radical ($\cdot\text{OH}$) because the KIE value of a Fenton-type reaction is generally in the range of 1.7–1.8.^[12]

A radical-chain reaction of $\cdot\text{O}_2\text{H}$ was proposed for the reaction of **2**,^[6] and may explain the low H_2O_2 efficiency of **2** because the $\cdot\text{O}_2\text{H}$ radical decomposes by disproportionation to O_2 and H_2O_2 . Therefore, to examine participation of $\cdot\text{O}_2\text{H}$ in the reaction employing **1**, 5,5'-dimethyl-1-pyrroline *N*-oxide (DMPO; 0.50 and 5.0 mM) was added as a radical trapping reagent. The resulting reaction of **1** was not affected by DMPO (see time courses of phenol production shown in Figure S4). Thus, the radical-chain mechanism by $\cdot\text{O}_2\text{H}$ can be excluded from consideration for the reaction of **1**, thus indicating that the dicopper core enables formation of alternative active species.

Kinetic studies were carried out for benzene oxidation with H_2O_2 , catalyzed by **1**. The initial rates were determined

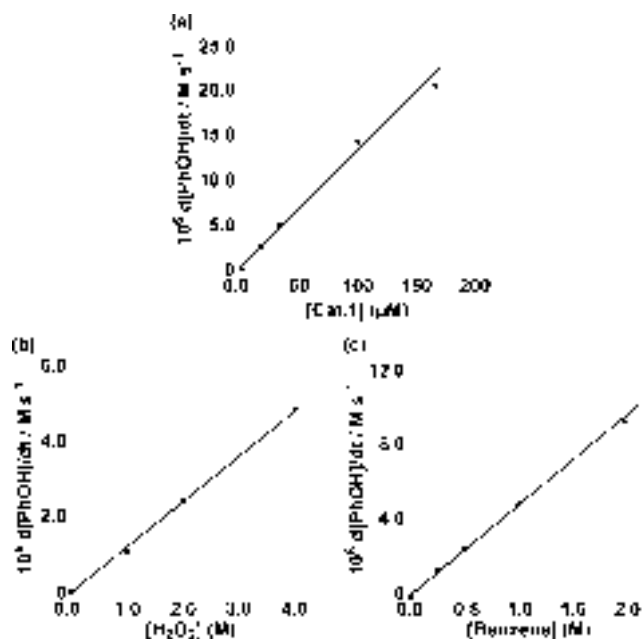


Figure 3. a) Dependence of the initial rate of phenol production estimated from the TOF (h^{-1}) at 50°C ($d[\text{PhOH}]/dt$) on the concentration of **1** ($[\text{I}] = 0\text{--}170 \mu\text{M}$, $[\text{C}_6\text{H}_6] = 1.0 \text{ M}$, $[\text{H}_2\text{O}_2] = 4.0 \text{ M}$). b) Dependence of $d[\text{PhOH}]/dt$ on the concentration of H_2O_2 ($[\text{H}_2\text{O}_2] = 0\text{--}4.0 \text{ M}$, $[\text{I}] = 33 \mu\text{M}$, $[\text{C}_6\text{H}_6] = 1.0 \text{ M}$). c) Dependence of $d[\text{PhOH}]/dt$ on the concentration of C_6H_6 ($[\text{C}_6\text{H}_6] = 0\text{--}2.0 \text{ M}$, $[\text{I}] = 33 \mu\text{M}$, $[\text{H}_2\text{O}_2] = 4.0 \text{ M}$).

from TOFs of phenol production under the typical reaction conditions, and were found to be proportional to concentrations of **1**, H_2O_2 , and benzene, as shown in Figures 3a–c. The rate equation for the phenol formation is derived on the basis of these kinetic studies and is shown in the Supporting Information. In the case of **2**, however, it was reported that the initial rate was proportional to the square root of the concentration of **2**.^[6] This rate showed that 2 equivalents of $\cdot\text{O}_2\text{H}$ were formed from 1 equivalent of **2** by formation of hydroperoxocopper(II) in equilibrium with **2** and H_2O_2 .

To the reaction mixture of **1**, NaBPh_4 and Et_2O were added, and yielded green crystals after standing for several days at 0°C. The X-ray analysis revealed the structure of a diphenoxodicopper(II) complex, $[\text{Cu}_2(\text{PhO})_2(6\text{-hpa})] \cdot (\text{BPh}_4)_2$ (**3**) (see ORTEP view in Figure S5). The structure shows that a phenoxide ion binds to each copper site, and that 6-hpa is kept intact in the recovered complex.

Besides benzene, nitrobenzene, toluene, and phenol were used as substrates for the reaction, catalyzed by **1**, to examine reactivity of the active species (Table 1). Time courses for oxidation of these substrates are shown in Figure S6. In the case of toluene, *o*- and *p*-cresol and benzaldehyde were produced as major products with a total TON of 4380 after 40 hours. The ratio of aromatic to aliphatic oxidations was 2.6:1.0. In the case of nitrobenzene, *o*-nitrophenol was the major product with *m*- and *p*-nitrophenol as minor products, and the total TON after 40 hours was 860. In the case of phenol, *p*-benzoquinone was the sole detectable product up to 10 hours, with a TON of 1630, after which catechol formation occurred, presumably because of a structural change to the catalyst. Phenol may also inhibit H_2O_2 activation by binding

Table 1: Product analysis in oxidation of benzene and its derivatives catalyzed by **1**.

Entry ^[a]	Substrate	Products [%] ^[b] (<i>o/p/m</i>) ^[c]	TOF ^[d] (h ⁻¹)	TON ^[e]
1	Benzene	Phenol [95.2], <i>p</i> -benzoquinone [4.8]	1010	12550
2	Benzene	Phenol [93.2], <i>p</i> -Benzoquinone [6.8]	540	6250
3	Toluene	Cresol [72] (57:43:trace) Benzaldehyde [26]	380	4320
4	Phenol	<i>p</i> -Benzoquinone [99]	350	1630 ^[f]
5	Nitrobenzene	Nitrophenol [99] (91:4:5)	72	860

[a] Reaction conditions: entry 1: benzene (60 mmol), H₂O₂ (10 mL of 30% aqueous H₂O₂, 120 mmol), **1** (1.0 μmol), and TEA (5.0 μmol) in MeCN (20 mL) at 50 °C under N₂. Entries 2, 3, 4, 5: 30 mmol of substrate was added under the same reaction conditions as entry 1. [b] Product yield based on substrate consumed after 40 h for Entries 1–3 and 5, and after 10 h for Entry 4. [c] Product ratio of hydroxylation at *ortho*-, *meta*-, and *para*-position in cresol and nitrophenol. [d] Turnover frequency of all product after 1 h. [e] Turnover number of all product after 40 h. [f] Turnover number of all product after 10 h.

to Cu^{II} as shown in the crystal structure of **3**, thus explaining the relatively low TON. Selective *p*-benzoquinone production in this reaction system suggests that the oxidation occurred at the *para*-position of a copper-bonded phenoxide, which is more reactive because of the radical character than free phenol, where *ortho*-positions did not react as a result of the steric hindrance of the 6-hpa.^[13] The relative reactivity order estimated from the initial rate (TOF, see Table 1) is phenol ≈ toluene ≫ nitrobenzene, and increases with increasing electron density of the aromatic ring, thus indicating an electrophilic character of the active species. The regioselectivity is *ortho* and *para* for toluene, *ortho* for nitrobenzene, and *para* for phenol, therefore indicating a radical character of the active species. Thus, based on these results, the active species may have an electrophilic radical character such as a metal-bonded oxyl radical, which was previously proposed as the active species in the reactions of Co, Ni, Cu, and Ru complexes with various oxidants.^[14]

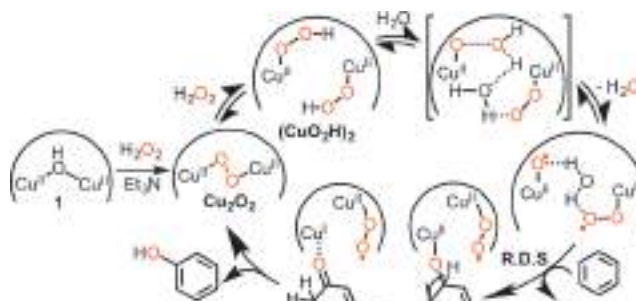
Two intermediates were spectroscopically detected in the reaction of **1** with H₂O₂ and provide insight into the mechanism of H₂O₂ activation. When 1 equivalent of H₂O₂ was added to **1** in the presence of Et₃N in MeCN at -40 °C, clear bands, which are typical of an end-on *trans*-peroxodicopper(II) (Cu₂O₂) complex, appeared at λ = 520 nm,^[15] and decayed with a half-life of 1200 s as shown in Figure S7. In contrast, upon addition of excess amounts of H₂O₂, the Cu₂O₂ complex that once formed rapidly decayed to give a new species that showed a band at λ = 380 nm, close to the band at λ = 379 nm for the hydroperoxocopper(II) (CuO₂H) complex.^[16] The Cu₂O₂ complex decayed with a half-life of 10 seconds in the presence of 100 equivalents of H₂O₂ at -40 °C. The reaction rate showed saturation kinetics with an increase of concentration of H₂O₂, as shown in Figure S8. The resonance Raman spectra of the Cu₂O₂ complex and the as-prepared new species showed clear bands at 821 and 846 cm⁻¹, respectively, and the corresponding

isotope shifts were 43 and 53 cm⁻¹ when H₂¹⁸O₂ was used (see Figure S9). These values are similar to bands at 827 (44) and 847 (55) cm⁻¹ attributed to O–O stretching bands for the Cu₂O₂ and CuO₂H complexes, respectively.^[15,16] Thus, the data confirm that the second intermediate contains a peroxo ligand and we hypothesize that it is a dihydroperoxodicopper(II) (CuO₂H)₂ complex, which is in equilibrium with the Cu₂O₂ complex and H₂O₂.

Here, we propose a mechanism (Scheme 1) for the H₂O₂ activation and benzene hydroxylation catalyzed by **1** and it is based on the relative reactivity and regioselectivity in oxidation of substituted benzenes, the spectroscopic studies of reaction intermediates, and DFT calculations. The reaction pathway is estimated by DFT calculations, and we confirmed the interaction between the Cu–O moiety of the active species and benzene in the transition state. The details are shown in Figures S11 and S12. The (CuO₂H)₂ complex is shown to be a precursor of the active species with an electrophilic radical character shown in the oxidation of substituted benzenes. The (CuO₂H)₂ complex releases H₂O reversibly with the assistance of H₂O to give a copper-bound oxyl and peroxy radical which is stabilized by hydrogen-bonding interactions with H₂O. Here, it reacts with benzene in the rate-limiting step. This reactivity is consistent with kinetic results for the phenol production. It is also not a radical-chain reaction as discussed previously. The active species may then react with DMPO to undergo decomposition, but does not form a stable radical, such as a ·O₂H-adduct, and this may be the reason why DMPO did not inhibit phenol production. The present mechanism is one of many possible pathways, and further studies are needed for clarification.

In a mechanism reported for benzene hydroxylation catalyzed by **2**,^[6] it was shown that ·O₂H was generated as an active oxygen species by O–O bond scission of the CuO₂H species, a step which is energetically unfavorable.^[17] In contrast, in the case of **1**, the active species is formed by a more energetically favorable intramolecular dehydration of the (CuO₂H)₂ complex as shown by DFT calculations, where the two CuO₂H moieties are encapsulated by 6-hpa. Therefore, it is concluded that the dinuclear structure of **1** is favorable for the formation of the active species to specifically enhance the catalytic activity.

In summary, a new dicopper complex with the dinucleating ligand 6-hpa, which specifically stabilizes a dinuclear



Scheme 1. Proposed mechanism of H₂O₂ activation and benzene hydroxylation catalyzed by **1**.

structure, enhances catalytic activity, selectivity, and H₂O₂ efficiency in selective hydroxylation of benzene to phenol with H₂O₂. This reactivity is clearly shown in the comparison with a monocopper complex. Moreover, the mechanism of H₂O₂ activation and benzene hydroxylation is consistently supported by kinetic studies of phenol production, product analysis of benzene derivatives, spectroscopic studies of reaction intermediates, and DFT calculations. Such a unique feature of the dicopper complex may provide a new concept around which future catalysts for the direct benzene hydroxylation may be developed.

Experimental Section

Catalytic reactions. A solution of **1** (1.0 μmol), Et₃N (5.0 μmol), substrate (30 or 60 mmol) in MeCN (20 mL) was placed in a flask, and quickly degassed with N₂ gas. 10 mL of 30% aqueous H₂O₂ (120 mmol) was added under N₂ atmosphere with stirred at 50 °C. After passing the reaction mixture through an alumina column (eluent: CHCl₃, CDCl₃ in the case of ¹H NMR analysis and assays), a fraction of the solution was analyzed and assayed by ¹H NMR spectroscopy, as well as GC and GC-MS on the basis of nitrobenzene or *o*-dichlorobenzene as an added standard.

Acknowledgments

This work was supported by a Grant-in-Aid for Scientific Research (B) JSPS KAKENHI Grant Number 26288027, and CREST, JST.

Conflict of interest

The authors declare no conflict of interest.

Keywords: arenes · copper · oxidation · reaction mechanisms · structure elucidation

How to cite: *Angew. Chem. Int. Ed.* **2017**, *56*, 7779–7782
Angew. Chem. **2017**, *129*, 7887–7890

- [1] a) R. A. Sheldon, J. K. Kochi in *Metal-Catalyzed Oxidations of Organic Compounds* (Eds.: R. A. Sheldon, J. K. Kochi), Academic Press, New York, **1981**, pp. 315–339; b) M. Weber, M. Kleine-Boymann in *Ullmann's Encyclopedia of Industrial Chemistry*, Wiley-VCH, Weinheim, **2000**.
- [2] a) R. Molinari, T. Poerio, *Asia-Pac. J. Chem. Eng.* **2010**, *5*, 191–206; b) J. R. Schmidt, *Appl. Catal. A* **2005**, *280*, 89–103.
- [3] a) S.-i. Niwa, M. Eswaramoorthy, J. Nair, A. Raj, N. Itoh, H. Shoji, T. Namba, F. Mizukami, *Science* **2002**, *295*, 105–107; b) T. Kusakari, T. Sasaki, Y. Iwasawa, *Chem. Commun.* **2004**, 992–993; c) M. Tani, T. Sakamoto, S. Mita, S. Sakaguchi, Y. Ishii, *Angew. Chem. Int. Ed.* **2005**, *44*, 2586–2588; *Angew. Chem.* **2005**, *117*, 2642–2644; d) K. Ohkubo, T. Kobayashi, S. Fukuzumi, *Angew. Chem. Int. Ed.* **2011**, *50*, 8652–8655; *Angew. Chem.* **2011**, *123*, 8811–8814; e) O. Shoji, T. Kunitatsu, N. Kawakami, Y. Watanabe, *Angew. Chem. Int. Ed.* **2013**, *52*, 6606–6610; *Angew. Chem.* **2013**, *125*, 6738–6742; f) A. Raba, M. Cokoja, W. A. Herrmann, F. E. Kuhn, *Chem. Commun.* **2014**, 50, 11454–11457; g) Y. Aratani, Y. Yamada, S. Fukuzumi, *Chem. Commun.* **2015**, *51*, 4662–4665.
- [4] a) F. Xiao, J. Sun, X. Meng, R. Yu, H. Yuan, D. Jiang, S. Qiu, R. Xu, *Appl. Catal. A* **2001**, *207*, 267–271; b) P. K. Khatri, B. Singh, S. L. Jain, B. Sain, A. K. Sinha, *Chem. Commun.* **2011**, 47, 1610–1612; c) G. B. Shul'pin, Y. N. Kozlov, L. S. Shul'pina, W. A. Carvalhoc, D. Mandellic, *RSC Adv.* **2013**, *3*, 15065–15074.
- [5] Y. Morimoto, S. Bunno, N. Fujieda, H. Sugimoto, S. Itoh, *J. Am. Chem. Soc.* **2015**, *137*, 5867–5870.
- [6] M. Yamada, K. D. Karlin, S. Fukuzumi, *Chem. Sci.* **2016**, *7*, 2856–2863.
- [7] E. I. Solomon, D. E. Heppner, E. M. Johnston, J. W. Ginsbach, J. Cirera, M. Qayyum, M. T. Kieber-Emmons, C. H. Kjaergaard, R. G. Hadt, L. Tian, *Chem. Rev.* **2014**, *114*, 3659–3853.
- [8] a) C. E. Elwell, N. L. Gagnon, B. D. Neisen, D. Dhar, A. D. Spaeth, G. M. Yee, W. B. Tolman, *Chem. Rev.* **2017**, *117*, 2059–2107; b) M. Kodera, Y. Kajita, Y. Tachi, K. Katayama, K. Kano, S. Hirota, S. Fujinami, M. Suzuki, *Angew. Chem. Int. Ed.* **2004**, *43*, 334–337; *Angew. Chem.* **2004**, *116*, 338–341; c) M. Kodera, K. Katayama, Y. Tachi, K. Kano, S. Hirota, S. Fujinami, M. Suzuki, *J. Am. Chem. Soc.* **1999**, *121*, 11006–11007.
- [9] a) H. R. Lucas, L. Li, A. A. N. Sarjeant, M. A. Vance, E. I. Solomon, K. D. Karlin, *J. Am. Chem. Soc.* **2009**, *131*, 3230–3245; b) C. Würtele, O. Sander, V. Lutz, T. Waitz, F. Tuczek, S. Schindler, *J. Am. Chem. Soc.* **2009**, *131*, 7544–7545; c) J. S. Woertink, P. J. Smeets, M. H. Groothaert, M. A. Vance, B. F. Sels, R. A. Schoonheydt, E. I. Solomon, *Proc. Natl. Acad. Sci. USA* **2009**, *106*, 18908–18913.
- [10] M. Kodera, M. Itoh, K. Kano, T. Funabiki, M. Reglier, *Angew. Chem. Int. Ed.* **2005**, *44*, 7104–7106; *Angew. Chem.* **2005**, *117*, 7266–7268.
- [11] Consumption of H₂O₂ in the hydroxylation of benzene catalyzed by the copper complexes **1** and **2** was determined by redox titration with an aqueous KMnO₄ solution to be 24 and 45%, respectively.
- [12] R. Augusti, A. O. Dias, L. L. Rocha, R. M. Lago, *J. Phys. Chem. A* **1998**, *102*, 10723–10727.
- [13] H. Higashimura, K. Fujisawa, Y. Moro-oka, M. Kubota, A. Shiga, A. Terahara, H. Uyama, S. Kobayashi, *J. Am. Chem. Soc.* **1998**, *120*, 8529–8530.
- [14] a) D. Maiti, H. R. Lucas, A. A. N. Sarjeant, K. D. Karlin, *J. Am. Chem. Soc.* **2007**, *129*, 6998–6999; b) K. Ray, F. Heims, F. F. Pfaff, *Eur. J. Inorg. Chem.* **2013**, 3784–3807; c) S. Hong, F. F. Pfaff, E. Kwon, Y. Wang, M. Seo, E. Bill, K. Ray, W. Nam, *Angew. Chem. Int. Ed.* **2014**, *53*, 10403–10407; *Angew. Chem.* **2014**, *126*, 10571–10575; d) T. Corona, A. Draksharapu, S. K. Padamati, I. Gamba, V. Martin-Diaconescu, F. Acuña-Parés, W. R. Browne, A. Company, *J. Am. Chem. Soc.* **2016**, *138*, 12987–12996; e) Y. Shimoyama, T. Ishizuka, H. Kotani, Y. Shiota, K. Yoshizawa, K. Mieda, T. Ogura, T. Okajima, S. Nozawa, T. Kojima, *Angew. Chem. Int. Ed.* **2016**, *55*, 14041–14045; *Angew. Chem.* **2016**, *128*, 14247–14251.
- [15] R. R. Jacobson, Z. Tyeklar, K. D. Karlin, S. Liu, J. Zubieta, *J. Am. Chem. Soc.* **1988**, *110*, 3690–3692.
- [16] T. Fujii, A. Naito, S. Yamaguchi, A. Wada, Y. Funahashi, K. Jitsukawa, S. Nagatomo, T. Kitagawa, H. Masuda, *Chem. Commun.* **2003**, 2700–2701.
- [17] S. Kim, J. W. Ginsbach, J. Y. Lee, R. L. Peterson, J. J. Liu, M. A. Siegler, A. A. Sarjeant, E. I. Solomon, K. D. Karlin, *J. Am. Chem. Soc.* **2015**, *137*, 2867–2874.
- [18] CCDC 1551785 (**1**) and 1551786 (**3**) contain the supplementary crystallographic data for this paper. These data can be obtained free of charge from The Cambridge Crystallographic Data Centre.

Manuscript received: March 3, 2017

Revised manuscript received: March 30, 2017

Version of record online: May 31, 2017



Efficient cleavage of DNA oligonucleotides by a non-FokI-type zinc finger nuclease containing one His₄-type finger domain derived from the first finger domain of Sp1



Shigeru Negi^{a,*}, Michiko Yoshioka^a, Hiroko Mima^a, Makoto Mastumoto^b, Michiko Suzuki^a, Mao Yokoyama^a, Koji Kano^b, Yukio Sugiura^a

^a Faculty of Pharmaceutical Science, Doshisha Women's University, 97-1 Minamihokotachi, Koudo, Kyotanabe, Kyoto 610-0395, Japan

^b Department of Molecular Chemistry and Biochemistry, Faculty of Science and Engineering, Doshisha University, Kyotanabe, Kyoto 610-0321, Japan

ARTICLE INFO

Article history:

Received 5 August 2015

Revised 12 August 2015

Accepted 14 August 2015

Available online 22 August 2015

Keywords:

Zinc finger protein

DNA binding

Oligonucleotide DNA cleavage

Non-FokI-type zinc finger nuclease

His₄-type zinc finger domain

ABSTRACT

In this study, we sought to improve the hydrolytic activity of a His₄-type single finger domain (f2), which was previously derived from the second finger domain (f2') of the Sp1 zinc finger protein (Sp1wt), which has 3 tandem finger domains (f1', f2', and f3'). To this end, 2 His₄-type single finger domains were generated by mutating 2 Cys residues participating in Zn(II) coordination with the His residues in the first (f1') and third finger (f3') domains of Sp1wt. Circular dichroism spectroscopy results showed that the first and second His₄-type zinc finger domains (f1 and f2) adopted folded ββ α structures in the presence of Zn(II), but that the third His₄-type zinc finger domain (f3) did not. Non-FokI-type zinc finger nucleases containing 3 or 4 finger domains were also prepared by combining a His₄-type zinc finger domain with the Sp1wt scaffold. We studied their DNA-binding abilities and hydrolytic activities against DNA oligonucleotides by performing gel-mobility-shift assays. The results showed that f1 had higher hydrolytic activity for a DNA oligonucleotide with a GC box (5'-GGG GCG GGG-3'), compared with that of f2, although both His₄-type single finger domains had similar DNA-binding affinities. The difference in the hydrolytic activity between f1 and f2 was ascribed not only to the zinc coordinate structure, but also to its folding structure and the stability of finger domain.

© 2015 Elsevier Ltd. All rights reserved.

Recently, artificial nucleases that promote efficient and selective cleavage of target DNA molecules have emerged as promising tools for gene editing and gene-therapy.^{1–3} In particular, artificial nucleases using protein-based platforms such as (i) zinc finger proteins, (ii) transcription activator-like (TAL) effector proteins, and (iii) clustered regularly interspaced short palindromic repeats (CRISPR)-associated proteins have attracted much attention as practical and facile genome-editing tools.^{1,4–6} Among them, zinc finger proteins are ideal protein-based platforms for redesigning and constructing artificial nucleases because of their (1) compact ββ α -folding structures, (2) precise metal- and DNA-binding abilities, (3) capacity for facile manipulation of the DNA-recognition pattern using engineered zinc finger libraries, and (4) tandemly connected structures.^{7–12} The most common strategy for creating an artificial zinc finger nuclease involves fusion of a DNA-cleaving domain with a zinc finger protein. Chandrasegaran's group reported the first example of an artificial zinc finger nuclease by

fusing a non-specific FokI restriction endonuclease with the C-terminal domain of zinc finger proteins.¹³ Subsequently, several FokI-type artificial zinc finger nucleases were engineered and have been widely used for manipulating and editing targeting DNA, both in vitro and in vivo.^{14–16}

Previously, we investigated the structure, function, and redesign of the Sp1 zinc finger protein (Sp1wt), which serves as a DNA-binding domain in the human transcription factor Sp1.^{7,8} The DNA-binding motif of Sp1wt is composed of 3 tandem Cys₂His₂-type zinc finger domains (f1', f2', and f3'; Fig. 1). We reported the first examples of non-FokI-type zinc finger nucleases based on His₄-type zinc finger domains (f2 in Fig. 2), which was prepared by mutating the 2 Zn(II)-binding Cys residues to His residues in the second finger domain of Sp1wt (Fig. 1).^{17–20} The artificial zinc finger nucleases possessing the f2 domain, which have no additional cleavage domain such as FokI restriction endonuclease, successfully hydrolyzed *p*-nitrophenol acetate (NA), bis(*p*-nitrophenyl)phosphate (BNPP), and plasmid DNA (pBS plasmid containing Sp1 binding site) with sequence selectivity.^{18,19} However, the hydrolytic activity of these artificial zinc finger nucleases for

* Corresponding author. Tel.: +81 774 65 8650; fax: +81 774 65 8652.

E-mail address: snegi@dwc.doshisha.ac.jp (S. Negi).

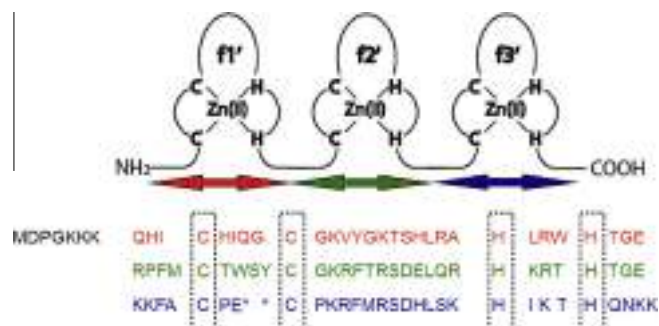


Figure 1. Primary sequence of Sp1 zinc finger protein (Sp1wt) and its tandem structure. The zinc-coordinating Cys and His residues are boxed. Sp1wt contains 3 classical Cys₂His₂-type zinc finger domains (f1', red; f2', green; and f3', blue).

plasmid DNA was much lower than those of natural restriction enzymes.^{18,19}

To improve their hydrolytic activities, we newly generated 2 His₄-type zinc finger domains (f1 and f3 in Fig. 2) corresponding to f1' and f3' of Sp1wt (Fig. 1). We also designed new types of non-FokI-type zinc finger nucleases based on the Sp1wt platform (f1f2'f3', f1'f2f3', f1'f2'f3'f1, and f1'f2'f3'f2), which contained a single His₄-type zinc finger domain (Fig. 2). The folding structure of His₄-type single finger domains (f1, f2, and f3) and the DNA-binding and hydrolytic activities of artificial non-FokI-type zinc finger nucleases for DNA oligonucleotides were investigated.

His₄-type single finger domains (f1, f2, and f3) were prepared by Fmoc-based solid-phase synthesis on the Rink amide resin using the TGS-RAM resin (Shimadzu Corporation, Kyoto, Japan), with a Shimadzu PSSM-8 peptide synthesizer (Shimadzu Corporation), as described in our previous study.²¹ The fidelity of the purified proteins was confirmed by matrix-associated laser desorption

ionization time-of-flight mass spectroscopy (MALDI-TOF-MS) using a Voyager-DE STR system (AB SCIEX, Framingham, MA, USA; Table S1). A plasmid encoding Sp1wt (pEV Sp1) was constructed according to our previous report.²² Expression vectors for 3-finger proteins (f1f2'f3' and f1'f2f3'), in which f1' and f2' finger domains of Sp1wt were replaced with the corresponding His₄-type finger domains f1 and f2, respectively, were constructed by inverse-PCR-based site-directed mutagenesis of the pEV Sp1 plasmid, using the KOD-Plus-Mutagenesis Kit (TOYOBO, Tokyo, Japan), following the manufacturer's instructions. We also prepared 4-finger proteins (f1'f2'f3'f1 and f1'f2'f3'f2), in which each fourth finger domain was joined to the C-terminus of Sp1wt by a consensus linker containing 5 amino acid residues (TGEKP), as we described previously.¹⁹ All constructed DNA sequences were confirmed by sequencing with a 3130 Genetic Analyzer (Applied Biosystems, Foster City, CA, USA). The 3 and 4-finger proteins were overexpressed in *Escherichia coli* BL21(DE3) codon-plus strain cells (Agilent Technologies, Santa Clara, CA, USA) and purified according to our previous procedures.²³ The purities of the produced proteins were confirmed by sodium dodecyl sulfate-polyacrylamide gel electrophoresis (data not shown) and MALDI-TOF-MS (Table S2).

The folding structures of f1, f2, and f3 were characterized by circular dichroism (CD) spectroscopy (see the [Supplemental information section for experimental details](#)). CD is an effective tool for determining the secondary structure characteristics of peptides and proteins in solution.²⁴ Figure 3 shows the CD spectra of f1, f2, and f3 single finger domains in the absence or presence of Zn(II). In all cases, negative bands at ~200 nm were observed in the absence of Zn(II), suggesting that the His₄-type single finger domains peptides mainly adopted random coil structures. Upon the addition of Zn(II), both f1 and f2 induced negative Cotton effects at ~208 and 222 nm. These CD spectral changes are similar to that of a typical Cys₂His₂-type zinc finger domain with a ββα

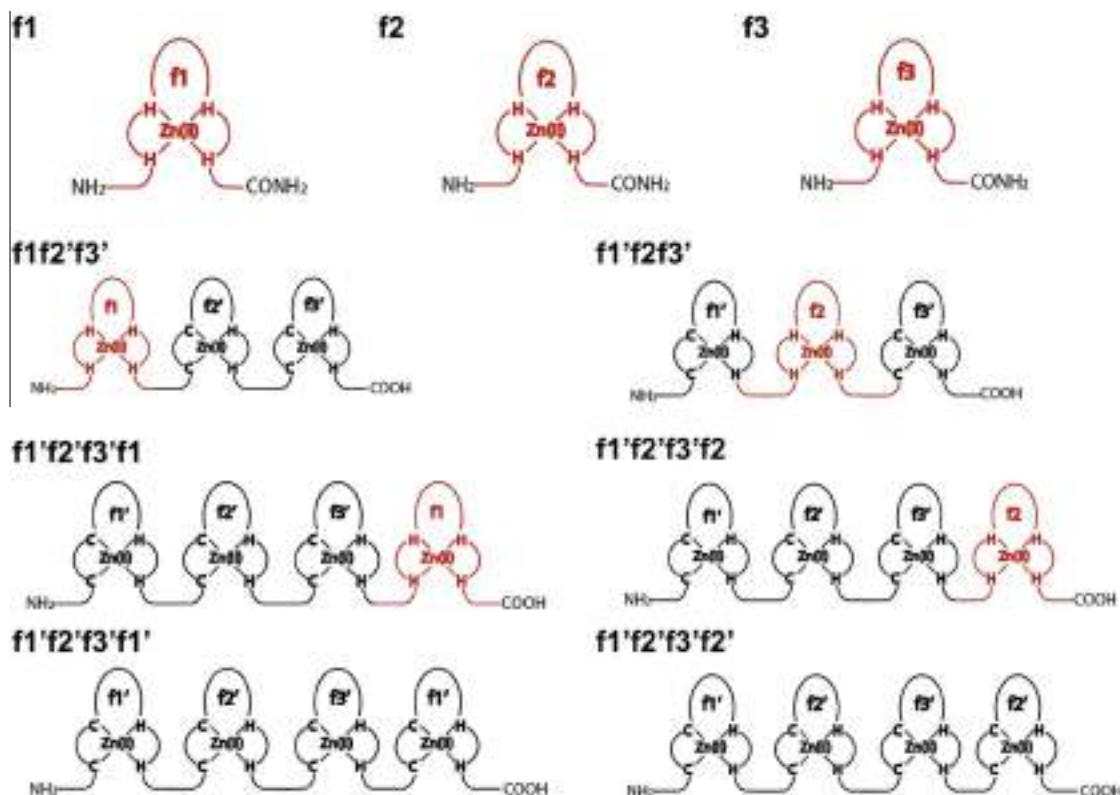


Figure 2. Schematic representation of various engineered His₄-type zinc finger proteins, based on the Sp1 zinc finger scaffold.

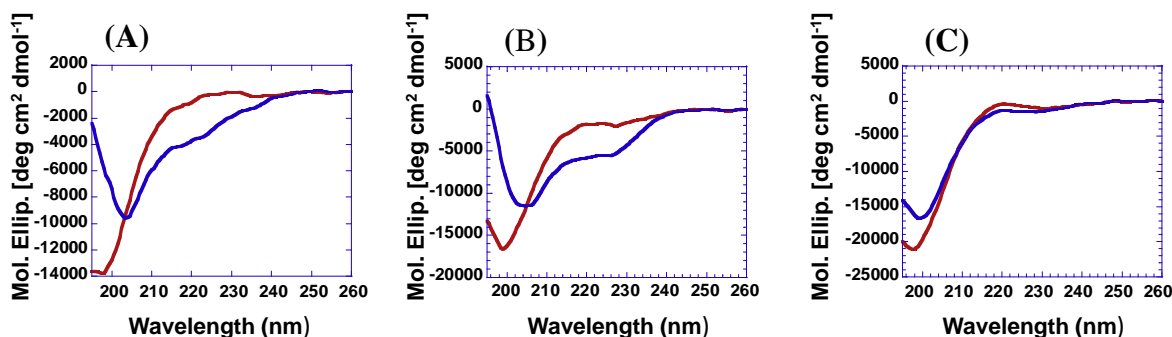


Figure 3. CD spectra of (A) f1, (B) f2, and (C) f3 (25 μ M) in the absence (red line) or presence of 1.5 equiv of Zn (II) (blue line) in 10 mM Tris–HCl buffer (pH 7.5), containing 50 mM NaCl and 100 μ M Tris(2-carboxyethyl)phosphine Hydrochloride at 20 $^{\circ}$ C.

Table 1

Sequences of DNA oligonucleotides (GC1 and GC2) with a GC box at different positions for use in gel-mobility-shift assays

Oligo DNA	Base sequence
GC1	5'-TAATACGACTCACTATAGTCTGGGGCGGGCCTACCTAGC 3'-ATTATGCTGAGTGATATCAGACCCCGCCCGGATGGATCG
GC2	5'-TAATACGACGGGGCGGGCCTCACTATAGTCTTACCTAGC 3'-ATTATGCTGCCCGCCCGGAGTGATATCAGAATGGATCG

secondary structure. These results suggest that f1 and f2 in the presence of Zn(II) take their ordered secondary structures. Meanwhile, only a slight spectral change was observed with f3 upon the addition of Zn(II), indicating that the mutation in f3 finger domain compromised the peptide folding.

Sp1wt specifically binds cognate DNA with a GC box (5'-GGG GCG GGG-3').²² The DNA-binding properties of non-FokI-type zinc finger nucleases (f1f2'f3', f1'f2f3', f1'f2'f3'f1, and f1'f2'f3'f2) for the 2 different types of DNA oligonucleotides containing 1 GC box site (GC1 or GC2; Table 1) were evaluated by gel-mobility-shift assays (see the [Supplemental information section for experimental details](#)). Binding between the DNA oligonucleotides and the proteins was performed in buffer solution at 25 $^{\circ}$ C for 30 min. Then the samples were electrophoresed in an 8% native polyacrylamide gel at 25 $^{\circ}$ C. Figure 4 shows gel-mobility-shift assay results for binding of Sp1wt, f1f2'f3', and f1'f2f3' with the GC1 DNA oligonucleotide. Both f1f2'f3' and f1'f2f3' showed band shifts that depended on the protein concentration, suggesting that these proteins bound the DNA oligonucleotide containing a GC box, though the DNA-binding affinity was considerably lower than that of Sp1wt. It is noteworthy that, in the case of f1f2'f3', additional shifted bands (red arrow in Fig. 4B) were observed at a lower position than the normal shifted band due to the GC1–f1f2'f3' complex. These bands can be ascribed to f1f2'f3' in complex with a DNA fragment formed by cleavage of the GC-box site in the GC1 DNA oligonucleotide by the f1 domain in f1f2'f3', indicating that the f1 domain possess hydrolytic activity for the appropriate DNA oligonucleotide.

To examine the hydrolytic activity of f1 in greater detail, we next studied the 4-zinc finger proteins (f1'f2'f3'f1 and f1'f2'f3'f2) proteins and their negative controls (f1'f2'f3'f1' and f1'f2'f3'f2'), as shown in Figure 2. The f1'f2'f3'f1 and f1'f2'f3'f2 zinc finger proteins are composed of 2 distinct functional sites, namely a DNA-binding site (Sp1wt) and a catalytic site (f1 and f2). The binding and catalytic sites are connected by a consensus 'TGEKP' linker, which is a widely conserved sequence in classical zinc finger proteins. We studied the DNA-binding affinity and hydrolytic activity of these 4-finger proteins for the GC1 target DNA oligonucleotide by gel-mobility-shift assays. As shown in Figure 5, the DNA-binding affinities of the f1'f2'f3'f1 and f1'f2'f3'f2 proteins for GC1 were almost the same as those of the f1'f2'f3'f1' and f1'f2'f3'f2' zinc finger proteins, respectively, suggesting that their DNA-binding affinities are mainly determined by the common Sp1wt domain (f1'f2'f3') in the 4-zinc finger proteins, but not by the fourth additional domains. In the case of the f1'f2'f3'f1, both the normal and the second shifted bands (red arrow in Fig. 5C) were also observed in the gel-shift assays, as observed with the f1f2'f3' zinc finger protein. However, only normal shifted bands were detected with f1'f2'f3'f2. These results strongly suggest that the difference in the hydrolytic activity between the f1'f2'f3'f1 and f1'f2'f3'f2 proteins may be attributed to the difference in the innate hydrolytic activities between the f1 and f2 domains in zinc finger nucleases, rather than differences in DNA-binding affinities. To confirm the sequence-selective hydrolysis of the f1'f2'f3'f1 zinc finger protein, gel-mobility-shift assays were performed using DNA oligonucleotide GC2, which has a GC box site located closer to the 5' end compared with GC1 (Table 1). The second shifted band (blue arrow in Fig. 5E) was observed at a position lower than that observed with the GC1–f1'f2'f3'f1 complex (Fig. 5C), indicating that the f1'f2'f3'f1 zinc finger protein bound to the GC box. The result indicated that f1'f2'f3'f1 protein could bind the GC box selectively, and efficiently cleave the DNA sequence in the vicinity of the GC box.

In summary, we successfully demonstrated the selective and efficient hydrolysis of a DNA oligonucleotide containing a GC box by artificial zinc finger nucleases (f1f2'f3' and f1'f2'f3'f1) with an f1 zinc finger domain, which was designed based on the first Cys₂-His₂-type finger domain (f1) of Sp1wt. Of special interest is the fact

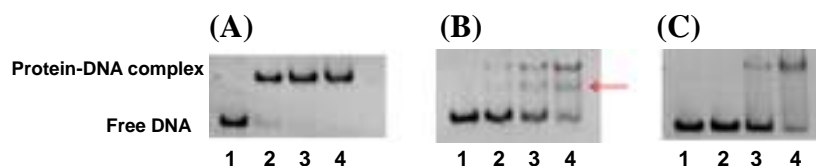


Figure 4. Gel-mobility-shift assays performed to study the binding of (A) Sp1wt, (B) f1f2'f3', and (C) f1'f2f3' to the 6-FAM-labeled DNA oligonucleotide, GC1. Peptide–DNA complexes were resolved by electrophoresis on 8% native poly-acrylamide gels. Lanes 1–4 were loaded with 0, 500, 1000, or 2000 nM peptides, respectively.

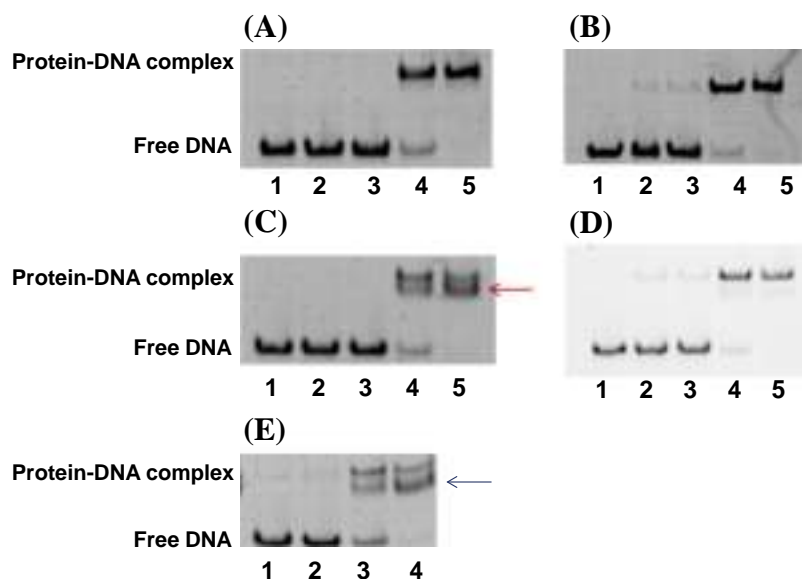


Figure 5. Gel-mobility-shift assays performed to study the binding of (A) f1'f2'f3'f1', (B) f1'f2'f3'f2', (C) f1'f2'f3'f1, and (D) f1'f2'f3'f2 to the 6-FAM-labeled DNA oligonucleotide, GC1. Lanes 1–5 were loaded with 0, 250, 500, 1000, and 2000 nM proteins, respectively. (E) Gel-mobility-shift assays performed to study the binding of f1'f2'f3'f1 to the 6-FAM-labeled DNA oligonucleotide, GC2. Lanes 1–4 were loaded with 0, 500, 1000, and 2000 nM proteins, respectively. Protein–DNA complexes were resolved by electrophoresis on an 8% native poly-acrylamide gel.

that the hydrolytic activity of a multi zinc finger protein involving an f1 domain is much higher than that involving an f2 domain. Based on this result, we propose that the hydrolytic activity of His₄-type zinc finger proteins is influenced not only by the Zn(II) coordinate structure, but also by its folding structure and the stability of the finger domain. Our design strategy using the His₄-type zinc finger domains might provide a valuable approach for producing artificial nucleases. Further studies are in progress to characterize the hydrolysis of plasmid and genomic DNA by f1f2'f3 and f1'f2'f3'f1 zinc finger proteins.

Acknowledgments

This study was supported by Grant-in-Aid for Scientific Research (No. 205102060 and 24390012) from the Ministry of Education, Culture, Sports, Science, and Technology, Japan, and by a grant from the Kurata Memorial Hitachi Science and Technology Foundation. We thank Dr. Yoko Amagase (Doshisha Women's University) for helpful discussions in preparing this manuscript.

Supplementary data

Supplementary data associated with this article can be found, in the online version, at <http://dx.doi.org/10.1016/j.bmcl.2015.08.045>.

References and notes

- Gaj, T.; Gersbach, C. A.; Barbas, C. F., III *Trends Biotechnol.* **2013**, *31*, 397.
- Aiba, Y.; Sumaoka, J.; Komiyama, M. *Chem. Soc. Rev.* **2011**, *40*, 5657.
- Mancin, F.; Scrimin, P.; Tecilla, P. *Chem. Commun.* **2012**, 5545.
- Scharenberg, A. M.; Duchateau, P.; Smith, J. *Curr. Gene Ther.* **2013**, *13*, 291.
- Bortesi, L.; Fischer, R. *Biotechnol. Adv.* **2015**, *33*, 41.
- Scott, J. N.; Kupinski, A. P.; Boyes, J. *FEBS J.* **2014**, *281*, 4583.
- Dhanasekaran, M.; Negi, S.; Suigura, Y. *Acc. Chem. Res.* **2006**, *39*, 45.
- Negi, S.; Imanishi, M.; Matsumoto, M.; Sugiura, Y. *Chem. Eur. J.* **2008**, *14*, 3236.
- Segal, D. J.; Dreier, B.; Beerli, R. R.; Barbas, C. F., III *Proc. Natl. Acad. Sci. U.S.A.* **1999**, *96*, 2758.
- Mandell, J. G.; Barbas, C. F., III *Nucleic Acids Res.* **2006**, *34*, W516.
- Sera, T.; Uranga, C. *Biochemistry* **2002**, *41*, 7074.
- Gersbach, C. A.; Gaj, T.; Barbas, C. F., III *Acc. Chem. Res.* **2014**, *47*, 2309.
- Kim, Y. G.; Cha, J.; Chandrasegaran, S. *Proc. Natl. Acad. Sci. U.S.A.* **1996**, *93*, 1156.
- Urnov, F. D.; Rebar, E. J.; Holmes, M. C.; Zhang, H. S.; Gregory, P. D. *Nat. Rev. Genet.* **2010**, *11*, 636.
- Carroll, D. *Curr. Gene Ther.* **2011**, *11*, 2.
- Jabalamei, H. R.; Zahednasab, H.; Karimi-Moghaddam, A.; Jabalamei, M. R. *Gene* **2015**, *558*, 1.
- Nomura, A.; Sugiura, Y. *Inorg. Chem.* **2004**, *43*, 1708.
- Nomura, A.; Sugiura, Y. *J. Am. Chem. Soc.* **2004**, *126*, 15374.
- Negi, S.; Umeda, Y.; Masuyama, S.; Kano, K.; Sugiura, Y. *Bioorg. Med. Chem. Lett.* **2009**, *19*, 2789.
- Imanishi, M.; Negi, S.; Sugiura, Y. *Methods Mol. Biol.* **2010**, *649*, 337.
- Negi, S.; Itazu, M.; Imanishi, M.; Nomura, A.; Sugiura, Y. *Biochem. Biophys. Res. Commun.* **2004**, *325*, 421.
- Yokono, M.; Saegusa, N.; Matsushita, K.; Sugiura, Y. *Biochemistry* **1998**, *37*, 6824.
- Negi, S.; Imanishi, M.; Sasaki, M.; Tatsutani, K.; Futaki, S.; Sugiura, Y. *Biochemistry* **2011**, *50*, 6266.
- Woody, R. W. *Methods Enzymol.* **2004**, *380*, 242.



Intrinsic cell permeability of the GAGA zinc finger protein into HeLa cells



Shigeru Negi^{*}, Yuka Terada, Misato Suzuyama, Haruka Matsumoto, Akino Honbo, Yoko Amagase, Yumiko Mizukawa, Akiko Kiriya, Katsumi Iga, Tetsuro Urushidaini, Yukio Sugiura

Faculty of Pharmaceutical Science, Doshisha Women's University, Koudo, Kyotanabe, Kyoto, 610-0395, Japan

ARTICLE INFO

Article history:

Received 7 July 2015

Accepted 11 July 2015

Available online 15 July 2015

Keywords:

GAGA zinc finger

Cell penetrating peptide (CPP)

Intrinsic cell permeability

ABSTRACT

We examined the intrinsic cell permeability of a GAGA zinc finger obtained from the *Drosophila melanogaster* transcription factor and analyzed its mechanism of cellular uptake using confocal microscopy and flow cytometry. HeLa cells were treated with the Cy5-labeled GAGA peptides (containing a fluorescent chromophore) to detect fluorescence signals from the fluorescent labeling peptides by confocal microscopy. The results clearly indicated that GAGA peptides possess intrinsic cell permeability for HeLa cells. Based on the results of the flow cytometry analysis and the theoretical net positive charge of the GAGA peptides, the efficiency of cellular uptake of the GAGA peptides was predicted to depend on the net positive charge of the GAGA peptide as well as the cationic component ratio of Arg residues to Lys residues.

© 2015 Elsevier Inc. All rights reserved.

1. Introduction

Various bioactive substances and functional materials containing cell-penetrating peptides (CPPs) consisting of fewer than 30 amino acid residues can be transported into cells and/or tissues in a non- or low-toxic manner [1–4]. Among these, cationic peptides, such as penetratin, HIV-1 Tat, and oligopeptides, contain a high percentage of basic amino acid residues (Arg and Lys) in the primary sequences, and are regarded to be the most representative CPPs [5–7]. These cationic CPPs are highly efficient in penetrating through biological membranes for the cells transport into cells. The basic mechanisms and applications of cationic CPPs have been widely studied [8–12]. Recent studies have reported the preparation of superpositively charged variants of green fluorescent protein (GFP) by mutating acidic amino acid residues (Glu and Asp) on the solvent-exposed surface to cationic amino acids residues (Arg and Lys), without a loss of proper folding [13–16]. Although wild-type GFP cannot permeate cells, superpositively charged GFPs can pass through cell membranes because of their highly positive two-dimensional cationic cluster on the solvent-exposed protein surface. In addition, superpositively charged GFPs can deliver

functional macromolecules into the cytoplasm of mammalian cells more efficiently than typical unstructured cationic CPPs. This indicates that extraneous cationic CPPs are not essential for the cellular uptake of a protein, and that a positively charged cluster on the well-folded protein surface enables a protein to be membrane permeable. Furthermore, designed small folded proteins with four to six Arg residues [17–19], naturally supercharged human proteins [20], and artificial proteins based on the zinc finger framework [21,22] have been shown to penetrate cells. This suggests that naturally occurring proteins with highly positive charges on the structural surface may penetrate cell membranes based on their intrinsic biological functions.

We previously examined the structure, function, and redesign of zinc finger proteins, which are among the most common DNA-binding domains of transcription factors [23,24]. A zinc finger protein binds to negatively charged DNA because of its positive charge; the positive charge is a result of the high density of basic amino acid residues, such as Arg and/or Lys on the surface. Barbas et al. recently reported that zinc finger nuclease and genetically fused zinc finger motifs can penetrate the cell membrane and efficiently deliver other proteins into cells without any dysfunction [21,22]. The intrinsic cellular uptake potential of native zinc finger proteins was investigated in the GAGA zinc finger, derived from the *Drosophila melanogaster* transcription factor [25]. In contrast to

^{*} Corresponding author.

E-mail address: snegi@dwc.doshisha.ac.jp (S. Negi).

other zinc finger proteins possessing multiple finger domains in tandem fashion, the GAGA zinc finger contains only one Cys2His2-type zinc finger domain (FD) and two basic regions (BR1 and BR2) (Fig. 1A); in addition, this protein can bind to a cognate DNA sequence (GAGAGAG). The GAGA zinc finger is a suitable model for examining the intrinsic cell permeability of zinc finger proteins because of its simple structure compared to other zinc finger proteins. In this study, a full-length GAGA zinc finger (GAGA) and its deleted mutants (FD, BR1-BR2, BR1, and BR2) were synthesized (Fig. 1B) in order to clarify the intrinsic cell permeability of the GAGA zinc finger. We also examined which regions of the GAGA zinc finger mainly contributed to HeLa cell penetration by confocal microscopy and fluorescence-activated cell sorting (FACS).

2. Materials and methods

2.1. Preparation and fluorescent labeling of GAGA peptides

The DNA fragment encoding GAGA was obtained from Life Technologies (Carlsbad, CA, USA) and used as an insert to construct the protein expression vector. The insert DNA was cleaved using *NdeI* and *EcoRI* and inserted into the multicloning site of the pET-17b vector (Novagen, Madison, WI, USA). The sequence of the constructed expression vector was confirmed using a 3130 Genetic Analyzer (Applied Biosystems, Foster City, CA, USA). BL21(DE3) codon plus strain (Agilent Technologies, Santa Clara, CA, USA) *Escherichia coli* cells were grown at 37 °C until an optical density at 600 nm (OD_{600}) of 0.6 was reached. *E. coli* were then incubated for an additional 12 h at 25 °C in the presence of 0.1 mM isopropyl β -D-1 thiogalactopyranoside and 0.1 mM $ZnCl_2$, in order to obtain soluble GAGA zinc finger protein. Overexpressed proteins were purified by cation-exchange chromatography using a Bio-Scale Mini High S (Bio-Rad, Hercules, CA, USA) and desalting using Bio-Gel P-6 (Bio-Rad) columns. Final purification was performed using a Cosmosil 5C₁₈-ARII (10 × 250 mm; Nacalai Tesque, Inc., Kyoto, Japan) reverse-phase high-performance liquid chromatography (RP-HPLC) column. The fidelity of the purified protein was confirmed by SDS-PAGE (data not shown) and matrix-associated laser desorption ionization time-of-flight mass spectroscopy (MALDI-TOF-MS) using a Voyager-DE STR system (AB SCIEX, Framingham, MA, USA).

Each deletion GAGA mutant (FD, BR1-BR2, BR1, and BR2) (Fig. 1B) was synthesized on TGS-RAM resin (Shimadzu Corporation, Kyoto, Japan) using a standard Fmoc solid-phase method (2-(1H-benzotriazole-1-yl)-1,1,3,3-tetramethyluronium hexafluorophosphate (HBTU)/1-hydroxybenzotriazole (HOBT) serving as the coupling reagent), with a PSSM-8 synthesizer (Shimadzu Corporation) (Fig. 1). The synthesized peptides were removed from the resin by incubation with 86% trifluoroacetic acid, 2.5% water, 5% 1,2-ethanedithiol, 5% thioanisole and 1.5% triethylsilane for 3 h. The crude peptides were then precipitated in ice-cold ether, separated by centrifugation, washed three times with cold diethyl ether, and dissolved in water and lyophilized. The peptide was purified using a Cosmosil 5C₁₈-ARII RP-HPLC column (10 × 250 mm; Nacalai Tesque). The fidelity of the products was confirmed by MALDI-TOF MS using a Voyager DE STR (AB SCIEX). GAGA peptides were fluorescently labeled by introducing a Lys-Cys-Lys sequence into the C-terminus of each peptide; the samples were fluorescently-labeled by treatment with 3 equivalents of Cy5 (GE Healthcare, Little Chalfont UK) in 100 mM HEPES (pH 7.5) for 18 h at room temperature, and subsequently purified using a Cosmosil 5C₁₈-ARII RP-HPLC column (10 × 250 mm; Nacalai Tesque). The fluorescently-labeled peptides were confirmed by MALDI-TOF MS using a Voyager DE STR (AB SCIEX). MALDI-TOF-MS data is summarized in Table 1.

2.2. Cell culture

HeLa cells were purchased from the Riken BRC Cell Bank (Ibaraki, Japan). HeLa cells were cultured in a growth medium (α -MEM supplemented with 10% heat-inactivated fetal bovine serum (Gibco, Grand Island, NY, USA) and MEM non-essential amino acids). Cells were grown in T75-flasks and incubated at 37 °C in a 5% CO₂ incubator, to an approximate confluence of 70%. The cells were sub-cultured every 3–4 days.

2.3. Confocal microscopy

HeLa cells (1×10^5 cells/2 mL) were plated onto the 35 mm glass-bottomed dishes (Iwaki) and cultured in growth medium for 24 h at 37 °C in a 5% CO₂ incubator. The nuclei of living HeLa cells

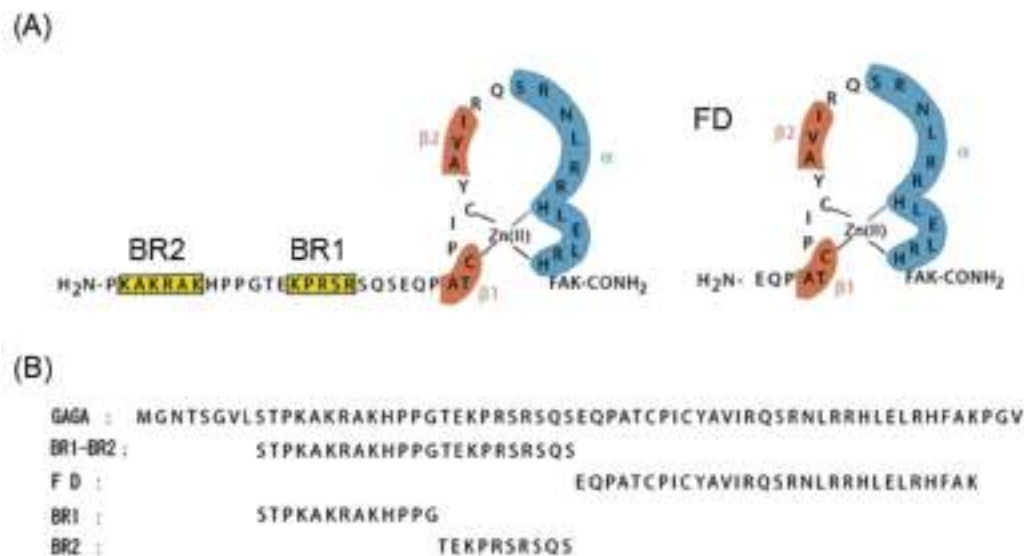


Fig. 1. (A) Schematic representation of the GAGA zinc finger protein. Yellow boxed sequences indicate the basic regions (BR1 and BR2) flanking the zinc finger domain (FD). (B) Amino acid sequences of full-length GAGA zinc finger protein and its deletion mutants used in this study. All GAGA peptides contained a KCK amino acid sequence at the C-terminus of the peptides. (For interpretation of the references to color in this figure legend, the reader is referred to the web version of this article.)

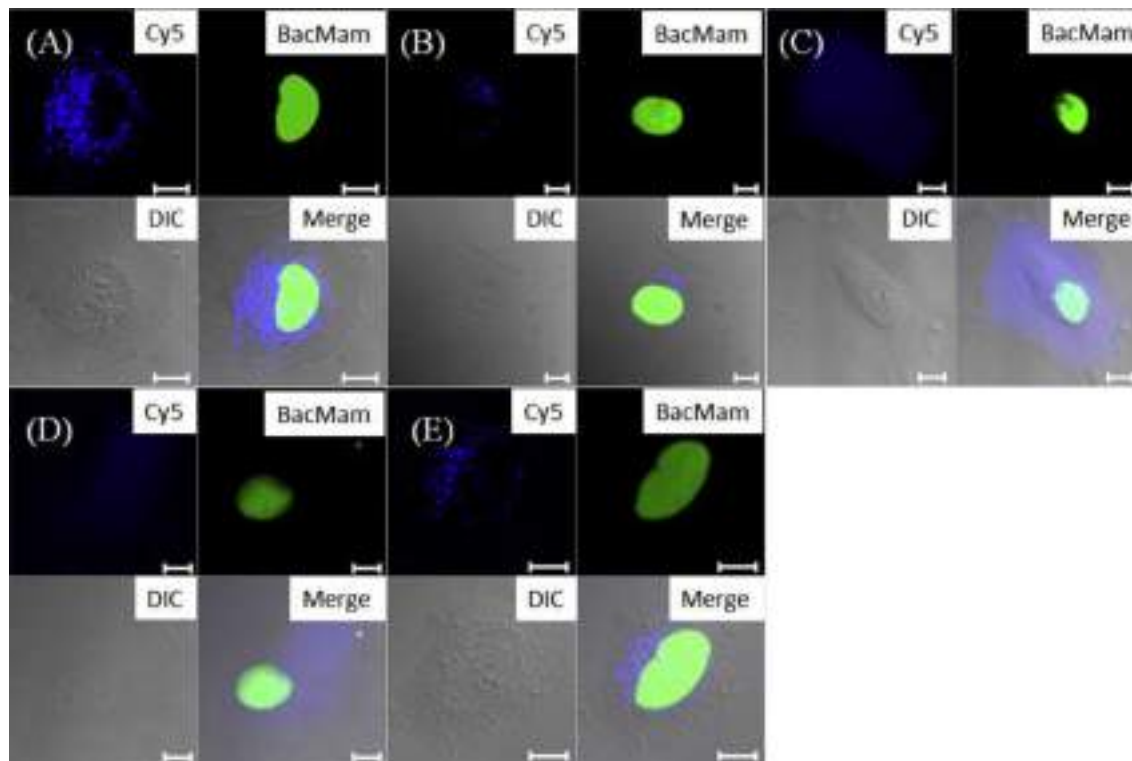


Fig. 2. Cy5-labeled GAGA zinc finger peptides (A; GAGA, B; FD, C; BR1–BR2, D; BR1, and E; BR) were transduced into HeLa cells. Peptide localization in the cells was observed by confocal microscopy ($\times 63$ objective lens). Scale Bar, 10 μm .

Table 1

Calculated and measured molecular weights of GAGA zinc fingers and their Cy5-labeled peptides.^a

Peptide	Calculated [MH ⁺]	Measured [MH ⁺]
GAGA	7489.0 (+Cy5 8267.0)	7357.0 (+Cy5 8139.5)
FD	3837.6 (+Cy5 4615.6)	3834.1 (+Cy5 4616.8)
BR1-BR2	3053.6 (+Cy5 3831.6)	3052.5 (+Cy5 3830.1)
BR1	1896.2 (+Cy5 2674.2)	1895.6 (+Cy5 2673.5)
BR2	1697.0 (+Cy5 2475.0)	1694.6 (+Cy5 2472.8)
FD(Ala)	3773.4 (+Cy5 4551.4)	3768.3 (+Cy5 4550.2)

^a Molecular weight is measured by MALDI-TOF-MASS.

were labeled with GFP by adding CellLight[®] Nucleus-RFP, BacMam 2.0 (30 particles/cell) to the culture medium. The concentrations of Cy5-labeled peptide stock solutions were spectrophotometrically estimated (absorbance of Cy5 at 650 nm; $\epsilon = 250,000$, where ϵ is the extinction coefficient ($\text{M}^{-1} \text{cm}^{-1}$)). The GAGA and FD stock solutions contained 1.5 equivalents of Zn(II) to apo-peptide and 50 μM TCEP. The medium was replaced at 24 h after seeding with fresh Opti-MEM reduced serum medium (Gibco) containing fluorescently labeled peptides (1 μM) and the cells were incubated for 30 min at 37 °C with 5% CO₂. The treated cells were washed five times with phosphate-buffered saline (PBS) and the medium was replaced with fresh growth medium. The distribution of the fluorescently labeled peptides was analyzed by confocal scanning laser microscopy using an LSM 510 (Carl Zeiss AG, Jena, Germany), equipped with a 63 \times or 40 \times objective.

2.4. Flow cytometry

HeLa cells (1×10^6 cells/5 mL) were plated onto 60 mm dishes (Iwaki) containing growth medium for 24 h at 37 °C in a 5% CO₂ incubator. The concentrations of Cy5-labeled peptide stock

solutions were spectrophotometrically estimated (absorbance of Cy5 at 650 nm; $\epsilon = 250,000$, where ϵ is the extinction coefficient ($\text{M}^{-1} \text{cm}^{-1}$)). The GAGA and FD stock solutions contained 1.5 equivalents of Zn(II) to apo-peptide and 50 μM TCEP. The medium was replaced at 24 h after seeding with fresh Opti-MEM reduced serum medium (Gibco) containing the fluorescently labeled peptide (1 μM), and the cells were incubated for 30 min at 37 °C with 5% CO₂. The treated cells were then washed with PBS five times and treated with 0.01% trypsin-EDTA (500 μL) for 5 min at 37 °C. Dissociated cells were suspended in PBS (2 mL) and filtered through a cell strainer (Falcon 70-mm mesh; Corning Life Sciences, Corning, NY, USA). The solution was fluorescently analyzed on a FACSCalibur (BD Biosciences, Franklin Lakes, NJ, USA) flow cytometer using a 635-nm laser excitation and 661-nm emission filter.

2.5. Circular dichroism (CD) measurements

CD was measured using a JASCO J-720 spectropolarimeter (Jasco, Tokyo, Japan). The spectra were recorded in the range of 195–260 nm in the continuous mode with a bandwidth of 1 nm, a response time of 1 s, and a scan speed of 50 nm min⁻¹. Each spectrum was represented by the average of 20 scans at 20 °C, performed in Tris–HCl buffer (10 mM, pH 7.5) containing NaCl (50 mM), in a capped cell with a 0.1-cm path length.

3. Results and discussion

3.1. Cellular uptake and internalization of GAGA peptides

Living HeLa cells were used to study the cellular uptake and internalization of the fluorescently labeled GAGA peptide and its deletion mutants (FD, BR1–BR2, BR1, and BR2) (Fig. 1). Living cells were analyzed by confocal microscopy because of the significant

effect of fixation on the cellular localization of peptides [26]. The GAGA peptide and its mutant peptides were successfully detected in the cells, indicating the capacity of all GAGA peptides to penetrate the cells without the aid of extraneous CPPs. Punctate fluorescent signals emitted as a result of the endosomal trap created by the endocytosis of the GAGA, FD, and BR2 peptides were detected around the cell nuclei. Additionally, the BR1 peptide showed cytosolic dispersion as a result of direct transmembrane and/or cytosol-release mechanisms. Although the confocal image for the BR1-BR2 peptide was similar to that of the BR1 peptide, punctate fluorescence signals were partially detected in the cytosol, suggesting that the cellular uptake of BR1-BR2 mainly occurred through direct transmembrane and/or cytosol-release mechanisms, and partially occurred through endocytosis control. These results indicate that the GAGA and its deleted mutant peptides have intrinsic cell-penetrating abilities; additionally, the presence of two different localized states in the cells was suggested, including the endosomal trapped structure and cytosolic dispersed localization.

3.2. Quantification of cellular uptake of GAGA peptides

The amount of GAGA peptides incorporated by HeLa cells was analyzed by FACS (Fig. 3) in order to quantitatively compare cell permeability. The amount of cellular uptake by the GAGA peptide increased in the order of GAGA > FD > BR1-BR2 > BR1 > BR2. McNaughton et al. [14] suggested that cellular uptake efficiency strongly depends on the magnitude of the net positive charge of a peptide. Therefore, the net charge on the GAGA peptides was calculated using the following equation: theoretical net charge = $(N_{\text{Arg}} + N_{\text{Lys}}) - (N_{\text{Glu}} + N_{\text{Asp}})$, where $N_{\text{a.a.}}$ indicates the total number of amino acids present in the primary sequence (Arg and Lys were positively charged, while Glu and Asp were negatively charged). The total number of total amino acids and the cationic and anionic amino acid residues in the GAGA peptides, as well as their calculated net charges are summarized in Table 2. The peptides in descending order of positive charge were GAGA (+12) > BR1-BR2 (+8) > BR1 (+6) > FD (+5) > BR2 (+4). Cellular uptake of GAGA peptides increased with increasing net positive charge; however, this did not apply for FD. Although the net positive charge of FD (+5) was the second lowest among the studied GAGA peptides, the cellular uptake level was the second highest after the GAGA peptide, with a net positive charge of +12. This confirmed that the net positive charge of a peptide is not the sole factor determining the efficiency of cellular uptake.

3.3. Importance of cationic amino acid composition ratio of Arg to Lys for cellular uptake of GAGA peptide

Schepartz et al. [19] reported that a dispersed arginine

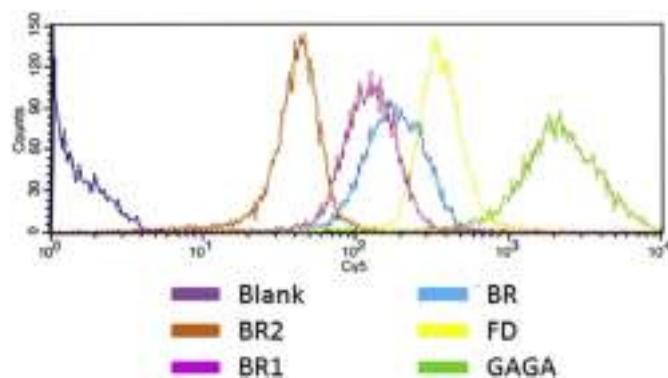


Fig. 3. Penetration of Cy5-labeled GAGA peptides into HeLa cells assessed by FACS.

arrangement on a well-folded structure is important for efficient cellular uptake. The two-dimensional cationic cluster with $\beta\beta\alpha$ secondary structure formed on the finger domain of FD may play a significant role in cellular uptake. In general, a zinc finger domain can fold into a $\beta\beta\alpha$ compact structure by Zn(II) binding. Therefore, mutated FD (FD(Ala)) lacking the Zn(II)-binding ability was prepared by replacing two Cys residues with non-coordinating Ala residues. The folding property of FD(Ala) was analyzed by CD measurement (Fig. S1), as the CD signature of the GAGA zinc finger domain has been well-documented [27]. In the absence of Zn(II), FD(Ala) showed a negative CD band near 200 nm, suggesting that the peptide is largely in a random coiled state. FD(Ala) displayed no spectral change upon addition of Zn(II). The CD data indicated that FD(Ala) did not fold into the characteristic zinc finger $\beta\beta\alpha$ structure because the Zn(II)-binding ability was lacking. Thus, we examined the relationship between the two-dimensional cationic cluster and the cell-penetrating ability of FD by comparing the cellular uptake of structured FD with that of unstructured FD(Ala). The cell permeability of FD(Ala) in HeLa cells was examined by confocal microscopy and FACS (Fig. 4). As shown in Fig. 4A, punctate fluorescence signals for FD(Ala) were detected around the cell nuclei, which were similar to those observed for FD (Fig. 2). Furthermore, the amount of cellular uptake of FD(Ala) was nearly identical to that of FD (Fig. 4B). These results strongly suggest that the two-dimensional cationic cluster formed on the $\beta\beta\alpha$ folding domain of FD does not directly participate in the high cellular permeability of this peptide, because of the small net positive charge.

We then focused on the amino acid ratio of Arg to Lys residues in order to determine the efficiency of cellular uptake of the GAGA peptides. CPPs commonly have a large number of Arg residues in their amino acid sequences. Futaki et al. [7] found that Arg residues play a more important role than Lys residues in the cellular uptake of CPPs. In addition, the hydrogen-bonding interaction between the positively charged guanidino group of an Arg residue and an H-bond acceptor on the cell surface (carboxylic, phosphate, and sulfate groups) resulting from the formation of bidentate hydrogen bonds also participates in membrane permeation [28,29]. Previous studies have compared the efficiency of the cellular uptake of oligoarginine with that of oligolysine [30,31]. In this study, the oligoarginine (Arg8) and oligolysine (Lys8) peptides were prepared with eight single amino acid residues [7], and the internalization and cellular uptake of these oligopeptides was analyzed by confocal microscopy and FACS, respectively. The results of this analysis are shown in Fig. S2. Both peptides had an equivalent positive charge (+8) under physiological conditions (pH 7.1–7.4), the pKa values for the guanidino group of Arg and primary amino group of Lys were 12.48 and 10.54, respectively. In both cases, living cell imaging revealed punctate fluorescent signals around the cell nuclei, suggesting that both peptides were similarly localized within cells. In contrast, internalization of Lys8 was less efficient than that of Arg8. These results agree with those of previous studies [7,30,31]. Despite the presence of the same net positive charge in both peptides, Arg8 showed higher cell permeability compared to Lys8, indicating that Arg residues play a more important role in efficient cellular uptake than do the Lys residues. The composition of cationic amino acid residues in FD for Arg:Lys was 5:2; thus, the ratio of Arg residues was greater than that of Lys residues, which may have resulted in higher cellular uptake of FD.

In summary, the native GAGA zinc finger and its deleted mutants penetrated HeLa cells without requiring additional CPPs. Our results indicate that the GAGA zinc finger peptide has innate cell permeability. Cellular uptake efficiency of the GAGA peptide was influenced by the net positive charge of the peptide, as well as the composition ratio of cationic amino acids (Arg and Lys) in the primary sequence. Because of its capacity for cell permeability, the

Table 2

Numbers of total, cationic and anionic amino acid residues in GAGA peptides and their total net positive charge.

	No. of total amino acid residues	No. of Arg residues	No. of Lys residues	No. of Glu residues	Total net positive charge
GAGA	64	8	7	3	+12
FD	30	5	2	2	+5
BR1–BR2	23	3	6	1	+8
BR1	13	1	5	0	+6
BR2	10	2	3	1	+4

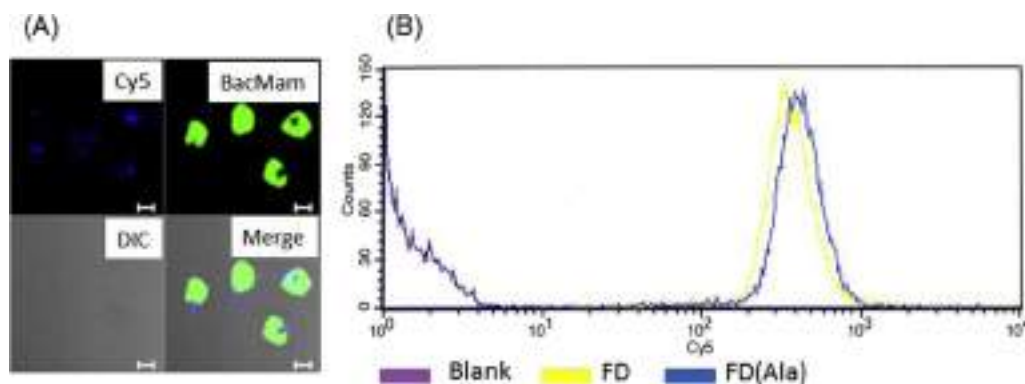


Fig. 4. (A) Localization of the FD(Ala) in the cells was observed by confocal microscopy ($\times 40$ objective lens). Scale Bar, 10 μm . (B) Penetration of Cy5-labeled FD and FD(Ala) into HeLa cells assessed by FACS.

zinc finger protein is a promising tool for delivering the various biological macromolecules (such as protein, nucleic acids, and lipids) into cells. In addition, the cell permeability of the zinc finger protein may contribute to intercellular communication as a signaling biomolecule. Naturally occurring zinc fingers with multi-finger domains require further study.

Acknowledgments

This work was supported in part by a Grant-in-Aid for Scientific Research (No. 23510266 and 26350962) from the Ministry of Education, Culture, Sports, Science, and Technology, Japan.

Appendix A. Supplementary data

Supplementary data related to this article can be found at <http://dx.doi.org/10.1016/j.bbrc.2015.07.060>.

Transparency document

Transparency document related to this article can be found online at <http://dx.doi.org/10.1016/j.bbrc.2015.07.060>.

References

- [1] D.M. Copolovici, K. Langel, et al., Cell-penetrating peptides: design, synthesis, and applications, *ACS Nano* 8 (2014) 1972–1994.
- [2] C. Bechara, S. Sagan, Cell-penetrating peptides: 20 years later, where do we stand? *FEBS Lett.* 587 (2013) 1693–1702.
- [3] E. Koren, V.P. Torchlin, Cell-penetrating peptides: breaking through to the other side, *Trends Mol. Med.* 18 (2012) 385–393.
- [4] F. Milletti, Cell-penetrating peptides: classes, origin, and current landscape, *Drug Discov. Today* 17 (2012) 850–860.
- [5] D. Derossi, A.H. Joliot, G. Chassaing, et al., The third helix of the Antennapedia homeodomain translocates through biological membranes, *J. Biol. Chem.* 269 (1994) 10444–10450.
- [6] E. Vives, P. Brodin, B. Lebleu, A truncated HIV-1 Tat protein basic domain rapidly translocates through the plasma membrane and accumulates in the cell nucleus, *J. Biol. Chem.* 272 (1997) 16010–16017.
- [7] S. Futaki, T. Suzuki, W. Ohashi, et al., Arginine-rich peptides. An abundant source of membrane-permeable peptides having potential as carriers for intracellular protein delivery, *J. Biol. Chem.* 276 (2001) 5836–5840.
- [8] S. Futaki, Special theme issue on membrane permeable peptide vectors: chemistry and functional design for the therapeutic applications, *Adv. Drug Deliv. Rev.* 60 (2008) 447–614.
- [9] A. van den Berg, S.F. Dowdy, Protein transduction domain delivery of therapeutic macromolecules, *Curr. Opin. Biotechnol.* 22 (2011) 888–893.
- [10] W. Wang, S. Abbad, Z. Zhang, et al., Cell-penetrating peptides for cancer-targeting therapy and imaging, *Curr. Cancer Drug. Targets* 15 (2015) 337–351.
- [11] N. Schmidt, A. Mishra, G.H. Lai, et al., Arginine-rich cell-penetrating peptides, *FEBS Lett.* 584 (2010) 1806–1813.
- [12] R. Brock, The uptake of arginine-rich cell-penetrating peptides: putting the puzzle together, *Bioconjug. Chem.* 25 (2014) 863–868.
- [13] S.M. Fuchs, R.T. Raines, Arginine grafting to endow cell permeability, *ACS Chem. Biol.* 2 (2007) 167–170.
- [14] B.R. McNaughton, J.J. Cronican, D.B. Thompson, et al., Mammalian cell penetration, siRNA transfection, and DNA transfection by supercharged proteins, *Proc. Natl. Acad. Sci. U. S. A.* 106 (2009) 6111–6116.
- [15] J.J. Cronican, D.B. Thompson, K.T. Beier, et al., Potent delivery of functional proteins into mammalian cells in vitro and in vivo using supercharged protein, *ACS Chem. Biol.* 5 (2010) 747–752.
- [16] M.S. Lawrence, K.J. Phillips, D.R. Liu, Supercharging proteins can impart unusual resilience, *J. Am. Chem. Soc.* 129 (2007) 10110–10112.
- [17] B.A. Smith, D.S. Daniels, A.E. Coplin, et al., Minimally cationic cell-permeable miniature proteins via α -helical arginine display, *J. Am. Chem. Soc.* 130 (2008) 2948–2949.
- [18] D.S. Daniels, A. Schepartz, Intrinsically cell-permeable miniature proteins based on a minimal cationic PPII motif, *J. Am. Chem. Soc.* 129 (2007) 14578–14579.
- [19] J.S. Appelbaum, J.R. LaRoche, B.A. Smith, et al., Arginine topology controls escape of minimally cationic proteins from early endosomes to the cytoplasm, *Chem. Biol.* 19 (2012) 819–830.
- [20] J.J. Cronican, K.T. Beier, T.N. Davis, et al., A class of human proteins that deliver functional proteins into mammalian cells in vitro and in vivo, *Chem. Biol.* 18 (2011) 833–838.
- [21] T. Gaj, J. Guo, Y. Kato, et al., Target gene knockout by direct delivery of zinc-finger nuclease proteins, *Nat. Methods* 9 (2012) 805–807.
- [22] T. Gaj, J. Liu, K.E. Anderson, et al., Protein delivery using Cys₂-His₂ zinc-finger domains, *ACS Chem. Biol.* 9 (2014) 1662–1667.
- [23] S. Negi, M. Imanishi, M. Matsumoto, et al., New redesigned zinc-finger proteins: design strategy and its application, *Chem. Eur. J.* 14 (2008) 3236–3249.
- [24] M. Dhanasekaran, S. Negi, Y. Sugiura, Designer zinc finger proteins: tools for creating artificial DNA-binding functional proteins, *Acc. Chem. Res.* 39 (2006) 45–52.
- [25] P.V. Pedone, R. Ghirlando, G.M. Clore, et al., The single Cys₂-His₂ zinc finger domain of the GAGA protein flanked by basic residues is sufficient for high-affinity specific DNA binding, *Proc. Natl. Acad. Sci. U. S. A.* 93 (1996) 2822–2826.
- [26] J.P. Richard, K. Melikov, E. Vives, et al., Cell-penetrating peptides. A reevaluation of the mechanism of cellular uptake, *J. Biol. Chem.* 278 (2003) 585–590.

- [27] M. Dhanasekaran, S. Negi, M. Imanishi, et al., DNA-binding ability of GAGA zinc finger depends on the nature of amino acids present in the β -hairpin, *Biochemistry* 46 (2007) 7506–7513.
- [28] J.B. Rothbard, T.C. Jessop, R.S. Lewis, et al., Role of membrane potential and hydrogen binding in the mechanism of translocation of guanidinium-rich peptides into cells, *J. Am. Chem. Soc.* 126 (2004) 9506–9507.
- [29] F. Perret, M. Nishihara, T. Takeuchi, et al., Anionic fullerenes, calixarenes, coronenes, and pyrens as activators of oligo/polyarginines in model membrane and live cells, *J. Am. Chem. Soc.* 127 (2005) 1114–1115.
- [30] D.J. Mitchell, D.T. Kim, L. Steinman, et al., Polyarginine enters more efficiently than other polycationic homopolymers, *J. Pept. Res.* 56 (2000) 318–325.
- [31] H.L. Amand, H.A. Rydberg, L.H. Fornander, et al., Cell surface binding and uptake of arginine- and lysine-rich penetratin peptides in absence and presence of proteoglycans, *Biochim. Biophys. Acta* 18 (2012) 2669–2678.

Arginine Residues Provide a Multivalent Effect for Cellular Uptake of a Hemoprotein Assembly

Koji Oohora,^{*1,2} Ryota Kajihara,¹ Misa Jiromaru,³ Hiroaki Kitagishi,^{*3} and Takashi Hayashi^{*1}

¹Department of Applied Chemistry, Graduate School of Engineering, Osaka University, Suita, Osaka 565-0871, Japan

²PRESTO, Japan Science and Technology Agency (JST), Kawaguchi, Saitama 332-0012, Japan

³Department of Molecular Chemistry and Biochemistry, Faculty of Science and Engineering, Doshisha University, Kyotanabe, Kyoto 610-0321, Japan

E-mail: oohora@chem.eng.osaka-u.ac.jp (K. Oohora), hkitagis@mail.doshisha.ac.jp (H. Kitagishi), thayashi@chem.eng.osaka-u.ac.jp (T. Hayashi)

Cellular uptake of rigid and flexible supramolecular hemoprotein assemblies formed by cytochrome *b*₅₆₂ was investigated. Multivalent cell-penetrating tags on the protein surfaces of the assemblies improve the efficiency of cellular uptake into HeLa cells in a manner which depends on the number of arginine residues in the tags and the main-chain rigidity of the assemblies. A rigid protein assembly with an arginine tetramer tag shows 10-fold higher cellular uptake efficiency than a corresponding assembly without an arginine tag.

Keywords: Supramolecular assembly | Arginine tag | Multivalent effect

Artificially-constructed supramolecular protein assembling systems are promising materials for biological applications due to their general biocompatibility and sub-micrometer size range.^{1,2} Over this past decade, great efforts of chemists and biologists have demonstrated several approaches for preparing supramolecular protein assemblies using synthetic and/or genetic strategies.³ Various structures and sizes of protein assemblies are now available and some of them can be directly observed by microscopy method and/or X-ray crystallography. While examples of applications of these systems have been limited so far, it is expected that such protein assemblies will soon be used in applications: artificial enzymes,⁴ light harvesting antennas⁵ and drug delivery systems^{6,7} among others. In this context, we have focused on the cellular uptake of proteins using a multivalent effect provided by the supramolecular assembly.⁸

It is known that assembled arginine (Arg, R) residues can induce cell penetration. It is also known that an arginine octamer (R8) tag acts as a cell penetrating peptide which is used to deliver various types of cargo into cells.⁹ As a starting point, we proposed that an arginine cluster formed in an artificially controlled protein self-assembly would allow us to construct a unique system for cellular uptake.¹⁰ While a protein monomer with a small arginine tag would not be taken up by cells, an assembly of the protein units would provide the arginine cluster needed to the penetrate the cell.

Our group has demonstrated the construction of a supramolecular assembling system based on cytochrome *b*₅₆₂ (Cyt *b*₅₆₂), a simple electron transfer hemoprotein (Figure 1).¹¹ Recently, the reaction of a maleimide-tethered heme analogue with an N80C mutant of Cyt *b*₅₆₂ was found to provide a rigid supramolecular assembly via a successive heme–heme pocket interaction and additional secondary hydrogen bonding interactions at the protein interfaces.¹² The rigid structure was characterized by molecular dynamics simulation, circular dichroism (CD) spectroscopy and atomic force microscopy as a

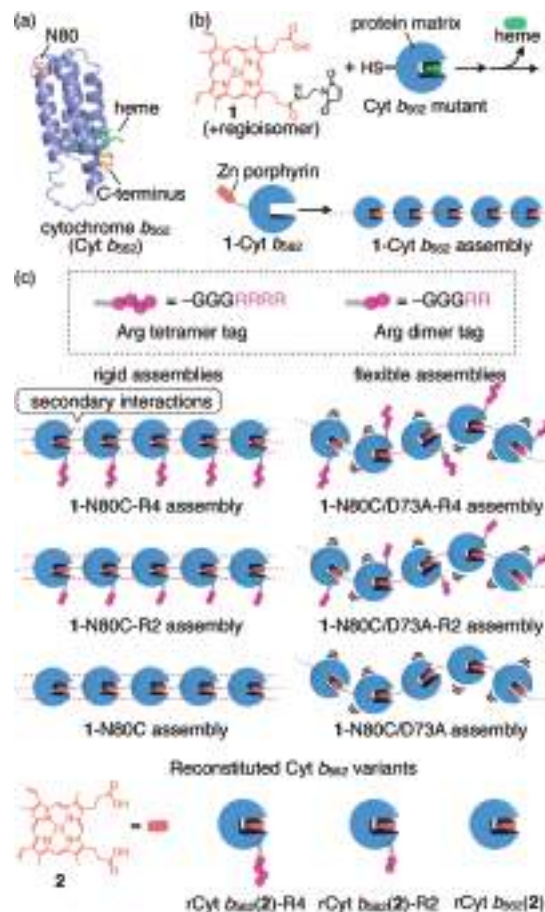


Figure 1. (a) Solution structure of wild type Cyt *b*₅₆₂ (PDB ID: 1QPU) (b) General scheme for preparation of 1-Cyt *b*₅₆₂ assembly. (c) Schematic representation of the rigid/flexible assemblies and rCyt *b*₅₆₂(2) variants used for cellular uptake in this study. Plausible helical structure of 1-N80C-R4 assembly is depicted in Figure S1.

periodic helical fiber with 3-nm pitches. Furthermore, a flexible assembly was generated in the same manner using an N80C/D73A mutant, suggesting that Asp73 is a key residue for secondary interactions in the rigid assembly. In this study, we investigated the cellular uptake of both the rigid and flexible hemoprotein assemblies with arginine tags where the arginine dimer R2 or tetramer R4 tag is attached onto each protein surface. R2 and R4 generally do not provide the ability to penetrate cells.⁹ It was believed that the rigid assembly would be efficiently taken up into the cells due to a multivalent interaction

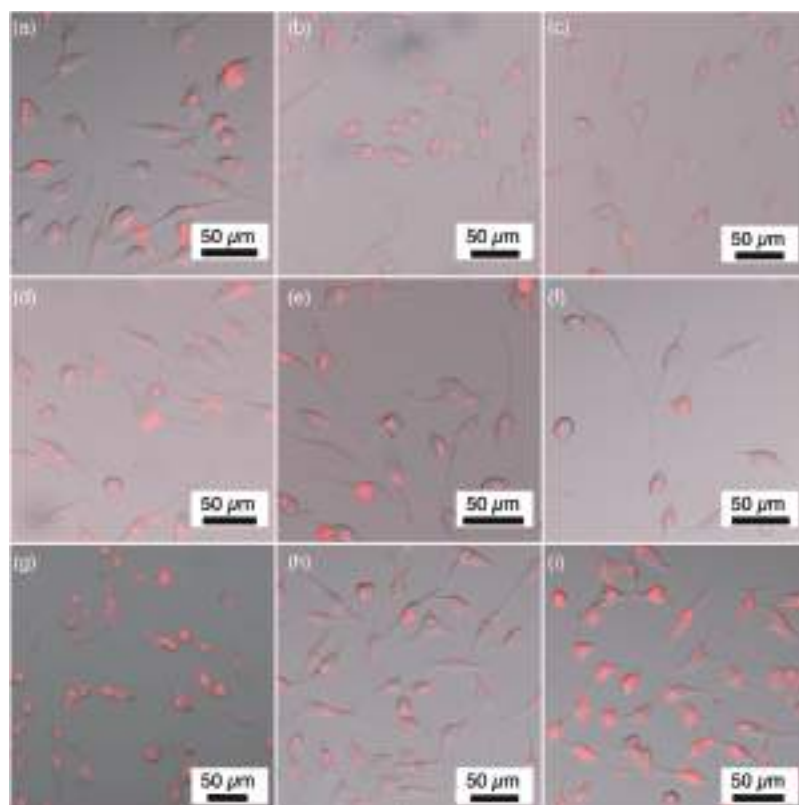


Figure 2. The overlaid fluorescence/bright field microscopic images of HeLa cells incubated with (a) **1-N80C-R4** assembly, (b) **1-N80C-R2** assembly, (c) **1-N80C** assembly, (d) **1-N80C/D73A-R4** assembly, (e) **1-N80C/D73A-R2** assembly, (f) **1-N80C/D73A** assembly, (g) **rCyt b_{562} (2)-R4** (h) **rCyt b_{562} (2)-R2** and (i) **rCyt b_{562} (2)**. $\lambda_{\text{ex}} = 488$ nm for assemblies or 561 nm for **rCyt b_{562} (2)** variants; $\lambda_{\text{obs}} = 570\text{--}620$ nm. The separated bright field and fluorescence images are shown in Figures S5 and S6.

between arginine residues and the cell surface. The multivalent effect provided by pre-organized arginine residues displayed on the same sides of the linear assembly is schematically shown as **1-N80C-R4** and **1-N80C-R2** in Figure 1.

We attached R4 and R2 via glycine trimers as linkers at the C-termini of the N80C mutant to obtain **N80C-R4** and **N80C-R2**, respectively, as shown in Figure 1c. Instead of heme, Zn porphyrin was employed as a cofactor¹³ because its fluorescence is useful for monitoring the cellular uptake events. The reaction of maleimide-tethered Zn porphyrin **1** with **N80C-R4**, **N80C-R2** and **N80C** mutants afforded **1-N80C-R4**, **1-N80C-R2** and **1-N80C**, respectively. After removal of the native heme cofactor from the protein, size exclusion chromatography and UV-vis/CD spectroscopy experiments (Figures S2–S4)¹⁴ indicated the formation of the **1-N80C**, **1-N80C-R2** and **1-N80C-R4** assemblies as shown in Figure 1. The CD spectra of the assemblies (Figure S4) are particularly useful because they show split-type Cotton effects at the Soret band absorptions. As described in our previous report, such split-type Cotton effects provide an indicator of a heme analogue within a rigid assembly. In a similar manner, **1-N80C/D73A-R4**, **1-N80C/D73A-R2** and **1-N80C/D73A** assemblies were designed as flexible assemblies, and then prepared and characterized (Figures 1, S2–S4). The CD spectra of these flexible assemblies are similar to the CD spectrum of monomeric Zn-substituted Cyt b_{562} as a result of their flexibility. As a control sample in investigation of the multivalent effect, we also prepared wild-type Cyt b_{562} recon-

stituted with Zn protoporphyrin IX (**2**), **rCyt b_{562} (2)**. The Arg tetramer (R4) and Arg dimer (R2)-attached variants, **rCyt b_{562} (2)-R4** and **rCyt b_{562} (2)-R2**, respectively, were also prepared.

Cellular uptake events of both of the rigid and flexible assemblies were investigated using HeLa cells and characterized by fluorescence microscopy. The culture medium (OPTI-MEM) containing the assemblies was added to cells adhered to a glass-bottom dish and the cells were incubated for 30 min at 37 °C. Fluorescence microscopy measurements of the cells were made after washing with phosphate buffered saline (PBS). Figures 2a–2f show the fluorescence micrographs. Interestingly, fluorescence intensity detected in the range of 570–620 nm, indicating fluorescence from Zn porphyrin, was observed in all cases, indicating uptake of all of the assemblies. The fluorescence intensities measured for the cells treated with **1-N80C-R4**, **1-N80C/D73A-R4** and **1-N80C/D73A-R2** assemblies are stronger than those observed in the case of **1-N80C** and **1-N80C/D73A** assemblies.¹⁵ These results indicate that cellular uptake efficiency is qualitatively enhanced by introduction of Arg dimer/tetramer tags onto the protein surface compared to the corresponding assemblies without Arg tags. In contrast, surprisingly, similar fluorescence was observed in the cells treated with corresponding monomer samples, **rCyt b_{562} (2)-R4** and **rCyt b_{562} (2)-R2**. The strong fluorescence was also detected with **rCyt b_{562} (2)** despite the absence of the Arg tag. Here, we doubted that the cofactor **2** itself was incorporated because **2** is non-covalently bound in the heme pocket via the reversible

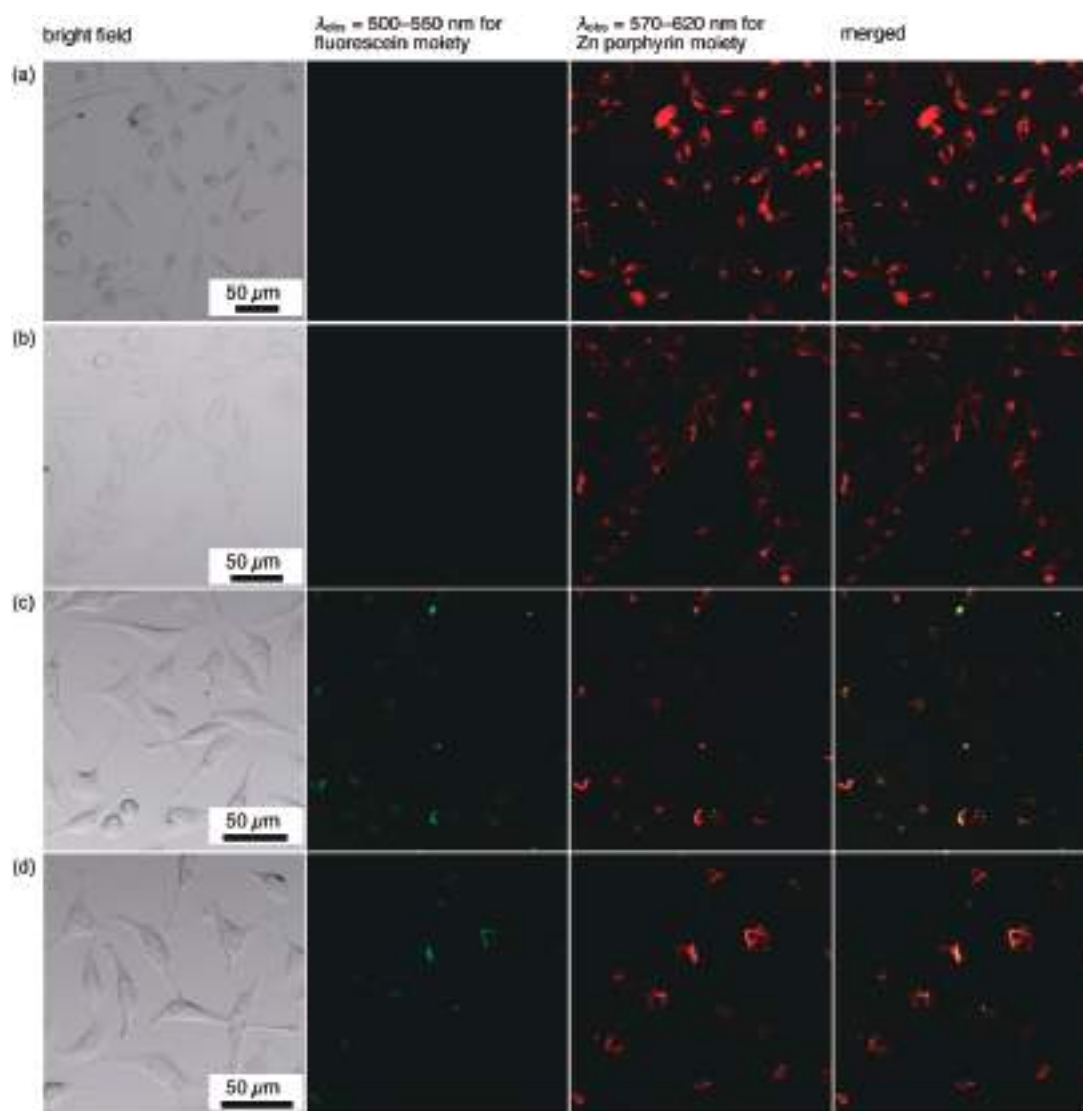


Figure 3. Bright field and fluorescence microscopic images of HeLa cells incubated with (a) Flu-rCyt $b_{562}(\mathbf{2})$, (b) Flu-rCyt $b_{562}(\mathbf{2})$ -R4, (c) FITC-labeled $\mathbf{1}$ -N80C-R4 assembly and (d) FITC-labeled $\mathbf{1}$ -N80C/D73A-R4 assembly. $\lambda_{\text{ex}} = 488$ nm (for fluorescein and $\mathbf{1}$) and 561 nm (for $\mathbf{2}$).

interactions ($K_d = 500$ nM in rCyt $b_{562}(\mathbf{2})$).¹⁶ To confirm this possibility, the protein surfaces of N80C and N80C-R4 reconstituted with $\mathbf{2}$ were quantitatively conjugated with fluorescein-5-maleimide at the Cys80 positions to provide Flu-rCyt $b_{562}(\mathbf{2})$ and Flu-rCyt $b_{562}(\mathbf{2})$ -R4, respectively. The cells were treated with these proteins and the cellular uptake was evaluated by fluorescence microscopy. Figures 3a and 3b show no green fluorescence from fluorescein moiety in the cells treated with rCyt $b_{562}(\mathbf{2})$ and Flu-rCyt $b_{562}(\mathbf{2})$ -R4, whereas strong red fluorescence was observed from $\mathbf{2}$. This finding clearly indicates that there is no incorporation of the protein scaffolds into the cells in the case of rCyt $b_{562}(\mathbf{2})$ and Flu-rCyt $b_{562}(\mathbf{2})$ -R4 and only the cofactor $\mathbf{2}$ which has dissociated from the heme pocket was internalized into the cells. The incorporation of the protein moieties in the assembly systems was confirmed using fluorescein isothiocyanate (FITC)-labeled $\mathbf{1}$ -N80C-R4 and $\mathbf{1}$ -N80C/D73A-R4 (Figures 3c and 3d).¹⁷ Both red and green fluorescence from Zn porphyrin and fluorescein moieties were well

matched in the merged images, indicating the incorporation of the whole system.¹⁸ In contrast to the Arg octamer tag, the Arg dimer/tetramer tags did not provide adequate cell penetration.⁹ However, the multivalent effect induced by the assembly appears to provide sufficient cell penetrating ability.¹⁹

Relative cellular uptake efficiencies of the protein assemblies were evaluated by measuring the fluorescence spectra of the cell lysates (Figure S8). The fluorescence intensities derived from Zn porphyrin were analyzed by peak fitting as shown in Figure S9. Figure 4 shows the cellular uptake efficiencies of $\mathbf{1}$ -N80C-R4, $\mathbf{1}$ -N80C-R2, $\mathbf{1}$ -N80C/D73A-R4, $\mathbf{1}$ -N80C/D73A-R2, and $\mathbf{1}$ -N80C/D73A relative to $\mathbf{1}$ -N80C. Introduction of the Arg dimer/tetramer tags significantly increases the cellular uptake efficiencies: 2.0-fold and 10-fold increases in $\mathbf{1}$ -N80C-R2 and $\mathbf{1}$ -N80C-R4 were respectively observed relative to $\mathbf{1}$ -N80C, and the 1.4-fold and 2.6-fold increases in $\mathbf{1}$ -N80C/D73A-R2 and $\mathbf{1}$ -N80C/D73A-R4 were respectively observed relative to $\mathbf{1}$ -N80C/D73A. In a comparison of the rigid and flexible

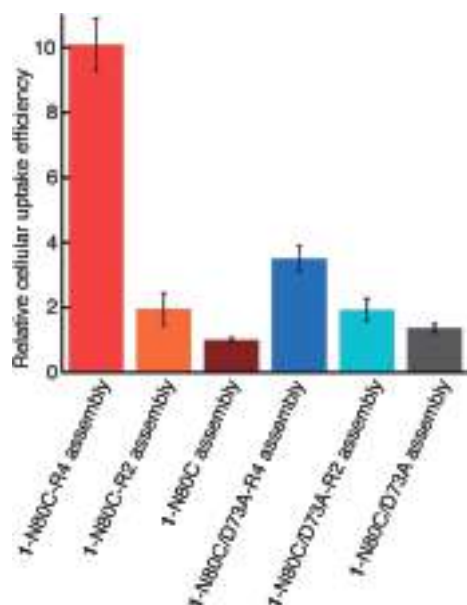


Figure 4. Relative cellular uptake efficiencies based on fluorescence intensities of the lysate of the cell treated with the assemblies.

assemblies, the rigid 1-N80C-R4 assembly demonstrates the 2.9-fold higher efficiency than the corresponding flexible assembly with the same arginine tag (1-N80C/D73A-R4). This finding suggests that the preorganized Arg tetramer moieties in the rigid assembly provide more effective cell-penetration than the randomly positioned Arg tetramer moieties in the flexible assembly, possibly because additional Arg residues are interacting with the negatively-charged cell surface.

In summary, cellular uptake efficiencies of flexible and rigid Zn-substituted cytochrome *b*₅₆₂ assemblies with Arg dimer/tetramer tags were investigated. The combination of the Arg tetramer tag and the rigid assembly provides the best cellular uptake efficiency. Although the Arg octamer (R8) is known as the best cell-penetration peptide tag, the multivalent effect of shorter Arg tags in the assembly provides enhanced cell-penetrating ability. The present rigid protein self-assembling system can induce the efficient multivalent effects of preorganized functional groups on the helical structure. This finding is expected to contribute to the development of artificial protein assemblies for use in cellular delivery applications based on the multivalent effect.

This work was supported by Grants-in-Aid for Scientific Research provided by JSPS KAKENHI Grant Numbers JP15H05804, JP15H00873, JP16K14036, JP16H06045, JP16H00837, JP18KK0156, and the MEXT-Supported Program for the Strategic Research Foundation at Private Universities (2015–2019). We appreciate support from JST PRESTO (JPMJPR15S2) and SICORP.

Supporting Information is available on <https://doi.org/10.1246/cl.180897>.

References and Notes

1 M. G. Ryadnov, D. N. Woolfson, in *Nanobiotechnology II*, ed. by C. A.

- Mirkin, C. M. Niemeyer, Wiley-VCH, Weinheim, **2007**, Ch. 2, pp. 17–38. doi:10.1002/9783527610389.ch2.
- 2 A. Fegan, B. White, J. C. T. Carlson, C. R. Wagner, *Chem. Rev.* **2010**, *110*, 3315.
- 3 a) J. C. T. Carlson, S. S. Jena, M. Flenniken, T. Chou, R. A. Siegel, C. R. Wagner, *J. Am. Chem. Soc.* **2006**, *128*, 7630. b) M. M. C. Bastings, T. F. A. de Greef, J. L. J. van Dongen, M. Merckx, E. W. Meijer, *Chem. Sci.* **2010**, *1*, 79. c) Y. Suzuki, G. Cardone, D. Restrepo, P. D. Zavattieri, T. S. Baker, F. A. Tezcan, *Nature* **2016**, *533*, 369. d) S. Gonen, F. DiMaio, T. Gonen, D. Baker, *Science* **2015**, *348*, 1365. e) T. Komatsu, X. Qu, H. Ihara, M. Fujihara, H. Azuma, H. Ikeda, *J. Am. Chem. Soc.* **2011**, *133*, 3246. f) Y.-T. Lai, D. Cascio, T. O. Yeates, *Science* **2012**, *336*, 1129. g) Y. Hsia, J. B. Bale, S. Gonen, D. Shi, W. Sheffler, K. K. Fong, U. Nattermann, C. Xu, P.-S. Huang, R. Ravichandran, S. Yi, T. N. Davis, T. Gonen, N. P. King, D. Baker, *Nature* **2016**, *535*, 136. h) T. Miyamoto, M. Kuribayashi, S. Nagao, Y. Shomura, Y. Higuchi, S. Hirota, *Chem. Sci.* **2015**, *6*, 7336. i) K. Oohora, S. Burazerovic, A. Onoda, Y. M. Wilson, T. R. Ward, T. Hayashi, *Angew. Chem., Int. Ed.* **2012**, *51*, 3818. j) S. van Dun, C. Ottmann, L.-G. Milroy, L. Brunsveld, *J. Am. Chem. Soc.* **2017**, *139*, 13960. k) Q. Luo, C. Hou, Y. Bai, R. Wang, J. Liu, *Chem. Rev.* **2016**, *116*, 13571. l) K. Matsuura, *Chem. Commun.* **2018**, *54*, 8944.
- 4 W. J. Song, F. A. Tezcan, *Science* **2014**, *346*, 1525.
- 5 L. Miao, J. Han, H. Zhang, L. Zhao, C. Si, X. Zhang, C. Hou, Q. Luo, J. Xu, J. Liu, *ACS Nano* **2014**, *8*, 3743.
- 6 S. Biswas, K. Kinbara, T. Niwa, H. Taguchi, N. Ishii, S. Watanabe, K. Miyata, K. Kataoka, T. Aida, *Nat. Chem.* **2013**, *5*, 613.
- 7 Q. Li, C. R. So, A. Fegan, V. Cody, M. Sarikaya, D. A. Vallera, C. R. Wagner, *J. Am. Chem. Soc.* **2010**, *132*, 17247.
- 8 a) K. Oohora, T. Hayashi, *Curr. Opin. Chem. Biol.* **2014**, *19*, 154. b) K. Oohora, A. Onoda, T. Hayashi, *Chem. Commun.* **2012**, *48*, 11714.
- 9 a) S. Futaki, T. Suzuki, W. Ohashi, T. Yagami, S. Tanaka, K. Ueda, Y. Sugiura, *J. Biol. Chem.* **2001**, *276*, 5836. b) S. Futaki, *Pept. Sci.* **2006**, *84*, 241. c) M. Kosuge, T. Takeuchi, I. Nakase, A. T. Jones, S. Futaki, *Bioconjugate Chem.* **2008**, *19*, 656.
- 10 a) S. van Dun, J. Schill, L.-G. Milroy, L. Brunsveld, *Chem.—Eur. J.* **2018**, *24*, 16445. b) Y.-R. Yoon, Y. Lim, E. Lee, M. Lee, *Chem. Commun.* **2008**, 1892.
- 11 H. Kitagishi, Y. Kakikura, H. Yamaguchi, K. Oohora, A. Harada, T. Hayashi, *Angew. Chem., Int. Ed.* **2009**, *48*, 1271.
- 12 K. Oohora, N. Fujimaki, R. Kajihara, H. Watanabe, T. Uchihashi, T. Hayashi, *J. Am. Chem. Soc.* **2018**, *140*, 10145.
- 13 A. Onoda, Y. Kakikura, T. Uematsu, S. Kuwabata, T. Hayashi, *Angew. Chem., Int. Ed.* **2012**, *51*, 2628.
- 14 Size exclusion chromatography traces in Figure S2 indicate that the assemblies have the broad molecular weight distributions: dimer to ca. 30 mer in 1-N80C-R4; dimer to ca. 20 mer in 1-N80C-R2; dimer to ca. 30 mer in 1-N80C; dimer to ca. 20 mer in 1-N80C/D73A-R4; dimer to ca. 15 mer in 1-N80C/D73A-R2 and dimer to ca. 20 mer in 1-N80C/D73A.
- 15 In the fluorescence microscopy, the differences in fluorescence intensity between cells treated with 1-N80C-R2 and 1-N80C assemblies is negligible.
- 16 E. A. D. Pia, Q. Chi, M. Elliott, J. E. Macdonald, J. Ulstrup, D. D. Jones, *Chem. Commun.* **2012**, *48*, 10624.
- 17 Approximately one FITC molecule per five Zn porphyrin moieties is attached to the protein unit in the FITC-labeled assemblies, which were confirmed by UV-vis spectra as shown in Figure S7.
- 18 In the present study, experimental results to evaluate the protein structure after the incorporation into the cell are unavailable and it is under investigation.
- 19 The mechanism of the incorporation is considered to be the typical endocytosis which is seen in other cell-penetrating peptides (ref 20). This is supported by the punctate fluorescence signals derived from Zn porphyrin moieties on the protein units incorporated into the cell as shown in Figures 2 and 3.
- 20 a) I. Nakase, H. Akita, K. Kogure, A. Gräslund, Ü. Langel, H. Harashima, S. Futaki, *Acc. Chem. Res.* **2012**, *45*, 1132. b) I. Nakase, A. Tadokoro, N. Kawabata, T. Takeuchi, H. Katoh, K. Hiramoto, M. Negishi, M. Nomizu, Y. Sugiura, S. Futaki, *Biochemistry* **2007**, *46*, 492.



Supramolecular Complexation in Biological Media: NMR Study on Inclusion of an Anionic Tetraarylporphyrin into a Per-O-Methylated β -Cyclodextrin Cavity in Serum, Blood, and Urine

Hiroaki Kitagishi,^{*,[a]} Mai Saito,^[a] Qiyue Mao,^[a] Akiko Kiriyama,^[b] Shigeru Negi,^[b] and Koji Kano^[a]

Abstract: The supramolecular complexation of 5,10,15,20-tetrakis(4-sulfonatophenyl)porphyrin (TPPS) with heptakis(2,3,6-tri-O-methyl)- β -cyclodextrin (TMCD) has been known to be highly specific in aqueous media. In this study, we have used NMR spectroscopy to reveal that this supramolecular system also works even in biologically crowded media such as serum, blood, and urine. A ^{13}C -labeled heptakis(2,3,6-tri-O-methyl- ^{13}C)- β -cyclodextrin (^{13}C -TMCD) was synthesized and studied using one-dimensional (1D) HMQC spectroscopy in serum and blood. The 1D HMQC spectrum of ^{13}C -TMCD showed clear signals due to the 2-, 3-, and 6- O^{13}CH_3 groups, whose chemical shifts changed upon addi-

tion of TPPS due to quantitative formation of the ^{13}C -TMCD/TPPS = 2/1 inclusion complex in such biological media. The ^1H NMR signals of non-isotope-labeled TPPS included by ^{13}C -TMCD were detected using the ^{13}C -filtered ROESY technique. A pharmacokinetic study of ^{13}C -TMCD and its complex with TPPS was carried out in mice using the 1D HMQC method. The results indicated that (1) 1D HMQC is an effective technique for monitoring the inclusion phenomena of ^{13}C -labeled cyclodextrin in biological media and (2) the intermolecular interaction between ^{13}C -TMCD and TPPS is highly selective even in contaminated media like blood, serum, and urine.

Introduction

Cyclodextrins (CDs) and their derivatives have been widely used in the pharmaceuticals field due to their ability to form inclusion complexes with hydrophobic drug molecules in aqueous media.^[1–4] The inclusion of drug molecules by CDs improves their water-solubilities, facilitating their delivery into tissues and organs. Chemically modified CD derivatives such as hydroxypropyl β -CDs without guest molecules have recently been proposed as drug candidates to remove accumulated lipophilic biomolecules like cholesterol via the host-guest complexation in vivo.^[5–8]

In general, the inclusion of a guest molecule into a CD cavity in aqueous solution has been studied by means of spectroscopic methods such as NMR, UV/Vis, circular dichroism, and fluorescence spectroscopies.^[9,10] Among them, NMR is the

most powerful tool providing fundamental information on the complexation process. However, NMR has serious limitations to observing complexation in biological media due to numerous contaminated signals arising from co-existing biomolecules. Rebek et al. reported the selective NMR-based detection of a host-guest complexation system using a deep cavitand host in human serum solution.^[11] Guest molecules included in the cavitand showed marked upfield chemical shifts (from -0.5 to -2.5 ppm) of the ^1H NMR signals due to a strong ring current effect by the cavitand. In the case of CDs, however, such a strong electronic effect is not inherently expected. To detect the CD component in vivo, high-performance liquid chromatographic (HPLC) analysis,^[12,13] radioisotope labeling,^[14,15] and fluorescence labeling techniques^[16] have been used in the pharmacokinetic studies of CDs. However, these approaches do not provide any structural information on the inclusion complexes of CDs. There are no well-studied methods to analyze the structures of the CD complexes in biological environments.

In the present study, we have used NMR spectroscopy to monitor the inclusion phenomena of heptakis(2,3,6-tri-O-methyl)- β -CD (TMCD) tagged with ^{13}C atoms. In our laboratory, highly specific intermolecular interaction between TMCD and water-soluble porphyrins such as 5,10,15,20-tetrakis(4-sulfonatophenyl)porphyrin (TPPS) has been studied.^[17,18] In particular, the iron complex of TPPS included by a per-O-methylated β -CD dimer having a pyridine linker has been utilized in vivo as an artificial oxygen carrier,^[19,20] cyanide antidote,^[21] and carbon monoxide removal agent.^[22–24] In these previous investigations, however, we did not provide satisfactory evidence to indicate that the inclusion complexes of CDs with porphyrins

[a] Dr. H. Kitagishi, M. Saito, Q. Mao, Prof. Dr. K. Kano
Department of Molecular Chemistry and Biochemistry
Faculty of Science and Engineering
Doshisha University
1-3 Tatara Miyakodani, Kyotanabe, Kyoto 610-0321 (Japan)
E-mail: hkitagis@mail.doshisha.ac.jp

[b] Dr. A. Kiriyama, Dr. S. Negi
Faculty of Pharmaceutical Science
Doshisha Women's College of Liberal Arts
Kyotanabe, Kyoto 610-0395 (Japan)

 The ORCID identification number(s) for the author(s) of this article can be found under:
<https://doi.org/10.1002/asia.201900983>.

 This manuscript is part of a special collection celebrating the 100th Annual Meeting of the Chemical Society of Japan (CSJ). Click here to see the Table of Contents of the special collection.

were sustained in the biological media. Then, we planned to synthesize an isotope-labeled TMCD (^{13}C -TMCD) bearing O^{13}CH_3 groups at the 2-, 3-, and 6-positions of the glucopyranose units. Isotope-labeling with NMR-active nuclei (^{13}C , ^{15}N , or ^2H) is a well-established method used in the detection of the biomolecules of interest, such as sugars, lipids, and proteins, in cells or organs to monitor their structures, biodistribution, and/or metabolic byproducts.^[25–28] To the best of our knowledge, however, NMR observation for the host-guest complexes of CDs in biologically crowded media has not been carried out yet. In this paper, we first describe the synthesis and characterization of isotope-labeled ^{13}C -TMCD. We then demonstrate the selective detection of ^{13}C -TMCD complexed with TPPS in serum and blood solutions using one-dimensional heteronuclear multiple quantum coherence (1D HMQC) and ^{13}C -filtered rotating frame nuclear Overhauser effect spectroscopy (ROESY) techniques. We demonstrate the quantitative 1D HMQC method for pharmacokinetic monitoring of the urinary excretions of mice injected with ^{13}C -TMCD with and without a guest molecule.

Results and Discussion

Synthesis and characterization of ^{13}C -TMCD: The synthesis of ^{13}C -TMCD was performed according to the standard procedure for methylation^[19,21] using sodium hydride (NaH) and isotope-labeled methyl iodide ($^3\text{CH}_3\text{I}$). The reaction product was confirmed by NMR spectroscopy, MALDI-TOF mass spectroscopy, and elementary analysis (see Experimental section). The ^1H NMR spectrum of ^{13}C -TMCD in CDCl_3 (Figure 1 a) showed

three characteristic doublet signals due to the heteronuclear coupling between the ^1H and ^{13}C ($J_{\text{CH}} = 143 \text{ Hz}$). Using the broad band decoupling (BBD) technique, three singlet signals were obtained (Figure 1 b). According to literature,^[17,18] these signals were assigned to the protons of 3-, 2-, and 6- O^{13}CH_3 groups, respectively. The ^1H -decoupled ^{13}C NMR spectrum of ^{13}C -TMCD in CDCl_3 with small scan times showed three intense signals at 59.7, 58.4, and 58.1 ppm (Figure 1 c). We then used the HMQC method for the selective detection of the ^1H NMR signals of ^{13}C -TMCD under biological conditions. The HMQC spectrum of ^{13}C -TMCD in D_2O showed clear ^1H - ^{13}C correlation signals corresponding to the O^{13}CH_3 groups (Figure 1 d). In the HMQC measurement, we extracted the spectrum displayed on the F2 (^1H) axis, whose resolution was set higher than usual to obtain the high-resolution ^1H NMR profile derived from HMQC (see Experimental section). To reduce the measurement time, the data point in the F1 (^{13}C) axis was set lower than usual, which did not affect the high-resolution spectrum on the F2 (^1H) axis. The spectrum of the F2 axis in HMQC is hereinafter referred to as the 1D HMQC spectrum.

We then obtained the ^{13}C -decoupled ^1H NMR spectra of ^{13}C -TMCD (0.1 mM) in D_2O (Figure 2 a) and in a serum containing 10% D_2O (Figure 2 b). In biological media, D_2O needs to be added to obtain the NMR lock signal. As expected, the ^1H NMR spectrum in serum (Figure 2 b) showed numerous complicated signals due to the presence of biological contaminants. It was difficult to identify the signals due to ^{13}C -TMCD. On the other hand, the 1D HMQC spectrum in serum containing 10% D_2O (Figure 2 c) showed only three signals at 3.52, 3.43, and 3.29 ppm, corresponding to the O^{13}CH_3 groups. These chemical

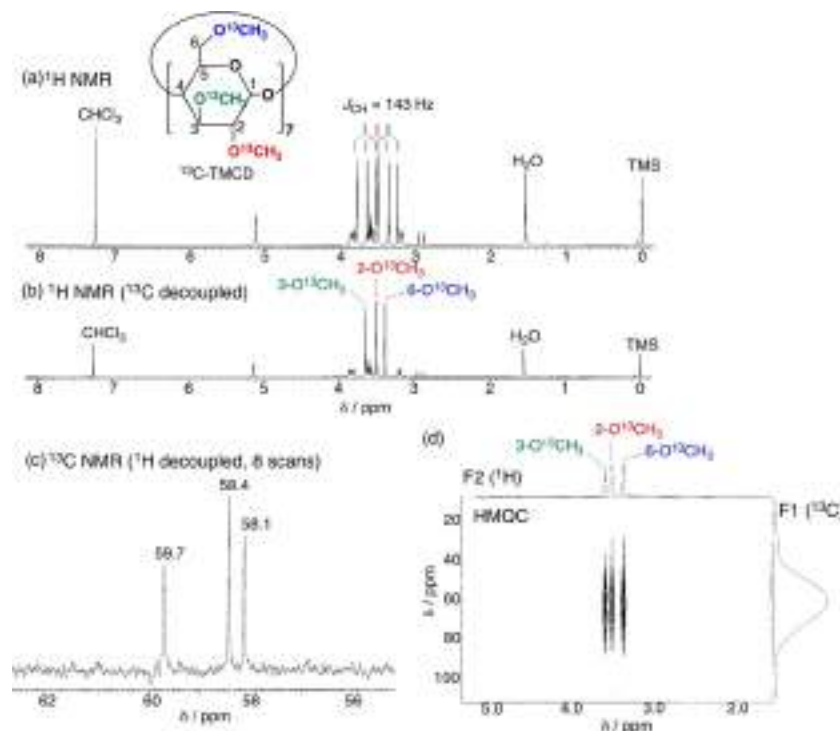


Figure 1. NMR spectral characterization of ^{13}C -TMCD. (a, b) ^1H NMR spectra of ^{13}C -TMCD in CDCl_3 (1.0 mM) without (a) and with ^{13}C broad band decoupling (b). (c) ^{13}C NMR spectrum of ^{13}C -TMCD (1.0 mM) in CDCl_3 with small scan times. (d) HMQC spectrum of ^{13}C -TMCD (1.0 mM) in D_2O . All the spectra were recorded at 25 °C.

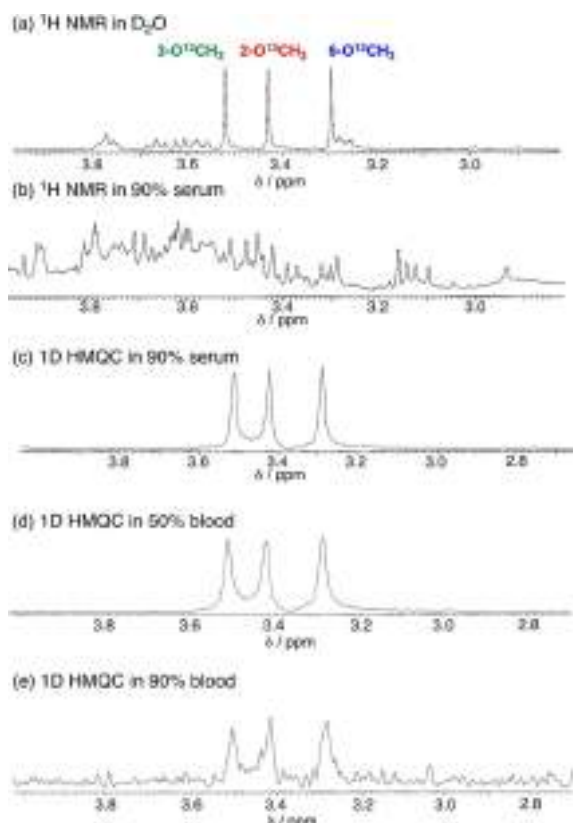


Figure 2. NMR spectra of ^{13}C -TMCD in biological media. (a, b) ^1H NMR spectra (^{13}C -decoupled) of ^{13}C -TMCD (0.1 mM) in D_2O (a) and in serum containing 10% D_2O (b). (c–e) 1D HMQC spectra of ^{13}C -TMCD (0.1 mM) in serum containing 10% D_2O (c), in whole blood containing 50% and 10% D_2O (d, e). All the spectra were recorded at 25°C .

shifts were consistent with those observed in D_2O (Figure 2a), indicating that the interaction between ^{13}C -TMCD and the serum components were weak. However, the signals observed in serum were considerably broader than those observed in D_2O . Since the 1D HMQC spectrum of ^{13}C -TMCD in the urine sample showed sharper signals as shown below, the signal broadening might be caused due to biomacromolecules, such as proteins and lipids, which are present in serum but absent in urine. This suggests the occurrence of weak but appreciable interactions between ^{13}C -TMCD and the biomacromolecules. The 1D HMQC spectrum recorded in the whole blood solution containing 50% D_2O (Figure 2d) was essentially the same as that recorded in the 90% serum solution. However, in the 90% blood solution (Figure 2e), the spectrum became significantly obscure with poor signal-to-noise ratio, potentially due to the high viscosity of the solution and/or a large amount of ferromagnetic contaminants in blood.

Host-guest complexation in serum and blood: In general, the ^1H NMR chemical shifts of CDs are affected by complexation with guest molecules. When TMCD forms inclusion complexes with tetraarylporphyrins like TPPS, the ^1H signals corresponding to the 2- and 3- OCH_3 groups of TMCD show large up-field shifts due to the ring-current effect of the porphyrin ring, whereas only a small shift is observed for the ^1H signal corresponding to the 6- OCH_3 group.^[17,18] Figure 3a shows the ^1H NMR spectral change of ^{13}C -TMCD (0.5 mM) in a 90% serum solution as a function of the concentration of TPPS ([TPPS]). In the ^{13}C -decoupled ^1H NMR spectra, biological contaminants produced a large number of unidentified signals in addition to the three signals (indicated with an asterisk *), whose intensities decreased upon the addition of TPPS. These three signals were assigned to the protons of the O^{13}CH_3 groups in ^{13}C -

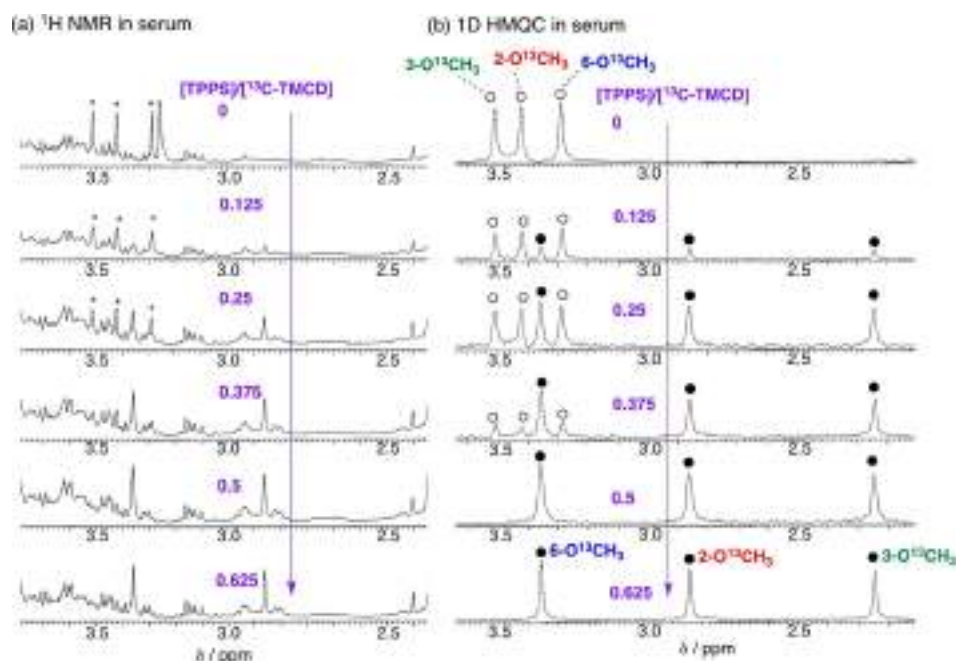


Figure 3. NMR titration experiments of ^{13}C -TMCD with TPPS. (a) ^{13}C -decoupled ^1H NMR and (b) 1D HMQC spectra of ^{13}C -TMCD (0.5 mM) as a function of [TPPS] in serum containing 10% D_2O . The open (○) and closed circles (●) indicate the signals assigned to free and complexed ^{13}C -TMCD with TPPS. All the spectra were recorded at 25°C .

TMCD, whose chemical shifts and signal intensities changed upon complexation with TPPS. Because ^{13}C -TMCD, as well as TMCD, has seven equivalent methyl groups per molecule (i.e. equivalent 21H per molecule), the highly concentrated protons of each methyl group could be detected even in the 90% serum solution. However, upon addition of TPPS, these methyl signals became to overlap with the signals due to biological contaminants. On the other hand, using the 1D HMQC method, the signals due to the protons of the $\text{O}^{13}\text{C}\text{H}_3$ groups of ^{13}C -TMCD were exclusively detected (Figure 3b). The signals systematically changed upon the addition of TPPS. The signal intensities of free ^{13}C -TMCD at 3.52, 3.43, and 3.29 ppm (○) were decreased along with appearance of new signals at 3.36, 2.87, and 2.25 ppm (●). These new signals were assigned to the 6-, 2-, and 3- $\text{O}^{13}\text{C}\text{H}_3$ protons of ^{13}C -TMCD complexed with TPPS, respectively, and the chemical shifts were corresponding to those observed in the TMCD/TPPS complex in D_2O .^[17,18] The spectral change was completely saturated in the presence of 0.5 equiv of TPPS, and no transitional spectral change was observed, indicating that quantitative 2:1 complexation occurred in the serum solution. A similar spectral change was observed when using the 1D HMQC technique in a 50% blood solution (Figure 4). These experiments clearly demonstrated that the complexation of ^{13}C -TMCD with TPPS is highly specific and quantitative even in the presence of biologically contaminated media such as serum and blood.

It is well known that chemically modified β -CDs (mostly methyl and hydroxypropyl β -CDs) interact with cholesterol and are thus often used as a cholesterol-depleting agents in living cells.^[7,8,29–31] The binding constant between methylated β -CD and cholesterol has been measured to be 10^{4-5} M^{-1} by the sol-

ubility method.^[32–34] Cholesterol is abundant in mammalian blood plasma ($\approx 200 \text{ mg dL}^{-1}$, $\approx 5 \text{ mM}$).^[35] Therefore, ^{13}C -TMCD dissolved in serum or blood possibly interacts with cholesterol. However, no significant changes in the chemical shifts of ^{13}C -TMCD were detected in the 1D HMQC spectra for serum and blood. TPPS also interacts strongly with serum albumin, the most abundant protein in plasma and the main component of blood (5 g dL^{-1} , $\approx 0.8 \text{ mM}$). The binding constant between TPPS and albumin has been reported to be 10^6 M^{-1} .^[36,37] Taking these intermolecular interactions into consideration, the complexation between ^{13}C -TMCD and TPPS in serum and blood should be competitive with complexation with the biological components. Nevertheless, the 1D HMQC measurements shown in Figures 3 and 4 indicate that the complexation between ^{13}C -TMCD and TPPS specifically occurred even in serum and blood. The binding constants (K_1 and K_2) for complexation between TMCD and TPPS to form the 2/1 inclusion complex are too large to be accurately determined in aqueous media.^[17] The present study reveals that the intermolecular interaction of ^{13}C -TMCD with TPPS is much stronger than those for the ^{13}C -TMCD and TPPS-biological component systems.

Using the present ^{13}C -TMCD/TPPS system with the 1D HMQC method, a reversible host-guest exchange reaction in blood was directly monitored. At first, as detailed above, the signals due to free ^{13}C -TMCD detected in the 1D HMQC spectrum changed upon the addition of TPPS because of the formation of the ^{13}C -TMCD/TPPS = 2/1 inclusion complex (Figures 5a and 5b). To the solution containing the ^{13}C -TMCD/TPPS complex, non-isotope-labeled TMCD (98.9% ^{12}C -TMCD with 1.1% ^{13}C -TMCD in natural abundance) was gradually added (Figures 5c–e). The signals of ^{13}C -TMCD complexed with TPPS

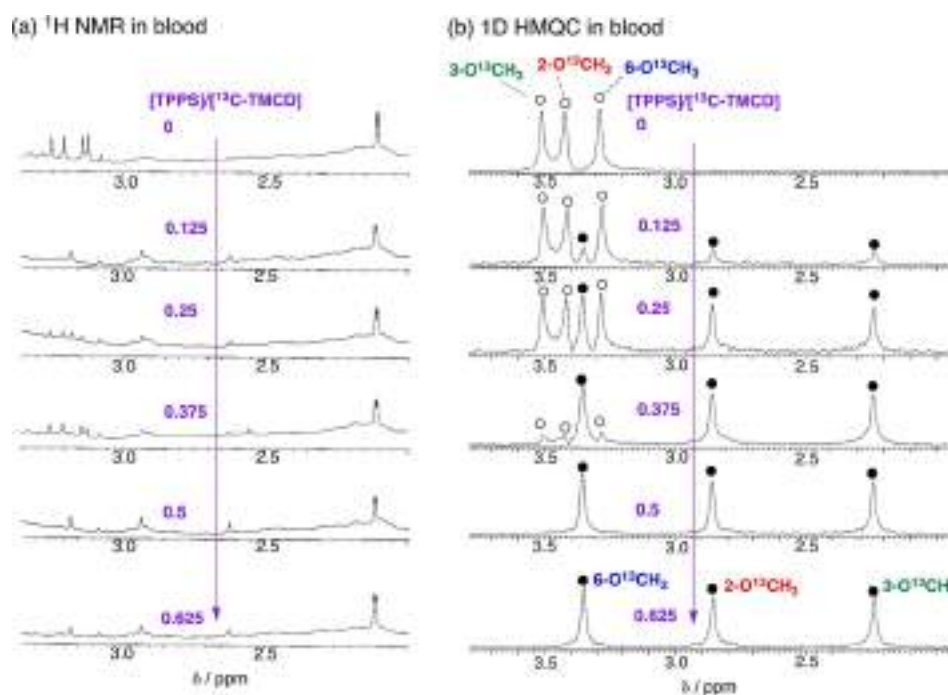


Figure 4. NMR titration experiments of ^{13}C -TMCD with TPPS. (a) ^{13}C -decoupled ^1H NMR and (b) 1D HMQC spectra of ^{13}C -TMCD (0.5 mM) as a function of TPPS in whole blood containing 50% D_2O . The open (○) and closed circles (●) indicate the signals assigned to free and complexed ^{13}C -TMCD with TPPS. All the spectra were recorded at 25°C .

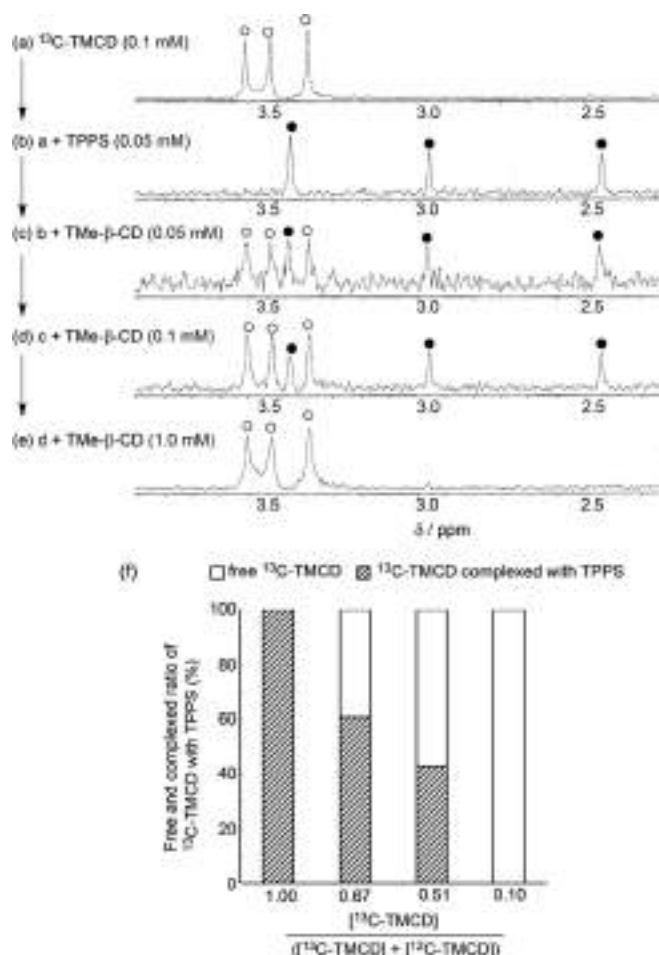


Figure 5. 1D HMQC spectra of ^{13}C -TMCD (0.1 mM) before (a) and after the successive additions of TPPS (0.05 mM) (b) and TMCD (0.05, 0.1, and 1.0 mM) (c, d, and e) in whole blood containing 50% D_2O . The open (○) and closed circles (●) indicate the signals assigned to free and complexed ^{13}C -TMCD with TPPS. All the spectra were recorded at 25 °C. (f) The ratio of free and complexed ^{13}C -TMCD with TPPS as a function of ^{13}C abundance.

(●) changed back to those of free ones (○). Under the 1D HMQC measurement conditions, only the signals due to ^{13}C -TMCD were detectable and ^{12}C -TMCD was NMR-spectroscopically silent. The signals of ^{13}C -TMCD complexed with TPPS were completely converted to free ones upon the addition of excess TMCD, indicating that the guest molecule, TPPS, was transferred from the ^{13}C -TMCD host cavity to that of ^{12}C -TMCD. Usually, such a host-guest exchange reaction is difficult to observe. Based on the signal intensities of free (○) and complexed ^{13}C -TMCD (●), the ratio of free and complexed ^{13}C -TMCD was easily determined as a function of the ^{13}C abundance in TMCD (Figure 5 f). This complexation ratio might be useful to determine the binding constants. As mentioned above, the binding constants between TMCD and TPPS have not been determined accurately because the interaction is too strong in aqueous media. In theory, if we use a host molecule with a known binding constant to TPPS as a competitor, it would be possible to determine the binding constants of ^{13}C -TMCD to TPPS. This is currently under investigation in our laboratory.

The molecular structure of the TMCD/TPPS inclusion complex in D_2O has been previously determined using the ROESY technique.^[17] In D_2O , the strong ROE signals were detected between the *O*-methyl protons at the secondary face (2- and 3-positions) of TMCD and the aromatic protons of TPPS, indicat-

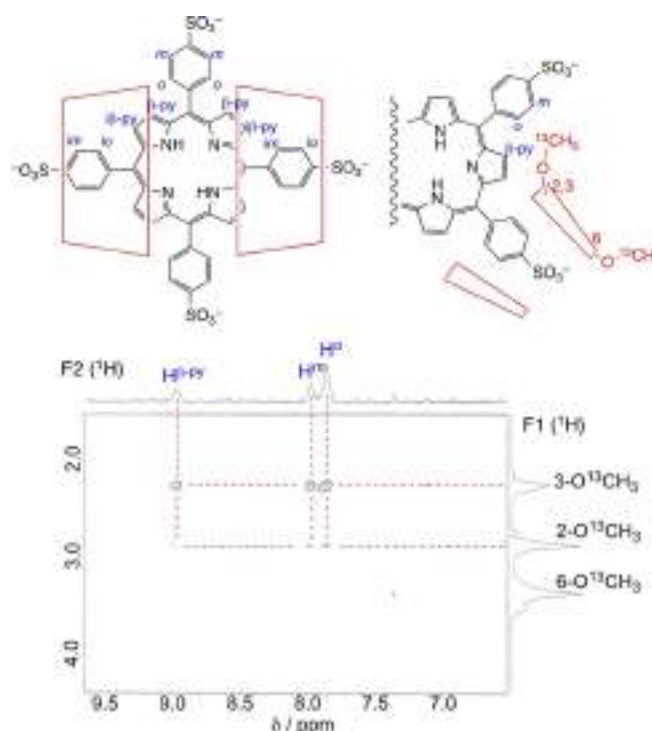


Figure 6. ^{13}C -filtered ROESY of ^{13}C -TMCD (1.0 mM) complexed with TPPS (0.5 mM) in whole blood containing 50% D_2O . The spectra were recorded at 25 °C with a mixing time of 180 ms.

ing the molecular structure of a *trans*-type TMCD/TPPS = 2/1 inclusion complex, as illustrated in the upper portion of Figure 6. To detect the ROE signals between ^{13}C -TMCD and TPPS in biologically crowded media, we applied the ^{13}C -filtered ROESY technique (Figure 6). The ^{13}C -TMCD/TPPS complex dissolved in 50% blood solution showed correlation signals between the 2- and 3- O^{13}CH_3 protons and the aromatic protons at 7.82, 7.95, and 8.98 ppm in ^{13}C -filtered ROESY. The chemical shifts of these aromatic proton signals were assigned to the β -pyrrole (β -py) and phenyl protons (*o* and *m*) of TPPS, respectively.^[17] The 1D projections of ROESY and ^{13}C -filtered ROESY spectra obtained for the ^{13}C -TMCD/TPPS complex are shown in Figure 7. Although no significant signals were detected in blood using the regular ROESY technique (Figure 7 a), three aromatic signals were clearly detected both in D_2O and blood using the ^{13}C -filtered ROESY method (Figures 7b and c). Upon comparison with the ^1H NMR spectrum of the TPPS/TMCD complex in D_2O (Figure 7d), the enhanced signals obtained by the ^{13}C -filtered ROESY method were obviously assigned to the β -py, *m*, and *o* protons of TPPS. These protons were located in close proximity to the secondary O^{13}CH_3 groups (2- and 3- O^{13}CH_3). The proton signals labeled with *i* β -py, *io* and *im* in Figure 7d, where *i* refers to "included", did not show any ROE sig-

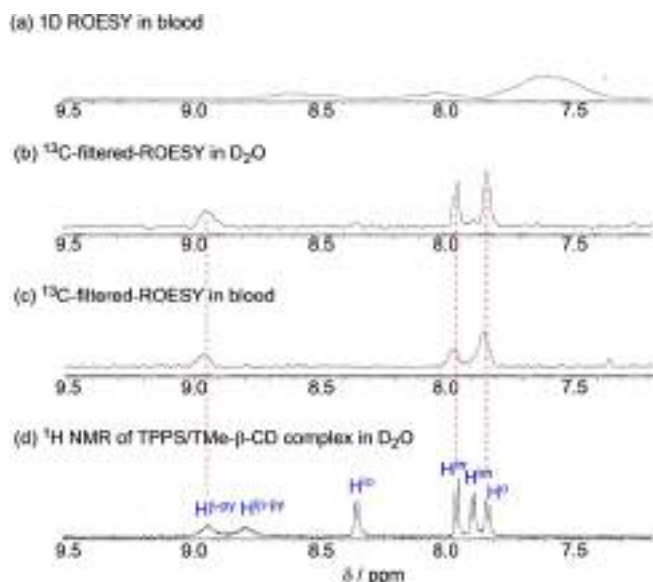


Figure 7. ^{13}C -filtered ROESY spectrum for detection of TPPS (0.5 mM) complexed with ^{13}C -TMCD (1.0 mM) in blood. (a) 1D ROESY of TPPS with ^{13}C -TMCD in the blood solution containing 50% D_2O , (b, c) ^{13}C -filtered ROESY of TPPS with ^{13}C -TMCD in D_2O (b) and in the blood solution containing 50% D_2O (c), (d) ^1H NMR spectrum of TPPS complexed with TMCD in D_2O . The spectra were recorded at 25°C with a mixing time of 180 ms.

nals with the O^{13}CH_3 groups. These “included” protons of TPPS showed strong ROE signals with the inner 3- and 5-protons of TMCD in D_2O ,^[17] where the inner protons in ^{13}C -TMCD will not give any signals in the present ^{13}C -filtered system. Therefore, the ^{13}C -filtered ROESY provided the structural information for the *trans*-type ^{13}C -TMCD/TPPS=2/1 inclusion complex in blood. It should be noted that non-isotope-labeled TPPS was used in this experiment. This non-isotope-labeled TPPS was able to be selectively detected in blood when it formed an inclusion complex with ^{13}C -TMCD. In other words, non-isotope-labeled guest molecules dissolved in the crowded media become detectable by ^{13}C -filtered 2D NMR spectroscopy when ^{13}C -labeled CD is used as a host molecule.

Pharmacokinetic application of 1D HMQC: In previous studies,^[22–24] we injected animals (rats and mice) with the inclusion complexes of TPPS and its iron complex (FeTPPS) with methylated β -CD derivatives. The complexes administered either intravenously or intraperitoneally were filtered through the renal glomeruli; thus partially excreted in the urine. The complexes contained in the urine samples were detected by measuring their absorption spectra. However, no evidence was obtained whether CD itself involved due to the absence of chromophores in the CD. Therefore, we applied the 1D HMQC method to determine the presence or absence of ^{13}C -TMCD and its complex with TPPS in the urine of mice. This method was expected to provide structural and quantitative information on the pharmacokinetic behavior of ^{13}C -TMCD.

A solution of ^{13}C -TMCD alone (1.0 mM, 0.15 mL) in phosphate buffered saline (PBS) was intraperitoneally injected into a mouse (22–24 g) and the excreted urine was collected for 30 min after administration. This urine sample was mixed with D_2O (10%, v/v) and then analyzed using the ^1H NMR and 1D

HMQC techniques. The ^1H NMR spectrum of the urine sample showed complicated signals due to the presence of biological contaminants and no signals could be assigned to ^{13}C -TMCD (Figure 8a). On the other hand, the 1D HMQC spectrum of the

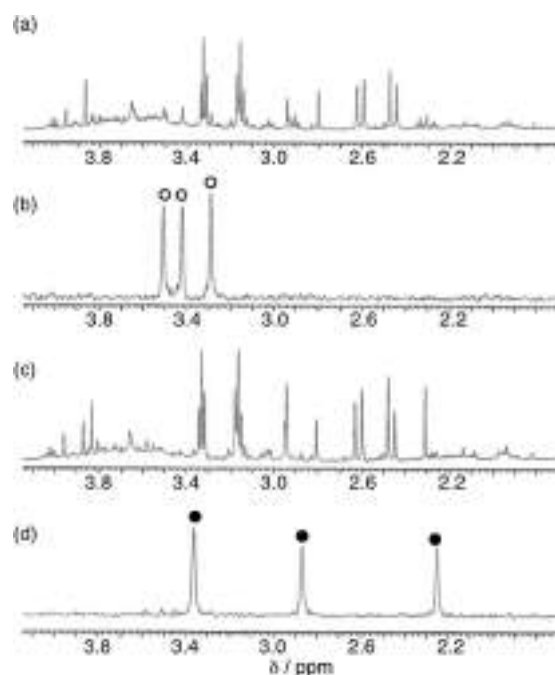


Figure 8. ^1H NMR (a, c) and 1D HMQC spectra (b, d) of the urine excreted from mice after administration of ^{13}C -TMCD (a, b) and the ^{13}C -TMCD/TPPS complex (c, d). D_2O (10%) was added to the urine before the measurements. The open (\circ) and closed circles (\bullet) indicate the signals assigned to free and complexed ^{13}C -TMCD with TPPS. All the spectra were recorded at 25°C .

same urine sample showed three characteristic signals (\circ) at 3.52, 3.43, and 3.29 ppm due to the presence of free ^{13}C -TMCD (Figure 8b). These signals were sharper in the urine samples when compared to those observed in serum and blood. This might be ascribed to the lower viscosity and/or the absence of large biomolecular components such as proteins in the urine. The chemical shifts of these ^{13}C -TMCD signals detected in the urine sample remained unchanged in comparison to those of free ^{13}C -TMCD in D_2O , indicating that ^{13}C -TMCD injected into the mouse was excreted in the urine without undergoing any chemical modification. The inclusion complex of ^{13}C -TMCD and TPPS was also detected in the urine when a solution (0.15 mL) containing ^{13}C -TMCD (1.0 mM) and TPPS (0.5 mM) was similarly injected into a mouse (Figures 8c and d). The chemical shifts of the three signals (\bullet) of the ^{13}C -TMCD/TPPS complex detected using the 1D HMQC method (3.37, 2.88, and 2.26 ppm) also remained unchanged in comparison to the chemical shifts observed in D_2O , indicating that the ^{13}C -TMCD/TPPS=2/1 inclusion complex retained its molecular structure even after urinary excretion from the animal body.

We then used the 1D HMQC method to measure the amount of ^{13}C -TMCD in the urine samples and obtain pharmacokinetic profiles. The solutions of ^{13}C -TMCD alone (3.0 mM, 0.15 mL in PBS) and its inclusion complex ($[^{13}\text{C}\text{-TMCD}] =$

3.0 mM and [TPPS] = 1.5 mM, 0.15 mL in PBS) were intraperitoneally injected into mice and the urine was then continuously collected for 90 min after administration. To these urine samples, an identical amount of methanol- ^{13}C ($^{13}\text{CH}_3\text{OH}$) was added as an internal standard for the quantitative analysis. The signal intensities of ^{13}C -TMCD relative to $^{13}\text{CH}_3\text{OH}$ revealed the pharmacokinetic profiles of the urinary excretion. The excretion time-courses of ^{13}C -TMCD and its inclusion complex of TPPS are shown in Figure 9. In both cases, bell-shaped profiles were

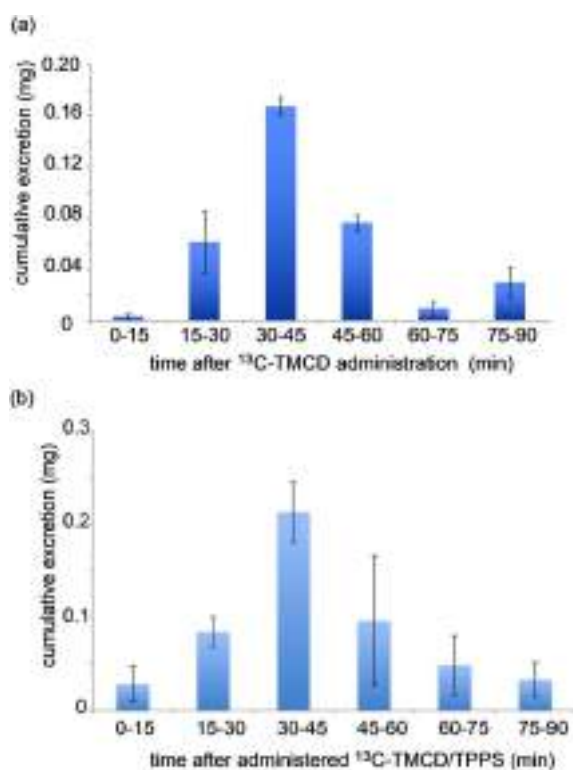


Figure 9. The urinary excretion profiles of ^{13}C -TMCD and the ^{13}C -TMCD/TPPS complex in mice after intraperitoneally injections of ^{13}C -TMCD (3.0 mM, 0.15 mL in PBS, a) and the complex (^{13}C -TMCD] = 3.0 mM and [TPPS] = 1.5 mM, 0.15 mL in PBS, b) to mice. The excreted compounds were quantified from peak integrations in the 1D HMQC spectra of the murine urine where ^{13}C -methanol was used as an internal standard. Each bar represents the means \pm SE ($n = 6$ mice per group).

obtained, indicating that ^{13}C -TMCD as well as its inclusion complex of TPPS exhibit similar pharmacokinetic behavior. From these profiles, ca. 0.21 mg (31%) of ^{13}C -TMCD and ca. 0.32 mg (18%) of the ^{13}C -TMCD/TPPS complex was detected in the excreted urine within 90 min. To investigate their distributions to other organs, the 1D HMQC method was used to study the blood and the liver lysates of mice injected intraperitoneally with ^{13}C -TMCD. However, no signals of ^{13}C -TMCD could be detected in the blood and liver, potentially due to the lack of ^{13}C concentration in samples and/or metabolism of ^{13}C -TMCD in the organs. The detection limit for ^{13}C -TMCD in the present system would be $\approx 20 \mu\text{M}$. A study on the whereabouts of TMCD and its inclusion complex would be the next topic of investigation.

Conclusions

The data collected from the above experiments brings us to the following conclusions:

- 1) The inclusion phenomena of ^{13}C -labeled per-*O*-methyl- β -cyclodextrin (^{13}C -TMCD) were selectively detected in the biological media (serum, blood, and urine) using the 1D HMQC method.
- 2) The 2:1 supramolecular complexation between ^{13}C -TMCD and TPPS was highly specific and quantitative even in biologically crowded media.
- 3) The ^1H NMR signals of the non-isotope labeled guest molecule, TPPS, that formed an inclusion complex with ^{13}C -TMCD under the biological conditions were selectively detected using the ^{13}C -filtered ROESY method.
- 4) Application of the present system to pharmacokinetic study provided information not only on the urinary excretion profiles of ^{13}C -TMCD and the ^{13}C -TMCD/TPPS complex, but also their molecular structure in the excreted urine.
- 5) The present ^{13}C -TMCD/TPPS host-guest system is highly specific and thus observable in biological media. We also believe that the current approach can be used to analyze other in vivo host-guest molecular systems that have seldom been studied to date.

Experimental Section

Materials. Heptakis-(2,3,6-tri-*O*-methyl- ^{13}C)- β -CD (^{13}C -TMCD) was synthesized as described below. 5,10,15,20-Tetrakis(4-sulfonatophenyl)porphyrin (TPPS) was purchased from Chemical Dojin and used as received. ^{13}C -Labeled reagents (iodomethane- ^{13}C and methanol- ^{13}C , 99 atom% ^{13}C) was purchased from Sigma-Aldrich. Serum (Fetal Bovine) was purchased from BIOWEST and used as received for the NMR measurements. Blood (mouse) was taken from mice and used after heparinization. Other general chemical reagents were purchased from commercial sources and used as received.

Synthesis of ^{13}C -TMCD. β -CD was purchased from Nacalai tesque and dried at 100°C in vacuo for 3 h before use. In a 50 mL three-neck flask, β -CD (0.11 g, 0.097 mmol) was dissolved in anhydrous *N,N*-dimethylformamide (5 mL, dried with calcium hydride and distilled under argon before use) with stirring at room temperature. The solution was then cooled on an ice bath. To the solution was added NaH (0.18 g, 7.5 mmol, the oil-coating of commercial NaH was washed out with hexane before use) followed by $^{13}\text{CH}_3\text{I}$ (0.22 mL, 3.5 mmol). The resulting solution was gradually warmed up to room temperature and stirred overnight. To the solution was added 1 mL of methanol and then the solvent was evaporated. The residue was dissolved in water and the aqueous solution was extracted with CHCl_3 (three times). The organic phase was separated, dried with Na_2SO_4 , and evaporated. The residue was passed through a silica gel column with $\text{CHCl}_3/\text{CH}_3\text{OH}$ (20/1, v/v) as the eluent. The fraction containing ^{13}C -TMCD, that could be monitored by TLC using anisaldehyde sulfuric acid stain, was collected and dried up to give ^{13}C -TMCD as a colorless solid (0.088 g, 63%): ^1H NMR (500 MHz, CDCl_3): $\delta = 5.14$ (d, 7H, $J = 3.5$ Hz), 3.88–3.77 (m, 14H), 3.65 (d, 21H, $J_{\text{CH}} = 143.0$ Hz), 3.68–3.55 (m, 14H), 3.50 (d, 21H, $J_{\text{CH}} = 143.0$ Hz), 3.38 (d, 21H, $J_{\text{CH}} = 143.0$ Hz), 3.20 ppm (dd, 7H, $J = 3.5, 11.0$ Hz); MS (MALDI-TOF, α -CHCA matrix, positive

mode) m/z 1473 ($M+Na$)⁺; Anal Calcd for $C_{42}^{13}C_{21}H_{112}O_{35} \cdot H_2O$: C, 52.95; H, 7.83. Found: C, 52.68; H, 7.63.

NMR measurements. NMR spectra were measured on a JEOL JNM-ECA500 spectrometer (500 MHz). In the spectra measured in aqueous media, the water resonance was suppressed using a conventional pre-saturation method with a dante pulse sequence for the chemical shift at 4.7 ppm. Heteronuclear multiple quantum correlation (HMQC) spectra were measured with 1.5 s relaxation delay and 4 scan times. The one-dimensional HMQC spectra showing the ¹H signals bound to ¹³C were acquired from the spectrum appeared in the F2 axis of HMQC. The data points on the F1 (¹³C) and F2 (¹H) axes set to 16 and 4096, respectively (resolution; 700 and 0.7 Hz/point for F1 and F2 axes, respectively). ¹³C-Filtered rotating frame nuclear Overhauser effect spectroscopy (ROESY) was measured for the ¹³C-TMCD/TPPS complex in the blood solution using the G-Bird pulse sequence incorporated into ROESY. The mixing time for ROESY was 180 ms. The 1D ROE spectrum was obtained from the F2 axis (4096 data point, 0.7 Hz/point resolution) of the 2D spectrum. In all NMR measurements, deuterium oxide (D₂O) was appropriately added to the biological solvents (serum, urine, and blood) in order to obtain NMR lock signals.

Animal experiments. All animal experiments were approved by the Animal Experimental Committee of Doshisha University and carried out in accordance with the Guidelines for Animal Experiments of Doshisha University. Male C57BL/6N mice weighing 20–22 g were used. A solution of ¹³C-TMCD (1.0 or 3.0 mM, 0.15 mL in phosphate buffer saline) or the ¹³C-TMCD/TPPS complex ([¹³C-TMCD] = 1.0 or 3.0 mM, [TPPS] = 0.5 or 1.5 mM in phosphate buffer saline) was intraperitoneally administered to the subject mouse. The urine was continuously collected after the administration. The urine was diluted with D₂O (10%, v/v) and then measured 1D HMQC as described above. To quantify the amount of ¹³C-TMCD contained in the urine, methanol-¹³C (1.0 mM) was used as an internal standard. Because of the difference in relaxation time between methanol-¹³C and ¹³C-TMCD, the ¹H signal intensity due to methanol-¹³C in 1D HMQC was detected smaller than the expected signal intensity for ¹³C-TMCD. To calibrate this, 1D HMQC spectra of methanol-¹³C (1.0 mM) as a function of ¹³C-TMCD (0.5, 0.4, and 0.3 mM) were taken before measuring the urine samples, and such a calibration curve obtained from the signal intensities of methanol-¹³C vs. ¹³C-TMCD was used for quantification of ¹³C-TMCD excreted in the urine. From the signal integration of ¹³C-TMCD vs. methanol-¹³C, the excreted amount of ¹³C-TMCD (mg) in the urine was determined. The ratio of the dose excreted into urine as ¹³C-TMCD and the ¹³C-TMCD/TPPS complex were calculated by dividing the cumulative amount of ¹³C-TMCD and the ¹³C-TMCD/TPPS complex into the urine by the administered dose, respectively.

Acknowledgements

We appreciate JEOL RESONANCE Co. Ltd. for advice on the ¹³C-filtered ROESY measurement. This work was financially supported by MEXT/JSPS KAKENHI (Grant No. 15H02569, 16K13092, 17H02208, 18KK0156, 19K22260), the MEXT-Supported Program for the Strategic Research Foundation at Private Universities (2015–2019), the Naito Foundation, Takeda Science Foundation, the NOVARTIS Foundation (Japan) for the Promotion of Science, Suntory Foundation for Life Sciences, and JGC-S Scholarship Foundation.

Conflict of interest

The authors declare no conflict of interest.

Keywords: biological media · cyclodextrin · NMR · porphyrin · supramolecular chemistry

- [1] K. Uekama, F. Hirayama, T. Irie, *Chem. Rev.* **1998**, *98*, 2045–2076.
- [2] M. E. Davis, M. E. Brewster, *Nat. Rev. Drug Discovery* **2004**, *3*, 1023–1035.
- [3] T. Loftsson, D. Duchêne, *Int. J. Pharm.* **2007**, *329*, 1–11.
- [4] T. Loftsson, M. E. Brewster, *J. Pharm. Pharmacol.* **2010**, *62*, 1607–1621.
- [5] K. B. Peake, J. E. Vance, *J. Biol. Chem.* **2012**, *287*, 9290–9298.
- [6] B. Liu, C. M. Ramirez, A. M. Miller, J. J. Repa, S. D. Turley, J. M. Dietschy, *J. Lipid Res.* **2010**, *51*, 933–944.
- [7] R. Onodera, K. Motoyama, A. Okamatsu, T. Higashi, H. Arima, *Sci. Rep.* **2013**, *3*, 1104.
- [8] R. Onodera, K. Motoyama, N. Tanaka, A. Ohyama, A. Okamatsu, T. Higashi, R. Kariya, S. Okada, H. Arima, *Sci. Rep.* **2014**, *4*, 4417.
- [9] K. A. Connors, *Chem. Rev.* **1997**, *97*, 1325–1357.
- [10] M. V. Rekharsky, Y. Inoue, *Chem. Rev.* **1998**, *98*, 1875–1917.
- [11] D. A. Ryan, J. Rebeck, Jr., *J. Am. Chem. Soc.* **2011**, *133*, 19653–19655.
- [12] H. W. Frijlink, J. Visser, N. R. Hefting, R. Oosting, D. K. F. Meijer, C. F. Lerk, *Pharm. Res.* **1990**, *8*, 1248–1252.
- [13] V. Hafner, D. Czock, J. Burhenne, K.-D. Riedel, J. Bommer, G. Mikus, C. Machleidt, T. Weinreich, W. E. Haefeli, *Antimicrob. Agents Chemother.* **2010**, *54*, 2596–2602.
- [14] A. Gerloczy, A. Fonagy, P. Keresztes, L. Perlaky, J. Szejtli, *Drug Res.* **1985**, *35*, 1042–1047.
- [15] B. Van Ommen, A. T. H. J. De Bie, A. Bär, *Regul. Toxicol. Pharmacol.* **2004**, *39*, 57–66.
- [16] J. Huang, S. Weinfurter, P. C. Pinto, M. Pretze, B. Kränzlin, J. Pill, R. Federica, R. Perciaccante, L. D. Ciana, R. Masereeuw, N. Gretz, *Bioconjugate Chem.* **2016**, *27*, 2513–2526.
- [17] K. Kano, R. Nishiyabu, T. Asada, Y. Kuroda, *J. Am. Chem. Soc.* **2002**, *124*, 9937–9944.
- [18] K. Kano, R. Nishiyabu, R. Doi, *J. Org. Chem.* **2005**, *70*, 3667–3673.
- [19] K. Kano, H. Kitagishi, M. Kodera, S. Hirota, *Angew. Chem. Int. Ed.* **2005**, *44*, 435–438; *Angew. Chem.* **2005**, *117*, 439–442.
- [20] K. Karasugi, H. Kitagishi, K. Kano, *Bioconjugate Chem.* **2012**, *23*, 2365–2376.
- [21] K. Watanabe, H. Kitagishi, K. Kano, *Angew. Chem. Int. Ed.* **2013**, *52*, 6894–6897; *Angew. Chem.* **2013**, *125*, 7032–7035.
- [22] H. Kitagishi, S. Negi, A. Kiriya, A. Honbo, Y. Sugiura, A. T. Kawaguchi, K. Kano, *Angew. Chem. Int. Ed.* **2010**, *49*, 1312–1315; *Angew. Chem.* **2010**, *122*, 1334–1337.
- [23] H. Kitagishi, S. Minegishi, A. Yumura, S. Negi, S. Taketani, Y. Amagase, Y. Mizukawa, T. Urushidani, Y. Sugiura, K. Kano, *J. Am. Chem. Soc.* **2016**, *138*, 5417–5425.
- [24] S. Minegishi, I. Sagami, S. Negi, K. Kano, H. Kitagishi, *Sci. Rep.* **2018**, *8*, 11996.
- [25] D. Sakakibara, A. Sasaki, T. Ikeya, J. Hamatsu, T. Hanashima, M. Mishima, M. Yoshimasu, N. Hayashi, T. Mikawa, M. Wälchli, B. O. Smith, M. Shirakawa, P. Güntert, Y. Ito, *Nature* **2009**, *458*, 102–105.
- [26] K. Inomata, A. Ohno, H. Tochio, S. Isogai, T. Tenno, I. Nakase, T. Takeuchi, S. Futaki, Y. Ito, H. Hiroaki, M. Shirakawa, *Nature* **2009**, *458*, 106–109.
- [27] H. Yamada, K. Mizukawa, R. Igarashi, H. Tochio, M. Shirakawa, Y. Tabata, Y. Kumura, T. Kondo, Y. Aoyama, S. Sando, *ACS Chem. Biol.* **2012**, *7*, 535–542.
- [28] H. Yamada, Y. Hasegawa, H. Imai, Y. Takayama, F. Sugihara, T. Matsuda, H. Tochio, M. Shirakawa, S. Sando, Y. Kimura, A. Toshimitsu, Y. Aoyama, T. Kondo, *J. Am. Chem. Soc.* **2015**, *137*, 799–806.
- [29] M. M. Fretz, N. A. Penning, S. Al-Taei, S. Futaki, T. Takeuchi, I. Nakase, G. Strom, A. T. Jones, *Biochem. J.* **2007**, *403*, 335–342.
- [30] S. Mahammad, I. Parmryd, *Methods Mol. Biol.* **2015**, *1232*, 91–102.
- [31] E. Christian, M. P. Haynes, M. C. Phillips, G. H. Rothblat, *J. Lipid Res.* **1997**, *38*, 2264–2272.
- [32] R. Breslow, B. Zhang, *J. Am. Chem. Soc.* **1996**, *118*, 8495–8496.

- [33] J. Nishijo, S. Moriyama, S. Shiota, *Chem. Pharm. Bull.* **2003**, *51*, 1253–1257.
- [34] H. W. Frijlink, A. C. Eissens, N. R. Hefting, K. Poelstra, C. F. Lerk, D. K. F. Meijer, *Pharm. Res.* **1991**, *8*, 9–16.
- [35] D. S. Goodman, S. B. Hulley, L. T. Clark, et al., *Arch Intern Med.* **1988**, *148*, 36–69.
- [36] J. Bartošová, I. Kalousek, Z. Hrkal, *Int. J. Biochem.* **1994**, *26*, 631–637.
- [37] E. Borissevitch, T. T. Tominaga, C. C. Schmitt, *J. Photochem. Photobiol. A* **1998**, *114*, 201–207.

Manuscript received: July 19, 2019
Revised manuscript received: August 8, 2019
Accepted manuscript online: August 12, 2019
Version of record online: August 22, 2019

SCIENTIFIC REPORTS



OPEN

Circadian clock disruption by selective removal of endogenous carbon monoxide

Saika Minegishi¹, Ikuko Sagami², Shigeru Negi³, Koji Kano¹ & Hiroaki Kitagishi¹ ¹

Circadian rhythms are regulated by transcription-translation feedback loops (TTFL) of clock genes. Previous studies have demonstrated that core transcriptional factors, NPAS2 and CLOCK, in the TTFL can reversibly bind carbon monoxide (CO) *in vitro*. However, little is known about whether endogenous CO, which is continuously produced during a heme metabolic process, is involved in the circadian system. Here we show that selective removal of endogenous CO in mice considerably disrupts rhythmic expression of the clock genes. A highly selective CO scavenger, hemoCD1, which is a supramolecular complex of an iron(II)porphyrin with a per-*O*-methyl- β -cyclodextrin dimer, was used to remove endogenous CO in mice. Intraperitoneal administration of hemoCD1 to mice immediately reduced the amount of internal CO. The removal of CO promoted the bindings of NPAS2 and CLOCK to DNA (E-box) in the murine liver, resulting in up-regulation of the E-box-controlled clock genes (*Per1*, *Per2*, *Cry1*, *Cry2*, and *Rev-erb α*). Within 3 h after the administration, most hemoCD1 in mice was excreted in the urine, and heme oxygenase-1 (HO-1) was gradually induced in the liver. Increased endogenous CO production due to the overexpression of HO-1 caused dissociation of NPAS2 and CLOCK from E-box, which in turn induced down-regulation of the clock genes. The down-regulation continued over 12 h even after the internal CO level recovered to normal. The late down-regulation was ascribed to an inflammatory response caused by the endogenous CO reduction. The CO pseudo-knockdown experiments provided the clear evidence that endogenous CO contributes to regulation in the mammalian circadian clock.

The circadian rhythm is a naturally occurring day-and-night oscillation system that controls physiological and behavioral cycles and is regulated in almost all cells^{1–4}. Figure 1 depicts the core circadian clock system in mammalian cells. This system involves a transcription-translation feedback loop (TTFL) for the rhythmic expression of clock components on approximately 24 h cycles^{1–4}. CLOCK and NPAS2 are the transcriptional factors that play central and overlapping roles in the TTFL^{1–7}. Both proteins form heterodimers with BMAL1 and bind to a specific DNA sequence called E-box. Transcription of clock genes, such as *periods* (*Per*) and *cryptochromes* (*Cry*), is enhanced by these heterodimers. The translated PER and CRY proteins also form a heterodimer, which acts on BMAL1:CLOCK(NPAS2) to repress the transcription of *Per* and *Cry*. Both PER and CRY proteins are gradually degraded through the post-transcriptional modifications such as phosphorylation and ubiquitination⁸, and then transcription of *Per* and *Cry* restarts, thus completing the TTFL.

Carbon monoxide (CO) is continuously produced in mammalian cells. The major source of endogenous CO is the degradation of heme by heme oxygenases (HOs)^{9,10}. Similar to nitric oxide (NO) and hydrogen sulfide (H₂S), CO acts as a gaseous signal messenger with several protective effects, such as anti-inflammation, anti-apoptosis, and anti-proliferation^{9–12}. In parallel with physiological studies on CO, CO-responsive transcriptional factors have been identified, such as NPAS2¹³, CoxA¹⁴, and RcoM^{15,16}. In contrast to NO and H₂S, which are highly reactive to metal ions, thiol groups in cysteine residues, and molecular oxygen, CO is relatively inert and only reactive to metal cofactors, mostly ferrous heme, in biological systems^{16–18}; therefore, these CO-sensing proteins possess heme cofactors, and binding of CO to the heme induces structural/functional changes of the proteins. Dioum *et al.* demonstrated that the BMAL1:NPAS2 heterodimer loses its DNA-binding character *in vitro* in the presence of CO¹³. The CLOCK protein also possesses heme as a prosthetic cofactor and the heme-based sensing function

¹Department of Molecular Chemistry and Biochemistry, Faculty of Science and Engineering, Doshisha University, Kyotanabe, Kyoto, 610-0321, Japan. ²Graduate School of Life and Environmental Sciences, Kyoto Prefectural University, Sakyo-ku, Kyoto, 606-8522, Japan. ³Faculty of Pharmaceutical Sciences, Doshisha Women's College of Liberal Arts, Kyotanabe, Kyoto, 610-0395, Japan. Correspondence and requests for materials should be addressed to H.K. (email: hkitagis@mail.doshisha.ac.jp)

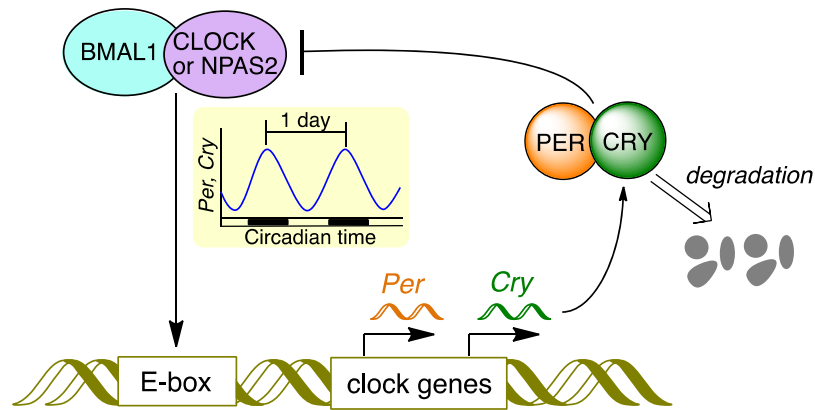


Figure 1. The core transcription-translation feedback loop in the circadian system of mammalian cells. The components of Fig. 1 were drawn using ChemBioDraw.

toward CO is suggested¹⁹. Therefore, endogenous CO might participate in the regulation of the TTFL in the circadian clock system²⁰. Tu and McKnight early demonstrated that endogenous/exogenous CO plays a regulatory role in the yeast metabolic cycle²¹. A recent pathological study showed that application of exogenous CO could adjust the disrupted circadian rhythms in injured cells^{22,23}. The role of endogenous CO in the circadian clock system has been recently studied by using HO-knockout/knockdown systems²⁴, suggesting that rhythmic heme degradation generating endogenous CO is required for keeping the E-box-controlled circadian rhythms. However, heme itself, whose internal level is controlled by the HO activity, has an effect on the regulation of circadian rhythms^{25,26}. In addition, heme degradation by HO consumes NADPH and generates not only CO, but also biliverdin and iron^{9,10}. Intracellular NADPH level is also an influencing factor in the regulation of circadian rhythms^{27,28}. Genetic or pharmacological inhibition of the HO activity has the potential to affect various biological events in addition to CO-depletion. Thus, the use of a selective CO-removal agent would be more favorable to clarify the contribution of endogenous CO to the circadian clock.

In this report, we show that selective removal of endogenous CO in mice significantly affects the expression levels of the E-box-controlled clock genes in the murine liver. We utilized hemoCD1, a highly selective CO scavenging agent working in aqueous media. HemoCD1 (Fig. 2) is a very stable 1:1 supramolecular inclusion complex comprised of 5,10,15,20-tetrakis(4-sulfonatophenyl)porphyrinatoiron(II) ($\text{Fe}^{\text{II}}\text{TPPS}$) encapsulated by a per-*O*-methylated β -cyclodextrin dimer with a pyridine ligand (Py3CD). Our group has extensively studied hemoCD1 as a water-soluble hemoprotein model compound^{29–32}. Similar to native hemoglobin and myoglobin, hemoCD1 reversibly binds oxygen (O_2) and CO in aqueous solutions at ambient temperature. It is noteworthy that the CO binding affinity of hemoCD1 is extremely high ($K_d = 0.02$ nM at 25 °C), approximately 100 times higher than that of hemoglobin in the R-state in aqueous solutions, whereas the O_2 binding affinity of hemoCD1 is moderate and close to that of hemoglobin in the T-state^{30,33,34}. To the best of our knowledge, the CO-binding affinity of hemoCD1 in aqueous solutions is the highest among the reported CO-binding hemoproteins. More advantageously, the NO-binding affinity of hemoCD1 is lower than that of hemoglobin³⁵. The coordination strength of H_2S to a hemoCD1 analog is also relatively weak, and the SH^- ligand is easily replaceable with CO ³⁶. Therefore, it might be possible to use hemoCD1 to selectively remove internal CO in mammals, creating an endogenous CO pseudo-knockdown state *in vivo*^{33–35}. The CO binding affinity of hemoCD1 is also much higher than those of NPAS2 ($K_d = 1–2$ μM at 25 °C)¹³ and CLOCK (PAS-A domain, $K_d = \text{ca. } 0.1$ mM at 22 °C)¹⁹. Using hemoCD1, therefore, it become possible to study of the effects of endogenous CO on the circadian clock system. Here, the pseudo-knockdown study for CO *in vivo* provides the clear experimental evidence that endogenous CO contributes to regulation of the mammalian circadian clock through acting on NPAS2 and CLOCK and modulating the clock genes related to inflammatory responses.

Results

Administration of hemoCD1 in mice. Before doing experiments, the mice were housed for two weeks under 12 h light/dark (LD) cycle (lights on at 7:00 and off at 19:00) with free feeding. From the day before hemoCD1 administration to the end of observation, the mice were housed under constant dark (DD) conditions without feeding to prevent the entrainment of their internal clocks by external stimuli. A solution containing hemoCD1 (1.0 mM), which existed as the O_2 adduct (O_2 -hemoCD1) under aerobic conditions, in phosphate-buffered saline (PBS, 0.15 mL) was intraperitoneally (i.p.) administered to the mice. After the i.p. administration of hemoCD1, endogenous CO in the mice was bound to hemoCD1 *via* ligand exchange with O_2 and excreted in the urine in a form complexed with hemoCD1 (CO-hemoCD1) as previously demonstrated³⁴. The amount of hemoCD1 administered was sufficient to deplete the endogenous CO in mice; the excreted amount of endogenous CO as CO-hemoCD1 was saturated when hemoCD1 was administered at concentrations higher than 1.0 mM (0.15 mL)³⁴. Throughout this study, we used mice treated with buffer (PBS) and the free-base complex of hemoCD1 (hemoCD1 without Fe^{II} , Fb-hemoCD1) as negative controls. In addition, we tested CO-hemoCD1 in place of O_2 -hemoCD1. Such a CO-adduct never altered the concentration of CO in mice and showed no effect on

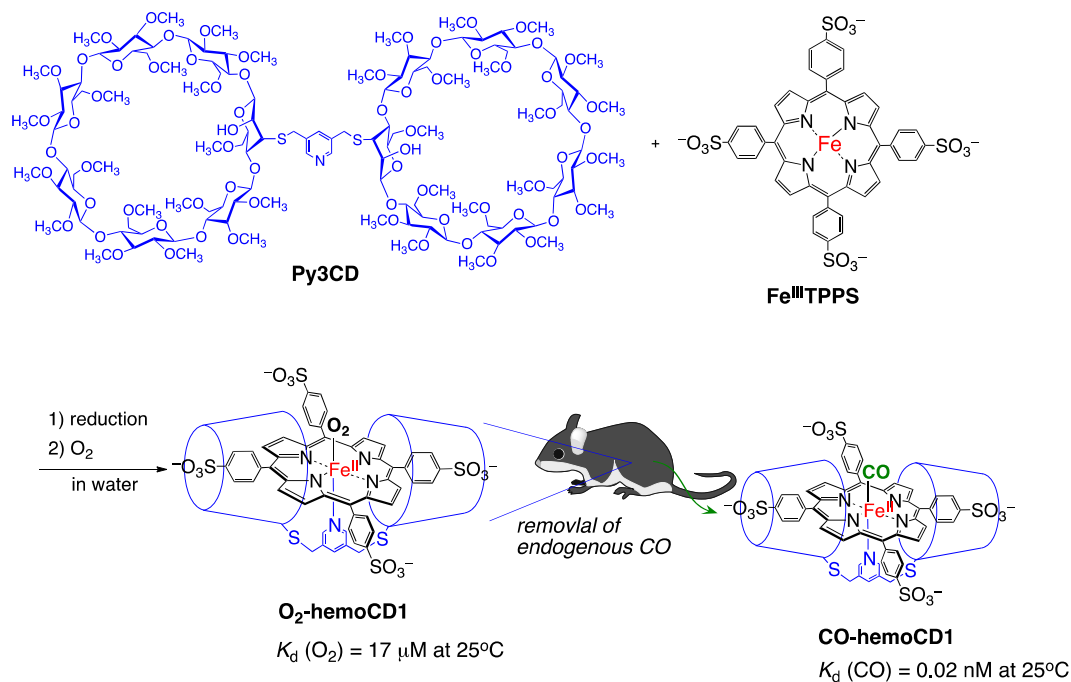


Figure 2. The structure of a CO-scavenging agent, hemoCD1, a 1:1 supramolecular inclusion complex of an ironporphyrin (FeTPPS) and a per-*O*-methylated cyclodextrin dimer (Py3CD). HemoCD1 is used for selective removal of endogenous CO in mice *via* the ligand exchange reaction of O₂ with CO. The binding affinity for CO ($P_{1/2}^{\text{CO}} = 0.000015 \text{ Torr}$) is much higher than that for O₂ ($P_{1/2}^{\text{O}_2} = 10 \text{ Torr}$)³⁴. The components of Fig. 2 were drawn using ChemBioDraw.

clock gene expression (Fig. S1). A series of control experiments confirmed that the changes in clock gene expression observed in the hemoCD1-treated mice must have arisen from the lack of endogenous CO.

Effects of endogenous CO depletion on the clock gene expression. After *i.p.* administration of hemoCD1 to mice at 14:30, the expression levels of the clock genes *Per1*, *Per2*, *Cry1*, and *Cry2* were measured by quantitative real-time PCR (RT-PCR) at different time points. The time profiles for the mRNA of the clock genes in the livers of the hemoCD1-treated mice were obviously different from those in the livers of the control groups (Fig. 3). The mRNA levels initially increased at clock time 15 (0.5 h after the administration), and then started to decline to levels lower than those in the control groups. The down-regulation of the clock genes continued until around 9:30 on day two (19 h after the administration). In addition, no significant changes in the mRNA levels were observed for the brains of the hemoCD1-treated mice (Fig. S2). HemoCD1 does not remove endogenous CO in the brain (Fig. S3), probably due to poor slipping ability of hemoCD1 through the blood brain barrier. This result suggests that administration of hemoCD1 to mice cannot possibly affect the master clock of the suprachiasmatic nucleus.

The disruption of clock gene expression affected the physical behavior of the mice. Analysis of wheel-running activity of mice (Fig. 4) showed that administration of hemoCD1 resulted in impaired locomotor action. This effect reached statistical significance on the second day after the administration. This observed behavioral effect is likely related to the down-regulation of *Cry* expression, as previously reported for *Cry*-null mice³⁷ and/or to the CO-removal-induced inflammatory response that increases TNF- α levels in the livers of mice during the third phase (*vide infra*).

CO depletion-induced activity changes in NPAS2 and CLOCK. To clarify the mechanism for the circadian rhythm disruption observed in the CO-reduced mice, we divided the mRNA expression profiles into four phases, as shown in Fig. 3. In the first phase (clock time 14.5–16.5), *i.p.* administration of hemoCD1 derived higher clock gene mRNA levels (Fig. 3). Quantification of endogenous CO in the murine tissues by the method developed by ourselves^{34,35} showed that endogenous CO levels were significantly reduced in the liver in the first phase (Fig. 5a), whereas they were unchanged in the brains of the hemoCD1-treated mice (Fig. S3). The relationship between the enhanced clock gene expression and the reduced CO level in the liver is interpreted in terms of the CO-responsive function of NPAS2 as previously reported *in vitro*¹³, *i.e.*, the binding of the BMAL1:NPAS2 heterodimer to the E-box sequence is facilitated under low CO concentrations.

In the second phase (16.5–19.5), the amount of endogenous CO in the liver of hemoCD1-treated mice increased much larger than those in the controls (Fig. 5a). We have previously demonstrated that endogenous CO in mice is quickly produced by inducing HO-1, an inducible form of HO, when endogenous CO is removed by hemoCD1, whereas HO-2, a constitutive form of HO, is not affected by hemoCD1³⁴. Indeed, we found that HO-1 protein expression was strongly induced in the hemoCD1-treated mice at clock time 17.5, leading to the

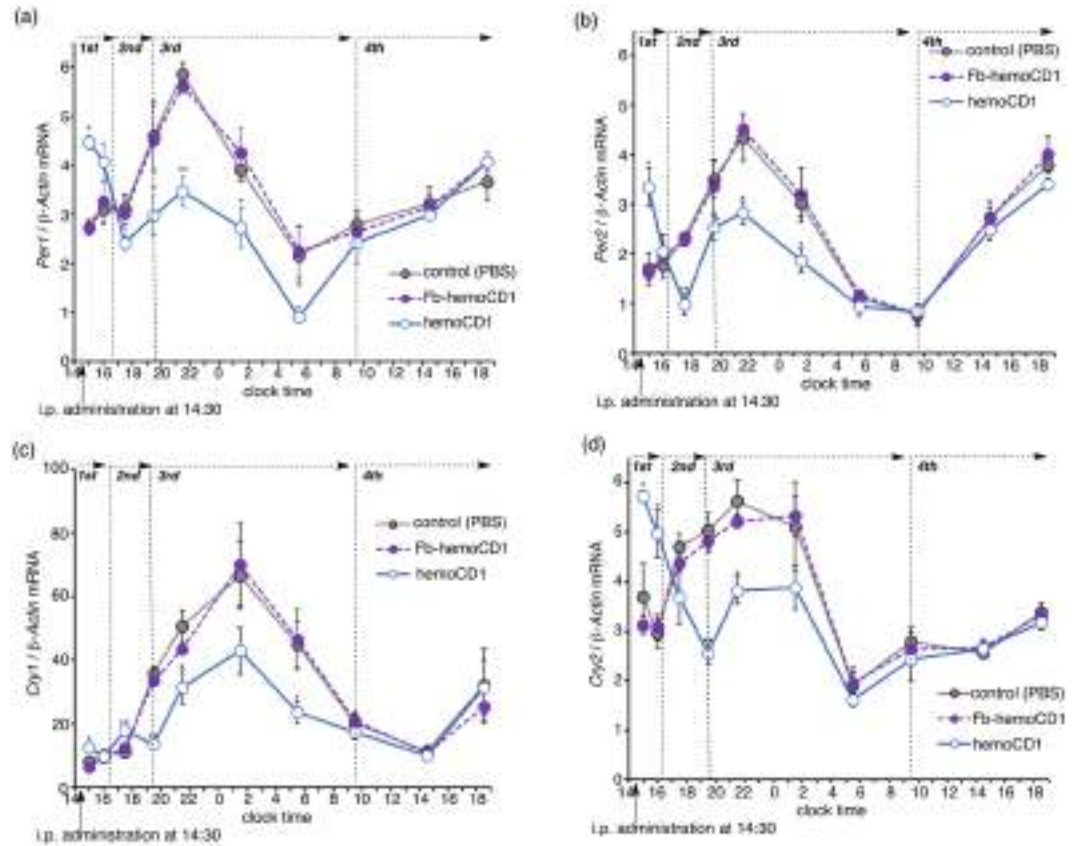


Figure 3. Changes in the mRNA levels of clock genes (*Per1*, **a**; *Per2*, **b**; *Cry1*, **c**; *Cry2*, **d**) in the murine liver after i.p. administration of hemoCD1 at clock time 14.5 (14:30). PBS and Fb-hemoCD1 were similarly administered as control samples. Each bar represents the mean \pm SE ($n = 3$ mice per group). The mice were housed for two weeks under a 12 h light/dark (LD) cycle (lights on at 7:00 and light off at 19:00) until the day before the experiments. The mice were then housed under constant dark (DD) conditions during the observations. Asterisk denotes statistical significance (* $P < 0.05$, ** $P < 0.01$), as compared to the controls. Note that the value on the vertical axis cannot be directly compared between the different panels (a–d) because the amount of cDNA used for real-time PCR varies with the gene of interest.

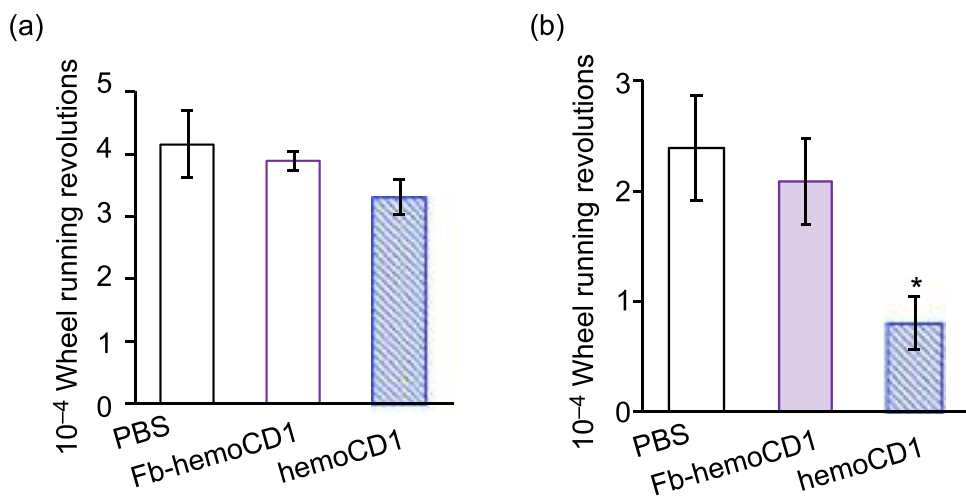


Figure 4. Cumulative wheel running revolutions in the first (**a**) and second 24 h periods (**b**) after i.p. administration of PBS, Fb-hemoCD1, and hemoCD1. Each bar represents the mean \pm SE ($n = 3$ mice per group). The mice were housed for two weeks under a 12 h light/dark (LD) cycle (lights on at 7:00 and light off at 19:00) until the day before the experiments. The mice were then housed under constant dark (DD) conditions during the observations. Asterisk denotes statistical significance (* $P < 0.05$), as compared to the controls. The raw actograms for measuring the wheel running activity are shown in Fig. S4.

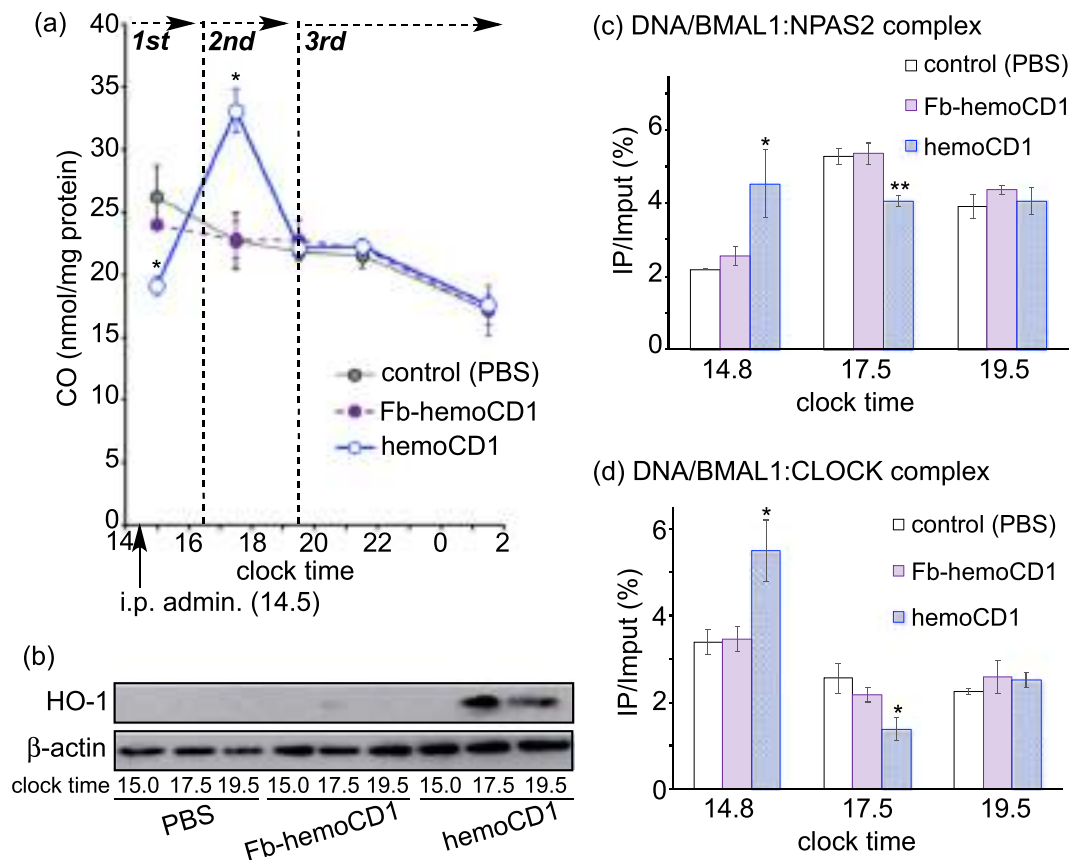


Figure 5. Quantification of CO, HO-1, and the DNA/protein complexes in the liver of the hemoCD1-treated mice. The mice were housed for two weeks under a 12 h light/dark (LD) cycle (lights on at 7:00 and light off at 19:00) until the day before the experiments. The mice were then housed under constant dark (DD) conditions during the observations. (a) Endogenous CO levels were measured by the assay using hemoCD1³⁵. (b) HO-1 levels were ascertained by western blotting with an anti-HO-1 antibody at clock time 15.0 (first phase), 17.5 (second phase), and 19.5 (third phase). (c,d) ChIP assays were conducted using anti-NPAS2 and anti-CLOCK antibodies to measure the corresponding DNA complexes at clock time 14.8 (first phase), 17.5 (second phase), and 19.5 (third phase). PBS and Fb-hemoCD1 were used as controls. Each bar represents the mean \pm SE ($n = 3$ mice per group). Asterisk denotes statistical significance (* $P < 0.05$, ** $P < 0.01$), as compared to the controls.

acceleration of endogenous CO production as shown in Figs 5b and S5. The increase in the amount of endogenous CO might cause down-regulation of the clock genes in the second phase, as shown in Fig. 3. Further, we confirmed the CO-dependent activity changes of NPAS2 and CLOCK using chromatin immunoprecipitation (ChIP) analysis with anti-NPAS2 and anti-CLOCK antibodies. The quantification of the amount of DNA bound to BMAL1:NPAS2 and BMAL1:CLOCK in the murine liver is displayed in Fig. 5c,d as a function of clock time. The changes in the quantities of DNA bound to these proteins were inversely correlated with the endogenous CO levels. It should be noted that the expression levels of *Npas2* and *Clock* mRNA were unaffected by administration of hemoCD1 (Fig. S6). Therefore, the significant increases and decreases in the DNA/protein complex levels observed at clock time 14.8 (the first phase) and 17.5 (the second phase) indicate that DNA binding of the BMAL1:CLOCK(NPAS2) heterodimers is modulated by endogenous CO level *in vivo*, resulting in up- and down-regulations of the clock genes.

CO depletion-induced inflammation affects clock gene expression. In the third phase (clock time after 19.5), endogenous CO and DNA/protein complex levels returned to normal (Fig. 5), whereas the levels of the clock genes (*Per1*, *Per2*, *Cry1*, and *Cry2*) were still down-regulated until around 9.5 on day two (Fig. 3). We hypothesized that the down-regulation was ascribed to the inflammatory responses caused by removal of endogenous CO. Our previous study³⁴ revealed that the removal of endogenous CO from CO-hemoglobin circulating in blood leads to accumulation of free heme in plasma. Indeed, the amount of free heme was temporally increased in the liver at 17.5 (the second phase) in the liver (Fig. 6a). Simultaneously, reactive oxygen species (ROS) levels in the hemoCD1-treated mice were much higher than those in normal mice (Fig. 6b). Free heme in organs produces ROS *via* a Fenton-type reaction³⁸. The ROS-induced oxidative stress enhanced the production of inflammatory cytokines, such as TNF- α (Fig. 6c)³⁹. Concurrently, TNF- α significantly accumulated in the hemoCD1-treated mice in the third phase (Fig. 6d). Inflammatory cytokines such as TNF- α affect clock gene expression through their inflammatory cascades^{40,41}. Therefore, the long-term down-regulation of the clock genes

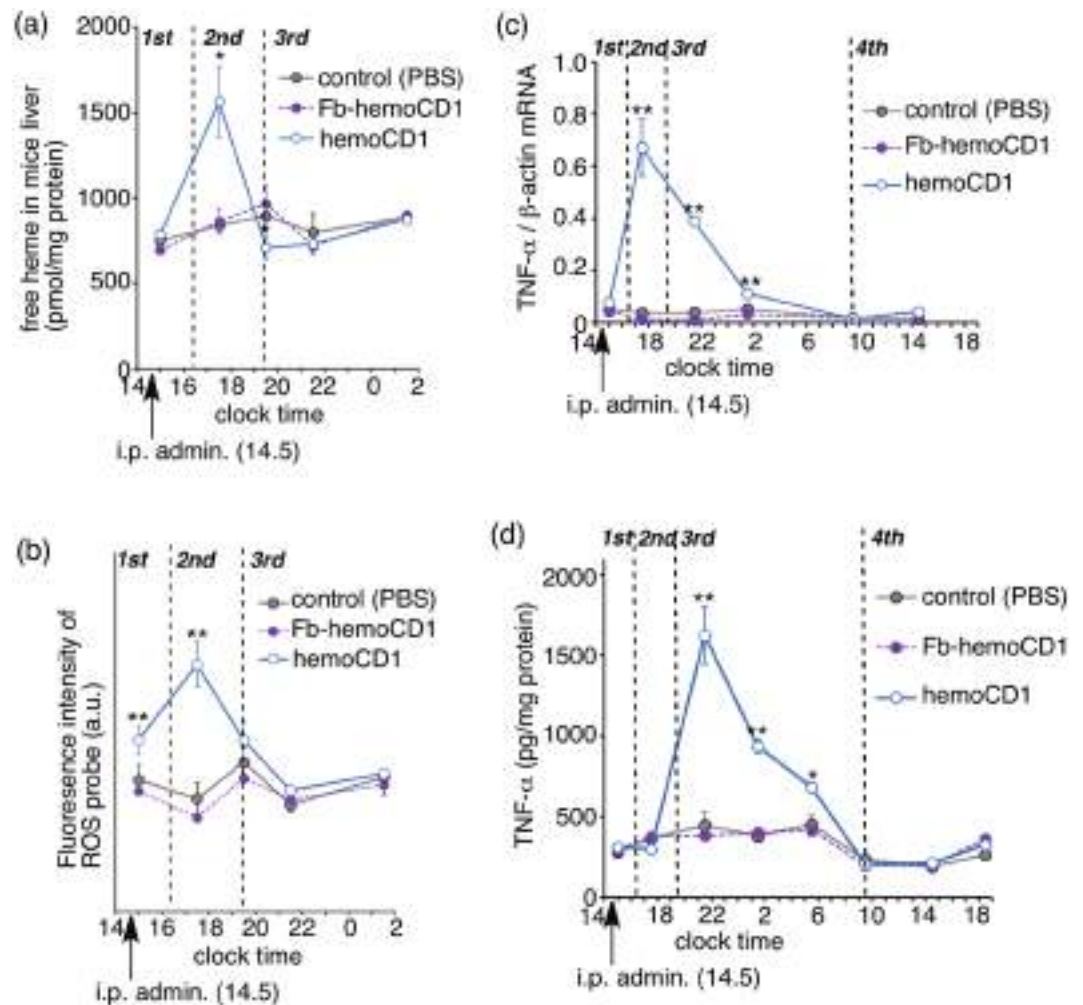


Figure 6. Changes in the amounts of free heme (a), ROS (b), and TNF- α (mRNA, (c); protein, (d)) in the liver of hemoCD1-treated mice. PBS and Fb-hemoCD1 were similarly administered as controls. Each bar represents the mean \pm SE ($n = 3$ mice per group). Asterisk denotes statistical significance (* $P < 0.05$, ** $P < 0.01$), as compared to the controls.

in the third phase seems to be due to the accumulation of inflammatory cytokines such as TNF- α . TNF- α protein levels returned to normal at clock time 9.5 on day two, at which the clock genes (*Per1*, *Per2*, *Cry1*, and *Cry2*) in the hemoCD1-treated mice recovered to normal (Fig. 3).

To confirm the participation of TNF- α in CO removal-induced circadian rhythm disruption, we measured the expression levels of *Rev-erba*, a circadian component induced by BMAL1:CLOCK(NPAS2)¹⁻³. It has been reported that, in contrast to *Per1/Per2*, the expression of *Rev-erba* is slightly enhanced by TNF- α (Fig. 7a)^{40,41}. Indeed, the mRNA levels of *Rev-erba* in the hemoCD1-treated mice were slightly but meaningfully higher than those in the controls at the third phase, whereas up- and down-regulations in the first and second phases were similar to those observed for *Per* and *Cry* (Fig. 7b). This result support a mechanism whereby changes in the mRNA levels in the first and second phases were caused by CO-dependent DNA-binding activity changes in NPAS2 and CLOCK, whereas the changes in the third phase were caused by an inflammatory response. The enhanced *Rev* expression possibly caused down-regulation of BMAL1 in the third phase (Fig. S6)¹⁻³, which might have contributed to down-regulation of *Per* and *Cry* in the third phase.

Discussion

The participation of CO in the circadian clock has been proposed since the important paper on the CO-responsive function of NPAS2 in 2002¹³. However, the study on the physiological contribution of endogenous CO to the circadian clock has been few, probably due to the difficulty in the loss-of-function approach for endogenous CO. The combinatorial use of HO-knockout/knockdown systems with exogenously applied gaseous CO or CO-releasing molecules (CO-RMs) has provided insights into the role of endogenous CO in the circadian clock²⁴. The E-box-controlled clock genes are significantly up-regulated in the HO-1-knockout cells, and further up-regulated by knockdown of HO-2. The addition of CO or CO-RMs to the cells partly suppresses the up-regulation. Interestingly, exogenous application of CO to wild-type cells hardly affects the clock gene expression. These findings suggest that endogenous CO is necessary and sufficient for playing a crucial role in regulation

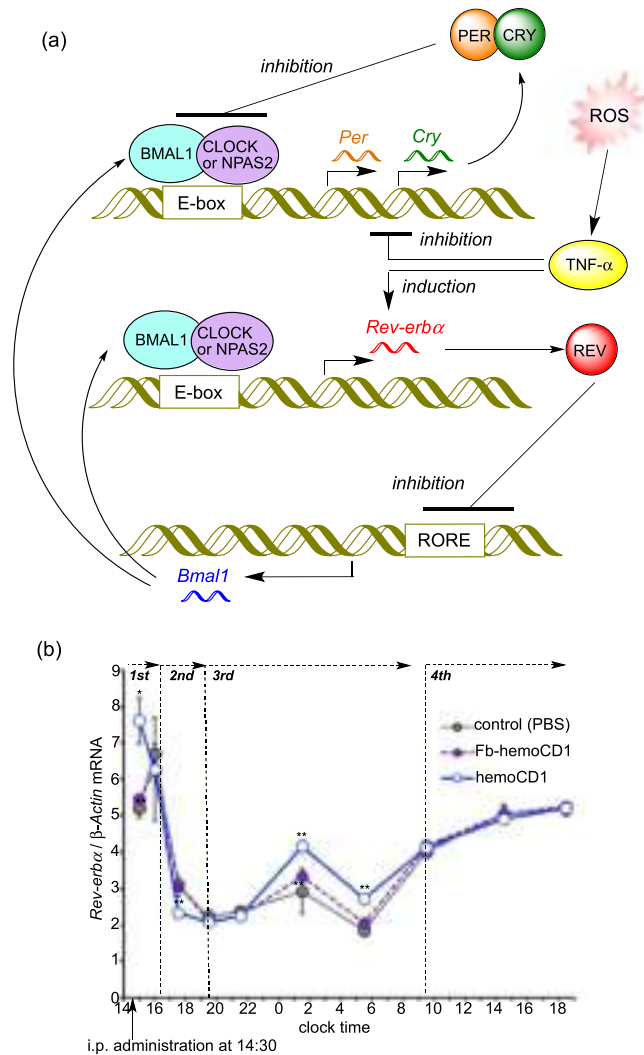


Figure 7. ROS-induced circadian rhythm disruption mediated by TNF- α . **(a)** Schematic representation of the clock system involving *Rev-erba*. Similar to *Per* and *Cry*, BMAL1:CLOCK(NPAS2) enhances transcription of *Rev-erba*. Additionally, TNF- α , which inhibits *Per* and *Cry*, slightly induces *Rev-erba*. REV proteins inhibits the expression of BMAL1. **(b)** Changes in the relative mRNA levels of *Rev-erba* in the murine liver after i.p. administration of hemoCD1. The mice were housed for two weeks under a 12 h light/dark (LD) cycle (lights on at 7:00 and light off at 19:00) until the day before the experiments. The mice were then housed under constant dark (DD) conditions during the observations. PBS and Fb-hemoCD1 were similarly administered as controls. Each bar represents the mean \pm SE ($n = 3$ mice per group). Asterisk denotes statistical significance ($^*P < 0.05$, $^{**}P < 0.01$), as compared to the controls. The components of Fig. 7a were drawn using ChemBioDraw.

of the circadian rhythms. However, the depletion of the HO activity seems to bring the side effects other than CO removal because the restoring effect by exogenous CO is quite limited in the HO-depleted system. As mentioned in the Introduction, inhibition of the HO activity might disturb several biological events, such as heme degradation, production of biliverdin and iron, and an intracellular NADPH concentration. In the present study, we used an endogenous CO-scavenging agent, hemoCD1, to see the effects of endogenous CO removal on the circadian clock of mice. This pseudo-knockdown approach for CO provided the clear evidence that endogenous CO contributes to regulation of the rhythmic expression of clock genes *in vivo*. Upon temporal removal of endogenous CO by hemoCD1, the circadian rhythms of the E-box-controlled clock genes were considerably interfered, and the locomotor activity of the mice was accordingly affected.

Figure 8 summarizes a plausible mechanism for the endogenous CO removal-induced circadian clock disruption. The i.p. administration of hemoCD1 immediately lowered endogenous CO levels in the murine liver in the first phase. The removal of endogenous CO facilitated the binding of BMAL1:CLOCK(NPAS2) heterodimers to E-box, resulting in enhancement of transcription of *Per* and *Cry*. This *in vivo* observation is consistent with the CO-responsive DNA-binding function of NPAS2 demonstrated *in vitro*¹³. The heme bound in the heme pocket of the CLOCK PAS-A domain also binds CO *in vitro* similarly to other gas-sensor proteins¹⁹, although the CO-dependent DNA-binding function has not been confirmed for CLOCK *in vitro*. Unlike NPAS2, it is difficult, as we have also tried several times, to confirm the CO-dependent DNA-binding of CLOCK by means

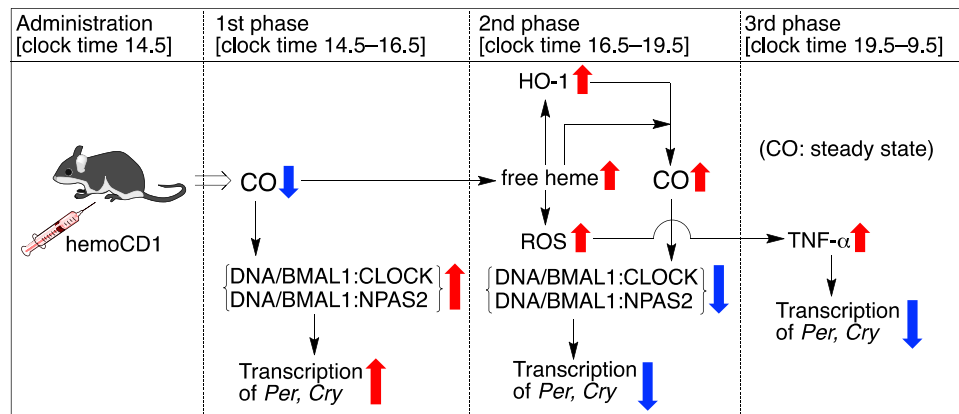


Figure 8. A mechanism for the circadian clock disruption caused by the hemoCD1-mediated endogenous CO depletion in mice. The components of Fig. 8 were drawn using ChemBioDraw.

of electrophoretic mobility shift assay, probably due to much lower CO binding affinity of CLOCK ($K_d = ca. 0.1 \text{ mM}$ at 22°C)¹⁹ than that of NPAS2 ($K_d = 1\text{--}2 \text{ }\mu\text{M}$ at 25°C)¹³. In contrast, the ChIP experiments for the hemoCD1-treated murine liver (Fig. 5c,d) clearly indicated that the DNA-bindings of BMAL1:CLOCK as well as BMAL1:NPAS2 were significantly altered by internal CO levels. The CO-responsive function of CLOCK has been rarely reported^{19,24}, and should be highlighted from the molecular biological point of view, although this would be beyond the scope of this study. We concluded that the up-regulation of the E-box-controlled clock genes observed in the first phase is ascribed to the enhanced transcriptional activities of both BMAL1:NPAS2 and BMAL1:CLOCK at E-box under the CO-reduced conditions.

HemoCD1 administered to mice primarily removes endogenous CO from cell-free CO-hemoglobin in blood, forming cell-free oxy-hemoglobin that is readily oxidized to met-hemoglobin (Fe^{III} state) by ROS in the blood plasma³⁴. CO-hemoglobin is resistant against the oxidation mediated by ROS, such as hydrogen peroxide³⁴. As cell-free met-hemoglobin easily dissociates to heme and apo-protein³⁸, free heme tends to be accumulated in the plasma and tissues in the endogenous CO-removed mice³⁴. The accumulated free heme is taken up by hepatic cells³⁸ and induces HO-1 *via* activation of Bach-1⁹, resulting in an increase of endogenous CO production *via* heme degradation. Indeed, the amount of endogenous CO is significantly increased in the hemoCD1-treated mice in the second phase (Fig. 6a). The excessively produced endogenous CO might cause additional dissociation of BMAL1:CLOCK(NPAS2) from E-box, resulting in down-regulation of the E-box-regulated clock genes in the second phase. Therefore, the data observed in the first and second phases strongly supports the scenario that the E-box-controlled clock gene transcriptions by both BMAL1:NPAS2 and BMAL1:CLOCK are modulated by internal CO *in vivo*. The expression of HO-1 shows a circadian rhythm²⁴. Endogenous CO production must also be circadian, as we show the time-dependent changes in the amounts of endogenous CO in the control groups (Fig. 5a). The circadian production of endogenous CO is possibly related to regulation of the core TTFL through acting on NPAS2 and CLOCK.

Circadian rhythms tend to be disrupted in injured cells and tissues^{22,23,41,42}. Increases in inflammatory cytokines, such as IL-1 β and TNF- α , affect the clock gene expression and function through acting mainly on the E-box regulatory elements^{40,41} although details have not been fully established. The murine cells treated with TNF- α *in vitro* and *in vivo* cause down-regulation of *Per1*, *Per2*, and other several clock genes, except for *Rev-Erba*⁴⁰. Interestingly, it has been recently demonstrated that inflammation-induced circadian rhythm disruption is suppressed by application of exogenous CO^{22,23}. In contrast, the endogenous CO-reduced mice by hemoCD1 showed an inflammatory response due to accumulation of free heme and ROS, as evidenced by the data in Fig. 6. TNF- α significantly accumulated in the third phase (*ca.* 5 h after the administration of hemoCD1), which might have caused further down-regulation of clock gene (*Per, Cry*) expression. The decreased wheel running activity observed in the hemoCD1-treated mice could be ascribed not only to down-regulation of *Cry*³⁷ but also to accumulation of TNF- α (40). Considering that hemoCD1 cannot reach the brain, the accumulation of TNF- α is likely the main reason for the decreased wheel running. The accumulated TNF- α can be sustained across the blood-brain barrier, which might affect clock gene expression in the suprachiasmatic nucleus⁴⁰. The down-regulation of *Per* and *Cry* ceased at 19 h after the administration of hemoCD1, at which TNF- α levels also returned to the normal state. Therefore, the temporal reduction of endogenous CO by hemoCD1 in mice has a long-term influence on the circadian clock due to the inflammatory response, and the circadian clock disruption continues until excess TNF- α is completely consumed.

The present pseudo-knockdown study for endogenous CO supports the hypothesis reported in the study using an HO-1 knockout system by Kramer *et al.*²⁴. In the HO-1 knockout mice, the E-box-controlled clock gene expression was significantly enhanced due to CLOCK activity changes. This is consistent with our observations of the hemoCD1-treated mice during the first phase. Unlike the reported HO-1 knockout system, our system selectively and temporally reduced the amount of endogenous CO in mice. Thus, the internal CO level can be dynamically altered, as shown in Fig. 5. Another advantage of our system is that hemoCD1 can also be used for internal CO quantification. As discussed in the paper by Kramer *et al.*²⁴, the amount of endogenous CO was

previously only roughly known *in vivo*. By using hemoCD1, we have succeeded in demonstrating the relation between internal CO levels and the core clock system.

In conclusion, based on the pseudo-knockdown strategy for CO, we identified the contribution of endogenous CO to regulation of the circadian clock *in vivo*. Temporal reduction of endogenous CO in mice by hemoCD1 significantly affected the circadian rhythms of the E-box-controlled clock genes. The mechanistic study suggested that the CO-dependent transcriptional activity changes of NPAS2 and CLOCK and the subsequent inflammatory response to produce TNF- α were both responsible for the CO-removal-induced circadian rhythm disruption. In principle, selective depletion of small biomolecules, such as gaseous signaling molecules, by genetic/pharmacological methods should not be possible without any side effects. We believe that, as demonstrated in this work, the pseudo-knockdown approach based on the highly selective molecular recognition by synthetic compounds will help to clarify the roles and functions of such small molecules in biological systems.

Materials and Methods

Preparation of hemoCD1 for administration. HemoCD1 and its free base complex (Fb-hemoCD1) were synthesized in our laboratory^{29,34}. The aqueous buffer solution containing the O₂ adduct of hemoCD1 (1.0 mM in PBS) was prepared according to the method as previously described^{34,35}. The solution was used for intraperitoneal (i.p.) administration to mice. The solution of Fb-hemoCD1 was similarly prepared with iron-free porphyrin.

Animal experiments. All animal experiments were approved by the Animal Experimental Committee of Doshisha University (Approval No. A 16001, A17033, A18040) and carried out in accordance with the Guidelines for Animal Experiments of Doshisha University. Male C57BL/6N mice weighing 20–22 g were used. For acclimatization, the mice were housed under a 12 h/12 h light/dark cycle with free feedings for two weeks before the day in the experiments. The mice were then housed under the dark condition without feeding from the experimental day in order to avoid the entrainment by external stimuli (light and food).

A solution of hemoCD1 (0.15 mL) was intraperitoneally administered to the subject mouse. The mice were sacrificed by cervical dislocation at different time points. The liver and/or whole brain samples were excised by disposable biopsy punch (5 mm), washed with saline, and soaked in RNA later stabilization reagent (QIAGEN). These were stored at 4 °C until use.

RT-PCR. Total RNA was isolated from the tissues using an RNA lipid tissue mini kit (QIAGEN) according to the manufacturer's instructions. The experimental procedures were the same as previously described^{34,35}. The amounts of total RNA used for reverse-transcription were appropriately adjusted in the range of 2–100 ng to see clear amplifications at the reasonable range in real-time PCR analyses (for *Per1*, *Per2*, *Cry2*, *Clock*, and *Rev-erba*, 2 ng; for *Cry1* and *Bmal1*, 10 ng; for *Npas2*, 100 ng; for β -*Actin*, 0.32 ng). The primers used in this study are listed in Table S1. Real-time PCR was performed using SYBR Green Master Mix (Applied Biosystems) and a StepOne real-time PCR system. β -Actin was used as a reference gene. All samples were measured in triplicate. Data were analyzed by the relative standard curve method using StepOne software v2.3 (Applied Biosystems).

Wheel running activity. Wheel running activity of mice was monitored using a RWC-15 automatic system (MELQUEST). For acclimatization, mice were housed in the system with a 12 h/12 h light/dark cycle for one week before being released into constant darkness. The monitoring started at 14:30 and the mice were i.p. administered at 14:30 of the second day. After administration, the monitor was continued for two consecutive days.

Quantification of endogenous CO. The liver or brain tissues (*ca.* 70 mg per sample, well-flashed to remove blood) were suspended in PBS and then homogenized on ice. The tissue suspensions in PBS (1 mL) were usually separated into 0.9 mL and 0.1 mL for CO and protein quantifications, respectively. The amount of endogenous CO in the tissues was measured by the hemoCD assay^{34,35}, where CO was detected by a simple photometric method using hemoCD1. To the tissue suspension (0.9 mL) was added hemoCD1 (1.0×10^{-8} mol) in PBS and then sonicated repeatedly on ice. The resulting suspension was filtered using an Amicon Ultra Centrifugal filter unit (MWCO 3000). The filtrate was measured by UV-vis spectrometer (SHIMADZU UV-2450). The calculation for determining the CO content from the absorbances was described previously^{34,35}. The CO contents in the tissues were normalized by protein contents determined by a bicinchoninic acid (BCA) method.

Western Blotting. Lysate of the mice liver was subjected to sodium dodecyl sulfate (SDS)-polyacrylamide gel electrophoresis (PAGE), and the proteins in the gels were electrophoretically transferred onto polyvinylidene difluoride membranes. The experimental procedure was the same as that previously described^{34,35}.

Chromatin Immunoprecipitation (ChIP) assay. The liver tissue (*ca.* 350 mg) was soaked in PBS containing 1% formaldehyde (10 mL/g) and shaken for 10 min at room temperature. To the solution was added glycine to a final concentration of 0.125 M and then incubated for additional 5 min. After homogenization of the tissue, the cells were collected by centrifugation, counted, and then suspended in Lysis buffer (ATTO, 0.75 mL/10⁷ cells) containing 1% protease inhibitor and 0.5 mM phenylmethylsulfonyl fluoride (PMSF). The cells were then disrupted by sonication (QSONICA, amplitude; 20%, ten times for 20 s each with 40 s intervals). The aliquot sample (20–40 μ L) was used for an BCA protein quantification assay. Another aliquot (100 μ L) was used for checking the chromatin size as follows; the aliquot solution was mixed with 5 M NaCl aqueous solution (5 μ L), heated at 65 °C for 5 h to reverse the cross-linking, and then the solution was heated at 45 °C for 1 h after the additions of RNase A (Wako, 10 mg/mL, 2 μ L) and proteinase K (Wako, 20 mg/mL, 2 μ L) to remove RNA and proteins. The DNA component in the solution was isolated using QIAquick PCR purification kit (QIAGEN), and then the chromatin

size was checked by agarose electrophoresis to ensure that the average size was between 100 and 1000 bp. The sonication was repeated until this size distribution was achieved.

The sonicated chromatin sample was diluted with Lysis buffer (ATTO) at the concentration of 1.25 mg protein/mL and then mixed with protein A/G plus agarose (Santa Cruz Biotechnology) bead slurry (30 μ L). After shaking the solution at 4 °C for 2 h, the solution was centrifuged, and the supernatant was collected. An aliquot (20 μ L) of the supernatant was separated for the use as the input sample, and therefore stored at -20 °C until the reverse cross-linking. The residual supernatant solution (410 μ L) was transferred to a new tube, and mixed with anti-NPAS2 antibody (3 μ L, H-270, Santa Cruz Biotechnology) or anti-CLOCK-antibody (5 μ L, ab3517, abcam). After the solution was gently shaken overnight at 4 °C, the solution was then mixed with protein A/G plus agarose bead slurry (30 μ L) that was preliminarily blocked with salmon sperm DNA. After further incubation for 2 h at 4 °C, the beads were collected by centrifugation, and washed repeatedly with low salt buffer (20 mM Tris-HCl, pH 8, 2 mM EDTA, 1% Triton X-100, 0.1% SDS, 200 μ L), high salt buffer (low salt buffer plus 0.5 M NaCl, 200 μ L), and LiCl salt buffers (0.25 M LiCl, 10 mM Tris-HCl, pH 8, 1 mM EDTA, 1% sodium deoxycholate, 1% NP-40, 200 μ L). The bound materials on the beads were eluted by heating at 65 °C for 20 min with an Elution buffer (70 mM Tris-HCl, pH 8, 1 mM EDTA, 1.5% SDS, 120 μ L). After centrifugation, the supernatant (500 μ L) was collected, mixed with 5 M NaCl aqueous solution (5 μ L), and then heated at 65 °C for 5 h to reverse the cross-linking. After that, the solution was heated at 45 °C for 1 h with RNase A (10 mg/mL, 2 μ L) and proteinase K (20 mg/mL, 2 μ L) to remove RNA and proteins. The DNA component in the resulting solution was isolated using QIAquick PCR purification kit (QIAGEN).

The resulting DNA samples were quantified by real-time PCR. The primers used in the ChIP assay are listed in Table S2. Real-time PCR was performed using SYBR Green Master Mix (Applied Biosystems) and a Step One real-time PCR system. β -Actin was used as a reference gene. All samples were measured in triplicate. Data were analyzed by the relative standard curve method using StepOne software v2.3 (Applied Biosystems).

Quantification of free heme. The liver tissues (*ca.* 200 mg) was homogenized with RIPA lysis buffer (500 μ L, ATTO, 20 mM HEPES, 150 mM NaCl, 1.0% IGEPAL CA- 630, 0.1% SDS, and 0.5% sodium deoxycholate). The supernatant was obtained by centrifugation. Aliquot was used for BCA protein quantification. The residual supernatant was passed through an Amicon Ultra Centrifugal filter units (MWCO 3000) to remove proteins. The concentration of free heme in the protein-depleted solution was quantified by a chromogenic assay according to the manufacturer's instructions (QuantiChrom heme assay kit, Bioassay Systems). The colorimetric change was monitored at 405 nm using a Filter Max F5 plate reader (Molecular Devices).

Quantification of ROS. The plasma samples were collected from the hemoCD1-treated mice blood after centrifugation (4000 g, 20 min). The tissue samples were also collected from the mice liver (*ca.* 50 mg). The tissue was mixed with buffer (1 mL) containing 150 mM KCl, 20 mM Tris, 0.5 mM EDTA, 5 mM glucose, 1 mM $MgCl_2$, 0.5 mM octanoic acid. After homogenization, the tissue samples were diluted to the 50 mg protein/mL concentrations, and then mixed with the solution of dihydrorhodamine (2 μ L, 10 mM DMSO solution) as a fluorescent ROS probe. After removing insoluble materials by centrifugation, fluorescence intensity of the supernatant (100 μ L each) was detected using a Filter Max F5 plate reader (Molecular Devices, $\lambda_{ex} = 485 \pm 20$ nm and $\lambda_{em} = 535 \pm 25$ nm).

Quantification of TNF- α protein. The mouse liver was homogenized in RIPA Lysis Buffer (ATTO, 20 mM HEPES, 150 mM NaCl, 1.0% IGEPAL CA- 630, 0.1% SDS, and 0.5% sodium deoxycholate) after the additions of the protease inhibitor (ATTO) and phosphatase inhibitor (ATTO). The total protein concentration was determined by an BCA assay. The amount of TNF- α protein in the liver was determined using a mouse TNF- α ELISA kit (Novex Life Technologies). The experiments were performed according to the manufacturer's instruction. The amount of TNF- α was quantified by a photometric measurement using a Filter Max F5 plate reader (Molecular Devices, Abs. at 450 nm).

Statistical analysis. All data represent the means \pm SE from at least three different experiments. Statistical analysis ($n \geq 3$) was performed by using an unpaired Student's *t*-test. The *P* value less than 0.05 was considered significant.

References

1. Reppert, S. M. & Weaver, D. R. Coordination of circadian timing in mammals. *Nature* **418**, 935–941 (2005).
2. Albrecht, U. Timing to perfection: The biology of central and peripheral circadian clocks. *Neuron* **74**, 246–260 (2012).
3. Buhr, E. D. & Takahashi, J. S. Molecular components of the Mammalian circadian clock. *Handb. Exp. Pharmacol.* **217**, 3–27 (2013).
4. Videnovic, A., Lazar, A. S., Barker, R. A. & Overeem, S. 'The clocks that time us'—circadian rhythms in neuro-degenerative disorders. *Nat. Rev. Neurol.* **10**, 683–693 (2014).
5. DeBruyne, J. P., Weaver, D. R. & Reppert, S. M. CLOCK and NPAS2 have overlapping roles in the suprachiasmatic circadian clock. *Nat. Neurosci.* **10**, 543–545 (2007).
6. DeBruyne, J. P. Oscillating perceptions: the ups and downs of the CLOCK protein in the mouse circadian system. *J. Genet.* **87**, 437–446 (2008).
7. Bertolucci, C. *et al.* Evidence for an overlapping role of CLOCK and NPAS2 transcription factors in liver circadian oscillators. *Mol. Cell. Biol.* **28**, 3070–3075 (2008).
8. Stojkovic, K., Wing, S. S. & Cermakian, N. A central role for ubiquitination within a circadian clock protein modification code. *Front. Mol. Neurosci.* **7**, 1–7 (2014).
9. Wu, L. & Wang, R. Carbon monoxide: endogenous production, physiological functions, and pharmacological applications. *Pharmacol. Rev.* **57**, 585–630 (2005).
10. Ryter, S. W., Alam, J. & Choi, A. M. Heme oxygenase-1/carbon monoxide: from basic science to therapeutic applications. *Physiol. Rev.* **86**, 583–650 (2006).

11. Motterlini, R. & Otterbein, L. E. The therapeutic potential of carbon monoxide. *Nat. Rev. Drug Discovery* **9**, 728–743 (2010).
12. Motterlini, R. & Foresti, R. Biological signaling by carbon monoxide and carbon monoxide-releasing molecules. *Am. J. Physiol. Cell Physiol.* **312**, C302–C313 (2017).
13. Dioum, E. M. *et al.* NPAS2: a gas-responsive transcription factor. *Science* **298**, 2385–2387 (2002).
14. Aono, S. Biochemical and Biophysical Properties of the CO-Sensing Transcriptional Activator CooA. *Acc. Chem. Res.* **36**, 825–831 (2003).
15. Kerby, R. L., Youn, H. & Roberts, G. P. RcoM: A New Single-Component Transcriptional Regulator of CO Metabolism in Bacteria. *J. Bacteriol.* **190**, 3336–3343 (2008).
16. Shimizu, T. *et al.* Gaseous O₂, NO, and CO in signal transduction: Structure and function relationships of heme-based gas sensors and heme-redox sensors. *Chem. Rev.* **115**, 6491–6533 (2015).
17. Szabo, C. Gasotransmitters in cancer: from pathophysiology to experimental therapy. *Nat. Rev. Drug Discovery* **15**, 185–203 (2016).
18. Fukuto, J. M. *et al.* Small molecule signaling agents: the integrated chemistry and biochemistry of nitrogen oxides, oxides of carbon, dioxygen, hydrogen sulfide, and their derived species. *Chem. Res. Toxicol.* **25**, 769–793 (2012).
19. Lukat-Rodgers, G. S., Correia, C., Botuyan, M. V., Mer, G. & Rodgers, K. R. Heme-based sensing by the mammalian circadian protein CLOCK. *Inorg. Chem.* **49**, 6349–6365 (2006).
20. Boehning, D. & Snyder, S. H. Circadian rhythms. Carbon monoxide and clocks. *Science* **298**, 2339–2340 (2002).
21. Tu, B. P. & McKnight, S. L. *Proc. Nat. Acad. Sci. USA* **106**, 14293–14296 (2009).
22. Schallner, N. *et al.* Carbon monoxide preserves circadian rhythm to reduce the severity of subarachnoid hemorrhage in mice. *Stoke* **48**, 2565–2573 (2017).
23. Correa-Costa, M. *et al.* Carbon monoxide protects the kidney through the central circadian clock and CD39. *Proc. Natl. Acad. Sci. USA* **115**, E2302–E2310 (2018).
24. Klemz, R. *et al.* Reciprocal regulation of carbon monoxide metabolism and the circadian clock. *Nat. Struct. Mol. Biol.* **24**, 15–22 (2017).
25. Kaasik, K. & Lee, C. C. Reciprocal regulation of haem biosynthesis and the circadian clock in mammals. *Nature* **430**, 467–471 (2004).
26. Damulewicz, M., Loboda, A., Jozkowicz, A., Dulak, J. & Pyza, E. Interactions between the circadian clock and heme oxygenase in the retina of drosophila melanogaster. *Mol. Neurobiol.* **54**, 4953–4962 (2017).
27. Rey, G. *et al.* The pentose phosphate pathway regulates the circadian clock. *Cell. Metab.* **24**, 462–473 (2016).
28. Yoshii, K., Tajima, F., Ishijima, S. & Sagami, I. Changes in pH and NADPH regulate the DNA binding activity of neuronal PAS domain protein 2, a mammalian circadian transcription factor. *Biochemistry* **54**, 250–259 (2015).
29. Kano, K., Kitagishi, H., Koder, M. & Hirota, S. Dioxygen binding to a simple myoglobin model in aqueous solution. *Angew. Chem. Int. Ed.* **44**, 435–438 (2005).
30. Kano, K. *et al.* Iron porphyrin–cyclodextrin supramolecular complex as a functional model of myoglobin in aqueous solution. *Inorg. Chem.* **45**, 4448–4460 (2006).
31. Kitagishi, H. *et al.* Oxoferryl porphyrin/hydrogen peroxide system whose behavior is equivalent to hydroperoxoferric porphyrin. *J. Am. Chem. Soc.* **132**, 16730–16732 (2010).
32. Watanabe, K., Kitagishi, H. & Kano, K. Supramolecular iron porphyrin/cyclodextrin dimer complex that mimics the functions of hemoglobin and methemoglobin. *Angew. Chem. Int. Ed.* **52**, 6894–6897 (2013).
33. Kitagishi, H. *et al.* A diatomic molecule receptor that removes CO in a living organism. *Angew. Chem. Int. Ed.* **49**, 1312–1315 (2010).
34. Kitagishi, H. *et al.* Feedback response to selective depletion of endogenous carbon monoxide in the blood. *J. Am. Chem. Soc.* **138**, 5417–5425 (2016).
35. Minegishi, S. *et al.* Detection and removal of endogenous carbon monoxide by selective and cell-permeable hemoprotein model complexes. *J. Am. Chem. Soc.* **139**, 5984–5991 (2017).
36. Watanabe, K., Suzuki, T., Kitagishi, H. & Kano, K. Reaction between a haemoglobin model compound and hydrosulphide in aqueous solution. *Chem. Commun.* **51**, 4059–4061 (2015).
37. Vitaterna, M. H. *et al.* Differential regulation of mammalian Period genes and circadian rhythmicity by cryptochromes 1 and 2. *Proc. Natl. Acad. Sci. USA* **96**, 12114–12119 (1999).
38. Ferreira, A., Balla, J., Jeney, V., Balla, G. & Soares, M. P. A central role for free heme in the pathogenesis of severe malaria: the missing link? *J. Mol. Med.* **86**, 1097–1111 (2008).
39. Aikawa, R. *et al.* Reactive oxygen species induce cardiomyocyte apoptosis partly through TNF- α . *Cytokine* **18**, 179–183 (2002).
40. Cavadini, G. *et al.* TNF- α suppresses the expression of clock genes by interfering with E-box-mediated transcription. *Proc. Natl. Acad. Sci. USA* **104**, 12843–12848 (2007).
41. Yoshida, K., Hashimoto, T., Sakai, Y. & Hashiramoto, A. Involvement of the circadian rhythm and inflammatory cytokines in the pathogenesis of rheumatoid arthritis. *J. Immunol. Res.* **2014**, 282495 (2014).
42. Buttgerit, F., Smolen, J. S., Coogan, A. N. & Cajochen, C. Clocking in: chronobiology in rheumatoid arthritis. *Nat. Rev. Rheumatol.* **11**, 346–356 (2015).

Acknowledgements

This work was financially supported by MEXT/JSPS KAKENHI (Grant No. 15H02569, 16K13092, 17H02208), the MEXT-Supported Program for the Strategic Research Foundation at Private Universities (2015–2019), the Naito Foundation, Takeda Science Foundation, Suntory Foundation for Life Sciences, and JGC-S Scholarship Foundation. SM is grateful to JSPS for a graduate fellowship.

Author Contributions

S.M. and H.K. designed the experiments and analyzed data. I.S., S.N. and K.K. contributed to the data analysis and discussion in the whole part of this study. All authors participated in the process of the writing and reviewing the manuscript.

Additional Information

Supplementary information accompanies this paper at <https://doi.org/10.1038/s41598-018-30425-6>.

Competing Interests: The authors declare no competing interests.

Publisher's note: Springer Nature remains neutral with regard to jurisdictional claims in published maps and institutional affiliations.



Open Access This article is licensed under a Creative Commons Attribution 4.0 International License, which permits use, sharing, adaptation, distribution and reproduction in any medium or format, as long as you give appropriate credit to the original author(s) and the source, provide a link to the Creative Commons license, and indicate if changes were made. The images or other third party material in this article are included in the article's Creative Commons license, unless indicated otherwise in a credit line to the material. If material is not included in the article's Creative Commons license and your intended use is not permitted by statutory regulation or exceeds the permitted use, you will need to obtain permission directly from the copyright holder. To view a copy of this license, visit <http://creativecommons.org/licenses/by/4.0/>.

© The Author(s) 2018

Detection and Removal of Endogenous Carbon Monoxide by Selective and Cell-Permeable Hemoprotein Model Complexes

Saika Minegishi,[†] Aki Yumura,[†] Hirotsuna Miyoshi,[†] Shigeru Negi,[‡] Shigeru Taketani,[§] Roberto Motterlini,^{||,⊥} Roberta Foresti,^{||,⊥} Koji Kano,[†] and Hiroaki Kitagishi^{*,†,⊥}

[†]Department of Molecular Chemistry and Biochemistry, Faculty of Science and Engineering, Doshisha University, Kyotanabe, Kyoto 610-0321, Japan

[‡]Faculty of Pharmaceutical Sciences, Doshisha Women's College of Liberal Arts, Kyotanabe, Kyoto 610-0395, Japan

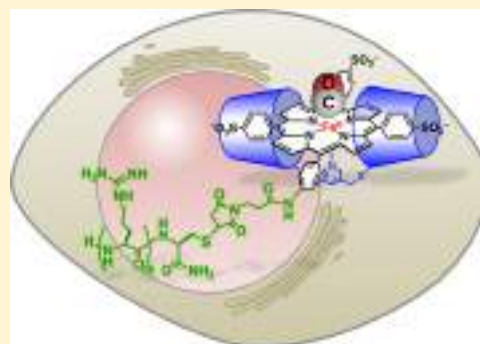
[§]Department of Microbiology, Kansai Medical University, Hirakata, Osaka 573-1010, Japan

^{||}Inserm U955, Team 12, Créteil 94000, France

[⊥]Université Paris Est, Faculty of Medicine, Créteil 94000, France

Supporting Information

ABSTRACT: Carbon monoxide (CO) is produced in mammalian cells during heme metabolism and serves as an important signaling messenger. Here we report the bioactive properties of selective CO scavengers, hemoCD1 and its derivative R8-hemoCD1, which have the ability to detect and remove endogenous CO in cells. HemoCD1 is a supramolecular hemoprotein-model complex composed of 5,10,15,20-tetrakis(4-sulfonatophenyl)porphyratoiron(II) and a per-*O*-methylated β -cyclodextrin dimer having a pyridine linker. We demonstrate that hemoCD1 can be used effectively to quantify endogenous CO in cell lysates by a simple spectrophotometric method. The hemoCD1 assay detected ca. 260 pmol of CO in 10⁶ hepatocytes, which was well-correlated with the amount of intracellular bilirubin, the final breakdown product of heme metabolism. We then covalently attached an octaarginine peptide to a maleimide-appended hemoCD1 to synthesize R8-hemoCD1, a cell-permeable CO scavenger. Indeed, R8-hemoCD1 was taken up by intact cells and captured intracellular CO with high efficiency. Moreover, we revealed that removal of endogenous CO by R8-hemoCD1 in cultured macrophages led to a significant increase (ca. 2.5-fold) in reactive oxygen species production and exacerbation of inflammation after challenge with lipopolysaccharide. Thus, R8-hemoCD1 represents a powerful expedient for exploring specific and still unidentified biological functions of CO in cells.



INTRODUCTION

Carbon monoxide (CO) is one of the gaseous signaling molecules that play key regulatory roles as second messengers in biological systems.^{1–6} Because CO exhibits physiological functions similar to nitric oxide (NO) and hydrogen sulfide (H₂S),^{7–12} these three biomolecules are often classified within the same category of “gasotransmitters”. However, CO differs from the other two gases on the basis of its reactivity and biological source. CO is an inert gas and hardly decomposes *in vivo*, whereas NO and H₂S are highly reactive with metal ions, cysteine residues of proteins, and molecular oxygen.^{6–8} In biological systems, CO almost exclusively reacts via coordination with metal cofactors, mostly with ferrous heme.^{6–8,13} Therefore, endogenous CO is stable when bound to hemoproteins *in vivo*, and is gradually eliminated from the lung through respiration. The major endogenous source of CO is the degradation of heme by constitutive (HO-2) and inducible (HO-1) heme oxygenase enzymes.^{1,2} To date, investigations assessing the role of HO-derived CO have relied mainly on the use of cells and animals lacking HO enzymes in

parallel with application of CO gas and CO-releasing compounds.^{3,14,15} However, deletion of HO enzymes results not only in the elimination of CO but also of biliverdin and iron, the other breakdown products of heme metabolism. Moreover, if the enzymatic activity of HO is depleted to stop endogenous CO production, then accumulation of excess heme would cause serious side effects in addition to CO deficiency.¹⁶

To study the physiological roles and functions of CO, selective CO scavengers that can detect and/or remove CO from metal cofactors are extremely useful. Alongside several methods that have been recently developed for detecting CO in cells and tissues,^{17–22} our group has been working on the development of chemical compounds that are capable of selectively removing CO *in vitro* and *in vivo*. We first accomplished this by synthesizing and using hemoCD1 (Figure 1), a supramolecular hemoprotein-model complex that we have studied for the past decade.^{23–34} HemoCD1 is composed of

Received: March 5, 2017

Published: April 7, 2017

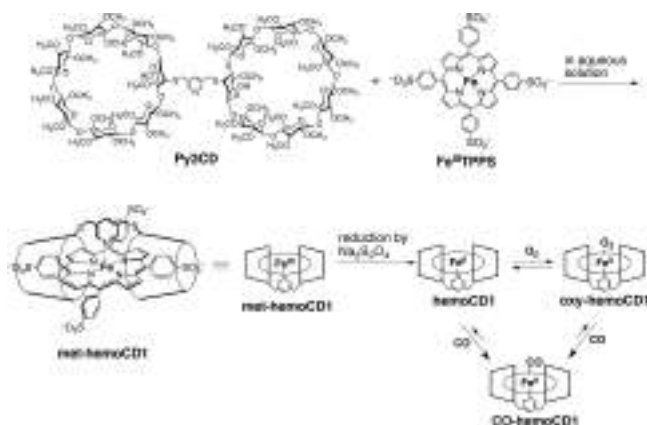


Figure 1. Structure of hemoCD1 used as a selective CO scavenger.

5,10,15,20-tetrakis(4-sulfonatophenyl)porphinatoiron(II) ($\text{Fe}^{\text{II}}\text{TPPS}$) and per-*O*-methylated β -cyclodextrin dimer (Py3CD) with a pyridine ligand. In the ferrous state, oxygen (O_2) and CO are reversibly bound to the iron(II) center of hemoCD1, similar to the binding of these two gases to hemoglobin (Hb) and myoglobin (Mb) in aqueous solution. However, because of the lack of the distal polar functional group that destabilizes CO-ferrous complexes in Hb and Mb,^{35,36} the CO binding affinity of hemoCD1 is much higher than that of Hb in the R-state and Mb.^{24,33} We have recently demonstrated that hemoCD1 can successfully remove CO from CO-bound Hb in the blood of living animals.^{27,33} Since hemoCD1 shows high water solubility and does not bind to endogenous NO in blood, it does not cause any toxicity or increase blood pressure in animals.^{27,29} Therefore, hemoCD1 is a useful chemical tool that allows a pseudoknockdown state of CO in animals without disrupting other physiological processes, such as heme metabolism by HO.

Here we advance on our technologies devised to scavenge CO by presenting data on the synthesis and characterization of a cell-permeable hemoCD1 derivative that targets endogenous CO in cells. First, we quantified CO produced in control and hemin-stimulated cells using a simple photometric method that utilized hemoCD1. Since hemoCD1 does not penetrate the cell membranes, an assay for intracellular CO quantification was established by preparing cell lysates. Next, we synthesized R8-hemoCD1 by conjugating hemoCD1 to an octaarginine chain as a cell-penetrating peptide, to capture intracellular CO without destroying the cells. Using R8-hemoCD1, we demonstrate that specific removal of endogenous CO in living cells is attainable and provides evidence for the crucial role of intracellular CO in inflammatory responses and in the regulation of reactive oxygen species (ROS) production.

RESULTS AND DISCUSSION

Preparation of hemoCD1. A solution of hemoCD1 in phosphate-buffered saline (PBS) was prepared as follows. The solution of met-hemoCD1, which contained $\text{Fe}^{\text{III}}\text{TPPS}$ and 1.2 equiv of Py3CD (Figure 1) in PBS, was reduced to ferrous (Fe^{II}) hemoCD1 by excess $\text{Na}_2\text{S}_2\text{O}_4$. The resulting solution was purified using a Sephadex G-25 desalting column to remove excess $\text{Na}_2\text{S}_2\text{O}_4$ and its decomposition products. During purification, hemoCD1 bound atmospheric O_2 to form the oxygen complex, oxy-hemoCD1.^{24,35} The eluted solution containing oxy-hemoCD1 was used for quantification of intracellular CO. Oxy-hemoCD1 binds CO very strongly via

the ligand exchange of O_2 to CO (Figure 1). Addition of oxy-hemoCD1 solution to the culture medium did not result in significant cytotoxicity at the concentration used in this study (up to 20 μM , Figure S1).

Quantification of Endogenous CO in Cells. A solution of oxy-hemoCD1 in PBS (1 mL) was added to cells (Figure 2a). Cells were then collected, counted, and disrupted by

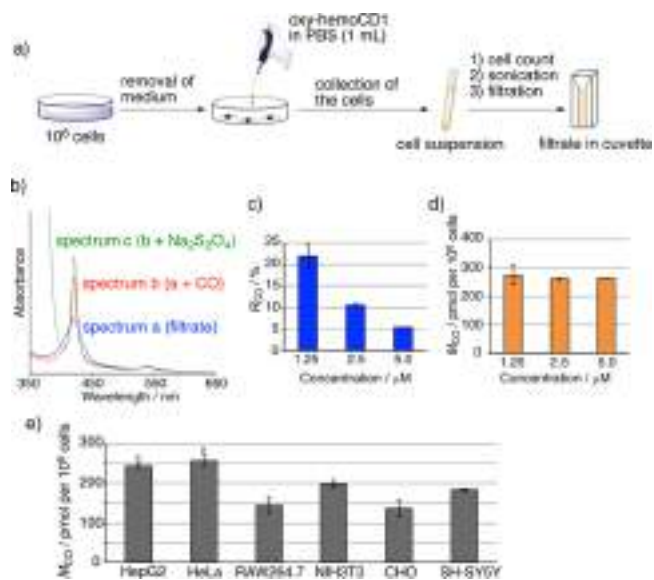


Figure 2. Quantification of endogenous CO in cells by hemoCD1. (a) Workflow of CO quantification by hemoCD1. (b) UV-vis absorption spectra of the filtrate in cuvettes before (blue) and after the addition of CO (red) and $\text{Na}_2\text{S}_2\text{O}_4$ (green). From these spectra, the amount of CO contained in cells was quantified. (c) Concentration dependency of the ratio (R_{CO}) of CO-hemoCD1 in the total hemoCD1 contained in the cell lysate from the 10^6 HepG2 cells. (d) Amount of CO (M_{CO}) detected in the 10^6 HepG2 cells by hemoCD1 at different concentrations. (e) Moles of endogenous CO detected in the untreated HepG2, HeLa, RAW264.7, NIH3T3, CHO, and SH-SY5Y cells (10^6 cells), as determined by hemoCD1 assays. Each bar represents the means \pm SE ($n = 3$ experiments per group). *, $P < 0.05$ as compared with control cells.

sonication.³⁷ Samples were filtered to remove insoluble materials, and the clear cell lysate (filtrate) was measured by UV-vis absorption spectroscopy. Characteristic Soret and Q-bands due to hemoCD1 were detected (Figure 2b, spectrum a).³⁸ The solution contained three different hemoCD1 states, i.e., oxy-hemoCD1, CO-hemoCD1, and met-hemoCD1. met-hemoCD1 was partly formed by autoxidation of oxy-hemoCD1 during the experiment (the half-life of oxy-hemoCD1 is ca. 30 h at 25 $^\circ\text{C}$).^{24,33} Introduction of CO gas into the solution caused a spectral change due to the conversion of residual oxy-hemoCD1 to CO-hemoCD1 (Figure 2b, spectrum b). Subsequently, the addition of excess $\text{Na}_2\text{S}_2\text{O}_4$ to the solution converted all hemoCD1 species to CO-hemoCD1 (Figure 2b, spectrum c). Based on the absorbances of these spectra at 422 nm, the total concentration of hemoCD1 (C_{total}) and the concentrations of each component (C_{oxy} , C_{CO} , and C_{met}) were determined using the molar absorption coefficients of oxy-, met-, and CO-hemoCD1 as described in the Experimental Section. The calculated spectrum using the C_{oxy} , C_{CO} , and C_{met} values was in good agreement with the observed spectrum (Figure S2). The ratio of CO-hemoCD1 in the total hemoCD1 species (R_{CO}) and the moles of CO contained as CO-

hemoCD1 in the cell lysate (M_{CO}) were determined. R_{CO} and M_{CO} are defined as follows:

$$R_{CO} (\%) = (C_{CO}/C_{total}) \times 100 \quad (1)$$

$$M_{CO} (\text{mol}) = C_{CO} \times V \quad (2)$$

where V is the volume of the oxy-hemoCD1 solution added to the cells (1×10^{-3} L). The R_{CO} values (Figure 2c) showed inverse dependence on the concentration of oxy-hemoCD1 added to the cells, i.e., as the concentration of oxy-hemoCD1 increased from 1.25 to 5.0 μM R_{CO} decreased from 22 to 5%. Accordingly, the ratio of oxy-hemoCD1 (R_{oxy}) increased as a function of the concentration (Figure S3), yielding M_{CO} values that were independent of the initial oxy-hemoCD1 concentration (Figure 2d). A constant amount of CO ($[2.6 \pm 0.09] \times 10^{-10}$ mol) was detected as CO-hemoCD1 from the 10^6 HepG2 cells with a high reproducibility. The amount of CO was almost equal to that of bilirubin in the cells (*vide infra*). Using this assay, we measured the amounts of endogenous CO in different types of cells (Figure 2e). Endogenous CO in the range of 140–260 pmol was detected in the respective 10^6 cells. Among the cell lines tested, cancer cell lines HepG2 and HeLa contained relatively large amounts of endogenous CO under normal culture conditions. This result is in accordance with the reported expression of cellular HO-1, the inducible isoform of HO, which is usually higher in cancer cells than that in normal cells.^{7,39}

Next, endogenous CO production was monitored after treatment of HepG2 cells (10^6 cells) with 20 μM hemin (ferric Fe^{III} state of heme), a substrate and inducer of HO-1 (Figure 3a). Intracellular CO and CO in the culture medium were

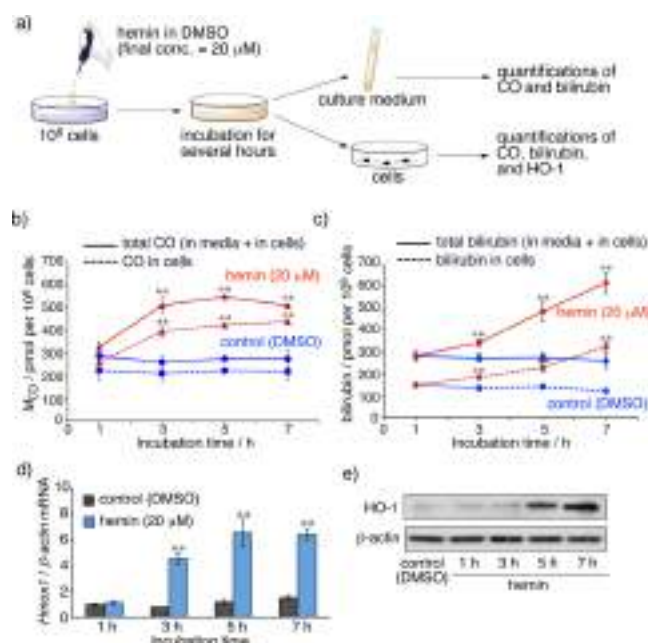


Figure 3. Quantifications of CO, bilirubin, and HO-1 in hemin-stimulated HepG2 cells. (a) Workflow of hemin stimulation and subsequent quantifications of CO, bilirubin, and HO-1 in cells and in the culture medium. (b) Time-course of CO production quantified by hemoCD1. (c) Time-course of bilirubin quantified by UnaG. (d, e) mRNA (*Hmox1*) and protein levels of HO-1 measured by real-time PCR and Western blotting using anti-HO-1 antibodies. *, $P < 0.05$ as compared with the controls.

quantified using hemoCD1 assays. We used UnaG, a recently identified bilirubin-binding fluorescent protein,⁴⁰ to quantify bilirubin in cells and in the culture medium.⁴¹ The time course (Figure 3b,c) showed a clear increase in endogenous CO and bilirubin in hemin-treated cells as compared with that in control cells incubated with the vehicle (DMSO). Without addition of hemin, endogenous CO was constant, and the amount of total CO (280 ± 54 pmol/ 10^6 cells) was completely consistent with that of total bilirubin (280 ± 21 pmol/ 10^6 cells).⁴² The result is expected because the enzymatic reaction of HO produces equimolar amounts of CO and biliverdin that is subsequently converted to bilirubin by NAD(P)H-dependent reductases.² The addition of hemin caused a time-dependent increase in both CO and bilirubin. The levels of total CO reached a plateau at 5 h and then started to decrease, probably due to atmospheric diffusion of CO from the medium, whereas bilirubin continued to accumulate in the medium.⁴³ Interestingly, bilirubin accumulation after the addition of hemin was slower than CO accumulation, suggesting that more time was required for enzymatic reduction of biliverdin to bilirubin after hemin degradation by HO. HO-1 protein expression was strongly induced after addition of hemin to cells (Figure 3d,e), which was consistent with previous findings.^{44,45} Competitive experiments using Sn-protoporphyrin IX (SnPPIX, an HO inhibitor)^{43,46,47} demonstrated that the hemin-induced intracellular CO production was blocked by SnPPIX, as quantified by hemoCD1 assays (Figure S4). Therefore, the amount of CO detected by hemoCD1 clearly reflected the enzymatic activity of HO in cells.

Preparation of a Cell-Permeable R8-hemoCD1. In order to capture and remove intracellular CO without disrupting cells, we synthesized a cell-permeable hemoCD1. For this purpose, we utilized a cell-penetrating peptide (CPP) that was covalently attached to hemoCD1. Octaarginine (Arg8 or R8) is a well-characterized CPP developed by Futaki et al.^{48–51} Recently, we established covalent attachments of R8 to the tetraarylporphyrin/per-*O*-methylated β -cyclodextrin supramolecular complexes, which enabled them to be delivered into the cells.^{52–54} In the present study, R8 with terminal Cys (Arg8-Cys) was conjugated to maleimide-appended met-hemoCD1 (Mal-met-hemoCD1) by the Michael addition reaction (Figure 4).

Before the reaction with Arg8-Cys, Py3CD was added to the maleimide-appended Fe^{III} porphyrin (Mal- Fe^{III} TPPS) in order to avoid the formation of insoluble aggregates between anionic

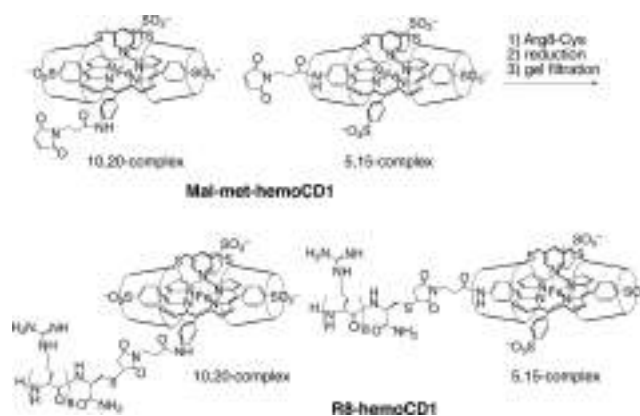


Figure 4. Preparation of R8-hemoCD1 as a scavenger of intracellular CO.

Mal-Fe^{III}TPPS and cationic Arg8-Cys (Figure S5). The supramolecular Mal-met-hemoCD1 complex exists as an approximate 1:1 mixture of the 5,15- and 10,20-complexes shown in Figure 4, as the structure has been characterized by ¹H NMR spectroscopy.⁵⁵ After conjugation of Mal-met-hemoCD1 with Arg8-Cys, the Fe^{III} complex was reduced by Na₂S₂O₄ followed by purification using gel-filtration chromatography to remove excess Arg8-Cys and Na₂S₂O₄. The purification was confirmed by the disappearance of reactive thiol groups, as monitored by Ellman's assay.^{56,57} The supramolecular R8-hemoCD1 complex was directly detected by MALDI-TOF MS (Figure S6). The supramolecular porphyrin-cyclodextrin complexes mostly dissociate upon laser irradiation and cannot be detected in the molecular complex form by MALDI-TOF MS.⁵⁵ Therefore, the undissociated component seems to originate from the 5,15-complex of R8-hemoCD1 (Figure 4), whose Py3CD moiety is sterically locked by Arg8 and cannot be dissociated.

The ferrous complex of R8-hemoCD1 (a mixture of the 5,15- and 10,20-complexes) formed stable O₂ and CO complexes in aqueous solution (Figure S7), in which the half-life for the autoxidation of the O₂ complex was 7.5 h at pH 7.4 and 37 °C (Figure S8). The O₂ and CO binding affinities of R8-hemoCD1 were measured using the gas equilibrium method (Figures S9 and S10); the affinities ($P_{1/2}^{O_2} = 21$ Torr and $P_{1/2}^{CO} = 1.3 \times 10^{-3}$ Torr at pH 7.4 and 37 °C) were comparable to those of hemoCD1 (Table S1). The selective removal of CO by R8-hemoCD1 was confirmed by the competitive assay with Hb (Figures S11 and S12). In this assay, we confirmed that R8-hemoCD1 quantitatively removed CO from CO-Hb and did not react with NO in the presence of ferrous Hb.

The cell-penetrating ability of R8-hemoCD1 was verified using its free-base analog (R8-Fb-hemoCD) as a fluorescent probe molecule. Confocal microscopy of HeLa cells showed effective cellular uptake of this complex (Figure S13), whereas the free-base complex of hemoCD1 (Fb-hemoCD1) and the noncovalent mixture of Arg8 with Fb-hemoCD1 could not be taken up by cells. Therefore, covalent attachment of the Arg8 peptide to hemoCD1 was effective for cell internalization of this complex. The fluorescence spectral profile measured inside the R8-Fb-hemoCD1-treated cells showed the two bands at 643 and 704 nm, which was characteristic of R8-Fb-hemoCD1 and distinguishable from free-base porphyrin without Py3CD (Figure S14). The results indicated that the structure of the inclusion complex of R8-Fb-hemoCD1 was maintained in cells.

R8-hemoCD1 Effectively Removes Intracellular CO. In order to verify the CO removal capacity of R8-hemoCD1 in cells, we used COP-1, a palladium-based fluorescent CO probe reported by Chang et al.,¹⁹ for visualization of intracellular CO. Before cell experiments, competition experiments for CO binding using hemoCD1 and COP-1 were carried out in the cuvette in the presence of a CO-releasing molecule ([Ru(CO)₃Cl(glycinate)] or CORM-3).¹⁵ Consistent with a previous report,¹⁹ the addition of CORM-3 to the solution of COP-1 caused a gradual increase in green fluorescence due to the reaction of COP-1 with CO (Figure S15). This reaction was completely blocked in the presence of hemoCD1, indicating that hemoCD1 captured CO released from CORM-3 more strongly than COP-1. The competitive reaction was demonstrated in HeLa cells. Consistent with the literature,¹⁹ COP-1 showed weak fluorescence in untreated cells (Figure 5a). When cells were incubated with CORM-3 prior to addition of COP-1 (Figure 5b), significantly intense

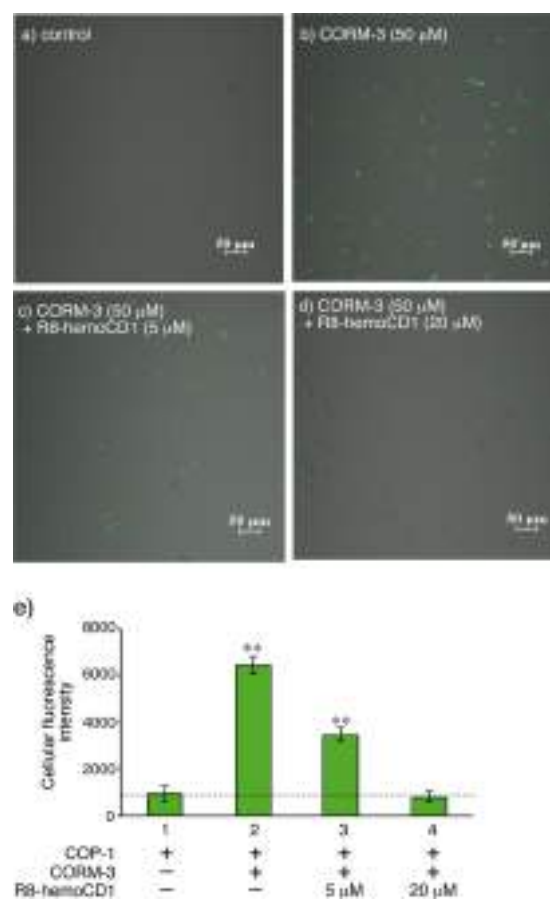


Figure 5. Confocal microscopy analysis of CO removal by R8-hemoCD1 in HeLa cells. The COP-1 probe (1 μM) was used for visualization of intracellular CO delivered by CORM-3 (50 μM). (a) Cells with COP-1. (b) Cells incubated with CORM-3 before the addition of COP-1. (c) Cells incubated with CORM-3, R8-hemoCD1 (5 μM), and then COP-1. (d) Cells incubated with CORM-3, R8-hemoCD1 (20 μM), and then COP-1. (e) Mean fluorescence intensities of representative images with (1) COP-1; (2) COP-1 and CORM-3; (3) COP-1, R8-hemoCD1 (5 μM), and CORM-3; and (4) COP-1, R8-hemoCD1 (20 μM), and CORM-3. Each bar represents the means ± SE ($n = 3$ experiments per group). **, $P < 0.01$ as compared to control (bar 1).

green fluorescence was detected in the cells. The fluorescence was weakened when R8-hemoCD1 was added to CORM-3-treated cells before the addition of COP-1 (Figure 5c,d), indicating that R8-hemoCD1 scavenged intracellular CO. The reaction of COP-1 with CO in cells was completely blocked when the CORM-3 (50 μM)-treated cells were incubated with 20 μM R8-hemoCD1 (Figure 5e).

Effects of CO Removal by R8-hemoCD1 on Cell Functions. The anti-inflammatory effects of CO in cells have been demonstrated using macrophages challenged with lipopolysaccharide (LPS).^{58,59} LPS induces the production of inflammatory cytokines, such as tumor necrosis factor- α (TNF- α), that has been reported to be markedly attenuated by administration of gaseous CO⁵⁸ or CO-RMs.⁵⁹ To explore whether R8-hemoCD1 blocks signaling pathways involving intracellular CO, RAW264.7 macrophages were treated with R8-hemoCD1 before stimulation by LPS, and the expression levels of TNF- α mRNA were then measured. In previous typical experiments, LPS stimulation was performed under a CO atmosphere or in the presence of CO-RMs in the medium

in order to evaluate the effects of CO on LPS-induced inflammation.^{58,59} In the present study, cells were first treated with CORM-3 (6 h) which was then washed out from the culture medium before the addition of R8-hemoCD1 in order to avoid extracellular reaction of R8-hemoCD1 with the compound. We confirmed that in this washing-out protocol, the CO liberated from CORM-3 in cells significantly inhibited TNF- α production (Figure 6, bars 2 and 3). Interestingly, the

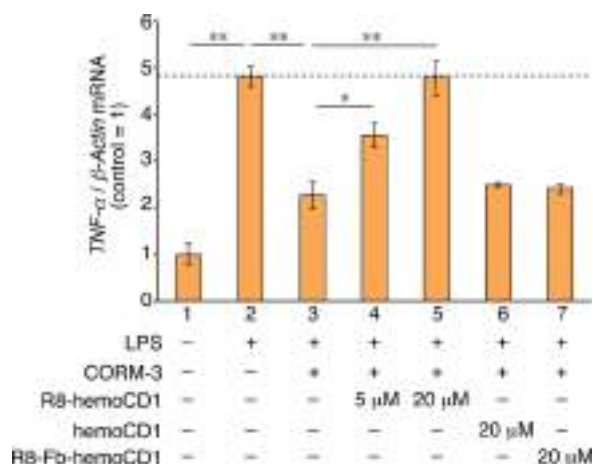


Figure 6. Effects of intracellular CO removal by R8-hemoCD1 on TNF- α mRNA expression in LPS-stimulated RAW264.7 macrophages. (1) Untreated cells (no LPS); (2) cells incubated with LPS (1 μ g/mL) for 1 h; (3) cells incubated with CORM-3 (50 μ M) for 6 h and then LPS (1 μ g/mL) for 1 h; (4, 5) cells incubated with CORM-3 (50 μ M) for 6 h, R8-hemoCD1 (5 and 20 μ M) for 30 min, and LPS (1 μ g/mL) for the final 1 h; (6, 7) negative controls to R8-hemoCD1 (20 μ M, bar 5) using hemoCD1 and R8-Fb-hemoCD1. Each bar represents the means \pm SE ($n = 3-6$ experiments per group). *, $P < 0.05$; **, $P < 0.01$.

suppressive effect of CO on TNF- α expression was inhibited by R8-hemoCD1 in a concentration-dependent manner (Figure 6, bars 4 and 5). Consistent with the confocal microscopy results shown in Figure 5, the anti-inflammatory effects of CO induced by CORM-3 were completely blocked when cells were incubated with 20 μ M R8-hemoCD1. Similar experiments conducted with hemoCD1 and R8-Fb-hemoCD1 as negative controls showed that these compounds did not affect the CORM-3-mediated anti-inflammatory action (Figure 6, bars 6 and 7), thus confirming that R8-hemoCD1 efficiently removed intracellular CO.

Finally, we followed the changes in intracellular ROS levels upon removal of intracellular CO. Earlier studies have shown that exogenously applied CO induces ROS generation in cells through inhibition of cytochrome *c* oxidases (complex IV) in mitochondria.⁶⁰ ROS is thought to mediate subsequent adaptive signaling for cellular protection. Additionally, Choi et al. reported that the anti-inflammatory effects of CO could be attributed to suppression of NADPH oxidase-dependent ROS generation.⁶¹ Several studies have suggested the importance of intracellular CO in ROS regulation.^{62,63} We measured ROS levels in R8-hemoCD1-treated HepG2 and RAW264.7 cells using 2',7'-dichlorofluorescein diacetate (DCFH-DA) as a cell-permeable fluorescent ROS probe. As shown in Figure 7, a marked fluorescence due to increased ROS production was observed in R8-hemoCD1-treated RAW264.7 macrophages compared to controls, whereas only a slight

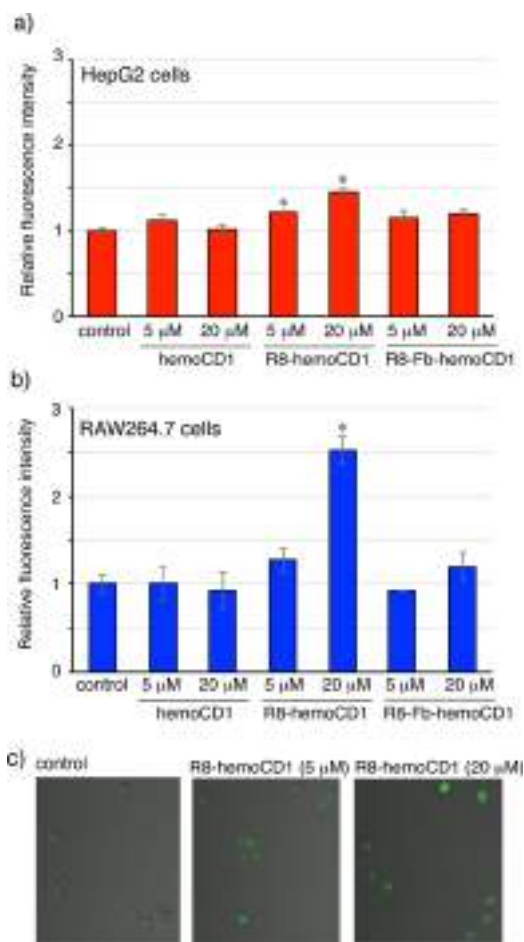


Figure 7. Effects of removal of endogenous CO by R8-hemoCD1 on ROS levels in HepG2 and RAW264.7 cells. Cells were incubated with R8-hemoCD1 or control samples for 1 h. ROS levels were then measured using a DCFH-DA probe. (a, b) Relative fluorescence intensities of HepG2 and RAW264.7 cell lysates. Bars represent means \pm SE ($n = 3-4$ experiments per group). *, $P < 0.05$ as compared with the control. (c) Confocal micrographs of RAW264.7 cells incubated with R8-hemoCD1 followed by DCFH-DA.

increase in fluorescence was observed in R8-hemoCD1-treated HepG2 cells. These cell-type dependent differences are possibly due to the high expression of NADPH oxidase in macrophages.⁶² Thus, the present results clearly show that endogenous CO plays an important role in the regulation of basal intracellular ROS production.

CONCLUSION

In summary, we established methods to quantify and remove efficiently intracellular CO using supramolecular hemoprotein model complexes hemoCD1 and R8-hemoCD1. The amount of endogenous CO detected by hemoCD1 in cell lysates was equimolar to bilirubin detected by UnaG, which confirmed the accuracy of the assays. The hemoCD1 assay presented in this study is convenient and can be applied for measurement of endogenous CO levels in blood, organs, and tissues without requiring special equipment except for a simple spectrophotometer. Most importantly, we showed for the first time that removal of intracellular CO by R8-hemoCD1 resulted in increased ROS generation in macrophages; moreover, R8-hemoCD1 was able to inhibit the anti-inflammatory effects mediated by a CO-releasing agent. Proteomic/transcriptomic

analyses of CO-depleted cells after treatment with R8-hemoCD1 will provide crucial information to further elucidate the specific signaling pathways directly affected by basal levels of CO or after HO-1 induction.⁶⁴ In addition, we believe that the combined use of hemoCD1/R8-hemoCD1 in cells and tissues will be a valuable tool for assessing the potential therapeutic effects of CO delivered by CO-RMs^{3,64} and will contribute to a comprehensive understanding of the HO enzymatic pathway in both physiological and pathophysiological conditions.

EXPERIMENTAL SECTION

Materials. HemoCD1 was synthesized in our laboratory.²³ The solution of oxy-hemoCD1 in PBS was prepared as previously described.³³ Synthesis of R8-hemoCD1 is described below. COP-1 was synthesized in our laboratory as described in the literature.¹⁹ CORM-3¹⁵ and recombinant UnaG protein⁴¹ were prepared as previously described. HepG2, HeLa, RAW264.7, and NIH3T3 cells were purchased from RIKEN Cell Bank. CHO and SH-SY5Y cells were kind gifts from Dr. Yasuomi Urano (Doshisha University). The other chemicals were purchased and used as received.

Preparation of R8-hemoCD1. Synthesis and characterization of Mal-met-hemoCD1⁵⁵ and Arg8-Cys⁵² were reported elsewhere. In a 1.5 mL Eppendorf tube, Mal-Fe^{III}TPPS (0.97 mg, 0.83 μ mol) and Py3CD (3.0 mg, 1.0 μ mol) were dissolved in PBS (pH 7.4). Arg8-Cys (1.7 mg, 1.2 μ mol) was added to the solution, and the solution was gently mixed for 30 min. Subsequently, Na₂S₂O₄ (1 mg) was added to reduce Fe^{III} to Fe^{II}. The solution was then passed through a Sephadex G-25 column (GE Healthcare Life Sciences) to remove excess Na₂S₂O₄ and Arg8-Cys peptide. During the chromatography, the Fe^{II}porphyrin was oxygenated to form the O₂-complex under aerobic conditions. Ellman's assays^{56,57} performed on the resulting solution containing the O₂ complex of R8-hemoCD1 showed no reactive thiol components. The increase in molecular size after this conjugation was assessed by size-exclusion chromatography (Superdex 75 column; GE Healthcare Life Sciences). R8-Fb-hemoCD1 was similarly prepared using free-base Mal-TPPS as the starting material. MALDI-TOF MS of R8-hemoCD1 and R8-Fb-hemoCD1 is shown in Figure S6.

Cell Cultures. Cell lines were cultured in D-10 medium containing Dulbecco's modified Eagle's medium (DMEM; Wako) supplemented with 10% fetal bovine serum (FBS; heat inactivated at 56 °C before use; Invitrogen GIBCO) and 1% penicillin/streptomycin/amphotericin B (Wako) at 37 °C in a humidified atmosphere with 5% CO₂.

Quantification of CO in Cells by hemoCD1. D-10 medium was removed from 10⁶ adherent cells, and 1 mL of oxy-hemoCD1 (2.5 μ M) in PBS was added to cells. Cells were then collected by scraping and transferred to tubes. After counting, cells in suspension were disrupted by sonication (time: 10 s \times 2, amplitude: 15; QSONICA). Samples were filtered using disposable syringe filters (DISMIC 13CP; ADVANTEC) to obtain a clear cell lysate. The lysate was measured by UV-vis absorption spectroscopy (spectrum a). Introduction of CO gas to the solution caused a spectral change (spectrum b) because of the conversion of residual oxy-hemoCD1 to CO-hemoCD1 in the cell lysate solution. Addition of Na₂S₂O₄ (approximately 1 mg to 1 mL of solution) caused further spectral changes (spectrum c); all hemoCD1 species in the cell lysates were converted to CO-hemoCD1. The concentration of total hemoCD1 contained in the cell lysates (C_{total}) was determined from the absorbance at 422 nm in spectrum c (the molar extinction coefficient of CO-hemoCD1, $\epsilon_{422}^{\text{CO}} = 3.71 \times 10^5 \text{ M}^{-1} \text{ cm}^{-1}$, was used for calculation). From the absorbance at 422 nm of spectrum b (A_{422}^{b}), the concentration of met-hemoCD1 (C_{met}) was determined by eq 3:

$$A_{422}^{\text{b}} = \epsilon_{422}^{\text{CO}}(C_{\text{total}} - C_{\text{met}}) + \epsilon_{422}^{\text{met}}C_{\text{met}} \quad (3)$$

where $\epsilon_{422}^{\text{met}} = 1.19 \times 10^5 \text{ M}^{-1} \text{ cm}^{-1}$ was used for the calculation. From the absorbance at 422 nm of spectrum a (A_{422}^{a}), the concentrations of CO-hemoCD1 (C_{CO}) and oxy-hemoCD1 (C_{oxy})

contained in the cell lysate were determined by eqs 4 and (5) as follows:

$$A_{422}^{\text{a}} = \epsilon_{422}^{\text{CO}}C_{\text{CO}} + \epsilon_{422}^{\text{oxy}}C_{\text{oxy}} + \epsilon_{422}^{\text{met}}C_{\text{met}} \quad (4)$$

$$C_{\text{total}} = C_{\text{CO}} + C_{\text{oxy}} + C_{\text{met}} \quad (5)$$

where $\epsilon_{422}^{\text{oxy}} = 1.64 \times 10^5 \text{ M}^{-1} \text{ cm}^{-1}$ was used for the calculation. The ratio of each component in total hemoCD1 (R_X , X = CO, oxy, or met) and the moles of CO contained as CO-hemoCD1 in the solution (M_{CO}) were determined by eqs 1 and 2.

Quantification of Bilirubin in the Cells. Bilirubin was measured using the recombinant UnaG protein as a fluorescent probe.^{40,41} Before the assay, cells were incubated for 14 h in bilirubin-free medium (OPTI-MEM) containing 2 mg/mL bovine serum albumin. Different agents (hemin, SnPPIX, or DMSO as a vehicle control) were added to the medium, and cells were incubated for 1, 3, 5, or 7 h. The recombinant His-tagged UnaG (0.38 mM aqueous solution, 15 μ L) was then added to the culture medium or cell lysate. Solutions containing UnaG were incubated for 2 h at 25 °C in the dark, after which the UnaG was trapped with Ni-NTA agarose (Invitrogen). After washing the resin with PBS, UnaG was eluted with PBS containing 300 mM imidazole (300 μ L). The fluorescence from the bilirubin-bound UnaG was monitored using a Filter Max F5 plate reader (Molecular Devices); $\lambda_{\text{ex}} = 485 \pm 20 \text{ nm}$ and $\lambda_{\text{em}} = 535 \pm 25 \text{ nm}$.

Real-Time PCR. RNA was isolated from the cells using an RNeasy Mini kit (Qiagen) according to the manufacturer's instructions. The experimental procedures were the same as previously described.³³ The following primers were used for the analyses: HO-1 forward, ATGGCCTCCCTGTACCACATC; HO-1 reverse, TGTTGCGCTCAATCTCCTCCT; β -actin forward, CTGGCACCAGCA-CAATG; and β -actin reverse, GCCGATCCACACGGAGTACT. Real-time PCR was performed using SYBR Green Master Mix (Applied Biosystems) and a Step One real-time PCR system. β -Actin was used as a reference gene.

Western Blotting. Lysates from HepG2 cells were subjected to sodium dodecyl sulfate (SDS)-polyacrylamide gel electrophoresis (PAGE), and the proteins in the gels were electrophoretically transferred onto polyvinylidene difluoride membranes. The experimental procedure was the same as that previously described.³³

Confocal Microscopy. Cell experiments using a COP-1 probe were performed according to the literature.¹⁹ Briefly, HeLa cells (6×10^4 cells/mL adhered on a 14 mm glass-bottom dishes) were incubated in D-10 medium without or with CORM-3 (50 μ M) at 37 °C for 30 min. The medium was then removed, and cells were washed with PBS. OPTI-MEM containing R8-hemoCD1 (0, 5, or 20 μ M) was added and the cells were incubated for 30 min. The medium was then removed, and cells were washed with PBS. COP-1 (1 μ M) in PBS was added and cells were incubated at 37 °C for 30 min. After washing, cells in D-10 medium were subjected to confocal fluorescence microscopic measurements. Confocal microscopic measurements were performed with a Nikon A1+ laser microscope system. Image analysis was performed using the ImageJ software.

LPS-Stimulation Experiments. RAW264.7 macrophages (1×10^6 cells/mL) were incubated with CORM-3 (50 μ M in D-10) at 37 °C for 6 h. The medium was then removed, and cells were washed with PBS and incubated with R8-hemoCD1 (5 or 20 μ M in OPTI-MEM) for 30 min. After washing, cells were incubated for 1 h with LPS (1 μ g/mL) in D-10 medium. TNF- α mRNA was then quantified by real-time PCR using the following primers: TNF- α forward, CCCTCACACTCAGATCATCTTCT; TNF- α reverse, GCTAC-GACGTGGGCTACAG; β -actin forward, AGAGGAAATCGTG-CGTGAC; and β -actin reverse, CAATAGTGATGACCTGGCCGT.

Detection of Intracellular ROS. Intracellular ROS levels were measured by DCF fluorescence assays.⁶⁰ HepG2 and RAW264.7 cells (1×10^6 cells/mL) were incubated with R8-hemoCD1 (5 or 20 μ M in OPTI-MEM) or control samples (hemoCD1 or R8-Fb-hemoCD1) for 1 h. After washing with PBS, cells were incubated with DCFH-DA (10 μ M in PBS; Sigma) for 1 h. Cells were then washed with PBS. Cells in D-10 were observed by confocal microscopy ($\lambda_{\text{ex}} = 485 \pm 20 \text{ nm}$) or

lysed with 0.1 M NaOH for photometric measurements ($\lambda_{\text{ex}} = 485 \pm 20$ nm and $\lambda_{\text{em}} = 535 \pm 25$ nm).

Statistical Analysis. All data represent the means \pm SE from at least three different experiments. Statistical analysis ($n \geq 3$) was performed using unpaired Student's *t* tests. Differences with *P* values of less than 0.05 were considered significant.

■ ASSOCIATED CONTENT

Supporting Information

The Supporting Information is available free of charge on the ACS Publications website at DOI: 10.1021/jacs.7b02229.

Cell viability after treatment of cells with hemoCD1 and R8-hemoCD1, the comparison of the calculated and observed spectra in the hemoCD1 assay, dose dependency of the R_{CO} , R_{Oxy} , and R_{met} values, effect of hemin and SnPIX on endogenous CO and bilirubin production, photographs of Mal-Fe^{III}TPPS aqueous solutions after the addition of Arg8-Cys in the absence and presence of Py3CD, MALDI-TOF MS of R8-hemoCD1 and R8-Fb-hemoCD1, UV-vis absorption spectra of R8-hemoCD1 under N₂, O₂, and CO atmospheres, autoxidation of the O₂-complex of R8-hemoCD1, determination of O₂ and CO affinities of R8-hemoCD1, competitive reaction assays for Hb and R8-hemoCD1, confocal micrographic analysis of HeLa cells with R8-Fb-hemoCD1, and reaction of COP-1 with CORM-3 in the absence or presence of hemoCD1 (PDF)

■ AUTHOR INFORMATION

Corresponding Author

*E-mail: hkitagis@mail.doshisha.ac.jp.

ORCID

Hiroaki Kitagishi: 0000-0003-4682-7217

Notes

The authors declare no competing financial interest.

■ ACKNOWLEDGMENTS

We thank Dr. Yasuomi Urano (Doshisha University) for providing several cell lines. This work was financially supported by Grants-in-Aid for Scientific Research (A) (No. 24249086), Challenging Exploratory Research (No. 16K13092), the MEXT-Supported Program for the Strategic Research Foundation at Private Universities (2015–2019), the Naito Foundation, Iketani Science and Technology Foundation, and Suntory Foundation for Life Sciences.

■ REFERENCES

- (1) Wu, L.; Wang, R. *Pharmacol. Rev.* **2005**, *57*, 585–630.
- (2) Ryter, S. W.; Alam, J.; Choi, A. M. *Physiol. Rev.* **2006**, *86*, 583–650.
- (3) Motterlini, R.; Otterbein, L. E. *Nat. Rev. Drug Discovery* **2010**, *9*, 728–743.
- (4) Heinemann, S. H.; Hoshi, T.; Westerhausen, M.; Schiller, A. *Chem. Commun.* **2014**, *50*, 3644–3660.
- (5) Durante, W.; Johnson, F. K.; Johnson, R. A. *J. Cell. Mol. Med.* **2006**, *10*, 672–686.
- (6) Shimizu, T.; Huang, D.; Yan, F.; Stranova, M.; Bartosova, M.; Fojtíková, V.; Martínková, M. *Chem. Rev.* **2015**, *115*, 6491–6533.
- (7) Szabo, C. *Nat. Rev. Drug Discovery* **2015**, *15*, 185–203.
- (8) Fukuto, J. M.; Carrington, S. J.; Tantillo, D. J.; Harrison, J. G.; Ignarro, L. J.; Freeman, B. A.; Chen, A.; Wink, D. A. *Chem. Res. Toxicol.* **2012**, *25*, 769–793.

(9) Andreadou, I.; Iliodromitis, E. K.; Rassaf, T.; Schulz, R.; Papapetropoulos, A.; Ferdinandy, P. *Br. J. Pharmacol.* **2015**, *172*, 1587–1606.

(10) Farrugia, G.; Szurszewski, J. H. *Gastroenterology* **2014**, *147*, 303–313.

(11) Prabhakar, N. R.; Semenza, G. L. *J. Mol. Med.* **2012**, *90*, 265–272.

(12) Olas, B. *Clin. Chim. Acta* **2015**, *445*, 115–121.

(13) Throughout this paper, the terms “heme” and “hemin” refer to the iron(II) and iron(III) complexes of protoporphyrin IX, respectively.

(14) Soares, M. P.; Lin, Y.; Anrather, J.; Cszmadia, E.; Takigami, K.; Sato, K.; Grey, S. T.; Colvin, R. B.; Choi, A. M.; Poss, K. D.; Bach, F. H. *Nat. Med.* **1998**, *4*, 1073–1077.

(15) Clark, J. E.; Naughton, P.; Shurey, S.; Green, C. J.; Johnson, T. R.; Mann, B. E.; Foresti, R.; Motterlini, R. *Circ. Res.* **2003**, *93*, e2–e8.

(16) Yachie, A.; Niida, Y.; Wada, T.; Igarashi, N.; Kaneda, H.; Toma, T.; Ohta, K.; Kasahara, Y.; Koizumi, S. *J. Clin. Invest.* **1999**, *103*, 129–135.

(17) Marks, G. S.; Vreman, H. J.; McLaughlin, B. E.; Brien, J. F.; Nakatsu, K. *Antioxid. Redox Signaling* **2002**, *4*, 271–277.

(18) Morimoto, Y.; Durante, W.; Lancaster, D. G.; Klattenhoff, J.; Tittel, F. K. *Am. J. Physiol.: Heart Circ. Physiol.* **2001**, *280*, H483–H488.

(19) Michel, B. W.; Lippert, A. R.; Chang, C. J. *J. Am. Chem. Soc.* **2012**, *134*, 15668–15671.

(20) Wang, J.; Karpus, J.; Zhao, B. S.; Luo, Z.; Chen, P. R.; He, C. *Angew. Chem., Int. Ed.* **2012**, *51*, 9652–9656.

(21) Yan, J.; Zhu, J.; Tan, Q.; Zhou, L.; Yao, P.; Lu, Y.; Tan, J.; Zhang, L. *RSC Adv.* **2016**, *6*, 65373–65376.

(22) Li, Y.; Wang, X.; Yang, J.; Xie, X.; Li, M.; Niu, J.; Tong, L.; Tang, B. *Anal. Chem.* **2016**, *88*, 11154–11159.

(23) Kano, K.; Kitagishi, H.; Kodera, M.; Hirota, S. *Angew. Chem., Int. Ed.* **2005**, *44*, 435–438.

(24) Kano, K.; Kitagishi, H.; Dagallier, C.; Kodera, M.; Matsuo, T.; Hayashi, T.; Hisaeda, Y.; Hirota, S. *Inorg. Chem.* **2006**, *45*, 4448–4460.

(25) Kano, K.; Itoh, Y.; Kitagishi, H.; Hayashi, T.; Hirota, S. *J. Am. Chem. Soc.* **2008**, *130*, 8006–8015.

(26) Kitagishi, H.; Tamaki, M.; Ueda, T.; Hirota, S.; Ohta, T.; Naruta, Y.; Kano, K. *J. Am. Chem. Soc.* **2010**, *132*, 16730–16732.

(27) Kitagishi, H.; Negi, S.; Kiriya, A.; Honbo, A.; Sugiura, Y.; Kawaguchi, A. T.; Kano, K. *Angew. Chem., Int. Ed.* **2010**, *49*, 1312–1315.

(28) Kano, K.; Chimoto, S.; Tamaki, M.; Itoh, Y.; Kitagishi, H. *Dalton. Trans.* **2012**, *41*, 453–461.

(29) Ueda, T.; Kitagishi, H.; Kano, K. *Org. Biomol. Chem.* **2012**, *10*, 4337–4347.

(30) Watanabe, K.; Kitagishi, H.; Kano, K. *Angew. Chem., Int. Ed.* **2013**, *52*, 6894–6897.

(31) Ueda, T.; Kitagishi, H.; Kano, K. *Inorg. Chem.* **2014**, *53*, 543–551.

(32) Watanabe, K.; Suzuki, T.; Kitagishi, H.; Kano, K. *Chem. Commun.* **2015**, *51*, 4059–4061.

(33) Kitagishi, H.; Minegishi, S.; Yumura, A.; Negi, S.; Taketani, S.; Amagase, Y.; Mizukawa, Y.; Urushidani, T.; Sugiura, Y.; Kano, K. *J. Am. Chem. Soc.* **2016**, *138*, 5417–5425.

(34) Kitagishi, H.; Kurosawa, S.; Kano, K. *Chem. - Asian J.* **2016**, *11*, 3213–3219.

(35) Tani, F.; Matsu-ura, M.; Ariyama, K.; Setoyama, T.; Shimada, T.; Kobayashi, S.; Hayashi, T.; Matsuo, T.; Hisaeda, Y.; Naruta, Y. *Chem. - Eur. J.* **2003**, *9*, 862–870.

(36) Collman, J. P.; Boulatov, R.; Sunderland, C. J.; Fu, L. *Chem. Rev.* **2004**, *104*, 561–588.

(37) The cell disruption by freeze–thaw cycles yielded the same results of CO quantification as that by sonication.

(38) The spectral interference due to other components of cell lysates was negligible because of the large absorption property of hemoCD1 at visible region.

(39) Was, H.; Dulak, J.; Jozkowicz, A. *Curr. Drug Targets* **2010**, *11*, 1551–1570.

(40) Kumagai, A.; Ando, R.; Miyatake, H.; Greimel, P.; Kobayashi, T.; Hirabayashi, Y.; Shimogori, T.; Miyawaki, A. *Cell* **2013**, *153*, 1602–1611.

(41) Takeda, T. A.; Mu, A.; Tai, T. T.; Kitajima, S.; Taketani, S. *Sci. Rep.* **2015**, *5*, 10488.

(42) Here we focused on the total amounts (in media + in cells) of CO and bilirubin because the degrees of extracellular diffusion and/or transport of CO and bilirubin to the media were different.

(43) Foresti, R.; Hoque, M.; Bains, S.; Green, C. J.; Motterlini, R. *Biochem. J.* **2003**, *372*, 381–390.

(44) Sun, J.; Hoshino, H.; Takaku, K.; Nakajima, O.; Muto, A.; Suzuki, H.; Tashiro, S.; Takahashi, S.; Shibahara, S.; Alam, J.; Taketo, M. M.; Yamamoto, M.; Igarashi, K. *EMBO J.* **2002**, *21*, 5216–5224.

(45) Ghattas, M. H.; Chuang, L. T.; Kappas, A.; Abraham, N. G. *Int. J. Biochem. Cell Biol.* **2002**, *34*, 1619–1628.

(46) Breslow, E.; Chandra, R.; Kappas, A. *J. Biol. Chem.* **1986**, *261*, 3135–3141.

(47) Foresti, R.; Goatly, H.; Green, C. J.; Motterlini, R. *Am. J. Physiol.: Heart Circ. Physiol.* **2001**, *281*, H1976–H1984.

(48) Futaki, S.; Suzuki, T.; Ohashi, W.; Yagami, T.; Tanaka, S.; Ueda, K.; Sugiura, Y. *J. Biol. Chem.* **2001**, *276*, 5836–5840.

(49) Futaki, S. *Biopolymers* **2006**, *84*, 241–249.

(50) Takeuchi, T.; Kosuge, M.; Tadokoro, A.; Sugiura, Y.; Nishi, M.; Kawata, M.; Sakai, N.; Matile, S.; Futaki, S. *ACS Chem. Biol.* **2006**, *1*, 299–303.

(51) Kosuge, M.; Takeuchi, T.; Nakase, I.; Jones, A. T.; Futaki, S. *Bioconjugate Chem.* **2008**, *19*, 656–664.

(52) Kitagishi, H.; Hatada, S.; Itakura, T.; Maki, Y.; Maeda, Y.; Kano, K. *Org. Biomol. Chem.* **2013**, *11*, 3203–3211.

(53) Kitagishi, H.; Minami, K.; Kano, K. *Chem. Lett.* **2014**, *43*, 1095–1097.

(54) Kitagishi, H.; Chai, F.; Negi, S.; Sugiura, Y.; Kano, K. *Chem. Commun.* **2015**, *51*, 2421–2424.

(55) Kitagishi, H.; Kawasaki, H.; Kano, K. *Chem. - Asian J.* **2015**, *10*, 1768–1775.

(56) Eyer, P.; Worek, F.; Kiderlen, D.; Sinko, G.; Stuglin, A.; Simeon-Rudolf, V.; Reiner, E. *Anal. Biochem.* **2003**, *312*, 224–227.

(57) Riener, C. K.; Kada, G.; Gruber, H. J. *Anal. Bioanal. Chem.* **2002**, *373*, 266–276.

(58) Choi, A. M.; Otterbein, L. E.; Bach, F. H.; Alam, J.; Soares, M.; Lu, H. T.; Wysk, M.; Davis, R. J.; Flavell, R. A. *Nat. Med.* **2000**, *6*, 422–428.

(59) Sawle, P.; Foresti, R.; Mann, B. E.; Johnson, T. R.; Green, C. J.; Motterlini, R. *Br. J. Pharmacol.* **2005**, *145*, 800–810.

(60) Zuckerbraun, B. S.; Chin, B. Y.; Bilban, M.; de Costa d'Avila, J.; Rao, J.; Billiar, T. R.; Otterbein, L. E. *FASEB J.* **2007**, *21*, 1099–1106.

(61) Nakahira, K.; Kim, H. P.; Geng, X. H.; Nakao, A.; Wang, X.; Murase, N.; Drain, P. F.; Wang, X.; Sasidhar, M.; Nabel, E. G.; Takahashi, T.; Lukacs, N. W.; Ryter, S. W.; Morita, K.; Choi, A. M. K. *J. Exp. Med.* **2006**, *203*, 2377–2389.

(62) Choi, Y. K.; Por, E. D.; Kwon, Y.-G.; Kim, Y.-M. *Oxid. Med. Cell. Longevity* **2012**, *2012*, 794237.

(63) Bilban, M.; Haschemi, A.; Wegiel, B.; Chin, B. Y.; Wagner, O.; Otterbein, L. E. *J. Mol. Med.* **2008**, *86*, 267–279.

(64) Motterlini, R.; Foresti, R. *Am. J. Physiol. Cell Physiol.* **2017**, *312*, C302–C313.

Feedback Response to Selective Depletion of Endogenous Carbon Monoxide in the Blood

Hiroaki Kitagishi,^{*,†} Saika Minegishi,[†] Aki Yumura,[†] Shigeru Negi,[‡] Shigeru Taketani,[§] Yoko Amagase,[‡] Yumiko Mizukawa,[‡] Tetsuro Urushidani,[‡] Yukio Sugiura,[‡] and Koji Kano[†]

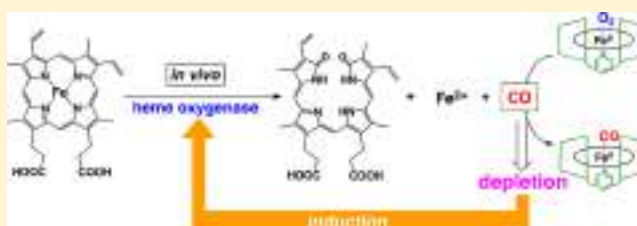
[†]Department of Molecular Chemistry and Biochemistry, Faculty of Science and Engineering, Doshisha University, Kyotanabe, Kyoto 610-0321, Japan

[‡]Faculty of Pharmaceutical Sciences, Doshisha Women's College of Liberal Arts, Kyotanabe, Kyoto 610-0395, Japan

[§]Department of Microbiology, Kansai Medical University, Hirakata, Osaka 573-1010, Japan

Supporting Information

ABSTRACT: The physiological roles of endogenous carbon monoxide (CO) have not been fully understood because of the difficulty in preparing a loss-of-function phenotype of this molecule. Here, we have utilized *in vivo* CO receptors, hemoCDs, which are the supramolecular 1:1 inclusion complexes of *meso*-tetrakis(4-sulfonatophenyl)porphyratoiron(II) with per-*O*-methylated β -cyclodextrin dimers. Three types of hemoCDs (hemoCD1, hemoCD2, and hemoCD3) that exhibit different CO-affinities have been tested as CO-depleting agents *in vivo*. Intraperitoneally administered hemoCD bound endogenous CO within the murine circulation, and was excreted in the urine along with CO in an affinity-dependent manner. The sufficient administration of hemoCD that has higher CO-affinity than hemoglobin (Hb) produced a pseudoknockdown state of CO in the mouse in which heme oxygenase-1 (HO-1) was markedly induced in the liver, causing the acceleration of endogenous CO production to maintain constant CO-Hb levels in the blood. The contents of free hemin and bilirubin in the blood plasma of the treated mice significantly increased upon removal of endogenous CO by hemoCD. Thus, a homeostatic feedback model for the CO/HO-1 system was proposed as follows: HemoCD primarily removes CO from cell-free CO-Hb. The resulting oxy-Hb is quickly oxidized to met-Hb by oxidant(s) such as hydrogen peroxide in the blood plasma. The met-Hb readily releases free hemin that directly induces HO-1 in the liver, which metabolizes the hemin into iron, biliverdin, and CO. The newly produced CO binds to ferrous Hb to form CO-Hb as an oxidation-resistant state. Overall, the present system revealed the regulatory role of CO for maintaining the ferrous/ferric balance of Hb in the blood.



INTRODUCTION

Carbon monoxide (CO) is continuously produced in mammalian organisms.¹ In the human body, about 10 mL of CO is produced per day through natural metabolic processes.² The major endogenous process of CO production (ca. 86%) is the degradation reaction of a heme prosthetic group, while a minor amount of CO arises from lipid oxidation.^{1,2} Therefore, the main precursor of CO in living organisms is hemin, the ferric form of the heme prosthetic group (Figure 1). Hemin is released from aged heme proteins, which arise primarily from cell-free hemoglobin (Hb) leaked from senescent red blood cells (RBCs).^{3,4} While Hb in RBCs exists in its ferrous form, cell-free Hb is rapidly oxidized to its ferric form (met-Hb) by reactive oxygen species (ROS) existing in the blood.^{3,4} The cell-free met-Hb easily dissociates to hemin and apo-globin, and serum proteins such as hemopexin transport hemin into cells.^{3–5} The enzymatic reaction of heme oxygenase (HO) in the cells causes the degradation of hemin to generate CO, biliverdin, and iron (Figure 1).^{1–5} The endogenously produced CO can then diffuse back out through the cell membrane. Most

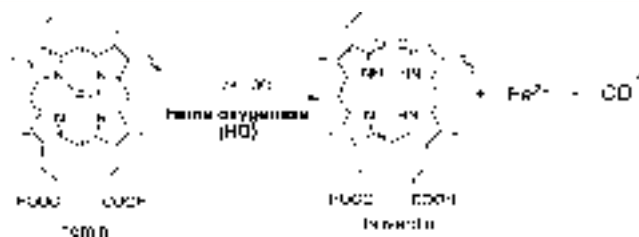


Figure 1. Metabolic degradation of hemin by a heme oxygenase enzyme (HO) to endogenously produce biliverdin, Fe²⁺, and CO.

of the endogenously produced CO (ca. 80%) circulates as CO-Hb in the blood;^{6,7} thus, normal human blood contains a fraction of CO-Hb ($1.2 \pm 0.3\%$ of total Hb) even in nonsmokers.⁸ Since the finding that CO at low concentration (below 500 ppm) exerts a remarkable protective effect against inflammation in cardiac transplant⁹ and ischemia/reperfusion

Received: February 29, 2016

Published: April 8, 2016

models,¹⁰ much effort has been directed toward the therapeutic use of CO as an anti-inflammatory agent.^{1,2,11,12} In particular, water-soluble, nontoxic metal carbonyl complexes have been developed as agents for the controlled release of CO in vivo.^{11–15}

The functional mechanisms of CO in biological systems have been extensively studied over the past two decades,^{1,2,12} but are not fully understood. In vitro as well as in vivo studies have clearly revealed that CO at low concentration inhibits the production of stress-induced pro-inflammatory cytokines through several signaling pathways, resulting in an anti-inflammatory effect.^{16–19} Furthermore, the discovery of CO-responsive transcriptional factors such as neuronal PAS domain 2²⁰ and CoxA²¹ has strongly suggested the existence of gene expression regulatory systems controlled by intracellular CO.^{22,23} However, the majority of endogenous CO primarily circulates in the blood as CO-Hb and is not retained within cells. Although the intracellular CO has been demonstrated to function as a signaling molecule, the role of endogenous CO in the blood remains unclear. To understand the overall role of endogenous CO, the phenotypes of HO-knockout mice have been characterized.^{1,24,25} Upon genetic deletion as well as chemical inhibition of HO activity, however, redundant hemin might accumulate in the blood and/or in cells. The primary role of endogenous CO itself in living systems remains uncertain owing to the difficulty in generating a loss-of-function phenotype of this gaseous molecule.

In the present study, we developed a selective in vivo CO-depletion system without the requirement for genetic manipulation. The key materials are the synthetic CO-receptors, hemoCDs, which are supramolecular 1:1 inclusion complexes of *meso*-tetrakis(4-sulfonatophenyl)porphyratoiron(II) (Fe^{II}TPPS) with per-*O*-methylated β -cyclodextrin dimers (Figure 2). We had designed hemoCDs as synthetic myoglobin (Mb) and/or Hb model complexes that reversibly bind molecular oxygen (O₂) in aqueous solution.²⁶ A series of hemoCDs (hemoCD1,^{26,27} hemoCD2,²⁸ and hemoCD3,²⁹ Figure 2) are reported as the model complexes showing different O₂ and CO binding affinities (Table 1). Since the CO binding affinity of hemoCD1 was much higher than that of Hb

Table 1. O₂ and CO Binding Affinities ($P_{1/2}^L$, L = O₂ or CO, Torr)^a and Half-Lives for the Autoxidation of the Oxygenated Complexes ($t_{1/2}^{O_2}$, h) in Aqueous Phosphate Buffer Solution at 25 °C

	$P_{1/2}^{O_2}$ /Torr	$10^3 P_{1/2}^{CO}$ /Torr	$t_{1/2}^{O_2}$ /h	ref.
hemoCD1	10	0.015	30	27
hemoCD2	176	16	>100	28
hemoCD3	18	0.56	53	29
Hb, human, R-state	0.22	1.4	>60	30

^a $P_{1/2}^L$ (L = O₂ or CO) represents the partial pressure of O₂ or CO at which half of the ferrous complexes are bound by O₂ or CO.

in the R-state,^{27,30} the O₂ complex of hemoCD1 (oxy-hemoCD1) intravenously injected to rats was capable of capturing endogenous CO in the blood of the animals.^{31,32} The supramolecular structure of hemoCD1 was so stable that no dissociation to its components was observed in the blood or in the urine.³¹ Throughout this study, we used oxy-hemoCDs as the CO-removal agents, which captured CO from CO-Hb through the ligand exchange reaction between O₂ and CO. The present study showed, for the first time, that the depletion of CO from the blood accelerates the endogenous production of CO by inducing HO-1, an inducible isoform of the HO enzymes. Accordingly, we propose a homeostatic feedback model for the endogenous CO/HO-1 system.

RESULTS AND DISCUSSION

Sample Preparation. The solution of hemoCD in phosphate buffer saline (PBS) for administration to mice was prepared as follows: The solution of met-hemoCD, which contained Fe^{III}-TPPS and 1.2 equiv of a CD dimer (Py3CD,²⁷ Py2CD,²⁸ or Py3OCD,²⁹ Figure 2) in PBS, was reduced to its ferrous form (hemoCD) by excess Na₂S₂O₄. The excess Na₂S₂O₄ and its decomposed products were then removed by passing the solution through a Sephadex G-25 desalting column. Under aerobic conditions, the ferrous complex was spontaneously oxygenated to form an O₂ complex (oxy-hemoCD) during the treatment. The eluted solution containing ferrous hemoCD in PBS was immediately used for administration to subject animals to minimize its autoxidation (Table 1).

Before the in vivo experiments, the CO-removal ability of each hemoCD from CO-Hb in vitro was assessed using the competitive reaction assay (Figure S1). According to the CO-affinities listed in Table 1, hemoCD1 and hemoCD3 removed CO quantitatively from equimolar CO-Hb, whereas only a fraction of CO was removed from CO-Hb by hemoCD2. In the reaction with hemoCD, CO-Hb was converted to oxy-Hb owing to the ligand exchange between CO and O₂.

Pharmacokinetic Study. To investigate how much hemoCD was necessary for complete removal of endogenous CO in the blood, the solutions of hemoCD1 (0.15 mL) at different concentrations (0.5, 1.0, and 1.5 mM) were intraperitoneally administrated to male C57BL/6N mice. To avoid biological reactions induced by anesthesia, we utilized intraperitoneal administration to the unanesthetized SPF mice. Following the administration, red-colored urine was spontaneously excreted owing to the renal clearance of hemoCD1. Figure 3a shows a typical example of the UV-vis spectrum of the urine. The Soret band that was sharper than that of oxy-hemoCD1 indicated the existence of CO-bound hemoCD1 (CO-hemoCD1) in the urine. This observation represents the

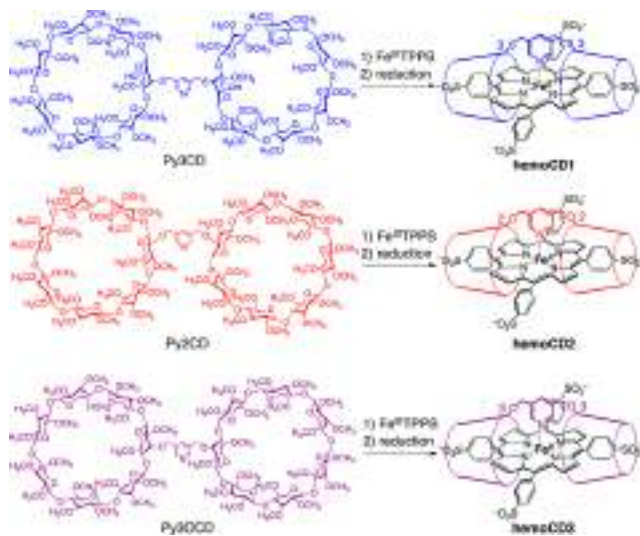


Figure 2. Structures of the hemoCD1, hemoCD2, and hemoCD3 complexes used in this study as supramolecular CO-depleting agents that function in vivo.

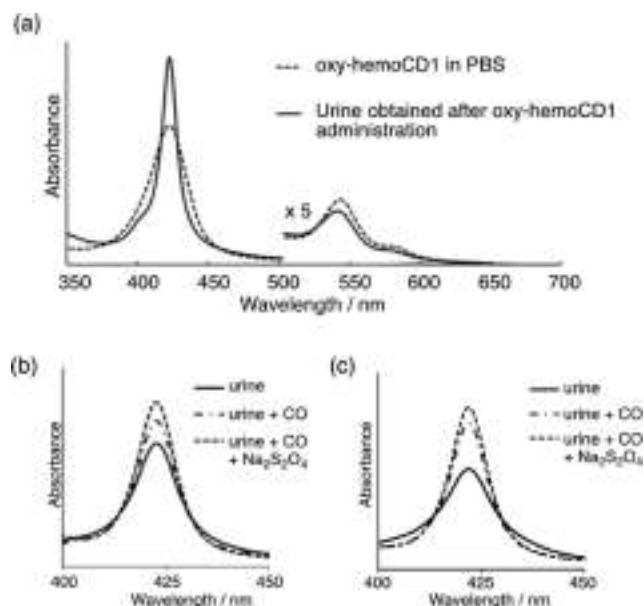


Figure 3. UV-vis spectral characterization of the urine. (a) UV-vis spectra of oxy-hemoCD1 in PBS (dashed line) and the urine solution diluted in PBS (solid line). The urine was obtained spontaneously after the administration of oxy-hemoCD1. (b, c) UV-vis spectra of the urine solutions obtained from the hemoCD1-treated mice (b, 0.5 mM, 0.15 mL; c, 1.0 mM, 0.15 mL) before and after the additions of CO and CO/excess $\text{Na}_2\text{S}_2\text{O}_4$. From the absorbances in these spectra, the amount of total hemoCD1 (M_{hemoCD1}) and the molar fractions of CO-, oxy-, and met-hemoCD1 in the urine were determined.

following processes: (1) absorption of hemoCD1 from the peritoneal cavity into the bloodstream, (2) ligand exchange of O_2 in oxy-hemoCD1 with endogenous CO, and (3) the glomerular filtration of CO-hemoCD1 into the urine. The transfer of hemoCD1 from the bloodstream into the urine accompanied by endogenous CO has been previously confirmed by resonance Raman spectroscopy as well as UV-vis spectroscopy.³¹ Endogenous nitric oxide (NO) was considered not to bind to hemoCD1 in the blood as previously studied using rats.³¹ Therefore, the urine contained three different states of hemoCD1, i.e., oxy-hemoCD1, CO-hemoCD1, and met-hemoCD1; the molar fractions of these components were determined using the CO/ $\text{Na}_2\text{S}_2\text{O}_4$ assay.^{31–33} Figures 3b and 3c show the typical UV-vis spectral changes of the urine solutions before and after the successive additions of CO and $\text{Na}_2\text{S}_2\text{O}_4$. Addition of CO gas into the urine sample caused an increase in the absorbance at 422 nm, owing to the conversion of residual oxy-hemoCD1 to CO-hemoCD1. Subsequent addition of $\text{Na}_2\text{S}_2\text{O}_4$ caused further enhancement of the absorption band at 422 nm, indicating that the urine included met-hemoCD1 as well.

Figure 4a shows the time courses of the excreted hemoCD1 (M_{hemoCD1}) after the intraperitoneal administration of hemoCD1 (applied doses: 0.5, 1.0, and 1.5 mM in PBS, 0.15 mL each). The time courses for M_{hemoCD1} showed a dependency on the dose concentration. The administered hemoCD1 completely disappeared at 180 min; this rapid renal clearance was also observed for rats,^{31,32} in which ca. 80% of intravenously administered hemoCD1 was transferred into the urinary bladder. In the present study, an average of $53 \pm 5\%$ administered hemoCD1 was spontaneously excreted in the urine after intraperitoneal injection in mice, as evaluated from

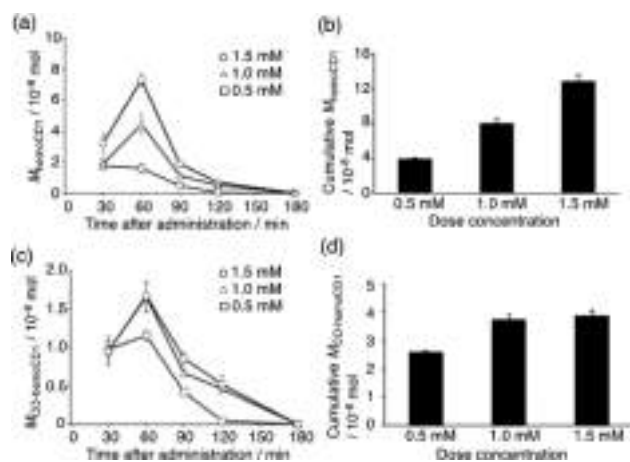


Figure 4. Urinary excretion profiles for the mice after intraperitoneal administration of hemoCD1 (0.5, 1.0, or 1.5 mM in PBS, 0.15 mL each). (a) Changes in the amount of hemoCD1 excreted in the urine (M_{hemoCD1} , mol) as a function of time; (b) the cumulative value of M_{hemoCD1} for 180 min after the administration; (c) changes in the amount of CO-hemoCD1 excreted in the urine ($M_{\text{CO-hemoCD1}}$, mol) as a function of time; and (d) the cumulative value of $M_{\text{CO-hemoCD1}}$ for 180 min after the administration. Each bar represents the means \pm SE ($n = 3$ mice per time point).

the cumulative M_{hemoCD1} values (Figure 4b). The renal clearance ratio was independent of its dose concentrations (0.5, 1.0, and 1.5 mM), whereas the molar fractions of the individual components (oxy-, CO-, and met-hemoCD1) in the total hemoCD1 in the urine showed strong dose-dependency (Figure S2); the fraction of the CO complex was lower when hemoCD1 at higher concentration was administered to the mice. The time-courses of the amount of the CO complex in the urine ($M_{\text{CO-hemoCD1}}$), which is equal to the amount of endogenous CO removed from the body, are shown in Figure 4c. The data showed no differences at the 1.0 and 1.5 mM applied doses. The cumulative $M_{\text{CO-hemoCD1}}$ values (Figure 4d) indicated that $(3.8 \pm 0.2) \times 10^{-8}$ mol of endogenous CO was removed by hemoCD1, which saturated at doses over 1.0 mM. The results indicate that the removable endogenous CO was completely excreted in the urine as CO-hemoCD1 when over 1.0 mM hemoCD1 (0.15 mL) was administered to the mouse.

HemoCD2 and hemoCD3, which show lower CO-binding affinities than hemoCD1 (Table 1), were administered to mice in the same manner as hemoCD1. Figure 5 shows the comparison of the pharmacokinetic profiles between hemoCD1, hemoCD2, and hemoCD3 (applied doses: 1.0 mM, 0.15 mL each). There was no difference in the amounts of the excreted hemoCD molecules (M_{hemoCD}) between the complexes (Figure 5a and b). HemoCD2, having a lower CO binding affinity than Hb, insufficiently removed endogenous CO whereas hemoCD3 removed similar amounts of CO as hemoCD1 (Figure 5c and d). The results indicated that a constant amount of endogenous CO could be removed by sufficient administration of hemoCDs that exhibit higher CO binding affinities than Hb.

The CO-Hb contents in the blood were measured after the administration of hemoCDs to mice as a function of time (Figure 6). In the control mice (PBS), the fraction of CO-Hb (%) in the total Hb was found to be ca. 0.2%, which is consistent with the reported value for the mouse blood.³⁴ At 30 min after the administration of hemoCD1 or hemoCD3, the

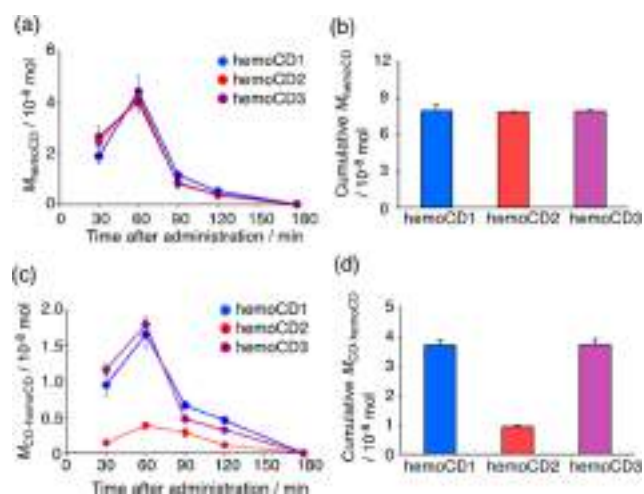


Figure 5. Urinary excretion profiles for the mice after intraperitoneal administration of hemoCD1, hemoCD2, or hemoCD3 (1.0 mM in PBS, 0.15 mL each). (a) Changes in the total amount of hemoCD excreted in the urine (M_{hemoCD} , mol) as a function of time; (b) the cumulative value of M_{hemoCD} for 180 min after the administration; (c) changes in the amount of CO-hemoCD1 excreted in the urine ($M_{\text{CO-hemoCD}}$, mol) as a function of time; and (d) the cumulative value of $M_{\text{CO-hemoCD}}$ for 180 min after the administration. Each bar represents the means \pm SE ($n = 3$ mice per time point).

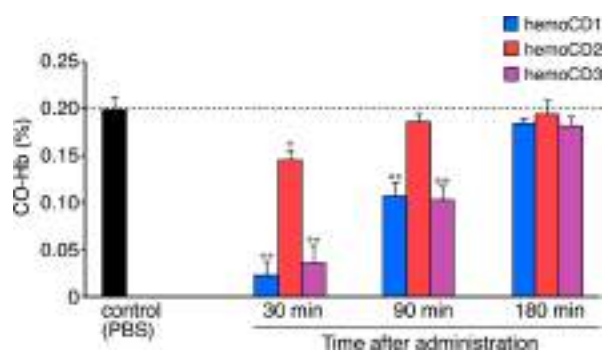


Figure 6. Time-courses of the fraction of CO-Hb (%) in the whole blood of the mice after the intraperitoneal administration of hemoCD1, hemoCD2, or hemoCD3 (1.0 mM, 0.15 mL each). The control data were obtained from the blood of mice at 30 min after the intraperitoneal administration of PBS (0.15 mL). Each bar represents the means \pm SE ($n = 3$ mice per time point). An asterisk denotes statistical significance: * $P < 0.05$, ** $P < 0.01$, as compared to the controls.

value was drastically reduced to below 0.03%, indicating that these hemoCDs removed endogenous CO from CO-Hb circulating in the blood. On the other hand, the effect of hemoCD2 was small, owing to its lower CO affinity than Hb (Table 1). The CO-Hb content returned smoothly to a normal level (ca. 0.2%) at 180 min after hemoCD administration, at which the dosed hemoCDs disappeared from the body (Figure 5a). Such rapid recovery of the CO-Hb content suggested that the endogenous CO was newly produced to compensate for the lack of CO in the blood.

Induction of HO-1 by CO-Depletion. The compensative production of endogenous CO that occurred in the hemoCD-treated mouse strongly suggested an enhancement of the enzymatic activity of HO. The HO enzyme is classified mainly as two isozymes, inducible HO-1 and constitutive HO-2.^{1,2} Therefore, the mRNA levels of HO-1 (*Hmox1*) and HO-2

(*Hmox2*) in the livers of mice were examined using a quantitative PCR method. The solution of hemoCD (1.0 mM, 0.15 mL) was administered to mice and total RNA was then extracted from the liver at 30, 90, and 180 min after the administration. Iron-free hemoCD1 (a mixed solution of 5,10,15,20-tetrakis(4-sulfonatophenyl)porphyrin (TPPS) and Py3CD, hereafter abbreviated as Fb-hemoCD1) was similarly administered to another mouse as a negative control. Met-hemoCD, a ferric form of hemoCD, could not be used as the negative control because it was partially reduced to its ferrous form during its circulation in the bloodstream.^{29,31} The intraperitoneally administered Fb-hemoCD1 was excreted in the urine without showing any UV-vis spectral change (Figure S3), indicating that no dissociation and no specific interaction with biomolecules occurred during its circulation and excretion.

Hmox1 expression levels were significantly enhanced in the mice treated by hemoCDs (Figure 7a). At 90 min after

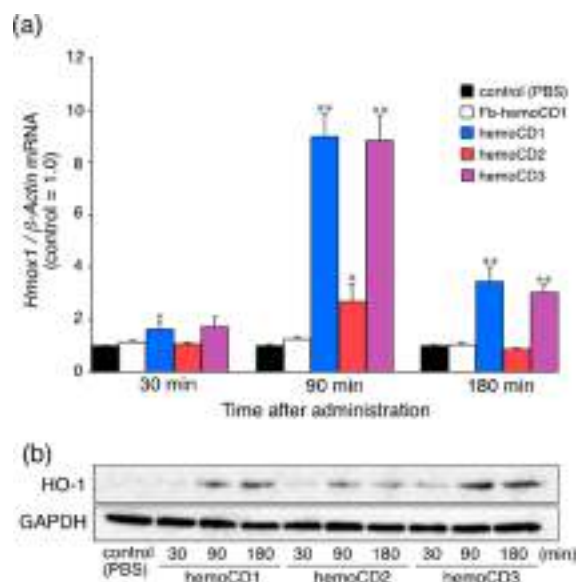


Figure 7. Induction of HO-1 following hemoCD administration. (a) Relative mRNA expression levels of HO-1 in the mice liver after the intraperitoneal administration of hemoCD1, hemoCD2, or hemoCD3 (1.0 mM, 0.15 mL each). PBS and Fb-hemoCD1 were similarly administered as controls. Each bar represents the means \pm SE ($n = 3$ mice per group). An asterisk denotes statistical significance, * $P < 0.05$, ** $P < 0.01$, as compared to the controls. (b) Western blot analysis of the liver using an anti-HO-1 antibody at 30, 90, and 180 min after the administration of hemoCD1, hemoCD2, or hemoCD3. The samples for the control were obtained from the mice at 30 min after the intraperitoneal administration of PBS (0.15 mL).

hemoCD1 or hemoCD3 injection, ca. 9-fold higher mRNA expression was observed as compared with the controls (PBS and Fb-hemoCD1). On the other hand, relatively weak induction (ca. 2.5-fold) was observed in the case of hemoCD2, indicating that *Hmox1* induction was dependent on the respective CO affinities of the hemoCDs. The enhanced mRNA gradually returned to a normal level. The time-courses of the transcriptional responses of *Hmox1* followed the depletion of CO-Hb in the blood as shown in Figure 6; the stronger depletion of CO-Hb in the blood caused a larger *Hmox1* mRNA induction in the mouse liver. In contrast, *Hmox2* expression levels were not affected by hemoCD administration (Figure S4).

The induction of mRNA in the mouse liver correlated with HO-1 protein expression, as confirmed by Western blot analysis using an anti-HO-1 antibody (Figure 7b). HO-1 protein began to accumulate in the liver at 90 min after the hemoCD dosing. The accumulated HO-1 protein is able to produce additional endogenous CO via the enzymatic degradation of hemin, leading to recovery of the reduced CO-Hb level in the blood as shown in Figure 6.

In Vitro Analysis. The expression level of *Hmox1* was also measured in vitro using mammalian hepatoma cells (HepG2) following incubation with hemoCD. We previously found that Fb-hemoCD cannot penetrate the cell membrane.³⁵ Therefore, it is reasonable to assume that hemoCD exists in the culture medium. Such conditions are similar to those of the in vivo experiments, wherein hemoCD circulated in the bloodstream without having any specific interactions with the surrounding cells. Unlike the in vivo experiments, however, the ferrous hemoCD1 (oxy-hemoCD1) in the culture medium did not affect the expression level of *Hmox1* in the HepG2 cells (Figure 8a). The individual components, i.e., met-hemoCD1,

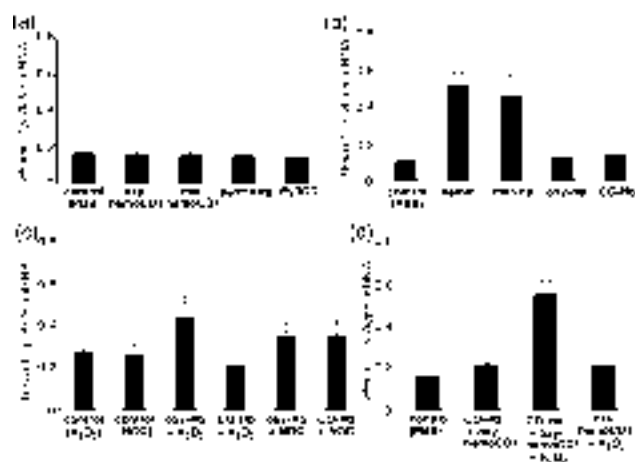


Figure 8. In vitro RT-PCR analysis of mRNA expression levels of HO-1 in HepG2 cells. Cells were incubated for 2 h with the following components prior to RT-PCR analysis: (a) Oxy-hemoCD1 (10 μ M), met-hemoCD1 (10 μ M), Fe^{III}TPPS (10 μ M), or Py3CD (10 μ M); (b) hemin (10 μ M), met-Hb (100 μ M), oxy-Hb (100 μ M), or CO-Hb (100 μ M); (c) H₂O₂ (200 μ M), NOC (a NO gas releasing agent, 250 μ M), oxy-Hb + H₂O₂ (100 μ M + 200 μ M), CO-Hb + H₂O₂ (100 μ M + 200 μ M), oxy-Hb + NOC (100 μ M + 250 μ M), or CO-Hb + NOC (100 μ M + 250 μ M); or (d) CO-Hb + oxy-hemoCD1 (100 μ M + 300 μ M), CO-Hb + oxy-hemoCD1 + H₂O₂ (100 μ M + 300 μ M + 200 μ M), or oxy-hemoCD1 + H₂O₂ (300 μ M + 200 μ M). Each bar represents the means \pm SE ($n = 3-7$ experiments per group). The asterisks denote statistical significance, * $P < 0.05$, ** $P < 0.01$, as compared to the controls.

Fe^{III}TPPS, and Py3CD, also did not induce *Hmox1*. It has been demonstrated that the natural biologic system does not recognize *meso*-tetraphenylporphyratoiron (FeTPP) derivatives as heme cofactor analogues because of the nonplanar structure of their peripheral phenyl substituents.^{36,37} In addition, hemoCD did not exhibit any cytotoxic and hemolytic activities.³⁸ Therefore, the induction of HO-1 observed in vivo cannot be ascribed to the direct interaction of the hemoCD molecules with the cells. Instead, the induction of HO-1 in vivo is attributable to the removal of endogenous CO by hemoCD in the blood.

As previously reported,³⁹ a strong *Hmox1* induction occurred in the HepG2 cells when they were incubated with hemin (Figure 8b). Hemin (Figure 1) is the substrate of HO-1 and thus a potent inducer for HO-1.⁴⁰ Hemin complexed with the globin protein (i.e., met-Hb) also induced *Hmox1*, whereas ferrous Hbs (oxy-Hb and CO-Hb) did not (Figure 8b). Ferrous heme is captured by globin protein more tightly than the ferric state (i.e., hemin).⁴¹ Therefore, met-Hb tends to partly dissociate to hemin and apo-globin in the culture medium. The released hemin from met-Hb in turn might penetrate the cell membrane to induce *Hmox1* in the cells. The release of hemin from met-Hb is considered to take place more efficiently in the bloodstream in vivo because of the presence of the intracellular transportation system for free hemin in the blood plasma.⁵

We hypothesized that the oxidation of ferrous Hb to met-Hb is the key reaction in the HO-1 induction observed in the CO-Hb depleted mice. The intravascular oxidation of ferrous Hb to met-Hb is known to be promoted by active oxidants such as hydrogen peroxide (H₂O₂) and NO in the blood,⁴² whose plasma concentrations range from 20–60 μ M for H₂O₂⁴³ and 0.003–1 μ M for NO.⁴⁴ Ferrous Hb is oxidized by H₂O₂ to met-Hb via ferryl intermediates.⁴⁵ H₂O₂ oxidizes deoxy-Hb ca.100-times more rapidly than oxy-Hb.⁴⁶ Because CO binds more strongly to the ferrous center of Hb than does O₂, the oxidation of CO-Hb by H₂O₂ is much slower than that of oxy-Hb, as shown in Figure S5. In other words, CO suppresses the H₂O₂-promoted oxidation of ferrous Hb to met-Hb. Such suppression has been previously proposed by Soares and Mota,⁴⁷ who reported that exogenously inhaled CO functions very effectively to reduce the generation of free hemin in the plasma of malaria-infected model mice.

On the other hand, NO promoted the oxidation of both oxy-Hb and CO-Hb to met-Hb with similar rates (Figure S6). NO binds to ferrous Hb more strongly than O₂ and CO,⁴⁸ and the resulting NO-Hb is readily oxidized to met-Hb under aerobic conditions.⁴⁹ The difference between H₂O₂ and NO in their reactivity to ferrous Hb (oxy- and CO-Hb) was clearly reflected in the *Hmox1* expression in the HepG2 cells (Figure 8c). *Hmox1* was induced when the oxidation of ferrous Hb by H₂O₂ or NO occurred in the culture medium. In contrast, CO-Hb did not induce *Hmox1* even in the presence of H₂O₂ (Figure 8c). When the CO ligand of CO-Hb was removed by oxy-hemoCD1 in the culture medium, *Hmox1* was significantly induced by H₂O₂ (Figure 8d). These results indicated that the removal of CO from CO-Hb caused an accumulation of met-Hb via the oxidation of oxy-Hb by H₂O₂, which led to the release of free hemin that subsequently induced *Hmox1*.

Blood Plasma Analysis. To determine whether the CO-depletion in the blood caused an accumulation of free hemin, blood samples were collected from the mice at 30, 90, and 180 min after the intraperitoneal administration of hemoCD1 (1.0 mM, 0.15 mL) and analyzed. The increase of met-Hb in the blood of the CO-depleted mice could not be measured clearly (data not shown). On the other hand, the free hemin accumulation was measured in the ultrafiltered plasma, from which hemoCD1 had been removed together with proteins by the ultrafiltration process. Figure 9a shows the changes in the free hemin concentration in the protein-depleted plasma of the hemoCD1-treated mice. Free hemin significantly increased upon the removal of endogenous CO by hemoCD1. The accumulation of free hemin was further evidenced by the subsequent down-regulation of ALAS-1 mRNA (*Alas1*) in the

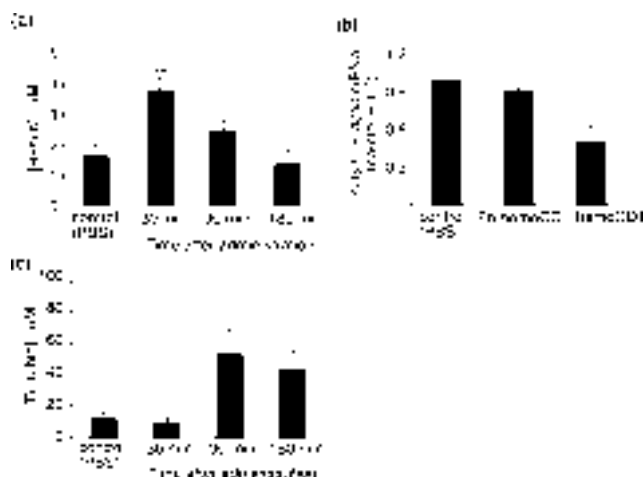


Figure 9. Accumulation of free hemin and bilirubin in the blood plasma of mice induced by CO-depletion. (a) Free hemin concentration in the protein-free plasma of mice after the administration of hemoCD1 (1.0 mM, 0.15 mL in PBS). The samples for the controls were obtained from the mice at 30 min after the intraperitoneal administration of PBS (0.15 mL). (b) The expression level of *Alas1* mRNA in the livers of mice at 90 min after the administration of hemoCD1 (1.0 mM, 0.15 mL in PBS). PBS and Fb-hemoCD1 were similarly administered as the negative controls. (c) Bilirubin concentration in the plasma of mice after the administration of hemoCD1 (1.0 mM, 0.15 mL in PBS). The samples for the controls were obtained from the mice at 30 min after the intraperitoneal administration of PBS (0.15 mL). Each bar represents the means \pm SE ($n = 3-4$ experiments per group). An asterisk denotes statistical significance; * $P < 0.05$, ** $P < 0.01$, as compared to the controls.

liver (Figure 9b). ALAS-1 is the enzyme that produces δ -aminolevulinic acid (ALA) for heme biosynthesis and it is known that the transcription system for this enzyme is inhibited by excess hemin.⁵⁰ The enhanced free hemin content in the plasma returned smoothly to a normal level (Figure 9a), suggesting the rapid degradation of hemin catalyzed by HO. In accordance with this, the concentration of bilirubin in the plasma was significantly increased (Figure 9c). The rise and decay in the time course of free hemin (Figure 9a) corresponded well with the depletion and recovery of CO-Hb, respectively, in the blood (Figure 6). In addition, the time course of the bilirubin concentration in the plasma (Figure 9c) appeared to be correlated to that of the *Hmox1* induction observed in the hemoCD-treated mice (Figure 7).

A Feedback Mechanism in the CO/HO-1 System. The present study revealed the relationship between the CO-depletion and the HO-1 induction in vivo. A plausible feedback mechanism is shown in Figure 10. The CO-removal from CO-Hb generates oxy-Hb. Oxy-Hb in RBC is very stable and is rarely oxidized to met-Hb because of the reduction system in the RBC membrane.⁴⁵ In contrast, cell-free oxy-Hb in the blood plasma is readily oxidized to met-Hb by ROS such as H_2O_2 and subsequently dissociates to hemin and apo-globin.⁴² The oxidation of CO-Hb by H_2O_2 should proceed much slower even in the blood plasma, resulting in the slow metabolism of cell-free CO-Hb by HO. Accordingly, the CO-depletion by hemoCD1 in vivo caused an accumulation of free hemin in the blood plasma. The unusual content of free hemin induces expression of HO-1 to metabolize this excess. The newly produced CO binds to ferrous Hb to form CO-Hb as the

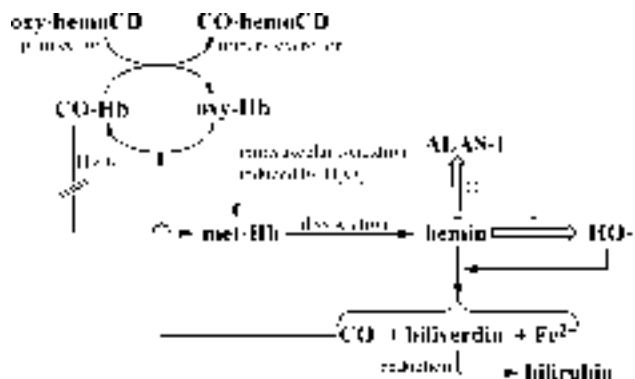


Figure 10. A homeostatic feedback model for the endogenous CO/HO-1 system in the blood plasma.

oxidation-resistant state, which restores the ferrous/ferric balance of cell-free Hb back to the homeostatic steady-state.

Endogenous CO contained in the whole blood and in the blood plasma from the untreated mice was quantified by the photometric assay using hemoCD1 (see Figure S7 in Supporting Information). We found that hemoCD1 could be used for quantification of endogenous CO in the blood because of its much higher CO affinity than Hb. Accordingly, $(2.2 \pm 0.2) \times 10^{-8}$ and $(9.2 \pm 0.6) \times 10^{-9}$ mol of CO were found in the whole blood and in the blood plasma, respectively. The amount of CO detected in the whole blood was consistent with that quantified by gas chromatography.⁵¹ The assay revealed that $42 \pm 4\%$ of endogenous CO was found in the blood plasma, indicating that a significant amount of endogenous CO is supposed to bind to cell-free Hb in the blood plasma. Because hemoCD cannot penetrate the cell membrane, administered hemoCD removes endogenous CO primarily from cell-free CO-Hb in the blood plasma, leading to the feedback response as shown in Figure 10.

CONCLUSIONS

The present study demonstrated the production of a pseudoknockdown state of endogenous CO in mice using the supramolecular complexes, hemoCDs. The CO-depletion caused a temporal decrease in the amount of CO-Hb in the blood of treated mice, which induced HO-1. The induced HO-1 accelerated endogenous CO production to compensate for the reduced CO in the blood. To our knowledge, this is the first example showing that the lack of CO in the blood causes a feedback-driven compensatory up-regulation of HO-1 to maintain constant CO-Hb level in the blood. The in vivo and in vitro experiments revealed a regulatory role of CO in maintaining the balance between ferrous Hb and ferric met-Hb. The strong coordination of CO to ferrous Hb can suppress the oxidation of cell-free Hb to met-Hb that is promoted by H_2O_2 . The CO-depletion in the blood resulted in the accumulation of free hemin, leading to rapid metabolism of free hemin by the HO enzyme to produce de novo endogenous CO. In summary, we have proposed a major regulatory role of endogenous CO in the blood through the use of hemoCDs. We believe that the present pseudoknockdown system will also be applicable for the investigation of other cryptic functions of CO in biological systems.

EXPERIMENTAL SECTION

Sample Preparation. $Fe^{III}TPPS$ (2.75 mg, $2.0 \mu\text{mol}$) and $Py3CD$ (7.05 mg, $2.4 \mu\text{mol}$)²⁶ were dissolved in PBS (1 mL) to yield a

solution of met-hemoCD1 (2 mM). The solutions of met-hemoCD2 and met-hemoCD3 were prepared as well using Py2CD²⁸ and Py3OCD.²⁹ To the solution of met-hemoCD was added Na₂S₂O₄ (ca. 1 mg) to reduce the met-hemoCD to ferrous hemoCD. Excess Na₂S₂O₄ was removed by passing the solution through a HiTrap desalting column (Sephadex G25, GE Healthcare Life Sciences). During this process under aerobic conditions, the ferrous hemoCDs bound O₂ in the air. The resulting solution containing ferrous hemoCD was appropriately diluted with PBS to obtain 0.5, 1.0, or 1.5 mM of the solution, the concentration of hemoCD being determined from its absorption coefficient as reported elsewhere.^{29,33} A solution of Fb-hemoCD (1.0 mM) was prepared by dissolving TPPS (0.94 mg, 1.0 μmol) and Py3CD (3.52 mg, 1.2 μmol) in PBS (1 mL).

Animal Experiments. The experiments were carried out in accordance with the Guidelines for Animal Experiments of Doshisha University and of Doshisha Women's College of Liberal Arts. Male C57BL/6N mice weighing 20–22 g were used. The mice were housed under controlled environmental conditions and fed commercial feed pellets. All mice had free access to food and water.

A solution of hemoCD (0.15 mL) was intraperitoneally administered to the subject mouse. The naturally excreted urine was collected (around 30 μL per 30 min), which was appropriately diluted with PBS and then measured by UV–vis spectroscopy (Shimadzu UV-2450). The assay for determining the amount of met-, oxy-, and CO complexes of hemoCD in the urine was described elsewhere.^{29,31–33} The mice were sacrificed by cervical dislocation at 30, 90, and 180 min after the administration, and the liver was excised by disposable biopsy punch (5 mmφ, Kai Medical), which was soaked in RNA later (Life Tech), and stored at 4 °C until use. For blood sampling, after the administration the mice were anaesthetized by isoflurane inhalation and the blood samples were collected from the postcava using a 23G syringe (Terumo). The blood samples were mixed with heparin and stored at –80 °C in the dark until use.

Cell Cultures. The human hepatoma cell line (HepG2) was obtained from RIKEN Cell Bank and cultured in Dulbecco's modified Eagle's medium (DMEM, Wako) supplemented with 10% fetal bovine serum (FBS, Invitrogen GIBCO, heat inactivated at 56 °C before use) and 1% penicillin/streptomycin/amphotericin B (Wako) at 37 °C in a humidified atmosphere with 5% CO₂. Cells were changed to serum-free medium (OPTI-MEM, Invitrogen GIBCO) before the treatments with agents. The cells were treated by hemoCD1, hemin (TCI, stock solution prepared using DMSO), human Hb (met-Hb was purchased from Sigma-Aldrich, ferrous Hb was prepared using Na₂S₂O₄ as a reducing agent, followed by purification using a HiTrap desalting column; the concentration of Hb was determined using reported absorption coefficients⁵²), H₂O₂ (Wako), 1-hydroxy-2-oxo-3-(3-aminopropyl)-3-isopropyl-1-triazene (NOC, a NO releasing molecule, Dojin Chemicals) or their mixed systems as described in Figure 8. After the incubation with these agents for 2 h, the cells were washed well with PBS and total RNA was then extracted, which was used for RT-PCR (below).

CO-Hb Content in Blood. The amount of CO-Hb in the blood was measured according to the reported method.⁵³ The blood samples (0.5 mL) obtained from the mice after the intraperitoneal administration of hemoCD were placed in a 5 mL 25G syringe (Terumo) sealed with a septum cap (natural rubber, for a 7 mm tube). To this, 3-drops of 4% Triton X-100 and 3-drops of *n*-octanol were injected through the septum. The mixture was then mixed well using a 5 mmφ glass ball. The atmosphere in the syringe (1 mL) was carefully replaced with He gas. Methane gas (10 μL) was added to the atmosphere through the septum in the syringe as an internal standard. Subsequently, 0.3 mL of 20% aqueous solution of K₃[Fe(CN)₆] was added to oxidize the ferrous Hb, and the liberated CO from CO-Hb in the gas phase (0.5 mL) was analyzed by means of gas chromatography (GC, Shimadzu GC-2014). It was confirmed that the CO gas was not liberated from CO-hemoCD by this treatment (CO-hemoCD was hardly oxidized by excess K₃[Fe(CN)₆] in the aqueous solution). The GC conditions were as follows: detector; TCD, column; SHINCARBON, carrier gas; He, column temperature; 40 °C, temperature at vaporizing chamber and detector; 120 °C; and flow rate: 50 mL/min.

The content of CO-Hb in the whole blood was determined from the amount of CO determined by GC and the amount of total Hb, which was measured by the CN-met-Hb method as previously reported.⁵⁴

RT-PCR. Total RNA was isolated from the mouse livers or HepG2 cells using the RNeasy Mini kit (Qiagen) according to the manufacturer's instructions. The RNA concentration and purity were determined by measuring the absorbances at 260 and 280 nm (Shimadzu BioSpec-nano). The resulting total RNA (1 μg) was reverse transcribed in a mixture (20 μL) of 5 × RT buffer (Toyobo, 4 μL), 10 mM dNTP (Toyobo, 2 μL), RNase Inhibitor (Toyobo, 1 μL), Oligo(dT)20 (Toyobo, 1 μL) and Rever Tra Ace (Toyobo, 1 μL). The sample was incubated at 30 °C for 10 min, at 42 °C for 20 min, and at 99 °C for 5 min. Real-time PCR was performed in a mixture (10 μL) of cDNA (1.0 ng/μL, 2 μL), forward and reverse primers (10 μM, 0.2 μL), distilled water (2.6 μL), and 2 × SYBR Green Master Mix (Applied Biosystems, 5 μL) using a Step One real time PCR system (Applied Biosystems). The primers are listed in Table S1. β-Actin was used as a reference gene. Forty cycles (95 °C for 30 s, 60 °C for 60 s) of PCR were performed after 10 min of denaturation at 95 °C. All samples were measured in triplicate. Data were analyzed by the relative standard curve method using StepOne software v2.3 (Applied Biosystems). Semiquantitative PCR was applied for the *in vitro* study. PCR was performed in a mixture of cDNA, PCR buffer (Toyobo), dNTP (Toyobo), forward and reverse primers, and DNA polymerase {KOD Dash (Toyobo) or Blend Taq (Toyobo)}. The primer sequences are listed in Table S2. The amplification reactions commenced with an initial denaturation step at 94 °C for 2 min, followed by denaturation at 94 °C for 1 min, annealing at 60 °C for 1 min, and extension at 72 °C for 2 min (15 cycles for KOD Dash, 21 cycles for blend-taq). For each reaction, a final extension of 72 °C for 5 min was carried out and the samples were then held at 4 °C until processed. The PCR products were analyzed by 2% agarose gel electrophoresis with ethidium bromide. The gel images were captured by a UV transilluminator (FAS-IV, Japan Genetics) and the band intensities were measured using the ImageJ software.

Western Blot. The mouse liver was homogenized in RIPA Lysis Buffer (ATTO, 20 mM HEPES, 150 mM NaCl, 1.0% IGEPAL CA-630, 0.1% SDS, and 0.5% sodium deoxycholate) after the additions of the protease inhibitor (ATTO) and phosphatase inhibitor (ATTO). The protein concentration was determined using a BCA Protein Assay Kit (Pierce). The protein sample (10 μL) was mixed with 2 × sample loading buffer (10 μL containing 4% SDS, 10% 2-mercaptoethanol, 20% glycerol, and 0.01% bromophenol blue in 125 mM Tris-HCl, pH 6.8), heated at 90 °C for 5 min, and separated by 12.5% SDS-PAGE. Proteins in the gels were electrophoretically transferred onto a polyvinylidene difluoride membrane at 144 mA for 50 min. The membrane was blocked with 5% skimmed milk in Tris buffer saline (TBS) for 1 h at room temperature. After washing the membrane with TBS-T (TBS containing 0.1% Tween), a polyclonal rabbit anti-HO-1 antibody (SPA-895, StressGen, 1:3000) was added and incubated overnight at 4 °C. The blots were incubated for 30 min at room temperature with HRP-conjugated secondary antibody (NA-931, Amersham Biosciences, 1:5000). Blots were processed with an ECL kit (Pierce) and the chemiluminescence signal was detected using an LAS-3000 mini image analyzer (Fuji Photo Film).

Quantification of Free Hemin in the Plasma. The concentration of free hemin in the blood plasma was measured according to the reported method.⁴⁷ After centrifuging the blood samples obtained from the mice (4 °C, 400g, 20 min), the plasma solution was collected and passed through an Amicon Ultra Centrifugal filter units (0.5 mL, MWCO 3000, centrifuged at 15 °C and 15 000g for 60 min) to remove proteins as well as hemoCD. The concentration of free hemin in the protein-depleted plasma was quantified by a chromogenic assay according to the manufacturer's instructions (QuantiChrom heme assay kit, Bioassay Systems). The colorimetric change was monitored at 405 nm using a Filter Max F5 plate reader (Molecular Devices).

Quantification of Bilirubin in the Plasma. The amount of bilirubin in the blood plasma was measured according to the reported method.^{55–57} After the centrifugation (4 °C, 400g, 20 min) of the blood sample obtained from the treated mice, the plasma solution (0.1

mL) was diluted 10-fold with PBS. To the solution (1 mL) was added recombinant his-tagged UnaG^{S7} (0.24 mM aqueous solution, 15 μ L) and then the solution was incubated for 2 h at 25 °C in the dark, after which the UnaG was trapped with Ni-NTA agarose (Invitrogen). After washing the resin with PBS, the UnaG was eluted with PBS containing 300 mM imidazole (300 μ L). The fluorescence from the bilirubin-bound UnaG was monitored using a Filter Max F5 plate reader (Molecular Devices, $\lambda_{\text{ex}} = 485 \pm 20$ nm and $\lambda_{\text{em}} = 535 \pm 25$ nm).

Statistical Analysis. All data represent the means \pm SE from at least three different experiments. Statistical analysis ($n \geq 3$) was performed by using an unpaired Student's *t*-test. The *P* value less than 0.05 was considered significant.

■ ASSOCIATED CONTENT

Supporting Information

The Supporting Information is available free of charge on the ACS Publications website at DOI: 10.1021/jacs.6b02211.

The primer sequences used for the RT-PCR experiments (Table S1 and S2), in vitro competitive reaction assay for Hb and hemoCD (Figure S1), time-courses of the molar fractions of oxy-, CO-, and met-hemoCD1 contained in the urine of the hemoCD1-treated mice (Figure S2), UV-vis spectra of TPPS, Fb-hemoCD, and the urine solution obtained after the intraperitoneal administration of Fb-hemoCD (Figure S3), mRNA expression levels of HO-2 (*Hmox2*) in the livers of mice after the administration of hemoCD1 (Figure S4), the UV-vis spectra for the reaction of oxy- and CO-Hb with H₂O₂ (Figure S5) and with NO (Figure S6) in aqueous solutions, and the photometric assay for the quantification of endogenous CO by hemoCD1 in the blood (Figure S7). (PDF)

■ AUTHOR INFORMATION

Corresponding Author

*hkitagis@mail.doshisha.ac.jp

Notes

The authors declare no competing financial interest.

■ ACKNOWLEDGMENTS

This work was financially supported by a Grant-in-Aid for Young Scientists (B) (No. 26870704) from the Japan Society for the Promotion of Science (JSPS), the MEXT-Supported Program for the Strategic Research Foundation at Private Universities (2015–2019), and The Uehara Memorial Foundation.

■ REFERENCES

- (1) Wu, L.; Wang, R. *Pharmacol. Rev.* **2005**, *57*, 585–630.
- (2) Ryter, S. W.; Alam, J.; Choi, A. M. *Physiol. Rev.* **2006**, *86*, 583–650.
- (3) Rother, R. P.; Bell, L.; Hillmen, P.; Gladwin, M. T. *JAMA* **2005**, *293*, 1653–1662.
- (4) Balla, J.; Vercellotti, G. M.; Jeney, V.; Yachie, A.; Varga, Z.; Eaton, J. W.; Balla, G. *Mol. Nutr. Food Res.* **2005**, *49*, 1030–1043.
- (5) Ferreira, A.; Balla, J.; Jeney, V.; Balla, G.; Soares, M. P. *J. Mol. Med.* **2008**, *86*, 1097–1111.
- (6) Piantadosi, C. A. *Antioxid. Redox Signaling* **2002**, *4*, 259–270.
- (7) Coburn, R. F. *Ann. N. Y. Acad. Sci.* **1970**, *174*, 11–22.
- (8) Miró, O.; Alonso, J. R.; Jarreta, D.; Casademont, J.; Urbano-Márquez, Á.; Cardellach, F. *Carcinogenesis* **1999**, *20*, 1331–1336.
- (9) Sato, K.; Balla, J.; Otterbein, L.; Smith, R. N.; Brouard, S.; Lin, Y.; Cszizmadia, E.; Sevigny, J.; Robson, S. C.; Vercellotti, G.; Choi, A. M.; Bach, F. H.; Soares, M. P. *J. Immunol.* **2001**, *166*, 4185–4194.

- (10) Amersi, F.; Shen, X. D.; Anselmo, D.; Melinek, J.; Iyer, S.; Southard, D. J.; Katori, M.; Volk, H. D.; Busuttill, R. W.; Buelow, R.; Kupiec-Weglinski, J. W. *Hepatology* **2002**, *35*, 815–823.
- (11) Johnson, T. R.; Mann, B. E.; Clark, J. E.; Foresti, R.; Green, C. J.; Motterlini, R. *Angew. Chem., Int. Ed.* **2003**, *42*, 3722–3729.
- (12) Motterlini, R.; Otterbein, L. E. *Nat. Rev. Drug Discovery* **2010**, *9*, 728–743.
- (13) Romão, C. C.; Blättler, W. A.; Seixas, J. D.; Bernardes, G. J. L. *Chem. Soc. Rev.* **2012**, *41*, 3571–3583.
- (14) Heinemann, S. H.; Hoshi, T.; Westerhausen, M.; Schiller, A. *Chem. Commun.* **2014**, *50*, 3644–3660.
- (15) Nikam, A.; Ollivier, A.; Rivard, M.; Wilson, J. L.; Mebarki, K.; Martens, T.; Dubois-Randé, J.-L.; Motterlini, R.; Foresti, R. *J. Med. Chem.* **2016**, *59*, 756–762.
- (16) Otterbein, L. E.; Bach, F. H.; Alam, J.; Soares, M.; Tao, L. H.; Wysk, M.; Davis, R. J.; Flavell, R. A.; Choi, A. M. *Nat. Med.* **2000**, *6*, 422–428.
- (17) Morse, D.; Pischke, S. E.; Zhou, Z.; Davis, R. J.; Flavell, R. A.; Loop, T.; Otterbein, S. L.; Otterbein, L. E.; Choi, A. M. *J. Biol. Chem.* **2003**, *278*, 36993–36998.
- (18) Bilban, M.; Bach, F. H.; Otterbein, S. L.; Ifedigbo, E.; d'Avila, J. C.; Esterbauer, H.; Chin, B. Y.; Usheva, A.; Robson, S. C.; Wagner, O.; Otterbein, L. E. *Immunity* **2006**, *24*, 601–610.
- (19) Nakahira, K.; Kim, H. P.; Geng, X. H.; Nakao, A.; Wang, X.; Murase, N.; Drain, P. F.; Wang, X.; Sasidhar, M.; Nabel, E. G.; Takahashi, T.; Lukacs, N. W.; Ryter, S. W.; Morita, K.; Choi, A. M. *J. Exp. Med.* **2006**, *203*, 2377–2389.
- (20) Dioum, E. M.; Rutter, J.; Tuckerman, J. R.; Gonzalez, G.; Gilles-Gonzalez, M. A.; McKnight, S. L. *Science* **2002**, *298*, 2385–2387.
- (21) Aono, S. *Acc. Chem. Res.* **2003**, *36*, 825–831.
- (22) Boehning, D.; Snyder, S. H. *Science* **2002**, *298*, 2339–2340.
- (23) Hou, S.; Reynolds, M. F.; Horrigan, F. T.; Heinemann, S. H.; Hoshi, T. *Acc. Chem. Res.* **2006**, *39*, 918–924.
- (24) Yachie, A.; Niida, Y.; Wada, T.; Igarashi, N.; Kaneda, H.; Toma, T.; Ohta, K.; Kasahara, Y.; Koizumi, S. *J. Clin. Invest.* **1999**, *103*, 129–135.
- (25) Morikawa, T.; Kajimura, M.; Nakamura, T.; Hishiki, T.; Nakanishi, T.; Yukutake, Y.; Nagahata, Y.; Ishikawa, M.; Hattori, K.; Takenouchi, T.; Takahashi, T.; Ishii, I.; Matsubara, K.; Kabe, Y.; Uchiyama, S.; Nagata, E.; Gadalla, M. M.; Snyder, S. H.; Suematsu, M. *Proc. Natl. Acad. Sci. U. S. A.* **2012**, *109*, 1293–1298.
- (26) Kano, K.; Kitagishi, H.; Kodera, M.; Hirota, S. *Angew. Chem., Int. Ed.* **2005**, *44*, 435–438.
- (27) Kano, K.; Kitagishi, H.; Dagallier, C.; Kodera, M.; Matsuo, T.; Hayashi, T.; Hisaeda, Y.; Hirota, S. *Inorg. Chem.* **2006**, *45*, 4448–4460.
- (28) Kano, K.; Itoh, Y.; Kitagishi, H.; Hayashi, T.; Hirota, S. *J. Am. Chem. Soc.* **2008**, *130*, 8006–8015.
- (29) Watanabe, K.; Kitagishi, H.; Kano, K. *Angew. Chem., Int. Ed.* **2013**, *52*, 6894–6897.
- (30) Collman, J. P.; Boulatov, R.; Sunderland, C. J.; Fu, L. *Chem. Rev.* **2004**, *104*, 561–588.
- (31) Kitagishi, H.; Negi, S.; Kiriya, A.; Honbo, A.; Sugiura, Y.; Kawaguchi, A. T.; Kano, K. *Angew. Chem., Int. Ed.* **2010**, *49*, 1312–1315.
- (32) Ueda, T.; Kitagishi, H.; Kano, K. *Org. Biomol. Chem.* **2012**, *10*, 4337–4347.
- (33) Kano, K.; Chimoto, S.; Tamaki, M.; Itoh, Y.; Kitagishi, H. *Dalton Trans.* **2012**, *41*, 453–461.
- (34) Matthew, E.; Warden, G.; Dedman, J. *Am. J. Physiol. Lung Cell. Mol. Physiol.* **2001**, *280*, L716–L723.
- (35) Kitagishi, H.; Minami, K.; Kano, K. *Chem. Lett.* **2014**, *43*, 1095–1097.
- (36) Mitrione, S. M.; Villalon, P.; Lutton, J. D.; Levere, R. D.; Abraham, N. G. *Am. J. Med. Sci.* **1988**, *296*, 180–186.
- (37) Shirataki, C.; Shoji, O.; Terada, M.; Ozaki, S.-i.; Sugimoto, H.; Shiro, Y.; Watanabe, Y. *Angew. Chem., Int. Ed.* **2014**, *53*, 2862–2866.
- (38) Karasugi, K.; Kitagishi, H.; Kano, K. *Bioconjugate Chem.* **2012**, *23*, 2365–2376.

- (39) Ghattas, M. H.; Chuang, L. T.; Kappas, A.; Abraham, N. G. *Int. J. Biochem. Cell Biol.* **2002**, *34*, 1619–1628.
- (40) Sun, J.; Hoshino, H.; Takaku, K.; Nakajima, O.; Muto, A.; Suzuki, H.; Tashiro, S.; Takahashi, S.; Shibahara, S.; Alam, J.; Taketo, M. M.; Yamamoto, M.; Igarashi, K. *EMBO J.* **2004**, *21*, 5216–5224.
- (41) Hargrove, M. S.; Olson, J. S. *Biochemistry* **1996**, *35*, 11310–11318.
- (42) Gladwin, M. T.; Kaniyas, T.; Kim-Shapiro, D. B. *J. Clin. Invest.* **2012**, *122*, 1205–1208.
- (43) Varma, S. D.; Devamanoharan, P. S. *Free Radical Res. Commun.* **1991**, *14*, 125–131.
- (44) Kelm, M. *Biochim. Biophys. Acta, Bioenerg.* **1999**, *1411*, 273–289.
- (45) Shikama, K. *Chem. Rev.* **1998**, *98*, 1357–1373.
- (46) Yusa, K.; Shikama, K. *Biochemistry* **1987**, *26*, 6684–6688.
- (47) Pamplona, A.; Ferreira, A.; Balla, J.; Jeney, V.; Balla, G.; Epiphany, S.; Chora, A.; Rodrigues, C. D.; Gregoire, I. P.; Cunha-Rodrigues, M.; Portugal, S.; Soares, M. P.; Mota, M. M. *Nat. Med.* **2007**, *13*, 703–710.
- (48) Tsai, A. L.; Berka, V.; Martin, E.; Olson, J. S. *Biochemistry* **2012**, *51*, 172–186.
- (49) Herold, S.; Röck, G. *Biochemistry* **2005**, *44*, 6223–6231.
- (50) Yamamoto, M.; Kure, S.; Engel, J. D.; Hiraga, K. *J. Biol. Chem.* **1988**, *263*, 15973–15979.
- (51) The amount of endogenous CO was estimated by gas chromatography to be 2.66×10^{-8} mol in the whole blood, where $[\text{Hb}] = 7.4$ mM (as monomer); the fraction of CO-Hb, 0.2%; blood volume, 1.8 mL.
- (52) Antonini, E.; Brunori, M. Hemoglobin and myoglobin in their reactions with ligands. In *Frontiers in Biology*; Neuberger, A., Tatum, E. L., Ed.; Elsevier: Amsterdam, 1971; Chapter 13.
- (53) Vreman, H. J.; Kwong, L. K.; Stevenson, D. K. *Clin. Chem.* **1984**, *30*, 1382–1386.
- (54) Rodkey, F. L.; Hill, T. A.; Pitts, L. L.; Robertson, R. F. *Clin. Chem.* **1979**, *25*, 1388–1393.
- (55) Takeda, T. A.; Mu, A.; Tai, T. T.; Kitajima, S.; Taketani, S. *Sci. Rep.* **2015**, *5*, 10488.
- (56) Liem, P. H.; Mu, A.; Kikuta, S.-i.; Ohta, K.; Kitajima, S.; Taketani, S. *Biol. Chem.* **2015**, *396*, 1265–1268.
- (57) Kumagai, A.; Ando, R.; Miyatake, H.; Greimel, P.; Kobayashi, T.; Hirabayashi, Y.; Shimogori, T.; Miyawaki, A. *Cell* **2013**, *153*, 1602–1611.

Structurally Simple Cell-permeable Porphyrins: Efficient Cellular Uptake and Phototoxicity of Porphyrins with Four Peripheral Primary-amine-terminated Oligo(ethylene oxide) Chains

Natsumi Ohashi,¹ Akiko Nomura,² Masahito Kodera,^{1,2} and Yutaka Hitomi*^{1,2}

¹Department of Applied Chemistry, Graduate School of Science and Engineering, Doshisha University, 1-3 Tatara Miyakodani, Kyotanabe, Kyoto 610-0321

²Center for Nanoscience Research, Doshisha University, 1-3 Tatara Miyakodani, Kyotanabe, Kyoto 610-0321

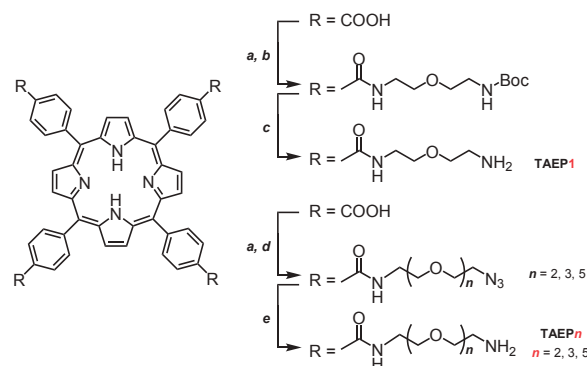
(E-mail: yhitomi@mail.doshisha.ac.jp)

A series of *meso*-tetraphenylporphyrins bearing four primary-amine-terminated oligo(ethylene oxide) chains have been synthesized from *meso*-tetrakis(4-carboxyphenyl)porphyrin. All the porphyrins with different lengths of oligo(ethylene oxide) chains accumulate in cells more efficiently than *meso*-tetrakis(*N*-methylpyridinium-4-yl)porphyrin, TMPyP. The porphyrin having the shortest ethylene oxide chains was found to accumulate the most within cells among the series, and exhibit phototoxicity under red light irradiation.

Keywords: Photodynamic therapy | Cell-permeable porphyrin | Phototoxicity

Photodynamic therapy is currently used for the treatment of certain types of cancer, as well as non-oncological diseases whereby a photosensitizer is administered and subsequently illuminated with red light, leading to the generation of reactive oxygen species to kill tumors.^{1,2} Porphyrins and related compounds that can accumulate in tumors are used in medical fields. Although these clinically successful photosensitizers are mostly non-ionic, cationic porphyrins have attracted attention because they effectively internalize in cells through endocytosis and/or the direct transmembrane mechanism.^{3–5} For instance, a commercially available water-soluble porphyrin, *meso*-tetrakis(*N*-methylpyridinium-4-yl)porphyrin, TMPyP, has been best studied as an intracellular photosensitizer.^{6–10} In addition, Vicente and co-workers have reported that AABB- and ABAB-type porphyrins bearing two *p*-trimethylammoniumphenyl groups exhibit higher cell-permeability than the corresponding tetracationic porphyrin, which clearly demonstrates importance of balance of hydrophilic and hydrophobic parts in designing efficient cell-permeable porphyrins.¹¹ However, AABB- and ABAB-type tetraphenylporphyrins require elaborate synthesis and tedious purification.

Recently we reported the synthesis and biological application of tetraphenylporphyrin with four poly(ethylene glycol) (PEG) chains, which is highly water-soluble and can be easily synthesized from the commercially available tetrakis(4-carboxyphenyl)porphyrin (TCPP) via amide condensation with mono-amine-terminated PEG.¹² However, the neutral PEGylated porphyrin does not show cell-permeability at all. We naively thought that introducing primary amine groups at the terminus of the four PEG chains may endow PEGylated porphyrins with cell-permeability. To this end, we have prepared a series of tetraphenylporphyrins bearing four primary-amine-terminated oligo(ethylene oxide) chains of different length (TAEP n : $n = 1, 2, 3,$ and 5) from TCPP according to Scheme 1, in order to perform a systematic investigation of cellular uptake of this type of porphyrin.



Scheme 1. Reagents: a) $(\text{COCl})_2$, DMF, CH_2Cl_2 ; b) $\text{BocNH-CH}_2\text{CH}_2\text{OCH}_2\text{CH}_2\text{NH}_2$, DIPEA, CH_2Cl_2 ; c) HCl aq., MeOH, and gel column chromatography; d) $\text{NH}_2\text{CH}_2(\text{CH}_2\text{OCH}_2)_n\text{CH}_2\text{-N}_3$, DIPEA, CH_2Cl_2 ; e) PPh_3 , THF, H_2O .

TAEP1 was obtained by amide condensation of TCPP with mono-Boc-protected bis(2-aminoethyl) ether, $\text{NH}_2\text{CH}_2\text{CH}_2\text{O-CH}_2\text{CH}_2\text{NH-Boc}$,¹³ followed by HCl-MeOH treatment and by gel chromatography on a Sephadex LH-20 column with methanol as an eluent. Other derivatives TAEP n , where $n = 2, 3,$ and 5 , were synthesized by amide condensation of TCPP with azide oligo(ethylene oxide) amine, $\text{NH}_2\text{CH}_2(\text{CH}_2\text{OCH}_2)_n\text{CH}_2\text{N}_3$,¹⁴ followed by Staudinger reduction with triphenylphosphine. The target compounds were easily obtained through extraction with chloroform.

The electronic absorption spectra of the solutions of TAEPs in DMSO were quite identical, indicating that the electronic structure of the porphyrin moiety was not affected by different peripheral groups of TAEP n . In contrast, the Soret bands were significantly broadened in the solution of TAEPs in cell culture media (Dulbecco's Modified Eagle Medium, D-MEM) compared with those observed in DMSO, except for TAEP1 (Figure 1). The FWHM values of the Soret bands were in order of $\text{TAEP2} > \text{TAEP3} > \text{TAEP5} > \text{TAEP1}$ (Figure 1 inset). The result suggests that TAEP n ($n = 2, 3,$ and 5) form some aggregate in D-MEM.

To address the aggregation of TAEP n , we measured the resonance light scattering (RLS) spectra of TAEP n in D-MEM (Figure 2).^{15,16} The RLS spectra were obtained by synchronously scanning the same excitation and emission wavelengths with a fluorescence spectrophotometer (HITACHI F-7000). TAEP1 and TAEP5 did not show significant elastic scattering. In contrast, TAEP2 and TAEP3 gave RLS signals, which gradually increased in intensity during the measurements.

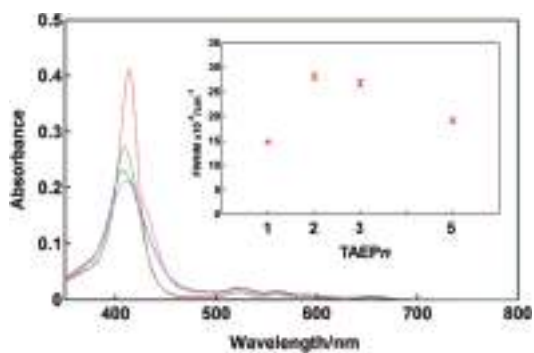


Figure 1. Electronic absorption spectra of TAEP1 (red), TAEP2 (pink), TAEP3 (blue), and TAEP5 (green) ($2\ \mu\text{M}$) in D-MEM. Inset: The full width at half-maximum (FWHM) of the Soret band of TAEP n ($n = 1, 2, 3,$ and 5).

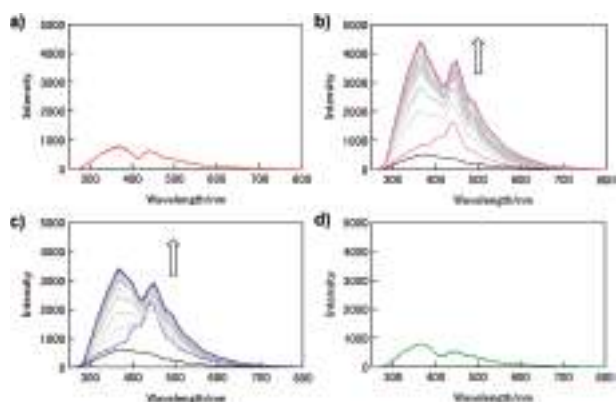


Figure 2. RLS spectra of a) TAEP1, b) TAEP2, c) TAEP3, and d) TAEP5 in D-MEM. Concentration: $2\ \mu\text{M}$. Black lines in b) and c) show the spectra of D-MEM without porphyrin. The spectra were taken every 10 min.

The electronic absorption measurement and RLS experiments indicate that TAEP2 and TAEP3 form larger aggregates than TAEP5, and that uniquely TAEP1 does not aggregate significantly in D-MEM. The aggregation behavior of TAEP n should be determined by the balance of hydrophobicity of the porphyrin core, cationic nature of the protonated primary amine groups, and amphiphilic nature of the oligo(ethylene oxide) chains. TAEP1 should be the most hydrophilic among the series, because it has four cationic moieties at closer position to the porphyrin core. The structural setting should allow TAEP1 to be solubilized in a more nearly monomeric form in D-MEM. We already reported structurally related PEGylated porphyrin is highly water soluble,¹² whose PEG chains should act as surfactants to wrap and solubilize the porphyrin core. It is likely that the longer ethylene oxide chains of TAEP5 partly inhibit the formation of porphyrin aggregates.

Next, we performed cellular uptake studies using the TAEP series together with TMPyP as a reference. HeLa cells were seeded at $100000\ \text{cells mL}^{-1}$ in $100\ \mu\text{L}$ of D-MEM containing fetal serum albumin (FBS) and phenol red in a 96 well plate and allowed to attach for 24 h. After counting cells in each well with an imaging cytometer (Molecular Devices, SpectraMax MiniMax 300), removing the media, and washing cells with

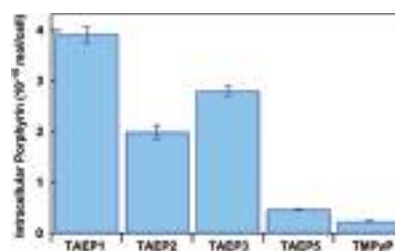


Figure 3. Cellular uptake of cationic porphyrins TAEP n and TMPyP at $2\ \mu\text{M}$ by HeLa cells after 3 h incubation.

Dulbecco's phosphate-buffered saline (D-PBS), porphyrin stock solutions were added to each well to give $2\ \mu\text{M}$ porphyrin in D-MEM containing no FBS. After incubation in a humidified, 5% CO_2 incubator at $37\ ^\circ\text{C}$ for 3 h, the medium was removed, the cells were washed with D-PBS twice, and solubilized with $20\ \mu\text{L}$ of 0.1% Triton X-100 in D-PBS for 20 min, and diluted with $180\ \mu\text{L}$ of DMSO. The intracellular accumulation of porphyrin was determined by measuring the fluorescence intensity of the porphyrin (Molecular Devices, SpectraMax i3x) based on separately prepared calibration curves. To our delight, TAEP n except for TAEP5 accumulated within cells much more efficiently than TMPyP under the current conditions (Figure 3). Among the TAEP series, the smallest TAEP1 accumulated the most in cells, and 16-fold more efficiently than TMPyP. The cellular uptake of TAEP2 and TAEP3 was about 0.5- and 0.7-fold lower that of TAEP1, although the former form relatively large aggregates. The amount of TAEP5 was only 2-fold higher than that of TMPyP. These results suggest that the cell-permeability of the TAEP series is primary determined by molecular size, but not by aggregation tendency.

We also monitored the cellular uptake of TAEP1 by confocal laser-scanning microscope (Figure 4). After 30 min exposure to $2\ \mu\text{M}$ TAEP1, fluorescence was observed only at the periphery of HeLa cells. After 1 and 3 h, punctate fluorescence was observed in cytosol region. These results suggest TAEP1 translocate and internalize through endocytosis. However, the amounts of cellular uptake of TAEP n were not suppressed by incubation at $4\ ^\circ\text{C}$, under which ATP-dependent endocytosis should be effectively inhibited.¹⁷ Thus, it is most likely that TAEP n are internalized by an energy-independent direct transmembrane-translocation mechanism as well as by endocytosis.

Finally, we examined the phototoxicity of TAEP1 under red light irradiation. HeLa cells were incubated with $0.5\ \mu\text{M}$ TAEP1 for 3 h. The medium was removed, and the cells was washed twice with PBS, and fed with D-MEM containing no serum and

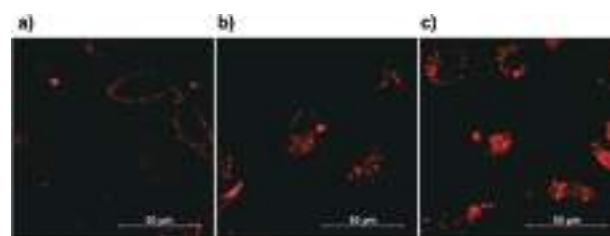


Figure 4. Confocal laser scanning microscope images of HeLa cells after a) 30 min, b) 1 h, and c) 3 h incubation with with $2\ \mu\text{M}$ TAEP1 (ex/em = $402.5/592.5\text{--}722.5\ \text{nm}$).

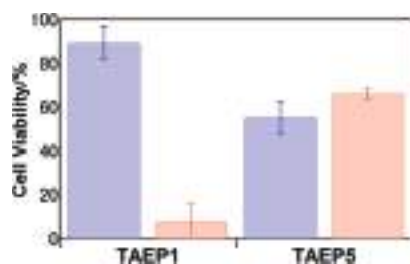


Figure 5. Cell viability of HeLa cells incubated with TAEP1 and TAEP5 (0.5 μM) in the dark (blue) or under light irradiation at 655 nm ($90 \pm 10 \mu\text{W cm}^{-2}$) for 30 min (red).

phenol red. An LED panel (CCS Inc., 655 nm, $90 \mu\text{W cm}^{-2}$) was used for irradiation for 30 min. After 24 h incubation at 37 °C, cell viability was evaluated by MTT assay. The experiment was also performed with TAEP5, because TAEP1 and TAEP5 have one of the Q-bands at ca. 655 nm with similar molar absorptivity in D-MEM. The results are shown in Figure 5, together with the results without irradiation, which clearly demonstrate that TAEP1 is an efficient intracellular photosensitizer.

In conclusion, we found that TAEP1 is an efficient cell-permeable porphyrin, which is structurally simple and easily synthesized. Thanks to these advantages, we anticipate that TAEP1 will provide a new opportunity for us to deliver various types of biologically useful metalloporphyrins within cells effectively and easily. This line of study is undergoing in our group.

This study was financially supported by JSPS KAKENHI Grant Numbers JP16H04124, JP16H01042, and JP15K05572, and the MEXT-Supported Program for the Strategic Research Foundation at Private Universities (2015–2019).

Dedicated to the late Professor Yoshihiko Ito on the occasion of the 10th anniversary of his sudden death.

References and Notes

1 S. Yano, S. Hirohara, M. Obata, Y. Hagiya, S. Ogura, A.

- Ikeda, H. Kataoka, M. Tanaka, T. Joh, *J. Photochem. Photobiol., C* **2011**, *12*, 46.
- 2 D. van Straten, V. Mashayekhi, H. S. de Bruijn, S. Oliveira, D. J. Robinson, *Cancers (Basel)* **2017**, *9*, 19.
- 3 H. Kitagishi, S. Hatada, T. Itakura, Y. Maki, Y. Maeda, K. Kano, *Org. Biomol. Chem.* **2013**, *11*, 3203.
- 4 B. P. P. McCormick, M. F. Pansa, L. N. M. Sanabria, C. M. B. Carvalho, M. A. F. Faustino, M. G. P. M. S. Neves, J. A. S. Cavaleiro, N. B. R. Vittar, V. A. Rivarola, *Laser Phys.* **2014**, *24*, 045603.
- 5 Á. Orosz, S. Bősze, G. Mező, I. Szabó, L. Herényi, G. Csík, *Amino Acids* **2017**, *49*, 1263.
- 6 S. M. Abdelghany, D. Schmid, J. Deacon, J. Jaworski, F. Fay, K. M. McLaughlin, J. A. Gormley, J. F. Burrows, D. B. Longley, R. F. Donnelly, C. J. Scott, *Biomacromolecules* **2013**, *14*, 302.
- 7 P. Acedo, J. C. Stockert, M. Cañete, A. Villanueva, *Cell Death Dis.* **2014**, *5*, e1122.
- 8 V. Cenklová, *J. Photochem. Photobiol., B* **2017**, *173*, 522.
- 9 S. Kim, T. Tachikawa, M. Fujitsuka, T. Majima, *J. Am. Chem. Soc.* **2014**, *136*, 11707.
- 10 S. Tada-Oikawa, S. Oikawa, J. Hirayama, K. Hirakawa, S. Kawanishi, *Photochem. Photobiol.* **2009**, *85*, 1391.
- 11 T. J. Jensen, M. G. H. Vicente, R. Luguia, J. Norton, F. R. Fronczek, K. M. Smith, *J. Photochem. Photobiol., B* **2010**, *100*, 100.
- 12 Y. Hitomi, T. Ekawa, M. Kodera, *Chem. Lett.* **2014**, *43*, 732.
- 13 H. Suzuki, A. Kanai, T. Uehara, F. L. G. Gomez, H. Hanaoka, Y. Arano, *Bioorg. Med. Chem.* **2012**, *20*, 978.
- 14 F. Bocard, A. Godinat, D. Staedler, H. C. Blanco, A.-L. Dumont, C. Chapuis-Bernasconi, C. Scaletta, L. A. Applegate, F. K. Juillerat, U. T. Gonzenbach, S. Gerber-Lemaire, L. Juillerat-Jeanneret, *Bioconjugate Chem.* **2011**, *22*, 1422.
- 15 R. F. Pasternack, K. F. Schaefer, P. Hambright, *Inorg. Chem.* **1994**, *33*, 2062.
- 16 G. De Luca, A. Romeo, L. M. Scolaro, *J. Phys. Chem. B* **2005**, *109*, 7149.
- 17 I. Nakase, H. Akita, K. Kogure, A. Gräslund, U. Langel, H. Harashima, S. Futaki, *Acc. Chem. Res.* **2012**, *45*, 1132.

DNA Cleavage through Reductive Dioxygen Activation by Iron-Bleomycin Mimics with Carboxamido Ligation: Correlation between DNA Cleavage Efficacy and Redox Potential

Akiko Nomura,¹ Yuji Iwamoto,^{1,2} Kengo Arakawa,² Akihiro Kashida,² Masahito Kodera,^{1,2} and Yutaka Hitomi*^{1,2}

¹Center for Nanoscience Research, Doshisha University, 1-3 Tatara Miyakodani, Kyotanabe, Kyoto 610-0321

²Department of Applied Chemistry, Graduate School of Science and Engineering, Doshisha University, 1-3 Tatara Miyakodani, Kyotanabe, Kyoto 610-0321

(E-mail: yhitomi@mail.doshisha.ac.jp)

DNA cleavage by a series of nonheme iron complexes supported by pentadentate carboxamido ligands, dpaq^R (R = OMe, H, Cl, and NO₂), was evaluated in the presence of a reducing agent under air and in the presence of hydrogen peroxide. Cleavage efficiency clearly increased as redox potential became more positive. These results provide an opportunity for the designing of Bleomycin mimics with higher activity.

Keywords: DNA cleavage | Iron-Bleomycin mimics | Redox potential

Bleomycins (BLMs) are natural glycopeptide antibiotics with a clinical activity against several types of tumors.^{1,2} The antitumor activity of this drug stems from the oxidative cleavage of double-stranded DNA by Fe-BLM complexes.³ BLMs exhibit low myelo- and immunosuppression,⁴⁻⁷ but they induce pneumonitis as a side effect.^{4,5} Therefore, there have been continuous efforts to develop new BLM analogues in the search for anticancer drugs with better efficacy and lower toxicity for normal cells.⁶ These may include artificial BLM analogues such as PYML^{7,8} and PMA.^{9,10} Both PYML and PMA have carboxamide functionality, as preserved in the metal binding domain of BLM. It has been shown that the iron(III) complexes of PYML and PMA are capable of inducing DNA strand breaks in an oxidative manner in the presence of both molecular oxygen (O₂) and additional reducing agents. Fe(III)OOH species of BLMs, known as activated BLM (ABLM),¹¹ are the last detectable intermediate before DNA cleavage occurs. The above-mentioned artificial BLMs also produce the corresponding Fe(III)OOH species when the iron(III) complexes of PYML or PMA either react with hydrogen peroxide (H₂O₂) or when the iron(II) complexes are exposed to air. Thus, iron(III) complexes of PYML and PMA are good structural and functional models for BLMs. However, a limited number of BLM mimics still exist,¹²⁻¹⁵ and there is no clear design guide for Fe-BLM analogues with higher DNA cleavage efficacy, although the mechanisms of O₂ activation by Fe-BLM complexes and the resulting DNA cleavage have been extensively investigated. In this study, we demonstrate that simple pentadentate carboxamido ligands can provide new functional mimics for Fe-BLM that promote DNA cleavage in the presence of a reducing agent under air, and report a clear correlation between the DNA cleavage efficacy and the reduction potentials of the Fe-BLM mimics.

Previously, we reported that an iron(III) complex, supported by the pentadentate carboxamido ligand 2-[bis(pyridin-2-ylmethyl)amino]-N-(quinolin-8-yl)acetamide (dpaq^H, Chart 1, R = H), catalyzes the hydroxylation of inert C–H bonds of alkanes with H₂O₂ in acetonitrile.¹⁶ Encouraged by this finding, we examined whether [Fe^{III}(dpaq^H)Cl]Cl and its ligand sub-

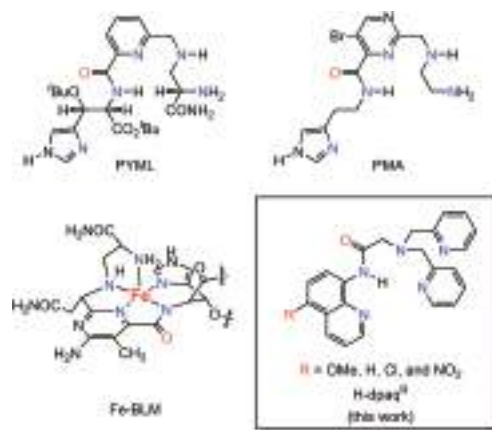


Chart 1. Chemical structure of Fe-BLM, PYML, PMA, and H-dpaq^R.

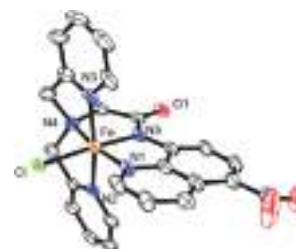


Figure 1. Crystal structure of the cation moiety of **1**^{NO₂} (50% probability). Selected bond lengths (Å): Fe–N1: 1.962(5); Fe–N2: 1.985(5); Fe–N3: 1.979(5); Fe–N4: 1.876(5); Fe–N5: 1.972(5); and Fe–Cl: 2.2693(16).

stituents (**1**^R, R = OMe, H, Cl, and NO₂, Chart 1)¹⁷ exhibited BLM-like activity in the presence of a reducing agent in water under air. In addition, we examined the substituent effect on the DNA cleavage efficacy.

Brown crystals suitable for X-ray diffraction were obtained as a tetrafluoroborate salt of [Fe^{III}(dpaqNO₂)Cl]⁺ by the diffusion of diethyl ether into a salt solution in ethanol. The cation moiety structure of **1**^{NO₂} shows that an Fe ion is supported by the dpaq^{NO₂} ligand in a pentadentate manner, which includes a carboxamido ligation, as reported for [Fe^{III}(dpaq^H)(H₂O)]-(ClO₄)₂;¹⁶ a chloride ion occupied the trans position to the carboxamido ligand (Figure 1).

Differential pulse voltammetry experiments were performed in an aqueous solution of **1**^H maintained at pH 8.0 using Tris-HCl buffer. A peak at 130 mV vs. NHE was observed, corresponding to the Fe(III)/Fe(II) reduction (Figure S1).



Figure 2. 1^R -promoted cleavage of pUC19 supercoiled plasmid DNA. Conditions: $1 \mu\text{M } 1^R$, 1 mM DTT , $0.1 \mu\text{g } \mu\text{L}^{-1}$ (0.15 mM in base pair) pUC19 DNA, $100 \mu\text{M EDTA}$ in 10 mM Tris-HCl ($\text{pH } 8.0$). Electrophoresis: 1% agarose gel in Tris-acetate-EDTA buffer.

The oxidative cleavage activity of 1^H was examined using pUC19 supercoiled plasmid DNA in the presence of 1 mM dithiothreitol (DTT) at $\text{pH } 8.0$ and 37°C under air. DNA cleavage reactions were initiated by adding 1^H to a buffered solution of pUC19 supercoiled plasmid DNA ($0.1 \mu\text{g } \mu\text{L}^{-1}$, 0.15 mM in base pair) and $100 \mu\text{M EDTA}$, and were subsequently quenched by adding an excess of NaCN at 10, 30, and 60 min. Agarose gel analysis showed that nicked DNA slowly increased up to 15% at 60 min, but linear DNA was not detected (Figure 2).

Ligand substitution is expected to affect the DNA cleavage activity. To explore this possibility, three additional derivatives of 1^H were prepared, with substituents at the 5-position of the quinoline ring (1^R , $R = \text{OMe}$, Cl , or NO_2 , Chart 1). Electrochemical measurements showed that the redox potentials of 1^R varied with the substituent R . The cathodic peak corresponding to the reduction of Fe(III) to Fe(II) species of 1^R was shifted more positively as the substituent R became more electron-withdrawing: $R = \text{OMe}$, 173 ; $R = \text{H}$, 185 ; $R = \text{Cl}$, 201 ; $R = \text{NO}_2$, 221 mV vs. NHE , indicating that the substitutions can tune the redox potentials at most by 48 mV (Figure S1).

DNA cleavage experiments on 1^R series revealed that the fraction of nicked DNA became larger as the substituent group on the ligand of 1^R becomes more electron-withdrawing; $R = \text{OMe}$, H , Cl , and NO_2 gave 1.7% , 6.5% , 12% , and 39% nicked DNA after incubation for 30 min, respectively (Figure 2 and Table S1). Thus, the fractions of nicked DNA are well correlated with the cathodic peak potentials of 1^R (Figure 3, black line).

Next, we examined DNA cleavage by the most active complex 1^{NO_2} and DTT in the presence of reactive oxygen species (ROS) scavengers (Figure 4). The addition of DMSO, a scavenger of hydroxyl radicals, did not suppress the formation of form II DNA, indicating no involvement of hydroxyl radicals in DNA cleavage. On the other hand, the addition of superoxide dismutase (SOD) decreased DNA cleavage efficiency. The result indicates the involvement of free superoxide radicals for 1^{NO_2} -mediated DNA cleavage because SOD rapidly converts superoxide into O_2 and H_2O_2 . The addition of catalase alone also decreased DNA cleavage efficiency, and the combined addition of SOD and catalase almost completely inhibited DNA cleavage. Since neither superoxide radicals nor H_2O_2 itself cannot cleave DNA effectively (Figure S2), it is most likely that free superoxide radicals and H_2O_2 are produced via reductive dioxygen activation by 1^R in the presence of reducing agents, and then react with 1^R to afford metal-based oxidants for DNA cleavage.

When $10 \mu\text{M H}_2\text{O}_2$ was used instead of DTT, nicked DNA also increased in a time-dependent manner (Figure S2 and Table S2). This indicates that the oxidizing species responsible for DNA cleavage can be generated by the reaction of 1^R with

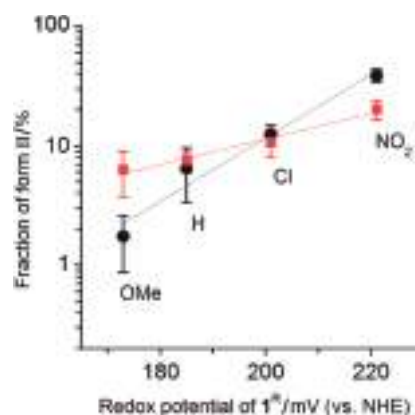


Figure 3. Plots of the fraction of nicked DNA after incubation for 30 min in Tris-HCl buffer ($\text{pH } 8.0$) with 1 mM DTT (black circle) or $0.01 \text{ mM H}_2\text{O}_2$ (red square) against the cathodic peak potential of 1^R .

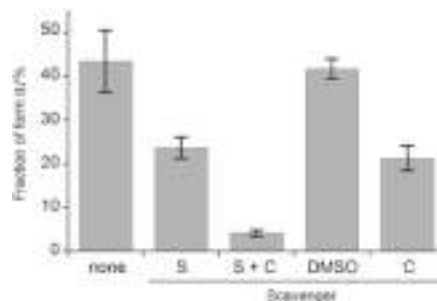


Figure 4. Fraction of form II pUC19 plasmid DNA in 10 mM Tris buffer ($\text{pH } 8.0$) in the presence of 1^{NO_2} ($1.0 \mu\text{M}$), 1 mM DTT , $100 \mu\text{M EDTA}$, and ROS scavengers after 30 min. S and C denote SOD and catalase, respectively.

H_2O_2 , supporting the idea that free H_2O_2 plays a role in DNA cleavage in the presence of DTT/O_2 . Interestingly, as per the results obtained in the presence of reducing agents, the fraction of nicked DNA increased as the substituent group on the ligand of 1^R became more electron-withdrawing; $R = \text{OMe}$, H , Cl , and NO_2 gave 6.3% , 7.5% , 11% , and 20% nicked DNA, respectively, at 30 min. The slope was shallower than that observed under DTT/O_2 conditions (Figure 3, red line), which is probably caused by the different amounts of active species generated under the different conditions.

It is important to know whether the Fe(III)OOH species as an initial oxidant is directly responsible for the oxidation of DNA, or whether it is a precursor to a high-valent iron species through homolysis or heterolysis of the O-O bond of Fe(III)OOH species. As mentioned above, we observed that DMSO did not suppress DNA cleavages, suggesting that it is unlikely that the Fe(III)OOH species undergoes the O-O bond homolysis to produce hydroxyl radicals and oxoiron(IV) species¹⁸ under the experimental conditions.

Meyer and co-workers reported that the oxoiron(V)/oxoiron(IV) redox couple of 1^H is 1.25 V vs. NHE at the pH range of 0.5 to 10.5 .¹⁹ Therefore, we expected that if the oxoiron(V) species is generated, 2'-azino-bis(3-ethylbenzothiazoline-6-sulfonic acid) (ABTS) should readily undergo one-electron

oxidation to give its blue-colored and relatively stable cation radical, because the oxidation potential of ABTS is 0.68 V vs. NHE.²⁰ However, we could not observe ABTS cation radical in the presence of $\mathbf{1}^{\text{NO}_2}$ and H_2O_2 , even when using 1 mM H_2O_2 (Figure S3), which is in accordance with our previous study that $\mathbf{1}^{\text{H}}$ exhibits no peroxidase activity at pH ranging from 4 to 9.²¹ The results suggest that $\mathbf{1}^{\text{R}}$ cannot generate oxoiron(V) species in the presence of H_2O_2 under the current conditions. Although more direct evidence should be required, we suppose that Fe(III)OOH species of $\mathbf{1}^{\text{R}}$ is directly responsible as a primary oxidant for the oxidation of DNA, as reported theoretically and experimentally for the Fe(III)OOH species of Fe-BLM, ABLM, by Solomon and co-workers.²²

The above results demonstrate that iron-carboxamido complexes $\mathbf{1}^{\text{R}}$ can act as new functional models for BLM. Significantly, an electron-withdrawing substituent on the dpq ligand positively shifts the redox potential and enhances DNA cleavage efficiency in the presence of DTT/ O_2 , as well as a H_2O_2 oxidant. These results provide an opportunity for the designing of BLM mimics with higher activity. Future work will focus on the synthesis of $\mathbf{1}^{\text{R}}$ variants bearing DNA recognition moieties and the exploration of the reactivity of the Fe(III)OOH species of $\mathbf{1}^{\text{R}}$.

This study is financially supported by JSPS KAKENHI Grant Numbers JP15K05572, JP15H00963, and JP16H01042.

Supporting Information is available on <http://dx.doi.org/10.1246/cl.170354>.

References

- 1 B. A. Chabner, D. L. Longo, *Cancer Chemotherapy and Biotherapy*, Lippincott Williams & Wilkins, Philadelphia, **2010**, p. 848.
- 2 H. Umezawa, K. Maeda, T. Takeuchi, Y. Okami, *J. Antibiot.* **1966**, *19*, 200.
- 3 J. Stubbe, J. W. Kozarich, *Chem. Rev.* **1987**, *87*, 1107.
- 4 L. H. Einhorn, *Proc. Natl. Acad. Sci. U.S.A.* **2002**, *99*, 4592.
- 5 S. Sleijfer, *Chest* **2001**, *120*, 617.
- 6 S.-X. Huang, Z. Feng, L. Wang, U. Galm, E. Wendt-Pienkowski, D. Yang, M. Tao, J. M. Coughlin, Y. Duan, B. Shen, *J. Am. Chem. Soc.* **2012**, *134*, 13501.
- 7 A. Kittaka, Y. Sugano, M. Otsuka, M. Ohno, Y. Sugiura, H. Umezawa, *Tetrahedron Lett.* **1986**, *27*, 3631.
- 8 Y. Sugano, A. Kittaka, M. Otsuka, M. Ohno, Y. Sugiura, H. Umezawa, *Tetrahedron Lett.* **1986**, *27*, 3635.
- 9 R. J. Guajardo, F. Chavez, E. T. Farinas, P. K. Mascharak, *J. Am. Chem. Soc.* **1995**, *117*, 3883.
- 10 R. J. Guajardo, S. E. Hudson, S. J. Brown, P. K. Mascharak, *J. Am. Chem. Soc.* **1993**, *115*, 7971.
- 11 R. M. Burger, J. Peisach, S. B. Horwitz, *J. Biol. Chem.* **1981**, *256*, 11636.
- 12 Q. Li, M. G. P. van der Wijst, H. G. Kazemier, M. G. Rots, G. Roelfes, *ACS Chem. Biol.* **2014**, *9*, 1044.
- 13 Q. Li, T. A. van den Berg, B. L. Feringa, G. Roelfes, *Dalton Trans.* **2010**, *39*, 8012.
- 14 Q. Jiang, N. Xiao, P. Shi, Y. Zhu, Z. Guo, *Coord. Chem. Rev.* **2007**, *251*, 1951.
- 15 E. L.-M. Wong, G.-S. Fang, C.-M. Che, N. Zhu, *Chem. Commun.* **2005**, 4578.
- 16 Y. Hitomi, K. Arakawa, T. Funabiki, M. Kodera, *Angew. Chem., Int. Ed.* **2012**, *51*, 3448.
- 17 Y. Hitomi, K. Arakawa, M. Kodera, *Chem.—Eur. J.* **2013**, *19*, 14697.
- 18 Y. Hitomi, K. Arakawa, M. Kodera, *Chem. Commun.* **2014**, *50*, 7485.
- 19 M. K. Coggins, M.-T. Zhang, A. K. Vannucci, C. J. Dares, T. J. Meyer, *J. Am. Chem. Soc.* **2014**, *136*, 5531.
- 20 S. L. Scott, W. J. Chen, A. Bakac, J. H. Espenson, *J. Phys. Chem.* **1993**, *97*, 6710.
- 21 Y. Hitomi, K. Hiramatsu, K. Arakawa, T. Takeyasu, M. Hata, M. Kodera, *Dalton Trans.* **2013**, *42*, 12878.
- 22 A. Decker, M. S. Chow, J. N. Kemsley, N. Lehnert, E. I. Solomon, *J. Am. Chem. Soc.* **2006**, *128*, 4719.



Cite this: *Chem. Commun.*, 2015, 51, 9539

Received 28th March 2015,
Accepted 7th May 2015

DOI: 10.1039/c5cc02566d

www.rsc.org/chemcomm

Uncaging a catalytic hydrogen peroxide generator through the photo-induced release of nitric oxide from a $\{\text{MnNO}\}^6$ complex†

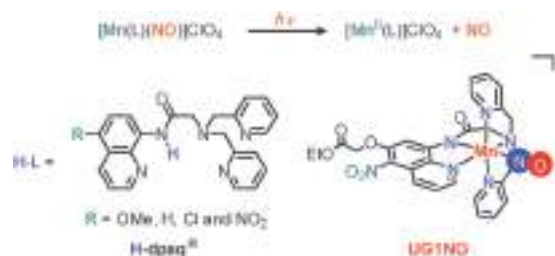
Yuji Iwamoto, Masahito Kodera and Yutaka Hitomi*

The photo-initiated cytotoxicity of a newly developed manganese nitrosyl $\{\text{MnNO}\}^6$ complex (UG1NO) to HeLa cells is described. The complex was found to be strongly cytotoxic after being exposed to light with a wavelength of 650 nm. Cell death was caused by a manganese(II) complex, UG1, generated from UG1NO through the photo-dissociation of NO, rather than by NO directly. Mechanistic studies revealed that UG1 consumes O_2 only in the presence of a reducing agent to catalytically produce H_2O_2 .

The development of photo-caged generators of small molecules has been intense in the past decade because these compounds can allow the spatially and temporally controlled release of biologically relevant small molecules, such as CO, H_2O_2 , H_2S , NO and peroxynitrite (ONOO^-), by the application of light.¹ For instance, Chang and co-workers recently developed an interesting compound, CPG1, which can be photo-activated to produce H_2O_2 on demand, and they demonstrated that CPG1 can be used to optically regulate cofilin-actin rod formation.² Xian and co-workers described a unique caged compound, WSP-1, which releases H_2S in cultured cells when stimulated by light.³ CPG1 and WSP-1 both contain one or more *ortho*-nitrobenzyl groups, and this group acts as a photo-cleavable protecting group.⁴ Nakagawa and co-workers have developed other unique photo-caged compounds without *ortho*-nitrobenzyl groups for releasing NO and ONOO^- .⁵ Transition metal NO or CO complexes that release NO or CO when the ligands photo-dissociate have also been developed.⁶ However, no photo-caged catalytic generators of the small molecules mentioned above have been developed. Here, we describe a manganese-nitrosyl $\{\text{MnNO}\}^6$ complex that acts as a photo-caged catalytic generator of H_2O_2 . When irradiated, the complex was found to induce changes in cell morphology and cell death efficiently. We discovered the compound as part

of our development of intracellular manganese–NO complexes for the photo-induced release of NO.

We recently prepared manganese nitrosyl $\{\text{MnNO}\}^6$ complexes with the general formula $[\text{Mn}(\text{dpaq}^{\text{R}})(\text{NO})]\text{ClO}_4$, where dpaq^{R} denotes a series of pentadentate mono-carboxylamido ligands, 2-[*N,N*-bis(pyridin-2-ylmethyl)]-amino-*N'*-quinolin-8-yl-acetyl-amido, with R = OMe, H, Cl or NO_2 at the 5-position of the quinoline moiety. We found that NO was released from this series of $\{\text{MnNO}\}^6$ complexes when they were irradiated with light (Scheme 1).⁷ The R = NO_2 derivative released NO more efficiently than the other derivatives when irradiated with red light with a wavelength of 650 nm. Encouraged by this result, we developed a strategy for achieving the light-induced release of NO from $\{\text{MnNO}\}^6$ complexes under the conditions in which cells are cultured. We synthesized a new $\{\text{MnNO}\}^6$ derivative with an ethyl ester moiety with the aim of increasing the intracellular retention of the complex (the ethyl ester group being expected to become hydrolysed by esterase inside a cell, giving the corresponding acid derivative, which would not be able to permeate through the cell membrane). The newly synthesized complex $[\text{Mn}(\text{L})(\text{NO})]\text{ClO}_4$ (UG1NO, shown on the right in Scheme 1), in which L is the carboxylamide-deprotonated form of ethyl $\{[8-\{[bis(pyridin-2-ylmethyl)amino]acetyl\}amino]-5\text{-nitroquinolin-6-yl}\}oxy\}acetate$, was synthesized as shown in Scheme S1 (ESI†). UG1NO absorbed light in the Vis-NIR region and responded to irradiation with red light in a similar way to $[\text{Mn}(\text{dpaq}^{\text{NO}_2})(\text{NO})]\text{ClO}_4$, despite the presence of an additional electron-donating



Scheme 1 Photo-induced release of NO from $\{\text{MnNO}\}^6$ complexes with pentadentate mono-carboxylamido ligands.

Department of Molecular Chemistry and Biochemistry, Faculty of Science and Engineering, Doshisha University, 1-3 Miyakodani, Tatara, 610-0321 Kyotanabe, Japan. E-mail: yhitomi@mail.doshisha.ac.jp

† Electronic supplementary information (ESI) available: Synthesis and characterization of UG1 and UG1NO. Fig. S1 to S7 and Scheme S1. See DOI: 10.1039/c5cc02566d

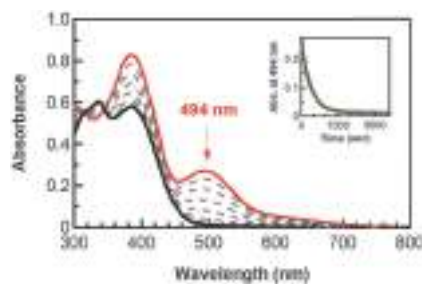


Fig. 1 Absorption spectral changes that occurred when UG1NO dissolved in a MES buffer (containing 5% DMSO and at pH 7.2) at 20 °C was irradiated with light with a wavelength of 650 nm. The arrow indicates where the band intensities decreased as the reaction proceeded. The inset shows the profile over time for absorbance at 494 nm.

1-(ethoxycarbonyloxy)ethyl ester at the 6-position of quinoline. As expected, UG1NO in a buffer solution at pH 7.2 was stable in the dark but was quickly converted into the corresponding Mn(II) complex (UG1) through the dissociation of NO when it was irradiated with light with a wavelength of 650 nm (Fig. 1). The same behaviour was observed in cell culture media containing serum. The quantum yield of NO release from UG1NO by light irradiation at 650 nm was determined to be 0.74 ± 0.01 , which is close to that reported for $[\text{Mn}(\text{dpaq}^{\text{NO}_2})(\text{NO})]\text{ClO}_4$.⁷

The ability of UG1NO to deliver NO to living cells was then investigated. Before the experiments were performed, we assessed the anti-proliferative effects of UG1NO on HeLa cells in the dark. HeLa cells were incubated with different concentrations of UG1NO for 24 h, and the cell viability was evaluated using the 3-(4,5-dimethylthiazol-2-yl)-2,5-diphenyltetrazolium bromide (MTT) assay. IC_{50} (the concentration required to induce 50% inhibition) was determined from the dose–response curves (Fig. S1, ESI†). We found that UG1NO was only weakly cytotoxic with an IC_{50} of more than 100 μM in the dark (Table 1). Therefore, HeLa was incubated with both UG1NO (10 μM) and an intracellular NO-selective fluorescent probe DAF2-DA⁸ (10 μM) for 30 min to visualize the NO released by UG1NO when light was applied. Green fluorescence emitted by the product of the reaction of DAF2 with NO was observed only when light was applied (Fig. 2A). These results

Table 1 IC_{50} values for the compounds that were tested on HeLa cells after 24 h of exposure

Compound	Conditions	IC_{50} ^a (μM)
UG1NO	Dark	> 100
UG1NO ^b	White light for 10 s ^{f,h}	17 ± 1
UG1NO ^b	650 nm light for 1 h ^{g,h}	33 ± 3
NOC-7 ^c	Dark	> 100
SIN-1 ^d	Dark	> 100
UG1	Dark	12.4 ± 0.2
UG1 ^e	Dark	> 100
Cisplatin	Dark	19 ± 3

^a The errors are the standard deviations. ^b The systems were exposed to light and incubated for 24 h. ^c NOC-7 = 3-(2-hydroxy-1-methyl-2-nitrosohydrazino)-N-methyl-1-propanamine, an NO donor. ^d SIN-1 = 3-(4-morpholinyl)sydnonimine, hydrochloride, an ONOO⁻ donor. ^e Co-incubated with esterase. ^f 385 to 740 nm with 0.1 mW cm⁻². ^g 5 $\mu\text{W cm}^{-2}$ through a band path filter (FWHM = 6 nm). ^h Light induced no cell death in the absence of the Mn complex.

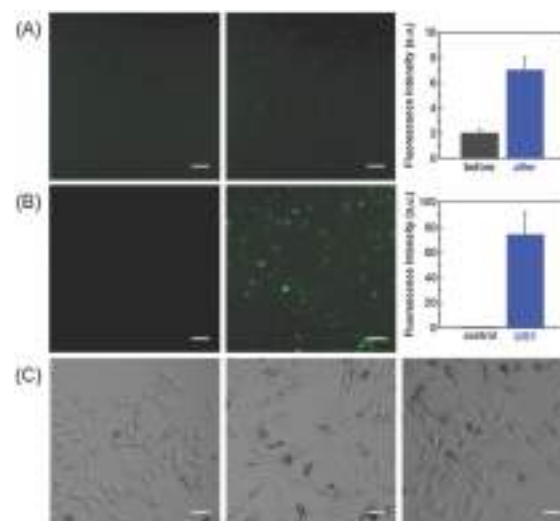


Fig. 2 (A) Fluorescence images of cells incubated with DAF-2-DA and UG1NO before (left) and after (middle) being exposed to light with a wavelength of 650 nm for 30 min. Each scale bar indicates 50 μm . The relative fluorescence intensities are shown on the right. (B) Fluorescence images of cells exposed to PF1 (left) and to PF1 and UG1 (middle) after being exposed to light. Each scale bar indicates 50 μm . The relative fluorescence intensities are shown on the right. (C) Bright field images of cells incubated with 10 μM UG1 (middle) and 100 μM H₂O₂ (right). The control is shown in the left.

clearly indicate that UG1NO is a photo-activated NO-releasing molecule that can deliver NO to the inside of cells. It is likely that the resulting Mn(II)L complex should have a weakly coordinated water molecule in place of NO in aqueous media.

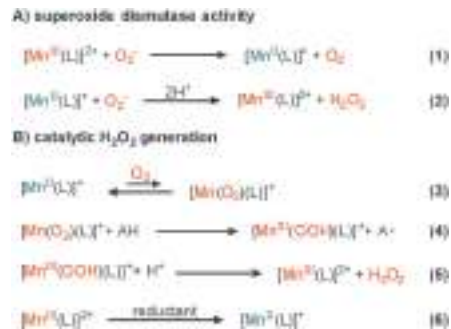
We next determined whether the photo-triggered dissociation of NO from UG1NO could induce the death of HeLa cells. HeLa cells were incubated with different concentrations of UG1NO for 24 h before being exposed to white light for 10 s or to light with a wavelength of 650 nm for 1 h, after which the cell viability was determined using the MTT assay. We found that UG1NO was strongly cytotoxic to HeLa cells, the IC_{50} values being 17 ± 1 and 33 ± 3 μM after the white and 650 nm light treatments, respectively. The low IC_{50} values suggested that the release of NO was not the main cause of cell death, because NO is rather weakly cytotoxic (Okuno and co-workers reported that 500 μM NO was required to induce cell death in HeLa cells, when *S*-nitroso-*N*-acetyl-DL-penicillamine was used as a thermally induced generator of NO).⁹ Even 500 μM of a thermally induced NO generator, NOC-7, did not induce cell death in HeLa cells in the tests we have performed. ONOO⁻ is another potential toxic agent, as it can be formed quickly by the reaction of NO with a superoxide anion radical (O₂^{•-}). However, the IC_{50} of SIN-1, a thermally induced ONOO⁻ donor, was above 100 μM . Taking these results together we concluded that NO and ONOO⁻ were not the main causes of the photo-induced cell death that was observed even though NO was released from UG1NO exposed to light.

We later found that the Mn(II)L complex UG1, which lacks an NO ligand, had a strong anti-proliferative effect on HeLa cells (the IC_{50} was 12.4 ± 0.2 μM after 24 h of incubation). The IC_{50} was comparable to that found for UG1NO after white light was

applied for 10 s or after light with a wavelength of 650 nm was applied for 1 h (Table 1). Notably, UG1 was found to be even more cytotoxic than cisplatin, which is an anti-cancer drug ($IC_{50} = 19 \pm 3 \mu\text{M}$).¹⁰ It should be noted that the ester functionality of UG1 was important to the ability of UG1 to cause cell death. The acidic form of UG1 was found to be not cytotoxic ($IC_{50} > 100 \mu\text{M}$), and the structurally similar manganese(II) complexes without ester functionality (*i.e.*, $[\text{Mn}^{\text{II}}(\text{dpaq}^{\text{R}})]\text{ClO}_4$, R = OMe, H, Cl or NO_2) shown in Scheme 1 were also found to be only moderately cytotoxic (with IC_{50} values between 30 and 70 μM , data not shown). We speculated that UG1 may cause cell death *via* oxidative stress. Therefore, we next visualized the production of reactive oxygen species using a H_2O_2 -specific fluorescent probe, PF1,¹¹ and a cell-membrane permeable fluorescent reactive-oxygen-species probe, 2,7-dichlorodihydrofluorescein diacetate (DCFH-DA). We observed green fluorescence inside cells incubated with UG1 and PF1 or DCFH-DA (Fig. 2B and Fig. S2, ESI†). These results suggest that UG1 can produce H_2O_2 inside a cell.

Interestingly, HeLa cells became elongated when incubated with 10 μM UG1, as shown in Fig. 2C (middle). A similar morphological change was observed when HeLa cells were treated with 100 μM H_2O_2 (Fig. 2C, right). HeLa cells have been found to become elongated after exposure to isophthalate derivatives¹² and as a consequence of knock-down by prohibitins.¹³ Isophthalate derivatives affect the reorganization of the cytoskeleton by binding to the C1 domain of protein kinase C. However, prohibitin plays an important role in mitochondrial functions, and its overexpression protects against oxidative stress.¹⁴ Bokoch and co-workers found that exogenously generated H_2O_2 can modulate cytoskeleton reorganization *via* the activation of the actin depolymerization factor cofilin.¹⁵ The similarities in the morphological changes caused by UG1 and H_2O_2 suggested that UG1 can produce H_2O_2 inside a cell. We speculated that H_2O_2 may be catalytically produced through the reductive dioxygen activation by UG1, resulting in the consumption of biological reducing agents inside the cell.

It has been found by several research groups that redox-active metal complexes, including water-soluble cationic manganese(III) porphyrins¹⁶ and iron(III) porphyrins,¹⁷ can cause enough oxidative stress to induce cell death through the formation of $\text{O}_2^{\bullet-}$ and H_2O_2 . Batinic-Haberle and co-workers found that a series of water-soluble cationic manganese(III) porphyrin complexes (MnPs) showed anti-cancer activities in several cancer models, and to achieve this the complexes acted as pro-oxidants (even though the complexes were originally developed for use as superoxide dismutase (SOD) mimics). Batinic-Haberle and co-workers showed that MnPs can promote the aerobic oxidation of ascorbic acid, producing $\text{O}_2^{\bullet-}$ and H_2O_2 , and that H_2O_2 is a major cytotoxic species, formed through the disproportionation of $\text{O}_2^{\bullet-}$ and through the reaction between $\text{O}_2^{\bullet-}$ and Mn(II) porphyrins. The latter reaction is part of the SOD cycle catalysed by MnPs. The SOD activity of SOD mimics strongly depends on the redox potential of SOD mimics, as the SOD cycle is made up of the reduction and oxidation reactions of $\text{O}_2^{\bullet-}$ (Scheme 2A). SOD mimics based on MnPs have redox potentials in the range -50 to 350 mV *vs.* NHE, which are between the reduction potential



Scheme 2 (A) Plausible reactions during superoxide disproportionation catalysed by UG1. (B) Proposed reaction mechanism for the generation of H_2O_2 catalysed by UG1. AH denotes a reductant.

of $\text{O}_2^{\bullet-}$ (891 mV *vs.* NHE; $\text{O}_2^{\bullet-}/\text{H}_2\text{O}_2$) and the oxidation potential of $\text{O}_2^{\bullet-}$ (-160 mV *vs.* NHE; $\text{O}_2/\text{O}_2^{\bullet-}$).¹⁸ We therefore measured the cyclic voltammogram of UG1 in 5% DMSO in H_2O (Fig. S3, ESI†). UG1 was found to have a Mn(II)/Mn(III) redox potential of 732 mV *vs.* NHE. As suggested from the redox potential, UG1 showed SOD activity *in vitro*, although the SOD activity of UG1 was rather lower than the SOD activities that were found for the MnPs mentioned above ($\log k_2 = 6.2 \pm 0.2 \text{ M}^{-1} \text{ s}^{-1}$; Fig. S4, ESI†). This SOD activity of UG1 suggests that, in the Mn(II) state, it can produce H_2O_2 by reacting with $\text{O}_2^{\bullet-}$ (eqn (2) in Scheme 2). However, the positive reduction potential of UG1 suggested that the Mn(II) centre of UG1 cannot reductively activate dioxygen to produce $\text{O}_2^{\bullet-}$. As expected, UG1 stably retained the Mn(II) state in aqueous solution and did not consume dioxygen (Fig. 3A). Jackson and co-workers found that the Mn(II) centre of a structurally related manganese(II) complex, Mn(dpaq^H), was aerobically oxidized to the corresponding Mn(III)OH species in acetonitrile.¹⁹ UG1 has an additional nitro-group at the 5-position of the quinoline moiety, which would make its redox potential more negative than the redox potential of Mn(dpaq^H), and therefore UG1 cannot react with dioxygen. However, we observed that UG1 catalytically consumed dioxygen in the presence of ascorbic acid (Fig. 3A), as Batinic-Haberle and co-workers found for SOD mimics based on MnPs.^{16g}

We also found that UG1 facilitated the oxidation of glutathione (GSH) to give GSSG under aerobic conditions, and this was monitored using the glutathione reductase/NADPH coupled method (Fig. S5, ESI†). We confirmed that UG1 could produce H_2O_2 only in the presence of the biological reducing agents GSH (-0.26 V *vs.* NHE)²⁰ and ascorbic acid (0.06 V *vs.* NHE)²¹ (Fig. S6, ESI† and Fig. 3B) using a H_2O_2 -specific fluorescent probe, PF1.¹¹ These results indicate that UG1 can reductively activate dioxygen at the manganese centre, with an assistance from biological reducing agents, to produce H_2O_2 .

The formation of H_2O_2 , catalysed by UG1 in the presence of ascorbic acid, was not altered by adding SOD (Fig. 3B), excluding the possibility that some free $\text{O}_2^{\bullet-}$ may be produced by the reaction of UG1 (in the Mn(II) state) with dioxygen. It is more likely that the dioxygen adduct of UG1 in the Mn(II) state will oxidize a biological reductant to yield the corresponding Mn(III)OOH, which would afford H_2O_2 and the Mn(III) complex (eqn (3)–(5) in Scheme 2).

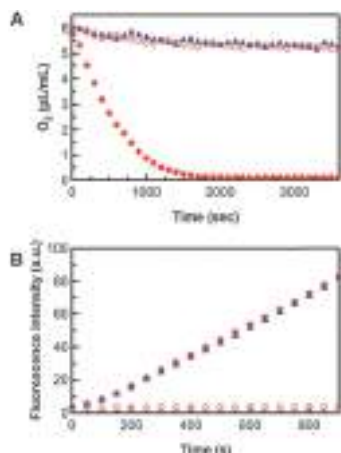


Fig. 3 (A) Oxygen consumption by UG1 (100 μM) in an air-saturated 20 mM phosphate buffer (pH 7.5) at 37 $^{\circ}\text{C}$. The open and filled red circles are data collected in the absence and the presence of 1 mM ascorbate, respectively. The blue filled triangles are data for the control (without UG1 present). (B) The generation of H_2O_2 by UG1 (25 μM) in an air-saturated 20 mM phosphate buffer (pH 7.5) at 37 $^{\circ}\text{C}$. The open and filled red circles are data collected in the absence and the presence of 1 mM ascorbate, respectively. H_2O_2 was detected using PF1 (10 μM). The blue filled triangles are data obtained in the presence of superoxide dismutase (100 Units per mL).

The dioxygen adduct, manganese(III)-superoxo complexes, would have enough reactivity toward hydrogen atom abstraction from a biological reductant.²² A similar reaction has been reported in which an air-stable mononuclear nonheme Fe(II) complex produced the corresponding Fe(III)OOH species in the presence of an NADH analogue.²³ These *in vitro* results suggest that H_2O_2 could be catalytically produced by UG1 inside a cell, although small amounts of H_2O_2 may be produced by the reaction between UG1 and $\text{O}_2^{\bullet-}$ generated endogenously through cellular processes, such as the mitochondrial respiratory chain (eqn (2) in Scheme 2).

In summary, we have found that a newly developed manganese nitrosyl complex releases NO when treated with light, and is also a photo-caged catalytic generator of H_2O_2 when a reducing agent is present. Many photo-caged molecules based on photo-labile protection groups, such as the *ortho*-nitrobenzyl group, have been prepared.²⁴ Our results demonstrate that ligand photo-dissociation is a useful method for achieving the photo-activation of the catalytic activity of metal complexes. We are now investigating the mechanism involved in the activation of dioxygen to produce H_2O_2 by UG1 in detail.

This work was partly supported by JSPS KAKENHI Grant Number 24550197 (to Y.H.).

Notes and references

1 C. Brieke, F. Rohrbach, A. Gottschalk, G. Mayer and A. Heckel, *Angew. Chem., Int. Ed.*, 2012, **51**, 8446–8476.

- 2 E. W. Miller, N. Taulet, C. S. Onak, E. J. New, J. K. Lanselle, G. S. Smelick and C. J. Chang, *J. Am. Chem. Soc.*, 2010, **132**, 17071–17073.
- 3 N. O. Devarie-Baez, P. E. Bagdon, B. Peng, Y. Zhao, C. M. Park and M. Xian, *Org. Lett.*, 2013, **15**, 2786–2789.
- 4 J. A. Barltrop, P. J. Plant and P. Schofield, *Chem. Commun.*, 1966, 822–823.
- 5 (a) N. Ieda, H. Nakagawa, T. Horinouchi, T. Peng, D. Yang, H. Tsumoto, T. Suzuki, K. Fukuhara and N. Miyata, *Chem. Commun.*, 2011, **47**, 6449–6451; (b) N. Ieda, H. Nakagawa, T. Peng, D. Yang, T. Suzuki and N. Miyata, *J. Am. Chem. Soc.*, 2012, **134**, 2563–2568; (c) N. Ieda, Y. Hotta, N. Miyata, K. Kimura and H. Nakagawa, *J. Am. Chem. Soc.*, 2014, **136**, 7085–7091.
- 6 (a) A. A. Eroy-Reveles, Y. Leung, C. M. Beavers, M. M. Olmstead and P. K. Mascharak, *J. Am. Chem. Soc.*, 2008, **130**, 4447–4458; (b) A. D. Ostrowski and P. C. Ford, *Dalton Trans.*, 2009, 10660–10669; (c) N. L. Fry and P. K. Mascharak, *Acc. Chem. Res.*, 2011, **44**, 289–298; (d) R. D. Rimmer, A. E. Pierri and P. C. Ford, *Coord. Chem. Rev.*, 2012, **256**, 1509–1519.
- 7 Y. Hitomi, Y. Iwamoto and M. Kodera, *Dalton Trans.*, 2014, **43**, 2161–2167.
- 8 H. Kojima, N. Nakatsubo, K. Kikuchi, Y. Urano, T. Higuchi, J. Tanaka, Y. Kudo and T. Nagano, *NeuroReport*, 1998, **9**, 3345–3348.
- 9 S. Okuno, S. Shimizu, T. Ito, M. Nomura, E. Hamada, Y. Tsujimoto and H. Matsuda, *J. Biol. Chem.*, 1998, **273**, 34272–34277.
- 10 UG1 showed lower cytotoxicity under hypoxic conditions (Fig. S7, ESI†). Thus, the present approach may not be applied for treatment of hypoxic tumours.
- 11 M. C. Chang, A. Pralle, E. Y. Isacoff and C. J. Chang, *J. Am. Chem. Soc.*, 2004, **126**, 15392–15393.
- 12 V. Talman, R. K. Tuominen, G. Boije af Gennas, J. Yli-Kauhaluoma and E. Ekokoski, *PLoS One*, 2011, **6**, e20053.
- 13 C. Sievers, G. Billig, K. Gottschalk and T. Rudel, *PLoS One*, 2010, **5**, e12735.
- 14 A. L. Theiss, R. D. Idell, S. Srinivasan, J. M. Klapproth, D. P. Jones, D. Merlin and S. V. Sitaraman, *FASEB J.*, 2007, **21**, 197–206.
- 15 J. S. Kim, T. Y. Huang and G. M. Bokoch, *Mol. Biol. Cell*, 2009, **20**, 2650–2660.
- 16 (a) P. R. Gardner, D. D. H. Nguyen and C. W. White, *Arch. Biochem. Biophys.*, 1996, **325**, 20–28; (b) W. Zhong, T. Yan, M. M. Webber and T. D. Oberley, *Antioxid. Redox Signaling*, 2004, **6**, 513–522; (c) J. Tian, D. M. Peehl and S. J. Knox, *Cancer Biother. Radiopharm.*, 2010, **25**, 439–448; (d) X. Ye, D. Fels, A. Tovmasyan, K. M. Aird, C. Dedeugd, J. L. Allensworth, I. Kos, W. Park, I. Spasojevic, G. R. Devi, M. W. Dewhirst, K. W. Leong and I. Batinic-Haberle, *Free Radical Res.*, 2011, **45**, 1289306; (e) M. Rawal, S. R. Schroeder, B. A. Wagner, C. M. Cushing, J. L. Welsh, A. M. Button, J. Du, Z. A. Sibenaller, G. R. Buettner and J. J. Cullen, *Cancer Res.*, 2013, **73**, 5232–5241; (f) I. Batinic-Haberle, A. Tovmasyan, E. R. Roberts, Z. Vujaskovic, K. W. Leong and I. Spasojevic, *Antioxid. Redox Signaling*, 2014, **20**, 2372415; (g) M. K. Evans, A. Tovmasyan, I. Batinic-Haberle and G. R. Devi, *Free Radical Biol. Med.*, 2014, **68**, 302–314.
- 17 (a) T. Ohse, S. Nagaoka, Y. Arakawa, H. Kawakami and K. Nakamura, *J. Inorg. Biochem.*, 2001, **85**, 201–208; (b) N. Kasugai, T. Murase, T. Ohse, S. Nagaoka, H. Kawakami and S. Kubota, *J. Inorg. Biochem.*, 2002, **91**, 349–355.
- 18 I. Batinic-Haberle, J. S. Reboucas and I. Spasojevic, *Antioxid. Redox Signaling*, 2010, **13**, 877–918.
- 19 G. B. Wijeratne, B. Corzine, V. W. Day and T. A. Jackson, *Inorg. Chem.*, 2014, **53**, 7622–7634.
- 20 K. K. Millis, K. H. Weaver and D. L. Rabenstein, *J. Org. Chem.*, 1993, **58**, 4144–4146.
- 21 *CRC Handbook of Biochemistry and Molecular Biology*, ed. G. D. Fasman, CRC Press, Cleveland, 1976.
- 22 A. Ansari, P. Jayapal and G. Rajaraman, *Angew. Chem., Int. Ed.*, 2015, **54**, 564–568.
- 23 S. Hong, Y. M. Lee, W. Shin, S. Fukuzumi and W. Nam, *J. Am. Chem. Soc.*, 2009, **131**, 13910–13911.
- 24 (a) H. Yu, J. Li, D. Wu, Z. Qiu and Y. Zhang, *Chem. Soc. Rev.*, 2010, **39**, 464–473; (b) C. Brieke, F. Rohrbach, A. Gottschalk, G. Mayer and A. Heckel, *Angew. Chem.*, 2012, **51**, 8446–8476.

Article

Curcumin Derivative GT863 Inhibits Amyloid-Beta Production via Inhibition of Protein N-Glycosylation

Yasuomi Urano ^{1,*}, Mina Takahachi ¹, Ryo Higashiura ¹, Hitomi Fujiwara ¹, Satoru Funamoto ¹, So Imai ², Eugene Futai ², Michiaki Okuda ³, Hachiro Sugimoto ^{1,3} and Noriko Noguchi ¹

¹ Department of Medical Life Systems, Faculty of Life and Medical Sciences, Doshisha University, 1–3 Miyakodani, Tatara, Kyotanabe, Kyoto 610 0394, Japan; ctuc2020@mail4.doshisha.ac.jp (M.T.); dmp2003@mail4.doshisha.ac.jp (R.H.); ko-sei11@mail.doshisha.ac.jp (H.F.); sfunamot@mail.doshisha.ac.jp (S.F.); hsugimot@mail.doshisha.ac.jp (H.S.); nnoguchi@mail.doshisha.ac.jp (N.N.)

² Department of Molecular and Cell Biology, Graduate School of Agricultural Science, Tohoku University, 468-1 Aramaki-zaaoba, Aobaku, Sendai, Miyagi 980-0845, Japan; kuku.sou99@gmail.com (S.I.); eugene.futai.e1@tohoku.ac.jp (E.F.)

³ Green Tech Co., Ltd., 1–7–7 Yaesu, Chuo-ku, Tokyo 103-0028, Japan; m.okuda.pharma8@gmail.com

* Correspondence: yurano@mail.doshisha.ac.jp; Tel.: +81-774-65-6260

Received: 27 December 2019; Accepted: 31 January 2020; Published: 3 February 2020



Abstract: Amyloid- β (A β) peptides play a crucial role in the pathogenesis of Alzheimer's disease (AD). A β production, aggregation, and clearance are thought to be important therapeutic targets for AD. Curcumin has been known to have an anti-amyloidogenic effect on AD. In the present study, we performed screening analysis using a curcumin derivative library with the aim of finding derivatives effective in suppressing A β production with improved bioavailability of curcumin using CHO cells that stably express human amyloid- β precursor protein and using human neuroblastoma SH-SY5Y cells. We found that the curcumin derivative GT863/PE859, which has been shown to have an inhibitory effect on A β and tau aggregation *in vivo*, was more effective than curcumin itself in reducing A β secretion. We further found that GT863 inhibited neither β - nor γ -secretase activity, but did suppress γ -secretase-mediated cleavage in a substrate-dependent manner. We further found that GT863 suppressed N-linked glycosylation, including that of the γ -secretase subunit nicastrin. We also found that mannosidase inhibitors that block the mannose trimming step of N-glycosylation suppressed A β production in a similar fashion, as was observed as a result of treatment with GT863. Collectively, these results suggest that GT863 downregulates N-glycosylation, resulting in suppression of A β production without affecting secretase activity.

Keywords: Alzheimer's disease; amyloid- β peptides; curcumin derivatives; glycosylation

1. Introduction

Alzheimer's disease (AD) is characterized by the accumulation of amyloid- β (A β) peptides in senile plaques and by intracellular accumulation of hyperphosphorylated tau [1]. An increasing body of evidence indicates that A β oligomers are neurotoxic, and trigger synapse dysfunction, memory loss, and cognitive deficits [2]. In the amyloidogenic pathway, A β is generated from transmembrane amyloid- β precursor protein (APP) by sequential proteolytic cleavage steps involving β -secretase and the γ -secretase complex [2]. On the other hand, β -secretase consists of a single protein—that is, β -site APP cleaving enzyme 1 (BACE1); γ -secretase is a multimeric complex consisting of four integral membrane proteins—these being presenilin 1 (PS1) or PS2, nicastrin, anterior pharynx-defective 1 (APH-1), and PS enhancer 2 (PEN-2). In an alternative pathway, APP is cleaved by α - and γ -secretases to release the nonamyloidogenic p3 peptide.

Major challenges in AD drug development include achievement of reduction of A β production through inhibition of β -secretase or γ -secretase, or achievement of increased A β clearance. However, many clinical trials have failed to satisfactorily achieve such challenges due either to lack of efficacy or adverse side effects [3,4]. It has also been suggested that clinical trials should start before appearance of AD symptoms. With regard to the adverse side effects that have been observed, it has been suggested that these may occur as a result of inhibition of secretase, as β - and γ -secretases cleave not only APP but also a number of other substrates [3,4]. For example, γ -secretase has been reported to cleave Notch, cadherins, and CD44. It would therefore be desirable to establish methods for inhibiting A β production that do not affect secretase activity.

Curcumin is a yellow-orange natural polyphenol compound which is found in abundance in the rhizome of the plant *Curcuma longa* (turmeric). Several lines of evidence suggest that curcumin has therapeutic effects on AD [5–9]. For example, curcumin can inhibit A β oligomer formation and aggregation, and can also inhibit A β production [5–7]. Several studies have further shown that curcumin can reduce A β deposition in the brain and significantly improve cognitive functions in experimental AD models [8,9]. On the other hand, there are a number of clinical trials that report no significant differences in cognitive function in placebo versus intervention groups [10–12]. It should be noted that the low solubility in water and poor bioavailability of curcumin have limited its use in clinical trials and in therapeutic applications [6,12]. We were therefore interested in studying whether derivatives of curcumin could be found which might be more effective in treatment of AD than curcumin itself.

Although curcumin derivatives have been the focus of studies seeking to develop inhibitors of A β and tau aggregation, and have been the focus of studies seeking to develop imaging probes for detection of A β and tau fibrils, there has been very little investigation into whether curcumin derivatives might serve as inhibitors of A β production [13–19]. We previously developed a series of curcumin derivatives and evaluated their inhibitory effects on A β production. Of these, we found that CU6/CNB-001 was more effective than curcumin itself in reducing A β secretion [13]. We further found that CU6/CNB-001 downregulates intracellular APP trafficking, resulting in suppression of A β production in a manner that is independent of secretase activity. Valera et al. has also reported that CU6/CNB-001 promotes A β clearance and improves memory in animal models of AD [14]. Although these results might suggest that CU6/CNB-001 should have beneficial effect on AD pathology, we observed that CU6/CNB-001 had little inhibitory effect on the production of A β 42, which is much more neurotoxic than A β 40 [13].

In the present study, we conducted in vitro screening in an attempt to identify curcumin derivatives that might inhibit A β production more effectively than either curcumin or CU6/CNB-001. As a result of screening of curcumin derivatives selected from a library on the basis of similarity in chemical structure to CU6/CNB-001, we found that GT863 reduced production of both A β 40 and A β 42. Interestingly, GT863 (formerly referred to as PE859) has been reported to inhibit A β and tau aggregation, and to ameliorate cognitive dysfunction, in AD mice models [15–17]. Although it has thus been shown that GT863 has beneficial effect in terms of suppressing A β aggregation, we were aware of no evidence indicating whether GT863 might suppress A β production. Upon finding in the present study that GT863 does suppress A β production, we further endeavored to examine the mechanism by which this occurs, demonstrating in the present study that GT863 inhibited A β production without affecting β - or γ -secretase activity. We further found that GT863 suppressed protein *N*-glycosylation, including that of γ -secretase subunit nicastrin, and observed that A β production was inhibited by mannosidase inhibitors of the type that cause abnormal *N*-glycan processing. We believe that these results provide insight into how GT863 and mannosidase inhibitors might be used to beneficial effect in the context of AD pathologies.

2. Materials and Methods

2.1. Materials

Curcumin was obtained from Sigma-Aldrich (St. Louis, MO, USA). CU6, GT832, GT855, GT857, GT863, GT934, and GT935 were kindly provided by Green Tech Co., Ltd. (Tokyo, Japan). Dulbecco's modified Eagle's medium/nutrient mixture Ham's F-12 (DMEM/F-12) and DMEM were from Thermo Fisher Scientific (Waltham, MA, USA). Fetal bovine serum (FBS) was from Sigma-Aldrich. Cell Counting Kit-8 was from Dojindo (Kumamoto, Japan). The following antibodies were from commercial sources: APP (6E10), Covance (Princeton, NJ, USA); APP (22C11), Millipore (Billerica, MA, USA); APP (A8717), nicastrin and β -actin, Sigma-Aldrich; N-cadherin, BD Biosciences (San Jose, CA, USA); ribophorin-1 (C-15), Santa Cruz (Santa Cruz, CA, USA); A β (82E1) and BACE1, IBL (Gunma, Japan); Notch intracellular domain (NICD, D3B8); myc (9B11), Cell Signaling (Danvers, MA, USA); and low-density lipoprotein (LDL) receptor-related protein 1 (LRP1), Abcam (Cambridge, United Kingdom). All other chemicals, of analytical grade, were from Sigma-Aldrich or Wako (Osaka, Japan).

2.2. Cell Lines and Cell Culture

Chinese hamster ovary (CHO) cells that stably expressed human wild-type APP751 (7WD10, CHO-APP) [20] were maintained in DMEM supplemented with 10% heat-inactivated FBS, antibiotics (100 U/mL penicillin, 100 μ g/mL streptomycin; Thermo Fisher Scientific), and 250 μ g/mL G418 (Nacalai Tesque, Kyoto, Japan). For CHO-APP cells that stably expressed mouse Notch1 Δ E (CHO-APP/Notch Δ E) [21], 500 μ g/mL hygromycin (Wako) was added to the above culture medium. SH-SY5Y human neuroblastoma cells (European Collection of Cell Cultures, Salisbury, United Kingdom) were maintained in DMEM/F-12 with 10% FBS and penicillin/streptomycin. Cells were grown at 37 °C in an atmosphere of 95% air and 5% CO₂.

2.3. Cell Treatment

Curcumin or curcumin derivative was dissolved in dimethyl sulfoxide (DMSO; Wako) to obtain stock solution (10 mM), and this stock solution was then stored at −20 °C. Each of the various compounds tested were added as DMSO solution to medium. For 24 h treatment, cells were treated with 10 μ M curcumin, 10 μ M curcumin derivative, or 3 μ M GT863. For 48 h treatment, cells were treated with 0.5–3 μ M GT863 for 24 h, following which an additional 0.5–3 μ M GT863 was added without changing the medium until 48 h. To confirm γ -secretase activity, cells were treated with 1 μ M N-[N-(3,5-difluorophenacetyl)-L-alanyl]-S-phenylglycine t-butyl ester (DAPT) (Wako) for 24 h. To inhibit N-glycosylation, cells were treated with 1 μ g/ml kifunensine (Cayman Chemical Company, Ann Arbor, MI), 1 μ g/ml swainsonine (Cayman), or 1 mM N-butyl-deoxyojirimycin (NB-DNJ, Wako) for 48 h.

2.4. Assessment of Cell Viability

To assess cell viability, 2-(2-methoxy-4-nitrophenyl)-3-(4-nitrophenyl)-5-(2,4-disulphophenyl)-2H-tetrazolium (WST-8) assay was performed using a Cell Counting Kit-8, as described previously [22]. After 22 h of curcumin derivative treatment, medium was replaced with fresh medium because curcumin has a yellowish pigment, following which WST-8 was added, and this was allowed to stand for an additional 2 h before measurements were conducted. Fluorescence intensity was measured at a wavelength of 450 nm.

2.5. ELISA for A β

Conditioned media was collected and cleared of cell debris by centrifugation. Secreted A β was measured by standard sandwich ELISA using human amyloid β (1–40) (FL) and (1–42) assay kits (both from IBL).

2.6. Preparation of Cell Samples and Immunoblotting

Whole cell extract and conditioned media were prepared and analyzed by immunoblotting, as described previously [13,23]. Human APP expressed in CHO cells was detected by 6E10 antibody. Human A β was detected by 82E1 antibody. C83 and C99 were detected by A8717 antibody. Secreted APP—APPs α or total APPs—was detected by 6E10 or 22C11 antibody, respectively. Endoglycosidase H (Endo H) and peptide-N-glycosidase F (PNGase F) treatments were performed according to the manufacturer's instructions (New England Biolabs, Beverly, MA, USA).

2.7. In Vitro Secretase Assay

In vitro γ -secretase assay using 3-[(3-cholamidopropyl)dimethylammonio]-2-hydroxypropanesulfonate (CHAPSO)-soluble microsomal fraction of CHO cells or yeast was performed, as described previously [21,24,25]. Immunoblotting was used to detect A β and NICD. Activity of α - or β -secretase was measured using a commercial kit (ANASPEC, Fremont, CA, USA). To measure total cellular α - or β -secretase activity, an equal amount of cellular protein (40 μ g) was used.

2.8. Statistical Analysis

Data are reported as mean \pm SD of at least three independent experiments unless otherwise indicated. The statistical significance of the difference between determinations was calculated by analysis of variance using ANOVA, Tukey–Kramer test for multiple comparisons and Student's *t*-test for comparison of two means. The difference was considered significant when the *P*-value was <0.05.

3. Results

3.1. GT863 was Identified as a Potent Inhibitor of A β 40 and A β 42 Production in CHO-APP Cells.

To assess the effects of six kinds of curcumin derivatives (Supplementary Figure S1) on APP processing, we used CHO cells that stably expressed wild-type human APP751 (CHO-APP) [20]. We first performed a WST-8 assay to evaluate the effect of curcumin derivatives on cell viability, with the results showing that 0.5–20 μ M GT832, GT855, or GT857 did not affect cell viability, but that an amount greater than 15 μ M of GT934, 5 μ M of GT935, or 4 μ M of GT863 had a significant cytotoxic effect (Figure 1a). Because we had previously found that 10 μ M CU6 for 24 h treatment showed an inhibitory effect on A β production in CHO-APP cells [13], we evaluated the effect of curcumin derivatives on A β production at the noncytotoxic concentrations of 10 μ M for GT832, GT855, GT857, or GT934, and 3 μ M for GT863 or GT935. We performed immunoblot assay (data not shown) and ELISA for A β 40 or A β 42 (Figure 1b), the results showing that there was a substantial decrease in A β 40 and A β 42 secretion in cells treated with GT863 for 24 h, but no significant reduction of A β in cells treated with curcumin, CU6, or any of the other derivatives tested. We therefore conducted further experiments to explore the effect of GT863 on APP metabolism.

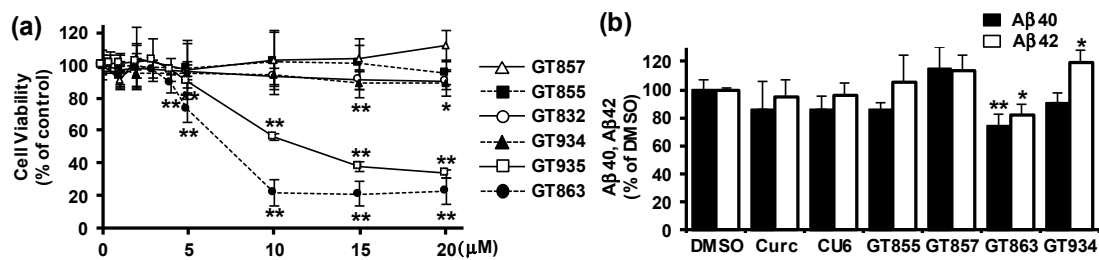


Figure 1. Screening of curcumin derivatives for effect on A β production in Chinese hamster ovary–amyloid- β precursor protein (CHO-APP) cells. (a) CHO-APP cells were treated with different concentrations of curcumin derivatives for 24 h. Cell viability was measured by 2-(2-methoxy-4-nitrophenyl)-3-(4-nitrophenyl)-5-(2,4-disulfophenyl)-2H-tetrazolium (WST-8) assay. $n = 3$. * $p < 0.05$, ** $p < 0.01$. (b) CHO-APP cells were treated with 10 μ M curcumin, CU6, GT855, GT857, or GT934, or with 3 μ M GT863, for 24 h. Secreted A β 40 or A β 42 in conditioned media was measured by ELISA. $n = 3$. * $p < 0.05$, ** $p < 0.01$. DMSO: dimethyl sulfoxide.

3.2. Treatment with GT863 for 48 h Reduced A β 40 and A β 42 Production and Increased C83 and C99 Levels in CHO-APP Cells

We next investigated the effect of long-term treatment with 0.5–3 μ M GT863 on A β production in CHO-APP cells. The chemical structure of GT863 is shown in Figure 2a. GT863 treatment for 48 h resulted in significant reduction of both A β 40 and A β 42 secretion in a dose-dependent manner (Figure 2b) without affecting cell viability (data not shown). The IC₅₀ value for A β 42 secretion was 1.7 μ M. Under the conditions tested, levels in whole cell lysate of full-length APP as well as secreted APP, APP α , and APP β —these latter two respectively being the products of α - or β -secretase cleavage of APP—were unchanged as compared with the DMSO control (Figure 2c). On the other hand, levels of APP C-terminal fragments (CTFs) C83 and C99—these respectively resulting from cleavage by α - and β -secretase—were significantly increased by long-term GT863 treatments as compared with the DMSO control. Because both C83 and C99 serve as substrate for cleavage by γ -secretase, these data indicate that treatment with GT863 caused a decrease in A β production, not as a result of inhibition of α - or β -cleavage of APP, but as a result of inhibition of γ -cleavage of C83 and C99.

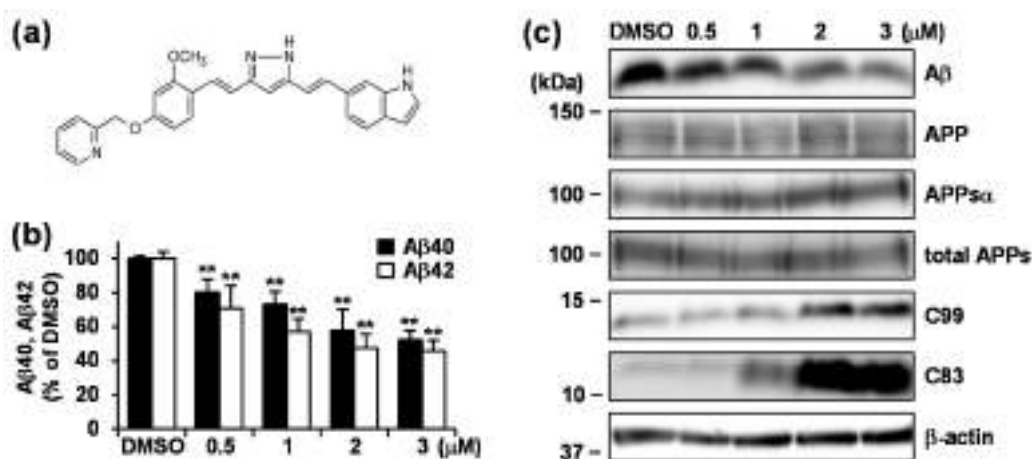


Figure 2. GT863 treatment for 48 h reduced secreted A β 40 and A β 42, and increased C99 and C83 levels in CHO-APP cells. (a) Chemical structural of GT863. (b,c) CHO-APP cells were treated with 0.5–3 μ M GT863 for 48 h. (b) Secreted A β 40 or A β 42 in conditioned media was measured by ELISA. $n = 3$. ** $p < 0.01$. (c) Whole cell lysates or conditioned media were immunoblotted with appropriate antibodies as indicated.

3.3. GT863 Did Not Inhibit γ -Secretase Activity in Vitro

To investigate whether the decrease in A β that was observed was the result of inhibition of γ -secretase activity by GT863, we examined the effect of GT863 on in vitro γ -secretase activity. We first performed in vitro γ -secretase assay using the CHAPSO-solubilized microsomal fraction of CHO cells and purified recombinant γ -secretase substrates (C99-FLAG and Notch-FLAG), which allows free collisions to occur between enzyme and substrates in solution [24]. Note that NICD is a γ -secretase cleavage product of Notch-FLAG. In a control experiment, co-incubation of the well-established γ -secretase inhibitor DAPT suppressed both the production of A β and NICD as compared with vehicle (Figure 3a, lanes 1–3). In contrast to what was observed with treatment with DAPT, we found that co-incubation with GT863 did not show significant reduction either A β or NICD production (Figure 3a, lane 4; Figure 3b).

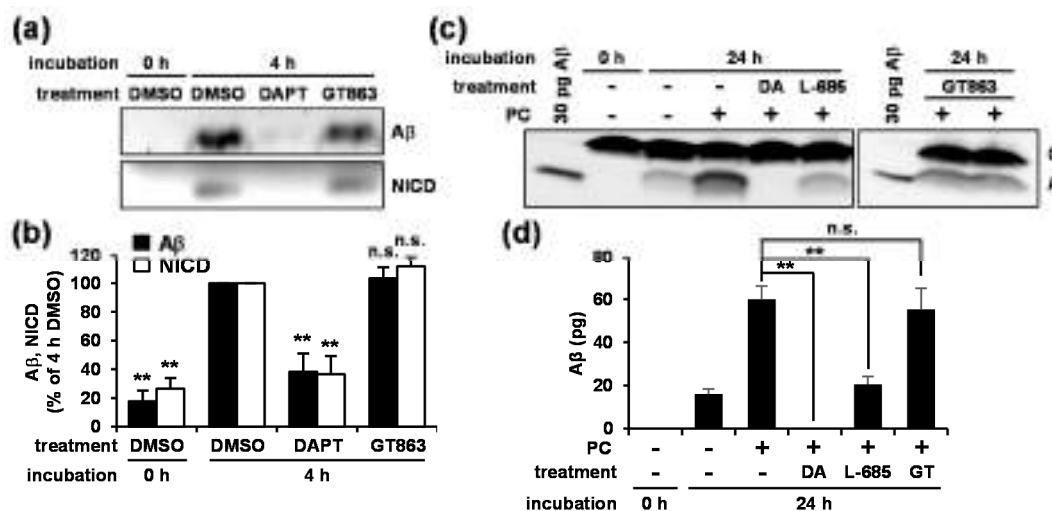


Figure 3. Effect of GT863 on in vitro γ -secretase activity. (a) 3-[(3-cholamidopropyl)dimethylammonio]-2-hydroxypropanesulfonate (CHAPSO)-solubilized microsomal fractions of CHO cells and substrates were incubated with or without 1 μ M N-[N-(3,5-difluorophenacetyl)-L-alanyl]-S-phenylglycine t-butyl ester (DAPT) or 3 μ M GT863 for 4 h at 37 $^{\circ}$ C. After incubation, reaction mixtures were subjected to immunoblotting with appropriate antibodies specific for A β or Notch intracellular domain (NICD). (b) Band intensities were quantified by densitometric scanning, relative intensity being shown. Mean \pm SD $n = 3$, ** $p < 0.01$, n.s. = not significant. (c) CHAPSO-solubilized microsomal fractions of yeast transformants were incubated in the presence of 1 mg/ml phosphatidylcholine (PC) with or without 1 μ M DAPT (DA), 1 μ M L-685,458 (L-685), or 3 μ M GT863 for 24 h at 37 $^{\circ}$ C. After incubation, reaction mixtures were subjected to immunoblotting. Synthetic A β 40 (30 pg) was loaded as a marker. (d) Band intensities were quantified by densitometric scanning, relative intensity being shown. mean \pm SD $n = 3$, ** $p < 0.01$, n.s. = not significant.

We further investigated the effect of GT863 on in vitro γ -secretase activity using CHAPSO-solubilized microsomal fractions of yeast transformants expressing the four subunits of γ -secretase (wild-type PS1, nicastrin, APH-1, and PEN-2) and the APP-based substrate C55 [25]. When the yeast microsomes were incubated with phosphatidylcholine (PC), A β production was observed (Figure 3c, lanes 2–4), with it further being observed that this A β production could be inhibited by co-incubation with γ -secretase inhibitor, DAPT, or L-685,458 (Figure 3c, lanes 5 and 6). Similar to our observations in Figure 3a, co-incubation with GT863 did not affect A β production (Figure 3c, lanes 8 and 9; Figure 3d). Taken together, these results suggested that GT863 did not cause inhibition of γ -secretase activity in vitro.

3.4. GT863 Inhibited γ -Cleavage in γ -Secretase Substrate-Selective Fashion in CHO-APP/Notch Δ E and SH-SY5Y Cells

To further investigate the mechanisms by which GT863 affects γ -secretase-mediated cleavage, we examined the effect of GT863 on γ -cleavage in CHO-APP/Notch Δ E cells. Notch Δ E is a truncated Notch1 protein that lacks the majority of the extracellular domain, and is a direct substrate of γ -secretase. In a control experiment, treatment with DAPT caused decrease in production of A β and NICD, and increased in the levels of C83, C99, and Notch Δ E, as compared with vehicle (Figure 4a,b). Although treatment with GT863 caused decreased production of A β and increased C83 levels, the effects of GT863 were less remarkable than those of DAPT. In contrast to the decrease in production of A β that was observed as being caused by GT863, we observed no significant difference in Notch Δ E cleavage relative to vehicle control in GT863-treated cells (Figure 4b).

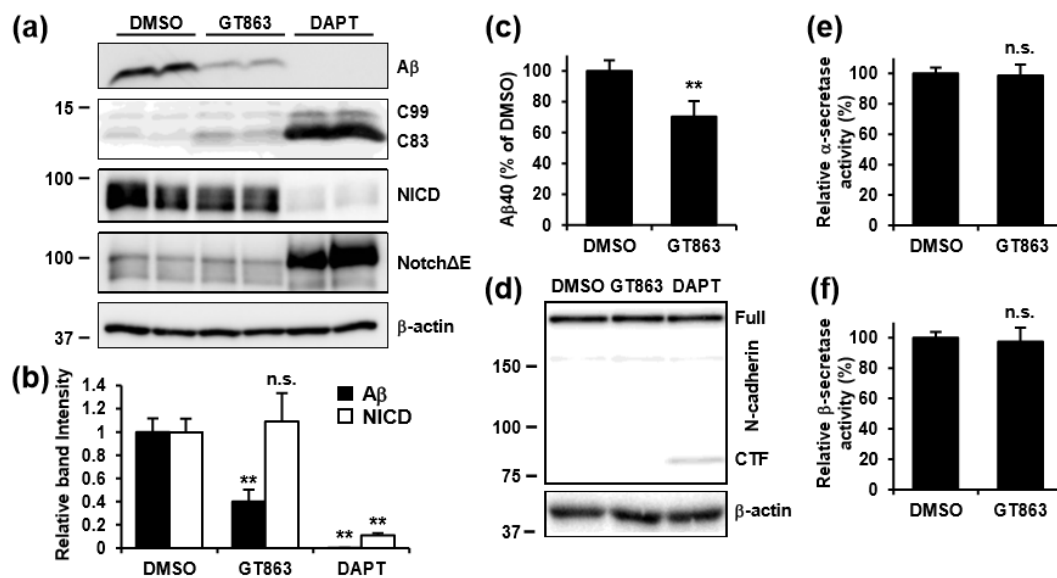


Figure 4. Effect of GT863 on activity of secretases. (a) CHO-APP/Notch Δ E cells were treated with 3 μ M GT863 or 1 μ M DAPT for 48 h. Whole cell lysates were immunoblotted with appropriate antibodies as indicated. (b) Band intensities were quantified by densitometric scanning, relative intensity being shown. Mean \pm SD $n = 3$, ** $p < 0.01$, n.s. = not significant. (c) SH-SY5Y cells were treated with 3 μ M GT863 for 24 h. Secreted A β 40 in conditioned media was measured by ELISA. $n = 3$. ** $p < 0.01$. (d) SH-SY5Y cells were treated with 3 μ M GT863 or 1 μ M DAPT for 24 h. Whole cell lysates were immunoblotted with appropriate antibodies specific for N-cadherin or β -actin. (e,f) α -secretase (e) or β -secretase (f) activity in SH-SY5Y cells treated with 3 μ M GT863 for 24 h was measured and normalized to control cells. $n = 3$. ** $p < 0.01$.

We next evaluated the effects of GT863 on A β production and γ -cleavage in SH-SY5Y human neuroblastoma cells that endogenously expressed APP. Similar to the results obtained with CHO-APP cells, we found that GT863 exhibited an inhibitory effect on A β 40 secretion in SH-SY5Y cells (Figure 4c). The amount of A β 42 in conditioned media was below our detection threshold (12.5 pg/ml) in SH-SY5Y cells. Using SH-SY5Y cells, we further examined whether there was cleavage of N-cadherin—N-cadherin being cleaved by α -secretase, and the CTF that is generated thereby being subsequently cleaved by γ -secretase [26]—finding as a result that N-cadherin CTF levels increased in cells treated with DAPT but not in cells treated with GT863 (Figure 4d). Collectively, these results suggest that the inhibitory effect of GT863 on γ -cleavage displays specificity with respect to γ -secretase substrate.

We also examined the effects of GT863 on α - and β -secretase activities in SH-SY5Y cells. Using in vitro enzymatic activity assays for α - and β -secretases, we found that there was no difference in α - or β -secretase activity in homogenates of cells treated with or without GT863 (Figure 4e,f). Taken

together, these results suggest that the decrease in A β production that was observed to occur upon treatment with GT863 was not due to direct inhibition of β - or γ -secretase activity.

3.5. GT863 Suppressed N-Glycosylation of Proteins Including Nicastrin

Because GT863 showed different effects depending on γ -secretase substrate, we examined the expression levels of nicastrin, as nicastrin is known to serve as a substrate receptor within the γ -secretase complex [27,28]. Nicastrin is a type I transmembrane protein with a large, heavily glycosylated ectodomain, and has been known to undergo a maturation process in the endoplasmic reticulum (ER) and the Golgi [29]. Human and Chinese hamster (*Cricetulus griseus*) nicastrin have 16 and 12 potential N-glycosylation sites, respectively. Although mature nicastrin manifests as a high molecular-mass band on SDS-PAGE and includes complex and high-mannose N-linked oligosaccharides, immature nicastrin manifests as a comparatively low molecular-mass band on SDS-PAGE and includes N-glycans that have not been subjected to complex glycosylation [29]. As shown in Figure 5a–c, we found that treatment with GT863 caused decrease in mature nicastrin levels (Figure 5b) and increase in immature nicastrin levels (Figure 5c). To determine whether the immature nicastrin band that had been observed to increase in intensity was sensitive to Endo H—with Endo H being specific for N-linked chains having high mannose and hybrid-type glycans—whole cell lysates were subjected to digestion with Endo H or PNGase F—with PNGase F being specific for all N-linked glycans. The results showed that the lower band that had been observed as increasing in intensity in GT863-treated cells was sensitive to digestion by both Endo H and PNGase F, resulting in the observation of a fully deglycosylated band at about 80 kDa (Figure 5d). Together, these results demonstrated that there was accumulation of immature nicastrin in GT863-treated cells.

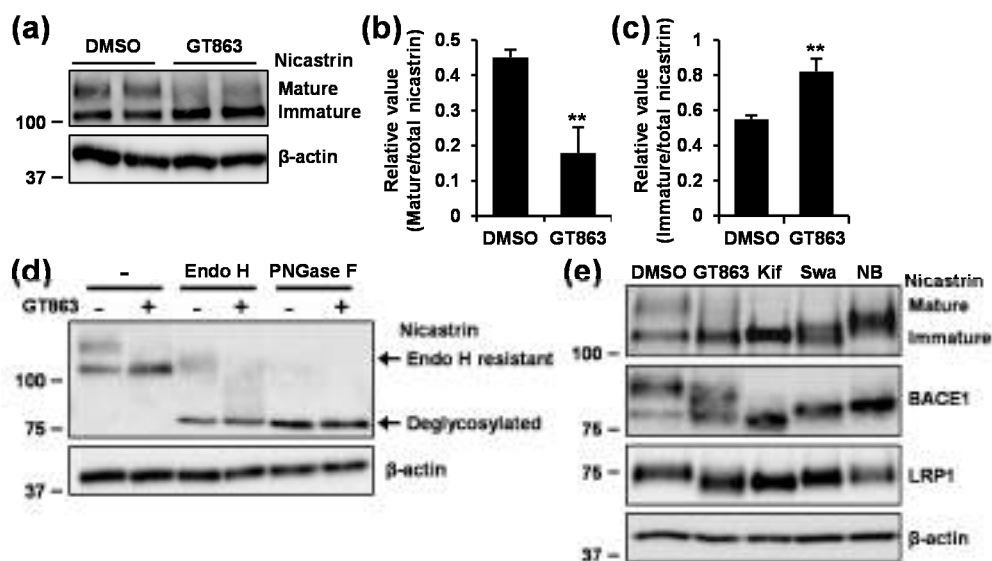


Figure 5. Effect of GT863 on nicastrin maturation. (a–d) CHO-APP/Notch Δ E cells were treated with 3 μ M GT863 for 48 h. (a) Whole cell lysates were immunoblotted with appropriate antibodies specific for nicastrin or β -actin. (b,c) Band intensities of mature (b) and immature (c) nicastrin were quantified by densitometric scanning, with the relative value being shown. Mean \pm SD $n = 3$, ** $p < 0.01$, n.s. = not significant. (d) Whole cell lysates were untreated or treated with endoglycosidase H (Endo H) or peptide-N-glycosidase F (PNGase F), and immunoblotted with appropriate antibodies specific for nicastrin or β -actin. (e) CHO-APP/Notch Δ E cells were treated with 3 μ M GT863, 1 μ g/mL kifunensine (Kif), 1 μ g/mL swainsonine (Swa), or 1 mM N-butyl-deoxynojirimycin (NB-DNJ) (NB) for 48 h. Whole cell lysates were immunoblotted with appropriate antibodies as indicated. LRP1: low-density lipoprotein (LDL) receptor-related protein 1; BACE1: β -site APP cleaving enzyme 1.

We further evaluated the glycosylation state of nicastrin by comparing the effect of several *N*-glycosylation inhibitors (kifunensine, a potent inhibitor of α -mannosidase I; swainsonine, a potent inhibitor of α -mannosidase II; and NB-DNJ, a potent inhibitor of α -glucosidase), finding as a result that the electrophoretic mobility of the immature nicastrin band that has been observed to increase in intensity in GT863-treated cells was similar to the electrophoretic mobility observed in kifunensine- or swainsonine-treated cells, but dissimilar to the electrophoretic mobility observed in NB-DNJ-treated cells (Figure 5e). We also found that the electrophoretic mobility of low-density lipoprotein (LDL) receptor-related protein 1 (LRP1) and BACE1—which are also *N*-glycosylated proteins—was altered in cells treated with GT863 in a similar fashion, as observed with kifunensine or swainsonine treatment. Together, these results suggested that GT863 inhibited the mannose trimming step but not the glucose trimming step of protein *N*-glycosylation.

3.6. Inhibition of Mannosidase Suppressed A β Production Without Affecting Notch Δ E Cleavage.

We then took a biochemical approach to evaluate the effect of mannosidase inhibition on A β and NICD production. Treatment with kifunensine or swainsonine caused reduction in mature nicastrin levels (Figure 6a,b). Under the condition tested, A β secretion was significantly reduced, whereas NICD production was unaffected in cells treated with either kifunensine or swainsonine (Figure 6c) as observed in cells treated with GT863 (Figure 4b). These results suggested that the inhibition of *N*-glycosylation, especially the mannose trimming step, suppressed A β production selectively.

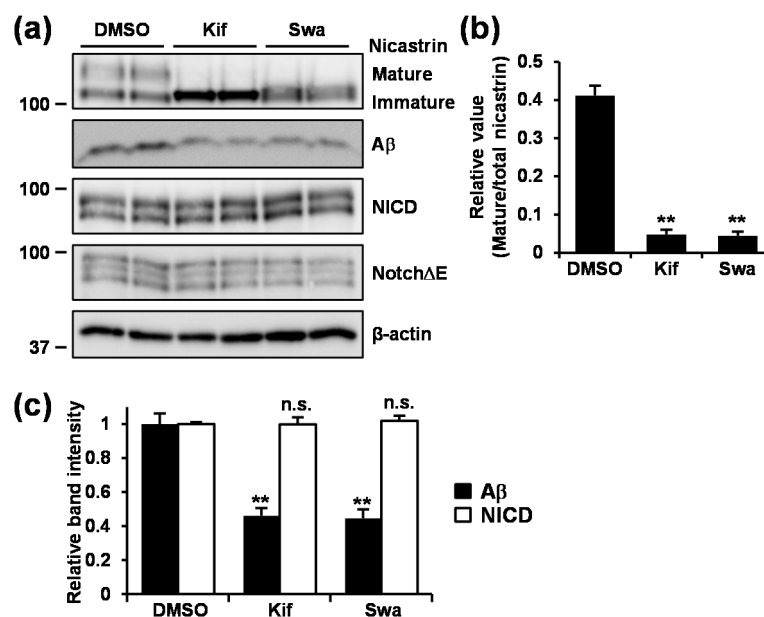


Figure 6. Effect of kifunensine or swainsonine treatment on A β and NICD production. (a–d) CHO-APP/Notch Δ E cells were treated with 1 μ g/mL kifunensine (Kif) or 1 μ g/mL swainsonine (Swa) for 48 h. (a) Whole cell lysates were immunoblotted with appropriate antibodies as indicated. (b–d) Band intensities of nicastrin (b), and A β and NICD (c) were quantified by densitometric scanning, relative value being shown. Mean \pm SD $n = 3$, ** $p < 0.01$, n.s. = not significant.

4. Discussion

Curcumin is a symmetric molecule (Supplementary Figure S1) in which there are three chemical entities, that is, two phenolic ring systems containing *o*-methoxy groups that are connected by a seven-carbon linker consisting of an α,β -unsaturated β -diketone moiety. Because the diketone of curcumin is substituted by a pyrazole moiety in CU6/CNB-001, we previously speculated that the pyrazole moiety of CU6/CNB-001 may play a role in inhibiting A β production [13]. Among the compounds tested in the present study, the pyrazole moiety is present in GT863, GT855, and GT857.

Of these, however, only GT863 showed an inhibitory effect on production of both A β 40 and A β 42. One of the hydrogens in the pyrazole moiety of GT863 is substituted by a benzene or nitrobenzene group in GT855 or GT857, respectively. We further note that although GT863 and GT832 differ only with respect to whether a pyrazole moiety or a diketone moiety is present, of these two compounds, only GT863 was observed to suppress A β production. Collectively, these observations are believed to confirm our speculation that the pyrazole moiety of GT863 may indeed play an important role in inhibiting A β production. We also speculate that the good inhibitory effect of GT863 on A β production as compared with CU6/CNB-001, GT855, or GT857 may have been due to presence of the hydrogen in the pyrazole moiety of GT863 at the location where there is a benzene or nitrobenzene group in the pyrazole moiety of CU6/CNB-001, GT855, and GT857. Regarding bioavailability, it has been confirmed that GT863 can cross the blood–brain barrier, GT863 being found in the brain for 24 h following oral administration in mice [15]. Furthermore, indications of drug toxicity such as weight loss were not observed in GT863-treated mice during a 6 month administration period [15], indicating the safety and tolerability of oral constant administration of GT863. Moreover, it has been demonstrated that GT863 treatment can reduce aggregated tau and delay onset and progression of motor dysfunction in human P301L tau transgenic mice [15], and can also inhibit both A β and tau aggregation, as well as ameliorate cognitive dysfunction, in senescence-accelerated mouse prone 8 (SAMP8) mice [17]. On the basis of our present study, we speculate that inhibition of A β production by GT863 may partly explain the beneficial effects on AD pathology that have been observed in *in vivo* experiments. Further experiments using AD mouse models should be performed to explore this possibility.

Glycosylation is one of the commonest types of post-translational modification observed to occur in proteins. Most commonly, a glycan is covalently attached to either an asparagine (*N*-glycan) or serine/threonine (*O*-glycan) residue of the protein. The functional properties of the *N*-glycan portion of a glycoprotein may include protein folding, trafficking, secretion, enzyme activity, and interaction with other biological molecules [30,31]. *N*-glycosylation begins in the ER with the transfer of a precursor oligosaccharide from dolichyl-pyrophosphate to the luminal side of a polypeptide chain. After the transfer of the oligosaccharide, the *N*-glycan is gradually trimmed by glucosidases and mannosidases in the ER and Golgi during protein folding. Subsequent processing steps occur in the Golgi through the actions of various glycosyltransferases, resulting in a wide variety of complex types of *N*-glycan structures. Because we found in the present study that treatment with GT863 induced accumulation of Endo H and PNGase F-sensitive immature nicastrin, which had similar electrophoretic mobility on SDS-PAGE as was observed in kifunensine- or swainsonine-treated cells, we consider it to be plausible that GT863 operates by inhibiting the mannose trimming step. Furthermore, because we found in the present study that treatment with GT863 inhibited *N*-glycosylation of not only nicastrin but also of LRP1 and BACE1, we consider it possible that GT863 may have inhibitory properties against any of the various enzymes involved in the mannose trimming step (e.g., α -mannosidase I or II, or *N*-acetylglucosaminyltransferase I). Further studies are needed to clarify the effect of GT863 on enzymatic activities in the mannose trimming step.

We furthermore demonstrated that not only GT863 but also kifunensine and swainsonine can inhibit A β production without affecting NICD production by γ -secretase. These results suggest that the mannose trimming step within the protein *N*-glycosylation pathway may play an important role in A β production. Because GT863 treatment induced an increase in C99 (and C83), the decrease in A β that we observed might have been due to suppression of the γ -cleavage step but not of the β -cleavage step. Although it was not clear which glycoprotein is responsible for the GT863-induced or mannosidase inhibitor-induced decrease in A β production that we observed, nicastrin is thought to be a likely candidate on the basis of its availability as a γ -secretase substrate, as nicastrin has been shown to function as a γ -secretase substrate receptor [27,28]. Recent papers have further shown that nicastrin serves as a molecular gatekeeper for γ -secretase substrates, sterically blocking longer substrates from gaining access to the active site on PS [32,33]. Because mature nicastrin primarily associates with the active γ -secretase complex [34], and because complex oligosaccharides are not

required for the binding of nicastrin to PS [35], it is possible that inhibition of nicastrin maturation might affect substrate recognition without affecting γ -secretase activity. In relation to our present observations, Moniruzzaman et al. reported that A β production was reduced in mutant CHO cells that lacked *N*-acetylglucosaminyltransferase I, resulting in increase in immature nicastrin [24]. On the other hand, several other papers have shown that inhibition of α -mannosidase I by kifunensine resulted in increased levels of immature nicastrin but did not affect A β production [35,36]. Though there is no clear explanation for this discrepancy, one explanation might be that our present study used CHO cells that stably expressed wild-type human APP (APPwt), whereas the aforementioned papers [35,36] used HEK293 cells that stably expressed Swedish mutant APP (APPswe). Indeed, in support of this possible explanation, we also confirmed that kifunensine treatment did not affect A β production despite the fact that it did suppress nicastrin maturation in CHO cells that stably expressed APPswe (Supplementary Figure S2). Several lines of evidence indicate that although APPwt is processed by β - and γ -secretases in acidic endosomal compartments originating at the cell surface, β -cleavage of APPswe occurs before it reaches the plasma membrane in the secretory pathway [37–39]. Furthermore, it has been reported that lipid rafts in post-Golgi and endosome membranes serve as the platform for amyloidogenic processing of APP [40–42]. There is therefore a possibility that the glycosylation state of nicastrin may affect substrate recognition by γ -secretase differently in different membrane microdomain environments. Another possibility that cannot be excluded is the possibility that the inhibitory effect of GT863 and mannosidase inhibitors on A β production that we observed might have been due to inhibition of or mediation by some other protein(s) and/or some aspect of *N*-glycosylation thereof. In this regard, there is growing evidence that *N*-glycans may play a significant role in AD development [30,31]. It should furthermore be noted that not only nicastrin but also APP, BACE1, α -secretase a disintegrin and metalloproteinase (ADAM10), and neprilysin are all known to be *N*-glycosylated. It is also of note that terminal sialylation of APP *N*-glycans has been reported to enhance A β production [43]. Further experiments will be required for in-depth analysis of these points.

In conclusion, we report that the curcumin derivative GT863 inhibits A β 40 and A β 42 production without affecting secretase activity. We also report that GT863 suppresses γ -cleavage in a γ -secretase-substrate-dependent manner. We further report that inhibition of the mannose trimming step in the protein *N*-glycosylation pathway is involved in inhibition of A β production by GT863. In addition to its ability to inhibit aggregation of both A β and tau, we found that GT863 also had a beneficial effect in terms of its ability to suppress A β production. Our findings also demonstrate that mannosidase inhibitor can suppress A β production without inhibiting Notch Δ E cleavage, suggesting the possibility that inhibition of enzymes involved in the mannose trimming step is a potential drug target for sporadic AD treatment.

Supplementary Materials: The following are available online at <http://www.mdpi.com/2073-4409/9/2/349/s1>: Figure S1: Chemical structural of curcumin derivatives. Figure S2: Effect of kifunensine treatment on A β production in CHO-APPswe (Swedish mutant APP) cells.

Author Contributions: Conceptualization, Y.U.; methodology, Y.U., S.F., and E.F.; formal analysis, Y.U., M.O., H.S., and N.N.; investigation, Y.U., M.T., R.H., H.F., and S.I.; resources, M.O. and H.S.; data curation, Y.U., H.S., and N.N.; writing—original draft preparation, Y.U.; writing—review and editing, Y.U. and N.N.; visualization, Y.U.; supervision, Y.U. and N.N.; project administration, Y.U.; funding acquisition, Y.U. and N.N. All authors have read and agreed to the published version of the manuscript.

Funding: This work was supported in part by JSPS KAKENHI Grant-in-Aid for Scientific Research (C) 16K08254 and 19K07093 to Y.U. and the MEXT-Supported Program for the Strategic Research Foundation at Private Universities in Japan for years 2015–2019.

Acknowledgments: We thank Norie Kato and Natsuki Botani for research support, and also thank Gerry Peters (JTT K.K., Takatsuki, Japan) for his careful editing of the manuscript.

Conflicts of Interest: H.S. is President of Green Tech Co., Ltd. Other authors declare no conflict of interest.

References

1. Selkoe, D.J. Alzheimer's disease is a synaptic failure. *Science* **2002**, *298*, 789–791. [[CrossRef](#)] [[PubMed](#)]
2. Thinakaran, G.; Koo, E.H. Amyloid precursor protein trafficking, processing, and function. *J. Biol. Chem.* **2008**, *283*, 29615–29619. [[CrossRef](#)] [[PubMed](#)]
3. De Strooper, B. Lessons from a failed γ -secretase Alzheimer trial. *Cell* **2014**, *159*, 721–726. [[CrossRef](#)]
4. Long, J.M.; Holtzman, D.M. Alzheimer Disease: An Update on Pathobiology and Treatment Strategies. *Cell* **2019**, *179*, 312–339. [[CrossRef](#)]
5. Kim, J.; Lee, H.J.; Lee, K.W. Naturally occurring phytochemicals for the prevention of Alzheimer's disease. *J. Neurochem.* **2010**, *112*, 1415–1430. [[CrossRef](#)]
6. Reddy, P.H.; Manczak, M.; Yin, X.; Grady, M.C.; Mitchell, A.; Tonk, S.; Kuruva, C.S.; Bhatti, J.S.; Kandimalla, R.; Vijayan, M.; et al. Protective Effects of Indian Spice Curcumin Against Amyloid- β in Alzheimer's Disease. *J. Alzheimers Dis.* **2018**, *61*, 843–866. [[CrossRef](#)]
7. Zhang, C.; Browne, A.; Child, D.; Tanzi, R.E. Curcumin decreases amyloid- β peptide levels by attenuating the maturation of amyloid- β precursor protein. *J. Biol. Chem.* **2010**, *285*, 28472–28480. [[CrossRef](#)]
8. Yang, F.; Lim, G.P.; Begum, A.N.; Ubeda, O.J.; Simmons, M.R.; Ambegaokar, S.S.; Chen, P.P.; Kaye, R.; Glabe, C.G.; Frautschy, S.A.; et al. Curcumin inhibits formation of amyloid beta oligomers and fibrils, binds plaques, and reduces amyloid in vivo. *J. Biol. Chem.* **2005**, *280*, 5892–5901. [[CrossRef](#)]
9. Garcia-Alloza, M.; Borrelli, L.A.; Rozkalne, A.; Hyman, B.T.; Bacskaï, B.J. Curcumin labels amyloid pathology in vivo, disrupts existing plaques, and partially restores distorted neurites in an Alzheimer mouse model. *J. Neurochem.* **2007**, *102*, 1095–1104. [[CrossRef](#)] [[PubMed](#)]
10. Baum, L.; Lam, C.W.; Cheung, S.K.; Kwok, T.; Lui, V.; Tsoh, J.; Lam, L.; Leung, V.; Hui, E.; Ng, C.; et al. Six-month randomized, placebo-controlled, double-blind, pilot clinical trial of curcumin in patients with Alzheimer disease. *J. Clin. Psychopharmacol.* **2008**, *28*, 110–113. [[CrossRef](#)] [[PubMed](#)]
11. Hamaguchi, T.; Ono, K.; Yamada, M. Curcumin and Alzheimer's disease. *CNS Neurosci. Ther.* **2010**, *16*, 285–297. [[CrossRef](#)]
12. Belkacemi, A.; Doggui, S.; Dao, L.; Ramassamy, C. Challenges associated with curcumin therapy in Alzheimer disease. *Expert Rev. Mol. Med.* **2011**, *13*, e34. [[CrossRef](#)] [[PubMed](#)]
13. Kotani, R.; Urano, Y.; Sugimoto, H.; Noguchi, N. Decrease of Amyloid- β Levels by Curcumin Derivative via Modulation of Amyloid- β Protein Precursor Trafficking. *J. Alzheimers Dis.* **2017**, *56*, 529–542. [[CrossRef](#)] [[PubMed](#)]
14. Valera, E.; Dargusch, R.; Maher, P.A.; Schubert, D. Modulation of 5-lipoxygenase in proteotoxicity and Alzheimer's disease. *J. Neurosci.* **2013**, *33*, 10512–10525. [[CrossRef](#)]
15. Okuda, M.; Hijikuro, I.; Fujita, Y.; Wu, X.; Nakayama, S.; Sakata, Y.; Noguchi, Y.; Ogo, M.; Akasofu, S.; Ito, Y.; et al. PE859, a novel tau aggregation inhibitor, reduces aggregated tau and prevents onset and progression of neural dysfunction in vivo. *PLoS ONE* **2015**, *10*, e0117511. [[CrossRef](#)] [[PubMed](#)]
16. Okuda, M.; Hijikuro, I.; Fujita, Y.; Teruya, T.; Kawakami, H.; Takahashi, T.; Sugimoto, H. Design and synthesis of curcumin derivatives as tau and amyloid β dual aggregation inhibitors. *Bioorg. Med. Chem. Lett.* **2016**, *26*, 5024–5028. [[CrossRef](#)] [[PubMed](#)]
17. Okuda, M.; Fujita, Y.; Hijikuro, I.; Wada, M.; Uemura, T.; Kobayashi, Y.; Waku, T.; Tanaka, N.; Nishimoto, T.; Izumi, Y.; et al. A Novel Curcumin Derivative, Inhibits Amyloid- β and Tau Aggregation, and Ameliorates Cognitive Dysfunction in Senescence-Accelerated Mouse Prone 8. *J. Alzheimers Dis.* **2017**, *59*, 313–328. [[CrossRef](#)]
18. Yanagisawa, D.; Ibrahim, N.F.; Taguchi, H.; Morikawa, S.; Hirao, K.; Shirai, N.; Sogabe, T.; Tooyama, I. Curcumin derivative with the substitution at C-4 position, but not curcumin, is effective against amyloid pathology in APP/PS1 mice. *Neurobiol. Aging* **2015**, *36*, 201–210. [[CrossRef](#)]
19. Serafini, M.M.; Catanzaro, M.; Rosini, M.; Racchi, M.; Lanni, C. Curcumin in Alzheimer's disease: Can we think to new strategies and perspectives for this molecule? *Pharmacol. Res.* **2017**, *124*, 146–155. [[CrossRef](#)]
20. Koo, E.H.; Squazzo, S.L. Evidence that production and release of amyloid beta-protein involves the endocytic pathway. *J. Biol. Chem.* **1994**, *269*, 17386–17389.
21. Funamoto, S.; Sasaki, T.; Ishihara, S.; Nobuhara, M.; Nakano, M.; Watanabe-Takahashi, M.; Saito, T.; Kakuda, N.; Miyasaka, T.; Nishikawa, K.; et al. Substrate ectodomain is critical for substrate preference and inhibition of γ -secretase. *Nat. Commun.* **2013**, *4*, 2529. [[CrossRef](#)] [[PubMed](#)]

22. Urano, Y.; Ho, V.D.K.; Araki, H.; Noguchi, N. 24(S)-Hydroxycholesterol induces ER dysfunction-mediated unconventional cell death. *Cell Death Discov.* **2019**, *113*. [[CrossRef](#)] [[PubMed](#)]
23. Urano, Y.; Ochiai, S.; Noguchi, N. Suppression of amyloid- β production by 24S-hydroxycholesterol via inhibition of intracellular amyloid precursor protein trafficking. *FASEB J.* **2013**, *27*, 4305–4315. [[CrossRef](#)] [[PubMed](#)]
24. Moniruzzaman, M.; shihara, S.; Nobuhara, M.; Higashide, H.; Funamoto, S. Glycosylation status of nicastrin influences catalytic activity and substrate preference of γ -secretase. *Biochem. Biophys. Res. Commun.* **2018**, *502*, 98–103. [[CrossRef](#)]
25. Yagishita, S.; Futai, E.; Ishiura, S. In vitro reconstitution of gamma-secretase activity using yeast microsomes. *Biochem. Biophys. Res. Commun.* **2008**, *377*, 141–145. [[CrossRef](#)]
26. Marambaud, P.; Wen, P.H.; Dutt, A.; Shioi, J.; Takashima, A.; Siman, R.; Robakis, N.K. A CBP binding transcriptional repressor produced by the PS1/epsilon-cleavage of N-cadherin is inhibited by PS1 FAD mutations. *Cell* **2003**, *114*, 635–645. [[CrossRef](#)]
27. Shah, S.; Lee, S.F.; Tabuchi, K.; Hao, Y.H.; Yu, C.; LaPlant, Q.; Ball, H.; Dann, C.E., 3rd; Südhof, T.; Yu, G. Nicastrin functions as a gamma-secretase-substrate receptor. *Cell* **2005**, *122*, 435–447. [[CrossRef](#)]
28. Zhang, X.; Hoey, R.J.; Lin, G.; Koide, A.; Leung, B.; Ahn, K.; Dolios, G.; Paduch, M.; Ikeuchi, T.; Wang, R.; et al. Identification of a tetratricopeptide repeat-like domain in the nicastrin subunit of γ -secretase using synthetic antibodies. *Proc. Natl. Acad. Sci. USA* **2012**, *109*, 8534–8539. [[CrossRef](#)]
29. Yang, D.S.; Tandon, A.; Chen, F.; Yu, G.; Yu, H.; Arawaka, S.; Hasegawa, H.; Duthie, M.; Schmidt, S.D.; Ramabhadran, T.V.; et al. Mature glycosylation and trafficking of nicastrin modulate its binding to presenilins. *J. Biol. Chem.* **2002**, *277*, 28135–28142. [[CrossRef](#)]
30. Schedin-Weiss, S.; Winblad, B.; Tjernberg, L.O. The role of protein glycosylation in Alzheimer disease. *FEBS J.* **2014**, *281*, 46–62. [[CrossRef](#)]
31. Kizuka, Y.; Kitazume, S.; Taniguchi, N. N-glycan and Alzheimer's disease. *Biochim. Biophys. Acta. Gen. Subj.* **2017**, *1861*, 2447–2454. [[CrossRef](#)]
32. Bolduc, D.M.; Montagna, D.R.; Gu, Y.; Selkoe, D.J.; Wolfe, M.S. Nicastrin functions to sterically hinder γ -secretase-substrate interactions driven by substrate transmembrane domain. *Proc. Natl. Acad. Sci. USA* **2016**, *113*, 509–518. [[CrossRef](#)] [[PubMed](#)]
33. Wolfe, M.S. Substrate recognition and processing by γ -secretase. *Biochim. Biophys. Acta. Biomembr.* **2019**, *183016*. [[CrossRef](#)] [[PubMed](#)]
34. Kimberly, W.T.; LaVoie, M.J.; Ostaszewski, B.L.; Ye, W.; Wolfe, M.S.; Selkoe, D.J. Complex N-linked glycosylated nicastrin associates with active gamma-secretase and undergoes tight cellular regulation. *J. Biol. Chem.* **2002**, *277*, 35113–35117. [[CrossRef](#)]
35. Herreman, A.; Van Gassen, G.; Bentahir, M.; Nyabi, O.; Craessaerts, K.; Mueller, U.; Annaert, W.; De Strooper, B. gamma-Secretase activity requires the presenilin-dependent trafficking of nicastrin through the Golgi apparatus but not its complex glycosylation. *J. Cell Sci.* **2003**, *116*, 1127–1136. [[CrossRef](#)]
36. Shirotani, K.; Edbauer, D.; Capell, A.; Schmitz, J.; Steiner, H.; Haass, C. Gamma-secretase activity is associated with a conformational change of nicastrin. *J. Biol. Chem.* **2003**, *278*, 16474–16477. [[CrossRef](#)]
37. Haass, C.; Lemere, C.A.; Capell, A.; Citron, M.; Seubert, P.; Schenk, D.; Lannfelt, L.; Selkoe, D.J. The Swedish mutation causes early-onset Alzheimer's disease by β -secretase cleavage within the secretory pathway. *Nat. Med.* **1995**, *12*, 1291–1296. [[CrossRef](#)]
38. Thinakaran, G.; Teplow, D.B.; Siman, R.; Greenberg, B.; Sisodia, S.S. Metabolism of the "Swedish" amyloid precursor protein variant in neuro2a (N2a) cells. Evidence that cleavage at the "beta-secretase" site occurs in the golgi apparatus. *J. Biol. Chem.* **1996**, *271*, 9390–9397. [[CrossRef](#)]
39. Yamakawa, H.; Yagishita, S.; Futai, E.; Ishiura, S. beta-Secretase inhibitor potency is decreased by aberrant beta-cleavage location of the "Swedish mutant" amyloid precursor protein. *J. Biol. Chem.* **2010**, *285*, 1634–1642. [[CrossRef](#)]
40. Riddell, D.R.; Christie, G.; Hussain, I.; Dingwall, C. Compartmentalization of beta-secretase (Asp2) into low-buoyant density, noncaveolar lipid rafts. *Curr. Biol.* **2001**, *11*, 1288–1293. [[CrossRef](#)]
41. Vetrivel, K.S.; Cheng, H.; Lin, W.; Sakurai, T.; Li, T.; Nukina, N.; Wong, P.C.; Xu, H.; Thinakaran, G. Association of gamma-secretase with lipid rafts in post-Golgi and endosome membranes. *J. Biol. Chem.* **2004**, *279*, 44945–44954. [[CrossRef](#)] [[PubMed](#)]

42. Urano, Y.; Hayashi, I.; Isoo, N.; Reid, P.C.; Shibasaki, Y.; Noguchi, N.; Tomita, T.; Iwatsubo, T.; Hamakubo, T.; Kodama, T. Association of active gamma-secretase complex with lipid rafts. *J. Lipid Res.* **2005**, *46*, 904–912. [[CrossRef](#)] [[PubMed](#)]
43. McFarlane, I.; Georgopoulou, N.; Coughlan, C.M.; Gillian, A.M.; Breen, K.C. The role of the protein glycosylation state in the control of cellular transport of the amyloid beta precursor protein. *Neuroscience* **1999**, *90*, 15–25. [[CrossRef](#)]



© 2020 by the authors. Licensee MDPI, Basel, Switzerland. This article is an open access article distributed under the terms and conditions of the Creative Commons Attribution (CC BY) license (<http://creativecommons.org/licenses/by/4.0/>).

ARTICLE

Open Access

24(S)-Hydroxycholesterol induces ER dysfunction-mediated unconventional cell death

Yasuomi Urano¹, Diep-Khanh Ho Vo¹, Araki Hirofumi¹ and Noriko Noguchi¹

Abstract

Endoplasmic reticulum (ER) stress induced by disruption of protein folding activates the unfolded protein response (UPR), which while generally pro-survival in effect can also induce cell death under severe ER stress. 24(S)-hydroxycholesterol (24S-OHC), which is enzymatically produced in the ER of neurons, plays an important role in maintaining brain cholesterol homeostasis but also shows neurotoxicity when subjected to esterification by acyl-CoA:cholesterol acyltransferase 1 (ACAT1) in the ER. In this study, we demonstrated that the accumulation of 24S-OHC esters in human neuroblastoma SH-SY5Y cells evoked the UPR with substantially no pro-survival adaptive response but with significant activation of pro-death UPR signaling via regulated IRE1-dependent decay (RIDD). We further found that accumulation of 24S-OHC esters caused disruption of ER membrane integrity and release of ER luminal proteins into cytosol. We also found that de novo synthesis of global proteins was robustly suppressed in 24S-OHC-treated cells. Collectively, these results show that ER dysfunction and the accompanying RIDD-mediated pro-death UPR signaling and global protein synthesis inhibition are responsible for 24S-OHC ester-induced unconventional cell death.

Introduction

Upon accumulation of unfolded/misfolded proteins in the endoplasmic reticulum (ER)—a condition referred to as ER stress—cells activate an adaptive response—this response being referred to as the unfolded protein response (UPR)—to restore ER homeostasis and maintain the fidelity of protein-folding¹. In mammalian cells, the UPR comprises three major signaling pathways, which are respectively mediated by inositol-requiring enzyme 1 (IRE1), protein kinase RNA-like ER kinase (PERK), and activating transcription factor 6 (ATF6). The UPR processes include induction of ER chaperones, inhibition of protein synthesis, and stimulation of retrograde transport of misfolded proteins from the ER into the cytosol for

ubiquitination and destruction by ER-associated degradation (ERAD)². However, under unresolvable ER stress conditions, the UPR represses the adaptive response and triggers cell death^{3–6}.

On activation of IRE1, phosphorylated IRE1 becomes an active endoribonuclease (RNase) that cleaves an intron of *X-box binding protein 1* (*XBPI*) mRNA, resulting in the translation of bZIP-containing transcription factor *XBPIs*¹. *XBPIs* induces the expression of several genes involved in the UPR to activate pro-survival mechanisms. IRE1 RNase activity also contributes to post-transcriptional degradation of a subset of ER-localized mRNAs through a process known as regulated IRE1-dependent decay (RIDD)^{7–9}. Although RIDD may help to reduce the folding load of nascent proteins and alleviate ER stress as a pro-survival mechanism, continuous decay of RIDD substrates by unmitigated ER stress leads to pro-death outputs^{4,10}. Activated IRE1 also promotes apoptosis through the activation of apoptosis signal-regulated kinase 1 (ASK1; also known as MAP3K5), JUN N-

Correspondence: Yasuomi Urano (yurano@mail.doshisha.ac.jp) or Noriko Noguchi (nnoguchi@mail.doshisha.ac.jp)

¹Department of Medical Life Systems, Faculty of Life and Medical Sciences, Doshisha University, Kyoto 610-0394, Japan

These authors contributed equally: Yasuomi Urano, Diep-Khanh Ho Vo
Edited by I. Lavrik

© 2019 The Author(s).



Open Access This article is licensed under a Creative Commons Attribution 4.0 International License, which permits use, sharing, adaptation, distribution and reproduction in any medium or format, as long as you give appropriate credit to the original author(s) and the source, provide a link to the Creative Commons license, and indicate if changes were made. The images or other third party material in this article are included in the article's Creative Commons license, unless indicated otherwise in a credit line to the material. If material is not included in the article's Creative Commons license and your intended use is not permitted by statutory regulation or exceeds the permitted use, you will need to obtain permission directly from the copyright holder. To view a copy of this license, visit <http://creativecommons.org/licenses/by/4.0/>.

terminal kinase (JNK), and p38 MAPK. Activation of PERK by autophosphorylation induces pro-survival signaling and pro-apoptotic signaling. Activated PERK phosphorylates eukaryotic translation initiator factor 2 α (eIF2 α) and causes general translational attenuation which is a pro-survival process, as it reduces the number of proteins entering the ER¹¹. In addition, phosphorylation of eIF2 α also induces the specific translation of ATF4. ATF4 controls the expression of genes that encode not only cytoprotective proteins but also pro-apoptotic proteins, including C/EBP-homologous protein (CHOP)¹². ATF6 is a type II transmembrane protein containing bZIP transcription factor in its cytosolic domain. Upon occurrence of ER stress, ATF6 translocates to the Golgi apparatus, where it is cleaved by site-1 protease and site-2 protease. The cleaved cytosolic domain of ATF6 activates transcription of target genes such as ER chaperones. There is growing evidence that not only accumulation of unfolded/misfolded proteins in the ER lumen, but also alterations in membrane lipid desaturation and aberrant phospholipid composition may also be potent in activating the UPR^{13,14}. There is, however, little known at present about whether oxidation products of lipids might activate the UPR.

24(S)-hydroxycholesterol (24S-OHC) is one of the enzymatic oxidation products of cholesterol and plays an important role in maintaining brain cholesterol homeostasis^{15–18}. While 24S-OHC has important physiological and protective functions in the brain, several lines of evidence suggest that dysregulation of 24S-OHC metabolism in the brain may contribute to the development of neurodegenerative diseases such as Alzheimer's disease (AD) and Parkinson's disease (PD)^{19–26}. Furthermore, we and other groups have shown that 24S-OHC possesses a potent neurotoxicity that may be involved in the etiology of neurodegenerative disease^{27,28}. We have previously demonstrated that 24S-OHC elicits caspase-independent cell death in human neuroblastoma SH-SY5Y cells, and rat primary cortical neuronal cells not expressing caspase-8²⁸. 24S-OHC-induced cell death is partially but significantly suppressed by Necrostatin-1 (Nec-1), an inhibitor of receptor interacting serine/threonine kinase 1 (RIPK1) or knockdown of RIPK1. However, as necroptosis is a form of regulated necrotic cell death that depends on MLKL, RIPK3, and (at least in some settings) on the kinase activity of RIPK1²⁹, and since we subsequently showed that RIPK1, but neither RIPK3 nor MLKL, is expressed in SH-SY5Y cells³⁰, we considered that the type of cell death induced by 24S-OHC in SH-SY5Y cells is necroptosis-like.

Acyl-CoA:cholesterol acyltransferase 1 (ACAT1), an ER-resident enzyme, catalyzes the esterification of free cholesterol to form cholesteryl esters³¹. We found that ACAT1 also utilizes 24S-OHC and long-chain

unsaturated fatty acid as substrates to form 24S-OHC ester^{32,33}. We further found that accumulation of 24S-OHC esters leads to formation of atypical lipid droplet (LD)-like structures coupled with an enlarged membrane structure that appears to be a swollen ER structure³³. Since ACAT inhibitor or ACAT1 siRNA suppresses both 24S-OHC-induced LD-like structure formation and cell death, we concluded that ACAT1-catalyzed 24S-OHC esterification and formation of atypical LD-like structures having abnormal ER morphology are initial key events in 24S-OHC-induced cell death; however, the specific mechanism by which 24S-OHC esterification activates cell death signaling still remains to be elucidated.

In this study, we found that esterification of 24S-OHC evoked the UPR but the downstream pro-survival adaptive response was not substantially activated, finding instead that RIDD is implicated in 24S-OHC-induced cell death. We also demonstrate that accumulation of 24S-OHC esters caused disruption of ER membrane integrity, resulting in the release of a number of ER-resident proteins into cytosol and the suppression of de novo protein synthesis. Taken together, we conclude that ER dysfunction, and the accompanying pro-death UPR signaling and protein synthesis inhibition, are responsible for cell death induced by ACAT1-catalyzed 24S-OHC esterification.

Results

Accumulation of 24S-OHC esters activated the UPR in SH-SY5Y cells

To investigate the activation of UPR signaling by 24S-OHC, we first examined IRE1 autophosphorylation by immunoblotting. In a control experiment, the well-established ER stress inducer thapsigargin, which inhibits ER Ca²⁺-ATPase, induced phosphorylation of IRE1 α as confirmed by observation of mobility shift of the IRE1 α band in SDS-PAGE as compared with vehicle condition in SH-SY5Y cells (Fig. 1a). The same shift in the IRE1 α band was observed in cells treated with 50 μ M 24S-OHC for 6 h, suggesting that 24S-OHC treatment induced IRE1 α phosphorylation. 24S-OHC-induced IRE1 α phosphorylation was inhibited by cotreatment with F12511 but not by Nec-1 (Fig. 1a). We further found that *XBP1* splicing was induced in cells treated with 24S-OHC in similar fashion as was observed with thapsigargin treatment (Fig. 1b). 24S-OHC-induced *XBP1* splicing was also inhibited by cotreatment with F12511. However, XBP1s protein expression was less remarkably induced in 24S-OHC-treated cells than in thapsigargin-treated cells (Fig. 1c), suggesting that IRE1 α was activated but that downstream XBP1s was not substantially activated in 24S-OHC-treated cells.

We also found that there was phosphorylation of PERK as demonstrated by the occurrence of mobility shift and reduction in the amount of full-length ATF6, which

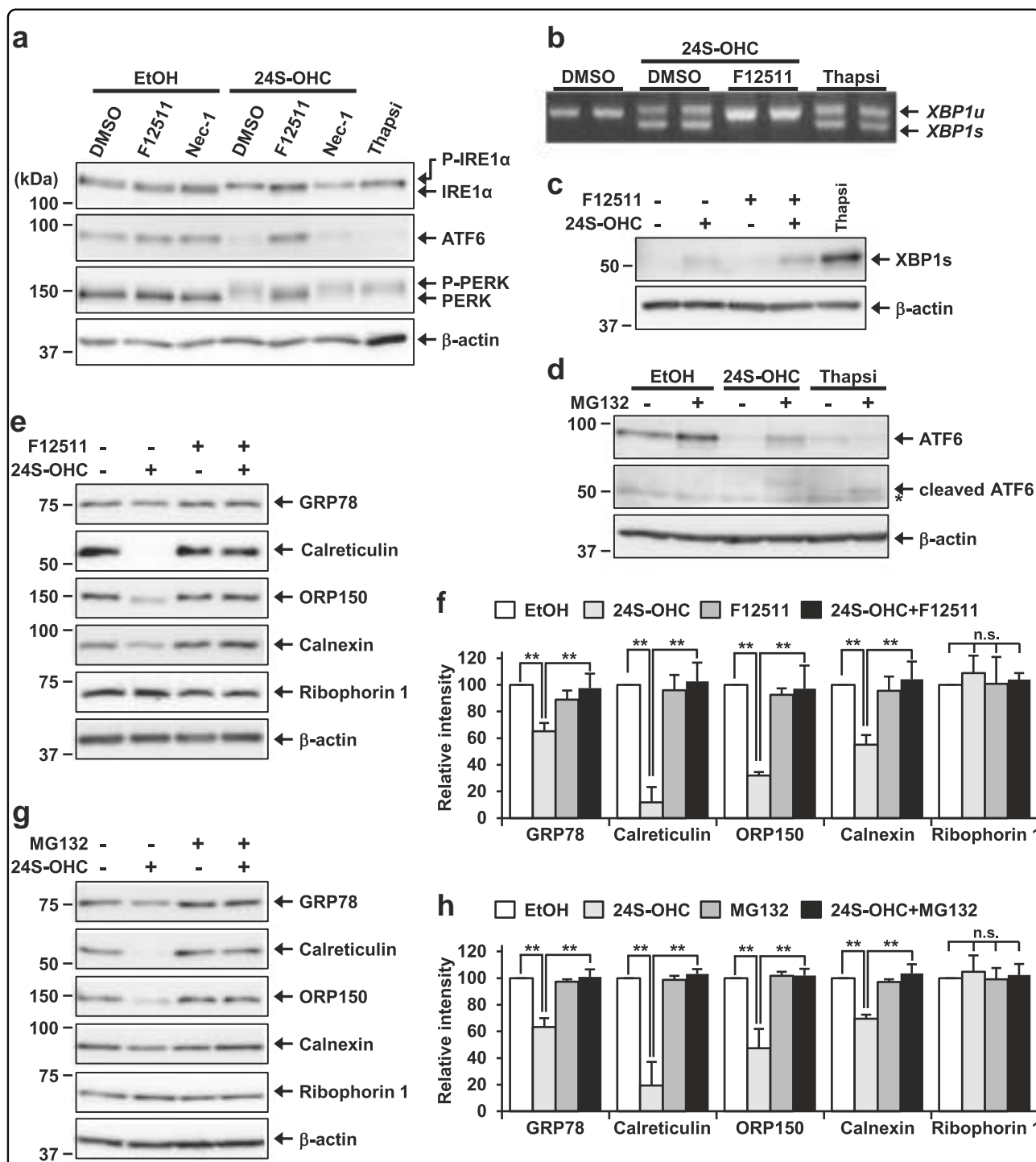


Fig. 1 Accumulation of 24S-OHC esters activated the UPR signaling pathway and downregulated expression of ER chaperone proteins in SH-SY5Y cells. **a-c** SH-SY5Y cells were pretreated with 5 μM F12511 for 15 min or with 100 μM Nec-1 (**a**) for 1 h and then exposed to 50 μM 24S-OHC for 6 h. Cells were also treated with 3 μM thapsigargin (Thapsi) for 3 h. **a** Whole-cell lysates were subjected to immunoblotting with appropriate antibodies as indicated. **b** The unspliced (*XBP1_u*) and spliced (*XBP1_s*) *XBP1* mRNAs were analyzed by RT-PCR. **c** Whole-cell lysates were immunoblotted with antibodies specific for XBP1s or β-actin. **d** Cells were pretreated with 20 μM MG132 for 30 min and then exposed to 50 μM 24S-OHC or 3 μM thapsigargin for 6 h. Whole-cell lysates were immunoblotted with antibodies specific for ATF6 or β-actin. Asterisks denote nonspecific bands. **e, f** Cells were treated as in panel **a**. **g, h** Cells were treated as in panel **d**. **e, g** Whole-cell lysates were subjected to immunoblotting with appropriate antibodies as indicated. **f, h** Band intensities were quantified by densitometric scanning, relative intensity is shown. Mean ± SD *n* = 3, ***P* < 0.01, n.s. not significant

occurred in cells treated with 24S-OHC in similar fashion as was observed with thapsigargin treatment (Fig. 1a). Similar to our observations with respect to IRE1 α , these changes were found to be suppressed by cotreatment with F12511, but not by Nec-1. Because the cleaved form of ATF6 is relatively unstable due to proteasomal degradation³⁴, we also examined activation of ATF6 in the presence of the proteasome inhibitor MG132, finding that the cleaved ATF6 was observed in cells treated with thapsigargin in the presence of MG132, but that uncleaved full-length ATF6 was observed in cells treated with 24S-OHC (Fig. 1d), suggesting that 24S-OHC-induced reduction of full-length ATF6 was not due to processing, but was instead due to proteasomal degradation.

We further found that expression of ER chaperone proteins (glucose-regulated protein 78 kDa (BiP/GRP78), calreticulin, ORP150, and calnexin) but not ribophorin 1 was reduced in 24S-OHC-treated cells, and that this reduction was suppressed by cotreatment with F12511 (Fig. 1e, f). We also found that this reduction was inhibited by cotreatment with MG132 (Fig. 1g, h), suggesting

that 24S-OHC-induced downregulation of ER chaperone proteins was due to proteasomal degradation. Time-course experiments revealed that IRE1 α phosphorylation occurred substantially, simultaneously with reduction in the amount of calreticulin (Fig. S1). Collectively, these data indicate that ACAT1-mediated 24S-OHC esterification induces ER stress, leading to activation of UPR signaling pathways, but that pro-survival mechanisms are not substantially activated in SH-SY5Y cells.

Upregulation of CHOP expression was not involved in 24S-OHC-induced cell death in SH-SY5Y cells

To investigate whether activation of pro-death UPR signaling was implicated in 24S-OHC-induced cell death, we first examined the induction of ATF4 and CHOP in SH-SY5Y cells, the results showing that ATF4 and CHOP expression was only moderately induced in 24S-OHC-treated cells as compared with the more pronounced expression, thereof observed in thapsigargin-treated cells (Fig. 2a). Furthermore, when 24S-OHC-induced CHOP upregulation was suppressed by CHOP siRNA (Fig. 2b), we found that cell death was not suppressed (Fig. 2c),

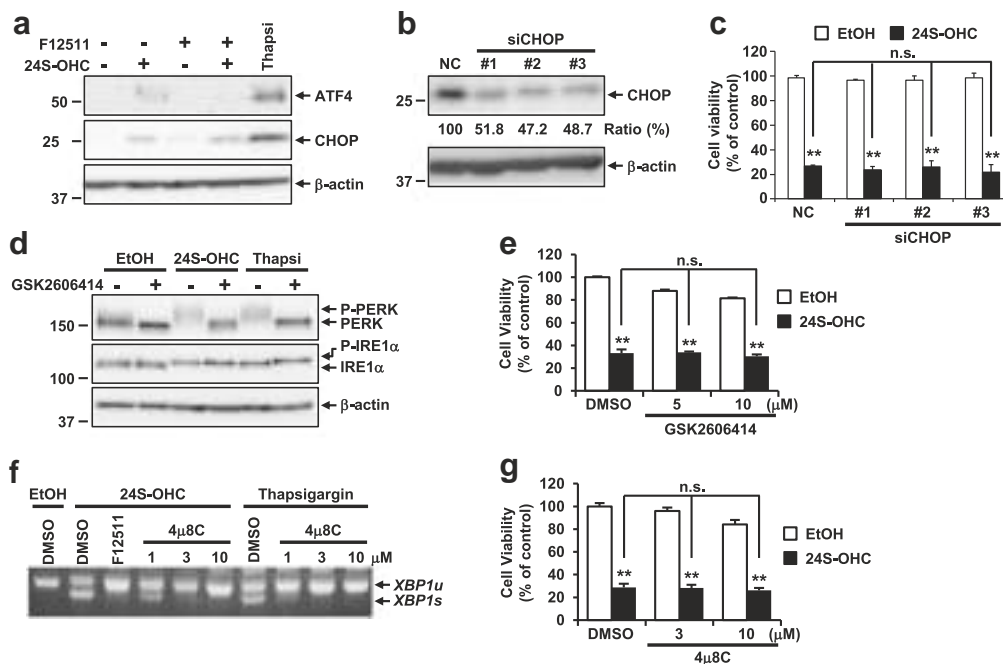


Fig. 2 PERK and IRE1-XBP1 axes were not involved in 24S-OHC-induced cell death in SH-SY5Y cells. **a** SH-SY5Y cells were treated as in Fig. 1a. Whole-cell lysates were immunoblotted with antibodies specific for ATF4, CHOP, or β -actin. **b, c** Cells were transfected with CHOP (siCHOP #1-#3) or negative control (NC) siRNA oligo for 24 h. **b** Whole-cell lysates were immunoblotted with antibodies specific for CHOP or β -actin. Relative expression levels of CHOP are shown. **c** The cells were exposed to 50 μ M 24S-OHC for 24 h. Cell viability was measured by LDH assay. ****P** < 0.01, when compared with cells treated with vehicle or among 24S-OHC-treated groups. **d** Cells were pretreated with 5 μ M GSK2606414 for 30 min then exposed to 50 μ M 24S-OHC or 3 μ M thapsigargin for 6 h. Whole-cell lysates were immunoblotted with antibodies specific for PERK, IRE1 α , or β -actin. **e** Cells were pretreated with 5 or 10 μ M GSK2606414 for 30 min then exposed to 50 μ M 24S-OHC for 24 h. Cell viability was measured by WST-8 assay. ****P** < 0.01. **f** Cells were pretreated with 5 μ M F12511 for 15 min or with 1–10 μ M 4 μ 8C for 1 h then exposed to 50 μ M 24S-OHC for 6 h or 1 μ M thapsigargin for 3 h, respectively. *XBP1* mRNAs were analyzed by RT-PCR. **g** Cells were pretreated with 3 or 10 μ M 4 μ 8C for 1 h and then exposed to 50 μ M 24S-OHC for 24 h. Cell viability was measured by WST-8 assay. ****P** < 0.01

suggesting that CHOP induction is not involved in the 24S-OHC-induced cell death machinery.

PERK, IRE1-XBP1, and IRE1-ASK1 axes were not involved in 24S-OHC-induced cell death in SH-SY5Y cells

We then evaluated the effect of the PERK inhibitor GSK2606414, the results showing that GSK2606414 treatment inhibited autophosphorylation of PERK in cells treated with either 24S-OHC or thapsigargin (Fig. 2d). As expected, 24S-OHC-induced IRE1 α phosphorylation was not inhibited by GSK2606414 treatment. Under the conditions tested, 24S-OHC-induced cell death was not suppressed by GSK2606414 (Fig. 2e), suggesting that the PERK activation was not involved in 24S-OHC-induced cell death.

We next evaluated the effects of the selective IRE1 α RNase inhibitor 8-formyl-7-hydroxy-4-methylcoumarin (4 μ 8C), results showing that 4 μ 8 C inhibited *XBP1* splicing in a concentration-dependent manner in cells treated with either 24S-OHC or thapsigargin (Fig. 2f), but that 4 μ 8C did not inhibit 24S-OHC-induced cell death (Fig. 2g). These results indicate that inhibition of IRE1 α -mediated *XBP1* splicing by 4 μ 8 C did not prevent 24S-OHC-induced cell death in SH-SY5Y cells.

We also evaluated the effect of the selective inhibitor of ASK1 (NQDI-1), p38 (SB203580), or JNK (SP600125) on 24S-OHC-induced cell death, the results showing that neither NQDI-1 nor SB203580 nor SP600125 was able to prevent 24S-OHC-induced cell death (Fig. S2A–C),

suggesting that neither ASK1 nor p38 or JNK is implicated in 24S-OHC-induced cell death.

As the small molecular chemical chaperone 4-phenylbutyric acid (4-PBA) was reported to protect against ER stress-mediated neuronal cell death by aiding in protein folding^{35,36}, we tested the effects of 4-PBA on 24S-OHC-induced cell death, finding as a result that cotreatment with 1 mM of 4-PBA significantly mitigated thapsigargin-induced cell death, but did not affect 24S-OHC-induced cell death (Fig. S2D), suggesting that the increase in ER folding capacity produced by 4-PBA was ineffective in decreasing 24S-OHC-induced cell death.

Inhibition of RIDD mitigated 24S-OHC-induced cell death in SH-SY5Y cells

We next investigated whether RIDD was implicated in 24S-OHC-induced cell death. Since RIDD targets multiple mRNA substrates^{37–39}, we evaluated the expression levels of a series of RIDD substrates including *ANGPTL3*, *BLOS1*, *COL6*, *PDGFRB*, and *SCARA3*, the results showing that the expression of all genes examined was significantly reduced in cells treated with 24S-OHC for 6 h compared to the vehicle-control condition in SH-SY5Y cells (Fig. 3a), suggesting that 24S-OHC treatment activated the RIDD pathway. Downregulation of all genes tested was inhibited by cotreatment with F12511, indicating that activation of RIDD occurred in response to ACAT1-mediated 24S-OHC esterification.

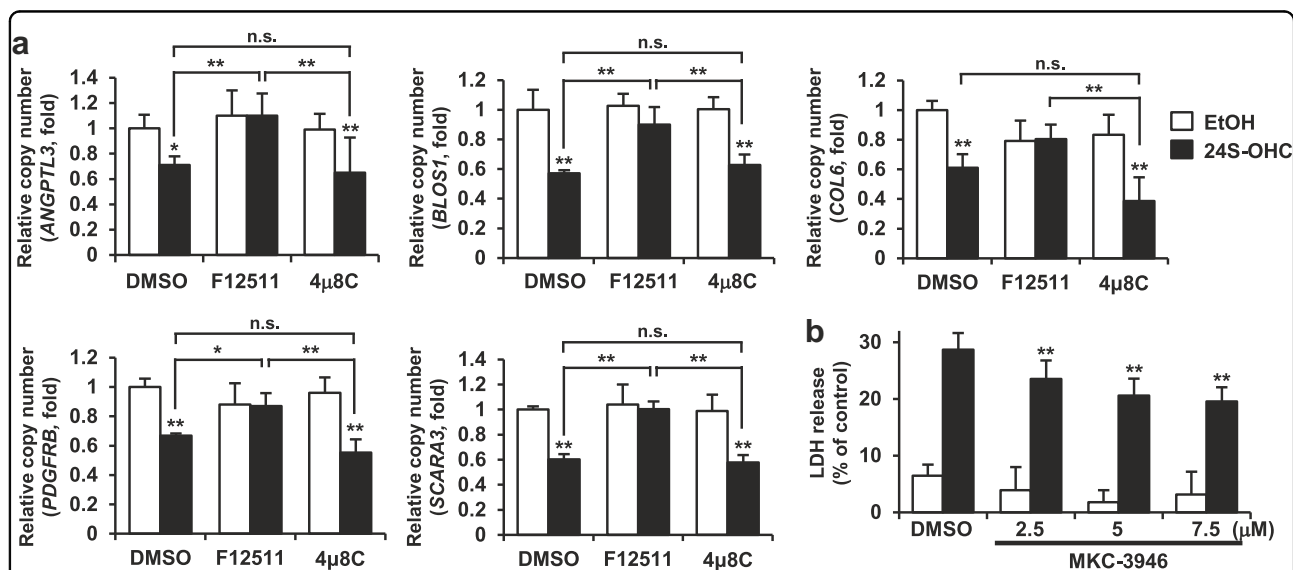


Fig. 3 Inhibition of RIDD mitigated 24S-OHC-induced cell death in SH-SY5Y cells. **a** SH-SY5Y cells were pretreated with 5 μ M F12511 for 15 min or with 10 μ M 4 μ 8 C for 1 h and then exposed to 50 μ M 24S-OHC for 6 h. The mRNA levels of RIDD target genes (*ANGPTL3*, *BLOS1*, *COL6*, *PDGFRB*, and *SCARA3*) were quantified by real-time PCR. Results are shown as normalized to levels measured for *RPL32*. * P < 0.05, ** P < 0.01, when compared with cells treated with vehicle or among 24S-OHC-treated groups. **b** Cells were pretreated with 2.5–7.5 μ M MKC-3946 for 1 h then exposed to 50 μ M 24S-OHC for 24 h. Cell viability was measured by LDH assay. ** P < 0.01, when compared with cells treated with 24S-OHC alone

We then sought to evaluate the involvement of IRE1 α -mediated RIDD in 24S-OHC-induced cell death. As it had been reported that knockdown of IRE1 α by siRNA induced cell death in SH-SY5Y cells⁴⁰, we therefore first examined the effect of 4 μ 8c on 24S-OHC-induced downregulation of RIDD substrates. Unlike the inhibitory effect of 4 μ 8C observed on IRE1 α -mediated *XBPI* splicing (Fig. 2f), 10 μ M, 4 μ 8 C did not suppress the downregulation of any gene examined in 24S-OHC-treated cells (Fig. 3a). Although other studies³⁸ reported that a high concentration of 4 μ 8 C is necessary to inhibit RIDD, we found that anything more than 15 μ M 4 μ 8 C had cytotoxic effect on SH-SY5Y cells (data not shown). We therefore chose another inhibitor of IRE1 α RNase activity, i.e., MKC-3946⁴¹, and found that MKC-3946 significantly inhibited 24S-OHC-induced cell death in a concentration-dependent manner (Fig. 3b). As expected, 7.5 μ M MKC-3946 significantly blocked the 24S-OHC-induced downregulation of *BLOS1* and *SCARA3* expression (Fig. S3). Taken together, these results indicated that IRE1 α -mediated RIDD plays an important role in the mechanism of 24S-OHC-induced neuronal cell death.

Accumulation of 24S-OHC esters induced disruption of ER membrane integrity in SH-SY5Y cells

To further examine 24S-OHC-induced ER stress in SH-SY5Y cells, we carried out morphological analysis using electron microscopy. To investigate changes in the ER structure during the early stages of 24S-OHC-induced cell death, cells were treated with 50 μ M 24S-OHC for 3 h. In contrast to the typical rough ER structures observed in EtOH-treated control cells (Fig. 4a, arrow), we observed broken-membrane ER structures in 24S-OHC-treated cells (Fig. 4a, arrowhead). We therefore assessed whether disturbance of ER membrane integrity was induced by 24S-OHC. To do this, we employed crude subcellular fractionation to sequentially extract proteins from cells in a digitonin-soluble fraction enriched for cytosolic protein and in a subsequent NP-40-soluble fraction enriched for membrane-bound organelles including ER. The results showed that in vehicle-treated cells, the cytosolic protein DJ-1 was found in the digitonin extract; we further found that all ER proteins examined were recovered in the NP-40 extract (Fig. 4b). In cells treated with 24S-OHC for 3 h, although recovered levels of ER membrane proteins (calnexin and ribophorin-1) in NP-40 extract were unchanged, recovered levels of ER luminal proteins (GRP78, ORP150, protein disulfide isomerase (PDI) and calreticulin) were reduced in the NP-40 extract, but these proteins, except calreticulin, were increased in the DJ-1-rich digitonin extract. These changes could be inhibited by cotreatment with F12511, suggesting that ER luminal proteins were released into cytosol as a consequence of 24S-OHC esterification. We also found that levels of

GRP78, ORP150, PDI, and calreticulin were increased in the digitonin extract of cells cotreated with 24S-OHC and MG132 for 6 h, indicating that these proteins were subjected to proteasomal degradation after being released into cytosol (Fig. 4c).

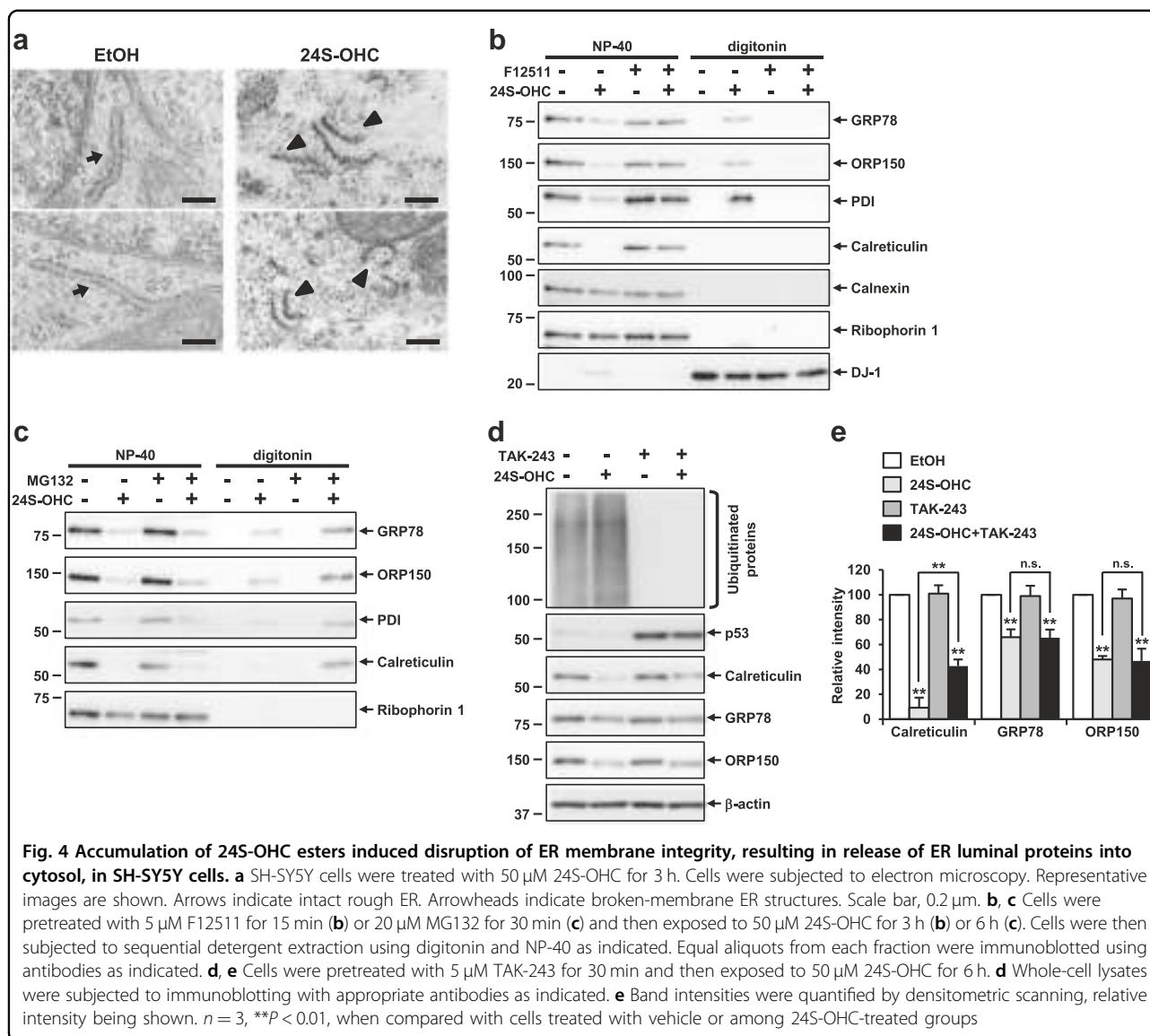
To investigate whether redistribution of ER luminal proteins to cytosol was the result of translocon-mediated retrotranslocation as ERAD substrates, we evaluated the effect of ubiquitination inhibition on 24S-OHC-induced chaperone degradation, because ubiquitination and retrotranslocation of luminal ERAD substrates have been shown to be coordinated by a membrane-embedded E3 ligase complex⁴². To do this, we used TAK-243, which targets the ubiquitin activating enzyme⁴³, as a result of which we found that protein ubiquitination was blocked, and that the degradation of p53, a well-studied ubiquitin-dependent proteasome substrate, was inhibited by TAK-243 (Fig. 4d). We further found that cotreatment with TAK-243 did not produce the same drastic inhibition of 24S-OHC-induced chaperone protein degradation (Fig. 4e) as was observed during cotreatment with MG132 (Fig. 1g), suggesting that chaperone proteins were being released into cytosol without ubiquitination.

Collectively, these results suggest that ACAT1-mediated 24S-OHC esterification caused disruption of ER membrane integrity, resulting in the release of ER luminal proteins into cytosol, followed by ubiquitin-independent proteasomal degradation of the released proteins.

Global protein synthesis was inhibited by 24S-OHC in SH-SY5Y cells

We further examined whether 24S-OHC-induced disruption of ER membrane integrity affected de novo protein synthesis. Because 24S-OHC is known to act as a ligand of liver X receptor (LXR)^{18,21}, we assessed the expression of the LXR target genes *ATP-binding cassette transporter A1 (ABCA1)* and *ABCG1*. Real-time PCR results showed that treatment for 6 h with either 24S-OHC or the synthetic LXR ligand T0901317 upregulated expression levels of *ABCA1* and *ABCG1* mRNA in a concentration-dependent manner (Fig. 5a).

Despite this observed concentration-dependent increase in *ABCG1* mRNA expression levels, however, we found that upregulation of ABCG1 protein levels was induced in cells treated with 5 μ M 24S-OHC (nontoxic concentration) but not in cells treated with 50 μ M 24S-OHC (Fig. 5b). We further found that cotreatment with 50 μ M 24S-OHC and F12511 caused ABCG1 protein levels to increase to similar extent as was observed with 5 μ M 24S-OHC, while cotreatment with 50 μ M 24S-OHC and MG132 did not induce upregulation of ABCG1 protein. These results suggested that 24S-OHC esterification suppressed ABCG1 protein upregulation not as a result of



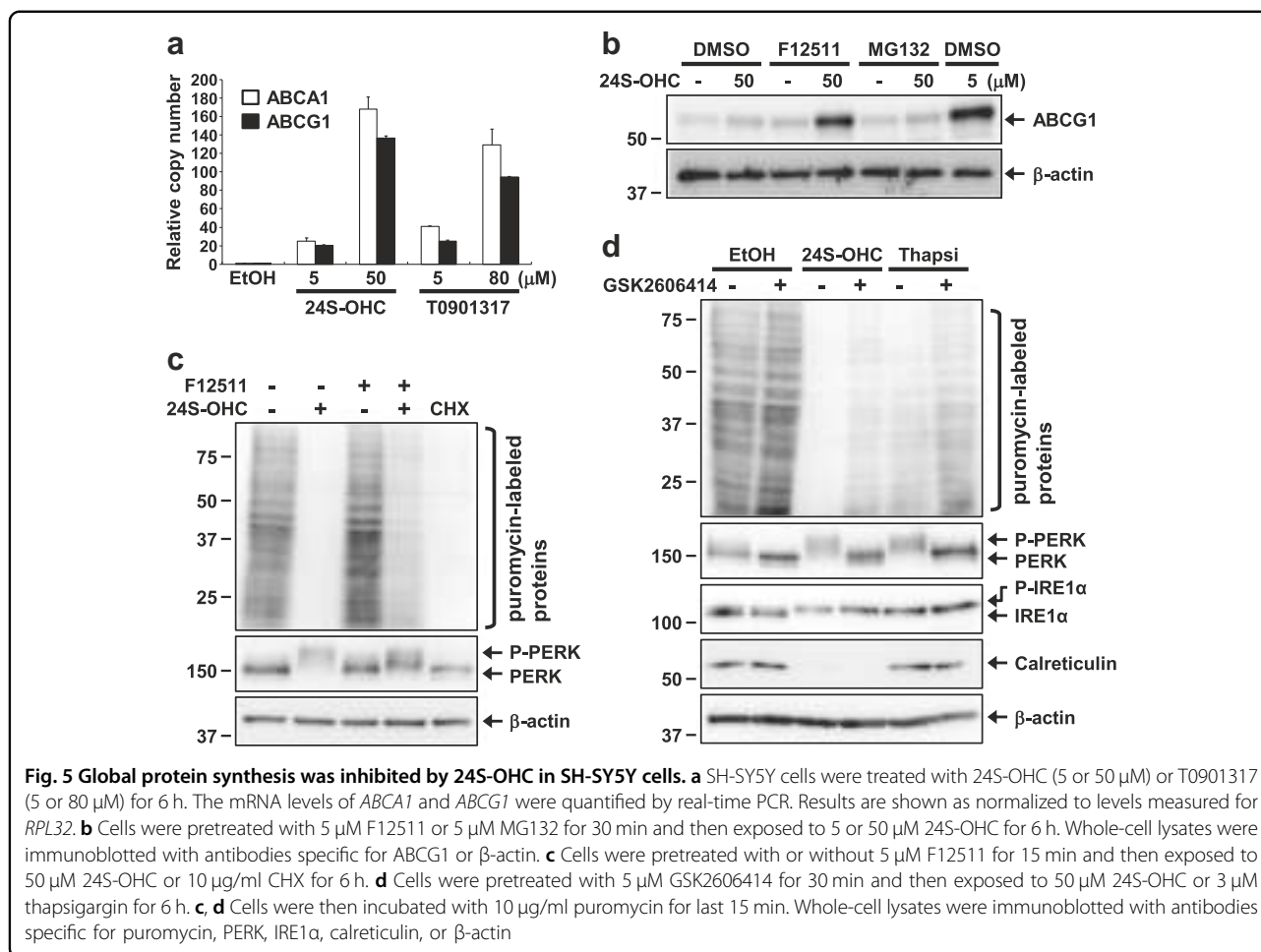
proteasomal degradation, but as a result of inhibition of de novo protein synthesis.

We then evaluated the effect of 24S-OHC esterification on global protein synthesis by using SUnSET, a non-radioactive assay method utilizing incorporation of puromycin into newly synthesized proteins and subsequent detection using anti-puromycin antibody⁴⁴. A robust decrease in puromycin-labeled proteins—not unlike that observed with the known protein synthesis inhibitor cycloheximide (CHX)—was observed in cells treated with 24S-OHC, and this decrease was found to be significantly suppressed by cotreatment with F12511 (Fig. 5c), suggesting that 24S-OHC inhibited not only ABCG1 protein synthesis but also global protein synthesis. Although 24S-OHC-induced PERK phosphorylation was completely

inhibited by GSK2606414 without affecting IRE1 α phosphorylation or the decrease in calreticulin levels that had been observed, the decrease in levels of puromycin-labeled proteins was partially suppressed by GSK2606414 (Fig. 5d), indicating that the observed 24S-OHC-induced robust decrease in protein synthesis was not only due to PERK-regulated translation attenuation.

Discussion

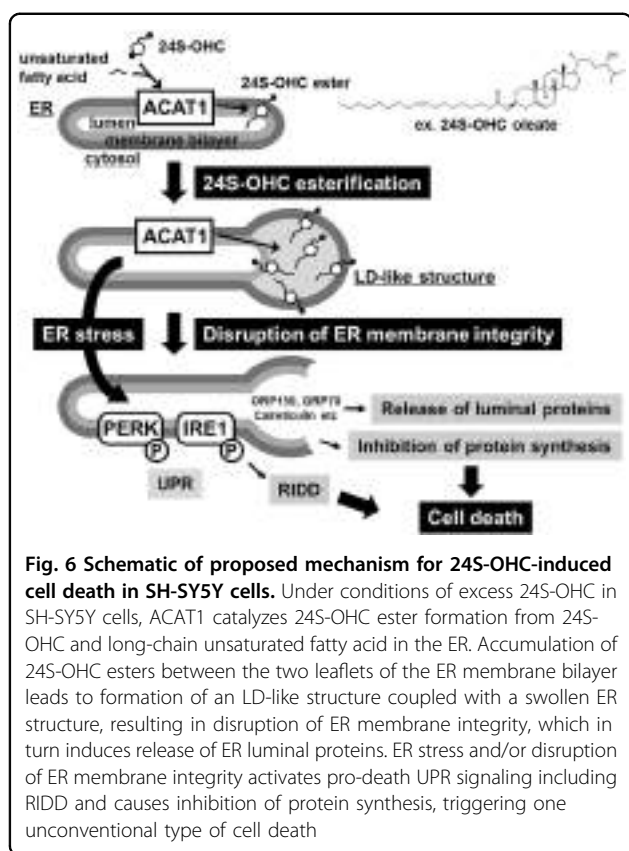
It has been indicated that an excess of lipid can induce ER stress. For example, saturated fatty acids can activate the UPR with subsequent induction of apoptosis^{13,14}. Moreover, excess cellular cholesterol can activate the UPR, resulting in induction of apoptosis in macrophages⁴⁵. In the case of oxysterol, cytotoxic oxysterols,



e.g., 7-ketocholesterol, produced by nonenzymatic auto-oxidation of cholesterol act as stressors to activate the UPR⁴⁶. In our present study, we showed that enzymatically formed oxysterol 24S-OHC also activates the UPR signaling pathway. Regarding possible mechanisms for 24S-OHC-induced UPR activation, it is thought likely that ER dysfunction due to abnormal morphological change of ER and/or decrease in protein folding capacity causes UPR activation, since our present study demonstrates that 24S-OHC treatment results in a decrease in ER chaperone proteins. As it has been known that GRP78 binds to IRE1, PERK, and ATF6, inhibiting activation of these UPR sensors in unstressed cells, and dissociates from these UPR sensors, activating the UPR during ER stress⁴⁷, it is also possible that reduction of luminal GRP78 levels might enforce UPR activation. Unlike the situation observed with conventional UPR, we found that 24S-OHC treatment resulted in insufficient activation of the pro-survival adaptive response, activating IRE1 and PERK but not ATF6 or XBP1. Regarding to pro-death UPR signaling, we found that RIDD plays an important role in the

24S-OHC-induced cell death machinery (Fig. 6). We postulate that since IRE1 inhibitor cannot by itself suppress 24S-OHC-induced ER membrane disruption, MKC-3946 may have some mild inhibitory effect on cell death.

Most conventional models of LD biogenesis have assumed that the neutral lipids including cholesteryl esters assemble into lens-like structures in the hydrophobic region of the ER membrane bilayer^{48,49}. Once the amount of neutral lipids reaches a critical mass, the nascent LD structure buds off from the ER, followed by growth to mature LDs. Based on this model, we posit that newly formed 24S-OHC esters synthesized by ER-resident ACAT1 might be packaged between the two leaflets of the ER membrane bilayer in similar fashion as would be the case with a cholesteryl esters (Fig. 6). Accumulation of 24S-OHC esters results in the formation of LD-like structures. As identified in our previous study³³, 24S-OHC esters have a hydroxyl group at position 24 in their steroid side chain (e.g., 24S-OHC oleate). More specifically, we postulate that because the 24S-OHC ester has the polar moiety of its side chain plus the nonpolar moiety



that results from combination of its sterol ring with an unsaturated fatty acid, 24S-OHC esters may possess amphipathic properties within the hydrophobic environment of the lipid bilayer. It is therefore plausible that, unlike cholesteryl esters which are entirely hydrophobic, amphipathic properties of 24S-OHC esters could present a detergent function to the ER bilayer. Indeed, electron microscopy and biochemical analysis revealed that treatment with 24S-OHC caused ER membrane integrity to be disrupted and ER luminal proteins to be subsequently released into cytosol. The possibility that some other proteins mediate 24S-OHC-induced disruption of ER membrane integrity cannot be excluded. It was interesting to note that the released ER proteins were subjected to proteasomal degradation without ubiquitination, suggesting that ubiquitin-independent degradation by the 20 S proteasome but not ubiquitin-dependent degradation by the 26 S proteasome might be responsible for degradation of the released proteins. We also found that not only ER luminal proteins but also some ER transmembrane proteins such as calnexin and ATF6 were degraded by proteasome during 24S-OHC-induced ER stress. Further studies are needed to clarify the biological mechanism for 24S-OHC-induced proteasomal degradation of ER proteins.

We also demonstrated that de novo synthesis of global protein was robustly suppressed in 24S-OHC-treated cells, and that the observed decrease in protein synthesis was only partially recovered by PERK inhibitor, suggesting that not only PERK-induced translational attenuation but also other mechanisms might be involved. Since it is well-established that global protein synthesis inhibition induces cell death, it is thought that the observed 24S-OHC-induced robust decrease in de novo protein synthesis may play an important role in the cell death machinery. Because we found that mRNA levels of LXR target genes were markedly upregulated in 50 μ M 24S-OHC-treated cells, it is unlikely that the observed robust decrease in nascent proteins was due to reduction in global transcription activity. Degradation of ER-localized mRNAs by RIDD might be partially implicated in the observed decrease in nascent proteins. Because 24S-OHC treatment caused disruption of ER membrane integrity, it is therefore plausible that protein synthesis was down-regulated due to disappearance of the scaffold for protein translation at the rough ER. There is a possibility that the weak induction levels of XBP1s, ATF4, and CHOP proteins we observed might be associated with the 24S-OHC-induced robust decrease in protein synthesis.

A growing body of experimental evidence has unveiled and characterized the existence of multiple types of cell death²⁹. In addition to apoptosis and necrosis, many nonapoptotic regulated cell death (RCD) pathways are emerging, including necroptosis (regulated necrosis), pyroptosis, parthanatos, ferroptosis, and several others. Furthermore, novel signaling pathways thought to orchestrate RCD are still being characterized. While multiple types of RCD share common morphological hallmarks and are regulated by overlapping and interconnected signaling pathways, the various modes of RCD are distinguishable to a certain degree based on features observed or inferred to exist during the various stages of the respective cell death processes^{29,50}. We have previously demonstrated that SH-SY5Y cells treated with 24S-OHC exhibited neither fragmentation of the nucleus nor caspase activation²⁸. We have also found that 24S-OHC-treated cells showed morphological changes resembling necrosis, but these did not induce ATP depletion²⁸. We might summarize the results of our current and previous findings by saying that the mode of 24S-OHC-induced cell death in SH-SY5Y cells is characterized by: (i) ACAT-mediated 24S-OHC esterification-dependency; (ii) activation of pro-death UPR signaling including RIDD; (iii) disruption of ER membrane integrity; and (iv) inhibition of protein synthesis (Fig. 6). Based on this unique combination of features, we conclude that 24S-OHC-induced cell death might be an unconventional type of RCDs. Since it has been reported that RIPK1 is a mediator of ER stress-induced apoptosis⁵¹, the

dependency with respect to RIPK1 suggests a possible connection with the downstream branch of 24S-OHC-induced cell death signaling. Moreover, we have shown that accumulation of 24S-OHC esters induces caspase-dependent apoptotic cell death in Jurkat cells or all-*trans*-retinoic acid-treated SH-SY5Y cells in which caspase-8 is expressed^{32,52}, suggesting that the executor(s) in the downstream pathway(s) of 24S-OHC-induced cell death may exhibit cell-type dependency. In studies with other oxysterols, we previously showed that 7-ketocholesterol, 7 α -OHC, 7 β -OHC, and 22R-OHC induced cell death in SH-SY5Y cells, and that this was not suppressed by ACAT inhibitor³². On the other hand, ACAT is implicated in 24(S),25-epoxycholesterol-induced apoptosis in mast cells⁵³, and in 7-ketocholesterol-induced apoptosis in macrophages⁵⁴. Since growing evidence suggests a link between accumulation of oxysterols and the pathophysiology of various diseases^{55,56}, further investigations will be required to address the features and specificities of 24S-OHC-induced cell death in oxysterol-induced cell death. In conclusion, our present study revealed that abnormal ER morphological change with disruption of ER membrane integrity is crucial for triggering of pro-death signaling under conditions in which there is accumulation of 24S-OHC esters by ACAT1.

Materials and methods

Materials

24S-OHC was synthesized as we previously reported⁵⁷, this has been dissolved in EtOH (Wako, Osaka, Japan) and stored at -20°C . F12511 ACAT inhibitor was the generous gift of Dr. Ta-Yuan Chang (Geisel School of Medicine at Dartmouth, Hanover, NH, USA). Thapsigargin, MG132, and CHX were purchased from Wako (Osaka, Japan). Nec-1, SP600125, and 4-PBA were from Sigma-Aldrich (St. Louis, MO, USA). 4 μ 8C and MKC-3946 were from Merck Millipore (Darmstadt, Germany). GSK2606414, T0901317, NQDI-1, and SB203580 were from Cayman Chemical (Ann Arbor, MI, USA). TAK-243 was from Active Biochem (Hong Kong, China). Thapsigargin, MG132, Nec-1, GSK2606414, 4 μ 8 C, T0901317, TAK-243, CHX, NQDI-1, SB203580, and SP600125 were dissolved in dimethyl sulfoxide (DMSO, Wako). 4-PBA was dissolved in 1 M NaOH. The following antibodies were from commercial sources: IRE1 α (Cat# 3294), PERK (Cat# 3192), ATF4 (Cat# 11815), and CHOP (Cat# 2895) were all from Cell Signaling (Danvers, MA, USA); ATF6 α (Cat# 73500) was from BioAcademia (Osaka, Japan); β -actin (Cat# A5441) was from Sigma-Aldrich. XBP1 (Cat# 24168-1-AP) was from Proteintech (Chicago, IL, USA); GRP78 (Cat# 610979), calreticulin (Cat# 612136), calnexin (Cat# 610523), and (PDI Cat# 610946) were from BD Biosciences (Franklin Lakes, NJ, USA); ORP150 (Cat# 10301) was from IBL (Gunma, Japan);

ribophorin 1 (Cat# sc-12614), ubiquitin (Cat# sc-8017), and DJ-1 (Cat# ab4150) were from Abcam (Cambridge, UK); p53 (Cat# OP43) and puromycin (Cat# MABE343) were from Merck Millipore; ABCG1 (Cat# NB400-132) was from Novus Biologicals (Littleton, CO, USA). All other chemicals, of analytical grade, were obtained from Sigma-Aldrich or Wako.

Cell lines and cell culture

Human neuroblastoma cells from the SH-SY5Y cell line were purchased from American Type Culture Collection (Manassas, VA, USA) or European Collection of Cell Cultures (Salisbury, UK). Cells were routinely maintained in the Dulbecco's Modified Eagle's Medium/Nutrient Mixture Ham's F-12 (Thermo Fisher Scientific, Waltham, MA, USA), which contained 10% heat-inactivated fetal bovine serum (Sigma-Aldrich), and antibiotics (100 U/ml penicillin, 100 $\mu\text{g}/\text{ml}$ streptomycin; Thermo Fisher Scientific). Cells were grown at 37°C under an atmosphere of 95% air and 5% CO_2 .

Cell treatment

To elucidate the mechanism of 24S-OHC-induced cell death, SH-SY5Y cells were treated with 50 μM 24S-OHC for the indicated period (final concentration of EtOH in the medium was 0.5%). Cells were also exposed to 3 μM thapsigargin for the indicated period as positive controls. EtOH or DMSO was used as a vehicle for control treatments. To evaluate the effect of various inhibitors, cells were pretreated with 5 μM F12511 for 15 min, or with 20 μM MG132, or with 5 μM TAK-243 for 30 min, before further treatment. Cells were also pretreated with variable concentrations of GSK2606414, 4 μ 8 C, MKC-3946, NQDI-1, SB203580, or SP600125 for 1 h, or 4-PBA for 24 h, before further treatment.

Immunoblotting

Whole-cell extract was prepared as described previously⁵⁸. Briefly, cells were suspended in lysis buffer (150 mM NaCl, 50 mM Tris-HCl at pH 7.5, 1% NP-40, 2 mM EDTA) containing PhosSTOP (Roche Applied Science, Mannheim, Germany) and a protease inhibitor cocktail (Nacalai Tesque, Kyoto, Japan) at 4°C for 30 min. Nuclei and unlysed cellular debris were removed by centrifugation at $13,000\times g$ for 5 min. Protein samples were subjected to SDS-PAGE and were transferred to a PVDF membrane for 1 h at 100 V. Immunoblotting with appropriate antibodies was visualized with enhanced chemiluminescence (Millipore, Billerica, MA, USA).

XBP1-splicing assay

The total RNA isolation and real-time PCR were conducted as described previously²⁰. Briefly, the total RNA was isolated by using Tripure Isolation Reagent (Roche

Applied Science) along with chloroform according to the manufacturer's instructions. Synthesis of cDNA was carried out using a PrimeScriptTM RT Master Mix (Takara Bio, Shiga, Japan) according to the manufacturer's instruction. The *XBPI*-splicing assay used human *XBPI*-specific primers that amplified and spliced (-26 nt) and unspliced *XBPI* mRNA (forward 5'-TTACGAGAGA AACTCATGGCC-3', reverse 5'-GGGTCCAAGTTGTC CAGAATGC-3'). PCR products were analyzed on a 3% agarose gel.

Determination of cell viability

For determination of cell viability, WST-8 assay and lactate dehydrogenase (LDH) assay were used. WST-8 assay was performed using Cell Counting Kit-8 according to the manufacturer's instructions (Dojindo, Kumamoto, Japan). LDH activity assay was performed as described previously³⁰. The data are expressed as the percentage of total LDH activity, after subtraction of background determined from the culture medium alone.

Knockdown of CHOP by small interfering RNA

Double-stranded small interfering RNAs (siRNA) targeting human *CHOP* were obtained from Thermo Fisher Scientific. The sense and antisense of siRNA specific for *CHOP* used here were as follows: #1: 5'-UAGCUGAAG AGAAUGAACGGCUCAA-3' and 5'-UUGAGCCGUUC AUUCUCUUCAGCUA-3'; #2: 5'-GCAAGAGGUCCUG UCUUCAGAUGAA-3' and 5'-UUCAUCUGAAGACAG GACCUCUUGC-3'; #3: 5'-UAGAGGCGACUCGCCGA GCUCUGAU-3' and 5'-AUCAGAGCUCGGCGAGUCG CCUCUA-3'. Stealth RNAi-negative control (NC) with medium GC content (48%) was obtained from Thermo Fisher Scientific. The siRNAs were transfected into SH-SY5Y cells at a concentration of 100pmol/well by Lipofectamine RNAiMAX (Thermo Fisher Scientific) for 24 h before further experiments. To confirm knockdown efficiency for *CHOP*, expression levels of protein were analyzed by immunoblotting analysis.

Real-time PCR

Quantitative detection of differentially expressed genes was performed with the 7900HT Fast Real-Time PCR system (Applied Biosystems, Foster City, CA, USA) and SYBR Green Master Mix (Thermo Fisher Scientific) under the following condition: one cycle of 95 °C for 10 min followed by 40 cycles of 95 °C for 15 s and 60 °C for 1 min. Human *RPL32* (ribosomal protein L32) was used for the normalization of each reaction. The following primers (Thermo Fisher Scientific) were used: human *ANGPTL3* forward 5'-ACATGATGGCATTCTGCTGA-3', reverse 5'-GAGTT GCTGGGTCTGATGGCA-3'; human *BLOS1* forward 5'-G AGGAGGCGAGAGGCTATCA-3', reverse 5'-ATCCCCA ATTTCTTGAGTGC-3'; human *COL6* forward 5'-CA

ACGACATTGCACCCCGAG-3', reverse 5'-CCGCACTT GCATTCACAGCA-3'; human *PDGFRB* forward 5'-CAGC AAGGACACCATGCGGC-3', reverse 5'-TGGGACATCC GTTCCCACAC-3'; human *SCARA3* forward 5'-ACGAGG ACATGCCGACCTTC-3', reverse 5'-TTCAGGGCTTTC GGATCCAGG-3'; human *RPL32* forward 5'-CCCCTT GTGAAGCCCAAGA-3', reverse 5'-TGACTGGTGCCGG ATGAAC-3'.

Electron microscopy analysis

For electron microscopy, ultrathin sections were prepared as described previously³³, and were subjected to TEM observation (JEM-1200 EX, JEOL) at Hanaichi Ultrastructure Research Institute (Okazaki, Japan).

Subcellular fractionation

Crude cytosolic and membrane/organelle fractions were isolated by sequential detergent extraction as described previously^{59,60}. Equal aliquots from each fractions were analyzed for immunoblotting.

Measurement of protein synthesis by SUnSET puromycin end-labeling assay

Following treatment, cells were incubated with 10 µg/ml puromycin for 15 min prior to cell lysis. Whole-cell lysates were then subjected to immunoblotting. An anti-puromycin antibody was used to detect levels of puromycin-labeled proteins.

Statistical analysis

The data are reported as mean ± SD of at least three independent experiments unless otherwise indicated. The statistical significance of the difference between the determinations was calculated by analysis of variance using ANOVA, Tukey–Kramer multiple comparisons test. The difference was considered significant when the *P*-value was <0.05.

Acknowledgements

We thank Dr. Ta-Yuan Chang (Geisel School of Medicine at Dartmouth, NH, USA) and Kowa Co. Ltd (Aichi, Japan) for providing valuable reagents. We also thank Norie Kato for research support and also thank Gerry Peters (JTT K.K., Takatsuki, Japan) for his careful editing of the paper. This work was supported in part by JSPS KAKENHI Grant-in-Aid for Scientific Research (C) 16K08254 and 19K07093 to Y.U., 16K00882 to N.N., and the MEXT-Supported Program for the Strategic Research Foundation at Private Universities in Japan for years 2012–2016 and 2015–2019.

Conflict of interest

The authors declare that they have no conflict of interest.

Publisher's note

Springer Nature remains neutral with regard to jurisdictional claims in published maps and institutional affiliations.

The online version of this article (<https://doi.org/10.1038/s41420-019-0192-4>) contains supplementary material, which is available to authorized users.

Received: 1 February 2019 Revised: 20 May 2019 Accepted: 30 May 2019
 Published online: 15 July 2019

References

- Hetz, C. The unfolded protein response: controlling cell fate decisions under ER stress and beyond. *Nat. Rev. Mol. Cell Biol.* **13**, 89–102 (2012).
- Moore, K. A. & Hollien, J. The unfolded protein response in secretory cell function. *Annu. Rev. Genet.* **46**, 165–183 (2012).
- Kim, I., Xu, W. & Reed, J. C. Cell death and endoplasmic reticulum stress: disease relevance and therapeutic opportunities. *Nat. Rev. Drug Discov.* **7**, 1013–1030 (2008).
- Tabas, I. & Ron, D. Integrating the mechanisms of apoptosis induced by endoplasmic reticulum stress. *Nat. Cell Biol.* **13**, 184–190 (2011).
- Sano, R. & Reed, J. C. ER stress-induced cell death mechanisms. *Biochim. Biophys. Acta* **1833**, 3460–3470 (2013).
- Iurlaro, R. & Munoz-Pinedo, C. Cell death induced by endoplasmic reticulum stress. *FEBS J.* **283**, 2640–2652 (2016).
- Hollien, J. & Weissman, J. S. Decay of endoplasmic reticulum-localized mRNAs during the unfolded protein response. *Science* **313**, 104–107 (2006).
- Hetz, C., Chevet, E. & Harding, H. P. Targeting the unfolded protein response in disease. *Nat. Rev. Drug Discov.* **12**, 703–719 (2013).
- Maurel, M., Chevet, E., Tavernier, J. & Gerlo, S. Getting RIDD of RNA: IRE1 in cell fate regulation. *Trends Biochem. Sci.* **39**, 245–254 (2014).
- Tam, A. B., Koong, A. C. & Niwa, M. Ire1 has distinct catalytic mechanisms for XBP1/HAC1 splicing and RIDD. *Cell Rep.* **9**, 850–858 (2014).
- Liu, Z., Lv, Y., Zhao, N., Guan, G. & Wang, J. Protein kinase R-like ER kinase and its role in endoplasmic reticulum stress-decided cell fate. *Cell Death Dis.* **6**, e1822 (2015).
- Oyadomari, S. & Mori, M. Roles of CHOP/GADD153 in endoplasmic reticulum stress. *Cell Death Differ.* **11**, 381–389 (2004).
- Ariyama, H., Kono, N., Matsuda, S., Inoue, T. & Arai, H. Decrease in membrane phospholipid unsaturation induces unfolded protein response. *J. Biol. Chem.* **285**, 22027–22035 (2010).
- Halbleib, K. et al. Activation of the unfolded protein response by lipid bilayer stress. *Mol. Cell* **67**, 673–684 e8 (2017).
- Noguchi, N., Saito, Y. & Urano, Y. Diverse functions of 24(S)-hydroxycholesterol in the brain. *Biochem. Biophys. Res. Commun.* **446**, 692–696 (2014).
- Dietschy, J. M. Central nervous system: cholesterol turnover, brain development and neurodegeneration. *J. Biol. Chem.* **390**, 287–293 (2009).
- Lütjohann, D. et al. Cholesterol homeostasis in human brain: evidence for an age-dependent flux of 24S-hydroxycholesterol from the brain into the circulation. *Proc. Natl Acad. Sci. USA* **93**, 9799–9804 (1996).
- Russell, D. W., Halford, R. W., Ramirez, D. M., Shah, R. & Kottli, T. Cholesterol 24-hydroxylase: an enzyme of cholesterol turnover in the brain. *Annu. Rev. Biochem.* **78**, 1017–1040 (2009).
- Jeitner, T. M., Voloshyna, I. & Reiss, A. B. Oxysterol derivatives of cholesterol in neurodegenerative disorders. *Curr. Med. Chem.* **18**, 1515–1525 (2011).
- Urano, Y., Ochiai, S. & Noguchi, N. Suppression of amyloid-beta production by 24S-hydroxycholesterol via inhibition of intracellular amyloid precursor protein trafficking. *FASEB J.* **27**, 4305–4315 (2013).
- Okabe, A. et al. Adaptive response induced by 24S-hydroxycholesterol through liver X receptor pathway reduce 7-ketocholesterol-caused neuronal cell death. *Redox Biol.* **2**, 28–35 (2014).
- Noguchi, N., Urano, Y., Takabe, W. & Saito, Y. New aspects of 24(S)-hydroxycholesterol in modulating neuronal cell death. *Free Radic. Biol. Med.* **87**, 366–372 (2015).
- Sun, M. Y. et al. 24(S)-Hydroxycholesterol as a modulator of neuronal signaling and survival. *Neuroscientist* **22**, 132–144 (2016).
- Lütjohann, D. et al. Plasma 24S-hydroxycholesterol (cerebrosterol) is increased in Alzheimer and vascular demented patients. *J. Lipid Res.* **41**, 195–198 (2000).
- Shafaati, M., Solomon, A., Kivipelto, M., Björkhem, I. & Leoni, V. Levels of ApoE in cerebrospinal fluid are correlated with Tau and 24S-hydroxycholesterol in patients with cognitive disorders. *Neurosci. Lett.* **425**, 78–82 (2007).
- Björkhem, I. et al. Oxysterols and Parkinson's disease: evidence that levels of 24S-hydroxycholesterol in cerebrospinal fluid correlates with the duration of the disease. *Neurosci. Lett.* **555**, 102–105 (2013).
- Kölsch, H., Lütjohann, D., Tulke, A., Björkhem, I. & Rao, M. L. The neurotoxic effect of 24-hydroxycholesterol on SH-SY5Y human neuroblastoma cells. *Brain Res.* **818**, 171–175 (1999).
- Yamanaka, K., Saito, Y., Yamamori, T., Urano, Y. & Noguchi, N. 24(S)-hydroxycholesterol induces neuronal cell death through necroptosis, a form of programmed necrosis. *J. Biol. Chem.* **286**, 24666–24673 (2011).
- Galluzzi, L. et al. Molecular mechanisms of cell death: recommendations of the Nomenclature Committee on Cell Death. *Cell Death Differ.* **25**, 486–541 (2018).
- Vo, D. K., Urano, Y., Takabe, W., Saito, Y. & Noguchi, N. 24(S)-Hydroxycholesterol induces RIPK1-dependent but MLKL-independent cell death in the absence of caspase-8. *Steroids* **99**, 230–237 (2015).
- Chang, T. Y., Li, B. L., Chang, C. C. & Urano, Y. Acyl-coenzyme A: cholesterol acyltransferases. *Am. J. Physiol. Endocrinol. Metab.* **297**, E1–E9 (2009).
- Yamanaka, K., Urano, Y., Takabe, W., Saito, Y. & Noguchi, N. Induction of apoptosis and necroptosis by 24(S)-hydroxycholesterol is dependent on activity of acyl-CoA:cholesterol acyltransferase 1. *Cell Death Dis.* **5**, e990 (2014).
- Takabe, W. et al. Esterification of 24S-OHC induces formation of atypical lipid droplet-like structures, leading to neuronal cell death. *J. Lipid Res.* **57**, 2005–2014 (2016).
- Thuerauf, D. J., Morrison, L. E., Hoover, H. & Glembotski, C. C. Coordination of ATF6-mediated transcription and ATF6 degradation by a domain that is shared with the viral transcription factor, VP16. *J. Biol. Chem.* **277**, 20734–20739 (2002).
- Marwarha, G., Dasari, B. & Ghribi, O. Endoplasmic reticulum stress-induced CHOP activation mediates the down-regulation of leptin in human neuroblastoma SH-SY5Y cells treated with the oxysterol 27-hydroxycholesterol. *Cell. Signal.* **24**, 484–492 (2012).
- Zamarbide, M. et al. Phenyl acyl acids attenuate the unfolded protein response in tunicamycin-treated neuroblastoma cells. *PLoS ONE* **8**, e71082 (2013).
- Hollien, J. et al. Regulated Ire1-dependent decay of messenger RNAs in mammalian cells. *J. Cell Biol.* **186**, 323–331 (2009).
- Cross, B. C. et al. The molecular basis for selective inhibition of unconventional mRNA splicing by an IRE1-binding small molecule. *Proc. Natl Acad. Sci. USA* **109**, E869–E878 (2012).
- So, J. S. et al. Silencing of lipid metabolism genes through IRE1alpha-mediated mRNA decay lowers plasma lipids in mice. *Cell Metab.* **16**, 487–499 (2012).
- Son, S. M., Byun, J., Roh, S. E., Kim, S. J. & Mook-Jung, I. Reduced IRE1alpha mediates apoptotic cell death by disrupting calcium homeostasis via the InsP3 receptor. *Cell Death Dis.* **5**, e1188 (2014).
- Mimura, N. et al. Blockade of XBP1 splicing by inhibition of IRE1alpha is a promising therapeutic option in multiple myeloma. *Blood* **119**, 5772–5781 (2012).
- Ruggiano, A., Foresti, O. & Carvalho, P. Quality control: ER-associated degradation: protein quality control and beyond. *J. Cell Biol.* **204**, 869–879 (2014).
- Hyer, M. L. et al. A small-molecule inhibitor of the ubiquitin activating enzyme for cancer treatment. *Nat. Med.* **24**, 186–193 (2018).
- Schmidt, E. K., Clavarino, G., Ceppi, M. & Pierre, P. SUNSET, a nonradioactive method to monitor protein synthesis. *Nat. Methods* **6**, 275–277 (2009).
- Feng, B. et al. The endoplasmic reticulum is the site of cholesterol-induced cytotoxicity in macrophages. *Nat. Cell Biol.* **5**, 781–792 (2003).
- Pedrucci, E. et al. NAD(P)H oxidase Nox-4 mediates 7-ketocholesterol-induced endoplasmic reticulum stress and apoptosis in human aortic smooth muscle cells. *Mol. Cell Biol.* **24**, 10703–10717 (2004).
- Shen, J., Chen, X., Hendershot, L. & Prywes, R. ER stress regulation of ATF6 localization by dissociation of BIP/GRP78 binding and unmasking of Golgi localization signals. *Dev. Cell* **3**, 99–111 (2002).
- Walther, T. C. & Farese, R. V. Jr. Lipid droplets and cellular lipid metabolism. *Annu. Rev. Biochem.* **81**, 687–714 (2012).
- Ohsaki, Y. et al. Biogenesis of cytoplasmic lipid droplets: from the lipid ester globule in the membrane to the visible structure. *Biochim. Biophys. Acta* **1791**, 399–407 (2009).
- Vanden Berghe, T., Linkermann, A., Jouan-Lanhouet, S., Walczak, H. & Vandenabeele, P. Regulated necrosis: the expanding network of non-apoptotic cell death pathways. *Nat. Rev. Mol. Cell Biol.* **15**, 135–147 (2014).
- Estornes, Y. et al. RIPK1 promotes death receptor-independent caspase-8-mediated apoptosis under unresolved ER stress conditions. *Cell Death Dis.* **5**, e1555 (2014).

52. Nakazawa, T. et al. Effect of vitamin E on 24(S)-hydroxycholesterol-induced necroptosis-like cell death and apoptosis. *J. Steroid Biochem. Mol. Biol.* **169**, 69–76 (2017).
53. Fukunaga, M. et al. Mast cell death induced by 24(S),25-epoxycholesterol. *Exp. Cell Res.* **316**, 3272–3281 (2010).
54. Freeman, N. E. et al. Acyl-coenzyme A:cholesterol acyltransferase promotes oxidized LDL/oxysterol-induced apoptosis in macrophages. *J. Lipid Res.* **46**, 1933–1943 (2005).
55. Poli, G., Biasi, F. & Leonarduzzi, G. Oxysterols in the pathogenesis of major chronic diseases. *Redox Biol.* **1**, 125–130 (2013).
56. Luu, W., Sharpe, L. J., Capell-Hattam, I., Gelissen, I. C. & Brown, A. J. Oxysterols: old tale, new twists. *Annu. Rev. Pharmacol. Toxicol.* **56**, 447–467 (2016).
57. Shibuya, K. et al. Synthesis of 24(S)-hydroxycholesterol esters responsible for the induction of neuronal cell death. *Bioorg. Med. Chem.* **24**, 2559–2566 (2016).
58. Kotani, R., Urano, Y., Sugimoto, H. & Noguchi, N. Decrease of amyloid- β levels by curcumin derivative via modulation of amyloid- β protein precursor trafficking. *J. Alzheimers Dis.* **56**, 529–542 (2017).
59. Holden, P. & Horton, W. A. Crude subcellular fractionation of cultured mammalian cell lines. *BMC Res. Notes* **2**, 243 (2009).
60. Urano, Y. et al. 6-Hydroxydopamine induces secretion of PARK7/DJ-1 via autophagy-based unconventional secretory pathway. *Autophagy* **14**, 1943–1958 (2018).

6-Hydroxydopamine induces secretion of PARK7/DJ-1 via autophagy-based unconventional secretory pathway

Yasuomi Urano, Chinatsu Mori, Ayano Fuji, Keito Konno, Takayuki Yamamoto, Shohei Yashirogi, Mayu Ando, Yoshiro Saito, and Noriko Noguchi

Department of Medical Life Systems, Faculty of Life and Medical Sciences, Doshisha University, Kyoto, Japan

ABSTRACT

PARK7/DJ-1 is a Parkinson disease- and cancer-associated protein that functions as a multifunctional protein involved in gene transcription regulation and anti-oxidative defense. Although PARK7 lacks the secretory signal sequence, it is secreted and plays important physiological and pathophysiological roles. Whereas secretory proteins that lack the endoplasmic reticulum-targeting signal sequence are secreted from cells by way of what is called the unconventional secretion mechanism, the specific processes responsible for causing PARK7 to be secreted across the plasma membrane have remained unclear. In the present study, we found that PARK7 secretion was increased by treatment with 6-OHDA via the unconventional secretory pathway in human neuroblastoma SH-SY5Y cells and MEF cells. We also found that 6-OHDA-induced PARK7 secretion was suppressed in *Atg5*-, *Atg9*-, or *Atg16l1*-deficient MEF cells or ATG16L1 knockdown SH-SY5Y cells, indicating that the autophagy-based unconventional secretory pathway is involved in PARK7 secretion. We moreover observed that 6-OHDA-derived electrophilic quinone induced oxidative stress as indicated by a decrease in glutathione levels, and that this was suppressed by pretreatment with antioxidant NAC. We further found that NAC treatment suppressed autophagy and PARK7 secretion. We also observed that 6-OHDA-induced autophagy was associated with activation of AMPK and ULK1 via a pathway which was independent of MTOR. Collectively these results suggest that electrophilic 6-OHDA quinone enhances oxidative stress, and that this is followed by AMPK-ULK1 pathway activation and induction of secretory autophagy to produce unconventional secretion of PARK7.

Abbreviations: 6-OHDA: 6-hydroxydopamine; AMPK: AMP-activated protein kinase; ATG: autophagy related; CAV1: caveolin 1; ER: endoplasmic reticulum; FN1: fibronectin 1; GSH: glutathione; IDE: insulin degrading enzyme; IL: interleukin; LDH: lactate dehydrogenase; MAP1LC3B/LC3B: microtubule associated protein 1 light chain 3 beta; MEF: mouse embryonic fibroblast; MTOR: mechanistic target of rapamycin kinase; NAC: N-acetyl-L-cysteine; PARK7/DJ-1: Parkinsonism associated deglycase; PD: Parkinson disease; RPS6KB1/p70S6K: ribosomal protein S6 kinase B1; RPN1: ribophorin I; ROS: reactive oxygen species; ULK1: unc-51 like autophagy activating kinase 1; WT: wild-type

ARTICLE HISTORY

Received 17 May 2017
Revised 12 June 2018
Accepted 19 June 2018

KEYWORDS

AMPK; oxidative stress; PARK7/DJ-1; parkinson disease; secretory autophagy; unconventional secretion

Introduction

Most secretory proteins have a signal sequence at the N-terminus which allows them to be transported from the endoplasmic reticulum (ER) to the Golgi and exported from the cell via the conventional secretion mechanism. There are a smaller number of proteins that lack the ER-targeting signal sequence which are secreted from the cell by what is referred to as the unconventional secretion mechanism [1–3]. Unconventionally secreted proteins include DBI (diazepam binding inhibitor, acyl-CoA binding protein), IL1B (interleukin 1 beta), IL18 (interleukin 18), HMGB1 (high mobility group box 1), and FGF2 (fibroblast growth factor 2) [4–7]. Although it is known that these unconventionally secreted proteins are released from the cell via an ER-/Golgi-independent pathway, the specific mechanism by which the soluble protein is able to

translocate across the hydrophobic plasma membrane still remains to be discussed. Multiple pathways have been proposed as possible routes by which such unconventional secretion might be accomplished, these proposed routes including secretory lysosomes, plasma membrane shedding, exosome derived from multivesicular bodies, and secretory autophagy [1–3,8]. Because some of the proteins that are secreted via the unconventional secretory pathway play important extracellular functional roles in developmental processes and inflammation, the unconventional secretion mechanism is being studied extensively.

PARK7/DJ-1 (Parkinsonism associated deglycase) was initially identified as an oncoprotein that cooperates with Ras to promote cell transformation [9]. PARK7 has been implicated as a protein encoded by one of the causative genes (*PARK7*) in a familial form of Parkinson disease (PD) [10]. It has also been suggested that PARK7 is related to a

sporadic form of PD [11,12]. Elevated levels of an oxidized form of PARK7 (oxPARK7) are observed in erythrocytes of PD patients at early stages [11]. oxPARK7 is also observed in the brains of human PD patients and animal PD models [12]. PARK7 is a multifunctional protein involved in several molecular processes such as gene transcription regulation, protein stabilization, and anti-oxidative defense [13,14]. Overexpression of PARK7 can protect dopaminergic neurons against several types of oxidative stress by increasing cellular glutathione (GSH) levels [15]. Knockdown of PARK7 increases susceptibility to oxidative stress [15,16]. Human PARK7 has three cysteine residues at amino acid numbers 46, 53, and 106, and undergoes preferential oxidation at position 106 (Cys106) under oxidative stress [17,18]. Replacement of Cys106 with alanine, serine, or aspartic acid causes PARK7 to lose its anti-oxidative properties.

PARK7 is localized in the cytoplasm and the nucleus; it has also been shown that some PARK7 is localized in the mitochondria [9,10,19,20]. Several lines of evidence suggest that PARK7 is secreted from cells into the circulation despite the fact that PARK7 lacks a secretory signal sequence [21–29]. Increase in PARK7 secretion into serum or plasma has been observed in patients with breast cancer, melanoma, stroke, familial amyloid polyneuropathy, and PD [21–27]. There have been conflicting reports of both increase [28] and decrease [29] in the amount of PARK7 in cerebrospinal fluid in sporadic PD patients as compared with control groups. Secreted PARK7 plays important physiological and pathophysiological roles which include involvement in anti-oxidative effects [30], extracellular signaling between neighboring neuronal cells [31], angiogenic and osteogenic factors [32], and degradation of aggregated protein [26]. Such findings indicate that PARK7 secretion may be implicated in the etiology and/or progression of diseases such as PD and cancer, possibly making it suitable for use as a biomarker. Despite the considerable number of such findings, however, it remains unclear how cytosolic PARK7 protein is able to translocate across the plasma membrane.

In our present study, to investigate the molecular mechanism of PARK7 secretion, we use 6-hydroxydopamine (6-OHDA), which is a catecholaminergic neurotoxin commonly used to generate experimental models for PD *in vivo* and *in vitro* [33]. As a result of our study, we find that PARK7 secretion is increased by treatment with 6-OHDA via the unconventional secretory pathway in human neuroblastoma SH-SY5Y cells and mouse embryonic fibroblast (MEF) cells. We demonstrate that 6-OHDA induces oxidative stress as indicated by a decrease in GSH levels, resulting in induction of macroautophagy/autophagy. We further show that 6-OHDA-induced autophagy is associated with activation of AMP-activated protein kinase (AMPK) and its downstream effector ULK1 (unc-51 like autophagy activating kinase 1) and that this occurs via a pathway that is independent of MTOR (mechanistic target of rapamycin kinase). We conclude that AMPK-ULK1-mediated secretory autophagy plays an important role in the unconventional secretion of PARK7.

Results

PARK7 is secreted under non-stress conditions in SH-SY5Y cells

To assess PARK7 secretion from human neuroblastoma SH-SY5Y cells, cells were cultured in serum-free medium for 0–6 h to prevent contamination by serum protein. As controls, FN1 (fibronectin 1) was used as a protein marker secreted via the conventional pathway and RPN1 (ribophorin I) was used as a cell resident protein. Our results showed that PARK7 was secreted in a time-dependent manner similar to the observed secretion of FN1 control, and that RPN1 was present only in the cell lysate fraction (Figure 1(A and B)). Evaluation was carried out to determine whether LDH (lactate dehydrogenase), an enzyme normally found only in the cytoplasm, was being released from the cell under the conditions tested, as a result of which it was found based on the small amount of LDH released that the PARK7 secretion observed was not due to plasma membrane leakage (Figure 1(B)). To evaluate whether PARK7 secretion was mediated by the conventional ER-/Golgi-dependent secretion mechanism, cells were treated with brefeldin A, an inhibitor of ER-Golgi transport, as a result of which it was found that treatment with brefeldin A inhibited FN1 secretion but not PARK7 secretion (Figure 1(C), suggesting that the conventional secretory pathway was not involved in PARK7 secretion. As previously reported [9,10], most of PARK7 was found to be in the cytosolic protein-enriched fraction obtained by subcellular fractionation (Figure 1(D)), supporting the idea that PARK7 was secreted via an ER-/Golgi-independent secretory pathway. We also used 2D-PAGE to examine the oxidative state of PARK7, as a result of which we found that the ratio of oxPARK7 to total PARK7 in medium was almost the same as that in cells, suggesting that secretion of PARK7 was not induced by its oxidation (Figure 1(E)).

Treatment with 6-OHDA enhances secretion of PARK7 from SH-SY5Y cells

We then evaluated the effect of 6-OHDA on PARK7 secretion. Because we had noticed that 6-OHDA in medium interfered with protein precipitation during the trichloroacetic acid precipitation procedure, protein secretion was evaluated using the conditioned medium obtained following 6-OHDA treatment as described in Materials and Methods. Results showed that 6-OHDA treatment for 3 h increased PARK7 secretion in a concentration-dependent manner (Figure 2(A)). Significant release of LDH from 100 μ M 6-OHDA-treated cells was not observed (Figure 2(B)), suggesting that the increase in PARK7 secretion was not the result of plasma membrane disruption by 6-OHDA. Brefeldin A treatment did not inhibit PARK7 secretion (Figure 2(C)), confirming that 6-OHDA-induced PARK7 secretion was mediated via an ER-/Golgi-independent secretory pathway. Because it had recently been reported that CASP1 (caspase 1) may act as regulator of unconventional protein secretion [34], we decided to assess the respective effects of a pan-caspase inhibitor (zVAD; i.e., Z-VAD [OMe]-FMK) and a specific CASP1 inhibitor (YVAD; i.e., Ac-YVAD-CMK) on PARK7 secretion. Our results indicated

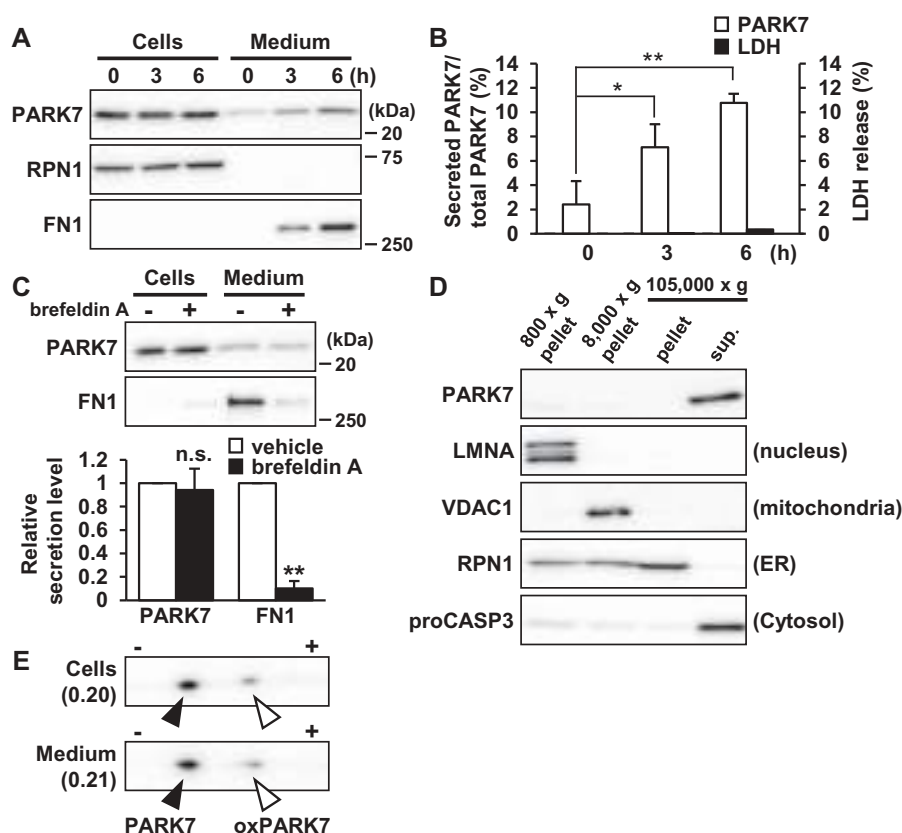


Figure 1. PARK7 was secreted from SH-SY5Y cells. (A and B) SH-SY5Y cells were cultured in serum-free medium for 0–6 h. (A) Whole cell lysates (Cells) and the conditioned medium (Medium) were immunoblotted using antibodies specific for PARK7, RPN1, or FN1. Representative image is shown. (B) PARK7 band intensities were quantified by densitometric scanning and the percentage of secreted PARK7/total PARK7 is shown. LDH release in the conditioned medium was analyzed by LDH assay. $n = 3$; mean \pm S.D.; *, $p < 0.05$; **, $p < 0.01$. (C) SH-SY5Y cells were treated with 2 $\mu\text{g/ml}$ brefeldin A in serum-free medium for 3 h. Whole cell lysates and the conditioned medium were immunoblotted with antibodies specific for PARK7 or FN1. PARK7 and FN1 band intensities were quantified by densitometric scanning and relative secretion level to vehicle-treated cells is shown. $n = 3$; **, $p < 0.01$; n.s., not significant. (D) SH-SY5Y cells were homogenized by using the Dounce homogenizer and homogenate was sequentially centrifuged as indicated. Equal aliquots from each fraction were immunoblotted using antibodies specific for PARK7, LMNA (lamin A/C), VDAC1, RPN1, or proCASP3 (caspase 3). (E) SH-SY5Y cells were cultured in serum-free medium for 3 h. Whole cell lysates and the conditioned medium were separated by 2D-PAGE and immunoblotted using antibody specific for PARK7. The ratio of oxPARK7 to total PARK7 is shown under each condition.

that 6-OHDA-induced PARK7 secretion was inhibited by either inhibitor (Figure 2(D)). Taken together, the foregoing series of results suggest that 6-OHDA induces PARK7 secretion via the unconventional secretory pathway.

6-OHDA-induced oxidative stress is implicated in PARK7 secretion

Considering the prominent effect of 6-OHDA on PARK7 secretion that we observed as reported above, we then sought to explore the mechanism of 6-OHDA-induced PARK7 secretion. It has been known that 6-OHDA is readily oxidized by molecular oxygen to produce superoxide anion, hydrogen peroxide (H_2O_2), and 2-hydroxy-5-(2-aminoethyl)-1,4-benzoquinone (6-OHDA quinone), resulting in induction of intracellular oxidative stress [35]. We therefore decided to examine whether 6-OHDA-induced oxidative stress affected PARK7 secretion. We first assessed the effect of 6-OHDA on intracellular antioxidant GSH content, finding as a result that there was a significant decrease in GSH levels in cells treated with 100 μM 6-OHDA for 3 h (Figure 3(A)). We next examined whether the 6-OHDA-induced reduction in GSH level caused PARK7 secretion in the presence or absence of the GSH precursor N-acetyl-L-cysteine (NAC), a well-established

cysteine supplier. We found that pretreatment with NAC suppressed the 6-OHDA-induced PARK7 secretion (Figure 3(B)). Since we had previously reported that about 260 μM H_2O_2 and 600 μM 6-OHDA quinone are formed from 600 μM 6-OHDA in medium [36], we decided to test the effect of H_2O_2 on PARK7 secretion, finding as a result that treatment with 100 μM H_2O_2 in the presence or absence of catalase did not increase PARK7 secretion (Figure 3(C)). Based on the foregoing series of results, we hypothesized that electrophilic quinone-induced oxidative stress might be responsible for 6-OHDA-induced PARK7 secretion. To test this possibility, we evaluated the effect of another electrophilic *p*-quinone, benzoquinone, on PARK7 secretion, finding as a result that, at non-cytotoxic concentrations (i.e., no release of LDH), benzoquinone induced PARK7 secretion in a concentration-dependent manner (Fig. S1A). Furthermore, NAC treatment was found to suppress the increase in 20 μM benzoquinone-induced PARK7 secretion (Fig. S1B). Similar to the effects of 6-OHDA treatment, 20 μM benzoquinone was found to reduce GSH content, and it was moreover found that this reduction could be abrogated by NAC treatment (Fig. S1C). Together, these results suggest that electrophilic quinone-induced oxidative stress underlies 6-OHDA-induced PARK7 secretion. We also examined whether PARK7

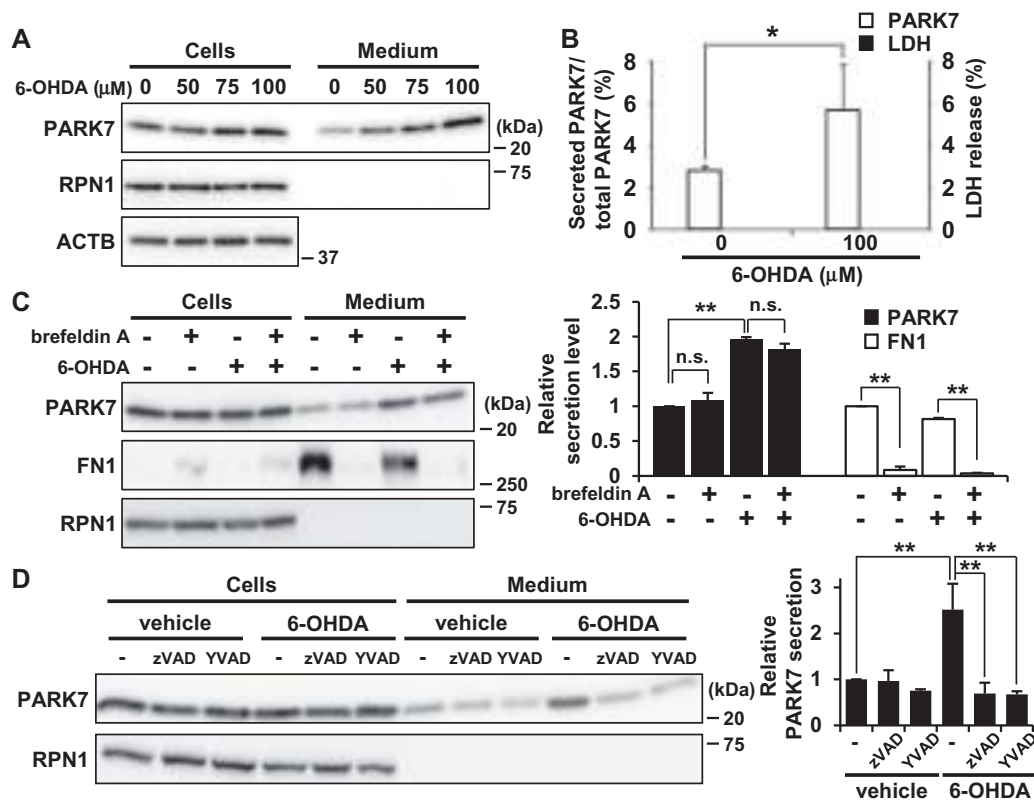


Figure 2. 6-OHDA treatment enhanced secretion of PARK7 from SH-SY5Y cells. **(A and B)** SH-SY5Y cells were treated with 0–100 μM 6-OHDA for 3 h and were then cultured in serum-free medium for 2 h. **(A)** Whole cell lysates and the conditioned medium were immunoblotted using antibodies specific for PARK7, RPN1, or ACTB. **(B)** PARK7 band intensities were quantified by densitometric scanning and the percentage of secreted PARK7/total PARK7 is shown. LDH release in the conditioned medium was analyzed by LDH assay. $n = 3$; mean \pm S.D.; *, $p < 0.05$. **(C)** SH-SY5Y cells were pre-treated with 2 $\mu\text{g/ml}$ brefeldin A for 3 h and were then treated with 100 μM 6-OHDA for 3 h, followed by culture in serum-free medium for 2 h. Whole cell lysates and the conditioned medium were immunoblotted with antibodies specific for PARK7, FN1, or RPN1. PARK7 and FN1 band intensities were quantified by densitometric scanning and relative secretion level to vehicle-treated cells is shown. $n = 3$; mean \pm S.D.; **, $p < 0.01$; n.s., not significant. **(D)** SH-SY5Y cells were pre-treated with or without 20 μM pan-caspase inhibitor (zVAD) or CASP1 inhibitor (YVAD) for 1 h and were then treated with 100 μM 6-OHDA for 3 h, followed by culture in serum-free medium for 2 h. Whole cell lysates and the conditioned medium were immunoblotted using antibodies specific for PARK7 or RPN1. PARK7 band intensities were quantified by densitometric scanning and relative secretion level to vehicle-treated cells is shown. $n = 3$; mean \pm S.D.; **, $p < 0.01$.

secretion was caused by another neurotoxin-induced oxidative stress. We tested the mitochondrial complex I inhibitor rotenone, which can cause reactive oxygen species (ROS) production and a decrease in GSH levels [37]. We found that treatment with rotenone at non-toxic concentrations for 24 h induced PARK7 secretion (Fig. S1D).

To evaluate whether the oxidized form of PARK7 was preferentially secreted from cells treated with 6-OHDA, 2D-PAGE analysis was carried out to determine the ratio of reduced:oxidized PARK7. Results showed that the ratio of oxPARK7 to total PARK7 in cells was increased by 6-OHDA treatment (Figs. 1E and 3D). Furthermore, reduced and oxidized forms of PARK7 were both observed in medium, and the ratio of oxPARK7 to total PARK7 in medium was similar to that in cells. To further assess the involvement of Cys106 in PARK7 secretion, HEK293 cells were transfected with either wild-type (WT) PARK7 or PARK7^{C106S}, the latter being a mutant form of PARK7 in which oxidation-sensitive cysteine at amino acid 106 is substituted by serine. Results of transfection indicated that 6-OHDA treatment induced PARK7^{C106S} secretion in a manner similar to that observed with endogenous PARK7 and WT PARK7 (Figure 3(E)). Together, the foregoing series of results suggest that oxidation of PARK7 at Cys106 is not involved in enhancement of PARK7 secretion.

6-OHDA induces autophagy in SH-SY5Y cells and MEF cells

To gain insight into the mechanism by which 6-OHDA treatment increased PARK7 secretion, we examined whether 6-OHDA induced autophagy, since it had recently been shown that the secretion of several proteins lacking a signal sequence is associated with the autophagy-based unconventional secretory pathway [38–40]. To exclude any possible effect of incubation of cells in serum-free medium on monitoring of autophagy induction, autophagic flux was evaluated using the lysate from the cells treated with 6-OHDA for 3 h. By monitoring the conversion of MAP1LC3B/LC3B (microtubule associated protein 1 light chain 3 beta) from a cytosolic form (LC3B-I) to its lipidated phagophore- and autophagosome-associated form (LC3B-II), we found that 6-OHDA treatment induced increase in LC3B-II levels in SH-SY5Y cells (Figure 4(A)).

In this context, to determine whether autophagy could be induced under the same conditions for which we had observed that 6-OHDA treatment increased PARK7 secretion, we assessed the effects of 6-OHDA on PARK7 secretion and autophagy induction in WT MEF cells, which have been widely used in autophagy research. We found that

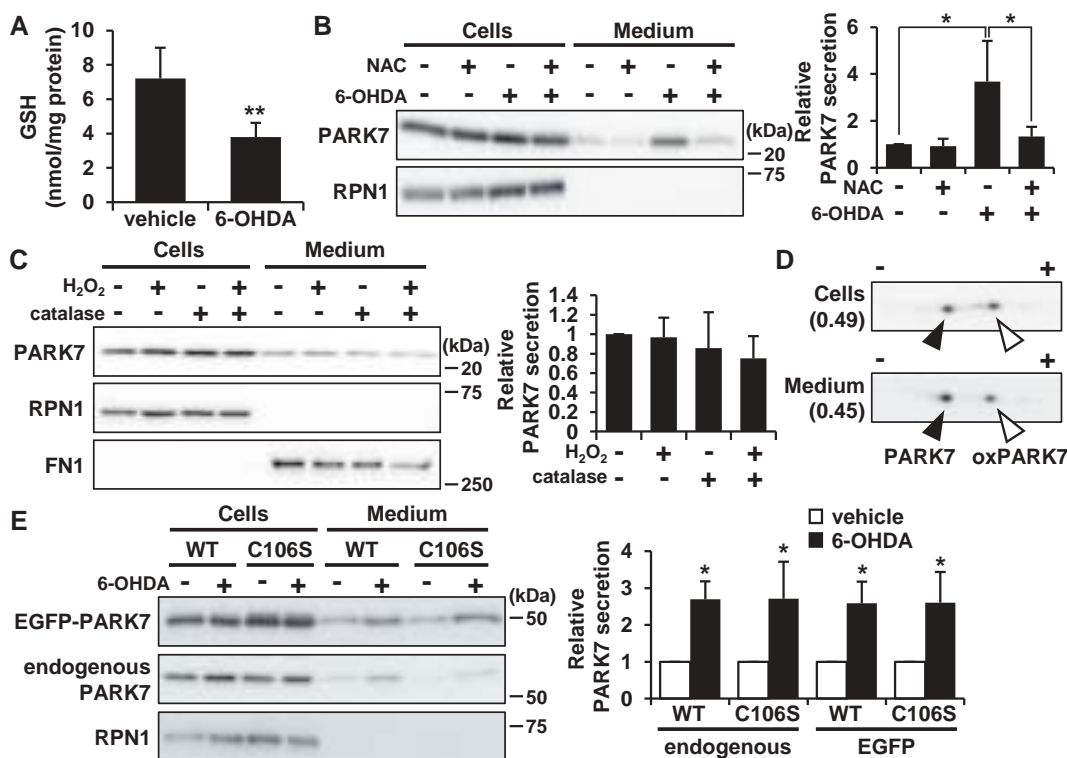


Figure 3. 6-OHDA-induced oxidative stress was implicated in PARK7 secretion. **(A)** SH-SY5Y cells were treated with 100 μ M 6-OHDA for 3 h and were subjected to GSH assay. $n = 5$; mean \pm S.D.; **, $p < 0.01$. **(B)** SH-SY5Y cells were pre-treated with or without 2 mM NAC for 2 h and were then treated with 100 μ M 6-OHDA for 3 h, followed by culture in serum-free medium for 2 h. Whole cell lysates and the conditioned medium were immunoblotted using antibodies specific for PARK7 or RPN1. PARK7 band intensities were quantified by densitometric scanning and relative secretion level to vehicle-treated cells is shown. $n = 3$; mean \pm S.D.; *, $p < 0.05$. **(C)** SH-SY5Y cells were treated with 100 μ M H₂O₂ in the presence or absence of 50 U/ml catalase in serum-free medium for 3 h. Whole cell lysates and the conditioned medium were immunoblotted with antibodies specific for PARK7, RPN1, or FN1. PARK7 band intensities were quantified by densitometric scanning and relative secretion level to vehicle-treated cells is shown. $n = 3$; mean \pm S.D. **(D)** SH-SY5Y cells were treated with 100 μ M 6-OHDA for 3 h and were then cultured in serum-free medium for 2 h. Whole cell lysates and the conditioned medium were separated by 2D-PAGE and immunoblotted using antibody specific for PARK7. The ratio of oxPARK7:total PARK7 is shown under each condition. **(E)** HEK293 cells stably expressing WT or C106S mutant of PARK7 were treated with 100 μ M 6-OHDA for 3 h and were then cultured in serum-free medium for 2 h. Whole cell lysates and the conditioned medium were immunoblotted using antibodies specific for PARK7 or RPN1. PARK7 band intensities were quantified by densitometric scanning and relative secretion level to vehicle-treated cells is shown. $n = 3$; mean \pm S.D.; *, $p < 0.05$.

6-OHDA treatment increased PARK7 secretion in MEF cells, although the amount of secreted PARK7 from 6-OHDA-treated MEF cells was less than that from 6-OHDA-treated SH-SY5Y cells (Figure 4(B)). Significant LDH release was not observed in cells treated with 100 μ M 6-OHDA (data not shown). We further found that significant increase in LC3B-II levels was observed in cells treated with 75 μ M 6-OHDA (Figure 4(C)). Since it had previously been indicated that an increase in LC3B-II level may be associated with either enhanced formation of autophagosomes or impairment of autophagosome turnover [41], we decided to evaluate the effect of co-treatment of 6-OHDA with bafilomycin A₁, which inhibits acidification inside the lysosome and to block fusion between the autophagosome and the lysosome. Results showed that LC3B-II levels increased in 6-OHDA-treated cells, and that this increase was enhanced by co-treatment of 6-OHDA with bafilomycin A₁, indicating that there was increase in autophagic flux during 6-OHDA treatment in MEF cells (Figure 4(D)). We also evaluated the effect of bafilomycin A₁ on autophagic degradation and on secretion of PARK7, finding as a result that although LC3B-II levels increased in response to treatment with bafilomycin A₁ alone (Figure 4), this did not result in induction of PARK7 secretion (Figure 4(E)). We further found that this increase in 6-OHDA-induced

PARK7 secretion was suppressed by co-treatment with bafilomycin A₁, suggesting the possibility that autophagic flux is important for PARK7 secretion and that PARK7 is not a substrate for autophagic degradation. We also used a fluorescent probe for lysosomes, LysoTracker Red, to evaluate the lysosomal membrane integrity. Decreased fluorescence of LysoTracker Red reflects lysosomal membrane permeabilization and/or an increase in lysosomal pH. As control, bafilomycin A₁ treatment caused a decrease in LysoTracker Red fluorescence both in SH-SY5Y cells (Fig. S2A) and WT MEF cells (Fig. S2B), as expected. In contrast, the staining pattern of LysoTracker Red puncta in 6-OHDA-treated cells was similar to that in vehicle-treated cells. The lysosomal membrane integrity was further evaluated by subcellular fractionation. Results showed that in vehicle-treated cells, lysosomal protease CT SB (cathepsin B) was found almost exclusively in the membrane organellar protein-rich NP-40 extract but not in the cytosolic protein-rich digitonin extract (Fig. S2C). 6-OHDA treatment did not significantly change the localization of CT SB. Together, these results suggest the conditions in which 6-OHDA induced secretion of PARK7 do not affect lysosomal membrane integrity.

We also performed transmission electron microscopy analysis to elucidate the induction of autophagy in 6-OHDA-treated WT MEF cells. Results indicated that while there

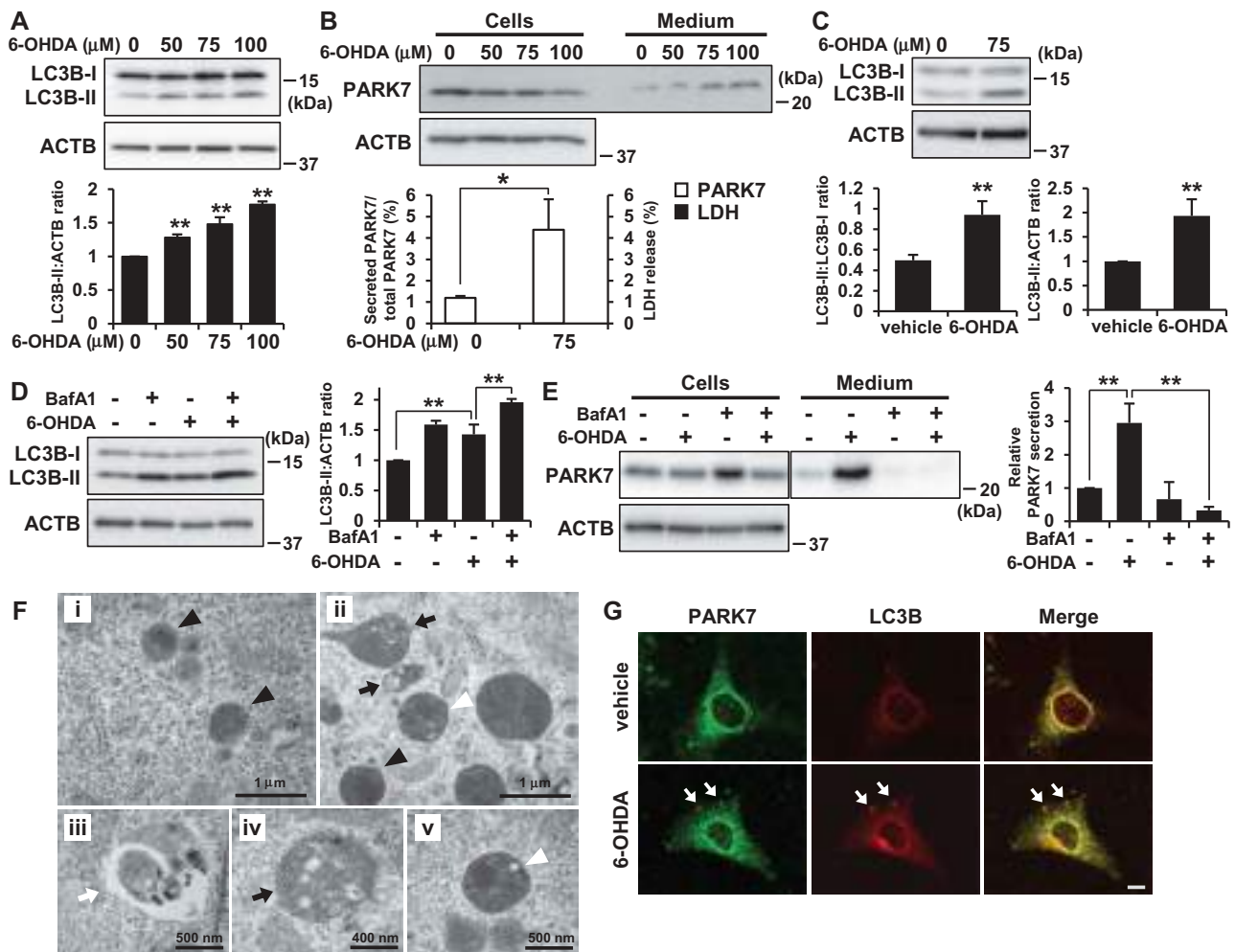


Figure 4. 6-OHDA treatment induced autophagy in SH-SY5Y cells and WT MEF cells. **(A)** SH-SY5Y cells were treated with 0–100 μM 6-OHDA for 3 h. Whole cell lysates were immunoblotted using antibodies specific for LC3B or ACTB. LC3B and ACTB band intensities were quantified by densitometric scanning and LC3B-II:ACTB ratio is shown. $n = 3$; mean \pm S.D.; **, $p < 0.01$. **(B)** WT MEF cells were treated with 0–100 μM 6-OHDA for 3 h and were then cultured in serum-free medium for 2 h. Whole cell lysates and the conditioned medium were immunoblotted using antibodies specific for PAK7 or ACTB. PAK7 band intensities were quantified by densitometric scanning and the percentage of secreted PAK7/total PAK7 is shown. LDH release in the conditioned medium was analyzed by LDH assay. $n = 3$; mean \pm S.D.; *, $p < 0.05$. **(C)** WT MEF cells were treated with 75 μM 6-OHDA for 3 h. Whole cell lysates were immunoblotted using antibodies specific for LC3B or ACTB. LC3B band intensities were quantified by densitometric scanning and LC3B-II:LC3B-I or LC3B-II:ACTB ratio is shown. $n = 3$; **, $p < 0.01$. **(D and E)** WT MEF cells were pretreated with 100 nM bafilomycin A₁ (BafA1) for 1 h and were then treated with 75 μM 6-OHDA for 3 h **(D)**, followed by culture in serum-free medium for 2 h **(E)**. Whole cell lysates and the conditioned medium were immunoblotted using antibodies specific for LC3, PAK7, or ACTB. PAK7, LC3B and ACTB band intensities were quantified by densitometric scanning. LC3B-II:ACTB ratio **(D)** and relative secretion level to vehicle-treated cells **(E)** are shown. $n = 3$; mean \pm S.D.; **, $p < 0.01$. **(F)** WT MEF cells were treated with vehicle **(i)** or 75 μM 6-OHDA **(ii–v)** for 3 h. Cells were subjected to electron microscopy. Representative images are shown. Black arrowheads indicate lysosome. Black arrows indicate autophagosome/amphisome and lysosome. White arrowhead indicates autolysosome. White arrow indicates phagophore. **(G)** WT MEF cells grown on coverslips were treated with 75 μM 6-OHDA for 3 h. Cells were processed for immunofluorescence staining with antibody against PAK7 or LC3B. Representative confocal images are shown. White arrows indicate co-localization. Scale bar: 10 μm .

were no obvious autophagic structures in the vehicle-treated cells (Figure 4Fi), there were structures (Figure 4Fii) in 6-OHDA-treated cells that seemed to be phagophores (Figure 4Fiii), autophagosomes, amphisomes (Figure 4Fiv), and autolysosomes (Figure 4Fv). We then evaluated intracellular localization of PAK7 by confocal microscopy. Although most of the PAK7 signal was observed in the cytoplasm, 6-OHDA treatment caused the modest but significant localization of PAK7 in LC3B-positive puncta (Figure 4(G)). Together, these results suggest that the same conditions in which 6-OHDA induces secretion of PAK7 also induce autophagy.

PARK7 secretion is suppressed in autophagy-deficient MEF cells and ATG16L1 knockdown SH-SY5Y cells

To further examine the involvement of autophagy in 6-OHDA-induced PAK7 secretion, we investigated the response to 6-OHDA in *Atg5*-deficient (*atg5*^{-/-}) MEF cells, as ATG5 is known to play an essential role in autophagosome formation [42]. Results for *atg5*^{-/-} MEF cells indicated that there was no LC3B-II formation and that 6-OHDA did not induce PAK7 secretion (Figure 5(A)). We further employed *Atg9*-deficient (*atg9*^{-/-}) and *Atg16l1*-deficient (*atg16l1*^{-/-}) MEF cells, in both of which autophagosome formation was

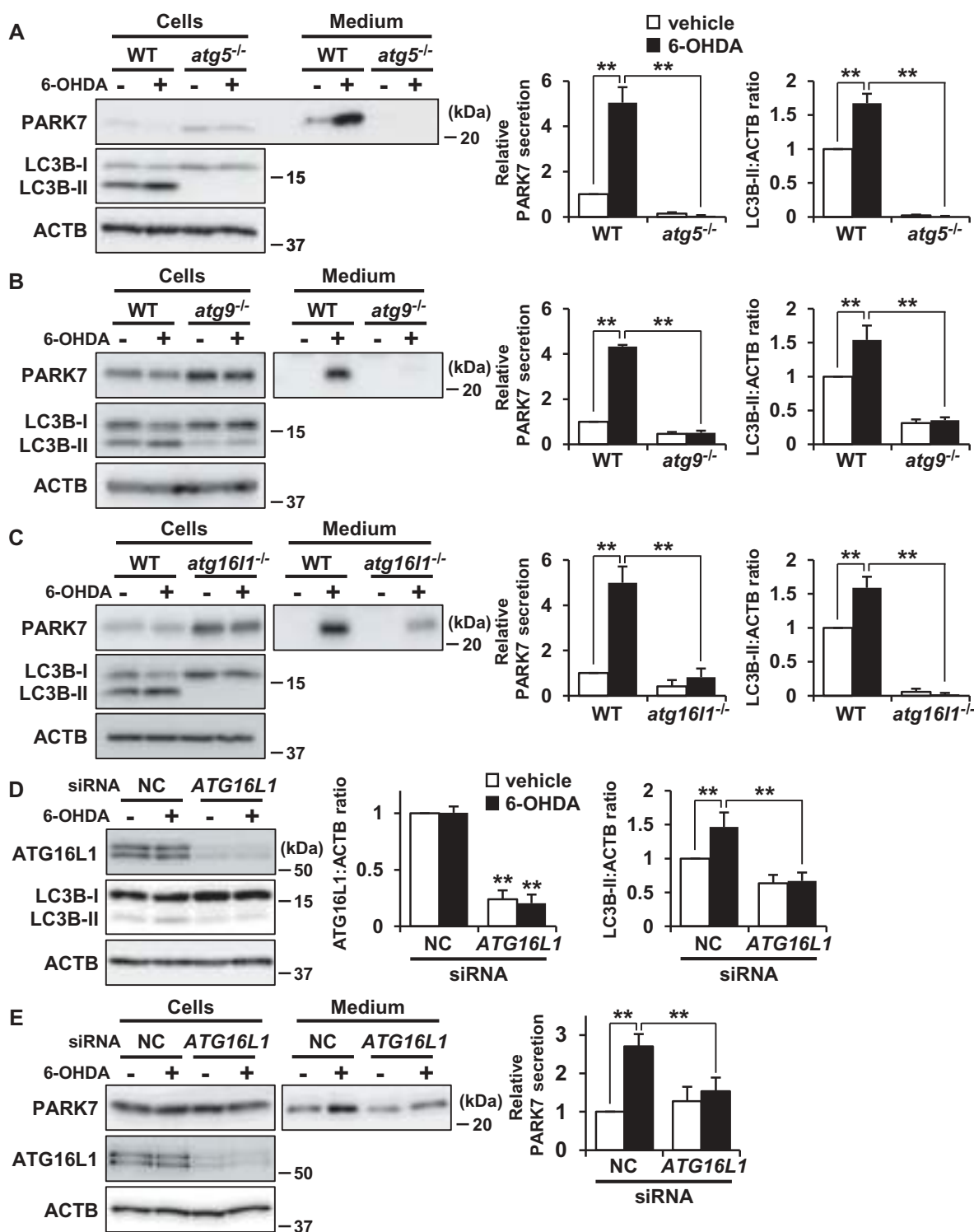


Figure 5. ATG5, ATG9, and ATG16L1 were involved in 6-OHDA-induced PARK7 secretion. (a-c) WT MEF, *atg5*^{-/-} MEF (A), *atg9*^{-/-} MEF (B) or *atg16l1*^{-/-} MEF (C) cells were treated with 75 μ M 6-OHDA for 3 h and were then cultured in serum-free medium for 2 h. Whole cell lysates and the conditioned medium were immunoblotted using antibodies specific for PARK7, LC3B, or ACTB. PARK7, LC3B and ACTB band intensities were quantified by densitometric scanning. Relative PARK7 secretion level to vehicle-treated cells and LC3B-II:ACTB ratio are shown. $n = 3$; mean \pm S.D.; **, $p < 0.01$. (D and E) WT MEF cells were transfected with ATG16L1 or negative control (NC) siRNA oligo for 72 h. The cells were treated with 75 μ M 6-OHDA for 3 h (D), followed by culture in serum-free medium for 2 h (E). Whole cell lysates and the conditioned medium were immunoblotted with using antibodies specific for ATG16L1, LC3B, PARK7, or ACTB. ATG16L1, LC3B, PARK7 and ACTB band intensities were quantified by densitometric scanning. ATG16L1:ACTB and LC3B-II:ACTB ratios (d) and relative PARK7 secretion level to vehicle-treated cells (e) are shown. $n = 3$; mean \pm S.D.; **, $p < 0.01$.

impaired [43,44]. Consistent with the results obtained for *atg5*^{-/-} MEF cells, 6-OHDA-induced PARK7 secretion and LC3B-II formation were each suppressed in both *atg9*^{-/-} MEF cells (Figure 5(B)) and *atg16l1*^{-/-} MEF cells (Figure 5

(C)). Furthermore, we performed siRNA knockdown of ATG16L1 in SH-SY5Y cells and confirmed a marked decline in ATG16L1 protein levels (Figure 5(D)). Under these conditions, 6-OHDA-induced increase in LC3B-II levels was

suppressed (Figures 5(D)) and 6-OHDA-induced PARK7 secretion was also significantly inhibited (Figure 5(E)) as observed in *atg16l1*^{-/-} MEF cells. Taken together, these results suggest that autophagic flux is required for unconventional secretion of PARK7.

To evaluate whether extracellular PARK7 was associated with small vesicles, we performed ultracentrifugation fractionation of conditioned medium at 100,000 x g to separate vesicle-associated proteins from soluble proteins. CAV1 (caveolin 1), secretion of which has been reported to occur with vesicles [45], was recovered from the pellet fraction, while PARK7 was recovered from the supernatant fraction, in both the medium collected from vehicle and 6-OHDA-treated cells (Fig. S3). These results suggest that extracellular PARK7 exists as soluble protein.

Oxidative stress is implicated in 6-OHDA-induced autophagy and PARK7 secretion

We then sought to test whether 6-OHDA-induced oxidative stress stimulated autophagy and PARK7 secretion. As had been observed in SH-SY5Y cells, we observed that GSH content was significantly reduced by 6-OHDA treatment in WT MEF cells (Figure 6(A)). We also used the fluorescent probe DCFH-DA to monitor intracellular ROS levels, finding as a result that treatment with 6-OHDA caused an increase in ROS levels as compared with vehicle-treated cells, and that this increase could be mitigated by treatment with NAC (Figure 6(B)). We further found that 6-OHDA-induced PARK7 secretion could be suppressed by treatment with NAC (Figure 6(C)) in a similar manner as had been observed in SH-SY5Y cells (Figure 3

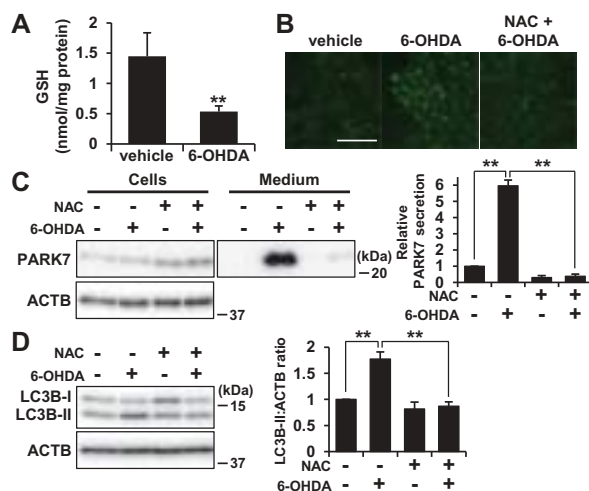


Figure 6. NAC treatment suppressed 6-OHDA-induced autophagy and PARK7 secretion. (A) WT MEF cells were treated with 75 μ M 6-OHDA for 3 h and were then subjected to GSH assay. $n = 3$; mean \pm S.D.; **, $p < 0.01$. (B-D) WT MEF cells were pre-treated with or without 2 mM NAC and were then treated with 75 μ M 6-OHDA for 3 h (B and D), followed by culture in serum-free medium for 2 h (C). (B) ROS generation was determined using a fluorescence probe, DCFH-DA. Fluorescence was detected using a fluorescence microscope. Representative fluorescence images are shown. Scale bar: 100 μ m. (C and D) Whole cell lysates and the conditioned medium were immunoblotted using antibodies specific for PARK7, LC3B, or ACTB. PARK7, LC3B and ACTB band intensities were quantified by densitometric scanning. Relative PARK7 secretion level to vehicle-treated cells (c) and LC3B-II:ACTB ratio (d) are shown. $n = 3$; mean \pm S.D.; **, $p < 0.01$.

(B)). Under conditions which were the same as the foregoing, we further noted that 6-OHDA induced an increase in LC3B-II levels, and that this increase could be suppressed by co-treatment with NAC (Figure 6(D)). Together, these results suggest that 6-OHDA-induced oxidative stress is implicated in autophagy-based unconventional secretion of PARK7.

Activation of AMPK and ULK1 is implicated in 6-OHDA-induced autophagy and PARK7 secretion

Because a cytotoxic concentration of 6-OHDA has been reported to induce AMPK-dependent autophagy in SH-SY5Y cells [46], we examined whether activation of the AMPK pathway could be made to occur under the same conditions as those for which we had observed that 6-OHDA caused secretion of PARK7. We investigated the effect of 6-OHDA on phosphorylation of AMPK at Thr172 (AMPK activation) and on phosphorylation by AMPK of its downstream effector ULK1 at Ser555 (ULK1 activation). Since the inhibitory function of MTOR in autophagy is well-established [41], the phosphorylation of RPS6KB1/p70S6K (ribosomal protein S6 kinase B1) at Thr389 by MTOR was also evaluated to assess MTOR activity. As a control, the MTOR inhibitor rapamycin was employed, this being observed to cause a decrease in RPS6KB1 phosphorylation without causing stimulation of AMPK and ULK1 phosphorylation (Figure 7(A)), as expected. In contrast, 6-OHDA treatment enhanced phosphorylation of AMPK and its substrate ULK1, but did not significantly change the degree of phosphorylation of RPS6KB1. We therefore evaluated the effect of NAC on AMPK phosphorylation, finding as a result that NAC treatment significantly diminished AMPK phosphorylation in a manner roughly paralleling the observed decrease in LC3B-II levels (Figure 7(B)). Because AMPK activation is regulated by the AMP:ATP ratio, we assessed AMP and ATP levels, upon which we found that 6-OHDA treatment increased the AMP:ATP ratio (Figure 7(C)). These results suggest that the same conditions which exist when 6-OHDA induces oxidative stress-mediated PARK7 secretion and autophagy also cause activation of the AMPK-ULK1 pathway without affecting MTOR activity.

To confirm the involvement of the AMPK-ULK1 pathway in 6-OHDA-induced autophagy and PARK7 secretion, SH-SY5Y cells were treated with MRT68921, a specific inhibitor of ULK1 [47], as a result of which it was found that 6-OHDA-induced increase in LC3B-II levels was suppressed by co-treatment with MRT68921 (Figure 7(D)). Furthermore, 6-OHDA-induced PARK7 secretion was suppressed by co-treatment with MRT68921 (Figure 7(E)). Consistent with the results obtained for SH-SY5Y cells, 6-OHDA-induced PARK7 secretion was suppressed in WT MEF cells treated with MRT68921 (Figure 7(F)). Together, these results suggest that AMPK-ULK1 pathway is involved in 6-OHDA-induced autophagy and PARK7 secretion.

Trehalose but not rapamycin promotes PARK7 secretion in WT MEF cells

We then investigated whether another stimulator of autophagy could induce PARK7 secretion. In WT MEF cells, rapamycin treatment increased LC3B-II levels both in the presence and

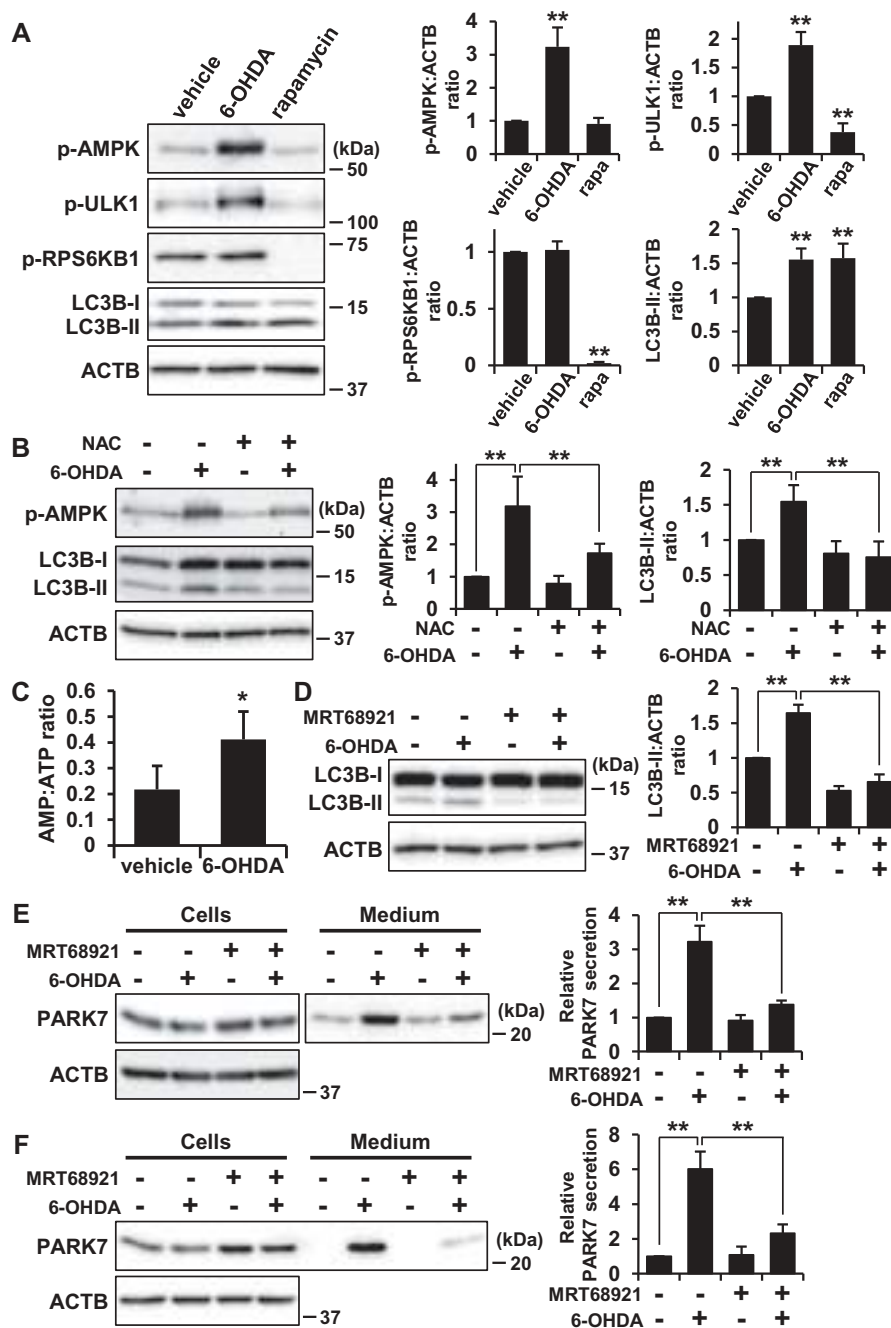


Figure 7. 6-OHDA-induced AMPK-ULK1 phosphorylation was associated with PARK7 secretion in WT MEF cells. **(A)** WT MEF cells were treated with 75 μ M 6-OHDA or 2 μ M rapamycin for 3 h. Whole cell lysates were immunoblotted using antibodies specific for phospho-AMPK (Thr172), phospho-ULK1 (Ser555), phospho-RPS6KB1 (Thr389), LC3B, or ACTB. Band intensities were quantified by densitometric scanning and p-AMPK:ACTB, p-ULK1:ACTB, p-RPS6KB1:ACTB and LC3B-II:ACTB ratios are shown. $n = 3$; mean \pm S.D.; **, $p < 0.01$. **(B)** WT MEF cells were pre-treated with or without 2 mM NAC and were then treated with 75 μ M 6-OHDA for 3 h. Whole cell lysates were immunoblotted using antibodies specific for phospho-AMPK, LC3B, or ACTB. Band intensities were quantified by densitometric scanning and p-AMPK:ACTB and LC3B-II:ACTB ratios are shown. $n = 3$; mean \pm S.D.; **, $p < 0.01$. **(C)** WT MEF cells were treated with 75 μ M 6-OHDA for 3 h and were then subjected to AMP:ATP assay. $n = 3$; mean \pm S.D.; *, $p < 0.05$. **(D and E)** SH-SY5Y cells were pre-treated with or without 1 μ M MRT68921 for 30 min and were then treated with 75 μ M 6-OHDA for 3 h **(D)**, followed by culture in serum-free medium for 2 h **(E)**. Whole cell lysates and the conditioned medium were immunoblotted using antibodies specific for LC3, PARK7, or ACTB. LC3B, PARK7 and ACTB band intensities were quantified by densitometric scanning. LC3B-II:ACTB ratio **(d)** and relative secretion level to vehicle-treated cells **(e)** are shown. $n = 3$; mean \pm S.D.; **, $p < 0.01$. **(F)** WT MEF cells were pre-treated with or without 2 μ M MRT68921 for 30 min and were then treated with 75 μ M 6-OHDA for 3 h, followed by culture in serum-free medium for 2 h. Whole cell lysates and the conditioned medium were immunoblotted using antibodies specific for PARK7 or ACTB. PARK7 band intensities were quantified by densitometric scanning and relative secretion level to vehicle-treated cells is shown. $n = 3$; mean \pm S.D.; **, $p < 0.01$.

absence of bafilomycin A_1 as expected (Figure 8(A)). When the cells were treated with 1–5 μ M rapamycin, an increase in PARK7 secretion was observed, but not to the same degree as had been observed with 6-OHDA treatment (Figure 8(B)). We next evaluated the effect of trehalose. Trehalose is a natural disaccharide

found in many non-mammalian species that induces MTOR-independent autophagy by inhibiting hexose uptake and subsequently activating the AMPK-ULK1 pathway [48,49]. It should be noted that it has recently been reported that release of SNCA (synuclein alpha) is upregulated by trehalose treatment in rat

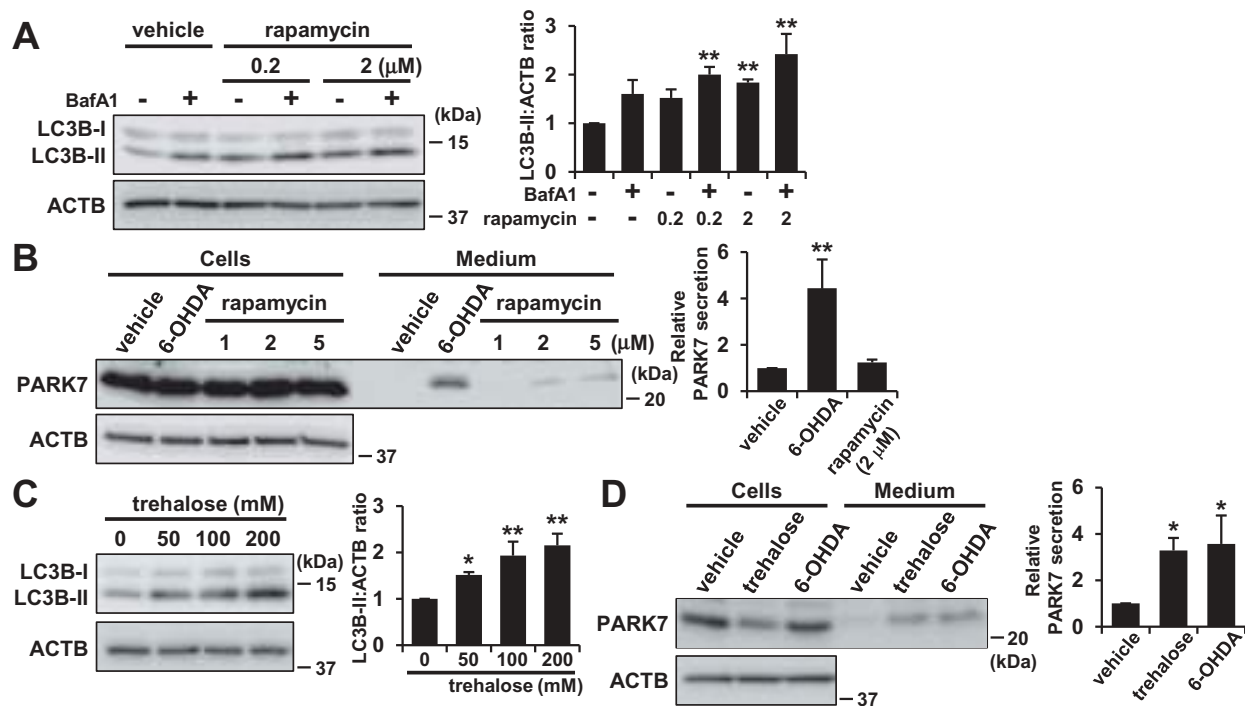


Figure 8. Trehalose but not rapamycin promoted PARK7 secretion in WT MEF cells. **(A)** WT MEF cells were treated with 100 nM BafA1 for 1 h and were then treated with 0–2 μ M rapamycin for 3 h. Whole cell lysates were immunoblotted using antibodies specific for LC3B or ACTB. LC3B and ACTB band intensities were quantified by densitometric scanning and LC3B-II:ACTB ratio is shown. $n = 3$; mean \pm S.D.; **, $p < 0.01$. **(B)** WT MEF cells were treated with 1–5 μ M rapamycin or 75 μ M 6-OHDA for 3 h and were then cultured in serum-free medium for 2 h. Whole cell lysates and the conditioned medium were immunoblotted using antibodies specific for PARK7 or ACTB. PARK7 band intensities were quantified by densitometric scanning and relative secretion level to vehicle-treated cells is shown. $n = 3$; mean \pm S.D.; **, $p < 0.01$. **(C)** WT MEF cells were treated with 0–200 mM trehalose for 48 h. Whole cell lysates were immunoblotted using antibodies specific for LC3B or ACTB. LC3B and ACTB band intensities were quantified by densitometric scanning and LC3B-II:ACTB ratio is shown. $n = 3$; mean \pm S.D.; *, $p < 0.05$; **, $p < 0.01$. **(D)** WT MEF cells were treated with 200 mM trehalose for 48 h or 75 μ M 6-OHDA for 3 h and were then cultured in serum-free medium for 2 h. Whole cell lysates and the conditioned medium were immunoblotted using antibodies specific for PARK7 or ACTB. PARK7 band intensities were quantified by densitometric scanning and relative secretion level to vehicle-treated cells is shown. $n = 3$; mean \pm S.D.; *, $p < 0.05$.

pheochromocytoma PC12 cells [50]. When WT MEF cells were treated with trehalose, we found that LC3B-II levels were increased in a concentration-dependent manner (Figure 8(C)), confirming that there was activation of autophagic flux under the conditions tested. Furthermore, 200 mM trehalose enhanced PARK7 secretion at the same level with 6-OHDA treatment (Figure 8(D)) without significant LDH release (data not shown). Together, these results suggest the possibility that 6-OHDA-induced PARK7 secretion is mainly mediated by MTOR-independent autophagy.

Discussion

In our present study, we demonstrate that PARK7 is secreted via the autophagy-mediated unconventional secretion mechanism. Autophagy is generally understood to be the process by which cytosolic proteins and damaged organelles are degraded within lysosomes [41]. During macroautophagy, which is the most prevalent form of autophagy, some cytoplasmic components including organelles are enclosed within a double-membraned structure referred to as an autophagosome. The autophagosome undergoes the fusion with a lysosome (autolysosome) to achieve degradation of its internal contents. The autophagosome can also fuse with an endosome to form an amphisome before

fusion with a lysosome. To understand the unconventional secretion mechanism, autophagy may be the mechanism by which cytosolic proteins are secreted into the extracellular space across the hydrophobic environment of the plasma membrane. It is conceivable that some form of autophagic structure (autophagosome, amphisome, or autolysosome) may fuse with the plasma membrane to release the enclosed cytosolic contents into the extracellular space. Indeed, autophagy-mediated unconventional secretion, termed secretory autophagy, has been implicated in the secretion of a subset of unconventionally secreted proteins which include yeast Acb1/DBI, mammalian IL1B, and IDE (insulin degrading enzyme) [8,38–40]. Our study indicates that PARK7 is also secreted via the secretory autophagy. It is however not clear how such a secretory protein might be selected for secretory autophagy and escape lysosomal degradation. One possibility is that the secretion rather than degradation of cytosolic constituents that occurs in secretory autophagy may be induced by a shared but partially divergent autophagic machinery. In our present study, we demonstrated that 6-OHDA-induced PARK7 secretion required the autophagy-related proteins ATG5, ATG9, and ATG16L1, suggesting that ATG proteins which govern biogenesis of autophagic membranes are needed for secretory autophagy-mediated PARK7 secretion. Interestingly, we

also showed that 6-OHDA induced MTOR-independent autophagy via the AMPK-ULK1 pathway. We furthermore observed that the MTOR-independent autophagy inducer trehalose caused PARK7 secretion to a degree on the same order as that observed with 6-OHDA treatment, but that the MTOR inhibitor rapamycin only poorly stimulated PARK7 secretion as compared with 6-OHDA treatment. Since MTOR senses cellular nutritional status and is involved in the induction of degradative autophagy that occurs in response to nutrient starvation [41], understanding the role that MTOR plays should assist in elucidating the respective contributions of the MTOR signaling pathway and the MTOR-independent signaling pathway to secretory autophagy.

Several cellular stresses, e.g., inflammation, nutrient stress, and ER stress, have been reported to trigger secretory autophagy [8,38–40]. In the present study, we demonstrated that oxidative stress induced by 6-OHDA also triggered secretory autophagy. Oxidative stress has been implicated in the induction of degradative autophagy [51]. It has been reported that oxidation of Atg4 at cysteine inactivates its delipidating activity on LC3, thereby leading to the induction of autophagosome formation [52]. It has also been proposed that AMPK may be activated in response to increased intracellular ROS levels, particularly through S-glutathionylation [53]. 6-OHDA has been reported to impair the mitochondrial respiratory chain, leading to a decrease in ATP levels [33]. We therefore concluded that 6-OHDA-induced oxidative stress, and the resulting increase in the AMP:ATP ratio and AMPK-ULK1 activation, were implicated in PARK7 secretion at least under the conditions tested. Indeed, we demonstrated in the present study that ULK1 inhibition suppressed 6-OHDA-induced PARK7 secretion. Because the AMPK inhibitor compound C has been reported to induce autophagy in some type of cells [54], it will be necessary to pay attention to evaluate the effect of AMPK inhibition by compound C or AMPK siRNA on PARK7 secretion.

Our study suggests that AMPK-ULK1-mediated but MTOR-independent signaling regulation plays an important role in the distinctive induction of secretory autophagy-mediated PARK7 secretion. In addition, we speculate that a dedicated molecular machinery for formation or intracellular trafficking of autophagic structures may account for the distinctive secretory pathway of PARK7. Further investigations to identify the involvement of other autophagy-related proteins in PARK7 secretion are required for in-depth analysis. It should be noted that Galluzi et al. encourage the use of molecularly-oriented descriptors for non-degradative functions of autophagic machinery [55]. In line with this definition, the mechanisms of PARK7 secretion may need to be referred to as ATG5, ATG9, and ATG16L1-dependent secretion instead of secretory autophagy-mediated secretion. In future studies, it would also be of interest to evaluate whether other known key proteins involved in secretory autophagy, such as RAB8A (RAB8A, member RAS oncogene family) and GORASP2/GRASP55 (golgi reassembly stacking protein 2) [39,40], are implicated in PARK7 secretion, and whether 6-OHDA-induced secretory autophagy is implicated in the secretion of other proteins. It has been recently reported that dedicated SNAREs participate in secretory autophagy-

mediated unconventional secretion of IL1B in response to lysosome damage [56]. Interestingly, secretion of IL1B depends on plasma membrane STX3 (syntaxin 3) and STX4 (syntaxin 4) instead of delivery to lysosomes via STX17 (syntaxin 17), which has been identified as a necessary protein for autophagosomal fusion with the endosome/lysosome [57]. To consider how autophagy-mediated PARK7 secretion separates from degradative autophagy, further investigations to elucidate the possible involvement of dedicated SNARE machinery in PARK7 secretion may provide another insight.

With respect to the differences between target proteins for degradative versus secretory autophagy, it is possible that secretory proteins in autophagic vacuoles may possess some protective modification or domain that contributes in some way to prevent lysosomal degradation. It has been demonstrated that the SlyX domain (EKPPHY) of IDE contributes to IDE secretion by preventing its lysosomal degradation [40,58]. Furthermore, KFERQ-like motifs of IL1B are thought to be required for entry of IL1B into the lumen of the phagophore so as to permit secretion as a soluble protein either through a direct fusion of the autophagosome with the plasma membrane or via the multi-vesicular body pathway [59]. It is also known that a KFERQ-like motif is present in substrates of chaperone-mediated autophagy [41]. In the case of PARK7, we found that there are several KFERQ-like motifs in the PARK7 amino acid sequence. Because we found in the present study that PARK7 secretion is mediated by secretory autophagy, studies to elucidate the possible involvement of KFERQ-like motifs in PARK7 secretion may provide further insight.

Electron microscopy analysis showed that 6-OHDA treatment induced formation of structures typically observed where there is involvement of the autophagic pathway, such as autophagosomes, amphisomes, and autolysosomes. Since ATG5, ATG9, and ATG16L1 are known to play essential roles in autophagosome formation [41–44], one possibility is that cytosolic PARK7 may be packaged within LC3-positive autophagic vacuoles for secretion. Indeed, in addition to cytosolic distribution of PARK7 signal, we observed the modest but significant localization of PARK7 in LC3B-positive puncta in the cells treated with 6-OHDA. Since our rough estimate of PARK7 band intensity suggested that less than 10% of PARK7 was secreted from cells in response to 6-OHDA treatment, we posit that this might affect the modest distribution of PARK7 in autophagic vacuoles. Since ultracentrifugation fractionation of conditioned medium showed that extracellular PARK7 was not associated with exosomes or other such small vesicles, we speculate that the PARK7-containing autophagic vacuole, if it exists, is most likely fusing with the plasma membrane to cause release of its soluble contents including PARK7 into the extracellular space, but we cannot exclude the possibility that PARK7 is first secreted via exosomes/ectosomes and then released from vesicle in the extracellular space.

Several lines of evidence suggest that secreted PARK7 may play a functional role in the extracellular space. For example, PARK7 secreted from osteoblasts has been found to promote

angiogenesis and osteogenesis [32]. Extracellular deposition of abnormal TTR (transthyretin) protein has been shown to cause familial amyloid polyneuropathy, and secreted PARK7 has been shown to degrade aggregated TTR to protect against the onset of amyloid polyneuropathy [26]. And with respect to PD, PARK7 has been detected in the cerebrospinal fluid of patients suffering from PD [28,29], and it has been found that administration of recombinant PARK7 into the brain of 6-OHDA-induced PD rat model improved PD phenotype [60], suggesting that extracellular PARK7 might exert a protective role against PD. There is a possibility that secreted PARK7 may protect neighboring cells from oxidative stress by means of a process similar to paracrine signaling, which possibility is thought to be supported by reports that PARK7 knockout astrocytes show inferior ability to protect neuronal cells against 6-OHDA-induced cell death both by co-culture and through astrocytes conditioned medium [61]. Since PARK7 has 3 reactive cysteine residues, it is also possible that secreted PARK7 itself receives oxidative modification by scavenging ROS within the extracellular space. Indeed, when the conditioned medium obtained from non-treated cells was incubated in the presence of 6-OHDA, the ratio of oxPARK7 to total PARK7 was increased, suggesting that oxidation of PARK7 occurred in the presence of 6-OHDA within the extracellular space (Fig. S4).

Here we have presented results indicating that PARK7 is secreted via the autophagy-based unconventional secretory pathway. In summary, our data suggest that electrophilic 6-OHDA quinone lowers GSH levels and induces oxidative stress, and that this is followed by AMPK-ULK1 activation

to induce secretory autophagy, resulting in unconventional secretion of PARK7 (Figure 9).

Materials and methods

Materials

6-hydroxydopamine hydrochloride (6-OHDA; H4381), catalase (C8531), rotenone (R8875), MRT68921 (SML1644), and trehalose (T9531) were obtained from Sigma-Aldrich. Bafilomycin A₁ (023-11641), benzoquinone (171-00242), H₂O₂ (080-01186), N-acetyl-L-cysteine (NAC; 017-05131), and Z-VAD (OMe)-FMK (zVAD; 269-02071) were from Wako. Brefeldin A (203729) was from Merck. Ac-YVAD-CMK (YVAD; 10014) was from Cayman Chemical Company. Rapamycin (S1039) was obtained from Selleck Chemicals. The following antibodies were from commercial sources: anti-PARK7/DJ-1 (ab4150), anti-CTSB (abcam, ab58802); anti-RPN1 (Santa Cruz Biotechnology, sc-12164); anti-FN1 (610077), anti-CAV1 (BD Biosciences, 610060); anti-VDAC1 (Merck, AP1059); anti-LMNA (2032), anti-CASP3 (9662), anti-ATG16L1 (8089), anti-phospho-AMPK Thr172 (2535), anti-phospho-ULK1 Ser555 (5869), anti-phospho-RPS6KB1/p70S6K Thr389 (Cell Signaling Technology, 9234); and anti-LC3B (L7543), and anti-ACTB (Sigma-Aldrich, A5441). Monoclonal antibody against PARK7 (Clone 3843) was prepared as previously described [62]. All other chemicals, of analytical grade, were obtained from Sigma-Aldrich or Wako.

Cell culture

Human neuroblastoma cells from the SH-SY5Y cell line (CRL-2266) were purchased from ATCC. WT MEF and *atg5*^{-/-} MEF cells [42] were kindly provided by Dr. Noboru Mizushima (The University of Tokyo). The *atg9*^{-/-} MEF and *atg16l1*^{-/-} MEF cells [43,44] were kindly provided by Dr. Shizuo Akira (Osaka University). Cells were maintained in Dulbecco's Modified Eagle's Medium/Nutrient Mixture F-12 (DMEM/F12; Thermo Fisher Scientific, 11320-033), to which 10% fetal bovine serum (Hyclone, SH30370.03) and antibiotics (100 U/ml penicillin, 100 µg/ml streptomycin; Thermo Fisher Scientific, 15140122) had been added. Cells were grown at 37°C in an atmosphere of 5% CO₂.

Cell treatment

6-OHDA was dissolved in phosphate-buffered saline (PBS; 137 mM NaCl [Wako, 195-01663], 2.7 mM KCl [Wako, 163-03545], 8.1 mM Na₂HPO₄ [Wako, 193-02845], 7.4 mM KH₂PO₄ [Wako, 169-04245]). Brefeldin A, zVAD, YVAD, and bafilomycin A₁ were dissolved in dimethyl sulfoxide (DMSO; Wako, 043-07216). To examine PARK7 secretion, SH-SY5Y or MEF cells plated on a 6-well dish were treated with 50–100 µM 6-OHDA for 3 h and were then cultured in serum-free medium for 2 h. To evaluate the effects of brefeldin A, zVAD, YVAD, NAC, bafilomycin A₁, MRT68921, trehalose, or rapamycin, cells were pretreated with 2 µg/ml brefeldin A for 3 h, or 20 µM zVAD or YVAD for 1 h, or with 2 mM NAC for

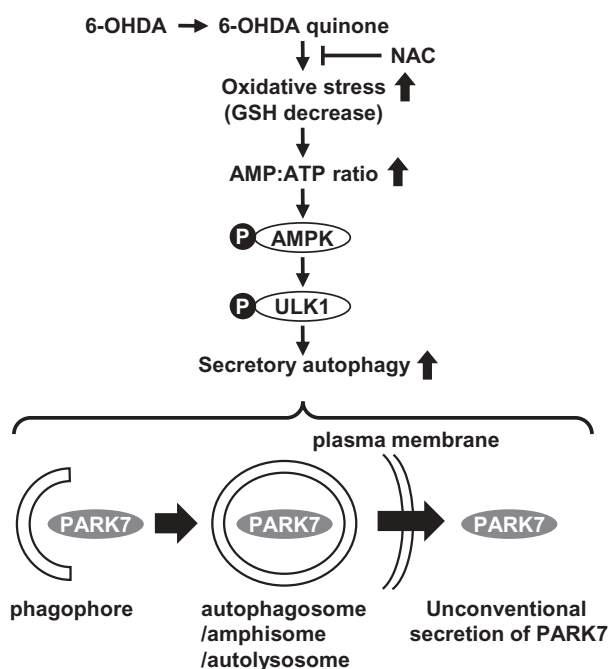


Figure 9. The proposed mechanism of autophagy-based unconventional secretion of PARK7 induced by 6-OHDA. The electrophilic 6-OHDA quinone formed from 6-OHDA lowers GSH levels and induces oxidative stress. Oxidative stress subsequently causes increase in AMP:ATP ratio and activates the AMPK-ULK1 pathway. This induces secretory autophagy, resulting in unconventional secretion of cytosolic PARK7.

2 h, or with 100 nM bafilomycin A₁ for 1 h, or 1–2 μM MRT68921 for 30 min, or 200 mM trehalose for 48 h, or 1–5 μM rapamycin for 3 h before further treatments. For benzoquinone treatment, cells were treated with 20 μM benzoquinone in serum-free medium for 3 h. For rotenone treatment, cells were treated with 0.1 or 0.2 μM rotenone for 24 h and were then cultured in serum-free medium for 2 h.

Assessment of protein secretion

Treated cells were harvested and whole cell lysates were prepared in lysis buffer (10 mM Tris-HCl, pH 7.4, 150 mM NaCl, 1% NP-40 [Sigma-Aldrich, I3021], 0.1% SDS [Wako, 191-07145], and 5 mM EDTA-2Na [Dojindo, 345-01865]) plus protease inhibitor cocktail (Nacalai Tesque, 25955-11). Protein concentration was determined by BCA assay kit (Thermo Fisher Scientific, 23225). Cultured medium from treated cells was collected and cell debris was removed by centrifugation. To concentrate the protein fraction in medium, 1 ml supernatant was mixed with 10 μg BSA carrier protein (Wako, 011-27055) and 110 μl of 100% w:v trichloroacetic acid and placed on ice for 1 h. Precipitated proteins were pelleted for 5 min at 16,000 x g at 4°C. Pelleted proteins were washed with 500 μl cold acetone and resuspended in 20 μl SDS-PAGE sample buffer (62.5 mM Tris-HCl, pH 6.8, 0.012% bromophenol blue [Wako, 029-02912], 2% SDS, 5% sucrose [Wako, 196-00015]). The protein samples were subjected to SDS-PAGE or 2D-PAGE, and to immunoblotting using appropriate antibodies as indicated in figures. An LDH (lactate dehydrogenase) release assay was performed as described previously [63]. Data are expressed as percentage of total LDH activity, after subtraction of background as determined from the medium alone.

2D-Page

Trichloroacetic acid-precipitated whole cell lysates or medium were mixed with rehydration buffer (9 M urea [Wako, 211-01213], 2% CHAPS [Dojindo, 347-04723], 65 mM dithioerythritol [Sigma-Aldrich, D8255], IPG buffer [pH 4–7; GE Healthcare Bioscience, 17-6000-86]) and applied to IPG gel strips (pH 4–7, non-linear, 7 cm; GE Healthcare Bioscience, 17-6001-10). Electrophoresis voltage was increased stepwise to reach a final voltage of 5,000 V or 8,000 V at a maximum current of 200 mA for 3–5 h. The second-dimension separation was carried out through SDS-PAGE. Densitometric analysis of reduced PARK7 and oxidized PARK7 spots were quantified by Multi Gauge software (Fujifilm), ratios (oxPARK7:total PARK7) shown being mean values.

Subcellular fractionation

SH-SY5Y cells were homogenized using a Dounce homogenizer with 60 strokes in 200 μl homogenization buffer (250 mM sucrose, 20 mM Tris-HCl, pH 7.4, 1 mM EDTA-2Na) with protease inhibitor cocktail as described previously [64]. The

resulting homogenate was centrifuged at 800 x g for 10 min twice at 4°C. The post-nuclear supernatant was pelleted at 8,000 x g for 10 min twice at 4°C. The resulting supernatant was further centrifuged at 100,000 x g for 30 min in a Beckman TLA100.3 rotor at 4°C. Each pellet was resuspended in 200 μl homogenization buffer. Equal aliquots from each fraction were analyzed for immunoblotting.

Crude cytosolic and membrane/organelle fractions were isolated from WT MEF cells by sequential detergent extraction as described previously [65]. Briefly, cells were resuspended by gentle pipetting in 200 μl digitonin buffer (150 mM NaCl, 10 mM Tris-HCl, pH 7.4, 40 μg/ml digitonin [Wako, 043-21371]). After 10 min incubation on ice, the cell suspension was centrifuged at 8,000 x g for 5 min at 4°C. The resulting supernatant was kept as cytosol-enriched digitonin extract. The resulting pellet was resuspended by vortexing in 200 μl NP-40 buffer (150 mM NaCl, 10 mM Tris-HCl, pH 7.4, 1% NP-40). After 30 min incubation on ice, samples were centrifuged at 13,000 x g for 5 min at 4°C. The resulting supernatant was kept as membrane organelle protein-enriched NP-40 extract. Equal aliquots from each fraction were analyzed for immunoblotting.

DNA constructs and transfection

Human WT or C106S PARK7 cDNA was cloned into pEGFP-N1 (Clontech, 6085-1). Human HEK293 cells (ATCC, CRL-1573) were transiently transfected using Lipofectamine 2000 (Thermo Fisher Scientific, 11668). To generate stable transfectant, cells were selected with 0.8 mg/ml G418 (Nacalai Tesque, 16512-94).

Determination of cellular GSH content

Cells were lysed in 0.2 M perchloric acid (Wako, 162-00695). The deproteinized supernatant was adjusted with 1 M CH₃COONa (Wako, 192-01075) to approximately pH 3, and this was then subjected to HPLC analysis using a column (Eicom, Eicompak SC-5ODS 3 × 150 mm) equipped with an electrochemical detection system (Eicom, HTEC-500). Flow rate of eluent (99% 0.1 M sodium phosphate buffer, pH 2.5, 1% methanol, 100 mg/l sodium octanesulfonate [Sigma-Aldrich, O0133], and 50 mg/l EDTA-2Na) was 0.5 ml/min. Glutathione (GSH) content was calculated using reduced GSH as standard, this being expressed as nmol per mg of total protein per assay.

Detection of lysosome or intracellular ROS by fluorescence microscopy

For lysosome staining, cells grown on coverslips were treated with 6-OHDA or bafilomycin A₁ for 3 h. Cells were then stained with LysoTracker Red DND-99 (Thermo Fisher Scientific, L7528) at a final concentration of 500 nM in serum-free medium for 1 h at 37°C. To detect intracellular ROS generation, cells were pre-incubated with 10 μM of DCFH-DA (Thermo Fisher Scientific, D399) for 1 h before 6-OHDA treatment. Cells were fixed with 4% paraformaldehyde (Wako, 166-2325)/PBS for 20 min and were washed with PBS twice. Cell nuclei were stained with Hoechst 33342

(Dojindo, 346–07951). Fluorescence was detected using a fluorescence microscope (OLYMPUS IX71).

Immunofluorescence staining

Cells grown on glass coverslips were fixed with cold methanol for 10 min at 4°C, and then blocked with 3% BSA in PBS for 1 h. The coverslips were incubated with anti-PARK7 (3843) and anti-LC3B antibodies for 3 h at room temperature. Confocal fluorescence images were obtained using a Zeiss LSM710 confocal microscope with oil objective lens and accompanying software (LSM Software ZEN2009).

Electron microscopy analysis

For electron microscopy, cells were fixed in phosphate-buffered 2% glutaraldehyde (Electron Microscopy Sciences, 16220), and subsequently post-fixed in 2% osmium tetroxide (Nisshin EM, 300–1) for 3 h in an ice bath, following which the cells were dehydrated in ethanol and embedded in epoxy resin. Ultrathin sections were obtained using the ultramicrotome technique. Ultrathin sections stained with uranyl acetate (Cerac) for 10 min and with lead staining solution (Sigma-Aldrich, 18–0875–2) for 5 min were subjected to TEM observation (JEM-1200 EX, JEOL) at Hanaichi Ultrastructure Research Institute (Okazaki, Japan).

Knockdown of ATG16L1 by small interfering RNA

ON-TARGETplus human *ATG16L1* siRNA (L-021033) or Non-targeting siRNA (D-001810) were obtained from Dharmacon. SH-SY5Y cells grown in 6-well plates were transfected with siRNA, at a concentration of 30 pmol/well with Lipofectamine RNAiMAX (Thermo Fisher Scientific, 13778) twice according to the manufacturer's instructions. Seventy-two h after transfection, cells were used for further analyses.

Determination of cellular AMP:ATP ratio

Cells were lysed in 0.25 ml of 0.6 N perchloric acid. Acid-insoluble material was removed by centrifugation at 1,000 x g for 5 min. The supernatant was adjusted with KOH to pH 5.0–7.0 and, after 10 min, was centrifuged at 8,000 x g for 5 min to remove KClO₄. HPLC analysis was carried out using an Inertsil ODS-2 column (GL Science). Flow rate of eluent (0.1 M sodium phosphate buffer, pH 6) was 0.5 ml/min. Nucleotides were detected by their absorbances at 260 nm, AMP:ATP ratios being calculated using standards for AMP and ATP.

Statistical analysis

Data are reported as mean ± S.D. of at least 3 independent experiments unless otherwise indicated. Statistical processing was conducted by variance analysis using Tukey test for multiple comparisons and Student t-test for comparison of 2 means. The difference was considered significant when the p value was < 0.05.

Acknowledgments

We thank Dr. Noboru Mizushima (The University of Tokyo) and Dr. Shizuo Akira (Osaka University) for providing cell lines. The authors thank Chihiro Satomi, Hitomi Takashima, Daichi Kawashima, Norie Kato for research support and Gerry Peters (JTT K.K., Takatsuki, Japan) for his careful editing of the manuscript.

Disclosure statement

No potential conflict of interest was reported by the authors.

Funding

This work was supported by the Ministry of Education, Culture, Sports, Science, and Technology-supported Program for the Strategic Research Foundation at Private Universities in Japan for the years 2012–2016 and 2015–2019, and the Cosmetology Research Foundation.

References

- [1] Nickel W, Rabouille C. Mechanisms of regulated unconventional protein secretion. *Nat Rev Mol Cell Biol.* 2009;10:148–155. PMID:19122676.
- [2] Zhang M, Schekman R. Unconventional secretion, unconventional solutions. *Science.* 2013;340:559–561. PMID:23641104.
- [3] Malhotra V. Unconventional protein secretion: an evolving mechanism. *EMBO J.* 2013;32:1660–1664. PMID:23665917.
- [4] Kineth MA, Anjard C, Fuller D, et al. The Golgi-associated protein GRASP is required for unconventional protein secretion during development. *Cell.* 2007;130:524–534. PMID:17655921.
- [5] Rubartelli A, Cozzolino F, Talio M, et al. A novel secretory pathway for interleukin-1 beta, a protein lacking a signal sequence. *EMBO J.* 1990;9:1503–1510. PMID:2328723.
- [6] Gardella S, Andrei C, Ferrera D, et al. The nuclear protein HMGB1 is secreted by monocytes via a non-classical, vesicle-mediated secretory pathway. *EMBO Rep.* 2002;3:995–1001. PMID:12231511. doi: 10.1093/embo-reports/kvf198
- [7] Temmerman K, Ebert AD, Müller HM, et al. A direct role for phosphatidylinositol-4,5-bisphosphate in unconventional secretion of fibroblast growth factor 2. *Traffic.* 2008;9:1204–1217. PMID:18419755.
- [8] Ponpuak M, Mandell MA, Kimura T, et al. Secretory autophagy. *Curr Opin Cell Biol.* 2015;35:106–116. PMID:25988755.
- [9] Nagakubo D, Taira T, Kitaura H, et al. DJ-1 a novel oncogene which transforms mouse NIH3T3 cells in cooperation with ras. *Biochem Biophys Res Commun.* 1997;231:509–513. PMID:9070310.
- [10] Bonifati V, Rizzu P, Van Baren MJ, et al. Mutations in the DJ-1 gene associated with autosomal recessive early-onset parkinsonism. *Science.* 2003;299:256–259. PMID:12446870.
- [11] Saito Y, Hamakubo T, Yoshida Y, et al. Preparation and application of monoclonal antibodies against oxidized DJ-1. Significant elevation of oxidized DJ-1 in erythrocytes of early-stage Parkinson disease patients. *Neurosci Lett.* 2009;465:1–5. PMID:19733211.
- [12] Akazawa YO, Saito Y, Hamakubo T, et al. Elevation of oxidized DJ-1 in the brain and erythrocytes of Parkinson disease model animals. *Neurosci Lett.* 2010;483:201–205. PMID:20708070.
- [13] Ariga H, Takahashi-Niki K, Kato I, et al. Neuroprotective function of DJ-1 in Parkinson's disease. *Oxid Med Cell Longevity.* 2013;2013:683920. PMID:23766857.
- [14] Taira T, Saito Y, Niki T, et al. DJ-1 has a role in antioxidative stress to prevent cell death. *EMBO Rep.* 2004;5:213–218. PMID:14749723.
- [15] Zhou W, Freed CR. DJ-1 up-regulates glutathione synthesis during oxidative stress and inhibits A53T alpha-synuclein toxicity. *J Biol Chem.* 2005;280:43150–43158. PMID:16227205.

- [16] Guzman JN, Sanchez-Padilla J, Wokosin D, et al. Oxidant stress evoked by pacemaking in dopaminergic neurons is attenuated by DJ-1. *Nature*. 2010;468:696–700. PMID:21068725.
- [17] Wilson MA. The role of cysteine oxidation in DJ-1 function and dysfunction. *Antioxid Redox Signal*. 2011;15:111–122. PMID:20812780.
- [18] Blackinton J, Lakshminarasimhan M, Thomas KJ, et al. Formation of a stabilized cysteine sulfinic acid is critical for the mitochondrial function of the parkinsonism protein DJ-1. *J Biol Chem*. 2009;284:6476–6485. PMID:19124468.
- [19] Miller DW, Ahmad R, Hague S, et al. L166P mutant DJ-1, causative for recessive Parkinson's disease, is degraded through the ubiquitin-proteasome system. *J Biol Chem*. 2003;278:36588–36595. PMID:12851414.
- [20] Canet-Avilés RM, Wilson MA, Miller DW, et al. The Parkinson's disease protein DJ-1 is neuroprotective due to cysteine-sulfinic acid-driven mitochondrial localization. *Proc Natl Acad Sci U S A*. 2004;101:9103–9108. PMID:15181200.
- [21] Le Naour F, Misek DE, Krause MC, et al. Proteomics-based identification of RS/DJ-1 as a novel circulating tumor antigen in breast cancer. *Clin Cancer Res*. 2001;7:3328–3335. PMID:11705844.
- [22] Tsuchiya B, Iwaya K, Kohno N, et al. Clinical significance of DJ-1 as a secretory molecule: retrospective study of DJ-1 expression at mRNA and protein levels in ductal carcinoma of the breast. *Histopathology*. 2012;61:69–77. PMID:22385318.
- [23] Oda M, Makita M, Iwaya K, et al. High levels of DJ-1 protein in nipple fluid of patients with breast cancer. *Cancer Sci*. 2012;103:1172–1176. PMID:22404125.
- [24] Allard L, Burkhard PR, Lescuyer P, et al. PARK7 and nucleoside diphosphate kinase A as plasma markers for the early diagnosis of stroke. *Clin Chem*. 2005;51:2043–2051. PMID:16141287.
- [25] Pardo M, García A, Thomas B, et al. The characterization of the invasion phenotype of uveal melanoma tumour cells shows the presence of MUC18 and HMG-1 metastasis markers and leads to the identification of DJ-1 as a potential serum biomarker. *Int J Cancer*. 2006;119:1014–1022. PMID:16570276.
- [26] Koide-Yoshida S, Niki T, Ueda M, et al. degrades transthyretin and an inactive form of DJ-1 is secreted in familial amyloidotic polyneuropathy. *Int J Mol Med*. 2007;19:885–893. PMID:17487420.
- [27] Waragai M, Nakai M, Wei J, et al. Plasma levels of DJ-1 as a possible marker for progression of sporadic Parkinson's disease. *Neurosci Lett*. 2007;425:18–22. PMID:17720313.
- [28] Waragai M, Wei J, Fujita M, et al. Increased level of DJ-1 in the cerebrospinal fluids of sporadic Parkinson's disease. *Biochem Biophys Res Commun*. 2006;345:967–972. PMID:16707095.
- [29] Hong Z, Shi M, Chung KA, et al. DJ-1 and alpha-synuclein in human cerebrospinal fluid as biomarkers of Parkinson's disease. *Brain*. 2010;133:713–726. PMID:20157014.
- [30] Yanagida T, Tsushima J, Kitamura Y, et al. Oxidative stress induction of DJ-1 protein in reactive astrocytes scavenges free radicals and reduces cell injury. *Oxid Med Cell Longev*. 2009;2:36–42. PMID: 20046643.
- [31] Kaneko Y, Shoji H, Burns J, et al. DJ-1 ameliorates ischemic cell death in vitro possibly via mitochondrial pathway. *Neurobiol Dis*. 2014;62:56–61. PMID:24060818.
- [32] Kim JM, Shin HI, Cha SS, et al. DJ-1 promotes angiogenesis and osteogenesis by activating FGF receptor-1 signaling. *Nat Commun*. 2012;3:1296. PMID:23250426.
- [33] Blum D, Torch S, Lambeng N, et al. Molecular pathways involved in the neurotoxicity of 6-OHDA, dopamine and MPTP: contribution to the apoptotic theory in Parkinson's disease. *Prog Neurobiol*. 2001;65:135–172. PMID:11403877.
- [34] Keller M, Rüegg A, Werner S, et al. Active caspase-1 is a regulator of unconventional protein secretion. *Cell*. 2008;132:818–831. PMID:18329368.
- [35] Cohen G, Heikkilä RE. The generation of hydrogen peroxide, superoxide radical, and hydroxyl radical by 6-hydroxydopamine, dialuric acid, and related cytotoxic agents. *J Biol Chem*. 1974;249:2447–2452. PMID:4362682.
- [36] Miyama A, Saito Y, Yamanaka K, et al. Oxidation of DJ-1 induced by 6-hydroxydopamine decreasing intracellular glutathione. *PLoS One*. 2011;6:e27883. PMID:22132160.
- [37] Watabe M, Nakaki T. Mitochondrial complex I inhibitor rotenone-elicited dopamine redistribution from vesicles to cytosol in human dopaminergic SH-SY5Y cells. *J Pharmacol Exp Ther*. 2007;323:499–507. PMID:17726156.
- [38] Duran JM, Anjard C, Stefan C, et al. Unconventional secretion of Acb1 is mediated by autophagosomes. *J Cell Biol*. 2010;188:527–536. PMID:20156967.
- [39] Dupont N, Jiang S, Pilli M, et al. Autophagy-based unconventional secretory pathway for extracellular delivery of IL-1 β . *EMBO J*. 2011;30:4701–4711. PMID:22068051.
- [40] Son SM, Cha MY, Choi H, et al. Insulin-degrading enzyme secretion from astrocytes is mediated by an autophagy-based unconventional secretory pathway in Alzheimer disease. *Autophagy*. 2016;12:784–800. PMID:26963025.
- [41] Klionsky DJ, Abdelmohsen K, Abe A, et al. Guidelines for the use and interpretation of assays for monitoring autophagy (3rd edition). *Autophagy*. 2016;12:1–222. PMID:26799652.
- [42] Kuma A, Hatano M, Matsui M, et al. The role of autophagy during the early neonatal starvation period. *Nature*. 2004;432:1032–1036. PMID:15525940.
- [43] Saitoh T, Fujita N, Hayashi T, et al. Atg9a controls dsDNA-driven dynamic translocation of STING and the innate immune response. *Proc Natl Acad Sci U S A*. 2009;106:20842–20846. PMID:19926846.
- [44] Saitoh T, Fujita N, Jang MH, et al. Loss of the autophagy protein Atg16L1 enhances endotoxin-induced IL-1 β production. *Nature*. 2008;456:264–268. PMID:18849965.
- [45] Llorente A, De Marco MC, Alonso MA. Caveolin-1 and MAL are located on prostasomes secreted by the prostate cancer PC-3 cell line. *J Cell Sci*. 2004;117:5343–5351. PMID:15466889.
- [46] Arsikin K, Kravic-Stevovic T, Jovanovic M, et al. Autophagy-dependent and -independent involvement of AMP-activated protein kinase in 6-hydroxydopamine toxicity to SH-SY5Y neuroblastoma cells. *Biochim Biophys Acta*. 2012;1822:1826–1836. PMID:22917563.
- [47] Petherick KJ, Conway OJ, Mpamhanga C, et al. Pharmacological inhibition of ULK1 kinase blocks mammalian target of rapamycin (mTOR)-dependent autophagy. *J Biol Chem*. 2015;290:11376–11383. PMID: 25833948.
- [48] Sarkar S, Davies JE, Huang Z, et al. Trehalose, a novel mTOR-independent autophagy enhancer, accelerates the clearance of mutant huntingtin and alpha-synuclein. *J Biol Chem*. 2007;282:5641–5652. PMID:17182613.
- [49] DeBosch BJ, Heitmeier MR, Mayer AL, et al. Trehalose inhibits solute carrier 2A (SLC2A) proteins to induce autophagy and prevent hepatic steatosis. *Sci Signal*. 2016;9:ra21. PMID:26905426.
- [50] Ejlerskov P, Rasmussen I, Nielsen TT, et al. Tubulin polymerization-promoting protein (TPPP/p25 α) promotes unconventional secretion of α -synuclein through exophagy by impairing autophagosome-lysosome fusion. *J Biol Chem*. 2013;288:17313–17335. PMID:23629650.
- [51] Filomeni G, De Zio D, Cecconi F. Oxidative stress and autophagy: the clash between damage and metabolic needs. *Cell Death Differ*. 2015;22:377–388. PMID:25257172.
- [52] Scherz-Shouval R, Shvets E, Fass E, et al. Reactive oxygen species are essential for autophagy and specifically regulate the activity of Atg4. *EMBO J*. 2007;26:1749–1760. PMID: 17347651.
- [53] Zmijewski JW, Banerjee S, Bae H, et al. Exposure to hydrogen peroxide induces oxidation and activation of AMP-activated protein kinase. *J Biol Chem*. 2010;285:33154–33164. PMID:20729205.
- [54] Vucicevic L, Misirkic M, Janjetovic K, et al. Compound C induces protective autophagy in cancer cells through AMPK inhibition-independent blockade of Akt/mTOR pathway. *Autophagy*. 2011;7:40–50. PMID: 20980833
- [55] Galluzzi L, Baehrecke EH, Ballabio A, et al. Molecular definitions of autophagy and related processes. *EMBO J*. 2017;36:1811–1836. PMID: 28596378.

- [56] Kimura T, Jia J, Kumar S, et al. Dedicated SNAREs and specialized TRIM cargo receptors mediate secretory autophagy. *EMBO J.* **2017**;36:42–60. PMID: 27932448.
- [57] Itakura E, Kishi-Itakura C, Mizushima N. The hairpin-type tail-anchored SNARE syntaxin 17 targets to autophagosomes for fusion with endosomes/lysosomes. *Cell.* **2012**;151:1256–1269. PMID: 23217709.
- [58] Glebov K, Schütze S, Walter J. Functional relevance of a novel SlyX motif in non-conventional secretion of insulin-degrading enzyme. *J Biol Chem.* **2011**;286:22711–22715. PMID:21576244.
- [59] Zhang M, Kenny SJ, Ge L, et al. Translocation of interleukin-1 β into a vesicle intermediate in autophagy-mediated secretion. *Elife.* **2015**;4:e11205. PMID:26523392. doi: [10.7554/eLife.11205](https://doi.org/10.7554/eLife.11205)
- [60] Inden M, Taira T, Kitamura Y, et al. PARK7 DJ-1 protects against degeneration of nigral dopaminergic neurons in Parkinson's disease rat model. *Neurobiol Dis.* **2006**;24:144–158. PMID:16860563.
- [61] Lev N, Barhum Y, Ben-Zur T, et al. Knocking out DJ-1 attenuates astrocytes neuroprotection against 6-hydroxydopamine toxicity. *J Mol Neurosci.* **2013**;50:542–550. PMID:23536331.
- [62] Saito Y, Akazawa-Ogawa Y, Matsumura A, et al. Oxidation and interaction of DJ-1 with 20S proteasome in the erythrocytes of early stage Parkinson's disease patients. *Sci Rep.* **2016**;6:30793. PMID:27470541.
- [63] Yamanaka K, Urano Y, Takabe W, et al. Induction of apoptosis and necroptosis by 24(S)-hydroxycholesterol is dependent on activity of acyl-CoA: cholesterolacyltransferase 1. *Cell Death Dis.* **2014**;5:e990. PMID:24407243.
- [64] Urano Y, Ochiai S, Noguchi N. Suppression of amyloid- β production by 24S-hydroxycholesterol via inhibition of intracellular amyloid precursor protein trafficking. *FASEB J.* **2013**;27:4305–4315. PMID:23839932.
- [65] Holden P, Horton WA. Crude subcellular fractionation of cultured mammalian cell lines. *BMC Res Notes.* **2009**;2:243. PMID:20003239.

Esterification of 24S-OHC induces formation of atypical lipid droplet-like structures, leading to neuronal cell death[■]

Wakako Takabe,* Yasuomi Urano,^{1,*} Diep-Khanh Ho Vo,* Kimiyuki Shibuya,[†] Masaki Tanno,[§] Hiroaki Kitagishi,[§] Toyoshi Fujimoto,** and Noriko Noguchi^{1,*}

Department of Medical Life Systems, Faculty of Life and Medical Sciences,* and Department of Molecular Chemistry and Biochemistry, Faculty of Sciences and Technology,[§] Doshisha University, Kyoto 610-0394, Japan; Tokyo New Drug Research Laboratories,[†] Pharmaceutical Division, Kowa Company, Ltd., Tokyo 189-0022, Japan; and Department of Anatomy and Molecular Cell Biology,** Nagoya University Graduate School of Medicine, Nagoya 466-8550, Japan

Abstract The 24(S)-hydroxycholesterol (24S-OHC), which plays an important role in maintaining brain cholesterol homeostasis, has been shown to possess neurotoxicity. We have previously reported that 24S-OHC esterification by ACAT1 and the resulting lipid droplet (LD) formation are responsible for 24S-OHC-induced cell death. In the present study, we investigate the functional roles of 24S-OHC esters and LD formation in 24S-OHC-induced cell death, and we identify four long-chain unsaturated fatty acids (oleic acid, linoleic acid, arachidonic acid, and DHA) with which 24S-OHC is esterified in human neuroblastoma SH-SY5Y cells treated with 24S-OHC. Here, we find that cotreatment of cells with 24S-OHC and each of these four unsaturated fatty acids increases prevalence of the corresponding 24S-OHC ester and exacerbates induction of cell death as compared with cell death induced by treatment with 24S-OHC alone. Using electron microscopy, we find in the present study that 24S-OHC induces formation of LD-like structures coupled with enlarged endoplasmic reticulum (ER) lumina, and that these effects are suppressed by treatment with ACAT inhibitor. Collectively, these results illustrate that ACAT1-catalyzed esterification of 24S-OHC with long-chain unsaturated fatty acid followed by formation of atypical LD-like structures at the ER membrane is a critical requirement for 24S-OHC-induced cell death.—Takabe, W., Y. Urano, D.-K. H. Vo, K. Shibuya, M. Tanno, H. Kitagishi, T. Fujimoto, and N. Noguchi. Esterification of 24S-OHC induces formation of atypical lipid droplet-like structures, leading to neuronal cell death. *J. Lipid Res.* 2016. 57: 2005–2014.

Supplementary key words acyl-CoA:cholesterol acyltransferase • Alzheimer's disease • electron microscopy • mass spectrometry • oxysterols • 24(S)-hydroxycholesterol

This work was supported in part by the Adaptable and Seamless Technology Transfer Program through target-driven R&D, Japan Science and Technology Agency Grant AS2532313Q (to Y.U.), and the Ministry of Education, Culture, Sports, Science, and Technology-supported Program for the Strategic Research Foundation at Private Universities in Japan for the years 2012–2016 and 2015–2019.

Manuscript received 16 May 2016 and in revised form 29 August 2016.

Published, JLR Papers in Press, September 19, 2016
DOI 10.1194/jlr.M068775

Copyright © 2016 by the American Society for Biochemistry and Molecular Biology, Inc.

This article is available online at <http://www.jlr.org>

The brain contains about 25% of the total amount of cholesterol in the human body (1). As the blood-brain barrier prevents cholesterol translocation between the brain and the circulation, brain cholesterol is locally produced. To maintain cholesterol homeostasis in the brain, cholesterol 24-hydroxylase (CYP46A1) converts excess amounts of cholesterol into 24(S)-hydroxycholesterol (24S-OHC), which readily crosses the blood-brain barrier (2). CYP46A1 mRNA and protein are present in neurons, but not in support cells (3). It has been reported that free 24S-OHC is present at concentrations of about 4–15 ng/mg wet weight in the human brain (4). Another report showed that 24S-OHC in four different brain areas of healthy controls was about 20 ng/mg tissue (5); assuming a volume of 1 μ l per 1 mg tissue, this would imply a concentration of 24S-OHC in brain tissue that is approximately 50 μ M. Several lines of evidence suggest that dysregulation of cholesterol and 24S-OHC metabolism in the brain has been linked to the development of neurodegenerative diseases such as Alzheimer's disease (AD) and Parkinson's disease (6–11). Several studies reported that 24S-OHC levels increase or decrease in plasma and cerebrospinal fluid of patients with AD or mild cognitive impairment (11–13); although inconclusive, the differing degrees of progression of disease may account for the different results observed. Selective expression of CYP46A1 around neuritic plaques has also been reported

Abbreviations: AA, arachidonic acid; AD, Alzheimer's disease; ADRP, adipose differentiation-related protein; CYP46A1, cholesterol 24-hydroxylase; DART, direct analysis in real time; ER, endoplasmic reticulum; EtOH, ethanol; LA, linoleic acid; LD, lipid droplet; MLKL, mixed lineage kinase domain-like; OA, oleic acid; PA, palmitic acid; RIPK, receptor-interacting protein kinase; SA, stearic acid; SCD1, stearoyl-CoA desaturase 1; 24S-OHC, 24(S)-hydroxycholesterol.

¹To whom correspondence should be addressed.

e-mail: yurano@doshisha.ac.jp (Y.U.); nnoguchi@mail.doshisha.ac.jp (N.N.)

■ The online version of this article (available at <http://www.jlr.org>) contains a supplement.

(14). Moreover, in the brains of patients with AD, increased CYP46A1 expression in astrocytes has been observed (15, 16). Furthermore, we and other groups have shown that 24S-OHC possesses a potent neurotoxicity that may be involved in the etiology of neurodegenerative disease (17, 18). We have also shown that high concentrations of 24S-OHC can induce caspase-independent cell death in human neuroblastoma SH-SY5Y cells and rat primary cortical neuronal cells (18).

Necroptosis is a form of caspase-independent programmed necrosis (19–21). Necroptosis can be caused by death receptor ligands or stimuli that induce expression of death receptor ligands under apoptotic-deficient conditions such as absence of functional caspase-8. This regulated cell death requires three proteins, these being: receptor-interacting protein kinase (RIPK)1, RIPK3, and mixed lineage kinase domain-like (MLKL). We have shown that necrostatin-1 (a specific inhibitor of RIPK1 kinase activity) or knockdown of RIPK1 significantly suppresses 24S-OHC-induced cell death (18). We further showed that RIPK1, but neither RIPK3 nor MLKL, was expressed in SH-SY5Y cells, suggesting that 24S-OHC induces RIPK1-dependent necroptosis-like cell death (22). Interestingly, we found that the neuronal cells used did not express caspase-8, which we understood to be the reason why 24S-OHC induced necroptosis-like cell death and not apoptosis. When we induced the expression of caspase-8 in SH-SY5Y cells by treating the cells with all-*trans*-retinoic acid, we found that apoptosis could be induced by 24S-OHC (23). We have also shown that 24S-OHC induces apoptosis in human T lymphoma Jurkat cells that endogenously express caspase-8, and that 24S-OHC induces RIPK1-dependent, but MLKL-independent, necroptosis-like cell death in caspase-8-deficient Jurkat cells (22). Despite clues drawn from the foregoing research, however, the specific molecular mechanisms responsible for induction of cell death have remained unclear.

ACAT1, an enzyme located in the endoplasmic reticulum (ER), forms cholesteryl esters to store or prevent cytotoxic build-up of cholesterol (24). We had previously found that ACAT1 catalyzes 24S-OHC esterification to produce at least four varieties of 24S-OHC esters, leading to formation of lipid droplets (LDs) that stained positive with the fluorescent probe, Nile red, in SH-SY5Y cells (25). Because selective ACAT1 inhibitor or ACAT1 siRNA suppresses both 24S-OHC-induced LD formation and cell death, we postulated that ACAT1-catalyzed esterification of 24S-OHC might be responsible for initiation of cell death signaling. However, even if our postulated explanation was correct, it was still unclear to us which varieties of 24S-OHC esters might have formed in the cells treated with 24S-OHC because, at the time of our previous study, no useful method had as yet been established for identifying oxysterol esters and no compounds suitable for use as 24S-OHC ester reference standards were as yet available. Moreover, it was still unclear to us at that time whether the cell death that we observed might be due to the specific cytotoxic effect of some particular 24S-OHC ester or whether it might be the accumulation of total 24S-OHC ester regardless of the

variety that was responsible. It was also unknown to us at that time whether it was accumulation of 24S-OHC ester or formation of LDs (or some other unknown phenomenon) that was responsible for cell death signaling.

In the present study, we investigate the precise association between 24S-OHC-induced cell death and the ACAT1-catalyzed 24S-OHC esterification that is responsible for LD formation. We find that there are increased amounts of esters produced by esterification of 24S-OHC with four varieties of long-chain unsaturated fatty acid in 24S-OHC-treated SH-SY5Y cells. We further show that 24S-OHC induces formation of atypical LD-like structures coupled with enlarged ER lumina in SH-SY5Y cells. We conclude that formation of atypical LD-like structures and the accompanying abnormal ER morphology, both of which are caused by accumulation of 24S-OHC esters, play an important role in 24S-OHC-induced cell death.

MATERIAL AND METHODS

Materials

ACAT inhibitor F12511 was the generous gift of Dr. Ta-Yuan Chang (Dartmouth Medical School, Hanover, NH). The 24S-OHC and various forms of esterified 24S-OHC were synthesized as we previously reported (26). All fatty acids and Nile red were obtained from Sigma-Aldrich (St. Louis, MO). BODIPY 493/503 and DAPI were from Thermo Fisher Scientific (Waltham, MA). Stearoyl-CoA desaturase 1 (SCD1) inhibitor was from BioVision (Milpitas, CA). All other chemicals, of analytical grade, were obtained from Sigma-Aldrich or Wako (Osaka, Japan).

Cell culture

Human neuroblastoma cells from the SH-SY5Y cell line were purchased from American Type Culture Collection (Manassas, VA). Cells were maintained in Dulbecco's modified Eagle's medium/nutrient mixture F-12 (Thermo Fisher Scientific), which contained 10% fetal bovine serum (Hyclone, Logan, UT) and antibiotics (100 U/ml penicillin, 100 mg/ml streptomycin; Thermo Fisher Scientific). Cells were grown at 37°C in an atmosphere of 5% CO₂.

Cell treatment

The 24S-OHC and oleic acids (OAs) were dissolved in ethanol (EtOH) and stored at –20°C. To examine toxicity or esterification of 24S-OHC in SH-SY5Y cells, cells were treated with 50 μM 24S-OHC (final concentration of EtOH in the medium was 0.5%) in the presence or absence of 50 μM of each fatty acid under study for the indicated period. To evaluate LD formation, cells were treated with 50 μM 24S-OHC or 200 μM OA for the indicated period. Control cells were treated with EtOH.

Knockdown of ACAT1 and RIPK1 by siRNA

Stealth siRNA targeting human RIPK1 (18), ACAT1 (25), and Stealth RNAi negative control were obtained from Thermo Fisher Scientific. Cells were transfected with siRNAs using Lipofectamine RNAiMax (Thermo Fisher Scientific) as previously described (18, 25). Forty-eight hours after transfection, cells were used for further analyses.

Neutral lipid staining

Neutral lipids were stained with Nile red as previously described (25) and fluorescence images were obtained using an inverted

fluorescence microscope (OLYMPUS IX71; Tokyo, Japan). To clarify the localization of neutral lipid-rich structures, cells were stained with BODIPY 493/503 (Thermo Fisher Scientific). Briefly, cells were fixed in a mixture of 3% formaldehyde and 0.025% glutaraldehyde in 0.1 M phosphate buffer (pH 7.4) for 15 min. Cells were then stained with 0.5 μ g/ml BODIPY 493/503 for 15 min at room temperature. Nuclei were counterstained by DAPI and images were obtained using confocal microscopy (Zeiss LSM710; Oberkochen, Germany).

Lipid extraction and HPLC analysis

Cellular lipids were extracted and HPLC analysis was performed as described previously (25). Briefly, after the treatment, the medium was removed and the cells were washed with PBS three times, lysed in 0.2 M NaOH, and neutralized immediately with 3 M HCl and 1 M KH_2PO_4 . The Folch method (2:1, v/v chloroform/methanol) was thereafter used to extract lipids, the chloroform phase being evaporated in a nitrogen gas environment. The dry residue was then dissolved in eluent without water, and this was subjected to HPLC analysis. HPLC was carried out using an Inertsil ODS-3 column (5 μ m, 4.6 \times 250 mm; GL Science, Tokyo, Japan) in combination with a pump (PU-980 Intelligent HPLC pump; Nihon Bunko, Tokyo, Japan), an UV detector outputting a signal in units of millivolts (UV-970 Intelligent UV/VIS detector; Nihon Bunko), and a data processor (EPC-500; Eicom, Kyoto, Japan) under conditions such that flow rate of eluent (acetonitrile/2-propanol/water, 43/53/4) was 1.0 ml/min.

Direct analysis in real time-MS analysis

Synthesized 24S-OHC esters were dissolved in CHCl_3 at concentrations of approximately 10^{-4} M and the resulting solutions were subjected to measurement of mass spectra. For cellular extract, lipid extracts were fractionated by HPLC, the eluent was removed using nitrogen gas, the dry residue was dissolved in CHCl_3 (approximately 100 μ l), and the resulting CHCl_3 solutions were subjected to MS analysis. Measurement of mass spectra was carried out using an LCMS 2020 instrument (Shimadzu, Kyoto, Japan) equipped with a direct analysis in real time (DART)-SVP ion source (IonSense, Inc., Saugus, MA). Helium was used as ionization gas at a temperature of 500°C. Mass spectra were obtained with the instrument set to positive ion mode.

Determination of cell viability

To determine cell viability, WST-8 assay was performed using a Cell Counting Kit-8 (Dojindo, Kumamoto, Japan) according to the manufacturer's protocol. MTT assay was performed as described previously (18). Data were expressed as percentages relative to cells treated with vehicle serving as control.

Isolation of LD-enriched fraction

Cells were resuspended in buffer A [25 mM Tris-HCl (pH 7.4), 100 mM KCl, 1 mM EDTA, 1 mM EGTA] with protease inhibitor cocktail (Nacalai Tesque, Kyoto, Japan). Cells were disrupted under high pressure by nitrogen bomb at 800 psi for 15 min, and the lysate was centrifuged for 10 min at 1,000 g at 4°C. The postnuclear supernatant was mixed with an equal volume of 1.08 M sucrose in buffer A (final sucrose concentration was 0.54 M). This postnuclear supernatant (1.25 ml) in 0.54 M sucrose in buffer A, 1.25 ml of 0.27 M sucrose in buffer A, 1.25 ml of 0.135 M sucrose in buffer A, and 1.25 ml of buffer A without KCl were layered sequentially in 5 ml tubes for ultracentrifugation (Beckman Coulter, Brea, CA). Tubes were centrifuged at 34,000 rpm at 4°C for 1 h using an Optima L-90K Ultracentrifuge (Beckman Coulter) with a swing rotor (SW 55 Ti). Following centrifugation, fractionated samples were collected at 0.5 ml intervals from the top of each tube.

Immunoblotting and MS analysis

Equal aliquots from each fraction were subjected to SDS-PAGE and immunoblotting by using primary antibodies specific for adipose differentiation-related protein (ADRP; Fitzgerald Industries International, Acton, MA), ribophorin-1 (Santa Cruz Biotechnologies, Dallas, TX), and RIPK1 (BD Biosciences, San Jose, CA) with appropriate secondary antibodies. Immunoblotting was visualized with enhanced chemiluminescence (Millipore, Billerica, MA). For each set of conditions, i.e., EtOH, 24S-OHC, and OA as indicated in Fig. 6B, the top three fractions were subjected to SDS-PAGE and were detected by silver staining using a Dodeca silver stain kit (Bio-Rad, Berkeley, CA). Visible bands obtained by silver staining were manually cut and subjected to LC-MS as described previously (6).

Electron microscopy analysis

For electron microscopy, cells cultured on glass coverslips were fixed for more than 2 h in a mixture of 2% formaldehyde and 2.5% glutaraldehyde in 0.1 M HEPES-NaOH (pH 7.4), to which 1 mM CaCl_2 had been added, and were thereafter postfixed for 1 h in a mixture of 1% osmium tetroxide and 0.1% potassium ferrocyanide in 0.1 M sodium cacodylate buffer (27), following which they were dehydrated and embedded in epoxy resin. Ultrathin sections were observed using a JEM1011 electron microscope (JEOL, Tokyo, Japan) operated at 100 kV.

Statistical analysis

Data are reported as mean \pm SD of at least three independent experiments. The statistical significance of the difference between the determinations was calculated by an ANOVA using Tukey's test for multiple comparisons. The difference was considered significant at $P < 0.05$.

RESULTS

The 24S-OHC-induced neutral lipid-rich structure formation occurred upstream of RIPK1 signaling in SH-SY5Y cells

We have previously shown that siRNA knockdown of either ACAT1 or RIPK1 significantly suppresses 24S-OHC-induced cell death (18, 25). In the present study, to examine the relationship between 24S-OHC-induced LD formation and RIPK1 activation, cells were transfected with ACAT1 (siACAT1), RIPK1 (siRIPK1), or negative control siRNA oligos for 48 h, and were then treated with 50 μ M 24S-OHC or vehicle (0.5% EtOH) for a further 6 h. Consistent with previous findings, knockdown of ACAT1 was found to suppress 24S-OHC-induced Nile red-positive LD formation (Fig. 1). In contrast, knockdown of RIPK1 did not affect 24S-OHC-induced LD formation. These data suggested that 24S-OHC-induced LD formation was occurring upstream of RIPK1 signaling.

Esterified forms of 24S-OHC in which 24S-OHC was esterified with four varieties of unsaturated fatty acid were identified in SH-SY5Y cells treated with 24S-OHC

Because we had previously observed that LD formation due to accumulation of 24S-OHC esters occurs in the early stage of 24S-OHC-induced cell death (25), we next focused on identifying which fatty acids it was that were esterifying with 24S-OHC. We previously reported being able to detect

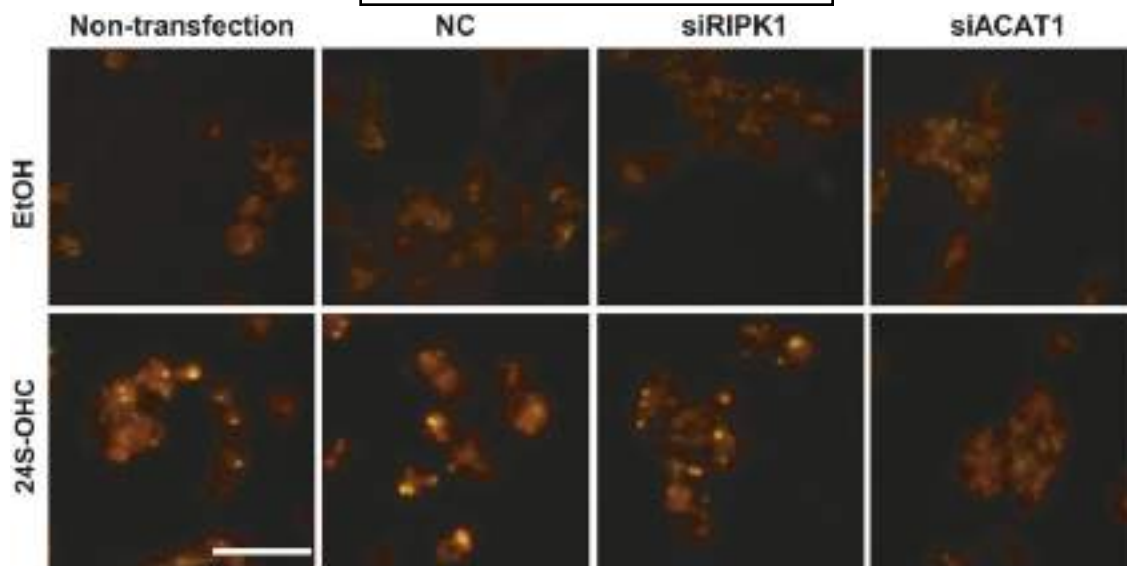


Fig. 1. Formation of Nile red-positive structure induced by 24S-OHC, which was attenuated by knockdown of ACAT1, but not by knockdown of RIPK1. SH-SY5Y cells were transfected with RIPK1 (siRIPK1), ACAT1 (siACAT1), or negative control (NC), siRNA oligo, for 48 h, and the cells were then treated with 50 μ M 24S-OHC for 6 h and were thereafter stained with Nile red. Representative images are shown. Scale bar, 50 μ m.

at least four different varieties of esterified 24S-OHC using HPLC in SH-SY5Y cells when cells were treated with 24S-OHC (25). In that study, we also confirmed that formation of 24S-OHC esters was diminished by ACAT inhibitor. Using the same technique as in our previous study, we first investigated those fatty acids which we had reason to expect might participate in 24S-OHC esterification. We focused on abundant fatty acids in the brain, such as DHA, arachidonic acid (AA), linoleic acid (LA), OA, stearic acid (SA), and palmitic acid (PA). In this first part of our present study, for each fatty acid under study, cells were cotreated with 50 μ M fatty acid and 50 μ M 24S-OHC for 6 h, and lipid extracts were thereafter subjected to HPLC analysis. As observed previously, significant increases in peak area were observed at four peaks in 24S-OHC-treated cells (Fig. 2A, 24S-OHC) as compared with the vehicle control condition (EtOH). When cells were cotreated with DHA, a marked increase in the area under peak 1 was observed (Fig. 2A, peak 1'). Similarly, treatment of cells with AA, LA, or OA showed marked increase in the area under peak 2, 3, or 4, respectively (Fig. 2A, peaks 2'–4'). In contrast, cotreatment with SA or PA did not affect the corresponding peak (Fig. 2B). These results suggested that ACAT1 favors unsaturated fatty acids for esterification of 24S-OHC.

For further identification of these four peaks, we synthesized candidate 24S-OHC esters (26), such as 24S-OHC-DHA, 24S-OHC-AA, 24S-OHC-LA, and 24S-OHC-OA (supplemental Fig. S1). We performed spiking experiments using these synthesized 24S-OHC esters by adding each synthesized 24S-OHC ester to lipid extract from 24S-OHC-treated cells, and then subjecting the ester-containing extract samples to HPLC analysis. When the lipid extract sample that contained 24S-OHC-DHA was analyzed, it was found that the area under peak 1 had increased as compared with lipid extract alone (Fig. 3, peak 1"). Similarly, lipid extract

samples that contained 24S-OHC-AA, 24S-OHC-LA, or 24S-OHC-OA showed a marked increase in the area under the respective peak 2, 3, or 4, as compared with lipid extract alone (Fig. 3, peaks 2"–4"). Note that we also measured the retention times of the peaks observed with synthesized 24S-OHC-SA and 24S-OHC-PA, and found that neither of these corresponded to any of the retention times measured for peaks 1–4 (data not shown).

Finally, we employed a novel mass spectrometric technique for yet further identification of the respective 24S-OHC esters. Prior to settling on the mass spectrometric technique that is reported below, we first tried to use gas chromatography-MS, matrix-assisted laser desorption/ionization time-of-flight-MS, and electrospray ionization-MS; despite our best attempts with each of these methods, however, we were unable to detect mass spectrographic patterns corresponding to the 24S-OHC esters due to difficulties experienced in ionizing these esters. But as we had recently established a novel technique using DART-MS that permits specific ion peaks derived from synthesized 24S-OHC esters to be detected (26), we decided to apply our DART-MS technique to identification of the 24S-OHC esters formed in SH-SY5Y cells using synthesized 24S-OHC esters as reference standards. Using a procedure similar to that described above with reference to Fig. 2, for each fatty acid under study, cells were treated with 50 μ M fatty acid and 50 μ M 24S-OHC for 6 h, following which each of the four peaks (peaks 1'–4') was collected by HPLC, and these were thereafter subjected to DART-MS analysis. For all DART-MS measurements, our instrument was operated in positive ion mode under conditions such that synthesized 24S-OHC esters were detected as $[M+NH_4]^+$ adduct ions (Fig. 4A). For example, synthesized 24S-OHC-DHA was detected by the presence of the parent ion peak at m/z 731 in the resulting spectra. The fragment ion peak at m/z 385

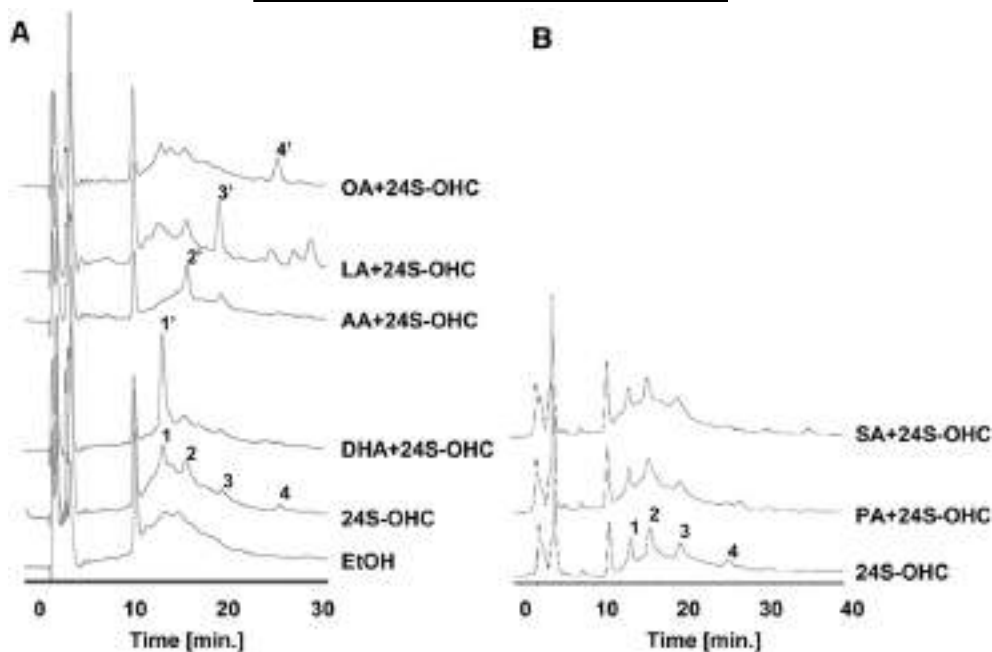


Fig. 2. The 24S-OHC preferentially formed esters with unsaturated fatty acids rather than saturated fatty acids in SH-SY5Y cells. A, B: SH-SY5Y cells were treated with vehicle (EtOH) or 50 μM 24S-OHC in the presence or absence of 50 μM unsaturated fatty acid (A) or 50 μM saturated fatty acid (B) for 6 h. Lipid extracts were subjected to HPLC analysis.

was attributed to the ester linkage. Based on comparison with synthesized 24S-OHC-DHA, -AA, -LA, -OA (Fig. 4A), and 24S-OHC-PA, -SA (supplemental Fig. S2), the adduct ion of m/z 731 at peak 1' (Fig. 4B) was found to be identical to that of synthesized 24S-OHC-DHA. Similarly, the adduct ion of m/z 707 at peak 3', m/z 683 at peak 2', and m/z 685 at peak 4' were respectively found to be identical to those of synthesized 24S-OHC-AA, 24S-OHC-LA, and 24S-OHC-OA. Collectively, these data suggest that DHA, AA, LA, and OA are fatty acids that are used for esterification of 24S-OHC in 24S-OHC-treated SH-SY5Y cells.

Effect that cotreatment with fatty acid had on 24S-OHC-induced cell death in SH-SY5Y cells

Because it was our observation that at least four varieties of 24S-OHC ester accumulate in 24S-OHC-treated cells, we considered it important to determine whether any particular 24S-OHC ester had specific cytotoxic effect or whether it was the formation of LD that triggered cell death signaling regardless of the variety of 24S-OHC ester. Unfortunately, synthesized 24S-OHC esters could not be introduced directly into cells due to their high hydrophobicity (data not shown). To evaluate the cytotoxic properties of these four varieties of 24S-OHC ester, for each unsaturated fatty acid under study, we therefore evaluated the effect of cotreatment with 24S-OHC and 50 μM unsaturated fatty acid for 24 h (Fig. 5) in SH-SY5Y cells, because in the present study we had already confirmed that there was increase of the corresponding 24S-OHC ester under the same treatment for 6 h (Fig. 2). WST-8 assay was performed to determine the effect of cotreatment with 24S-OHC and fatty acid on cell death. As a result, we found that cotreatment with 24S-OHC and each of the fatty acids under

study, except DHA, decreased cell viability as compared with treatment with 24S-OHC alone. Because we found that, at the concentration employed, none of the fatty acids induced cell death in SH-SY5Y cells, this supports our conclusion that, for all fatty acids under study for which reduction of cell viability was observed, it was cotreatment with the fatty acid and not any cytotoxicity on the part of the fatty acid itself that was responsible for the reduction of cell viability that we observed. These data suggest that it may be the accumulation of total esterified 24S-OHC and the resulting LD formation that causes cell death, independent of any specificity on the part of the ester employed for cotreatment.

The 24S-OHC induced LD-like structures along with swollen ER in SH-SY5Y cells

It is generally believed that LDs are formed to store excess lipids and protect cells against toxicity of lipids (28, 29). However, our present study showed that 24S-OHC-derived LD formation might actually be a cause of cell death. To compare 24S-OHC-induced LDs that we observed with fatty acid-induced TG-rich typical LDs, treatment with OA at high concentration (200 μM) was employed to induce LD formation. We first investigated the localization of LDs in SH-SY5Y cells in response to 50 μM 24S-OHC or 200 μM OA for 6 h by using Nile red (Fig. 6A) or the fluorescent probe, BODIPY 493/503, both of which stain neutral lipids (supplemental Fig. S3). We found as a result of our investigation that OA-treated cells had abundant LDs, these being dispersed throughout the cytoplasm, while 24S-OHC-treated cells had only a limited number of LDs, these being present near the nuclei. Cotreatment with 24S-OHC and 50 μM OA, which decreased cell viability as

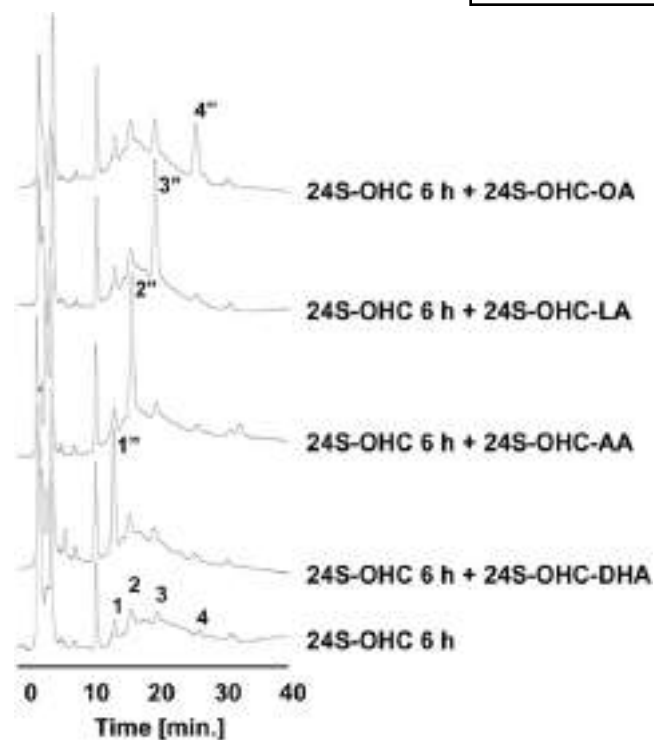


Fig. 3. Retention times of four synthesized 24S-OHC esters corresponded to those of four peaks observed in 24S-OHC-treated cells. SH-SY5Y cells were treated with 50 μ M 24S-OHC for 6 h. Lipid extracts were mixed with synthesized 4 nmol 24S-OHC-DHA, -LA, -OA, or 2 nmol 24S-OHC-AA for spiking and were thereafter subjected to HPLC analysis.

compared with treatment with 24S-OHC alone (Fig. 5), showed increases in both the number and the size of Nile red-positive LDs (Fig. 6A).

To further evaluate 24S-OHC-treated cells versus OA-treated cells with respect to formation of LDs, we applied sucrose density gradient centrifugation to attempt to isolate LD-enriched fractions from 24S-OHC-treated cells and OA-treated cells. ADRP, which is an LD-associated protein (28), was used as marker for LDs. LDs were generally recovered at the top surface, while other organelles were recovered at lower fractions along the gradient. The results showed that, for OA-treated cells, ADRP was detected at the top fraction (fraction #1), whereas the ER marker protein, ribophorin-1, and the cytosolic protein, RIPK1, were enriched in the bottom fractions (fractions #9, #10) (Fig. 6B, right panel). However, no ADRP was observed in any fraction recovered from 24S-OHC-treated cells (Fig. 6B, center panel), even though Nile red-positive and BODIPY-positive structures were observed in those cells (Figs. 1, 6A). Three fractions from the top in each condition were further subjected to silver staining and MS analysis (supplemental Fig. S4). The results showed that various proteins reported to exist in LDs (29) were detected in the top fraction obtained from OA-treated cells, but were not detected in the top fraction obtained from 24S-OHC-treated cells. Cell viability assays of 24S-OHC-treated cells and OA-treated cells showed that while significant cell death occurred in cells treated with 24S-OHC for 24 h, treatment with OA for 24 h did not induce cell death (Fig. 6C), suggesting that

typical LD formation itself was not a cytotoxic event in SH-SY5Y cells.

To further examine 24S-OHC-induced LDs in SH-SY5Y cells, we performed morphological analysis using electron microscopy. Cells were treated with either 50 μ M 24S-OHC or 200 μ M OA for 6 h, following which conventional ultrathin sections were prepared. While no LD structure was observed in EtOH-treated control cells (Fig. 7A), typical LD structures were observed in the cytoplasm of OA-treated cells (Fig. 7B). In contrast to the typical LD structures observed in OA-treated cells, in 24S-OHC-treated cells we observed atypical LD-like structures (Fig. 7C, white asterisk) that appeared to be attached to some sort of enlarged membrane structure (black star). Because our observations suggested that these enlarged membrane structures were connected to the ER membrane (Fig. 7C, arrow), we theorized that these structures might have formed as a result of enlargement of the ER lumen. Cells cotreated with 50 μ M OA and 24S-OHC showed an increased amount of 24S-OHC-OA (Fig. 2A) and decreased cell viability (Fig. 5), and it was further observed that there was an increase in the size of the atypical LD-like structures (Fig. 7D, white asterisk) that were attached to the enlarged membrane structures (Fig. 7D, black star). When cells were treated with 24S-OHC in the presence of F12511, an ACAT inhibitor, the 24S-OHC-induced atypical LD-like structures disappeared, but unknown multilamellar structures were observed (Fig. 7E, arrowhead). These observations led us to conclude that 24S-OHC induces ACAT-dependent atypical LD-like structures along with enlarged ER lumina, these being features that are different from typical OA-induced LDs, in SH-SY5Y cells.

DISCUSSION

ACAT generally catalyzes the esterification of free cholesterol with fatty acid to yield cholesteryl ester in the ER (19). Two ACAT isoenzymes, ACAT1 and ACAT2, have been identified. ACAT1 is the main isoenzyme in the brain (30). We have found that *ACAT1* mRNA, but not *ACAT2* mRNA, is expressed in SH-SY5Y cells (25). One study reported that ACAT1 showed a slight preference for oleoyl-CoA, compared with palmitoyl-, linoleoyl-, or arachidonyl-CoA, as substrate in insect cells expressing human ACAT1 (31). Another study has shown that microsomes isolated from human ACAT1-expressing CHO cells showed strong substrate preference for oleoyl-CoA, compared with linolenoyl-, arachidonyl-, or eicosapentaenoyl-CoA (32). In our present study, we showed that ACAT1 preferentially utilizes long-chain unsaturated fatty acids (OA, LA, AA, and DHA) rather than saturated fatty acids (PA and SA) for esterification of 24S-OHC. Our previous (25) and present results suggest that 24S-OHC ester forms in SH-SY5Y cells in relative amounts such that 24S-OHC-OA > 24S-OHC-LA > 24S-OHC-AA > 24S-OHC-DHA, but there was no significant difference among these four fatty acids in terms of any observed preference as substrate for ACAT1. The present study showed that at least four varieties of 24S-OHC ester

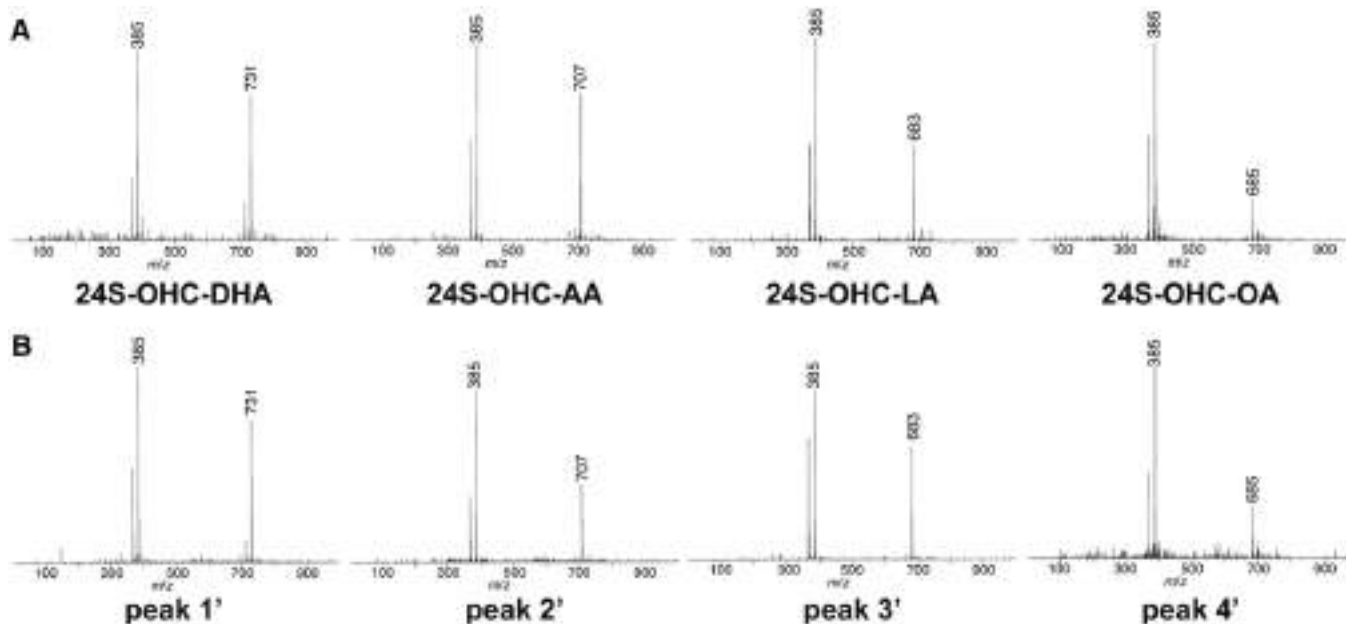


Fig. 4. DART-MS spectra of synthesized 24S-OHC esters and of fractions collected by HPLC from 24S-OHC-treated cells. For each unsaturated fatty acid under study, SH-SY5Y cells were treated with 50 μ M 24S-OHC and 50 μ M fatty acid for 6 h as in Fig. 2. Lipid extracts were subjected to HPLC analysis. Synthesized 24S-OHC esters (A) and fractions collected by HPLC (B) were further subjected to DART-MS analysis.

accumulated in 24S-OHC-treated cells, though it is possible that other minor esterified forms of 24S-OHC may also have formed in the cells. We also found that cotreatment with 24S-OHC and any of the four unsaturated fatty acids tested resulted in a cell death that was enhanced as compared with that which was induced by 24S-OHC alone. Specific enhancement of 24S-OHC-induced cell death as a result of cotreatment with any particular one of the unsaturated fatty acids tested was not observed, suggesting that it was the accumulation of total 24S-OHC ester regardless of variety, and not the specific cytotoxicity of any particular 24S-OHC ester, that was responsible for the 24S-OHC-induced cell death that we observed. We also found that 24S-OHC-induced cell death was significantly reduced when cells were cotreated with an inhibitor of SCD1 (supplemental Fig. S5); because SCD1 catalyzes the synthesis of mono-unsaturated fatty acids from saturated fatty acids, this supported the idea that esterification of 24S-OHC with unsaturated fatty acid is responsible for 24S-OHC-induced cell death. Interestingly, extracellular esterification of 24S-OHC by lecithin:cholesterol acyltransferase reduces the cytotoxic effect of 24S-OHC by limiting uptake of 24S-OHC esters by cells (33), suggesting that ACAT1-catalyzed intracellular esterification of 24S-OHC plays an important role in 24S-OHC-induced cell death.

In our present study, biochemical and morphological analysis revealed that ACAT1-mediated 24S-OHC esterification induced formation of atypical LD-like structures coupled with what appeared to be a swollen ER structure, but that the presence of OA induced typical LD formation without affecting cell viability in SH-SY5Y cells. Many lines of evidence suggest that LDs are formed within the ER membrane (28, 29). Most conventional models have assumed that formation of LDs occurs with an initial accumulation

of TG or sterol ester between the two leaflets of the ER membrane. It is believed that at some point the prenascent LD structure presumably buds off from the ER, forming a nascent LD, followed by growth of the LD. Because ACAT1 is localized in the ER membrane, the conventional thinking has been that newly produced 24S-OHC esters might accumulate between the two membrane leaflets of the ER in similar fashion as would be the case with a cholesteryl ester. However, unlike cholesteryl esters, which are entirely hydrophobic, 24S-OHC esters have a hydroxyl group at position 24 in their steroid side chain (supplemental Fig. S1). It is therefore plausible that the polar moiety at the side chain and the nonpolar moiety at the sterol ring in combination with the fatty acid portion of the 24S-OHC ester might act together to upset orientation of the 24S-OHC

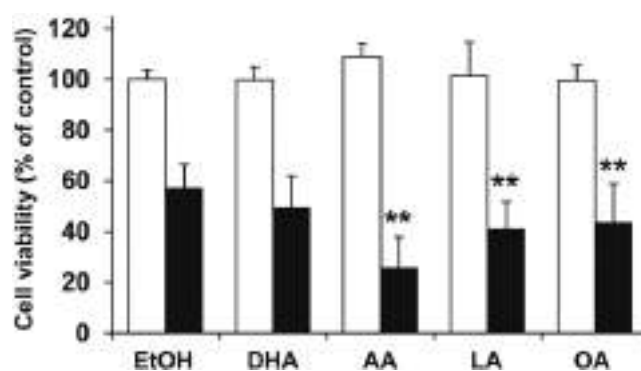


Fig. 5. Cotreatment with unsaturated fatty acid and 24S-OHC enhanced 24S-OHC-induced cell death. For each fatty acid under study, SH-SY5Y cells were treated with 50 μ M 24S-OHC in the presence or absence of 50 μ M fatty acid for 24 h. Cell viability was measured by WST-8 assay. ** $P < 0.01$, when compared with cells with 24S-OHC and EtOH.

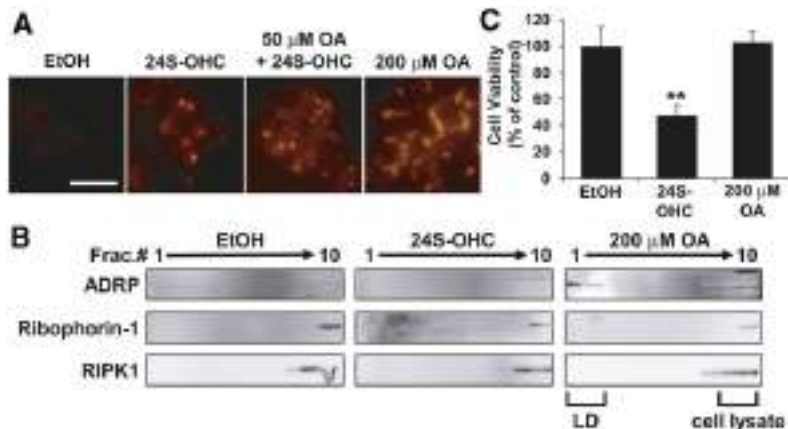


Fig. 6. The 24S-OHC-induced LD-like structures were different from OA-induced TG-rich LDs. A–C: SH-SY5Y cells were treated with 50 μ M 24S-OHC or 200 μ M OA for 6 h (A), 16 h (B), or 24 h (C). A: Cells were also cotreated with 50 μ M 24S-OHC and 50 μ M OA for 6 h. Cells were thereafter stained with Nile red. Representative images are shown. Scale bar, 20 μ m. B: The postnuclear supernatants were fractionated by using ultracentrifugation with different densities of sucrose. Equal aliquots from each fraction were subjected to immunoblotting with appropriate antibodies as indicated. C: Cell viability was measured by MTT assay. ** $P < 0.01$, when compared with cells with EtOH.

ester in the membrane bilayer, thereby disturbing ER membrane integrity and causing LD formation to become atypical. Because it has been reported that dysregulation of ER function, such as that which is caused by severe ER stress, can induce cell death (34–36), we postulated that disturbance of ER homeostasis by accumulation of 24S-OHC ester could trigger cell death signaling. Another possibility is that the atypical LD-like structures and/or swollen ER structures that we observed could be providing an intracellular platform to permit association of certain proteins that promote cell death signaling. Further experiments will be required to address these possibilities. It is noted that unknown multilamellar structures were observed in 24S-OHC-treated cells that had been cotreated with ACAT inhibitor. It is thought that formation of such unknown multilamellar structures might occur as a result of accumulation of free 24S-OHC. Because ACAT inhibitor suppressed

24S-OHC-induced cell death, these unknown multilamellar structures were not thought to be associated with cell death signaling. Interestingly, it has been reported that treatment with polar oxysterol (7-ketocholesterol, 7 β -hydroxycholesterol, cholesterol-5 β , 6 β epoxide) induced a multilamellar cytoplasmic structure that was predominantly lysosomal in origin in various cell types (37, 38). Further studies are needed to characterize the multilamellar structures that were observed in the present study.

With respect to methodology, in our present study we found that we were able to effectively ionize 24S-OHC esters using the DART method. Although mass spectrometric analysis is a powerful tool to investigate unknown biochemical compounds, inability to ionize esterified forms of sterols and sterol derivatives has forced many researchers to employ the saponification method, which unfortunately only permits evaluation of total sterol content (25, 39). In

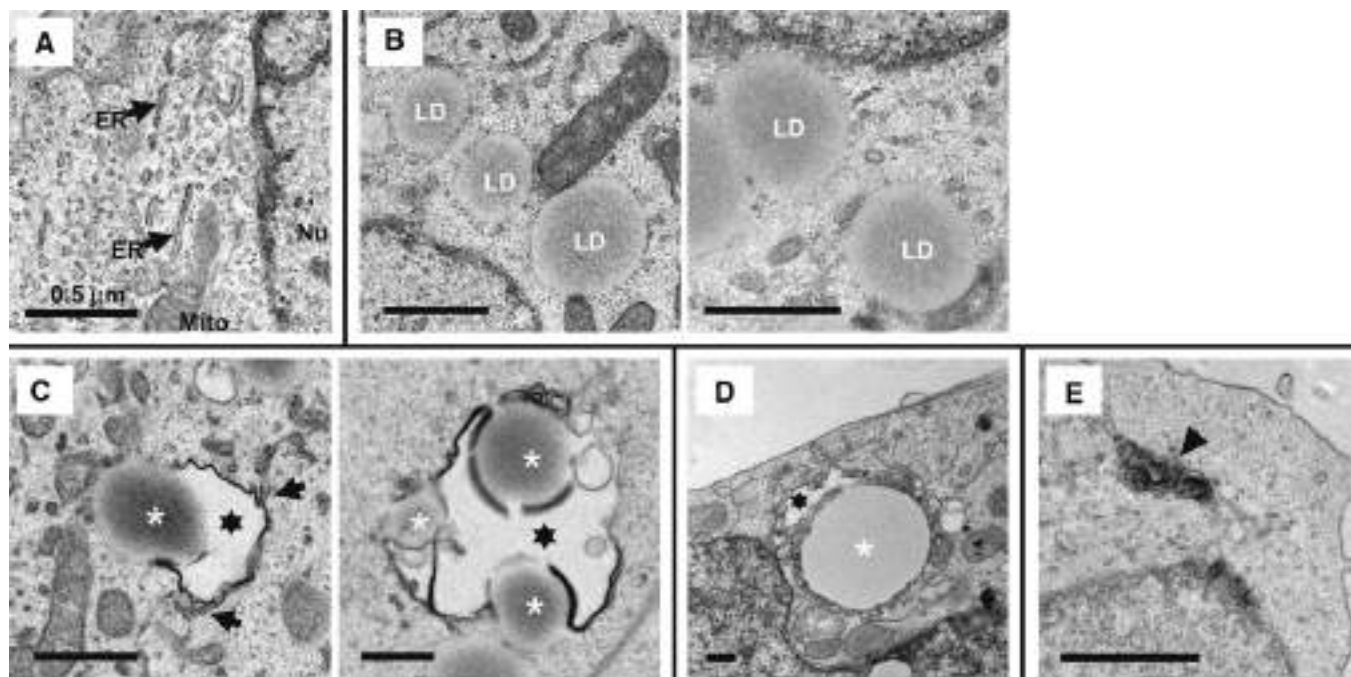


Fig. 7. The 24S-OHC induced atypical LD-like structures in SH-SY5Y cells. A–E: SH-SY5Y cells were treated with EtOH (A), 200 μ M OA (B), 50 μ M 24S-OHC (C), 50 μ M 24S-OHC with 50 μ M OA (D), or 50 μ M 24S-OHC with 5 μ M F-12511 (E) for 6 h. Cells were subjected to electron microscopy. Representative images are shown. Scale bar, 0.5 μ m. Arrows indicate ER. White asterisks indicate LD-like structures. Black star indicates swelling of ER lumen. Arrowhead indicates unknown multilamellar structure.

contrast, with DART analysis, it is possible to detect the parent ion peak of molecules as they exist in their esterified form, without the need for additives, pretreatment, or other such potentially sample-altering methods of preparation. Because DART-MS analysis cannot easily distinguish between different isomers under current conditions, DART-MS analysis must be coupled with a chromatographic technique, such as HPLC, using a suitable column and the synthetic standard compounds if it to be used for identification of compounds. We propose that DART-MS analysis may serve as a useful tool for investigation not just of 24S-OHC esters, as in our present study, but of a wide variety of esters of sterols and fatty acids. For example, there has been growing interest in oxysterol research because there are a number of bioactivities of oxysterols that have received much attention (40, 41), and oxysterols also have potential for use as biomarkers of neurodegenerative diseases (10, 42, 43). Although it will be necessary to devise appropriate techniques before DART-MS can be used for precise quantitative analysis, it is thought that the DART-MS method will ultimately be valuable for evaluation not only of free oxysterol, but also of oxysterol esters in the tissue, plasma, and cerebrospinal fluid of patients suffering from neurodegenerative disease.

Because we have previously shown that ACAT1-mediated 24S-OHC esterification occurs upstream of the switching point at which the determination is made as to whether cell death will be apoptotic or necroptosis-like (22, 25), the atypical LD-like structures and swollen ER that we observed to form as a result of treatment with 24S-OHC should also play an important role in 24S-OHC-induced caspase-dependent apoptosis. Unlike the extrinsic pathway for programmed cell death in which the cell surface death receptor is stimulated by its ligand (44), the morphological abnormalities that we observed to occur as a result of treatment with 24S-OHC, i.e., atypical LD-like structures and swollen ER, are intracellular events. It is therefore thought likely that the cell death machinery that is activated in 24S-OHC-induced cell death is different from that which is activated in death receptor-mediated cell death. In line with our observations, it has recently been reported that ER stress induces ligand-independent necroptosis in L929 mouse fibroblast cells (45). It should be noted, however, with regard to physiological relevance, that it is not clear that the changes observed in our present study would necessarily occur in accompaniment to the increase in CYP46A1 expression (14–16) or the increase in brain 24S-OHC level that has been observed in early- and middle-stage AD (11–13). Whereas LD structures have been observed in brain tissue from AD patients and in AD mouse models (46–48), there remains a need to elucidate whether an increase in 24S-OHC esters and formation of atypical LD-like structures, as reported in our present study, occur in vivo as a consequence of the normal progression of AD. In conclusion, our present study suggests that ACAT1-mediated esterification of 24S-OHC with long-chain unsaturated fatty acid and formation of atypical LD-like structures with abnormal ER morphology play important roles in 24S-OHC-induced cell death in SH-SY5Y cells. ■

The authors thank Dr. Ta-Yuan Chang for providing valuable reagents. The authors also thank Norie Kato and Kyoko Urano for research support and Gerry Peters (JTT K.K., Takatsuki, Japan) for his careful editing of the manuscript.

REFERENCES

1. Dietschy, J. M., and S. D. Turley. 2004. Cholesterol metabolism in the central nervous system during early development and in the mature animal. *J. Lipid Res.* **45**: 1375–1397.
2. Russell, D. W., R. W. Halford, D. M. Ramirez, R. Shah, and T. Kotti. 2009. Cholesterol 24-hydroxylase: an enzyme of cholesterol turnover in the brain. *Annu. Rev. Biochem.* **78**: 1017–1040.
3. Lund, E. G., J. M. Guileyardo, and D. W. Russell. 1999. cDNA cloning of cholesterol 24-hydroxylase, a mediator of cholesterol homeostasis in the brain. *Proc. Natl. Acad. Sci. USA.* **96**: 7238–7243.
4. Lütjohann, D., O. Breuer, G. Ahlborg, I. Nennesmo, A. Sidén, U. Diczfalusy, and I. Björkhem. 1996. Cholesterol homeostasis in human brain: evidence for an age-dependent flux of 24S-hydroxycholesterol from the brain into the circulation. *Proc. Natl. Acad. Sci. USA.* **93**: 9799–9804.
5. Heverin, M., N. Bogdanovic, D. Lütjohann, T. Bayer, I. Pikuleva, L. Bretillon, U. Diczfalusy, B. Winblad, and I. Björkhem. 2004. Changes in the levels of cerebral and extracerebral sterols in the brain of patients with Alzheimer's disease. *J. Lipid Res.* **45**: 186–193.
6. Noguchi, N., Y. Saito, and Y. Urano. 2014. Diverse functions of 24(S)-hydroxycholesterol in the brain. *Biochem. Biophys. Res. Commun.* **446**: 692–696.
7. Noguchi, N., Y. Urano, W. Takabe, and Y. Saito. 2015. New aspects of 24(S)-hydroxycholesterol in modulating neuronal cell death. *Free Radic. Biol. Med.* **87**: 366–372.
8. Urano, Y., S. Ochiai, and N. Noguchi. 2013. Suppression of amyloid- β production by 24S-hydroxycholesterol via inhibition of intracellular amyloid precursor protein trafficking. *FASEB J.* **27**: 4305–4315.
9. Okabe, A., Y. Urano, S. Itoh, N. Suda, R. Kotani, Y. Nishimura, Y. Saito, and N. Noguchi. 2013. Adaptive responses induced by 24S-hydroxycholesterol through liver X receptor pathway reduce 7-ketocholesterol-caused neuronal cell death. *Redox Biol.* **2**: 28–35.
10. Jeitner, T. M., I. Voloshyna, and A. B. Reiss. 2011. Oxysterol derivatives of cholesterol in neurodegenerative disorders. *Curr. Med. Chem.* **18**: 1515–1525.
11. Sun, M. Y., A. J. Linsenbardt, C. M. Emmett, L. N. Eisenman, Y. Izumi, C. F. Zorumski, and S. Mennerick. 2016. 24(S)-Hydroxycholesterol as a modulator of neuronal signaling and survival. *Neuroscientist.* **22**: 132–144.
12. Shafaati, M., A. Solomon, M. Kivipelto, I. Björkhem, and V. Leoni. 2007. Levels of ApoE in cerebrospinal fluid are correlated with Tau and 24S-hydroxycholesterol in patients with cognitive disorders. *Neurosci. Lett.* **425**: 78–82.
13. Lütjohann, D., A. Papassotiropoulos, I. Björkhem, S. Locatelli, M. Bagli, R. D. Oehring, U. Schlegel, F. Jessen, M. L. Rao, K. von Bergmann, et al. 2000. Plasma 24S-hydroxycholesterol (cerebrosterol) is increased in Alzheimer and vascular demented patients. *J. Lipid Res.* **41**: 195–198.
14. Brown 3rd, J., C. Theisler, S. Silberman, D. Magnuson, N. Gottardi-Littell, J. M. Lee, D. Yager, J. Crowley, K. Sambamurti, M. M. Rahman, et al. 2004. Differential expression of cholesterol hydroxylases in Alzheimer's disease. *J. Biol. Chem.* **279**: 34674–34681.
15. Bogdanovic, N., L. Bretillon, E. G. Lund, U. Diczfalusy, L. Lannfelt, B. Winblad, D. W. Russell, and I. Björkhem. 2001. On the turnover of brain cholesterol in patients with Alzheimer's disease. Abnormal induction of the cholesterol-catabolic enzyme CYP46 in glial cells. *Neurosci. Lett.* **314**: 45–48.
16. Tian, G., Q. Kong, L. Lai, A. Ray-Chaudhury, and C. L. Lin. 2010. Increased expression of cholesterol 24S-hydroxylase results in disruption of glial glutamate transporter EAAT2 association with lipid rafts: a potential role in Alzheimer's disease. *J. Neurochem.* **113**: 978–989.
17. Kölsch, H., D. Lütjohann, A. Tulke, I. Björkhem, and M. L. Rao. 1999. The neurotoxic effect of 24-hydroxycholesterol on SH-SY5Y human neuroblastoma cells. *Brain Res.* **818**: 171–175.
18. Yamanaka, K., Y. Saito, T. Yamamori, Y. Urano, and N. Noguchi. 2011. 24(S)-hydroxycholesterol induces neuronal cell death through

- necroptosis, a form of programmed necrosis. *J. Biol. Chem.* **286**: 24666–24673.
19. Christofferson, D. E., and J. Yuan. 2010. Necroptosis as an alternative form of programmed cell death. *Curr. Opin. Cell Biol.* **22**: 263–268.
20. Vandenabeele, P., L. Galluzzi, T. Vanden Berghe, and G. Kroemer. 2010. Molecular mechanisms of necroptosis: an ordered cellular explosion. *Nat. Rev. Mol. Cell Biol.* **11**: 700–714.
21. Vanden Berghe, T., A. Linkermann, S. Jouan-Lanhouet, H. Walczak, and P. Vandenabeele. 2014. Regulated necrosis: the expanding network of non-apoptotic cell death pathways. *Nat. Rev. Mol. Cell Biol.* **15**: 135–147.
22. Vo, D. K., Y. Urano, W. Takabe, Y. Saito, and N. Noguchi. 2015. 24(S)-Hydroxycholesterol induces RIPK1-dependent but MLKL-independent cell death in the absence of caspase-8. *Steroids*. **99(Pt B)**: 230–237.
23. Nakazawa, T., Y. Miyanoki, Y. Urano, M. Uehara, Y. Saito, and N. Noguchi. Effect of vitamin E on 24(S)-hydroxycholesterol-induced necroptosis-like cell death and apoptosis. *J. Steroid Biochem. Mol. Biol.* Epub ahead of print. March 4, 2016; doi:10.1016/j.jsmb.2016.03.003.
24. Chang, T. Y., B. L. Li, C. C. Chang, and Y. Urano. 2009. Acyl-coenzyme A:cholesterol acyltransferases. *Am. J. Physiol. Endocrinol. Metab.* **297**: E1–E9.
25. Yamanaka, K., Y. Urano, W. Takabe, Y. Saito, and N. Noguchi. 2014. Induction of apoptosis and necroptosis by 24(S)-hydroxycholesterol is dependent on activity of acyl-CoA:cholesterol acyltransferase 1. *Cell Death Dis.* **5**: e990.
26. Shibuya, K., T. Watanabe, Y. Urano, W. Takabe, N. Noguchi, and H. Kitagishi. 2016. Synthesis of 24(S)-hydroxycholesterol esters responsible for the induction of neuronal cell death. *Bioorg. Med. Chem.* **24**: 2559–2566.
27. White, D. L., J. E. Mazurkiewicz, and R. J. Barnett. 1979. A chemical mechanism for tissue staining by osmium tetroxide-ferrocyanide mixtures. *J. Histochem. Cytochem.* **27**: 1084–1091.
28. Walther, T. C., and R. V. Farese, Jr. 2012. Lipid droplets and cellular lipid metabolism. *Annu. Rev. Biochem.* **81**: 687–714.
29. Ohsaki, Y., J. Cheng, M. Suzuki, Y. Shinohara, A. Fujita, and T. Fujimoto. 2009. Biogenesis of cytoplasmic lipid droplets: from the lipid ester globule in the membrane to the visible structure. *Biochim. Biophys. Acta.* **1791**: 399–407.
30. Bryleva, E. Y., M. A. Rogers, C. C. Chang, F. Buen, B. T. Harris, E. Rousselet, N. G. Seidah, S. Oddo, F. M. LaFerla, T. A. Spencer, et al. 2010. ACAT1 gene ablation increases 24(S)-hydroxycholesterol content in the brain and ameliorates amyloid pathology in mice with AD. *Proc. Natl. Acad. Sci. USA.* **107**: 3081–3086.
31. Cases, S., S. Novak, Y. W. Zheng, H. M. Myers, S. R. Lear, E. Sande, C. B. Welch, A. J. Lusis, T. A. Spencer, B. R. Krause, et al. 1998. ACAT-2, a second mammalian acyl-CoA:cholesterol acyltransferase. Its cloning, expression, and characterization. *J. Biol. Chem.* **273**: 26755–26764.
32. Seo, T., P. M. Oelkers, M. R. Giattina, T. S. Worgall, S. L. Sturley, and R. J. Deckelbaum. 2001. Differential modulation of ACAT1 and ACAT2 transcription and activity by long chain free fatty acids in cultured cells. *Biochemistry.* **40**: 4756–4762.
33. La Marca, V., M. S. Spagnuolo, L. Cigliano, D. Marasco, and P. Abrescia. 2014. The enzyme lecithin-cholesterol acyltransferase esterifies cerebrosterol and limits the toxic effect of this oxysterol on SH-SY5Y cells. *J. Neurochem.* **130**: 97–108.
34. Tabas, I., and D. Ron. 2011. Integrating the mechanisms of apoptosis induced by endoplasmic reticulum stress. *Nat. Cell Biol.* **13**: 184–190.
35. Hetz, C. 2012. The unfolded protein response: controlling cell fate decisions under ER stress and beyond. *Nat. Rev. Mol. Cell Biol.* **13**: 89–102.
36. Sano, R., and J. C. Reed. 2013. ER stress-induced cell death mechanisms. *Biochim. Biophys. Acta.* **1833**: 3460–3470.
37. Miguet-Alfonsi, C., C. Prunet, S. Monier, G. Bessède, S. Lemaire-Ewing, A. Berthier, F. Ménétrier, D. Néel, P. Gambert, and G. Lizard. 2002. Analysis of oxidative processes and of myelin figures formation before and after the loss of mitochondrial transmembrane potential during 7beta-hydroxycholesterol and 7-ketocholesterol-induced apoptosis: comparison with various pro-apoptotic chemicals. *Biochem. Pharmacol.* **64**: 527–541.
38. Vejux, A., E. Kahn, F. Ménétrier, T. Montange, J. Lherminier, J. M. Riedinger, and G. Lizard. 2007. Cytotoxic oxysterols induce caspase-independent myelin figure formation and caspase-dependent polar lipid accumulation. *Histochem. Cell Biol.* **127**: 609–624.
39. Griffiths, W. J., and Y. Wang. 2009. Analysis of neurosteroids by GC-MS and LC-MS/MS. *J. Chromatogr. B Analyt. Technol. Biomed. Life Sci.* **877**: 2778–2805.
40. Luu, W., L. J. Sharpe, I. Capell-Hattam, I. C. Gelissen, and A. J. Brown. 2016. Oxysterols: old tale, new twists. *Annu. Rev. Pharmacol. Toxicol.* **56**: 447–467.
41. Olsen, B. N., P. H. Schlesinger, D. S. Ory, and N. A. Baker. 2012. Side-chain oxysterols: from cells to membranes to molecules. *Biochim. Biophys. Acta.* **1818**: 330–336.
42. Hughes, T. M., C. Rosano, R. W. Evans, and L. H. Kuller. 2013. Brain cholesterol metabolism, oxysterols, and dementia. *J. Alzheimers Dis.* **33**: 891–911.
43. Leoni, V., and C. Caccia. 2011. Oxysterols as biomarkers in neurodegenerative diseases. *Chem. Phys. Lipids.* **164**: 515–524.
44. Galluzzi, L., I. Vitale, J. M. Abrams, E. S. Alnemri, E. H. Baehrecke, M. V. Blagosklonny, T. M. Dawson, V. L. Dawson, W. S. El-Deiry, S. Fulda, et al. 2012. Molecular definitions of cell death subroutines: recommendations of the Nomenclature Committee on Cell Death 2012. *Cell Death Differ.* **19**: 107–120.
45. Saveljeva, S., S. L. Mc Laughlin, P. Vandenabeele, A. Samali, and M. J. Bertrand. 2015. Endoplasmic reticulum stress induces ligand-independent TNFR1-mediated necroptosis in L929 cells. *Cell Death Dis.* **6**: e1587.
46. Gómez-Ramos, P., and M. Asunción Morán. 2007. Ultrastructural localization of intraneuronal Abeta-peptide in Alzheimer disease brains. *J. Alzheimers Dis.* **11**: 53–59.
47. Hamilton, L. K., A. Aumont, C. Julien, A. Vadnais, F. Calon, and K. J. Fernandes. 2010. Widespread deficits in adult neurogenesis precede plaque and tangle formation in the 3xTg mouse model of Alzheimer's disease. *Eur. J. Neurosci.* **32**: 905–920.
48. Yang, D. S., P. Stavrides, M. Saito, A. Kumar, J. A. Rodriguez-Navarro, M. Pawlik, C. Huo, S. U. Walkley, M. Saito, A. M. Cuervo, et al. 2014. Defective macroautophagic turnover of brain lipids in the TgCRND8 Alzheimer mouse model: prevention by correcting lysosomal proteolytic deficits. *Brain.* **137**: 3300–3318.

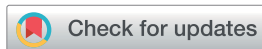

 Cite this: *RSC Adv.*, 2020, 10, 15947

Photo-responsive azobenzene interactions promote hierarchical self-assembly of collagen triple-helical peptides to various higher-order structures†

Nobuyuki Higashi, * Ryo Yoshikawa and Tomoyuki Koga *

Collagen is an essential structural protein in animal tissues and plays key roles in cellular modulation. We investigated methods to discover collagen model peptides (CMPs) that would self-assemble into triple helices and then grow into supramolecular organizations with diverse morphological features, which would be valuable as biomaterials. This challenging undertaking was achieved by placing azobenzene groups on the ends of the CMPs, (GPO)_{*n*} (*n* = 3–10), Azo-(GPO)_{*n*}. In a dilute aqueous solution (80 μM), CD spectra indicated that the Azo-(GPO)_{*n*} (*n* > 4) formed triple helices due to strong hydrophobic azobenzene interactions, and that helix stability was increased with the peptide segment length. The resulting triple helices induced a specific azobenzene orientation through turned and twisted configurations as shown by CD spectra. TEM observations for the same solutions disclosed the morphologies for the Azo-CMPs. Azo-(GPO)₃, having the shortest peptide segment, showed no nanostructure, both Azo-(GPO)₄ and Azo-(GPO)₅ provided consistent well-developed nanofiber structures resembling the natural collagen fibers, and Azo-(GPO)_{*n*}s (*n* = 6–10) grew into flexible rod-like micelle fibers. In addition, alkyl chain-attached C_{*m*}Azo-(GPO)₅ displayed a toroidal morphology, and Azo-deg-(GPO)₅ having a hydrophilic spacer assembled into a bilayer vesicle structure. These diverse morphological features are considered to be due to the characteristics of the pre-organized triple helix units. Photo-isomerization of the azobenzene moiety brought about the disappearance of such characteristic nano-architectures. When the solution concentration was increased up to 1 wt%, only Azo-(GPO)₄ and Azo-(GPO)₅ spontaneously formed hydrogels exhibiting a satisfactory gel-to-sol transition upon UV irradiation.

 Received 29th January 2020
 Accepted 2nd April 2020

DOI: 10.1039/d0ra02906h

rsc.li/rsc-advances

Introduction

Collagen, which is known to be the most abundant protein in mammals, is composed of three parallel helices and exists in the extracellular matrix (ECM) as interwoven fiber networks that serve as a scaffold for tissue growth and stability.^{1–3} Its high natural abundance and good biocompatibility have brought about the development of collagen as a potential biomaterial.⁴ Although natural collagen has been valued as a useful biomaterial and is conducive to various applications, challenges which have been identified in its reproduction include difficulty in the precise control of scaffold morphology and limited ability

to make site-specific chemical modifications to the collagen structure. To overcome these difficulties, numerous strategies have been developed to assemble synthetic collagen model peptides (CMPs) into a higher-order structure.^{5–10} CMPs with repeating units of Pro-Hyp-Gly (GPO) have been shown to adopt a collagen triple helix structure.¹¹ This core triple helical unit has been used in the formation of CMP fibers *via* the use of electrostatic interactions,^{12–14} native chemical ligation,¹⁵ cysteine knots,^{16–18} π–π stacking,^{19,20} aromatic–proline interaction,²¹ metal–ligand coordinations,^{22–24} and cation–π interactions,²⁵ all of which favorably assist the self-assembly of CMPs into micrometer-scale collagen fibers. In the present study, we sought to discover CMPs that would form triple helices and self-assemble into supramolecular structures with diverse morphological features without reorganizing the peptide chains by covalent linkages. This challenging objective was accomplished by attaching an azobenzene group and its derivatives to the N-terminal regions of peptides, (GPO)_{*n*} (*n* = 3–10). Azobenzene is known to not only show hydrophobicity based on its strong stacking capability but also behave as a spectroscopic

Department of Molecular Chemistry and Biochemistry, Faculty of Science and Engineering, Doshisha University, Kyotanabe, Kyoto 610-0321, Japan. E-mail: nhigashi@mail.doshisha.ac.jp; tkoga@mail.doshisha.ac.jp

† Electronic supplementary information (ESI) available: Experimental procedures and analyses for preparation of Azo-CMPs, Fig. S1–S6; MALDI-TOF MS and ¹H NMR spectra, AFM images for Azo-CMPs (*trans*-form), TEM images for Azo-CMPs after UV irradiation, and photographs of Azo-CMPs (*trans*-form) in the concentrated situation. See DOI: 10.1039/d0ra02906h



probe elucidating its interaction mode. Thus the azobenzene moiety would become a useful template to assemble the CMP molecules and to promote them to a higher-order structure. In addition to these characters, azobenzene shows photo-isomerization (photo-switching) accompanying a slight polarity change. Such photo-switching of the azobenzene groups introduced into CMP molecules has been able to control the stability and the structure of collagen triple helices.^{26–28}

One of the key factors in the morphological diversity accomplished through the self-assembly of peptides is now known to be hydrophilic/hydrophobic balance (amphiphilicity), which is based on the peptide sequence. For instance, the peptides composed of Ala and Lys (A₃K, A₆K and A₉K) have provided different morphological assemblies due to differences in amphiphilic balance.²⁹ We have previously described that the triblock and diblock peptides composed of Leu and Lys show β -sheet-based nanofiber, α -helix-based nanoplate and micelle structures which are dependent on the amphiphilicity and block length of the peptides.³⁰ In the case of CMPs, however, since the stability of the collagen triple helix structure is dependent on the peptide length (n), it does not contribute to the hierarchical variation in morphology. In fact, a short CMP of $n = 5$ (15mer) is unable to form triple helices.³¹ Substantial stabilization of the triple helical structures can be achieved with the introduction of covalent links between the C-terminal regions of three peptide chains^{32,33} or by use of a Kemp triacid (KTA) and a TREN (tri(2-aminoethyl) amine) template linked to the N-terminus of three peptide chains.^{34–37} Triple helical stabilization is considered to be due to the tight alignment of the three termini achieved by tethering the peptide to the self-assembled aggregates. Ideally, a system by which synthetic linear peptide chains self-assemble into desirable higher-order structures is beneficial because some of the covalently linked triple helical peptide compounds makes them difficult to prepare and/or purify owing to their large molecular size. Fields' and Tirrell's groups have developed a noncovalent, self-assembly approach to construct a collagen-like structural motif, in which two long alkyl chains are attached to the N-terminus of a peptide chain mimicking a lipid structure.^{38–42} Their amphiphilic peptide-lipid has provided a stable triple helical structure even though its peptide length is quite short (12-mer ($n = 4$)),³⁹ and has formed only a spherical micelle structure.^{40,41} Stupp's and Hartgerink's groups have also applied the self-assembly strategy of single-alkyl chain peptide amphiphiles to form collagen-like fibers.^{43,44} By using this strategy, Tong and coworker have shown that an epitope-containing collagen-mimetic amphiphile holds a potential for tissue regeneration applications.⁴⁵

In an effort to strengthen potential hydrophobic interactions between the termini of the triple helices, we designed peptides that contained repeating units of GPO directly terminating with an azobenzene group (**Azo-(GPO)_n**, $n = 3–10$) or through the use of flexible diethylene glycol (deg) as a spacer (**Azo-deg-(GPO)₅**) (Fig. 1). Peptides terminating in a more hydrophobic azobenzene having a long alkyl chain (**C_mAzo-(GPO)₅**, $m = 6$ and 12) were also designed for comparison. Herein we disclose the hierarchical assembly of these triple helices into various

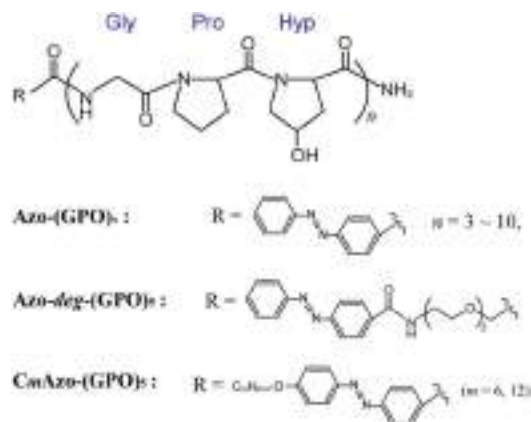


Fig. 1 Chemical structures of the azobenzene-terminated collagen-mimetic oligopeptides: **Azo-(GPO)_n** ($n = 3–10$), **Azo-deg-(GPO)₅**, and **C_mAzo-(GPO)₅** ($m = 6$ and 12).

architectures, depending on the peptide chain length (n), the polarity balance (hydrophobic/hydrophilic balance), and photo-isomerization of the azobenzene moiety.

Results and discussion

Design and syntheses of azobenzene-terminated collagen-model peptides (**Azo-CMPs**)

The hydrophilic/hydrophobic balance of peptides is one of the critical factors to control self-assembling behaviors.^{29,30} Thus we designed a new CMP whose N-terminus was modified with an azobenzene group. Azobenzene is known to be more hydrophobic than the peptide moieties and shows photo-isomerization, accompanied with a slight change in polarity. A triad repeating sequence of Gly-Pro-Hyp (GPO) was employed as the peptide segment forming the basis of the triple helix as it has been reported to be most stable triplet for collagen triple helices.¹¹ The C-termini are amidic so as to prevent ionization, which can cause phenomena that complicate self-assembly. Fig. 1 displays the basic molecular structures of azobenzene-terminated peptides (**Azo-(GPO)_n**) having various numbers of repeats ($n = 3–10$), and its derivatives which contain a flexible, hydrophilic diethylene glycol (deg) spacer connecting the (GPO)₅ segment with the azobenzene group (**Azo-deg-(GPO)₅**) and a long alkyl chain (**C_mAzo-(GPO)₅**, $m = 6$ and 12). The azobenzene moiety at the N-terminus is expected to show an effective hydrophobic interaction due to its stacking ability in water and to behave as a template that stabilizes collagen triple helical conformation. The additional introduction of the spacer (deg) and the alkyl chains into **Azo-(GPO)₅** would clarify the role of the azobenzene moiety in self-assembly. Furthermore, the resulting azobenzene aggregate in the N-terminal region of the collagen triple helices must be a driving force for developing into higher-order structures. All of these peptides were prepared by solid phase synthesis using Fmoc chemistry. Characterizations were carried out by using matrix-assisted laser desorption/ionization time-of-flight (MALDI-TOF) mass spectroscopy (MS)



and proton nuclear magnetic resonance (^1H NMR) spectroscopy (see ESI†).

Conformational properties of Azo-(GPO) $_n$ in water

The secondary structures of the Azo-CMPs obtained were first evaluated by measuring the circular dichroism (CD) spectra for their aqueous solutions (containing 5% trifluoroethanol (TFE); [peptide] = 80 μM). Natural collagen has a unique CD spectrum in which a small positive peak appears at around 220 nm and a large trough at approximately 197 nm.^{46–48} These spectral features have been used as a reference to determine the presence of collagen-like triple helices in water. Fig. 2a shows time dependence of CD spectra measured for Azo-(GPO) $_5$, a typical

CMP (and others are shown in Fig. S1, ESI†), in water at 4 °C. The measurement was started when the sample solution was cooled to 4 °C from 60–90 °C, which are the points above which thermal denaturation of the peptides occur. The spectra are indicative of triple helical conformations, where the positive peak is at 225 nm and the trough around 200 nm. These absorbances and the Rpn value (ratio of the ellipticities for positive and negative peaks; the triple helical conformation shows a value from 0.1–0.2) proposed by Goodman *et al.*^{34,49} are comparable to known collagen triple helical conformations since the Rpn value was evaluated to be 0.2. In a longer wavelength region around 320 nm, which is a specific absorption band derived from the azobenzene moiety, an induced CD (ICD) effect is clearly observed at 348 nm (negative first Cotton effect) and at 307 nm (positive second Cotton effect), likely due to a specific interaction of azobenzene moieties. Such an observed Cotton effect strongly suggests that an exciton coupling between azobenzene chromophores occurs in a twisted configuration.⁵⁰ That is to say, the formation of a triple helical structure would induce such a specific orientation of the N-terminal azobenzene groups. In fact, Azo-(GPO) $_3$, with the shortest peptide segment, does not assemble into a triple helical structure and presented no ICD phenomenon (Fig. 2b, c and S1, ESI†). In spite of the formation of a stable triple helical structure, the spacer-containing Azo-deg-(GPO) $_5$ also showed no ICD signal (Fig. 2b, c and S1, ESI†), likely due to the presence of the flexible spacer (deg) which blocked the peptide segments ((GPO) $_5$) from assembling into triple helical structures. These results support the hypothesis that the ICD effect derives from the triple helical structure composed of the peptide segment directly connected with the azobenzene group at the N-terminus. Fig. 2b and c display the time dependency of molar ellipticities at 225 nm due to the triple helical conformation ($[\theta]_{225}$) and at 307 nm due to the ICD of the azobenzene moiety ($[\theta]_{307}$) on the basis of CD spectra for Azo-(GPO) $_n$ ($n = 3–10$) and Azo-deg-(GPO) $_5$. As mentioned above, the $[\theta]_{225}$ and $[\theta]_{307}$ values for Azo-(GPO) $_3$, having the shortest peptide length ($n = 3$), are very small and almost time independent, meaning that it does not take a triple helical conformation. The time dependency of $[\theta]_{225}$ values for Azo-(GPO) $_n$ ($n = 6–10$) provide very similar profiles; that is, quick increases in $[\theta]_{225}$ values are observed at the beginning, and after incubation for a few hours the values level off between 0.4 and 0.5. The Rpn values were evaluated to be 0.10–0.12 from CD spectra, which are very consistent with those for the collagen triple helix. From the time dependency of $[\theta]_{307}$ values (Fig. 2c), we found that the ICD of the azobenzene moiety increases with incubation time and in particular, its enhancement in the early stage depends strongly on the peptide length (n). Interestingly, the enhancement of ICD becomes much more remarkable for Azo-(GPO) $_n$ with shorter peptide segments (n). Such further incremental changes in ICD $[\theta]_{307}$ values after even a few hours of incubation suggest that the triple helical assembly behaves as a precursor to higher-order nano-architectures triggered by specific interactions of N-terminal azobenzene aggregates and/or C-terminal amide groups, as the $[\theta]_{225}$ values due to triple helix formation level off. Furthermore, Azo-(GPO) $_n$ with shorter peptide segments could more favorably assemble into a higher-order structure due to easier inter-terminal interactions. In

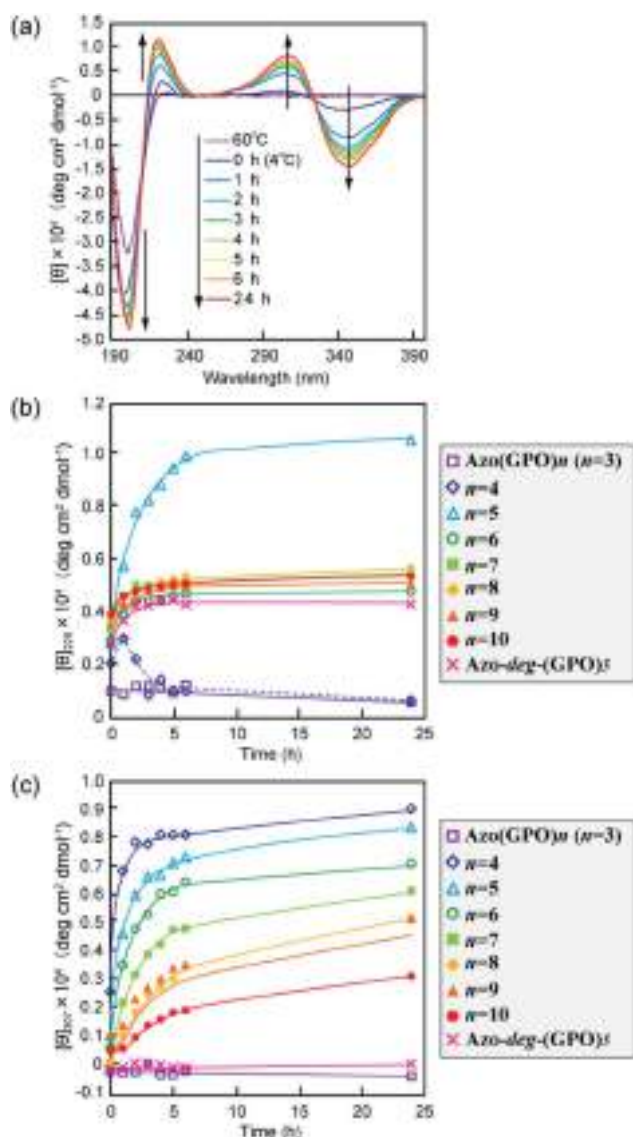


Fig. 2 (a) Changes in the CD spectra of Azo-(GPO) $_5$ (*trans*-form) in water upon incubation at 4 °C after the thermal treatment at 60–90 °C, at which the peptides denature. (b and c) Denote time courses of the $[\theta]_{225}$ and $[\theta]_{307}$ values, respectively, for aqueous Azo-(GPO) $_n$ (*trans*-form, $n = 3–10$) and Azo-deg-(GPO) $_5$ (*trans*-form) at 4 °C. [peptide] = 80 μM .



Fig. 2b, we found that the time dependency of $[\theta]_{225}$ values for **Azo-(GPO)₄** and **Azo-(GPO)₅** are somewhat unique, compared to the others (**Azo-(GPO)₆₋₁₀**). In particular, **Azo-(GPO)₅** shows an extremely rapid increase in $[\theta]_{225}$ reaching much larger values, and the $[\theta]_{225}$ value of **Azo-(GPO)₄** increases similar to the others for 1 h and then decreases gradually to that of **Azo-(GPO)₃**, which does not assume the triple helix conformation. On the other hand, since the ICD signals of $[\theta]_{307}$ for both **Azo-(GPO)₅** and **Azo-(GPO)₄** are the most markedly enhanced, they can be assumed to assume the triple helical conformation. However, precipitation occurred in the solution of **Azo-(GPO)₄** after 24 h of incubation, likely due to its growth to a huge aggregate resulting in the unique time dependency of the $[\theta]_{225}$ profile. For alkyl chain-attached **C_mAzo-(GPO)₅** ($m = 6$ and 12), the same CD experiments were performed, and as a result, **C_mAzo-(GPO)₅** was found to assume a triple helical structure (Rpn > 0.10) and shows the ICD of the specific azobenzene interactions, which were observed for **Azo-(GPO)_n** ($n = 5-10$). However, the CD spectra showed no time dependency within 24 h, suggesting that rapid self-assembly of **C_mAzo-(GPO)₅** into triple helices and other organizations proceeded because of strong hydrophobic interactions of the alkyl chain-attached azobenzene moiety.

Morphological observation for Azo-CMPs

In order to reveal morphological features for these Azo-CMPs, transmission electron microscopy (TEM) observations of the samples after 24 h of incubation were made by negative staining with phosphotungstic acid (Fig. 3). **Azo-(GPO)₃**, with the shortest peptide segment, which did not form a triple helical conformation and was not observed to have any specific nanostructures in the TEM picture (Fig. 3a). Both **Azo-(GPO)₄** and **Azo-(GPO)₅**, showing peculiar profiles in the time dependency of the $[\theta]_{225}$ value, provided consistent fiber structures with lengths on the order of micro-meters. Closer inspection appeared to show bundles of thinner fibers of approximately

4 nm in width (Fig. 3b and c). This value is similar to the width of the fiber structure of natural collagen^{51,52} as shown schematically in Fig. 4. The fiber structure is an assembly composed of five triple helix precursors which are elongated one-dimensionally due to interactions between the N-terminal azobenzene aggregates and C-terminal amide groups through hydrogen bonding, and aligned in the same direction. With a further increase in the number of peptide repeats ($n = 6-10$), nanofibers with homogeneous diameters appear in TEM images. The diameters are observed to increase linearly with lengthening of the peptide segment; that is, in the order of 12 nm ($n = 6$), 14 nm ($n = 7$), 16 nm ($n = 8$), 18 nm ($n = 9$), and 20 nm ($n = 10$). Interestingly, these values of diameters are approximately twice as long as those of the theoretical molecular length evaluated by assuming complete triple helical conformation. Thus, we suppose that **Azo-(GPO)_n** ($n = 6-10$) first formed a triple helical conformation and then grew to rod-like micelle fibers induced by the formation of an azobenzene core through hydrophobic interactions (Fig. 4). **Azo-deg-(GPO)₅** containing hydrophilic and flexible diethylene glycol (deg) as the spacer formed a single-walled vesicle structure (Fig. 3i), whose thickness is approximately 14 nm. This value corresponds well to twice that of the molecular length of triple helical **Azo-deg-(GPO)₅**. We surmise that the assemblies must be bilayer vesicle structures in which there are hydrophilic triple helices and spacers placed at the periphery of the assembly with azobenzene moiety aggregates at the inner core, as shown in Fig. 4. Alkyl chain-attached **C_mAzo-(GPO)₅** (Fig. 3j and k) shows a characteristic toroidal morphology as well as a turned and twisted fiber structure. By considering the observed width of toroidal rings and fibers (13–14 nm) and the theoretical molecular length of **C_mAzo-(GPO)₅** in triple helical form (6.2 nm and 7.1 nm for $m = 6$ and $m = 12$, respectively), **C_mAzo-(GPO)₅** likely forms a rod-like micelle fiber. Such a rod-like micelle fiber can spontaneously transform to a toroidal structure by ring closure. As was mentioned above, **Azo-(GPO)_n** ($n = 6-10$) also assembled into rod-like micelle fiber structures, but did not assume toroidal ring morphologies. It can be seen from the

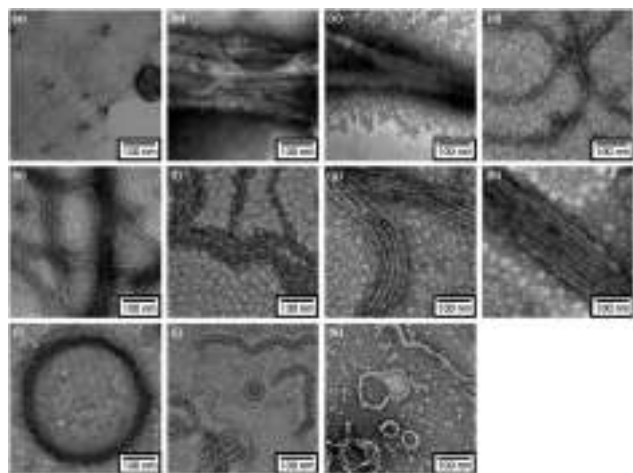


Fig. 3 TEM images stained by phosphotungstic acid for **Azo-(GPO)_n** (*trans*-form) ($n = 3$ (a), 4 (b), 5 (c), 6 (d), 7 (e), 8 (f), 9 (g), and 10 (h)), **Azo-deg-(GPO)₅** (*trans*-form) (i), and **C_mAzo-(GPO)₅** (*trans*-form) ($m = 6$ (j) and 12 (k)) incubated for 24 h at 4 °C.

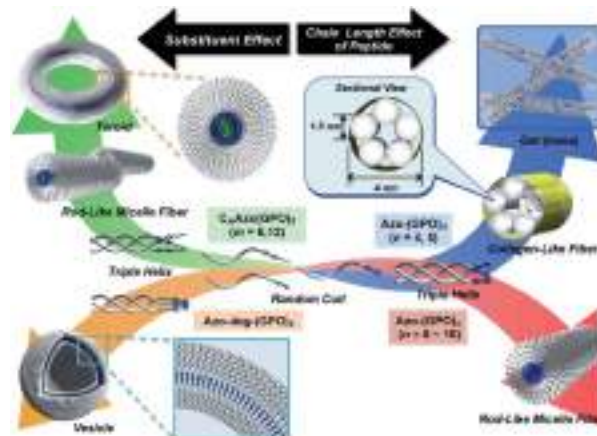


Fig. 4 Proposed model for a hierarchical self-assembly system from azobenzene-terminated collagen-mimetic oligopeptides.



TEM images that there are considerable differences in flexibility of nanofiber structures between those of Azo-(GPO)_n ($n = 6-10$) and $\text{C}_m\text{Azo-(GPO)}_5$ ($m = 6$ and 12). Apparently, the nanofibers for the latter seem to be more flexible, and turn and twist more than those of the former. Therefore, such pliability of a nanofiber might be an important factor for assembly into toroidal rings. The attachment of the alkyl chain to the rigid azobenzene moiety likely induces relatively loose assemblies of $\text{C}_m\text{Azo-(GPO)}_5$. The atomic force microscopy (AFM) observations were also performed for the same samples (Fig. S2, ESI[†]), and the observed morphologies were basically consistent with those of the TEM observations. From these morphological results, we can conclude that the morphological diversity of higher-order assemblies of Azo-CMPs is derived from the characteristics of the pre-organized triple helix unit; that is, through the variation in hydrophilic/hydrophobic balance achieved by changing the peptide length and introducing the soft substituent groups to the rigid azobenzene moiety.

Effects of photo-isomerization of azobenzene on self-assembly

The effects of *trans-cis* isomerization of the azobenzene moiety on collagen triple helical structures and their self-assemblies were examined spectroscopically and morphologically. Fig. 5a shows representative changes in the absorption spectra of the Azo-(GPO)_5 aqueous solution upon UV irradiation at 365 nm and 4 °C. The absorption peak at 320 nm due to the *trans*-form

of the azobenzene was found to decrease with UV irradiation, and at the same time the peak of the *cis*-isomer at 450 nm increased. After 60 minutes of irradiation, the isomerization reaches a photo-stationary state. Fig. 5b is a plot of the absorbance at 320 nm (*trans*-form) and the UV irradiation time measured for Azo-(GPO)_n ($n = 3-10$) and Azo-deg-(GPO)_5 under the same conditions. The isomerization behavior can be roughly grouped into three types: (I) Azo-(GPO)_n ($n = 6-10$), (II) Azo-(GPO)_n ($n = 4$ and 5), and (III) Azo-(GPO)_3 and Azo-deg-(GPO)_5 . Azo-CMPs belonging to type (I) exhibit the slowest and lowest degree of isomerization, compared with types (II) and (III). Such trends become more remarkable with increasing peptide length (n). Since the peptide length contributes strongly to the stability of triple helical conformation, the stability may lead to a tight stacking of the azobenzene moiety that presumably inhibits the isomerization. In fact, Azo-deg-(GPO)_5 , having a flexible spacer, shows a relatively rapid decrease in the *trans*-form with UV irradiation, and only 30 minutes of irradiation is sufficient to reach the photo-stationary state. Similar effective isomerization for Azo-(GPO)_3 , which does not take a triple helical conformation at all (type (III)), was observed. Therefore, from the isomerization behavior for Azo-(GPO)_4 and Azo-(GPO)_5 (type (II)), we suggest that the isomerization induces the conformational transition from a loose triple helical structure to a random coil structure. The measurements of the CD spectra also support this conformational transition. Fig. 6a displays changes in the CD spectra with UV irradiation for the Azo-(GPO)_5 aqueous solution. The UV irradiation was performed for the sample incubated for 24 h at 4 °C. Both $[\theta]$ values of the triple helix conformation at 225 nm and the ICD value of the azobenzene group at 307 nm decrease by UV irradiation, meaning that the photo-isomerization of the azobenzene moiety leads to the decay of the triple helix structure and simultaneously stacking of the twisted azobenzenes. On the other hand, the $[\theta]$ values at 225 nm for Azo-(GPO)_n ($n = 6-10$) showed no irradiation time dependency although the $[\theta]$ values at 307 nm decrease similarly to those of Azo-(GPO)_5 due to the disappearance of the *trans*-form by isomerization (Fig. 6b and c). This result again suggests that peptide length (n) determines the stability of the triple helix conformation. The triple helix conformation of Azo-deg-(GPO)_5 , which has a spacer, retains its stability regardless of the isomerization as was expected (Fig. 6b). In the case of alkyl chain-attached $\text{C}_m\text{Azo-(GPO)}_5$ ($m = 6$ and 12), the triple helices did not decay in spite of the progress of azobenzene photo-isomerization because the hydrophobic interaction of the attached alkyl chain could compensate for the steric and slight polar changes of the azobenzene groups resulting from their isomerization from the *trans*- to *cis*-forms. Subsequently, the effect of UV irradiation on the aggregation morphology for all Azo-CMPs was examined by TEM observation (Fig. S3, ESI[†]). For all of the Azo-CMPs, the *cis*-form of the azobenzene causes the disappearance of characteristic nano-architectures as observed in the *trans*-form, although only $\text{C}_{12}\text{Azo-(GPO)}_5$ retains a partly fragmented flexible fiber structure. Therefore, we conclude that the *trans*-form is essential to the formation of the characteristic nano-architecture

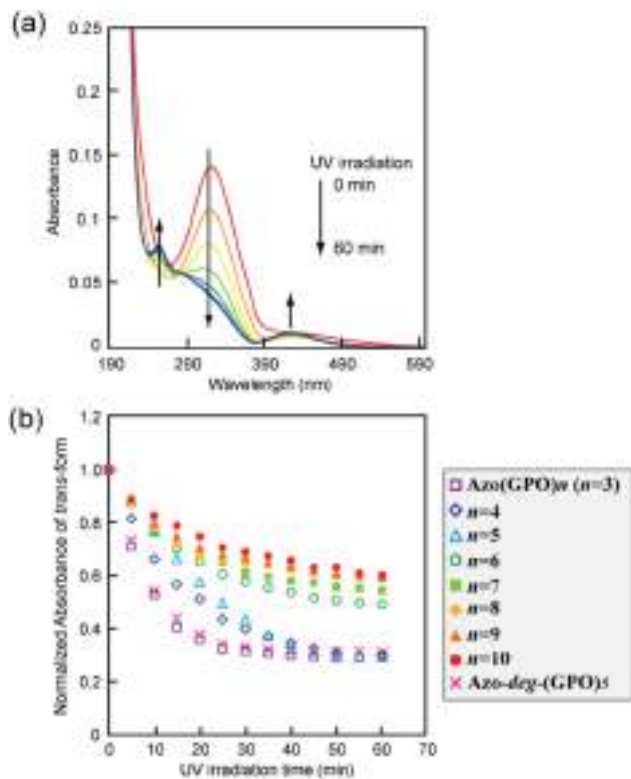


Fig. 5 (a) Changes in the absorption spectra of Azo-(GPO)_5 upon UV irradiation (365 nm) in water at 4 °C. [peptide] = 80 μM . (b) Photo-isomerization processes for Azo-(GPO)_n ($n = 3-10$) and Azo-deg-(GPO)_5 in water at 4 °C.



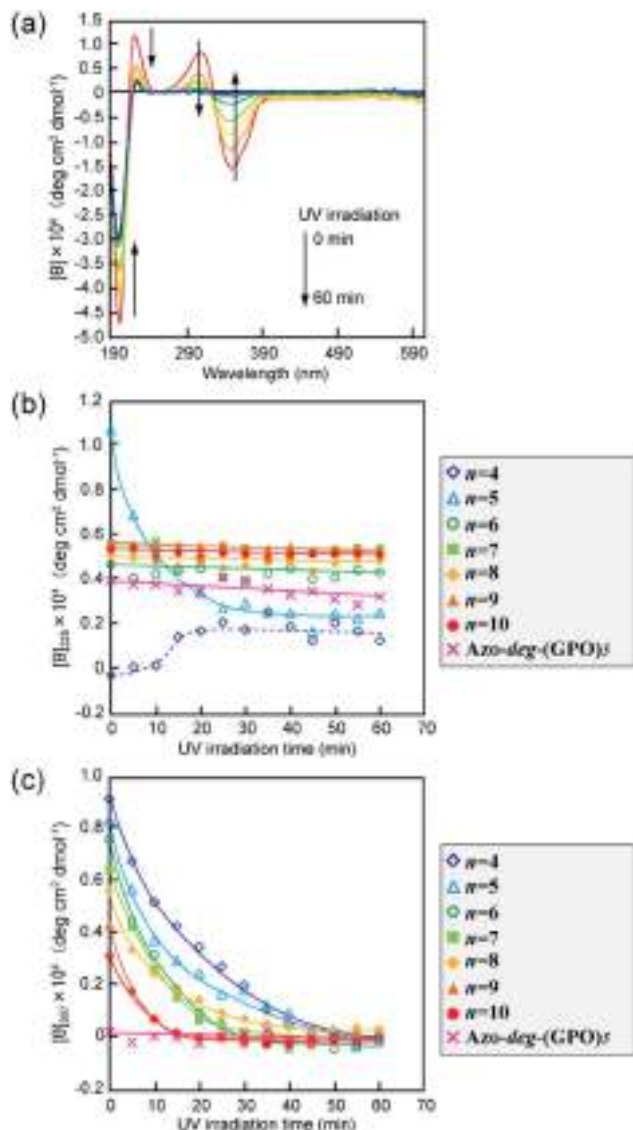


Fig. 6 (a) Changes in the CD spectra of Azo-(GPO)₅ upon UV irradiation (365 nm) in water at 4 °C. [peptide] = 80 μM. (b and c) Denote time courses of the $[\theta]_{225}$ and $[\theta]_{307}$ values, respectively, for Azo-(GPO)_n (n = 4–10) and Azo-deg-(GPO)₅ in water at 4 °C during UV irradiation. [peptide] = 80 μM.

dependent on molecular structures such as the peptide segment length, and the presence of a flexible spacer and alkyl chains.

Self-assembly of Azo-CMPs under concentrated conditions

The self-assembly of these Azo-CMPs was further investigated in a concentrated aqueous solution (6 wt%; [peptide] = 8–10 mM). Only Azo-(GPO)₄ and Azo-(GPO)₅, which self-organize in a dilute aqueous solution similar to natural collagen-like, well-developed fiber structures, formed hydrogels at 6 wt% concentration. C₆Azo-(GPO)₅ and C₁₂Azo-(GPO)₅ were insoluble in water at this concentration due to their higher hydrophobicity. Others such as Azo-(GPO)_n (n = 6–10) and Azo-deg-(GPO)₅ provided merely fluid, viscous solutions, except for Azo-(GPO)₃ whose aqueous solution caused partial precipitation (Fig. S4,

ESI†). These results suggest that gelation of these types of CMPs needs a tightly bundled structure of nanofibers as well as a suitable hydrophobic/hydrophilic balance of CMP molecules to generate cross-linking points for network formation. The prepared hydrogel of Azo-(GPO)₅ (azobenzene moiety: *trans*-form) was further characterized by dynamic rheology measurements. A strain sweep experiment was first carried out by measuring the evolution of the moduli while increasing the deformation of the gel. The hydrogel showed a mechanical-responsive gel-to-sol transition when the shear strain amplitude was increased (Fig. 7a). During measurement, the storage (*G'*) and the loss (*G''*) moduli showed a plateau up to a deformation of approximately 1%. Although the amplitude of the strain was increased, both moduli remained almost constant. At a higher strain above 1%, the hydrogel showed a gel-to-sol transition. The dynamic property of the hydrogel was then examined in the linear viscoelasticity by frequency sweep measurements. In the present frequency range, the elastic moduli are constant and the storage moduli are about one order of magnitude higher than the loss moduli (Fig. 7b). Subsequently, the effect of photo-isomerization on the gelation property was examined. Fig. 7c displays photographs of the Azo-(GPO)₅ hydrogel before and after UV irradiation for 2 h at 4 °C. The gel-to-sol transition proceeded smoothly. The results of rheological measurements for the sample after 2 h of irradiation also support the hypothesis that the collapse of the gel state arises from the *trans*-to-*cis* isomerization of the azobenzene moiety that triggered the disintegration of 3D-network structures (Fig. 7a and b).

Experimental

Materials

N,N-Dimethylformamide (DMF), piperidine, methanol, ethanol, phenol, ethylacetate, acetone, diethyl ether, tetrahydrofuran (THF) hexane, MgSO₄ anhydrous, dimethylsulfoxide (DMSO)-*d*₆,

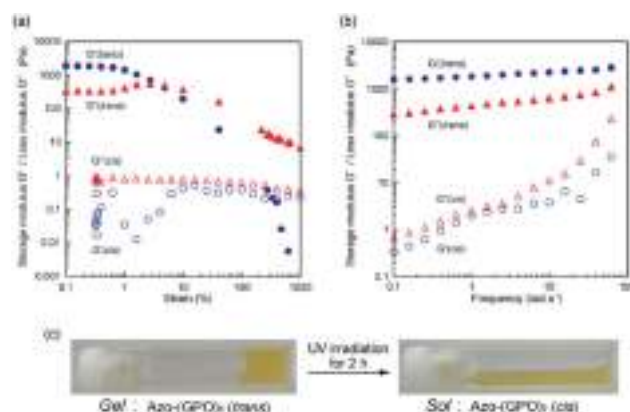


Fig. 7 (a) Dynamic storage (*G'*) and loss (*G''*) moduli for Azo-(GPO)₅-hydrogel (6 wt%) as a function of the strain (frequency: 6 rad s⁻¹) at 4 °C before (●, ▲) and after (○, △) UV irradiation. (b) *G'* and *G''* moduli for Azo-(GPO)₅-hydrogel (6 wt%) as a function of the frequency (strain: 0.1%) at 4 °C. (c) Photographs of Azo-(GPO)₅-hydrogel before and after UV irradiation.



and 2,2,2-trifluoroethanol (TFE) were purchased from Nacalai Tesque. Chloroform-*d*, 4-(phenylazo)benzoic acid and 2,5-dihydroxybenzoic acid (DHBA) were purchased from Sigma Aldrich. *N,N'*-Diisopropylcarbodiimide (DIPC), dichloromethane (DCM), 4-aminobenzoic acid, 1-bromohexane, 1-bromodecane and 18-crown-6-ether were purchased from Wako Pure Chemical. *N*-(9-Fluorenylmethoxycarbonyl) (Fmoc)-NH-SAL-MBHA Resin, Fmoc-Hyp(Bu^t)-OH, Fmoc-Gly-OH, trifluoroacetic acid (TFA) and 1-hydroxy-7-aza-benzotriazol (HOAt) were purchased from Watanabe Chemical Industries. Fmoc-Pro-OH and Fmoc-8-amino-3,6-dioxaoctanoic acid (Fmoc-deg-OH) were purchased from Peptide Institute. All reagents were used as received.

Measurements

¹H NMR spectra were recorded using a JEOL JNM-AL-400 (JEOL Resonance) spectrometer (400 MHz). MALDI-TOF MS analyses were performed on an Autoflex speed (Bluker Daltonics) using DHBA as a matrix. CD spectra were recorded on a J-820 spectropolarimeter (JASCO Ltd.) under N₂ atmosphere equipped with a Peltier type thermostatic cell holder coupled with a controller PTC-432L (JASCO Ltd.). Samples were prepared in water to be [peptide] = 80 μM, and incubated at 4 °C after thermo-treatment at 60–90 °C. Experiments were performed in a quartz cell with a 1 mm path length over the range of 190–600 nm at 4 °C. UV-vis spectra were acquired using a V-650 spectrophotometer (JASCO Ltd.) equipped with a Peltier type thermostatic cell holder ETSC-761 (JASCO Ltd.). The AFM images were collected on a SPM-9700 (Shimadzu Co.) operated by tapping using a silicone tip (MPP-1110, tip radius < 1.2 nm, Bruker Nano surfaces). A 10 mL of the aqueous solution of the peptide (80 μM), which was obtained after incubation for 24 h at 4 °C, was placed on freshly cleaved mica. After 10 s, the excess solution was removed by absorption onto filter paper, and the sample was dried at 4 °C. The scanning speed was at a line frequency of 1 Hz, and the original images were sampled at a resolution of 1024 × 1024 points. The TEM images were collected on a JEM 2100F (JEOL Resonance) at 200 kV accelerating voltage. After a small volume of the aqueous sample solution (80 μM, treated for 24 h at 4 °C) was applied to a TEM grid for 20 min, the excess solution was blotted with filter paper and stained with phosphotungstic acid aqueous solution (1 wt%), and the sample was dried in a covered container at room temperature overnight. Photo-isomerization was performed with a Handy UV Lamp SLUV-4 at 365 nm, 4 W (AS ONE Co.). Rheological measurements were performed on a Discover HR-1 TA Instruments equipped with a Peltier device for temperature control. During all rheological measurements, a solvent trap was used to minimize the evaporation. The measurement was carried out using a parallel plate (diameter: 40 mm). The gap was adjusted to be 300 μm to ensure that the geometry is completely filled. The gel samples were loaded and measured after incubation for 24 h at 4 °C.

Syntheses of Azo-CMPs

All Azo-CMPs employed in this study were prepared by SPPS using an Fmoc chemistry. These peptides were synthesized on

an Fmoc-NH-SAL-MBHA resin using Fmoc-L-amino acid derivatives [Fmoc-Hyp(Bu^t)-OH, Fmoc-Pro-OH, Fmoc-Gly-OH], DIPC, and HOAt in DMF for coupling and piperidine (25%)/DMF for Fmoc removal. Finally, azobenzene derivatives were attached to the N-terminus of the corresponding peptide as follows: 4-(phenylazo)benzoic acid (**Azo-(GPO)_n**), Fmoc-deg-OH and 4-(phenylazo) benzoic acid (**Azo-deg-(GPO)₅**), 4-(4-hexyloxyphenylazo)benzoic acid (see the ESI†) (**C₆Azo-(GPO)₅**) or 4-(4-dodecyloxyphenylazo)benzoic acid (see the ESI†) (**C₁₂Azo-(GPO)₅**) were coupled with the corresponding (GPO)_n-resins in DMF, including DIPC and HOAt. Treatment with TFA/DCM (v/v 9 : 1) cleaved the Azo-CMPs from the resins. After purification, the obtained Azo-CMPs were identified by MALDI-TOF MS and ¹H NMR spectroscopies as described in the ESI.†

Conclusions

We have introduced the concept of collagen-based supramolecular assemblies having widespread morphological features through the attachment of azobenzene to the short collagen mimetic peptides, Azo-CMPs, *via* an azobenzene stacking assisted self-assembling trigger. In a dilute solution, we found that such morphological shapes derived from Azo-CMPs such as well-developed nanofibers, rod-like micelle fibers, bilayer vesicles, and toroidal rings. These structures can be individually created by varying the peptide length of triple helices and by incorporating substituents such as an alkyl chain and a flexible spacer, resulting in an appropriate tune of hydrophobic/hydrophilic balance of the Azo-CMP molecules themselves. In a concentrated solution, specific Azo-CMPs (**Azo-(GPO)₄** and **Azo-(GPO)₅**, which gave well-developed collagen-like fiber structure in a dilute solution) spontaneously formed hydrogels that demonstrated a satisfactory gel-to-sol transition triggered by the *trans*-to-*cis* photo-isomerization of azobenzene. The ability to include nanometer to micrometer scale features and versatile morphology variation into designed biomaterial scaffolds may have significant potential for future biomedical applications.

Conflicts of interest

There are no conflicts to declare.

Acknowledgements

This work was partly supported by Grants-in-Aid for Scientific Research (KAKENHI) (26390022, No. 16K05800 and No. 17K04994) from the Japan Society for the Promotion of Science (JSPS), and a MEXT-Supported Program for the Strategic Research Foundation at Private University.

References

- 1 K. Beck and B. Brodsky, *J. Struct. Biol.*, 1998, **122**, 17–29.
- 2 B. Brodsky and A. V. Persikov, *Adv. Protein Chem.*, 2005, **70**, 301–339.



- 3 M. D. Shoulders and R. T. Raines, *Annu. Rev. Biochem.*, 2009, **78**, 929–958.
- 4 C. H. Lee, A. Singla and Y. Lee, *Int. J. Pharm.*, 2001, **221**, 1–22.
- 5 R. S. Erdmann and H. Wennemers, *J. Am. Chem. Soc.*, 2010, **132**, 13957–13959.
- 6 N. Dai and A. Etzkorn, *J. Am. Chem. Soc.*, 2009, **131**, 13728–13732.
- 7 M. D. Shoulders, J. A. Hodges and R. T. Raines, *J. Am. Chem. Soc.*, 2006, **128**, 8112–8113.
- 8 A. V. Persikov, J. A. M. Ramshaw, A. Kirkpatrick and B. Brodsky, *J. Am. Chem. Soc.*, 2003, **125**, 11500–11501.
- 9 D. E. Przybyla and J. Chmielewski, *Biochemistry*, 2010, **49**, 4411–4419.
- 10 R. Strawn, F. Chen, P. J. Haven, S. Wong, A. Park-Arias, M. D. Leeuw and Y. Xu, *Biopolymers*, 2018, **109**, 23226–23235.
- 11 A. V. Persikov, J. A. Ramshaw, A. Kirkpatrick and B. Brodsky, *Biochemistry*, 2000, **39**, 14960–14967.
- 12 S. Rele, Y. Song, R. P. Apkarian, Z. Qu, V. P. Conticello and E. L. Chaikof, *J. Am. Chem. Soc.*, 2007, **129**, 14780–14787.
- 13 L. E. O'Leart, J. A. Fallas, E. L. Bakota, M. K. Kang and J. D. Hartgerink, *Nat. Chem.*, 2011, **3**, 821–828.
- 14 I. C. Tanrikulu, A. Forticaux, S. Jin and R. T. Raine, *Nat. Chem.*, 2016, **8**, 1008–1014.
- 15 S. E. Paramonov, V. Gauba and J. D. Hartgerik, *Macromolecules*, 2005, **38**, 7555–7561.
- 16 F. W. Kotch and R. T. Raines, *Proc. Natl. Acad. Sci. U. S. A.*, 2006, **103**, 3028–3033.
- 17 C. M. Yamazaki, S. Asada, K. Kitagawa and T. Koide, *Biopolymers*, 2008, **90**, 816–823.
- 18 O. D. Krishna and K. L. Kiick, *Biomacromolecules*, 2009, **10**, 2626–2631.
- 19 M. A. Cejas, W. A. Kinney, C. Chen, G. C. Leo, B. A. Tounge, J. G. Vinter, P. P. Joshi and B. E. Maryanoff, *J. Am. Chem. Soc.*, 2007, **129**, 2202–2203.
- 20 M. A. Cejas, W. A. Kinney, C. Chen, G. C. Leo, B. A. Tounge, H. R. Almond Jr, C. A. Maryanoff, K. Balss, M. Breslav, E. Lacy and B. E. Maryanoff, *Proc. Natl. Acad. Sci. U. S. A.*, 2008, **105**, 8518–8525.
- 21 K. Kar, S. Ibrar, V. Nanda, S. P. Kunapuli and B. Brodsky, *Biochemistry*, 2009, **48**, 7959–7968.
- 22 D. E. Przybyla and J. Chmielewski, *J. Am. Chem. Soc.*, 2008, **130**, 12610–12611.
- 23 M. M. Pires and J. Chmielewski, *J. Am. Chem. Soc.*, 2009, **131**, 2706–2712.
- 24 D. E. Przybyla and J. Chmielewski, *J. Am. Chem. Soc.*, 2010, **132**, 7866–7867.
- 25 C.-C. Chen, W. Hsu, T.-C. Kao and J.-C. Horng, *Biochemistry*, 2011, **50**, 2381–2383.
- 26 U. Kusebauch, S. A. Cadamuro, H.-J. Musiol, L. Moroder and C. Renner, *Chem.–Eur. J.*, 2007, **13**, 2966–2973.
- 27 S. Samanta and A. Woolley, *ChemBioChem*, 2011, **12**, 1712–1723.
- 28 V. Kubyshev, *Org. Biomol. Chem.*, 2019, **17**, 8031–8047.
- 29 H. Xu, J. Wang, S. Han, J. Wang, D. Yu, H. Zhang, D. Xia, X. Zhao, T. A. Waigh and J. R. Lu, *Langmuir*, 2009, **25**, 4115–4123.
- 30 T. Koga, T. Higuchi, T. Kinoshita and N. Higashi, *Chem.–Eur. J.*, 2006, **12**, 1360–1367.
- 31 S. Sakakibara, K. Inoue, K. Shudo, Y. Kishida, Y. Kobayashi and D. J. Prockop, *Biochem. Biophys. Acta*, 1973, **303**, 198–202.
- 32 H.-P. Germann and E. Heidemann, *Biopolymers*, 1988, **27**, 157–163.
- 33 C. G. Fields, D. J. Mickelson, S. L. Drake, J. B. McCarthy and G. B. Fields, *J. Biol. Chem.*, 1993, **268**, 14153–14160.
- 34 Y. Feng, G. Melacini, J. P. Taulane and M. Goodman, *J. Am. Chem. Soc.*, 1996, **118**, 10351–10358.
- 35 M. Goodman, Y. Feng, G. Melacini and J. P. Taulane, *J. Am. Chem. Soc.*, 1996, **118**, 5156–5157.
- 36 G. Melacini, Y. Feng and M. Goodman, *J. Am. Chem. Soc.*, 1996, **118**, 10359–10364.
- 37 J. Kwak, A. D. Capua, E. Locardi and M. Goodman, *J. Am. Chem. Soc.*, 2002, **124**, 14085–14091.
- 38 P. Berndt, G. B. Fields and M. Tirrell, *J. Am. Chem. Soc.*, 1995, **117**, 9515–9522.
- 39 Y.-C. Yu, P. Berndt, M. Tirrell and G. B. Fields, *J. Am. Chem. Soc.*, 1996, **118**, 12515–12520.
- 40 Y.-C. Yu, M. Tirrell and G. B. Fields, *J. Am. Chem. Soc.*, 1998, **120**, 9979–9987.
- 41 Y.-C. Yu, V. Roontga, V. A. Daragan, K. H. Mayo, M. Tirrell and G. B. Fields, *Biochemistry*, 1999, **38**, 1659–1668.
- 42 T. Gore, Y. Dori, Y. Talmon, M. Tirrell and H. Bianco-Peled, *Langmuir*, 2001, **17**, 5352–5360.
- 43 J. D. Hartgerink, E. Beniash and S. I. Stupp, *Proc. Natl. Acad. Sci. U. S. A.*, 2002, **99**, 5133–5138.
- 44 H. W. Jun, S. E. Paramonov and J. D. Hartgerink, *Soft Matter*, 2006, **2**, 177–181.
- 45 J. Luo and Y. W. Tong, *ACS Nano*, 2011, **5**, 7739–7747.
- 46 S. Sakakibara, Y. Kishida, K. Okuyama, N. Tanaka, T. Ashida and M. Kakudo, *J. Mol. Biol.*, 1972, **65**, 371–372.
- 47 F. R. Brown III, J. P. Carver and E. R. Blout, *J. Mol. Biol.*, 1969, **39**, 307–313.
- 48 F. R. Brown III, A. di Corato, G. P. Lorenzi and E. R. Blout, *J. Mol. Biol.*, 1972, **63**, 85–99.
- 49 Y. Feng, G. Melacini and M. Goodman, *Biochemistry*, 1997, **36**, 8716–8724.
- 50 S. Allenmark, *Chirality*, 2003, **15**, 409–422.
- 51 I. T. Weber, R. W. Harrison and R. V. Iozzo, *J. Biol. Chem.*, 1996, **271**, 31767–31770.
- 52 S. M. Sweeney, J. P. Orgel, A. Fertala, J. D. McAuliffe, K. R. Turner, G. A. Di Lullo, S. Chen, O. Antipova, S. Permul, L. Ala-Kokko, A. Forlino, W. A. Cabral, A. M. Barnes, J. C. Marini and D. S. Antonio, *J. Biol. Chem.*, 2008, **283**, 21187–21197.



Photocleavable Peptide–Poly(2-hydroxyethyl methacrylate) Hybrid Graft Copolymer via Postpolymerization Modification by Click Chemistry To Modulate the Cell Affinities of 2D and 3D Materials

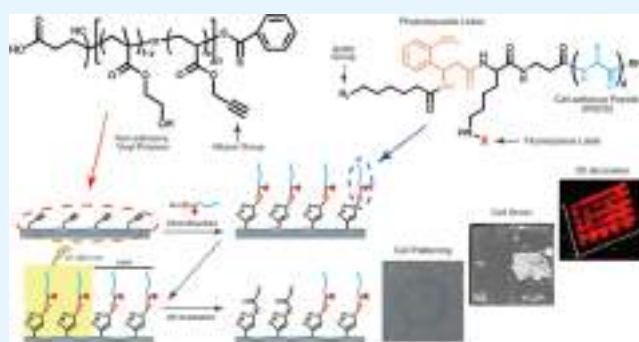
Shin-nosuke Nishimura,[†] Naoki Hokazono,[‡] Yukiko Taki,[‡] Hideki Motoda,[†] Yusuke Morita,^{*,‡} Koji Yamamoto,[‡] Nobuyuki Higashi,[†] and Tomoyuki Koga^{*,†}

[†]Department of Molecular Chemistry and Biochemistry, Faculty of Science and Engineering and [‡]Department of Biomedical Engineering, Faculty of Life and Medical Sciences, Doshisha University, Kyotanabe, Kyoto 610-0321, Japan

Supporting Information

ABSTRACT: Controlling the surface properties of engineered materials to enhance or reduce their cellular affinities remains a significant challenge in the field of biomaterials. We describe a universal technique for modulating the cytocompatibilities of two-dimensional (2D) and three-dimensional (3D) materials using a novel photocleavable peptide-grafted poly(2-hydroxyethyl methacrylate) (PHEMA) hybrid. The reversible addition–fragmentation chain transfer copolymerization of HEMA and propargyl acrylate was successfully controlled. The resultant alkyne-containing PHEMA was then used to modify the azide-terminated oligopeptides [Arg–Gly–Asp–Ser (RGDS)] with a photolabile 3-amino-3-(2-nitrophenyl)propanoic acid moiety via the copper-catalyzed alkyne–azide click chemistry. This strategy was readily used to decorate the surfaces of both hydrophilic and hydrophobic materials with RGDS peptides due to the high film-forming abilities of the PHEMA unit. The resultant thin film acted as an effective scaffold for improving cell adhesion and growth of NIH/3T3 fibroblasts and MC3T3-E1 osteoblast-like cells in vitro. In addition, UV irradiation of the surface led to the detachment of cells from the material surface accompanied by the photocleavage of RGDS grafts and enabled the 2D-patterning of cells and cell sheet engineering. The applicability of this system to 3D materials was investigated, and the cell adhesion was remarkably enhanced on a 3D-printed poly(lactic acid) object. This facile, biocompatible, and photoprocessable peptide–vinyl polymer hybrid system is valuable for its ability to advance the fields of tissue engineering, cell chips, and regenerative medicine.

KEYWORDS: peptide–polymer hybrid, photocleavable peptide, cell micropatterning, cell sheet engineering, postpolymerization modification, 2D and 3D coatings



INTRODUCTION

Significant efforts have been made recently toward designing functional scaffolds that control cell adhesion, shape, and proliferation for tissue engineering and regenerative medicine applications.^{1,2} The interaction strength between cells and a material's surface can be controlled by the biochemical cues (i.e., cell-binding ligands, their densities and distributions, etc.) as well as the physical factors such as surface wettability, stiffness, and topographic and nanograin structures.^{3–8} Mechanical forces, which are generated from the extracellular microenvironment, can also substantially affect the cell response and development.^{9,10} In vivo, the extracellular matrix (ECM), which is consisted of proteins and polysaccharides with nano- and microscale structures, acts as a scaffold to regulate cell behavior and cell-to-cell communication.¹¹ Fibronectin (FN) is one of the important ECM proteins that mediates the adhesion and spreading of many cells. The cell-binding activity of FN is attributed to the arginine-glycine-

aspartic acid (RGD) sequence in the protein, which specifically binds to integrin receptors present on a cell's surface.^{12–14} Chemically synthesized short RGD and RGD-serine (RGDS) peptides, which can be prepared easily using solid-phase peptide synthesis (SPPS) methods, can also function as cell recognition epitopes and have, therefore, been used to engineer ECM-mimicking surfaces.^{3,4,15–17} The hybridization of biofunctional oligopeptides and synthetic polymers having an appropriate biocompatibility and mechanical strength may offer a good material engineering strategy.

One successful approach to preparing peptide–polymer hybrid materials involves combining SPPS and controlled radical polymerization (CRP) methods, including nitroxide-mediated polymerization, atom transfer radical polymerization,

Received: April 18, 2019

Accepted: June 12, 2019

Published: June 25, 2019

and reversible addition–fragmentation chain transfer (RAFT) polymerization.^{18–21} Recent significant advances in CRP using peptide-based initiators, macromonomers, or chain transfer agents enables the sequence-controlled peptides to incorporate into well-defined vinyl polymers as block,^{22–25} multi-block,^{26–30} or graft^{31–33} segments. In fact, various RGD peptide-containing hybrids have been developed using this approach for use as artificial scaffolds for tissue engineering.^{15,22,31,33–37}

An alternative approach to hybrid synthesis involves postpolymerization modifications,^{26,27,38–41} for example, via the alkyne–azide cycloaddition click chemistry. Click chemistry was first proposed in 2001 as an addition reaction that proceeds rapidly and selectively without side reactions.⁴² The Huisgen 1,3-dipolar cycloaddition is a representative example of click chemistry⁴³ and proceeds between alkyne and azide groups via a copper catalyst, even in the presence of water.⁴⁴ This method enables the versatile and selective modification of synthetic polymers using biomolecules without undesirable side reactions (e.g., chain transfer reactions during polymerization), even on a solid surface (i.e., in the film form), and provides more flexibility to material design.^{26,27,39,41,45}

Hybrid polymer-based coatings that can form stable thin films with switchable cell–material interactions under the control of external stimuli are particularly valuable for the surface engineering of two-dimensional (2D) and three-dimensional (3D) materials and for facilitating cell sheet engineering and cell micropatterning for cell-based sensing and drug discovery applications. Herein, we report the preparation of a graft-type photocleavable RGDS peptide–biocompatible vinyl polymer hybrid using a postpolymerization modification approach as a novel functional artificial ECM that enables spatial control over cell adhesion and detachment by photolithography.

Several methods have been employed for cell micropatterning, including microcontact printing, inkjet printing, photolithography, and laser-guided writing.^{5,46} Among these, the photolithographic approach using photodegradable molecules, such as RGD with a photolabile linker or caged RGD,^{47–50} is especially attractive for constructing both RGD peptide micropatterned and gradient surfaces, permitting control over cell behavior, such as adhesion and migration, because light can be easily focused and its intensity controlled. Although cell adhesion has been successfully controlled by directly grafting light-sensitive RGD peptides onto engineered solid materials, in most cases, this approach is applicable only to a limited range of substrates, such as 2D glasses and silicon plates. The photodegradable peptide–polymer hybrid system described here overcomes limitations and will be a universal platform for decorating various materials, including simple 2D plates and complex 3D-printed objects.

In this study, we designed an azide-terminated RGDS peptide with a photolabile 3-amino-3-(2-nitrophenyl)propanoic acid (ANP) linker that decomposed rapidly under mild UV light.⁵¹ Moreover, an alkyne-containing poly(2-hydroxyethyl methacrylate) (PHEMA) prepared by RAFT polymerization was used as a base polymer to react with the peptide via a copper-catalyzed cycloaddition, leading to the desired photoprocessable hybrid graft copolymer (Figure 1). PHEMA is a biocompatible polymer commonly used in biomaterials for its ability to form films and hydrogels with sufficient mechanical strength and resist the nonspecific adsorption of proteins and cells.^{52,53} Spatially controlled UV

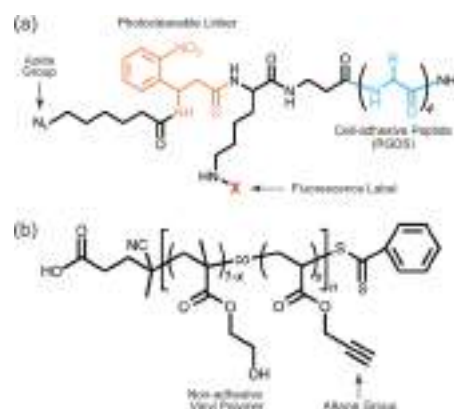


Figure 1. Chemical structure of the novel photocleavable and clickable oligopeptide (a) and alkyne-containing poly(HEMA-co-PgA) (b) used as a biofunctional coating.

irradiation induces partial photocleavage of the RGDS grafts to generate regions with opposing surface properties: cell adhesive and nonadhesive (nonfouling) surfaces. To evaluate the versatility of this hybrid coating as a novel functional ECM, two different cells were employed as model cell lines: NIH/3T3 fibroblast cell, which has been widely used for soft tissue engineering including cell sheet, and MC3T3-E1 osteoblast-like cell, which has usually been used to assess cell–material interaction, including cell migration, as well as for bone tissue engineering. A detailed analysis of cell behavior on the hybrid film was conducted, especially in view of the effect of the photocleavage of the RGDS grafts. Furthermore, the applicability of this system to 3D-printed poly(lactic acid) (PLA) objects was confirmed. PLA is a biocompatible and biodegradable hydrophobic polymer derived from renewable biomass and has been used in biomedical applications, such as bone plates, surgical sutures, and drug delivery system carriers. We believe that this work provides a useful method to fabricate various scaffolds with a photocontrollable cell affinity for soft and hard tissue engineering.

EXPERIMENTAL SECTION

Materials. Analytical grade solvents were used as received. *N,N*-Dimethylformamide (DMF), methanol, 2,2,2-trifluoroacetic acid (TFA), dichloromethane, diethylether, hexane, ethyl acetate, acetonitrile, hydrochloric acid (12 M HCl), triethylamine, *N*-methylmorpholine (NMM), piperidine, 2,2,2-trifluoroethanol (TFE), 2,2'-azobisisobutyronitrile (AIBN), sodium sulfate anhydrous (anhydrous Na₂SO₄), sodium azide (NaN₃), ammonia water (25 vol % NH₃), dimethyl sulfoxide (DMSO)-*d*₆, chloroform-*d*, and D₂O were purchased from Nacalai Tesque. 2-Hydroxyethyl methacrylate (HEMA), rhodamine B (RhB), 4-(4,6-dimethoxy-1,3,5-triazin-2-yl)-4-methylmorpholinium chloride (DMT-MM), *N,N'*-diisopropylcarbodiimide (DIPC), *N*-(9-fluorenylmethoxycarbonyloxy)succinimide (Fmoc-OSu), CuBr₂, *N,N,N',N'',N'''*-pentamethyldiethylenetriamine (PMDETA), and LiBr were purchased from Wako Pure Chemical (Japan). Fmoc-L-Arg(Pbf), Fmoc-L-Asp(OtBu), Fmoc-β-Ala, Fmoc-Gly, Fmoc-L-Lys(Mtt), Fmoc-L-Ser(tBu), Fmoc-NH-SAL 4-methylbenzhydrylamine (MBHA) resin (0.67 mmol/g), and 1-hydroxybenzotriazole anhydrous (HOBT) were purchased from Watanabe Chemical Industries. 2,5-Dihydroxybenzoic acid (DHBA), 4-cyano-(4-thiobenzoylthio)pentanoic acid (CTPA), propargyl acrylate (PgA), and 6-bromohexanoic acid were purchased from Sigma-Aldrich. Ascorbic acid (AsAc) was purchased from Tokyo Chemical Industries. 3-Amino-3-(2-nitrophenyl)propanoic acid (ANP) was purchased from Alfa Aesar. Poly(lactic acid) (PLA) (MakerBot PLA filament 1.75 mm) for 3D printing was purchased from B&H

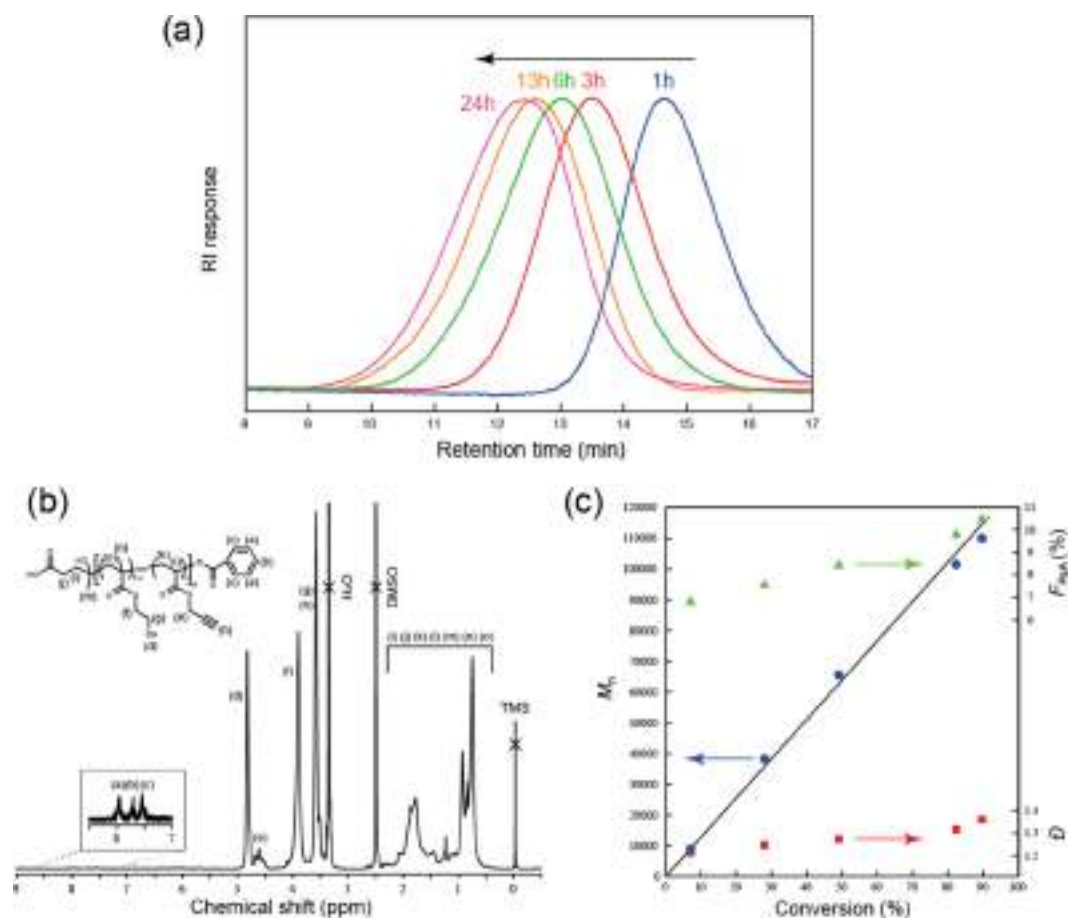


Figure 2. (a) SEC traces (DMF containing LiBr, 40 °C) of poly(HEMA-*co*-PgA) obtained after RAFT polymerization for 1, 3, 6, 13, or 24 h. (b) ^1H NMR spectrum of poly(HEMA-*co*-PgA) obtained after polymerization for 13 h in $\text{DMSO-}d_6$ at 25 °C. (c) Plots of M_n (blue circles), D (red squares), and F_{PgA} (green triangles) as a function of monomer conversion. The solid line represents the calculated theoretical M_n as a function of the monomer conversion, assuming a constant F_{PgA} feed composition.

Foto & Electronics Corp. HEMA and PgA were purified by passing through an activated alumina prior to use.

Measurements. ^1H NMR spectra were recorded using a JEOL JNM-ECA500 (JEOL Resonance) spectrometer (500 MHz). The values of polydispersity indexes (D , M_w/M_n) of the polymers were evaluated by size exclusion chromatography (SEC) using a JASCO LC-net II/AD (JASCO Ltd.) with a refractive index detector. DMF (containing 10 mM LiBr) was used as an eluent (0.6 mL/min, 40 °C, TSKgel α -4000). Poly(methyl methacrylate)s (GL Sciences Inc.) was used as the calibration standard. Matrix-assisted laser desorption/ionization time-of-flight MS (MALDI-TOF MS) analyses were performed on an Autoflex speed (Bruker Daltonics). DHBA was used as a matrix. Fourier transform infrared (FTIR) spectra were recorded on FT/IR-4600 (JASCO Ltd.) using a deuterated L-alanine triglycine sulfate detector fitted with an attenuated total reflection (ATR) accessory that used a germanium internal reflection element (resolution: 4 cm^{-1} , 32 scans). Absorption spectra were recorded by a V-650 spectrophotometer (JASCO Ltd.). AFM images were measured at room temperature on an SPM9700 (Shimadzu Co.) by contact mode (OMCL-TR800PSA-1, tip radius $<20\text{ nm}$) and tapping mode (MPP-11100, tip radius $<12\text{ nm}$) to evaluate the film thickness and the surface roughness, respectively. Confocal laser scanning microscopy (CLSM) images were collected at room temperature using Fluorescence Imaging System AF6000 (Leica Microsystems). Water contact angles of polymer thin films were evaluated at room temperature by a DropMaster-501 (Kyowa Interface Science Co., Ltd.).

Copolymerization of HEMA with PgA by RAFT Polymerization. HEMA (2.06 mL, 17 mmol), PgA (0.335 mL, 3 mmol),

CTPA (5.6 mg, 0.02 mmol), and AIBN (1.6 mg, 0.01 mmol) were dissolved in DMF [monomer concentration: 4 M (five sets)], and the solutions were degassed over freeze–pump–thaw cycles (three times) under dry N_2 . After polymerization for 1–24 h at 60 °C, the resulting copolymers were purified by a reprecipitation method with DMF/diethylether (pale pink-colored solid). The chemical structures were determined by ^1H NMR and FTIR spectroscopies. The number-average molecular weights (M_n), D , and copolymer composition (F_{PgA} : mole fraction of PgA units) of the copolymers were characterized by SEC and ^1H NMR analyses (Figure 2a,b). The M_n of all polymers were determined on the basis of the area ratio of the signals of HEMA and PgA units to that of the aromatic ring signal in CTPA. The F_{PgA} values were calculated using the area ratio of the signal of HEMA (3.80–4.20 ppm, 2H) to that of CH_2 in PgA (4.45–4.75 ppm, 2H).

^1H NMR [$\text{DMSO-}d_6$, tetramethylsilane (TMS), polymn. time: 13 h, $x = F_{\text{PgA}}$] (Figure 2b): 0.50–2.45 ppm [PHEMA, methylene (main chain), $2(1-x)n\text{H}$; PHEMA, methyl (main chain), $3(1-x)n\text{H}$; PPgA, methylene (main chain), $2xn\text{H}$; PPgA, methine (main chain), $xn\text{H}$; CTPA, methyl, 3H; CTPA, methylene, 4H]; 3.37–3.75 ppm [PPgA, $-\text{COOCH}_2\text{CCH}$, $xn\text{H}$; PHEMA, $-\text{COOCH}_2\text{CH}_2\text{OH}$, $2(1-x)n\text{H}$]; 3.80–4.20 ppm [PHEMA, $-\text{COOCH}_2\text{CH}_2\text{OH}$, $2(1-x)n\text{H}$]; 4.45–4.75 ppm [PPgA, $-\text{COOCH}_2\text{CCH}$, $2xn\text{H}$]; 4.75–4.95 ppm [PHEMA, $-\text{COOCH}_2\text{CH}_2\text{OH}$, $(1-x)n\text{H}$]; 7.45–8.10 ppm (CTPA, phenyl, 5H).

ATR-FTIR (polymn. time: 13 h): 3423 cm^{-1} (ν_s : O–H), 3262 cm^{-1} (ν_s : O–H), 2987 cm^{-1} [ν_s : C–H (methyl)], 2951 cm^{-1} [ν_s : C–H (methylene)], 2888 cm^{-1} [ν_s : C–H (methylene)], 2127 cm^{-1} (ν_s : $\text{C}\equiv\text{C}$), 1725 cm^{-1} (ν_s : $\text{C}(\text{=O})\text{O}$).

Polymn. time: 1 h: $F_{P_{gA}} = 6.9$, $M_n = 9000$, $n = 70$, and $\bar{D} = 1.21$. 3 h: $F_{P_{gA}} = 7.6$, $M_n = 38\,300$, $n = 298$, and $\bar{D} = 1.25$. 6 h: $F_{P_{gA}} = 8.5$, $M_n = 65\,600$, $n = 510$, and $\bar{D} = 1.28$. 13 h: $F_{P_{gA}} = 9.9$, $M_n = 101\,500$, $n = 792$, and $\bar{D} = 1.31$. 24 h: $F_{P_{gA}} = 10.4$, $M_n = 111\,000$, $n = 859$, and $\bar{D} = 1.37$.

Synthesis of Photocleavable and Clickable RGDS Peptides.

Photocleavable and clickable RGDS peptides were synthesized by Fmoc-based SPPS. The target sequence was prepared on an Fmoc-NH-SAL MBHA resin using Fmoc-L-Ser(*t*Bu), Fmoc-L-Asp(*O**t*Bu), Fmoc-Gly, Fmoc-L-Arg(Pbf), Fmoc- β -Ala, Fmoc-L-Lys(Mtt), Fmoc-ANP,³³ and 6-azidohexanoic acid (N_3 -HA) (see Figure S1, Supporting Information) (3 equiv) in DMF. 1-Hydroxybenzotriazole anhydrous (HOBt) (3 equiv) and 1,3-diisopropylcarbodiimide (DIPC) (3 equiv) were used for coupling, and piperidine (20 vol %)/DMF was used for Fmoc removal. The 4-methyltrityl (Mtt) group of the Lys residue was deprotected on resin by treating with TFA/dichloromethane/triisopropylsilane (TIS) (1/98/1 in vol) for 30 min. The resultant resin was treated with the mixture of RhB (3 equiv), DMT-MM (3 equiv), and NMM (3 equiv) in DMF/methanol (4/1 in vol) for 24 h. After the modification, the target peptide was obtained by cleaving from the resin using TFA/dichloromethane/TIS (8.5/1/0.5 in vol). In this case, the counterion of the RhB group was exchanged from chloride to trifluoroacetate ions. The obtained peptide (reddish-pink-colored solid) was refined by a reprecipitation method with methanol/diethylether and characterized by MALDI-TOF MS, FTIR, and ¹H NMR analyses.

MALDI-TOF MS (Figure 3): obsd $[M + Na]^+$, $[M + K]^+$ (calcd $[M + H]^+$, $[M + Na]^+$, $[M + K]^+$); 1523.94, 1540.00 (1502.60, 1524.58, 1540.69).

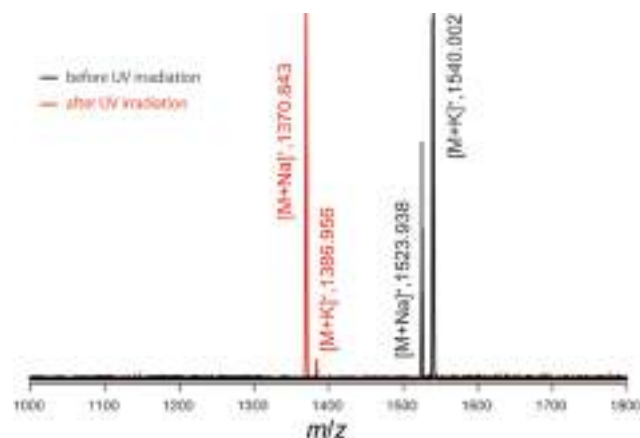


Figure 3. MALDI-TOF MS spectra of the photocleavable and clickable peptide obtained before (black) and after (red) UV irradiation for 30 min in water.

¹H NMR (DMSO-*d*₆, TMS) (Figure S2a): 0.75–2.45 ppm [RhB, $-N(CH_2CH_3)_2$, 6H; RhB, $=N^+(CH_2CH_3)_2$, 6H; methylene of N_3 -HA, 8H; Lys, γ -CH₂, 2H; Lys, δ -CH₂, 2H; Arg, γ -CH₂, 2H; Lys, β -CH₂, 2H; Arg, β -CH₂, 2H; β -Ala, α -CH₂, 2H]; 2.60–4.70 ppm (methylene of N_3 -HA, 2H; ANP, $-CH-CH_2-$, 2H; Asp, β -CH₂, 2H; Arg, δ -CH₂, 2H; Lys, ϵ -CH₂, 2H; β -Ala, β -CH₂, 2H; Gly, CH₂, 2H; Ser, β -CH₂, 2H; amino acids, α -CH, 5H); 3.30 ppm [RhB, $-N(CH_2CH_3)_2$, 4H; RhB, $=N^+(CH_2CH_3)_2$, 4H]; 6.25–6.45 ppm [RhB, $-CH=CH-C(N(CH_2CH_3)_2)=CH-$, 3H; RhB, $-CH=CH-C(N^+(CH_2CH_3)_2)-CH=$, 3H]; 6.75–8.45 ppm [ANP, $-C=CH-C=CH-CH=C(NO_2)-$, 4H; RhB, $-CH=CH-CH=CH-C-$, 4H; $-CONH_2$, 2H; $-CONH-$, 9H].

Transmission FTIR (KBr pellet) (Figure S2b): 3330 cm⁻¹ (ν_s : O–H), 3196 cm⁻¹ (ν_s : CON–H), 3076 cm⁻¹ (ν_s : CON–H), 2945 cm⁻¹ [ν_s : C–H (methylene)], 2873 cm⁻¹ [ν_s : C–H (methylene)], 2104 cm⁻¹ (ν_s : N=N=N), 1662 cm⁻¹ (ν_s : NHC=O), 1533 cm⁻¹ (δ : CON–H).

Preparation of a Poly(HEMA-co-PgA) Thin Film onto 2D and 3D Materials.

A 2D thin film of poly(HEMA-co-PgA) ($M_n = 101\,500$, $\bar{D} = 1.31$) was prepared by spin-coating method from TFE solution of the polymer (20 mg/mL, 30 μ L) at 3000 rpm for 30 s on a glass plate (1 cm²). The sample was dried overnight at room temperature. The glass substrate was treated by O₂ plasma before use for preparing a superhydrophilic surface using the dry etching system FA-1-UZ, SAMCO. The thickness of the obtained polymer thin film was estimated by scratching with an AFM cantilever in contact mode (Figure S3). A 3D-printed poly(lactic acid) (PLA) mesh object (1 cm \times 1 cm \times 0.2 cm, 100 μ m interval) was created by a fused deposition modeling (FDM) type 3D-printer (Replicator Desktop 3D-Printer, MakerBot Inds.). The 3D-printed PLA was then dipped into methanol solution of poly(HEMA-co-PgA) ($M_n = 101\,500$, $\bar{D} = 1.31$) (20 mg/mL) for 3 min and was then carefully pulled up at a speed of 1 mm/s. The sample was dried overnight at room temperature. Dust particles in the polymer solution were removed by filtration using a Cosmonice filter (Nacalai Tesque, pore size: 0.45 μ m).

Decoration of RGDS Peptides on a Poly(HEMA-co-PgA) Film Using the Click Reaction.

N_3 -HA-ANP-K(RhB)- β A-RGDS-*Am* 134 μ g (96 nmol), CuBr₂ 39 μ g (175 nmol), PMDETA 73 μ g (349 nmol), and AsAc 15 mg (85 μ mol) were dissolved in 15 mL of MeOH/water (5/7 in vol) (as final concentration). The solution was degassed over freeze–pump–thaw cycles (three times) under dry N₂ and poured into a separable flask. Poly(HEMA-co-PgA)-coated substrates were immersed in the solution under N₂ gas bubbling at room temperature. After bubbling was applied for 30 min, the separable flask was closed and placed in an incubator at 40 $^\circ$ C for 24 h to promote the copper-catalyzed alkyne–azide cycloaddition. Excess reaction reagents were removed by washing the substrates with MeOH/water (5/7 in vol), 1 M HCl_{aq}, 1 M ethylenediaminetetraacetate aqueous (aq) (pH 8.0), and distilled water for 10 min, separately, followed by drying in air. The surface concentration of the modified peptide was estimated from UV analysis. A calibration curve was prepared by measuring the absorbance of the RhB-labeled peptide at 552 nm in TFE ($\epsilon = 91\,000$ L/mol cm). The concentration of peptides bound to the PHEMA copolymer film (1 cm \times 1 cm \times 150 nm) was measured by dissolving the film in TFE. Three replicate measurements were performed. We assumed that only the peptide epitopes in the top 1 nm of the surface were useful for integrin binding, based on previous reports.^{36,40} The click reaction was carried out on the 3D-printed PLA object in a similar manner.

In Vitro Cell Assay. Fibroblast cells (NIH/3T3) and osteoblast-like cells (MC3T3-E1) were cultured to 80% confluence on a dish at 37 $^\circ$ C under 5% CO₂ with Dulbecco's modified Eagle's medium (L7A0439, Nacalai Tesque, Inc.), and minimum essential medium Eagle alpha modification (α -MEM) (12571-963, Life Technologies Japan Ltd.), containing 10% fetal bovine serum (S15314S1760, Biowest) and an antibiotic mixture (A5995-100ML, Sigma-Aldrich), respectively. The cells were seeded at a density of 6.0×10^3 or 3.0×10^4 cells/cm² onto the polymer thin films in serum(-free) medium at 37 $^\circ$ C under 5% CO₂ for 24 or 48 h, depending on the type of experiment. After incubation for the prescribed period, the number of attached cells was counted in phase contrast images obtained by confocal microscopy. Fluorescence images of cells were also obtained from the same samples by staining with 1000-fold diluted dyes (calcein-AM (C1359-100UL, Sigma-Aldrich) or 4',6-diamidino-2-phenylindole (DAPI) (KL092, Wako Pure Chemical)) in phosphate buffer solutions (PBS) for 5 min. DAPI staining was performed after fixing the cells in a 4%-paraformaldehyde phosphate buffer solution for 12 min.

For immunofluorescence staining, MC3T3-E1 cells were seeded on the poly(HEMA-co-PgA) and the RGDS-modified films placed in a 24-well plate at a density of 1.0×10^4 cells/cm² in serum-free α -MEM at 37 $^\circ$ C under 5% CO₂ for 24 h. After the cells were fixed in 4%-paraformaldehyde/PBS(-) for 12 min, the cells were washed twice with PBS(-) and permeabilized with 0.2% Triton X-100 (T8787, Sigma-Aldrich). Next, the treated cells were washed with 0.05% Tween-20/PBS(-) and blocked with 5% normal donkey serum/

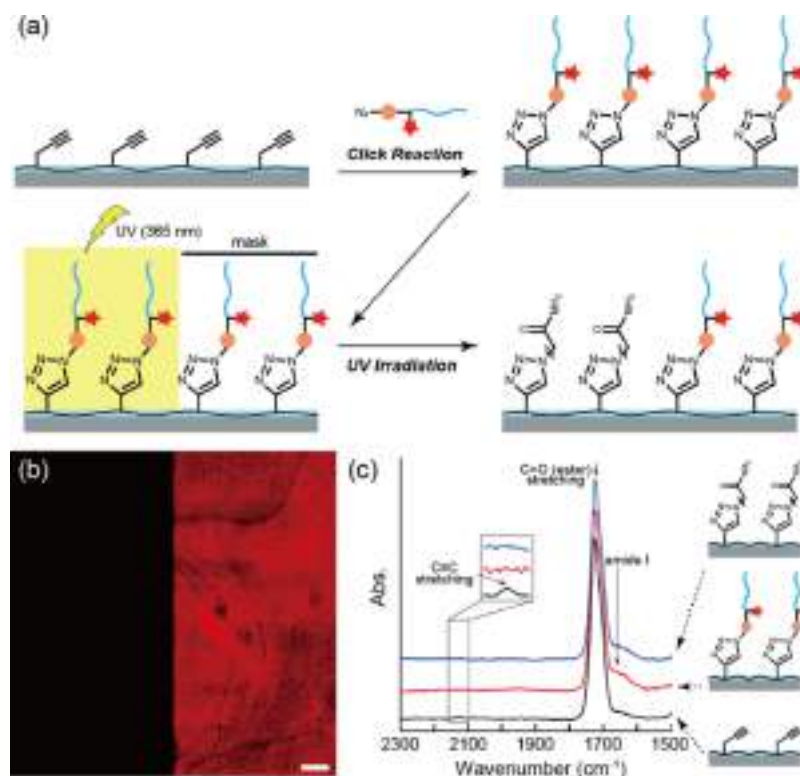


Figure 4. (a) Conceptual scheme for the modification of poly(HEMA-co-PgA) films with the RGDS peptide via a click reaction, and the 2D peptide patterning by UV irradiation. (b) Confocal microscopy image of the RGDS-patterned film (left: UV-irradiated region, right: nonirradiated region). The scale bar indicates 500 μm . (c) ATR-FTIR spectra of the poly(HEMA-co-PgA) film (black line), RGDS-modified film (red line), and UV-irradiated film (blue line).

PBS(-) for 30 min. The cells were immunostained with 100-fold diluted rat anti-integrin $\beta 1$ primary antibody (ab95623, Abcam) at 4 $^{\circ}\text{C}$ for 20 h. Subsequently, the Alexa Fluor-conjugated secondary anti-rat antibody (1:500) (ab169346, Abcam) and 50-fold diluted Fluor 546 phalloidin (A22283, Invitrogen) were added into the wells. After incubation for 1 h, the cell nuclei were stained with 500-fold diluted DAPI for 2 min. The stained cells were mounted with 50% glycerol and observed with CLSM.

Two-Dimensional (2D) Patterning of Cells on the RGDS-Modified Poly(HEMA-co-PgA) Thin Film. A ring pattern was designed to be five times the size of the final objective sample pattern dimensions using PowerPoint software and was printed on a film for use with an overhead projector (OHP film VF-1101N, Kokuyo). The OHP film and an emulsion mask (High Precision Photo Plate HRP-SN-2 4 \times 4 30Z, Konica Minolta) were used in a simple mask fabrication machine (MM605, Nanometric Technology Inc.) in a dark room. The emulsion mask was exposed to UV light directed through the OHP film, and the OHP film pattern was transferred onto the emulsion mask in one-fifth scale. The exposed emulsion mask was treated in a developer (High-Resolution Plate Developer CDH-100, Konica Minolta) and a fixer (High-Resolution Plate Fixer CFL-881P, Konica Minolta). As a result, the patterned photomask was successfully obtained (inner diameter: 3 mm, outer diameter: 4 mm, 500 μm interval). The ring-patterned photomask was set under a glass plate covered with NIH/3T3 cells bound to the peptide/PHEMA hybrid film. UV light (365 nm, 8 W) was applied using a handy lamp (SLUV-8, AS ONE Co.) for 30 min, directed toward the back side of the surface. After UV exposure, the cells were stained with calcein-AM and observed by CLSM.

RESULTS AND DISCUSSION

Synthesis and Characterization of Alkyne-Containing Poly(HEMA-co-PgA). Herein, PHEMA copolymers with clickable alkyne groups were prepared for use as a base

polymer coating, as illustrated in Figure 1. We employed RAFT polymerization using DMF, AIBN, and 4-cyano-4-(thiobenzoylthio)pentanoic acid (CTPA) as a solvent, initiator, and chain transfer agent, respectively, for the copolymerization of HEMA with propargyl acrylate (PgA). Previously, an alkyne-containing compound was successfully used in a RAFT polymerization with efficient retention of the functional alkyne group, even after the radical polymerization reaction.²⁷ Therefore, we selected the combination of an alkyne polymer and an azide peptide as an orthogonal click partner. The obtained copolymers were characterized using SEC and ¹H NMR analyses, and the results are summarized in Figure 2. The SEC traces of the copolymers obtained after polymerization for 1, 3, 6, 13, and 24 h were symmetrically unimodal and shifted clearly toward high molecular weights as the polymerization progressed (Figure 2a). Figure 2b shows a representative ¹H NMR spectrum of poly(HEMA-co-PgA) (13 h polymerization). The presence of PgA units on the PHEMA chain was confirmed by the characteristic ¹H signal at 4.45–4.75 ppm as well as by the presence of a $\text{C}\equiv\text{C}$ stretching band at 2127 cm^{-1} in the FTIR spectrum (Figure 4c, black line). Figure 2c plots M_n , \bar{D} , and F_{PgA} of all polymers against the monomer conversion. The theoretical values of M_n , $M_{n,\text{theor}}$ are included as a solid line. The observed F_{PgA} values of the obtained polymers were found to be 7–11%. These values were slightly lower than those of the feed composition (15%), probably due to differences in the monomer reactivity. The \bar{D} values of the copolymers were below 1.4 throughout the polymerization. In addition, the linearity of the M_n against the conversion plot was similar to the theoretical value, which

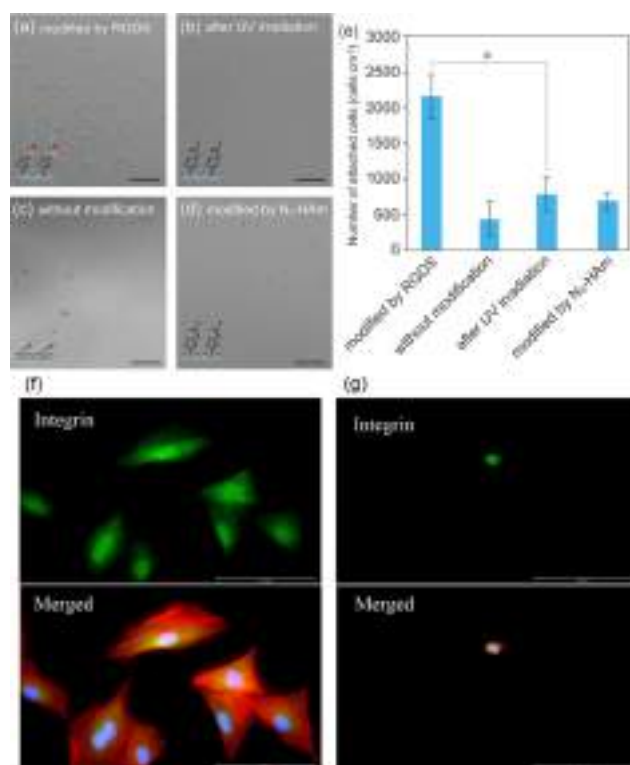


Figure 5. Phase contrast microscopy images of MC3T3-E1 cells cultured on various polymer thin films in serum-free medium for 24 h. Scale bar: 100 μm . (a) RGDS-modified hybrid film. (b) UV-irradiated hybrid thin film. (c) Poly(HEMA-*co*-PgA) film. (d) Poly(HEMA-*co*-PgA) thin film modified by N₃-HAM. Insets show schematic models of the surface structures. (e) Summary of the cell adhesion experiments. Statistical analysis was performed using the *t* test ($N = 6$). Error bars represent the standard deviation. * $p < 0.01$. Fluorescence microscopy images of MC3T3-E1 cells cultured on the (f) RGDS-modified hybrid film and (g) poly(HEMA-*co*-PgA) film. Cells stained with actin filaments (red), cell nuclei (blue), and integrin (green). Scale bar: 100 μm .

means that RAFT copolymerization proceeded by a well-controlled living mechanism.

Preparation of a Photocleavable RGDS Peptide-Modified Poly(HEMA-*co*-PgA) Thin Film via a Click Reaction. A clickable RGDS peptide with an azide group at the N-terminus via a photodegradable ANP moiety was successfully synthesized by Fmoc-based SPPS. Fluorescence labeling was performed on resin by removing the Mtt group of the Lys residue and then condensing with RhB. After cleavage from the resin, the obtained peptide was refined by a reprecipitation method with methanol/diethylether and then characterized by MALDI-TOF MS (Figure 3, black), ¹H NMR (Figure S2a), and FTIR analyses (Figure S2b) to verify the retention of the functional azide group. Moreover, the resultant peptide was found to be photodegradable by MALDI-TOF MS analysis. Figure 3 shows the MALDI-TOF MS spectra of the RGDS peptide before and after UV irradiation (365 nm, 8 W) for 30 min in water. After UV irradiation, two new peaks were observed at 1370.84 [M + Na]⁺ and 1386.96 [M + K]⁺ with the disappearance of the peaks from the original peptide. This result demonstrated that photocleavage of the peptide occurred promptly at the C(H)–N(H) linkage in the ANP moiety by UV irradiation.

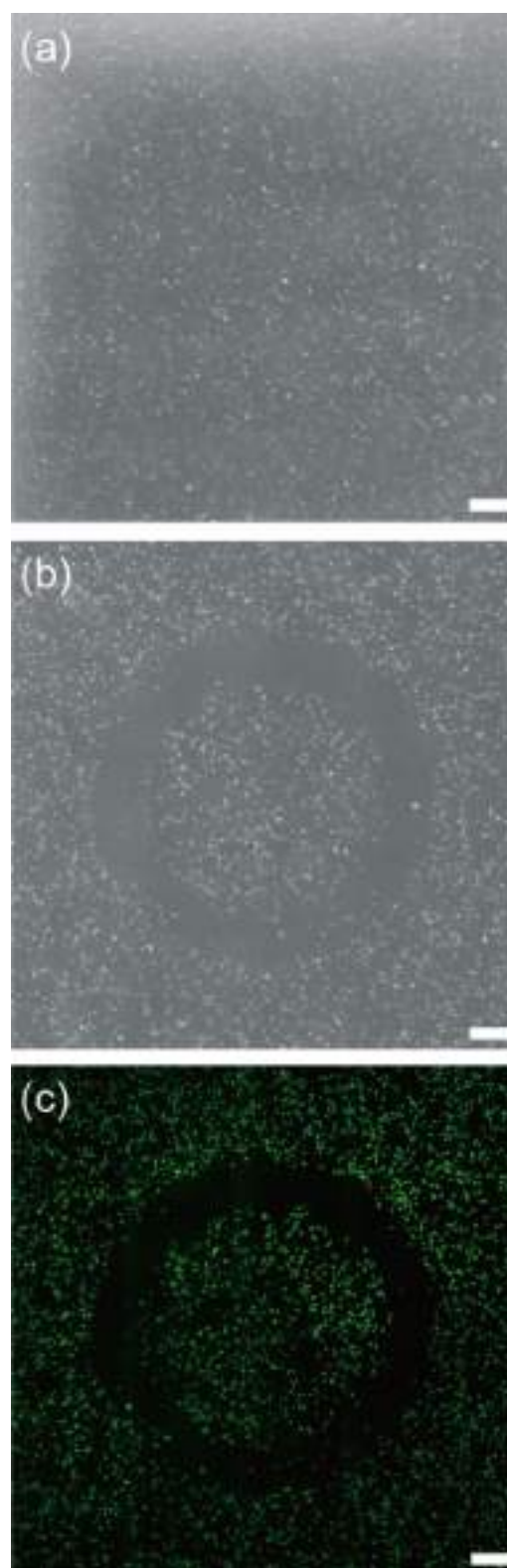


Figure 6. Phototriggered cell release from the hybrid thin film. Phase contrast microscopy images of NIH/3T3 cells cultured on an RGDS-modified hybrid film in serum-free medium over 24 h (a) before and (b, c) after UV irradiation through a circular ring-patterned photomask. Living cells in the image (c) were stained by calcein-AM. Scale bar: 500 μm .

We next examined the modification of a poly(HEMA-*co*-PgA) thin film with the azide-containing clickable RGDS

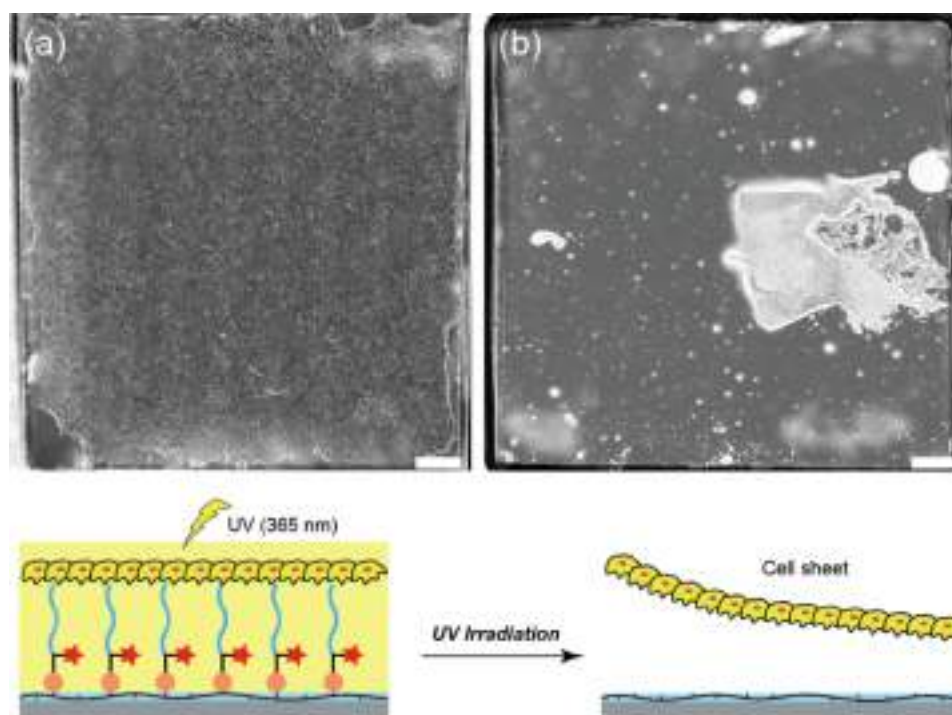


Figure 7. Phase contrast microscopy images of NIH/3T3 cells cultured on an RGDS-modified film in the presence of serum for 48 h (a) before and (b) after UV irradiation. Scale bar: 1000 μm . The cell sheet was successfully recovered from the confluent cells by UV irradiation.

peptide and its controlled removal by photolithographic techniques (Figure 4a). We chose a poly(HEMA-co-PgA) with a relatively large molecular weight obtained at 13 h polymerization ($M_n = 101\,500$, $D = 1.31$) for subsequent film experiments. A thin film of poly(HEMA-co-PgA) with a thickness of 150 nm (Figure S3) was easily prepared on a superhydrophilic glass substrate by spin-coating. Note that this film was stable in water as a gel film and could be prepared successfully not only on hydrophilic glass but also on a hydrophobic substrate, such as PLA. The thin film was then reacted with an azide-functionalized RGDS peptide labeled with RhB using the $\text{CuBr}_2/\text{PMDETA}/\text{AsAc}$ system in MeOH/water (5/7 in vol) under a N_2 atmosphere at 40 $^\circ\text{C}$ for 24 h. To evaluate whether the peptide was covalently attached to the gel film, CLSM images and ATR-FTIR spectra were obtained. Uniform fluorescence from RhB in the peptide was clearly observed in the CLSM image (Figure 4b, right). In addition, the ATR-FTIR spectrum revealed complete loss of the alkyne peak ($\text{C}\equiv\text{C}$ stretching) at 2127 cm^{-1} , together with a significant increase in the absorption at 1656 cm^{-1} (amide I) after the click reaction (Figure 4c, red line). The ATR equipment used in this study contains a germanium internal reflective element with a sample depth of penetration of approximately 320 nm at a wavenumber of 2100 cm^{-1} for the IR laser beam. These results indicated that the RGDS peptides were covalently bound to both the surface and the inside of the film. This conclusion was supported by cell assays (described below). The surface density of the RGDS peptide attached to the film was estimated from the RhB absorbance at 552 nm to be 12.4 pmol/cm^2 (the top 1 nm of the surface). This value is expected to promote cell adhesion and spreading. In fact, Klok et al. previously reported that a surface concentration of GGGRGDS peptide of 5.3 pmol/cm^2 was sufficient to induce human umbilical vein endothelial cell adhesion.³⁶ Biesalski et al. reported that polymer surfaces comprising at least 0.8

pmol/cm^2 GRGDS peptide (up to 20 pmol/cm^2) promoted fibroblast cell adhesion from a serum-free solution.³⁷ The observed amide I band also indicated that the secondary structure of the peptide grafts assumed a random coil conformation.⁵⁴ Since the RGD epitope occupies a loop segment without specific secondary structures such as α -helix and β -sheet in type III module of FN, unstructured peptide epitopes of this hybrid are favorable for cell adhesion. It should be noted that the surface topography and roughness of poly(HEMA-co-PgA) films were almost unchanged before and after the click reaction. The average roughness (R_a) of the RGDS-modified film was slightly higher than that of the poly(HEMA-co-PgA) film (ca. 1 nm) but was in the narrow range of $R_a = 1.82 \pm 0.24$ nm ($2\ \mu\text{m} \times 2\ \mu\text{m}$) and $R_a = 2.27 \pm 0.30$ nm ($10\ \mu\text{m} \times 10\ \mu\text{m}$) (Figure S4).

Subsequently, the peptide grafts were removed from the gel film under photocontrol via UV irradiation (365 nm, 30 min) using a photomask, followed by washing with water of pH 3.0. Figure 4b shows a CLSM image of an RGDS-modified film prepared with (left side) or without (right side) UV irradiation. The dark region caused by UV irradiation indicates detachment of the RGDS grafts from the film via photodegradation at the ANP moiety. The fluorescence intensity of the UV-irradiated area was almost zero, where strong fluorescence was observed in the nonirradiated area. Moreover, a significant decrease in absorbance of the amide I band was observed for the UV-irradiated area, which was normalized to that of the carbonyl stretching (ester) at 1725 cm^{-1} (Figure 4c, blue line). The peptide graft photocleavage rate, which was evaluated by comparing the amide I intensity after UV irradiation to that of a model surface prepared separately by a click reaction of poly(HEMA-co-PgA) with 6-azidohexanamide ($\text{N}_3\text{-HAM}$) (i.e., the same structure as the photocleaved surface), was nearly 100% (Figure S5). Compared to the previously reported hybrid polymer prepared by free-radical copolymerization

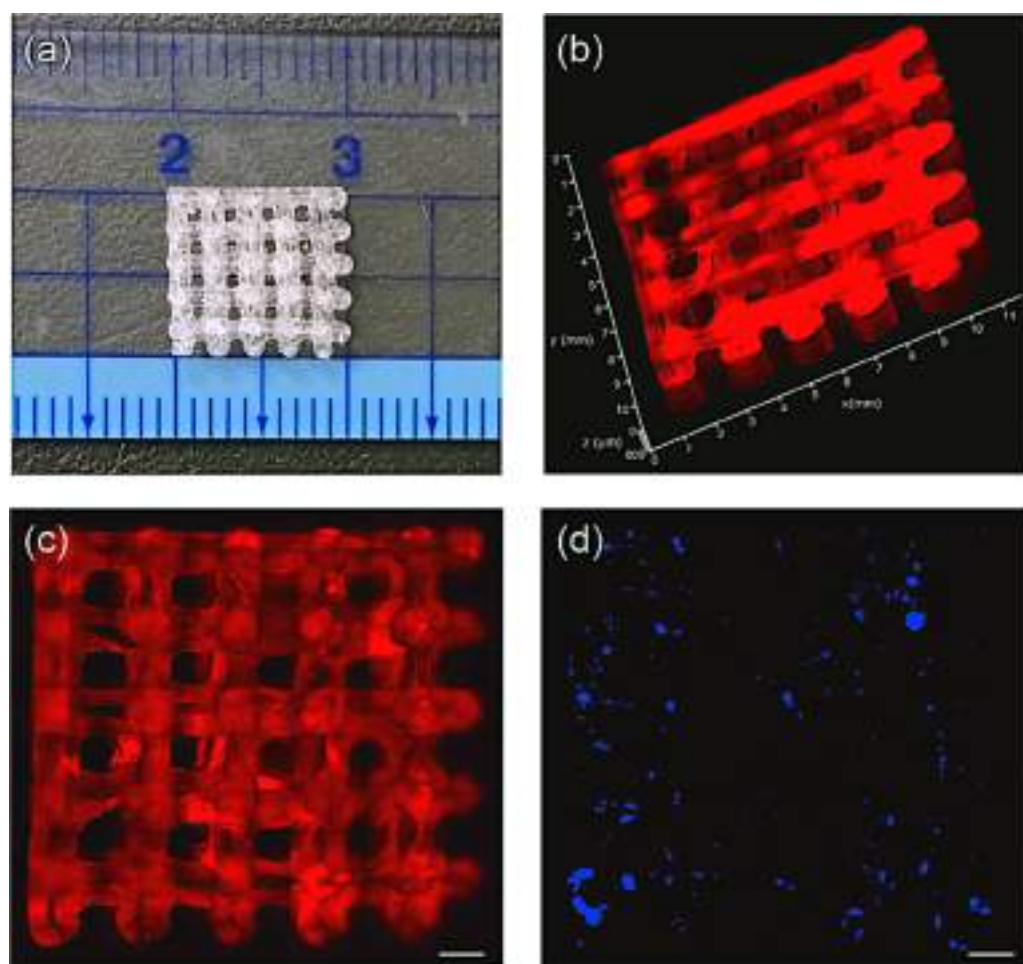


Figure 8. (a) Photograph of a 3D-printed PLA construct (1 cm \times 1 cm \times 0.2 cm). (b, c) Confocal microscopy images of the hybrid polymer-coated PLA construct (b: 3D view, c: top view). Red fluorescence corresponds to the RhB-labeled RGDS peptide grafts. (d) Fluorescence image of MC3T3-E1 cells attached to the RGDS-modified PLA 3D construct. The cells were cultured in serum-free medium for 24 h and were stained with DAPI. Scale bar: 1000 μ m.

using the RGDS peptide-macromonomer, in which the RGDS grafts were incompletely removed by UV irradiation (a 45% decrease),³³ the photopatterning efficiency of the RGDS grafts improved significantly in the hybrid polymer subjected to the postpolymerization modification approach. Thus, the peptide-polymer hybrid system prepared via postpolymerization modification may be applied to photolithography with excellent efficiency, enabling the spatially controlled decoration of material surfaces with bioactive peptides.

Cell Adhesion Properties of the RGDS-Modified Poly(HEMA-co-PgA) Film. The ability of the hybrid film to switch its cell-material interaction properties under light control was observed by monitoring the cell adhesion behaviors of the surfaces. MC3T3-E1 osteoblast-like cells and NIH/3T3 fibroblast cells were used in the cell assay. First, MC3T3-E1 cells (6.0×10^3 cells/cm²) were seeded on the surfaces of the RGDS-modified poly(HEMA-co-PgA) films before and after UV irradiation. The cells were cultured in serum-free medium at 37 °C for 24 h (Figure 5a,b). The same experiment was carried out on a poly(HEMA-co-PgA) film without modification (Figure 5c) and with modification by N₃-HAM (model surface) (Figure 5d) as a control. Compared with the original poly(HEMA-co-PgA) film (Figure 5c), the RGDS-modified film (Figure 5a) displayed a much higher cell adhesive and spreading ability. The number of cells adhered to

the RGDS-modified film surface was at least four times that of the poly(HEMA-co-PgA) film (Figure 5e). According to immunofluorescence microscopy, the expression of integrin β 1 and actin stress fibers in the MC3T3-E1 cells cultured on the RGDS-modified film (Figure 5f) was promoted more obviously than those on the unmodified film (Figure 5g), which means that the click-mediated RGDS grafts stimulate both formation of focal adhesion and polymerization of actin fibers in MC3T3-E1 cells. These results clearly demonstrated that cell adhesion on the film prepared with RDGS grafts was facilitated by integrin-specific interactions. In addition, the viability of the cells on the film indicated that the copper catalyst used for the click reaction was easily removed by a simple washing process. Note that a small number of cells adhered even to the peptide-free poly(HEMA-co-PgA) film, although the PHEMA homopolymer film³³ did not display any cell adhesion. This baseline adhesion was probably due to the slightly larger hydrophobic surface character of the peptide-free film (water contact angle: 54°) compared to the PHEMA homopolymer film (40°).

Interestingly, the cell adhesion behavior on the hybrid film was easily controlled by removing the RGDS grafts. As described above, the peptide grafts were completely removed from the PHEMA chain by photocleavage at the ANP site. MC3T3-E1 cells were seeded on the peptide-cleaved film and

cultured for 24 h (Figure 5b). A remarkable decrease in cell affinity was observed after photocleavage, and the number of attached cells was one-third (ca. 700 cells/cm²) of the value observed over the peptide hybrid film (ca. 2200 cells/cm²) ($p < 0.01$). The number of cells attached to the peptide-cleaved film was almost equal to the value obtained from the model film, which had the same surface structure (i.e., a N₃-HAM-modified film, Figure 5e). Thus, the hybrid polymer system prepared using the postmodification method via a click reaction enabled switching of the cell–2D material interactions under UV light control.

Cell Micropatterning and Cell Sheet Engineering. We anticipated that the cell–material interactions in the peptide–PHEMA hybrid system could be precisely controlled on demand via photocleavage of the RGDS peptide. Therefore, we next investigated the light-triggered detachment of surface-adhered cells with the goal of achieving cell micropatterning and cell sheet engineering. NIH/3T3 cells were seeded (3.0×10^4 cells/cm²) on the surface of an RGDS-modified poly-(HEMA-*co*-PgA) film and were cultured in serum-free medium at 37 °C for 24 h. UV light was directed locally for 30 min onto the cell-attached film through the back side of the glass plate through a ring-shaped photomask (inner diameter: 3 mm, outer diameter: 4 mm, 500 μm interval), whereas the cells were incubated in PBS(–) buffer at room temperature. Figure 6a,b shows phase contrast images of the NIH/3T3 cells before and after UV irradiation, respectively. Spatially controlled cell detachment was observed: the illuminated area (ring shape) released almost all cells from its surface, whereas cells continued to adhere to the nonilluminated surface. Fluorescence images of living cells (Figure 6c) demonstrated successful 2D-micropatterning and excluded the possibility that this photolithographic technique damaged the remaining cells. These results guaranteed that cell adhesion to the film occurred not through nonspecific interactions but in an RGDS-mediated manner. In other words, the PHEMA-based film swelled in the aqueous environment and effectively suppressed nonspecific protein adsorption, which is required for cell–material adhesion.

The photoresponsive character of the peptide–PHEMA hybrid film allowed cell sheets to be easily prepared. A pioneering study on cell sheet engineering was reported by Okano et al., who employed a thermoresponsive poly(*N*-isopropyl acrylamide)(PNIPAM)-grafted surface to successfully recover cultured cells as a sheet by applying a temperature change.^{55,56} PNIPAM-grafted surfaces are hydrophobic at 37 °C and permit cell adhesion. The surfaces become reversibly hydrophilic at temperatures below 32 °C and do not permit cell adhesion due to the hydration of the surface-grafted polymers. Cell sheets may be recovered from a photo-responsive peptide–PHEMA hybrid film using a variety of mechanisms. Cell–film interactions may be suppressed by cleaving the RGDS peptides, and the resulting hydrophilic surface promotes simultaneous cell detachment. NIH/3T3 cells were seeded (3.0×10^4 cells/cm²) on a film and cultured at 37 °C in the presence of serum. After these cells became ca. 80% confluent (48 h, Figure 7a), UV light was directed over the surface for a few minutes in a PBS(–) buffer at room temperature. Rapid detachment of the cell sheet monolayer was observed (Figure 7b), although the cell sheet shrank significantly due to strong cell–cell interactions. The cell sheet recovery was detectable with the naked eye. Importantly, cells in the cell sheet survived after phototriggered detachment, as

confirmed by the calcein staining assay (Figure S6). As a control, we confirmed that the cell sheets could not be recovered from the hybrid surface if the RGDS peptide was functionalized without a photolabile ANP linker. The bound cells remained present on the film, even after UV irradiation over a long period of time, 60 min (data not shown). Hence, the ability of the hybrid polymer system to effectively control cell attachment and release from a 2D material offers a promising opportunity for the design of novel biomedical materials.

Improvement in the Cell Affinity of a 3D-Printed PLA Object. Importantly, the hybrid polymer system can be used to tune the cell affinity of 2D materials, as described above, as well as of 3D materials having complex shapes and geometries. Recent advances in 3D printing enable the precise construction of tailor-made 3D objects from various polymeric materials. PLA has been employed as a feedstock material in fused deposition modeling (FDM), the most common 3D printing process. PLA is a fascinating polymer with biocompatible and biodegradable character but has no reactive groups and generally shows poor cell adhesiveness; therefore, surface modifications via a physical adsorption strategy could significantly improve the cell affinity. We first constructed a 3D-printed PLA mesh object (1 cm × 1 cm × 0.2 cm) as an example using the FDM method (Figure 8a). The 3D object was coated with poly(HEMA-*co*-PgA) using the dip-coating method and subsequently modified with the RGDS peptide via the click reaction, as described above. Poly(HEMA-*co*-PgA) can interact with various solid surfaces, including PLA, due to its strong hydrogen bonding abilities. Figure 8b,c shows CLSM images of the RGDS-modified 3D-printed PLA object. Red fluorescence based on the RhB-labeled RGDS peptide was clearly observed across the entire object, demonstrating successful 3D decoration with RGDS. Notably, the RGDS peptides were not immobilized if the PLA object was not treated with poly(HEMA-*co*-PgA) or was treated with the polymer but without the click reaction. Many MC3T3-E1 cells were found to adhere only to the scaffold surface of the RGDS-modified PLA open-mesh object, as shown in Figure 8d, in which the fluorescence signals of cells (blue color from the nuclear stain DAPI) are clearly observed. MC3T3-E1 cell attachment was not observed on the hybrid polymer-free PLA constructs. This facile method is effective for imparting good cell attachment properties to a 3D-printed PLA object and would be applicable to 3D spatial cell patterning via photolithography.

CONCLUSIONS

In this study, we described the synthesis of a photocleavable peptide–PHEMA hybrid graft copolymer via postpolymerization modification using a click reaction. We explored the utility of this method for producing novel surface coatings with a tunable cell affinity. The RAFT copolymerization of HEMA and propargyl acrylate proceeded by a well-controlled living mechanism, resulting in a well-defined alkyne-containing PHEMA with a narrow polydispersity. Azide-terminated RGDS peptides prepared with a photolabile ANP linker were newly synthesized using SPPS. The surfaces of the 2D and 3D materials were successfully modified with the peptide using a simple process: spin (or dip)-coating of the PHEMA copolymer and subsequent alkyne–azide cycloaddition. The resultant photoprocessable and bioactive peptide–polymer hybrid surface promoted cell adhesion and spreading of NIH/

3T3 and MC3T3-E1 cells. In vitro cell studies demonstrated the high potential of this method for spatially controlling cell micropatterning and cell sheet engineering by integrating photolithographic techniques. Remarkably, this new approach might be applicable to various materials, including 2D solids and 3D-printed materials with complex shapes. This facile and flexible strategy has great potential for advancing biomedical fields, such as tissue engineering, cell chip technologies, and regenerative medicine, especially in cartilage and bones.

■ ASSOCIATED CONTENT

📄 Supporting Information

The Supporting Information is available free of charge on the ACS Publications website at DOI: 10.1021/acsami.9b06807.

Additional experimental procedures; ^1H NMR and FTIR spectra of 6-azidoheptanoic acid; ^1H NMR and FTIR spectra of the photocleavable and clickable RGDS peptide; AFM image of the poly(HEMA-co-PgA) film (thickness measurement); surface structures of the poly(HEMA-co-PgA) film before and after RGDS modification; ATR-FTIR spectra of the UV-irradiated RGDS-modified film and N_3 -HAM-modified film; CLSM images of cell sheet; and ^1H NMR and FTIR spectra of 6-azidoheptanamide (PDF)

■ AUTHOR INFORMATION

Corresponding Authors

*E-mail: ymorita@mail.doshisha.ac.jp (Y.M.)

*E-mail: tkoga@mail.doshisha.ac.jp (T.K.).

ORCID

Nobuyuki Higashi: 0000-0001-9122-0479

Tomoyuki Koga: 0000-0002-2040-7188

Notes

The authors declare no competing financial interest.

■ ACKNOWLEDGMENTS

This work was partly supported by Grants-in-Aid for Scientific Research (KAKENHI) (Nos. 17K04994 and 16K05800) from the Japan Society for the Promotion of Science (JSPS) and a MEXT-Supported Program for the Strategic Research Foundation at Private Universities.

■ REFERENCES

- (1) Stevens, M. M.; George, J. H. Exploring and Engineering the Cell Surface Interface. *Science* **2005**, *310*, 1135–1138.
- (2) Lutolf, M. P.; Hubbell, J. A. Synthetic Biomaterials as Instructive Extracellular Microenvironments for Morphogenesis in Tissue Engineering. *Nat. Biotechnol.* **2005**, *23*, 47–55.
- (3) Shin, H.; Jo, S.; Mikos, A. G. Biomimetic Materials for Tissue Engineering. *Biomaterials* **2003**, *24*, 4353–4364.
- (4) Hirano, Y.; Mooney, D. J. Peptide and Protein Presenting Materials for Tissue Engineering. *Adv. Mater.* **2004**, *16*, 17–25.
- (5) Falconnet, D.; Csucs, G.; Grandin, H. M.; Textor, M. Surface Engineering Approach to Micropattern Surfaces for Cell-based Assays. *Biomaterials* **2006**, *27*, 3044–3068.
- (6) Curtis, A. S. G.; Varde, M. Control of Cell Behavior: Topological Factors. *JNCL, J. Natl. Cancer Inst.* **1964**, *33*, 15–26.
- (7) Nikkhab, M.; Edalat, F.; Manoucheri, S.; Khademhosseini, A. Engineering Microscale Topographies to Control the Cell-Substrate Interface. *Biomaterials* **2012**, *33*, 5230–5246.
- (8) Bagherifard, S.; Ghelichi, R.; Khademhosseini, A.; Guagliano, M. Cell Response to Nanocrystallized Metallic Substrates Obtained through Severe Plastic Deformation. *ACS Appl. Mater. Interfaces* **2014**, *6*, 7963–7985.
- (9) DuFort, C. C.; Paszek, M. J.; Weaver, V. M. Balancing Forces: Architectural Control of Mechanotransduction. *Nat. Rev. Mol. Cell Biol.* **2011**, *12*, 308–319.
- (10) Vining, K. H.; Mooney, D. J. Mechanical Forces Direct Stem Cell Behaviour in Development and Regeneration. *Nat. Rev. Mol. Cell Biol.* **2017**, *18*, 728–742.
- (11) Hynes, R. O. The Extracellular Matrix: Not Just Pretty Fibrils. *Science* **2009**, *326*, 1216–1219.
- (12) Pierschbacher, M. D.; Ruoslahti, E. Cell Attachment Activity of Fibronectin Can Be Duplicated by Small Synthetic Fragments of the Molecule. *Nature* **1984**, *309*, 30–33.
- (13) Ruoslahti, E. Fibronectin and Its Receptors. *Annu. Rev. Biochem.* **1988**, *57*, 375–413.
- (14) Ruoslahti, E.; Pierschbacher, M. D. New Perspectives in Cell Adhesion: RGD and Integrins. *Science* **1987**, *238*, 491–497.
- (15) Hersel, U.; Dahmen, C.; Kessler, H. RGD Modified Polymers: Biomaterials for Stimulated Cell Adhesion and Beyond. *Biomaterials* **2003**, *24*, 4385–4415.
- (16) McCracken, J. M.; Badea, A.; Kandel, M. E.; Gladman, A. S.; Wetzel, D. J.; Popescu, G.; Lewis, J. A.; Nuzzo, R. G. Programming Mechanical and Physicochemical Properties of 3D Hydrogel Cellular Microcultures via Direct Ink Writing. *Adv. Healthcare Mater.* **2016**, *5*, 1025–1039.
- (17) Badea, A.; McCracken, J. M.; Tillmaand, E. G.; Kandel, M. E.; Oraham, A. W.; Mevis, M. B.; Rubakhin, S. S.; Popescu, G.; Sweedler, J. V.; Nuzzo, R. G. 3D-Printed pHEMA Materials for Topographical and Biochemical Modulation of Dorsal Root Ganglion Cell Response. *ACS Appl. Mater. Interfaces* **2017**, *9*, 30318–30328.
- (18) Georges, M. K.; Veregin, R. P. N.; Kazmaier, P. M.; Hamer, G. K. Narrow Molecular Weight Resins by A Free-Radical Polymerization Process. *Macromolecules* **1993**, *26*, 2987–2988.
- (19) Matyjaszewski, K.; Xia, J. Atom Transfer Radical Polymerization. *Chem. Rev.* **2001**, *101*, 2921–2990.
- (20) Kamigaito, M.; Ando, T.; Sawamoto, M. Metal-Catalyzed Living Radical Polymerization. *Chem. Rev.* **2001**, *101*, 3689–3746.
- (21) Moad, G.; Rizzardo, E.; Thang, S. H. Living Radical Polymerization by the RAFT Process. *Aust. J. Chem.* **2005**, *58*, 379–410.
- (22) Mei, Y.; Beers, K. L.; Michelles Byrd, H. C.; VanderHart, D. L.; Washburn, N. R. Solid-Phase ATRP Synthesis of Peptide–Polymer Hybrids. *J. Am. Chem. Soc.* **2004**, *126*, 3472–3476.
- (23) Hentschel, J.; Börner, H. G. Peptide-Directed Microstructure Formation of Polymers in Organic Media. *J. Am. Chem. Soc.* **2006**, *128*, 14142–14149.
- (24) Koga, T.; Kamiwatari, S.; Higashi, N. Preparation and Self-Assembly Behavior of β -Sheet Peptide-Inserted Amphiphilic Block Copolymer as a Useful Polymeric Surfactant. *Langmuir* **2013**, *29*, 15477–15484.
- (25) Koga, T.; Aso, E.; Higashi, N. Novel Self-Assembling Amino Acid-Derived Block Copolymer with Changeable Polymer Backbone Structure. *Langmuir* **2016**, *32*, 12378–12386.
- (26) Grieshaber, S. E.; Farran, A. J. E.; Lin-Gibson, S.; Kiick, K. L.; Jia, X. Synthesis and Characterization of Elastin-mimetic Hybrid Polymers with Multiblock, Alternating Molecular Architecture and Elastomeric Properties. *Macromolecules* **2009**, *42*, 2532–2541.
- (27) Luo, K.; Yang, J.; Kopečková, P.; Kopeček, J. Biodegradable Multiblock Poly[N-(2-hydroxypropyl)methacrylamide] via Reversible Addition-Fragmentation Chain Transfer Polymerization and Click Chemistry. *Macromolecules* **2011**, *44*, 2481–2488.
- (28) Nishimura, S.; Higashi, N.; Koga, T. Facile Synthesis of Multiblock Copolymers Containing Sequence-Controlled Peptides and Well-Defined Vinyl Polymers by Nitroxide-Mediated Polymerization. *Chem. – Eur. J.* **2017**, *23*, 15050–15058.
- (29) Nishimura, S.; Higashi, N.; Koga, T. Synthesis of Peptide–Vinyl Polymer Multiblock Hybrids by Nitroxide-Mediated Polymerization: Breaking the Limitations of Monomer Compatibility. *Polym. Chem.* **2019**, *10*, 71–76.

- (30) Nishimura, S.; Higashi, N.; Koga, T. A Novel Thermo-Responsive Multiblock Architecture Composed of a Sequential Peptide and an Amino Acid-Derived Vinyl Polymer: Toward Protein-Mimicking Single-Chain Folding. *Chem. Commun.* **2019**, *55*, 1498–1501.
- (31) Irvine, D. J.; Mayes, A. M.; Griffith, L. G. Nanoscale Clustering of RGD Peptides at Surfaces Using Comb Polymers. 1. Synthesis and Characterization of Comb Thin Films. *Biomacromolecules* **2001**, *2*, 85–94.
- (32) Higashi, N.; Yasufuku, Y.; Matsuo, M.; Matsumoto, T.; Koga, T. Thermo-Responsive Multilayer Films from Ionic Polymers with Elastin-like Peptide as Graft Chains. *Colloids Interface Sci. Commun.* **2014**, *1*, 50–53.
- (33) Nishimura, S.; Hirata, A.; Taki, Y.; Morita, Y.; Higashi, N.; Koga, T. Photocleavable and Polymerizable Peptide for Micropatterning of Bioactive Segments in Polymer Soft Materials. *Chem. Lett.* **2018**, *47*, 555–558.
- (34) Massia, S. P.; Hubbell, J. A. Covalently Attached GRGD on Polymer Surface Promotes Biospecific Adhesion of Mammalian Cells. *Ann. N. Y. Acad. Sci.* **1990**, *589*, 261–270.
- (35) Woerly, S.; Pinet, E.; de Robertis, L.; Van Diep, D.; Bousmina, M. Spinal Cord Repair with PHPMA Hydrogel Containing RGD Peptides (NeuroGel). *Biomaterials* **2001**, *22*, 1095–1111.
- (36) Tugulu, S.; Silacci, P.; Stergiopoulos, N.; Klok, H.-A. RGD-Functionalized Polymer Brushes as Substrates for the Integrin Specific Adhesion of Human Umbilical Vein Endothelial Cells. *Biomaterials* **2007**, *28*, 2536–2546.
- (37) Loschonsky, S.; Shroff, K.; Prucker, O.; Ruhe, J.; Biesalski, M. Surface-Attached PDMAA-GGRGDSP Hybrid Polymer Monolayers that Promote the Adhesion of Living Cells. *Biomacromolecules* **2008**, *9*, 543–552.
- (38) Kubinová, Š.; Horák, D.; Kozubenko, N.; Vaněček, V.; Proks, V.; Price, J.; Cocks, G.; Syková, E. The Use of Superporous ACGGASIKVAVS-OH-Modified PHEMA Scaffolds to Promote Cell Adhesion and the Differentiation of Human Fetal Neural Precursors. *Biomaterials* **2010**, *31*, 5966–5975.
- (39) Such, G. K.; Johnston, A. P. R.; Liang, K.; Caruso, F. Synthesis and Functionalization of Nanoengineered Materials using Click Chemistry. *Prog. Polym. Sci.* **2012**, *37*, 985–1003.
- (40) Santander-Borrego, M.; Green, D. W.; Chirila, T. V.; Whittaker, A. W.; Blakey, I. Click Functionalization of Methacrylate-based Hydrogels and Their Cellular Response. *J. Polym. Sci., Part A: Polym. Chem.* **2014**, *52*, 1781–1789.
- (41) He, F.; Luo, B.; Yuan, S.; Liang, B.; Choong, C.; Olavi Pehkonen, S. PVDF Film Tethered with RGD-click-poly(glycidyl methacrylate) Brushes by Combination of Direct Surface-Initiated ATRP and Click Chemistry for Improved Cytocompatibility. *RCS Adv.* **2014**, *4*, 105–117.
- (42) Kolb, H. C.; Finn, M. G.; Sharpless, K. B. Click Chemistry: Diverse Chemical Function from a Few Good Reactions. *Angew. Chem., Int. Ed.* **2001**, *40*, 2004–2021.
- (43) Huisgen, R. 1,3-Dipolar Cycloadditions. *Proc. Chem. Soc.* **1961**, 357–369.
- (44) Rostovtsev, V. V.; Green, L. G.; Fokin, V. V.; Sharpless, K. B. A Stepwise Huisgen Cycloaddition Process: Copper(I)-Catalyzed Regioselective “Ligation” of Azides and Terminal Alkynes. *Angew. Chem., Int. Ed.* **2002**, *41*, 2596–2599.
- (45) Boyer, C.; Liu, J.; Bulmus, V.; Davis, T. P.; Barner-Kowollik, C.; Stenzel, M. H. Direct Synthesis of Well-Defined Heterotelechelic Polymers for Bioconjugations. *Macromolecules* **2008**, *41*, S641–S650.
- (46) Kane, R. S.; Takayama, S.; Ostuni, E.; Ingber, D. E.; Whitesides, G. M. Patterning Proteins and Cells using Soft Lithography. *Biomaterials* **1999**, *20*, 2363–2376.
- (47) Ohmuro-Matsuyama, Y.; Tatsu, Y. Photocontrolled Cell Adhesion on a Surface Functionalized with a Caged Arginine-Glycine-Aspartate Peptide. *Angew. Chem., Int. Ed.* **2008**, *47*, 7527–7529.
- (48) Petersen, S.; Alonso, J. M.; Specht, A.; Duodu, P.; Goeldner, M.; del Campo, A. Phototriggering of Cell Adhesion by Caged Cyclic RGD Peptides. *Angew. Chem., Int. Ed.* **2008**, *47*, 3192–3195.
- (49) Wirkner, M.; Alonso, J. M.; Maus, V.; Salierno, M.; Lee, T. T.; Garcia, A. J.; del Campo, A. Triggered Cell Release from Materials Using Bioadhesive Photocleavable Linkers. *Adv. Mater.* **2011**, *23*, 3907–3910.
- (50) Wegner, S. V.; Sentürk, O. I.; Spatz, J. P. Photocleavable Linker for the Patterning of Bioactive Molecules. *Sci. Rep.* **2015**, *5*, No. 18309.
- (51) Brown, B. B.; Wagner, D. S.; Geysen, H. M. A Single-Bead Decode Strategy Using Electrospray Ionization Mass Spectrometry and a New Photolabile Linker: 3-Amino-3-(2-nitrophenyl)propionic acid. *Mol. Diversity* **1995**, *1*, 4–12.
- (52) Montheard, J.-P.; Chatzopoulos, M.; Chappard, D. 2-Hydroxyethyl Methacrylate (HEMA): Chemical Properties and Applications in Biomedical Fields. *J. Macromol. Sci., Polym. Rev.* **1992**, *32*, 1–34.
- (53) Lee, K. Y.; Mooney, D. J. Hydrogels for Tissue Engineering. *Chem. Rev.* **2001**, *101*, 1869–1880.
- (54) Miyazawa, T.; Blout, E. R. The Infrared Spectra of Polypeptides in Various Conformations: Amide I and II Bands. *J. Am. Chem. Soc.* **1961**, *83*, 712–719.
- (55) Okano, T.; Yamada, N.; Sakai, H.; Sakurai, Y. A Novel Recovery System for Cultured Cells Using Plasma-Treated Polystyrene Dishes Grafted with Poly(*N*-isopropylacrylamide). *J. Biomed. Mater. Res.* **1993**, *27*, 1243–1251.
- (56) Yang, J.; Yamato, M.; Nishida, K.; Ohki, T.; Kanzaki, M.; Sekine, H.; Shimizu, T.; Okano, T. Cell Delivery in Regenerative Medicine: The Cell Sheet Engineering Approach. *J. Controlled Release* **2006**, *116*, 193–203.



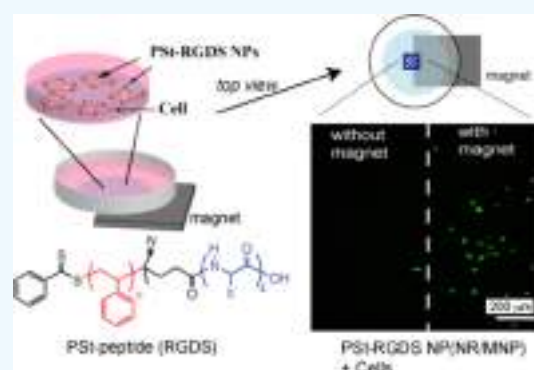
Spontaneous Formation of Nanoparticles from Peptide–Vinyl Polymer Diblock Hybrids Prepared by RAFT Polymerization and Their Interactions with Cells

Nobuyuki Higashi,^{*†} Kiyoshiro Narimatsu, Minori Okumura, Shin-nosuke Nishimura, and Tomoyuki Koga^{*†}

Department of Molecular Chemistry and Biochemistry, Faculty of Science and Engineering, Doshisha University, Kyotanabe, Kyoto 610-0321, Japan

Supporting Information

ABSTRACT: Novel polymeric nanoparticles (NPs) with uniform sizes were prepared from peptide–vinyl polymer diblock hybrids by the self-organized precipitation method. Hybrid polymers of polystyrene (PSt) and tetrapeptide (cell-binding epitope RGDS, reverse SDGR, cationic KKKK, and anionic DDDD) were successfully synthesized by combining solid-phase peptide synthesis and reversible addition fragmentation chain transfer polymerization methods. Narrowly dispersed hybrid polymers (polydispersity index < 1.25, M_n 14 000–17 000) were obtained. Altering the preparation conditions easily tuned the size and size distribution of the NPs. When the ζ -potentials for the NP suspensions were measured at pH 6.0, the obtained values corresponded to the net charge of each peptide segment. More importantly, the NPs could encapsulate fluorescent Nile red (NR) and magnetic iron oxide NP (MNP), which might be suitable for fluorescent imaging and magnet-induced patterning of cells, respectively. The interactions of NPs with cells (NIH/3T3 fibroblast) and the magnetic effects were examined for NR/MNP-loaded PSt–RGDS and –SDGR NPs. Both NPs were readily incorporated into cells, but only NR/MNP-loaded PSt–RGDS NP showed magnetic responsiveness in cell adhesion and cultures.



INTRODUCTION

In biological applications ranging from drug delivery to cellular imaging, polymeric nanoparticles (NPs) with a biocompatible exterior are becoming increasingly more important.^{1–6} These applications are based on the intrinsic properties of polymeric NPs and depend on the constituent polymeric materials and the surface functionalization. The surface properties are typically controlled after particle preparation by surface modifications, including surface-initiated polymerization and grafting-onto methods, for an appropriate polymer chain through covalent or noncovalent interactions⁸ and layer-by-layer polymer deposition.⁹

Herein, we describe the spontaneous formation of polymer NPs with a cell-adhesive function without surface modifications from block polymers composed of a short peptide block and a polystyrene (PSt) block through a self-organized precipitation (SORP)^{10–12} route. Such peptide–polymer hybrids have recently been investigated to fabricate biofunctional nanostructured materials.^{13–22} The conjugation of synthetic polymers with peptides offers well-defined nano-objects, including lamellae, cylindrical micelles, spherical micelles, and vesicles in appropriate media. The nano-objects depend on both the character and combination of each block segment.

Peptides mainly play roles in self-organization, whereas polymeric blocks provide structural (physical) stability. Additionally, peptide segments introduced as one block show interesting biofunctions when the peptide sequence is suitably designed. Examples include cell binding, cell spreading, and cell proliferation.^{23,24}

In cell biology, materials ranging from 50 to 200 nm uptake NPs into a wide variety of cells.^{25,26} NPs with a narrow size distribution yield a higher substrate encapsulation efficiency and exhibit a better biocompatibility with cells and tissues than polydisperse NPs.^{27–30}

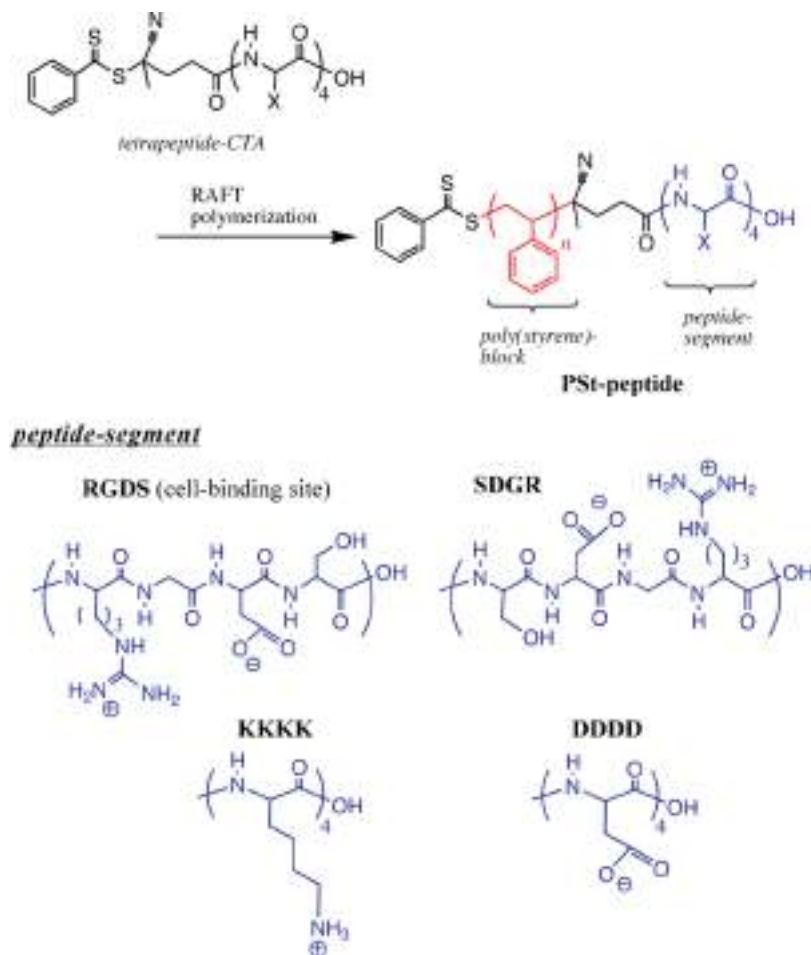
Herein, we prepare uniform biocompatible NPs from hybrid block polymers with a tetrapeptide segment and a PSt block via the SORP method. This method has recently been used to prepare narrowly distributed polymer NPs, which can be spontaneously formed based on nonequilibrium processes during slow evaporation of a polymer solution. Adjusting the preparation conditions tunes both the particle size and the size distribution. Additionally, multifunctional NPs are fabricated by encapsulating fluorescent dye (Nile red, NR) and magnetic

Received: March 31, 2019

Accepted: April 24, 2019

Published: May 2, 2019

Scheme 1. Synthesis of Peptide–Polymer Hybrids via RAFT Polymerization



iron oxide NPs (MNPs) into our polymeric NPs. The feature should be useful for fluorescent imaging and magnet-induced patterning of cells. Magnetically responsive NPs have also received much attention because of their widespread potential applications.^{31,32}

Hybrid block polymers are prepared by combining solid-phase peptide synthesis (SPPS) and a reversible addition fragmentation chain transfer (RAFT) polymerization.^{33,34} As the hydrophobic polymer block, PSt is synthesized via polymerization in the presence of a peptide chain transfer agent (CTA). The RGDS (Arg-Gly-Asp-Ser) sequence is employed as a peptide segment of the block polymer since this sequence binds to the integrin receptors present on the cell surface.^{35,36} For comparison, three other sequential peptides (reverse sequence SDGR, cationic KKKK, and anionic DDDD), whose numbers of repeating amino acid units are adjusted to that of the RGDS peptide (four units), are also prepared and attached to the PSt block in the same manner. Scanning electron microscopy (SEM) observations and ζ -potential measurements characterize the prepared particles, whereas phase contrast and confocal microscopic observations estimate the interactions with cells and cellular uptake.

RESULTS AND DISCUSSION

Synthesis and Characterization of Peptide–Polymer Hybrids. The hybrid block polymers were prepared by combining SPPS and RAFT polymerization. The RGDS sequence was employed as a peptide segment of the block

polymer since it had a cell-binding ability. Three other sequential peptides were prepared and used for comparison: the reverse sequence SDGR, cationic KKKK (K_4), and anionic DDDD (D_4). In these sequences, the number of repeating amino acids was adjusted to that of the RGDS peptide (four units). PSt was chosen as a hydrophobic polymer block because it should behave as a constituent for the particle core. Scheme 1 outlines the synthesis of hybrid block polymers.

The objective peptides (RGDS, SDGR, K_4 , and D_4) were successfully prepared by SPPS by Fmoc (9-fluorenylmethoxycarbonyl) chemistry. The N-termini of the resultant peptides were reacted with 4-cyano-4-(phenylcarbonothioylthio) pentanoic acid as a RAFT agent. The obtained peptide-CTAs, which contained the protective groups, were characterized by matrix-assisted laser desorption/ionization time-of-flight mass spectrometry (MALDI-TOF) MS and ^1H NMR spectroscopy analyses (Supporting Information). Subsequently, RAFT polymerizations of St were carried out in acetone initiated with azobisisobutyronitrile (AIBN) in the presence of the corresponding peptide-CTAs as a chain transfer agent at 60 °C for the prescribed periods.

Figure 1a shows the SEC traces for peptide side-chain-protected PSt–RGDS hybrid polymers prepared with different polymerization times. All SECs displayed unimodal chromatograms, and their peak tops shifted systematically to a higher molecular weight as polymerization progressed. Figure 1b plots the number-average molecular weight (M_n) and the polydispersity index ($\text{PDI} = M_w/M_n$) based on the SEC charts as a

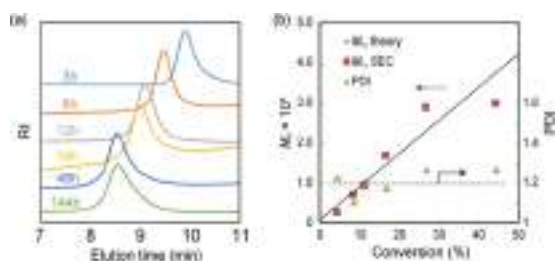


Figure 1. (a) SEC charts for the PSt–RGDS hybrid polymers obtained at various polymerization times and (b) relationship between the number-average molecular weight (M_n) or polydispersity index (PDI) and the conversion (%).

function of conversion. The PDI values ranged from 1.1 to 1.27, indicating that nearly monodispersed polymers were formed. The linearity of the M_n versus conversion plot was similar to the theoretical values calculated from the ratio of the monomer (St) and RAFT agent (RGDS-CTA) in the feed and the monomer conversion. Hence, the polymerization proceeded via a controlled, living mechanism. Removal of the protective groups from the peptide block eventually yielded the objective PSt–RGDS hybrid polymer. The three other hybrid polymers (PSt–SDGR, PSt–K₄, and PSt–D₄) were prepared in a similar manner.

Preparation of Peptide–Polymer Hybrid NPs from SORP. The SORP method was used to prepare peptide–polymer hybrid NPs. Compared to conventional particle preparation methods, the SORP method had three main advantages: (i) changing the preparation conditions controlled the particle size and its distribution. (ii) Surfactants and protective colloids were not necessary. (iii) Its preparation procedures were simple.

Tetrahydrofuran (THF) and water were used as a good and a poor solvent for the hybrid polymers, respectively. The use of water should facilitate the localization of the polar peptide segments of the hybrid polymers at the periphery of the resultant NPs. Such hydrophilic sequence effects on the NP structure have previously been reported by Yabu et al.^{37,38}

The SORP method generated uniform polymer NPs. Typically, PSt–RGDS (M_n 17 000) was dissolved in THF (good solvent) to form a homogeneous solution (0.1 mg mL⁻¹). Then, water (2 mL, precipitant) was added to this polymer solution (1 mL) while gently stirring at a constant speed of 1 mL min⁻¹. Then, the preparation conditions, including the molecular weight of the polymer (M_n), the concentration of THF polymer solution, the ratio of THF solution and water, their total volumes, and the rate of water addition, were adjusted to synthesize NPs (ca. 100 nm as a target size with a relatively narrow size distribution).

The resulting solution was left in air at room temperature until THF completely evaporated, yielding the NP suspension. Figure 2 shows the SEM images for the PSt–RGDS NP as well as those for PSt–SDGR (M_n 17 000) and the peptide-segment-free PSt homopolymer for comparison. The PSt homopolymer was prepared by conventional radical polymerization of St initiated with AIBN in the absence of the RAFT agent.

Figure 2d plots the particle size distribution based on the SEM observations. PSt–RGDS and PSt–SDGR provided uniform NPs with an average size of 100 nm and a relatively narrow size distribution. Meanwhile, the peptide-free PSt showed a broad particle size distribution ranging from 100 to 600 nm. These differences in the size and the size distribution

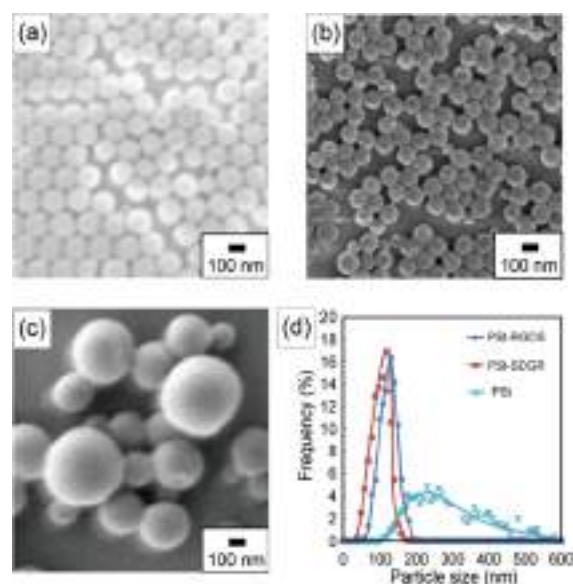


Figure 2. SEM images for (a) PSt–RGDS NPs, (b) PSt–SDGR NPs, and (c) PSt NPs prepared through the SORP route. (d) Plots of the size distributions as functions of the particle sizes observed in the SEM images. Concentrations of the polymer THF solutions are 0.1 mg mL⁻¹.

were attributed to the presence of the peptide segment in the polymer.

The existence of the polar peptide segment was important not only to stabilize the interface between the particle surface and the water phase during particle formation but also to yield a well-controlled size and size distribution. In the case of peptide-free PSt, the coalescence of growing particles appeared random due to the unstable interface of the particles. Generally, as the polymer concentration of THF solution increased, the number density of precipitated particles increased during particle preparation. This often resulted in coalescence among particles, which led to heterogeneity in their sizes and distributions. Neither the PSt particle size nor its distribution could be controlled when the polymer concentration was increased from 0.1 to 1.0 mg mL⁻¹ as both ranged from the nanometer to the micrometer scale (Figure S1). In contrast, when the same experiment was performed for PSt–RGDS and –SDGR, the average particle size definitely increased from 100 to 200 nm while maintaining the original narrow size distribution. Hence, the peptide segment in the polymer molecule preferred the water phase due to its polar nature and was located predominantly at the particle surface. The effect of molecular weight (M_n) of the polymers on the NP structure is also important to elucidate the role of hydrophilic peptide segments. Thus, we synthesized PSt–RGDSs having different molecular weights (M_n = 9500, 17 000, and 33 000) by varying the conversion in the RAFT polymerization (Table S1). The NPs were prepared by the SORP method in the same manner as described above, and the SEM images together with their size distributions are shown in Figure S2. It can be seen from the SEM pictures that the PSt–RGDSs with molecular weight M_n = 17 000 and 33 000 show spherical particles with a smooth surface and about 100 nm size, although the size distribution of the larger polymer of M_n = 33 000 is somewhat broader than that of the polymer with M_n = 17 000. The PSt–RGDS having the lowest molecular weight of M_n = 9500 provides a huge particle (average size =

260 nm) with a remarkable uneven surface, probably due to swelling of the particles in water derived from a higher content of the polar peptide segment per particle. Therefore, we decided to use the PSt–RGDS with a molecular weight of $M_n = 17\,000$ in the following experiments. Consequently, the peptide segment played an important role in controlling both the size and the size distribution of the resultant particles.

To confirm that the peptide segments preferentially existed near the surface of the NPs, the SORP method was applied to other two peptide–polymer hybrids [PSt–K₄ (M_n 14 000) and PSt–D₄ (M_n 17 000)] under the same conditions. Figure 3

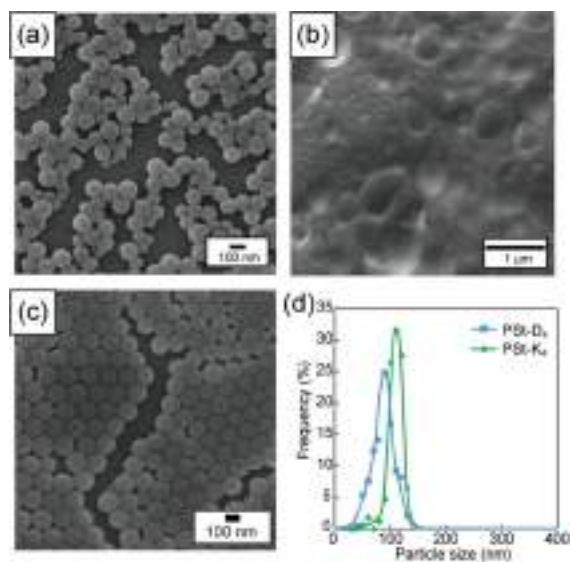


Figure 3. SEM images for (a) PSt–D₄ NP and (b) PSt–K₄ NP prepared through the SORP route at pH 6.0 and (c) for PSt–K₄ NP prepared at pH 11. (d) Plots of the size distributions as functions of the observed particle sizes in SEM images ((a) and (c)). Concentrations of the polymer THF solutions are 0.1 mg mL^{−1}.

shows the SEM images. PSt–D₄, whose peptide segment had an anionic net charge at pH 6.0, provided uniform NPs with the almost same size (ca. 100 nm) as those for PSt–RGDS and PSt–SDGR NPs. At pH 6.0, the cationic PSt–K₄ did not show a globular shape with a nonuniform distribution. This was attributed to the difference in hydrophobicity³⁹ between the cationic lysine residue and the anionic aspartic acid residue, which might cause a slight change in the interface stability during particle formation; that is, the anionic aspartic acid residue (hydrophobic index −3.5) was slightly more hydrophobic than the cationic lysine residue (hydrophobic index

−3.9). Another factor attributed to the interface unstabilization might be a cation– π interaction⁴⁰ being present only in the case of PSt–K₄, that is, intramolecular interaction between the cationic Lys residue of the K₄ segment and phenyl group of the PSt block. The ammonium group of the lysine residues should be deprotonated when the aqueous phase has a pH of 11. Increasing the pH to 11 provided 100 nm size PSt–K₄ particles with a narrow distribution similar to the anionic PSt–D₄ (Figure 3d). Note that the C-termini of all peptide segments were carboxylate anions in such a pH region.

If the peptide moiety in the block polymers helped stabilize the NPs dispersions, it would accumulate predominantly near the NP surfaces during particle preparation. The ζ -potentials of the NPs containing different types of peptide segments were measured. Table S2 summarizes their values and the corresponding net charge of the peptide segments at pH 6.0. Both PSt–D₄ and PSt–RGDS NPs with a negative charge showed negative values (−43.6 and −51.1 mV, respectively), whereas the positive PSt–K₄ provided a positive value of the ζ -potential (+33.1 mV). These results strongly suggested that the peptide segments were oriented toward the water phase during particle preparation, resulting in the location of peptide segments near the NP surface. It was supposed that the peptide moiety of the block polymers existing in the hydrophobic inner part of the NPs might be stabilized to weaken its polarity with hydrogen bonding.

Multifunctional NPs from PSt–RGDS through SORP.

Multifunctional NPs were prepared by encapsulating a fluorescent dye (NR) and/or magnetic iron oxide NP (MNP) into the PSt–RGDS NPs. These features would be useful for bioimaging and magnet-induced cell patterning, respectively. During the precipitation process, NR and/or MNP were simultaneously encapsulated into PSt–RGDS NPs due to the hydrophobicity of the substrates. First, fluorescent NR was encapsulated. Figure S3 shows the SEM image and the size distribution estimated from the image. The SORP approach generated uniform NPs with a particle size (about 100 nm) and distribution similar to those for the NR-free PSt–RGDS NP, which is shown in Figure S3 for comparison.

Figure 4a displays the fluorescence emission spectra recorded on NR-encapsulated PSt–RGDS NP, free NR in water, and NR in toluene when excited at 530 nm. NR in water had an emission maximum at 640 nm. Encapsulation in PSt–RGDS NP simultaneously enhanced the fluorescence intensity and blue-shifted the peak top to 566 nm, indicating that NR existed in the more hydrophobic inner core of the PSt–RGDS NP. In fact, the emission maximum of NR in toluene appeared at 566 nm, which was consistent with that for NR-encapsulated

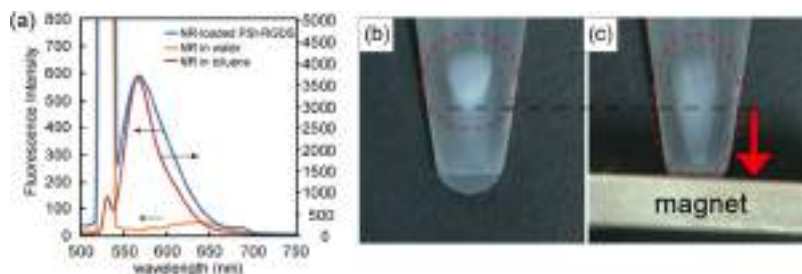


Figure 4. (a) Fluorescence spectra for NR-loaded PSt–RGDS NP in water ($[NR] < 0.1$ mg mL^{−1}), NR in water ($[NR] = 0.03$ mg mL^{−1}), and NR in toluene ($[NR] = 0.1$ mg mL^{−1}), excited at 530 nm. Photos for the aqueous suspensions of MNP-loaded PSt–RGDS NP (b) without and (c) with a magnet attached to the bottom of the test tube.

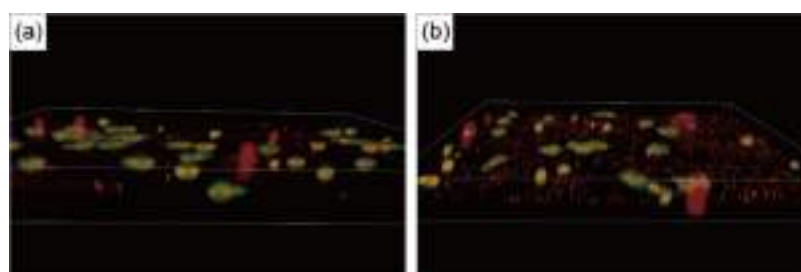


Figure 5. Confocal microscopic images of NIH/3T3 fibroblast cells treated with NR/MNP-loaded (a) PSt-RGDS NP and (b) -SDGR NP for 24 h after adding the NP suspension in serum-free medium. Note that the cells are stained with calcein-AM and ethidium D prior to fluorescence microscopic observations. Green emissions indicate live cells. Red emissions indicate NPs and dead cells, whose sizes are on the nanometer and micrometer scales.

PSt-RGDS NP. This spectral consistency strongly supported encapsulation of NR into the polymer NP.

MNP encapsulation was carried out in a similar manner. The SEM images shown in Figure S3c,d indicate that MNP was incorporated in the PSt-RGDS NP (size 130 ± 30 nm). The encapsulated MNPs did not greatly influence the shape and size of the NP, compared with those of MNP-free PSt-RGDS NP. Figure 4b,c shows photographic images of the suspensions of MNP-loaded PSt-RGDS NP without and with a magnet, respectively. When a magnet was attached, the milky-white suspension marked with a dashed red circle moved to the bottom of the test tube, suggesting that a magnetically responsive PSt-RGDS NP was realized. This feature would be useful in cell engineering such as cell patterning and manipulation.

Interaction of PSt-RGDS NPs with Cells and Uptake Behavior. Both NR and MNP (NR/MNP)-loaded PSt-RGDS and SDGR NPs were prepared in a similar manner (Figure S4 shows particle size and size distribution). Their interactions with a cell of a mouse NIH/3T3 fibroblast were examined in serum-free medium from the viewpoints of cellular uptake and its magnetic control. Figure 5 shows confocal microscopic pictures where the living cells are stained with calcein-acetoxymethyl (calcein-AM) at 24 h after adding each particle suspension to the cell-attached substrates. Both NPs emitted a red fluorescence due to NR encapsulated into NP from the living cell stained in green with calcein-AM, suggesting the uptake of NPs into the cells and/or the attachment of NPs onto the cell surfaces. Such cellular uptake and/or attachment of NPs proceeded smoothly and was completed within 1 h. As mentioned in the Introduction, one of the effects specific for materials in the range of 50–200 nm was the uptake of NPs into a wide variety of cells.^{25,26} Therefore, the particle size of our hybrid polymers (ca. 150 nm) might play an important role for uptake into the cell; it might influence the kind of peptide sequence (RGDS or SDGR), although the cell attachment ability of the RGDS sequence would be definitely superior to that of the reverse SDGR sequence. Thus, the effect of a permanent magnet field on the cell culture was examined for cells containing NR/MNP-loaded PSt-RGDS or SDGR NP.

Figure 6 schematically illustrates a top-view of a PSt-coated glass-bottomed dish, where the suspension of cells, including NR/MNP-loaded PSt-RGDS or SDGR NP, is seeded on a magnet plate. After a 24 h culture, the living cells were stained with calcein-AM. They were then observed using a confocal microscope. The pictures (Figure 6b,c) were taken at the shaded part drawn in Figure 6a. In the case of PSt-SDGR NP,

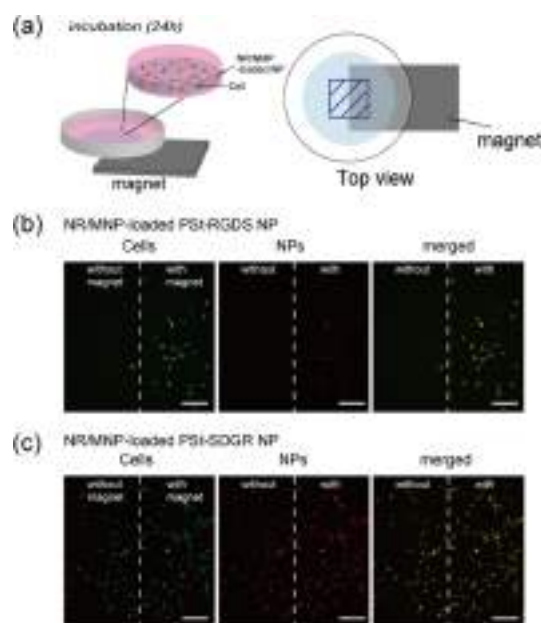


Figure 6. Magnetic field effects on the NP-treated NIH/3T3 cell adhesion. Schematic illustration for the top-view of a PSt-coated glass-bottomed dish, where the suspension of cells, including NR/MNP-loaded PSt-RGDS or SDGR NP, is seeded on a magnet plate. After 24 h culture, living cells stained with calcein-AM are observed with a confocal microscope. Pictures ((b) and (c) correspond to the cases of NR/MNP-loaded PSt-RGDS and SDGR NPs, respectively) are taken at the shaded part drawn in (a). Scale bar: 200 μm .

cell adhesion was observed both with and without a magnet plate, whereas in the case of PSt-RGDS NP, the cell adhesion proceeded predominantly with the magnet plate, although the number of attached cells for the PSt-RGDS NP was somewhat smaller than that for PSt-SDGR NP in the presence of the magnet plate. This difference in the attached number of cells might be reasonably explained by considering the difference in cell-binding ability between the NPs; that is, the PSt-RGDS NP has a much higher binding ability to the cell compared with the PSt-SDGR NP and thus more PSt-RGDS NPs attached to the cell surfaces would disturb adhesion of the drifting cells to the hydrophobic substrate. As a result, the number of cells appearing in Figure 6b might be restricted, compared with that in Figure 6c. The numbers of cells attached (N , cells per cm^2) with (N_{magnet}) and without (N_0) the magnet plate were then evaluated, and the ratio (N_{magnet}/N_0) was calculated to be 4.7. On the other hand, for PSt-RGDS NP, cell adhesion predominantly proceeded in the

presence of the magnet, and the ratio of N_{magnet}/N_0 was 10, which is about twice larger value than that for the case of PSt–SDGR NP. The observed magnetic effect was probably because the PSt–RGDS NP with a higher binding ability to the cell inhibited adhesion of drifting cells to the hydrophobic substrate and the magnetic field helped such an adhesion.⁴¹ The usage of the NR/MNP-loaded PSt–RGDS NP might realize two-dimensional control of the cell alignment by supplying a magnetic field.

CONCLUSIONS

This study prepared novel polymeric NPs from peptide–vinyl polymer diblock hybrids via the SORP approach. The synthesis combined SPPS and RAFT polymerization to fabricate well-defined hybrid polymers. The polymers consisted of PSt as a hydrophobic vinyl polymer segment and RGDS with cell-binding ability as the peptide segment. For comparison, three other peptide segments were synthesized: the reverse SDGR, cationic KKKK (K_4), and anionic DDDD (D_4). Adjusting the experimental parameters easily tuned the size and size distribution of the NPs.

The ζ -potentials measured for the NP suspensions reflected the net charge of the corresponding peptide sequence. The peptide segment was located near the periphery of the NPs. Hydrophobic fluorescent dye (NR) and magnetic NP were effectively encapsulated in the hybrid NPs to produce multifunctional (NR/MNP-loaded) NPs.

The interactions of these NR/MNP-loaded PSt–RGDS and –SDGR NPs with NIH/3T3 fibroblast cells were examined. Both NPs, whose sizes ranged between 100 and 200 nm, were smoothly incorporated into the cells. Finally, the effect of a permanent magnetic field on the cell culture was investigated. For NR/MNP-loaded PSt–RGDS NP, cell adhesion proceeded predominantly in the presence of a magnet. In contrast, cell adhesion occurred without a magnet for the SDGR counterpart. Employing NR/MNP-loaded PSt–RGDS NP would allow a magnetic field to manipulate the cell pattern.

EXPERIMENTAL SECTION

Materials and Methods. 2-Chlorotriylchloride resin for solid-phase peptide synthesis (SPPS) was purchased from the Peptide Institute (Osaka, Japan). 9-Fluorenylmethoxycarbonyl (Fmoc)-Ser(Bu^t)-OH, Fmoc-Asp(OBu^t)-OH, Fmoc-Gly-OH, Fmoc-Arg(Pbf)-OH, Fmoc-Lys-(Boc)-OH, and 1-hydroxybenzotriazole (HOBt) were purchased from Watanabe Chemical Industries (Hiroshima, Japan). *N,N*-Diisopropylcarbodiimide (DIPC), dichloromethane (DCM), diisopropylethylamine (DIPEA), and hexafluoro-2-propanol (HFIP) were purchased from Wako Pure Chemical Industries (Osaka, Japan). THF, piperidine, methanol, chloroform, dimethylformamide (DMF), trifluoroacetic acid (TFA), AIBN, styrene (St), CD_3OD , CDCl_3 , and acetone- d_6 were purchased from Nacalai Tesque (Kyoto, Japan). All except DMF and St were used as received. DMF and St were purified by distillation before use. The RAFT agent, 4-cyano-4-(phenylcarbonothioylthio) pentanoic acid, was purchased from Sigma-Aldrich (Missouri). NR and triisopropylsilane (TIS) were purchased from Tokyo Chemical Industry (Tokyo, Japan). Iron oxide magnetic nanoparticles coated with oleic acid (size 5 nm in toluene) were purchased from Cosmo Bio (Tokyo, Japan).

^1H NMR spectra were recorded using a JEOL JNM-AL 400 (JEOL Resonance, Tokyo, Japan) spectrometer (400 MHz).

MALDI-TOF MS analyses were carried out on an Autoflex speed instrument (Bruker Daltonics, Massachusetts) using DHBA as a matrix. The number-average molecular weight (M_n) and the polydispersity index ($\text{PDI} = M_w/M_n$) of the polymers were determined by size exclusion chromatography (SEC) using a JASCO LC-net II/AD (JASCO, Tokyo, Japan) equipped with a refractive index (RI) detector (column, GF-710F; eluent, THF; flow rate, 1.0 mL min^{-1} ; temperature, $40 \text{ }^\circ\text{C}$). Nearly monodispersed polystyrene was purchased from GL Science (Tokyo, Japan) and used as the calibration standard. Scanning electron microscopy (SEM) was conducted on a JEOL JSM7500FD (JEOL Resonance, Tokyo, Japan). Fluorescence spectra were recorded on an FP-8300 fluorescence spectrophotometer (JASCO, Tokyo, Japan). ζ -Potential measurements for the particle suspensions were performed on an ELS-8000 (Otsuka Electric, Osaka, Japan). Cell adhesion and spreading observations were performed via optical phase contrast microscopy (CKX41, Olympus, Tokyo, Japan). Fluorescence images were obtained on an A1+ confocal laser microscope system (Nikon, Tokyo, Japan).

Preparation of Tetrapeptide Chain Transfer Agent (Peptide-CTA). Four kinds of peptide-CTAs were prepared by SPPS using Fmoc chemistry. These peptides were synthesized on a 2-chlorotriylchloride resin using Fmoc-L-amino acid derivatives [Fmoc-Ser(Bu^t)-OH, Fmoc-Asp(OBu^t)-OH, Fmoc-Gly-OH, Fmoc-Arg(Pbf)-OH], DIPEA, DIPC, and HOBt in DMF for coupling and piperidine (25%)/DMF for Fmoc removal. Finally, 4-cyano-4-(phenylcarbonothioylthio) pentanoic acid as the RAFT agent was coupled with RGDS-resin in DMF, including DIPC and HOBt.

Treatment with DCM/HFIP (v/v 7:3) cleaved the peptide-CTAs from the resins. After purification, the obtained peptide-CTAs were identified by MALD TOF MS and ^1H NMR spectroscopies. The data are summarized in the [Supporting Information](#).

RAFT Polymerization of St with Peptide-CTA. A typical preparation procedure of PSt–RGDS was as follows. The monomer St (0.42 g, 4.0 mmol) was dissolved in acetone followed by the addition of RGDS-CTA (5.3 mg, $5.3 \mu\text{mol}$) and the initiator (AIBN, 0.41 mg, $2.5 \mu\text{mol}$). The solvent was added to adjust the total solution volume to 1.0 mL. This solution was poured into a polymerization glass tube, which was subsequently degassed by repeating freeze–vacuum–nitrogen filling–thaw cycles. The glass tube was then sealed into an ampule. Polymerizations were carried out at $60 \text{ }^\circ\text{C}$ with various polymerization times. After the prescribed time, the ampules were opened and the solvent was removed. Residues were purified by washing with cold methanol several times. The dried samples were subjected to SEC analyses. The data are summarized in [Table S1](#) (Supporting Information). Finally, the protective groups were removed by treating with a DCM solution of TFA/TIS (v/v 7:1) overnight. Complete removal of the protective groups was confirmed by ^1H NMR spectroscopy.

Preparation of NPs through SORP and Encapsulation of NR and MNP. Typically, 1 mg of PSt–peptide was dissolved in 10 mL of THF (0.1 mg mL^{-1}), which is a good solvent for the polymer. While gently stirring at room temperature at a constant speed of 1 mL min^{-1} , 2 mL of water, which is a precipitant for the polymer, was added to 1 mL of the polymer solution. The polymer solution remained optically transparent during this mixing process. The resulting polymer solution was placed in a small vial and left open to the

air at room temperature until the THF completely evaporated, yielding NPs suspensions.

To achieve multifunctional polymeric NPs, MNP (0.5 wt % relative to the polymer) was dissolved simultaneously with PSt-peptide in THF, and a similar preparation procedure was carried out as described above. Hydrophobic NR as a fluorescent dye was entrapped in the NPs when 0.2 wt % NR relative to the polymer was added to the THF solution of the polymer prior to adding the precipitant. Moreover, MNP and both of NR and MNP (NR/MNP) could be entrapped in the NPs in a similar manner.

Interaction of NPs with Cells and Cellular Uptake.

Cell culture was performed as follows. NIH/3T3 fibroblasts were cultured using Dulbecco's modified Eagle's medium (DMEM) supplemented with 10% calf serum and 1% penicillin/streptomycin. Cells were incubated at 37 °C under 5% CO₂. Cells grown to 80% confluence were passaged by trypsinization, diluted, and inoculated into a fresh tissue culture dish. Fibroblasts were seeded at a density of ca. 2 × 10⁴ cells per cm² onto the PSt-coated glass-bottomed dish. After incubating for 40 min, the dish was washed with the PBS (–) buffer to remove unattached cells. Then, the NR/MNP-loaded NPs suspensions (4 mL, 25 μg mL⁻¹, serum-free DMEM) were added. After the prescribed period, the cells were stained with calcein (calcein-AM, 6 μM) and ethidium D (EthD-1, 4 μM) for 15 min. Fluorescence images were obtained on a confocal microscope system. Green and red cells corresponded to live and dead cells, respectively. The magnetic effects on NP-containing cell adhesion were estimated by confocal microscopic observations for calcein-AM-stained cells in the presence or the absence of a permanent magnet (Neodymium magnet). NP-containing cells were prepared by incubating the cell (ca. 4 × 10⁵ cells) in the NR/MNP-loaded NPs suspensions (4 mL, 25 μg mL⁻¹, serum-free DMEM) for 12 h and then by recovering via centrifugation at 1200 rpm. Cell viability assays were conducted using a live/dead cell staining kit II (Takara Bio, Shiga, Japan).

■ ASSOCIATED CONTENT

Supporting Information

The Supporting Information is available free of charge on the ACS Publications website at DOI: 10.1021/acsomega.9b00899.

Experimental details for characterization of the peptide-CTAs by means of MALDI-TOF MS and ¹H NMR spectroscopies; polymerizations of St initiated with AIBN in the presence of RGDS-CTAs, SDGR-CTA, K₄-CTA, or D₄-CTA; ζ-potentials of the hybrid polymer NP suspensions at pH 6.0; SEM images of PSt-RGDS NPs: effect of polymer concentration and M_n; SEM images of NR or MNP-loaded PSt-RGDS NPs and NR/MNP-loaded PSt-RGDS NPs (PDF)

■ AUTHOR INFORMATION

Corresponding Authors

*E-mail: nhigashi@mail.doshisha.ac.jp (N.H.).

*E-mail: tkoga@mail.doshisha.ac.jp (T.K.).

ORCID

Nobuyuki Higashi: 0000-0001-9122-0479

Tomoyuki Koga: 0000-0002-2040-7188

Author Contributions

The manuscript was written through contributions of all authors. All authors have given approval to the final version of the manuscript.

Notes

The authors declare no competing financial interest.

■ ACKNOWLEDGMENTS

The authors acknowledge funding for this work provided by a Grant-in-Aid for Scientific Research (KAKENHI) (nos 16K05800 and 17K04994) from the Japan Society for the Promotion of Science (JSPS) and MEXT-Supported Program for the Strategic Research Foundation at Private Universities. The authors would like to thank Professor Yasushige Mori at Doshisha University for help with ζ-potential measurements.

■ REFERENCES

- (1) De, M.; Ghosh, P. S.; Rottelo, V. M. Applications of nanoparticles in biology. *Adv. Mater.* **2008**, *20*, 4225–4241.
- (2) Alivisatos, A. P.; Gu, W. W.; Larabell, C. Quantum dots as cellular probes. *Annu. Rev. Biomed. Eng.* **2005**, *7*, 55–76.
- (3) Kohane, D. S. Microparticles and nanoparticles for drug delivery. *Biotechnol. Bioeng.* **2007**, *96*, 203–209.
- (4) Michalet, X.; Pinaud, F. F.; Bentolila, L. A.; Tsay, J. M.; Doose, S.; Li, J. J.; Sundaresan, G.; Wu, A. M.; Gambhir, S. S.; Weiss, S. Quantum dots for live cells, in vivo imaging, and diagnostics. *Science* **2005**, *307*, 538–544.
- (5) Pridgen, E. M.; Langer, R.; Farokhzad, O. C. Biodegradable, polymeric nanoparticle delivery system for cancer therapy. *Nanomedicine* **2007**, *2*, 669–680.
- (6) Mailänder, V.; Landfester, K. Interaction of nanoparticles with cells. *Biomacromolecules* **2009**, *10*, 2379–2400.
- (7) Edmondson, S.; Osborne, V. L.; Huck, W. T. S. Polymer brushes via surface-initiated polymerizations. *Chem. Soc. Rev.* **2004**, *33*, 14–22.
- (8) Fleischer, C. C.; Payne, C. K. Nanoparticle-cell interactions: molecular structure of the protein corona and cellular outcomes. *Acc. Chem. Res.* **2014**, *47*, 2651–2659.
- (9) Hammond, P. T. Form and function in multilayer assembly: new applications at the nanoscale. *Adv. Mater.* **2004**, *16*, 1271–1293.
- (10) Yabu, H.; Higuchi, T.; Ijro, K.; Shimomura, M. Spontaneous formation of polymer nanoparticles by good-solvent evaporation as a nonequilibrium process. *Chaos* **2005**, *15*, No. 047505.
- (11) Yabu, H. Creation of functional and structured polymer particles by self-organized precipitation (SORP). *Bull. Chem. Soc. Jpn.* **2012**, *85*, 265–274.
- (12) Yabu, H. Self-organized precipitation: an emerging method for precipitation of unique polymer particles. *Polym. J.* **2013**, *45*, 261–268.
- (13) Perly, B.; Douy, A.; Gallot, B. Block copolymers poly(butadiene/poly(benzyl-L-glutamate) and polybutadiene/poly(N⁵-hydroxypropyl-glutamate) preparation and structural study by X-ray and electron microscopy. *Makromol. Chem.* **1976**, *177*, 2569–2589.
- (14) Lecommandoux, S.; Achard, M.-F.; Langenwaller, J. F.; Klok, H.-A. Self-assembly of rod-coil diblock oligomers based on α-helical peptides. *Macromolecules* **2001**, *34*, 9100–9111.
- (15) Eckhardt, D.; Groenewolt, M.; Krause, E.; Bötner, H. G. Rational design of oligopeptide organizers for the formation of poly(ethylene oxide) nanofibers. *Chem. Commun.* **2005**, 2814–2816.
- (16) Smeenk, J. M.; Otten, M. B. J.; Thies, J.; Tirrell, D. A.; Stunnenberg, H. G.; van Hest, J. C. M. Controlled assembly of macromolecular β-sheet fibrils. *Angew. Chem., Int. Ed.* **2005**, *44*, 1968–1971.
- (17) Marsden, H. R.; Korobko, A. V.; van Leeuwen, E. N. M.; Pouget, E. M.; Veen, S. J.; Sommerdijk, N. A. J. M.; Kros, A. Noncovalent triblock copolymers based on a coiled-coil peptide motif. *J. Am. Chem. Soc.* **2008**, *130*, 9386–9393.

- (18) Koga, T.; Koike, M.; Kamiwatari, S.; Higashi, N. Morphological variation of peptide-synthetic hybrid block copolymer assemblies in nonaqueous media. *Chem. Lett.* **2011**, *40*, 1244–1246.
- (19) Koga, T.; Kamiwatari, S.; Higashi, N. Preparation and self-assembly behavior of β -sheet peptide-inserted amphiphilic block copolymer as a useful polymeric surfactant. *Langmuir* **2013**, *29*, 15477–15484.
- (20) Nishimura, S.; Higashi, N.; Koga, T. Facile Synthesis of multiblock copolymers containing sequence-controlled peptides and well-defined vinyl polymers by nitroxide mediated polymerization. *Chem. - Eur. J.* **2017**, *23*, 15050–15058.
- (21) Nishimura, S.; Higashi, N.; Koga, T. Synthesis of peptide–vinyl polymer multiblock hybrids by nitroxide-mediated polymerization: breaking the limitations of monomer compatibility. *Polym. Chem.* **2019**, *10*, 71–76.
- (22) Nishimura, S.; Higashi, N.; Koga, T. A novel thermo-responsive multiblock architecture composed of a sequential peptides and an amino acid-derived vinyl polymers: toward protein-mimicking single-chain folding. *Chem. Commun* **2019**, *55*, 1498–1501.
- (23) Koga, T.; Teraguchi, Y.; Higashi, N. Preparation of PHEMA copolymers containing cell-binding peptides as graft chains and their cell adhesive properties. *Trans. Mater. Res. Soc. Jpn.* **2012**, *37*, 533–536.
- (24) Koga, T.; Nakamoto, K.; Odawara, K.; Matsuoka, T.; Higashi, N. Fabrication of thermo-responsive molecular layers from self-assembling elastin-like oligopeptides containing cell-binding domain for tissue engineering. *Polymers* **2015**, *7*, 134–146.
- (25) Lorenz, M. R.; Holzapfel, V.; Musyanovych, A.; Nothelfer, K.; Walther, P.; Frank, H.; Landfester, K.; Schrezenmeier, H.; Mailander, V. Uptake of functionalized, fluorescent-labeled polymeric particles in different cell lines and stem cells. *Biomaterials* **2006**, *27*, 2820–2828.
- (26) Rejman, J.; Oberle, V.; Zuhorn, I. S.; Hoekstra, D. Size-dependent internalization of particles via the pathways of clathrin- and caveolae-mediated endocytosis. *Biochem. J.* **2004**, *377*, 159–169.
- (27) Champion, J. A.; Walker, A.; Mitragotri, S. Role of particle size in phagocytosis of polymeric microspheres. *Pharm. Res.* **2008**, *25*, 1815–1821.
- (28) Siepmann, J.; Faisant, N.; Akiki, J.; Richard, J.; Benoit, J. P. Effect of the size of biodegradable microparticles on drug release: experiment and theory. *J. Controlled Release* **2004**, *96*, 123–134.
- (29) Gaumet, M.; Gurny, R.; Delie, F. Localization and quantification of biodegradable particles in an intestinal cell model: the influence of particle size. *Eur. J. Pharm. Sci.* **2009**, *36*, 465–473.
- (30) Shakweh, M.; Besnard, M.; Nicolas, V.; Fattal, E. Poly(lactide-co-glycolide) particles of different physicochemical properties and their uptake by peyer's patches in mice. *Eur. J. Pharm. Biopharm.* **2005**, *61*, 1–13.
- (31) Horák, D.; Babic, M.; Mackova, H.; Benes, M. J. Preparation and properties of magnetic nano- and micro-sized particles for biological and environmental separation. *J. Sep. Sci.* **2007**, *30*, 1751–1772.
- (32) Ohno, K.; Sakane, M.; Mori, C. Magnetically responsive assemblies of polymer-brush-decorated nanoparticle cluster that exhibit structural color. *Langmuir* **2018**, *34*, 9532–9539.
- (33) Moad, G.; Rizzardo, E.; Thang, S. H. Living radical polymerization by the RAFT process. *Aust. J. Chem.* **2005**, *58*, 379–410.
- (34) Chen, C.; Kong, F.; Wei, X.; Thang, S. H. Syntheses and effectiveness of functional peptide-based RAFT agents. *Chem. Commun.* **2017**, *53*, 10776–10779.
- (35) Pierschbacher, M. D.; Ruoslahti, E. M. Cell attachment activity of fibronectin can be duplicated by small synthetic fragments of the molecules. *Nature* **1984**, *309*, 30–33.
- (36) Ruoslahti, E. M.; Pierschbacher, M. D. New perspectives in cell adhesion: RGD and integrins. *Science* **1987**, *238*, 491–497.
- (37) Motoyoshi, K.; Tajima, A.; Higuchi, T.; Yabu, H.; Shimomura, M. Static and dynamic control of phase separation structures in nanoparticles of polymer blends. *Soft Matter* **2010**, *6*, 1253–1257.
- (38) Kanahara, M.; Satoh, H.; Higuchi, T.; Takahara, A.; Jinnai, H.; Harano, K.; Okada, S.; Nakamura, E.; Matsuo, Y.; Yabu, H. Fabrication of NIR-excitable SERS-active composite particles composed of densely packed Au nanoparticles on polymer microparticles. *Part. Part. Syst. Charact.* **2015**, *32*, 441–447.
- (39) Kyte, J.; Doolittle, R. F. A simple method for displaying the hydrophobic character of a protein. *J. Mol. Biol.* **1982**, *157*, 105–132.
- (40) Ma, J. C.; Dougherty, D. A. The cation- π interaction. *Chem. Rev.* **1997**, *97*, 1303–1324.
- (41) Yamada, T.; Matsushima, M.; Inaka, K.; Ohkubo, T.; Uyeda, A.; Maeda, T.; Titani, K.; Sekiguchi, K.; Kikuchi, M. Structural and functional analyses of the Arg-Gly-Asp sequence introduced into human lysozyme. *J. Biol. Chem.* **1993**, *268*, 10588–10592.

Cite this: *Chem. Commun.*, 2019, 55, 1498Received 14th November 2018,
Accepted 9th January 2019

DOI: 10.1039/c8cc09051c

rsc.li/chemcomm

A novel thermo-responsive multiblock architecture composed of a sequential peptide and an amino acid-derived vinyl polymer: toward protein-mimicking single-chain folding†

Shin-nosuke Nishimura,^{id} Nobuyuki Higashi* and Tomoyuki Koga^{id}*

A novel multiblock architecture composed of an alternating β -sheet forming oligopeptide and a thermo-responsive glycine-derived vinyl polymer was synthesized. The polymer exhibited lower critical solution temperature (LCST) behavior in water, unlike the behavior of a glycine-derived homopolymer, and formed nanoparticles through protein-mimicking folding driven by thermal cycle-induced β -sheet formation.

Naturally occurring biopolymers, such as proteins and nucleic acids, are functional copolymers with perfectly regulated primary structures (*i.e.*, monomer sequences and chain lengths). The controlled monomer sequences enable folding into well-defined three-dimensional (3D) architectures. Tertiary protein structures are formed through the intramolecular collapse of single polypeptide chains *via* non-covalent interactions among secondary structural elements, such as α -helices and β -sheets, which are ultimately dictated by the sequence of amino acid residues. The resultant globular proteins assume a nano-scale 3D-geometry that enforces the spatial dispositions of the side chains, such that the hydrophilic groups are mainly positioned on the protein surfaces and hydrophobic elements tend to be sequestered into the interior of the structure.¹ The unique folded structures with isolated interiors provide precise functions, such as specific molecular recognition and efficient catalysis.

By contrast, it is generally difficult to regulate the 3D geometries of linear vinyl polymers in solution due to their conformational freedom, which enables unrestricted backbone C–C bond rotation. Significant efforts have been applied toward the design of foldable synthetic polymers that form well-defined single-chain 3D-structures, similar to proteins, in solution.^{2–7} Precisely designed vinyl polymer chains with controlled molecular weights, dispersities, and side-chain functionalities have been prepared successfully using living radical polymerization techniques^{8–11} to achieve single-chain folding into polymeric nanoparticles through intramolecular

covalent,^{12–15} dynamic covalent,^{16–18} and non-covalent^{19–24} interactions. These single-chain nanoparticles are important new polymeric nanomaterials with potential applications in the fields of drug delivery, sensors, and catalysis, as well as they provide structural models of biopolymers. Consequently, this relatively new research field has grown rapidly over the last few years.

Herein, we report the unique thermal cycle-induced folding of a novel water-soluble peptide–vinyl polymer multiblock copolymer into nanoparticles. The multiblock copolymer was designed to have hydrophobic and β -sheet forming tetra-leucine (Leu) blocks²⁵ that act as supramolecular cross-linking points for folding, arranged at equal intervals in a thermo-responsive glycine (Gly)-derived vinyl polymer (Fig. 1). Amino acid-based vinyl polymers are fascinating smart polymers with excellent water solubility, biocompatibility, and readily tunable thermo-responsiveness, depending on the amino acids present and their combinations.^{26–30} Novel synthetic polymer scaffolds capable of collapsing into protein-like higher-order structures with specific nano-compartments in water are important for their value in the fields of single-chain nanotechnology³¹ and

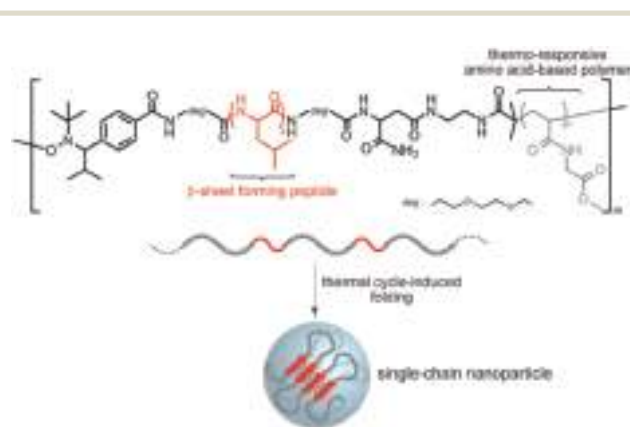


Fig. 1 Chemical structure of a multiblock hybrid polymer composed of an alternating aligned tetra-leucine β -sheet and a thermo-responsive glycine-derived vinyl polymer (top), and schematic illustration of the folding process to form single-chain nanoparticles *via* intramolecular cross-links among the peptide multiblocks (bottom).

Department of Molecular Chemistry & Biochemistry, Faculty of Science & Engineering, Doshisha University, Kyotanabe, Kyoto, 610-0321, Japan.
E-mail: tkoga@mail.doshisha.ac.jp, nhigashi@mail.doshisha.ac.jp

† Electronic supplementary information (ESI) available: Experimental details and supplemental schemes and figures. See DOI: 10.1039/c8cc09051c

biomedicine. The exploration of such novel polymer scaffolds presents a significant challenge in polymer chemistry.

We previously reported an efficient method of using cyclic peptides bearing an alkoxyamine bond in the framework to produce well-defined peptide–vinyl polymer multiblock architectures in one step. In the initial system, the 2,2,6,6-tetramethyl piperidine 1-oxyl (TEMPO)-derived alkoxyamine-containing peptide initiator was used to polymerize styrenes.³² Recently, we expanded the compatibility of monomers using this method to include acrylamide and acrylate by developing a 2,2,5-trimethyl-4-phenyl-3-azahexane-3-nitroxide (TIPNO)-based cyclic peptide NMP initiator.³³ The cyclic peptide-based NMP approach ensured the successful synthesis of the objective multiblock copolymer in one step using *N*-acryloyl-Gly *O*-methyl ester (NAGMe) as the vinyl monomer. The TIPNO-derived alkoxyamine-containing cyclic peptide ((Leu)₄ domain) was prepared as described previously,³³ and polymerization of NAGMe was carried out in DMF at 120 °C over 18 h (Scheme S1, see the ESI† for details). In this system, the thermally promoted homolysis of the alkoxyamine bond generated a reactive carbon radical and a stable nitroxide radical simultaneously at both ends of the peptide. As a result, chain extension and multimerization proceeded in one step. The structural features of the obtained polymer were characterized by size-exclusion chromatography (SEC), ¹H NMR, circular dichroism (CD), and fragmentation analyses. The SEC trace was symmetrically unimodal and indicated a relatively high molecular weight and broad polydispersity based on the multiblock structure ($M_n = 80\,400\text{ g mol}^{-1}$, $D = 2.89$ (PMMA standards)) (Fig. 2A, blue line). The structure of the constituent block was analyzed in a fragmentation experiment, in which the multiblock was broken into (Leu)₄-*b*-PNAGMe diblock units using a radical crossover reaction³⁴ in the presence of a large excess of TIPNO (800 equiv.) in *N*-methyl-2-pyrrolidone at 120 °C over 12 h (Scheme S2). The M_n value of the fragmented polymer ($12\,100\text{ g mol}^{-1}$, in comparison to those of PMMA standards) is in agreement with the theoretical value³⁵ ($M_{n,\text{Theor.}} = 13\,400\text{ g mol}^{-1}$), calculated based on the conversion rate (86.4%), and the polydispersity of the PNAGMe block was satisfyingly low ($D = 1.25$) (Fig. 2A, red line). Furthermore, the repeat number (m) of the diblock unit was estimated to be $m \approx 7$ from the M_n values determined before and after fragmentation (*i.e.* a total of 14 blocks). The structural characterization

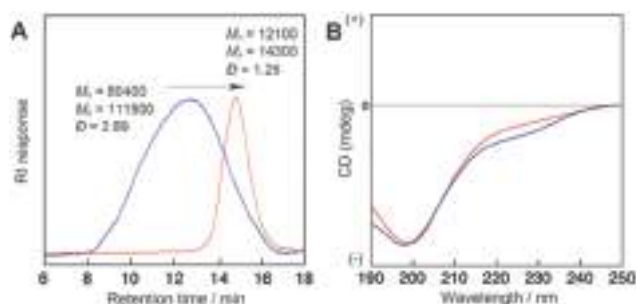


Fig. 2 (A) SEC traces (DMF, 40 °C) of the multiblock hybrid polymer obtained before (blue) and after (red) fragmentation by radical crossover reactions using a large excess of TIPNO. RI = refractive index. (B) CD spectra of the multiblock (blue) and fragmented diblock (red) hybrids in pure water at 20 °C. [Polymer] = 0.05 wt%.

experiments of the polymers are described in detail in the ESI† (Fig. S1). The unique multiblock hybrid was fully soluble in water, and the peptide blocks assumed a random coil structure with a negative maximum at 198 nm (Fig. 2B, blue line). Note that fragmentation did not extensively alter the peptide block conformations, as shown in Fig. 2B (red line).

The thermo-responsive behaviors of the multiblock hybrid in an aqueous solution were investigated using turbidimetry. Fig. 3A shows the turbidity curves of the multiblock hybrid solution measured at 600 nm during heating (1 °C min^{-1}) in a heating–cooling cycle (20–80 °C, 30 cycles). Data obtained from the peptide-free PNAGMe homopolymer, which was prepared by free radical polymerization using AIBN ($M_n = 39\,000\text{ g mol}^{-1}$), are shown in Fig. 3B for comparison. The multiblock hybrid exhibited a lower critical solution temperature (LCST)-type thermo-response, but the thermal profile was quite different from that of the PNAGMe homopolymer. During the first heating process, the transition temperature (T_t) for the hybrid was apparently shifted to a lower temperature (*ca.* 62 °C) compared with that for the homopolymer (73 °C). This was attributed to the increase in the hydrophobicity due to the introduction of (Leu)₄ multiblocks. Interestingly, the turbidity curves of the multiblock hybrid gradually shifted to higher temperatures after repeated heating–cooling cycles, approaching the curve obtained for the homopolymer after 30 cycles, although slight broadening was observed in the transition (Fig. 3A).

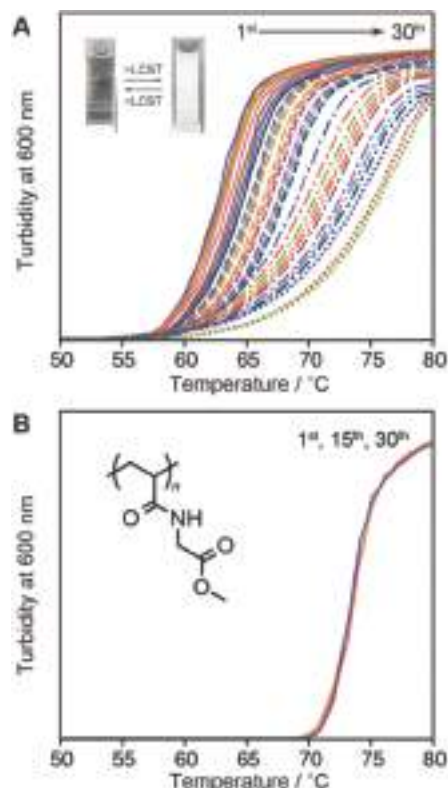


Fig. 3 Temperature dependence of the turbidity at 600 nm for the multiblock hybrid (A) and the PNAGMe homopolymer (B) aqueous solutions during the heating process of the heating–cooling cycles (20 to 80 °C). [Polymer] = 1.0 wt%. The inset in (A) shows photographs of the hybrid solutions at 20 °C (left) and 80 °C (right), acquired over 30 cycles.

Fragmentation and side chain hydrolysis (NAGMe unit) of the multiblock hybrid did not occur at 80 °C (Fig. 4B and Fig. S2, ESI[†]). Moreover, the turbid solution (above T_t) turned perfectly transparent (*i.e.*, 100% transmittance recovery), even after repeating the thermal cycles (Fig. 3A inset). Therefore, the remarkable hysteresis observed during heating of the multiblock hybrid was attributed to the folding of the linear polymer chain, rather than the formation of large intermolecular aggregates. Upon heating, the conformation of the PNAGMe chain changed from an extended and hydrated chain below T_t into a collapsed chain above T_t . This repeated transition seems to promote non-covalent interactions among the peptide multiblocks specifically aligned in the polymer chain (described in detail later), leading to folding, in which the hydrophobic peptide blocks were isolated from the hydrophilic PNAGMe blocks to minimize their contact with water. As a result, the hydrophobic nature of the peptide blocks was apparently shielded by the surface-exposed hydrophilic PNAGMe chains and the turbidity curve of the hybrid polymer approached the curve

obtained from the homopolymer under repeated thermal cycles (*i.e.*, T_t increased from 62 to 73 °C, $\Delta T_t = 11$ °C).

The folding behavior was investigated in more detail by collecting the CD spectra, SEC traces, atomic force microscopy (AFM) images, and transmission electron microscopy (TEM) images. Fig. 4A shows the CD spectra of a multiblock hybrid polymer before and after a heating–cooling cycle (30 times). Under repeated thermal cycles, highly ordered structures formed from the disordered random coil, as evidenced by a decrease in the ellipticity at 220 nm and an increase at 198 nm. The differential spectrum^{36,37} (inset) showed a pattern typical of a β -sheet structure, with negative and positive maxima at 220 nm and 198 nm, respectively, indicating the specific interactions among the peptide multiblocks. The SEC data supported the formation of non-covalent cross-links. The SEC traces obtained from the multiblock hybrid showed a clear increase in the retention times before and after the thermal cycles (a 12% decrease in the apparent molecular weight, Fig. 4B), indicating the collapse of the polymer chain with a decrease in the hydrodynamic volume.³⁸ Note that the SEC analysis was carried out in DMF using the lyophilized multiblock hybrid after the thermal cycles in water. Thus, once the folded structure had formed in water, it was relatively stable and appeared to be maintained to some extent, even after dissolution in DMF.

The folded structure of the multiblock hybrid was visualized using TEM and tapping-mode AFM. The TEM image obtained on a carbon-coated copper grid deposited from an aqueous solution after the thermal cycles clearly revealed nanospheres with a relatively uniform diameter of 40–50 nm (Fig. 4C). These nanostructures are in good agreement with the AFM image obtained for the same sample on mica, which showed well-defined nanoparticles with a uniform height and diameter (Fig. 4D). Note that such nanoparticles were not observed before the thermal cycle (Fig. S3, ESI[†]). The AFM cross-sectional analysis revealed the particle size, 1.5–2.5 nm in height, with diameters of 50–70 nm (Fig. S4, ESI[†]). The comparable nanostructures, which were observed using TEM on a carbon-coated copper grid and AFM on mica, demonstrated that nanoparticle formation was not induced by the surface interactions with the solid substrates, but rather reflected the structure in an aqueous solution. It should be noted that the nanoparticle heights were quite small compared with the widths, probably due to flattening under gravity during the deposition process. Thus, the nanoparticles adopted a half-ellipsoid shape on the solid surfaces. Given the half-ellipsoid shape, with an average height of 2 nm and a diameter of 60 nm (radius 30 nm), the volume of the nanoparticle was calculated to be $V = [4/3\pi(30 \times 30 \times 2)]/2 = 3770 \text{ nm}^3$. We therefore estimated the nanoparticle diameter in water to be 19.3 nm ($r = 9.65 \text{ nm}$) by converting the calculated volume to that expected for a spherical particle ($V = 4/3\pi r^3$). Dynamic light scattering (DLS) analysis also supported the folding of the multiblock hybrid into nanoparticles in water (Fig. 4E). Before the thermal cycle, a relatively broad size distribution was observed including a large component with a hydrodynamic diameter of *ca.* 160 nm (Fig. 4E, top). Similar aggregates were reported to exist in the aqueous solution of a diblock copolymer composed of thermo-responsive poly(*N*-isopropyl acrylamide) and hydrophilic poly(*N*-vinyl-2-pyrrolidone) even below the

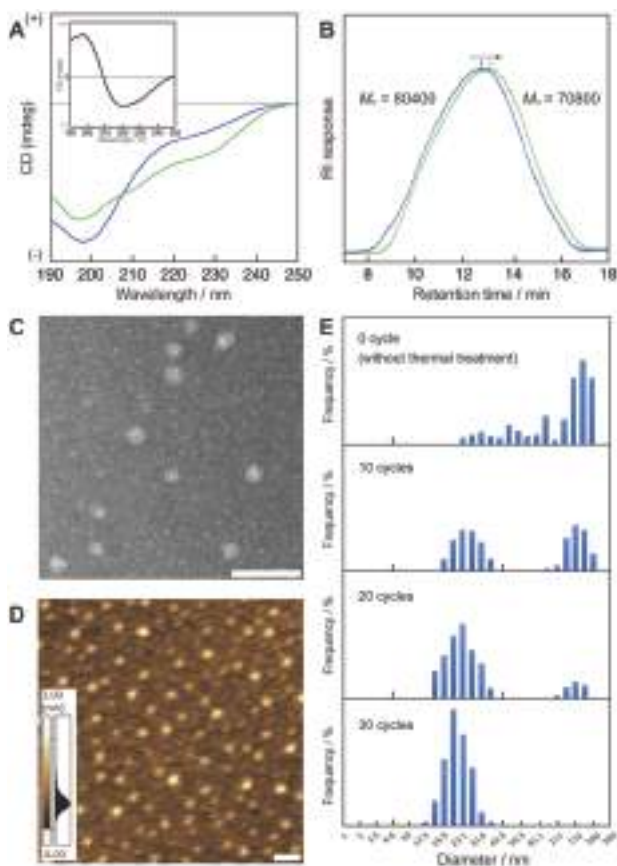


Fig. 4 Folding behavior of the multiblock hybrid polymer in pure water, driven by thermal cycling (20 to 80 °C, 30 cycles). (A) CD spectral change before (blue) and after (green) the thermal cycles. The inset shows the differential spectrum. (B) SEC traces (DMF, 40 °C, RI detector) of the multiblock hybrid polymer in the expanded (blue) and folded (green) states. (C) TEM image of the folded multiblock hybrid polymer stained negatively with 1% phosphotungstic acid; scale bar = 200 nm. (D) Tapping-mode AFM image of the folded hybrid polymer on mica; scale bar = 200 nm. [Polymer] = 0.05 wt%. (E) Hydrodynamic diameters of the multiblock hybrid polymer in water (1 wt%) during the thermal cycles, as measured by DLS at 20 °C.

LCST.³⁹ Upon repeated thermal cycles, the large component disappeared gradually and the particle size reached a value of ca. 20 nm. This value corresponded reasonably with the theoretical size (ca. 22 nm) based on the flower-like unimer micelle structure, as illustrated in Fig. 1, considering the molecular length of each block (that is, β -sheet (Leu)₄ (1.4 nm) and the extended length of PNAGMe (21 nm for 76-mer)). Taken together, these data strongly indicated the generation of single-chain nanoparticles *via* non-covalent intramolecular cross-linking, as illustrated in Fig. 1, although the possibility that the well-defined nanoparticles consist of multiple polymer chains⁷ cannot be excluded completely. The most interesting feature of this polymer system is that the multi-block hybrid formed well-defined nanoparticles with a uniform shape and size, despite a broad polydispersity ($D = 2.89$). These features were attributed to the characteristic molecular structures and the protein-mimicking folded forms. Indeed, this multiblock hybrid was polydisperse, but the dispersities of the constituent blocks were satisfyingly low ($D = 1.0$ for the peptide blocks, and $D = 1.25$ for the PNAGMe blocks). Consequently, the thickness of the coronal layer (looped hydrophilic PNAGMe chains) covering the non-covalently cross-linked hydrophobic peptide core remained constant, leading to the production of uniform nanoparticles. In fact, fluorescence analysis using an environmentally sensitive Nile red dye supported the formation of a hydrophobic pocket isolated from the hydrophilic environment by thermal cycle-induced folding. A blue shift ($\lambda_{\text{em}} = 616$ nm) and a remarkable intensity increase of the Nile red emission was clearly observed in the aqueous solution of the folded multiblock polymer compared to that in pure water ($\lambda_{\text{em}} = 650$ nm) and in the aqueous solution of the expanded form ($\lambda_{\text{em}} = 645$ nm) (Fig. S5, ESI†).

In conclusion, we have demonstrated the fascinating potential of a multiblock peptide/amino acid-based vinyl polymer hybrid for use as a novel foldable polymer scaffold. Well-defined and thermo-responsive single-chain nanoparticles were successfully obtained in water. The advantages of this multiblock backbone are (i) its high water solubility, (ii) a biocompatible amino acid-derived composition, (iii) the spatial arrangement of the peptide blocks in a single polymer chain, which could be easily controlled by changing the chain length of the vinyl polymer block, (iv) the structural and functional diversity of the peptide block, which could be precisely designed using the primary amino acid sequence, and (v) the widely tunable LCST behavior,²⁷ which could be realized *via* copolymerization with different amino acid-derived vinyl monomers. These findings open a route to a new family of single-chain nanoparticles and will enable the advance of the fields of nanomedicine and synthetic protein design.

This work was partly supported by the Grants-in-Aid for Scientific Research (KAKENHI) (No. 17K04994 and 16K05800) from the Japan Society for the Promotion of Science (JSPS), and a MEXT-Supported Program for the Strategic Research Foundation at Private University.

Conflicts of interest

There are no conflicts to declare.

Notes and references

- 1 C. B. Anfinsen, *Science*, 1973, **181**, 223–230.
- 2 O. Altintas and C. Barner-Kowollik, *Macromol. Rapid Commun.*, 2012, **33**, 951–971.
- 3 O. Altintas and C. Barner-Kowollik, *Macromol. Rapid Commun.*, 2016, **37**, 29–46.
- 4 S. Mavila, O. Eivgi, I. Berkovich and N. G. Lemcoff, *Chem. Rev.*, 2016, **115**, 878–961.
- 5 H. K. Murnen, A. R. Khokhlov, P. G. Khalatur, R. A. Segalman and R. N. Zuckermann, *Macromolecules*, 2012, **45**, 5229–5236.
- 6 E. Huerta, P. J. M. Stals, E. W. Meijer and A. R. A. Palmans, *Angew. Chem., Int. Ed.*, 2013, **127**, 2906–2910.
- 7 M. Shibata, M. Matsumoto, Y. Hirai, M. Takenaka, M. Sawamoto and T. Terashima, *Macromolecules*, 2018, **51**, 3738–3745.
- 8 M. Georges, R. P. N. Veregin, P. M. Kazmaier and G. K. Hamer, *Macromolecules*, 1993, **26**, 2987–2988.
- 9 K. Matyjaszewski and J. Xia, *Chem. Rev.*, 2001, **101**, 2921–2990.
- 10 M. Kamigaito, T. Ando and M. Sawamoto, *Chem. Rev.*, 2001, **101**, 3689–3746.
- 11 G. Moad, E. Rizzardo and S. H. Thang, *Aust. J. Chem.*, 2005, **58**, 379–410.
- 12 E. Harth, B. V. Horn, V. Y. Lee, D. S. Germack, C. P. Gonzales, R. D. Miller and C. J. Hawker, *J. Am. Chem. Soc.*, 2002, **124**, 8563–8660.
- 13 J. J. Jiang and S. Thayumanavan, *Macromolecules*, 2005, **38**, 5886–5891.
- 14 O. Altintas, J. Willenbacher, K. N. R. Wuest, K. K. Oehlenschlaeger, P. Krolla-Sidenstein, H. Gliemann and C. Barner-Kowollik, *Macromolecules*, 2013, **46**, 8092–8101.
- 15 J. P. Cole, J. J. Lessard, C. K. Lyon, B. T. Tuten and E. B. Berda, *Polym. Chem.*, 2015, **6**, 5555–5559.
- 16 B. S. Murray and D. A. Fulton, *Macromolecules*, 2011, **44**, 7242–7252.
- 17 B. T. Tuten, D. Chao, C. K. Lyon and E. B. Berda, *Polym. Chem.*, 2012, **3**, 3068–3071.
- 18 D. E. Whitaker, C. S. Mahon and D. A. Fulton, *Angew. Chem., Int. Ed.*, 2013, **52**, 956–959.
- 19 M. Seo, B. J. Beck, J. M. J. Paulusse, C. J. Hawker and S. Y. Kim, *Macromolecules*, 2008, **41**, 6413–6418.
- 20 E. J. Foster, E. B. Berda and E. W. Meijer, *J. Am. Chem. Soc.*, 2009, **131**, 6964–6966.
- 21 T. Terashima, T. Mes, T. F. A. De Greef, M. A. J. Gillissen, P. Besenius, A. R. A. Palmans and E. W. Meijer, *J. Am. Chem. Soc.*, 2011, **133**, 4742–4745.
- 22 E. A. Appel, J. Dyson, J. del Barrio, Z. Walsh and O. A. Scherman, *Angew. Chem., Int. Ed.*, 2012, **51**, 4185–4189.
- 23 T. Terashima, T. Sugita, K. Fukae and M. Sawamoto, *Macromolecules*, 2014, **47**, 589–600.
- 24 F. Wang, H. Pu, Y. Ding, H. Pan, Z. Chang and M. Jin, *Polymer*, 2018, **141**, 86–92.
- 25 T. Koga, S. Kamiwatari and N. Higashi, *Langmuir*, 2013, **29**, 15477–15484.
- 26 H. Mori, H. Iwaya, A. Nagai and T. Endo, *Chem. Commun.*, 2005, 4872–4874.
- 27 N. Higashi, R. Sonoda and T. Koga, *RSC Adv.*, 2015, **5**, 67652–67657.
- 28 N. Higashi, A. Hirata, S. Nishimura and T. Koga, *Colloid Surf., B*, 2017, **159**, 39–46.
- 29 N. Higashi, D. Sekine and T. Koga, *J. Colloid Interface Sci.*, 2017, **500**, 341–348.
- 30 N. Higashi, S. Matsubara, S. Nishimura and T. Koga, *Materials*, 2018, **11**, 424.
- 31 M. Ouchi, N. Badi, J.-F. Lutz and M. Sawamoto, *Nat. Chem.*, 2011, **3**, 917–924.
- 32 S. Nishimura, N. Higashi and T. Koga, *Chem. – Eur. J.*, 2017, **23**, 15050–15058.
- 33 S. Nishimura, N. Higashi and T. Koga, *Polym. Chem.*, 2019, **10**, 71–76.
- 34 H. Otsuka, K. Aotani, Y. Higaki and A. Takahara, *Chem. Commun.*, 2002, 2838–2839.
- 35 Theoretical number-average molecular weight of the fragmented polymer was calculated by the following equation: $M_{n, \text{Theor.}} = [\text{monomer}]/[\text{initiator}] \times \text{conversion} \times \text{molecular weight of the monomer} + \text{molecular weight of the initiator}$.
- 36 F. Eker, K. Griebenow and R. Schweitzer-Stenner, *J. Am. Chem. Soc.*, 2003, **125**, 8178–8185.
- 37 I. Gokce, R. W. Woody, G. Anderluh and J. H. Lakey, *J. Am. Chem. Soc.*, 2005, **127**, 9700–9701.
- 38 J. A. Pomposo, I. Perez-Baena, L. Buruaga, A. Alegria, A. J. Moreno and J. Colmenero, *Macromolecules*, 2011, **44**, 8644–8649.
- 39 T. Sato, K. Tanaka, A. Toyokura, R. Mori, R. Takahashi, K. Terao and S. Yusa, *Macromolecules*, 2013, **46**, 226–235.

Photocleavable and Polymerizable Peptide for Micropatterning of Bioactive Segments in Polymer Soft Materials

Shin-nosuke Nishimura,¹ Ayaha Hirata,¹ Yukiko Taki,² Yusuke Morita,² Nobuyuki Higashi,*¹ and Tomoyuki Koga*¹

¹Department of Molecular Chemistry and Biochemistry, Faculty of Science and Engineering, Doshisha University, Kyotanabe, Kyoto 610-0321, Japan

²Department of Biomedical Engineering, Faculty of Life and Medical Sciences, Doshisha University, Kyotanabe, Kyoto 610-0321, Japan

E-mail: tkoga@mail.doshisha.ac.jp (T. Koga), nhigashi@mail.doshisha.ac.jp (N. Higashi)

Herein, we report a novel photocleavable and polymerizable oligopeptide for versatile design of biofunctional polymers. Radical copolymerizations of the peptide with various vinyl monomers successfully produce graft-type peptide-polymer hybrids. The resultant RGDS peptide/PHEMA hybrid film is applied to photolithography, and provides spatially limited location of the bioactive RGDS peptides. Furthermore, such photocleavage of the RGDS-graft chains can also tune cell adhesion to the surface.

Keywords: Photocleavable peptide-polymer hybrid | Cell adhesion | Thin film

Artificial peptides are fascinating and versatile molecular units due to their exceptional ability to self-organize into precisely defined high-order nanostructure¹ as well as their biofunctions such as cell adhesion, antioxidative and antimicrobial properties.² Their chemical and physiological properties can be designed intrinsically by the primary sequence of amino acids. Solid phase peptide synthesis (SPPS) allows monodispersed oligopeptides to be prepared with perfectly controlled chain lengths and amino acid sequences.³ However, SPPS is a time-consuming method, often expensive, difficult to scale up, and is unsuited to synthesize high-molecular weight polypeptide. Therefore, a hybridization of structurally and functionally controlled oligopeptides and conventional synthetic polymers is a very attractive strategy to overcome these limitations in materials science and to construct new classes of polymeric materials with tailored characters and structures. Various peptide-polymer hybrids have been reported to fabricate biofunctional and nanostructured materials.⁴ We have also reported the synthesis of AB-type diblock,⁵ ABC-type triblock,⁶ multiblock⁷ and graft-type hybrids,⁸ and their structural and functional properties.

Herein, we report a new type of peptide-polymer hybrid whose bioactivity can be controlled by light. The newly prepared oligopeptide contains a photolabile linker and polymerizable group at the *N*-terminus. Radical copolymerizations of this peptide-macromonomer with vinyl monomers enable photocleavable peptide grafts that can be facilely inserted into a variety of vinyl polymers. In this study, we employed the RGDS (arginine-glycine-aspartic acid-serine) sequence as a bioactive peptide. The RGDS peptide has been identified as a principal cell adhesive ligand in extracellular matrix such as fibronectin (FN),^{2a,9} and has been used by attaching to a material surface to control cell adhesion, proliferation and differentiation.¹⁰ Recently, photocontrolled adhesions of cells to solid surfaces have also been achieved by combining the RGD-epitope with

photosensitive molecules (i.e. caged RGD (or RGDS)¹¹ and RGD with photolytic linker¹²). Such two-dimensional (2D)-patterning is an important technique for tissue engineering and screening based on cell chips. In our system, bioactive RGDS peptides are grafted from vinyl polymers through photosensitive 3-amino-3-(2-nitrophenyl)propanoic acid (*ANP*) linker. *ANP* is a photodegradable molecule, which is decomposed rapidly via Norrish II mechanism by mild UV light.¹³ Since light can be readily focused and controlled over intensity, this photoprocessable peptide-polymer hybrid system allows the controlled micropatterning of bioactive RGDS peptides that can guide cell behavior in 2D- and 3D-soft materials such as thin films and hydrogels.

The general strategy of this polymer system is presented in Figure 1. The peptide contained (1) a polymerizable methacryl group at the *N*-terminus, (2) a photolabile *ANP* linker, (3) a single lysine (Lys) residue to react with a fluorescence dye, and (4) a specifically designed amino acid sequence (RGDS). The objective peptide-macromonomer was successfully prepared by SPPS using 9-fluorenylmethoxycarbonyl (Fmoc) chemistry. First, the Fmoc-*ANP* was prepared by the reaction of *ANP* with Fmoc-succinimide in acetonitrile/water mixed solution,^{13a} and identified by ¹HNMR spectroscopy (Figure S1). After construction of the peptide segment on a Fmoc-NH-SAL MBHA resin by using various Fmoc-derivatives, a methacryl group was introduced to the *N*-terminus of the peptide by treating the resin with methacrylic anhydride. Fluorescence labeling was also carried out on the resin by removal of the 4-methyltrityl (Mtt)

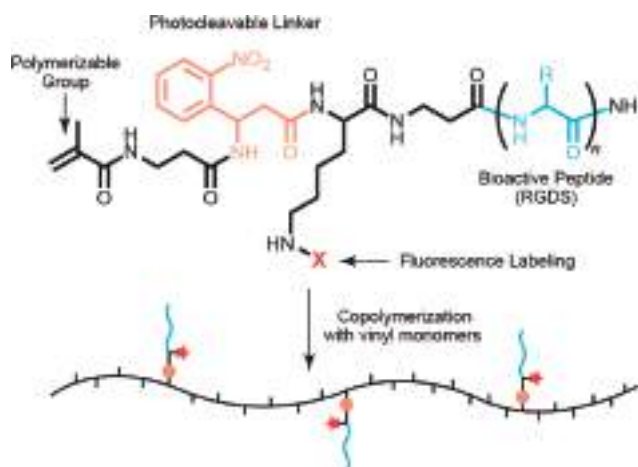


Figure 1. Novel photocleavable and polymerizable peptide for versatile design of functional peptide-polymer hybrids.

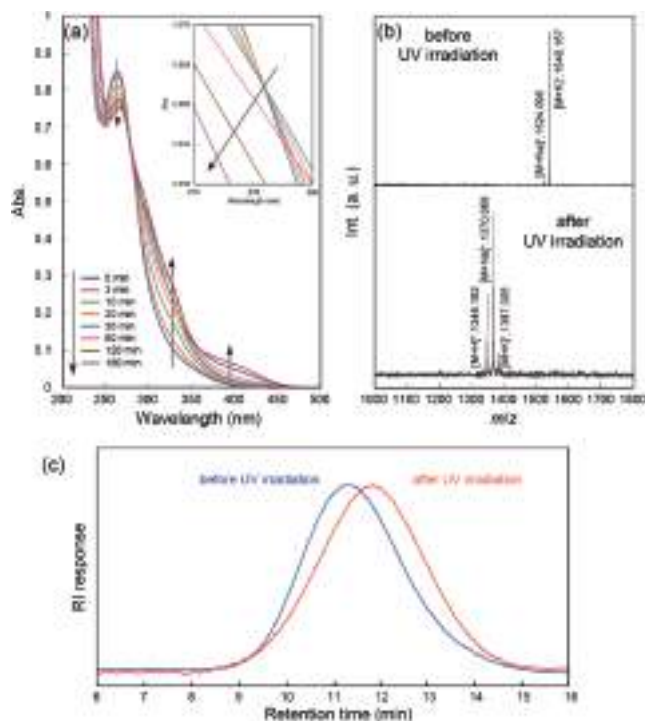


Figure 2. (a) UV-vis spectral change of peptide-macromonomer (without RhB) by UV irradiation (365 nm) in water at RT. Inset shows magnified spectral change at around 279 nm. [peptide] = 100 μ M. (b) MALDI-TOF MS spectra of peptide-macromonomer (with RhB) obtained before and after UV irradiation for 30 min in water. (c) SEC charts (DMF eluent (containing 10 mM LiBr), 40 $^{\circ}$ C, refractive index (RI) detector) of the peptide/PHEMA hybrid obtained before and after UV irradiation (365 nm, 30 min).

group of Lys residue and condensation of the resulting amino group with rhodamine B (RhB). To cleave the peptide-macromonomer from the resin, the resin was treated with TFA/dichloromethane/TIS (v/v/v = 8.5/1/0.5). The obtained peptide was purified by repeated precipitation from a methanol/diethyl ether system, and subsequently identified by MALDI-TOF MS (Figure 2b, top) and 1 H NMR analyses (Figure S2).

To test the photodegradability of the ANP moiety, the peptide-macromonomer was first exposed to a UV handy lamp (365 nm, 8 W) in water at room temperature, and the reaction was investigated by UV-vis and MALDI-TOF MS analyses. Note that we used RhB-free peptide-macromonomer for the case of UV analysis to monitor the spectral change of ANP moiety directly. Their UV spectra are shown in Figure 2a. Upon UV irradiation, a decrease in the absorbance at 264 nm is observed, together with an increase in absorbance both at 325 nm and 400 nm. These spectral changes within the period of 30 min are found to proceed through an isosbestic point at around 279 nm (Figure 2a inset). This result shows that the phototriggered decomposition of ANP moiety took place smoothly within 30 min. Further exposure to UV light leads to production of by-products; a shift from the isosbestic point is observed. Further evidence of such photolytic reaction at the ANP site is obtained from MALDI-TOF MS analysis (Figure 2b). The RhB-labeled peptide-macromonomer was dissolved in water (100 μ M) and

exposed to light (365 nm) for 30 min at room temperature. After irradiation for 30 min, three strong peaks are newly observed at 1348.2 [M+H]⁺, 1370.1 [M+Na]⁺ and 1387.0 [M+K]⁺, along with complete disappearance of the peaks at 1524.1 [M+Na]⁺ and 1540.2 [M+K]⁺ from the starting compound.

Radical copolymerizations of this peptide-macromonomer with vinyl monomers (2-hydroxyethyl methacrylate (HEMA), styrene (St) and methyl methacrylate (MMA)) produce facilely various graft-type peptide-polymer hybrids. As a representative example, an SEC chart of peptide/PHEMA hybrid obtained using AIBN as an initiator is shown in Figure 2c (blue line). The SEC trace is symmetrically unimodal and shows relatively high molecular weight ($M_n = 195000$, polydispersity index $D = 1.61$, PMMA standard). We also confirmed successful copolymerizations of the peptide-macromonomer with St and MMA (data not shown). It should be noted that copolymer compositions (i.e. grafting ratio of peptide chain), which are evaluated by 1 H NMR spectroscopy (Figure S3), are easily changeable by varying the feed composition of peptide-macromonomer and vinyl monomers. These results suggest that radical copolymerization of this system is successful even using peptide-macromonomer. Most importantly, photocleavage reactions of peptide-grafts occur even in the copolymer system. Figure 2c (red line) shows the SEC chart of peptide/PHEMA hybrid obtained after UV irradiation for 30 min in DMF. The shift in the RI peak to a longer retention time is clearly observed, demonstrating decrease in molecular weight.

We chose the peptide/PHEMA hybrid (grafting ratio = 2.5%) for the following cell adhesion experiments. PHEMA is a well-studied biocompatible polymer, which has been used for biomaterials because it can form hydrogel and film, resist non-specific adhesion of protein and cells, and has good mechanical strength.¹⁴ Thin films of the peptide/PHEMA hybrid and PHEMA homopolymer were prepared on a superhydrophilic glass substrate (1 cm \times 1 cm) by spin-coating from TFE solution (20 mg mL⁻¹). In order to estimate the film thickness, two films were scratched by an AFM cantilever in contact mode (Figure S4). According to the height profile analysis, the film thicknesses are evaluated to be ca. 100 nm for both films. ATR-FTIR spectrum of the hybrid film provides information on the secondary structure of peptide-graft chains (Figure S5). In the amide I and amide II regions, characteristic absorptions are observed at 1668 cm⁻¹ and 1540–1535 cm⁻¹, respectively. These spectral features indicate the random coil conformation¹⁵ of peptide segments. The additional C=O stretching band, arising from the ester groups of HEMA units, is observed at 1724 cm⁻¹. Such non-structural conformation of peptide-graft chains is convenient for cell attachment since the RGD sequence of FN also exists in the loop region of two connecting type III domains in vivo. In addition, the surface of the hybrid film afforded relatively hydrophilic surface with a water contact angle of 58 $^{\circ}$. However, this value is somewhat high compared to that for PHEMA homopolymer film (40 $^{\circ}$) probably due to higher hydrophobicity of peptide chain than HEMA unit. Thus, it seems that RGDS-grafts are exposed to the film surface and may therefore be a relevant epitope for cell adhesion. To address the potential of this peptide/PHEMA hybrid film as a bioactive surface, fibroblast cells (NIH/3T3) were seeded on the film and cultured at 37 $^{\circ}$ C in serum-free medium for 24 h (Figure 3b). As a control, the same experiment was performed on the PHEMA

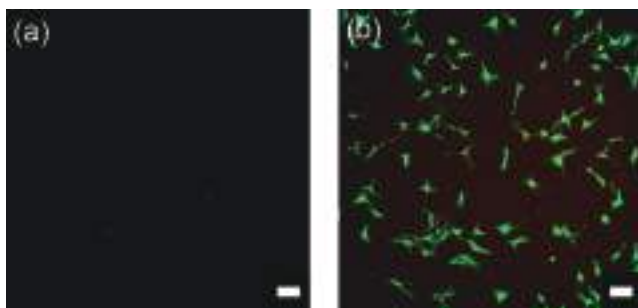


Figure 3. Confocal microscope images of NIH/3T3 cells cultured on PHEMA homopolymer film (a) and peptide/PHEMA hybrid film (b) for 24 h. Living cells were stained by Calcein-AM. Scale bar: 100 μm .

homopolymer film (Figure 3a). Negligible cell attachment is observed on the PHEMA film, suggesting that the hydrophilic surface character suppresses non-specific adsorption of the cells. In contrast, sufficient cell adhesion and well-spreading are observed on the peptide/PHEMA hybrid film. Moreover, most of the attached cells remain viable (green fluorescent cell). These results obviously demonstrate that cell adhesion on the hybrid film that contains RGDS-graft chains is facilitated by integrin-specific interactions.

We next examined the controlled removal of peptide-epitopes from the film surface by photolithographic technique. As we described above, the peptide-graft chain was smoothly cleaved at *ANP* moiety by UV irradiation from PHEMA main chain. By using a photomask for the UV irradiation step, patterns of bioactive peptides can be generated (Figure 4a). Figure 4b shows the confocal microscope image of the RhB-labeled peptide pattern obtained after UV irradiation (365 nm) for 30 min with a photomask and subsequent washing with acidic water (pH 3.0). The irradiated region appears dark indicating site-controlled detachment of the RGDS peptides from the film. Fluorescence intensity of irradiated region decreased by ca. 45% over the non-irradiated one. Likewise, FTIR analysis supports the photocleavage and removal of peptide-grafts from the film. The peak intensity for the amide I (1668 cm^{-1}) in irradiated region, which is normalized with the peak intensity for C=O stretching band of ester (1724 cm^{-1}), reduced almost by half to that in non-irradiated region (Figure S6). Note that residual fluorescence was observed even in the irradiated region. This may be attributed to the entrapment of photocleaved peptide by PHEMA film, which is not removable by washing, although the possibility of an incomplete photolysis cannot be excluded.

The micropatterning of the bioactive peptides is successfully accomplished by locally irradiating the film in the geometry of interest using an appropriate photomask. As shown in Figure 4c, various micropatterns of RGDS-peptides are easily obtained (star, circles, spiral and stripe-micropatterns). To assess the ability of such patterned hybrid film to attach cells selectively, NIH/3T3 cells are seeded on the stripe-patterned film (Figure 4d). Spatially restricted cell adhesion is achieved, namely the NIH/3T3 cells preferentially adhere on the stripes that were not illuminated (Figure 4e). The number of attached cells on the regions containing RGDS-grafts (i.e. red area) is at least 2.5 times higher than that on the illuminated regions (i.e. dark area).

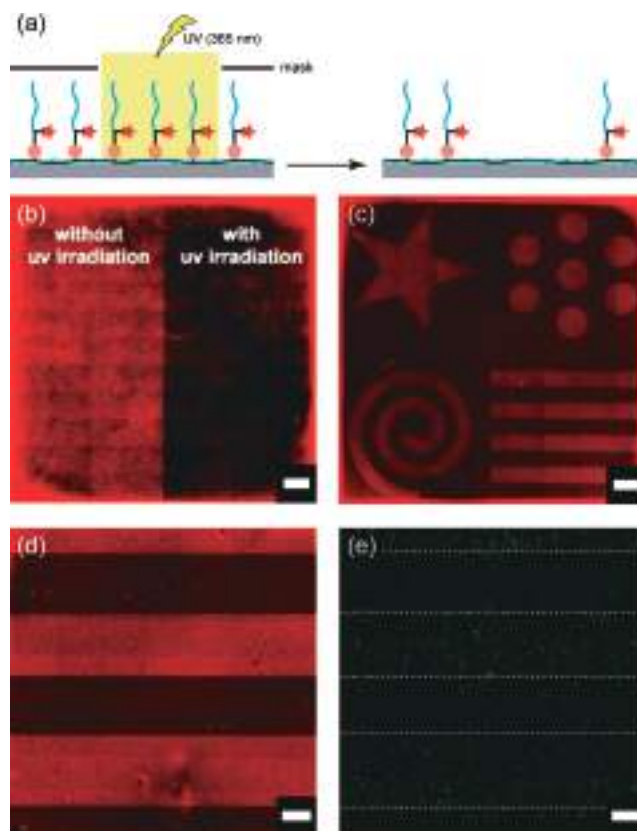


Figure 4. (a) Conceptual scheme for the patterning of RGDS peptide by UV irradiation. (b and c) Confocal microscope images of peptide-patterned PHEMA films prepared by photolithographic technique. (d and e) Spatial control of NIH/3T3 cell adhesion by using stripe-patterned peptide/PHEMA hybrid film. Living cells in image e were stained by Calcein-AM. Scale bar: 500 μm .

In summary, we have demonstrated that a new type of peptide-macromonomer with photolabile *ANP* linker is a convenient and facile tool to introduce bioactivity to conventional polymeric materials through a radical copolymerization and that these bioactive peptides can be cleaved on demand in a designed micropattern by light. Since the density and sequence of peptide chain can be easily manipulated in our method, this photoresponsive peptide-polymer hybrid will enable the fabrication of smart interfaces with tunable bioactivity not only in 2D-film systems described here but also in 3D-hydrogel systems. We believe that this research will open up a new avenue for the design of stimuli-responsive polymer materials with potential in various fields, such as biomedical, controlled self-assembly and degradable polymer materials.

This work was partly supported by Grants-in-Aid for Scientific Research (KAKENHI) (Nos. 17K04994 and 16K05800) from the Japan Society for the Promotion of Science (JSPS), and a MEXT-Supported Program for the Strategic Research Foundation at Private University.

Supporting Information is available on <http://dx.doi.org/10.1246/cl.171235>.

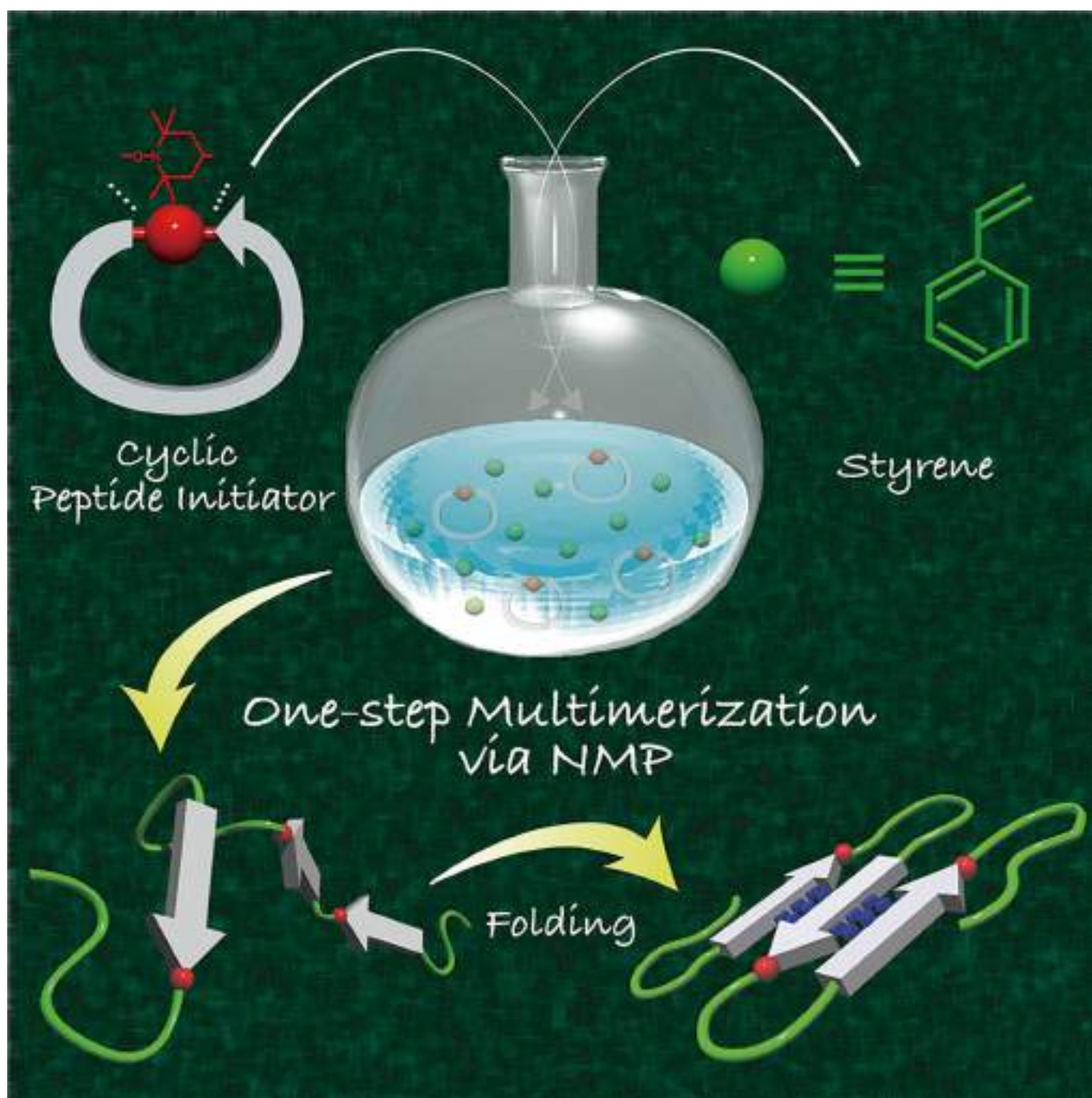
References

- 1 a) W. A. Petka, J. L. Harden, K. P. McGrath, D. Wirtz, D. A. Tirrell, *Science* **1998**, *281*, 389. b) J. D. Hartgerink, E. Beniash, S. I. Stupp, *Science* **2003**, *300*, 625. c) H. A. Lashuel, S. R. LaBrenz, L. Woo, L. C. Serpell, J. W. Kelly, *J. Am. Chem. Soc.* **2000**, *122*, 5262. d) Y. Takahashi, A. Ueno, H. Mihara, *Chem.—Eur. J.* **1998**, *4*, 2475. e) T. Koga, M. Matsuoka, N. Higashi, *J. Am. Chem. Soc.* **2005**, *127*, 17596.
- 2 a) M. D. Pierschbacher, E. Ruoslahti, *Nature* **1984**, *309*, 30. b) F. G. Hopkins, *Biochem. J.* **1921**, *15*, 286. c) T. Ganz, M. E. Selsted, D. Szklarek, S. S. Harwig, K. Daher, D. F. Bainton, R. I. Lehrer, *J. Clin. Invest.* **1985**, *76*, 1427.
- 3 R. B. Merrifield, *J. Am. Chem. Soc.* **1963**, *85*, 2149.
- 4 a) B. Perly, A. Douy, B. Gallot, *Makromol. Chem.* **1976**, *177*, 2569. b) J. M. Smeenk, M. B. J. Otten, J. Thies, D. A. Tirrell, H. G. Stunnenberg, J. C. M. van Hest, *Angew. Chem., Int. Ed.* **2005**, *44*, 1968. c) D. Eckhardt, M. Groenewolt, E. Krause, H. G. Börner, *Chem. Commun.* **2005**, 2814. d) Y. Mei, K. L. Beers, H. C. M. Byrd, D. L. VanderHart, N. R. Washburn, *J. Am. Chem. Soc.* **2004**, *126*, 3472. e) S. Tugulu, P. Silacci, N. Stergiopoulos, H.-A. Klok, *Biomaterials* **2007**, *28*, 2536.
- 5 a) T. Koga, K. Kitamura, N. Higashi, *Chem. Commun.* **2006**, 4897. b) T. Koga, M. Koike, S. Kamiwatari, N. Higashi, *Chem. Lett.* **2011**, *40*, 1244. c) T. Koga, E. Aso, N. Higashi, *Langmuir* **2016**, *32*, 12378.
- 6 T. Koga, S. Kamiwatari, N. Higashi, *Langmuir* **2013**, *29*, 15477.
- 7 S. Nishimura, N. Higashi, T. Koga, *Chem.—Eur. J.* **2017**, *23*, 15050.
- 8 a) T. Koga, K. Taguchi, Y. Kobuke, T. Kinoshita, M. Higuchi, *Chem.—Eur. J.* **2003**, *9*, 1146. b) T. Koga, Y. Teraguchi, N. Higashi, *Trans. Mater. Res. Soc. Jpn.* **2012**, *37*, 533. c) N. Higashi, K. Yasufuku, Y. Matsuo, T. Matsumoto, T. Koga, *Colloid Interface Sci. Commun.* **2014**, *1*, 50.
- 9 E. Ruoslahti, *Annu. Rev. Biochem.* **1988**, *57*, 375.
- 10 a) B. T. Houseman, M. Mrksich, *Biomaterials* **2001**, *22*, 943. b) D. J. Irvine, A. M. Mayes, L. G. Griffith, *Biomacromolecules* **2001**, *2*, 85. c) T. W. Jensen, B.-H. Hu, S. M. Delatore, A. S. Garcia, P. B. Messersmith, W. M. Miller, *J. Am. Chem. Soc.* **2004**, *126*, 15223.
- 11 a) Y. Ohmuro-Matsuyama, Y. Tatsu, *Angew. Chem., Int. Ed.* **2008**, *47*, 7527. b) S. Petersen, J. M. Alonso, A. Specht, P. Duodu, M. Goeldner, A. del Campo, *Angew. Chem., Int. Ed.* **2008**, *47*, 3192.
- 12 a) M. Wirkner, J. M. Alonso, V. Maus, M. Salierno, T. T. Lee, A. J. Garcia, A. del Campo, *Adv. Mater.* **2011**, *23*, 3907. b) S. V. Wegner, O. I. Sentürk, J. P. Spatz, *Sci. Rep.* **2015**, *5*, 18309.
- 13 a) B. B. Brown, D. S. Wagner, H. M. Geysen, *Mol. Diversity* **1995**, *1*, 4. b) C. G. Bochet, *J. Chem. Soc., Perkin Trans. 1* **2002**, 125.
- 14 K. Y. Lee, D. J. Mooney, *Chem. Rev.* **2001**, *101*, 1869.
- 15 T. Miyazawa, E. R. Blout, *J. Am. Chem. Soc.* **1961**, *83*, 712.

■ Synthesis Design

Facile Synthesis of Multiblock Copolymers Containing Sequence-Controlled Peptides and Well-Defined Vinyl Polymers by Nitroxide-Mediated Polymerization

Shin-nosuke Nishimura, Nobuyuki Higashi,* and Tomoyuki Koga*[a]



Abstract: Precisely incorporating a wide range of structural and functional multiblocks along a polymer backbone is a significant challenge in polymer chemistry and offers promising opportunities to design highly ordered materials, including controlled polymer folding. Herein, a facile and versatile strategy for preparing functional multiblock copolymers composed of sequential peptides and well-defined vinyl polymers with a narrow polydispersity is reported. Cyclic oligopeptides have been developed that contain an alkoxyamine bond in the framework. By using this type of cyclic initiator, peptide-containing multiblock copolymers are suc-

cessfully synthesized by nitroxide-mediated polymerization of styrene. To demonstrate the versatility of this method, radical (co)polymerizations were carried out for different monomers (*p*-chlorostyrene, 4-vinylpyridine, and styrene/acrylonitrile) and by three different cyclic peptide initiators with specific amino acid sequences. The resultant multiblock copolymer is foldable through intramolecular interactions between peptide blocks. It is believed that this approach will significantly advance the field of controlled polymer synthesis for complex structures and single-chain folding.

Introduction

Block copolymers are potentially fascinating soft materials in both industrial and biomedical fields. Combining chemically and physically different polymer blocks can form various nano-scaled structures through self-assembly.^[1] Recent dramatic advances in polymer synthesis, especially considerable progress in living radical polymerization techniques,^[2] such as nitroxide-mediated radical polymerization (NMP),^[2a] atom-transfer radical polymerization (ATRP),^[2b,c] and reversible addition fragmentation chain transfer polymerization (RAFT),^[2d] offer opportunities to design well-defined block copolymers with regulated block lengths and narrow dispersities, as well as more complex architectures possessing multiblock and sequence-controlled structures.^[3]

In contrast to such synthetic polymer systems, a living organism system has already accomplished the precise synthesis of complex and functional biopolymers with perfectly regulated sequences, such as proteins. Their controlled sequences (i.e., primary structures) enable folding of a single peptide chain into precisely defined three-dimensional high-order structures, which play a key role in defining their excellent functions and unique nature. Applying the structural and functional principles of biopolymers to a synthetic macromolecular system is of great interest, especially for designing polymer folding/self-assembly systems.^[4]

Solid-phase peptide synthesis (SPPS) allows monodispersed oligopeptides to be prepared with perfectly controlled chain lengths and monomer sequences.^[5] In addition, major secondary structural motifs with well-regulated shapes and sizes, such as α helices and β sheets, can be designed intrinsically by the primary sequence of amino acids. SPPS is a time-consuming method and is unsuited to synthesize high-molecular-weight polypeptides. However, the resultant peptides are

useful both as structuring and biofunctional units, even with relatively short chain lengths of $n = 2-4$.^[6] Thus, employing artificial peptides as one of the block segments (i.e., hybridization of structurally and functionally controlled peptides and conventional synthetic polymers) is a very attractive strategy for constructing new classes of polymeric materials with tailored characters and structures.

Various peptide-polymer hybrids have been reported to fabricate biofunctional nanostructured materials.^[7] However, the majority of these hybrid block polymers are simple AB-type diblock and ABA- or ABC-type triblock architectures. Despite their fascinating molecular structures, in which multiple peptide blocks are specifically distributed along the polymer backbone, the preparation of multiblock hybrids is limited due to the lack of efficient synthetic methodologies.

A general strategy for the synthesis of such multiblock hybrids is the covalent connection of preprepared peptide and polymer blocks through polycondensation or polyaddition reactions.^[8] Because this method limits the applicability of synthetic polymer blocks (i.e., reactive functional groups are necessary at both chain ends), α,ω -telechelic polyethers have been employed in most cases.^[8a,b] Another approach to combine a peptide and a polymer block has recently been reported by exploiting click chemistry, which can be applied to vinyl polymers.^[9] However, both of these approaches require precise transformations of the chain ends of each employed block to the appropriate reactive groups before multimerization. In addition, the intrinsic restriction of consecutive macromolecular coupling leads to a nonquantitative reaction that yields unreacted blocks. Therefore, purification steps are usually required to isolate the pure objective polymer. Unfortunately, these experimental procedures often include time-consuming work, undesirable impurities, and limitations on multiblock preparation with relatively large polymer blocks. Consequently, developing a new concept to synthesize multiblock peptide-polymer hybrids would circumvent such difficulties and facilitate the field of controlled polymer synthesis and single-chain folding.^[10]

Herein, we report, for the first time, a novel synthetic method that provides functional multiblock copolymers composed of alternately aligned sequence-ordered peptides and well-controlled vinyl polymers in a facile manner. The newly

[a] S.-n. Nishimura, Prof. Dr. N. Higashi, Prof. Dr. T. Koga
Department of Molecular Chemistry & Biochemistry
Faculty of Science & Engineering, Doshisha University
Kyotanabe, Kyoto 610-0321 (Japan)
E-mail: nhigashi@mail.doshisha.ac.jp
tkoga@mail.doshisha.ac.jp

Supporting information for this article can be found under:
<https://doi.org/10.1002/chem.201703655>.

prepared cyclic oligopeptides contain a thermally labile alkoxyamine bond in the framework as a macroinitiator for NMP. Radical polymerization in the homogeneous liquid phase by this type of initiator enables multiple peptide blocks to be directly inserted into the vinyl polymer backbone during polymerization. To demonstrate the versatility of this approach, various multiblock hybrids are constructed from four different (co)monomers (aromatic vinyl monomer family) by three different cyclic peptide initiators. This universal method not only allows the facile synthesis of functional multiblock copolymers, but also provides more flexibility to complex polymer design.

Results and Discussion

The synthesis of multiblock copolymers containing sequence-controlled peptides and vinyl polymers was carried out through an NMP reaction in a facile manner (Figure 1). In the initial NMP system,^[2a] a nitroxide radical, such as 2,2,6,6-tetramethyl piperidine 1-oxyl (TEMPO), was used as an additive to reversibly terminate the growing polymer chains, which were initiated by a separate initiator, such as benzoyl peroxide. The resultant thermally labile alkoxyamine bond acts as a “dormant species”, and consequently, can control radical polymerization. Hawker et al. successfully developed various unimolecular and universal NMP initiators, which produced both initiating and stable radicals from a single molecule.^[11] In our system, the thermally promoted homolysis of the alkoxyamine bond induces ring opening of the cyclic peptide and generates a reactive carbon radical and a nitroxide radical simultaneously at the N and C termini, respectively (Figure 1). The reactive radical allows the chain to be extended in the presence of monomers from the peptide terminus. On the other hand, the stable nitroxide at the C terminus cannot initiate polymerization, but should trap the intermediate growing polymer radical. As a

result, the multiblock architecture would be generated through the reversible capping reaction.

The objective cyclic peptide initiators were successfully prepared by SPPS by using 9-fluorenylmethoxycarbonyl (Fmoc) chemistry. First, the TEMPO-containing alkoxyamine derivative, Fmoc-NH-TEMPO-COOH, was newly designed and synthesized for Fmoc-based SPPS. We employed a commercially available 4-amino-TEMPO as a starting compound, and the amino group was protected with the Fmoc group through treatment with a solution of Fmoc-succinimide in dichloromethane (Figure S1 in the Supporting Information). The atom-transfer radical coupling reaction^[12] between Fmoc-NH-TEMPO and *tert*-butyl 2-bromoisobutyrate was then carried out in the presence of Cu⁰ in methanol. The resulting Fmoc-NH-TEMPO-COOtBu was purified by column chromatography on silica gel and characterized by ¹H NMR spectroscopy (Figure S2 in the Supporting Information). The desired Fmoc-NH-TEMPO-COOH was finally obtained by removing the *tert*-butyl group in a solution of trifluoroacetic acid (TFA)/CH₂Cl₂/triisopropylsilane (TIS; Figure S3 in the Supporting Information).

A series of cyclic peptides 1–3 were subsequently synthesized by conventional SPPS. All peptides contained 1) a tertiary TEMPO derivative for controlled NMP, 2) a single aspartic acid (Asp) residue for the cyclization reaction, 3) flexible diethylene glycol (deg) spacers, and 4) a specifically designed amino acid sequence ((Leu)₄ (1), (Leu-Gly)₂ (2), and [Glu(OBzl)]₄ (3; OBzl = benzyl ester)). The cyclization reaction proceeded completely on the resin through condensation between the N terminus and the Asp side chain. As a representative example, MALDI-TOF MS analyses of linear and cyclic [Asp-deg-(Leu)₄-deg-TEMPO] (1) demonstrate that the difference in molecular weight between the two is $\Delta m/z$ 18 (Figure S4 in the Supporting Information). Thus, cyclic peptide initiators 1–3 were successfully characterized by MS and ¹H NMR spectroscopy analyses (Figures S4–S6 in the Supporting Information).

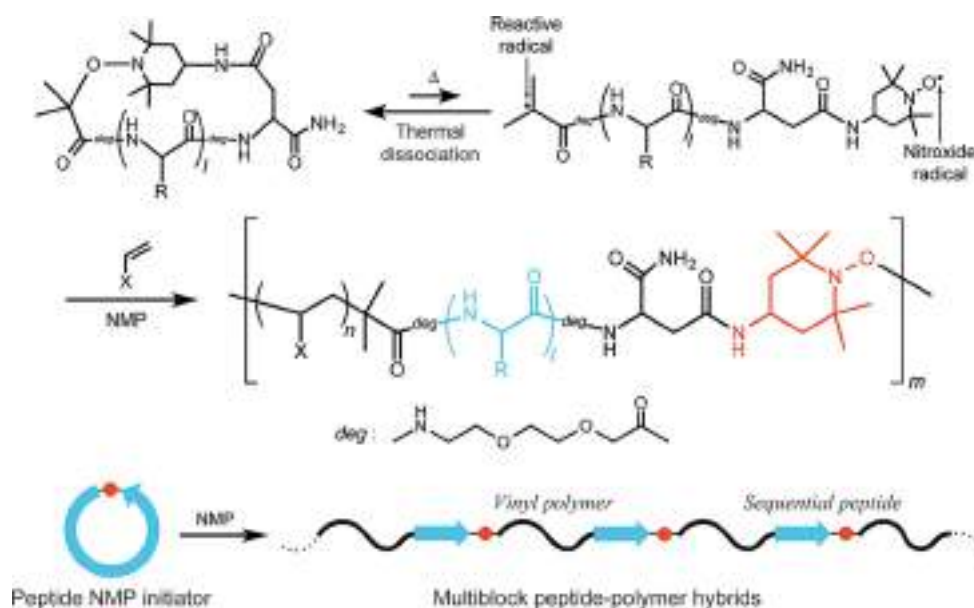


Figure 1. Conceptual scheme for the synthesis of multiblock peptide-polymer hybrids through NMP.

Initially, we used cyclic peptide **1** and styrene (St) as the initiator and monomer for solution polymerization, respectively, due to their easy characterization and the well-known suitability of St for NMP. Polymerization was conducted in DMF at 110 °C. The molecular weights and polydispersity indexes (\mathcal{D}) of the products obtained after polymerization for 18 (**P1**), 36 (**P2**), 70 (**P3**), and 140 h (**P4**) were analyzed by size-exclusion chro-

matography (SEC). Table 1 summarizes the results (**P1–P4**). The SEC traces of all polymers are symmetrically unimodal and show a clear shift toward high molecular weights with conversion. However, the number-average molecular weights (M_n) of these polymers deviate from the calculated theoretical values ($M_{n,Theor}$) based on monomer conversion assuming one peptide segment per chain (e.g., for **P2** (Figure 2B, blue line); $M_n =$

Polymer	Initiator	Monomer ^[a]	Peptide sequence	Polymerization		Conversion [%]	$M_{n,Theor}$ ^[b] [g mol ⁻¹]	Before fragmentation			After fragmentation		
				t [h]	T [°C]			M_n [g mol ⁻¹]	M_p ^[c] [g mol ⁻¹]	\mathcal{D} (M_w/M_n)	M_n [g mol ⁻¹]	M_p ^[c] [g mol ⁻¹]	\mathcal{D} (M_w/M_n)
P1	1	St	Leu ₄	18	110	4.4	1560	4340 ^[d]	4430	1.41	1690 ^[d]	1440	1.27
P2	1	St	Leu ₄	36	110	14.8	2640	9600 ^[d]	14 500	2.08	3100 ^[d]	3300	1.15
P3	1	St	Leu ₄	70	110	34.2	4660	10 800 ^[d]	18 900	2.31	4500 ^[d]	6700	1.22
P4	1	St	Leu ₄	140	110	72.5	8650	21 300 ^[d]	27 500	1.90	8800 ^[d]	9500	1.18
P5	2	St	(Leu-Gly) ₂	48	110	58.6	7060	15 800 ^[d]	21 600	2.46	9900 ^[d]	13 100	1.42
P6	3	St	[Glu(OBzl)] ₄	48	110	65.9	8360	22 700 ^[d]	26 000	1.99	11 500 ^[d]	16 400	1.33
P7	1	<i>p</i> -ClSt	Leu ₄	18	110	18.3	3630	9800 ^[d]	13 500	1.86	3300 ^[d]	3700	1.23
P8	1	4VP	Leu ₄	48	120	42.6	5580	13 300 ^[e]	17 800	2.58	4500 ^[e]	6800	1.16
P9	1	St/AN (4/1)	Leu ₄	18	120	–	–	23 700 ^[e]	35 400	2.05	9400 ^[e]	12 000	1.13

[a] *p*-ClSt = *p*-chlorostyrene, 4VP = 4-vinylpyridine, AN = acrylonitrile. [b] Theoretical number-average molecular weight of the fragmented polymer calculated by using the following equation: $M_{n,Theor} = [\text{monomer}]/[\text{initiator}] \times \text{conversion} \times \text{molecular weight of monomer} + \text{molecular weight of initiator}$. [c] Molecular weight at the top of the peak in the SEC curve. [d] Number-average molecular weight calculated by SEC analysis (PSt standard) in THF at 40 °C. [e] Number-average molecular weight calculated by SEC analysis (PSt standard) in DMF (containing 10 mM LiBr) at 40 °C.

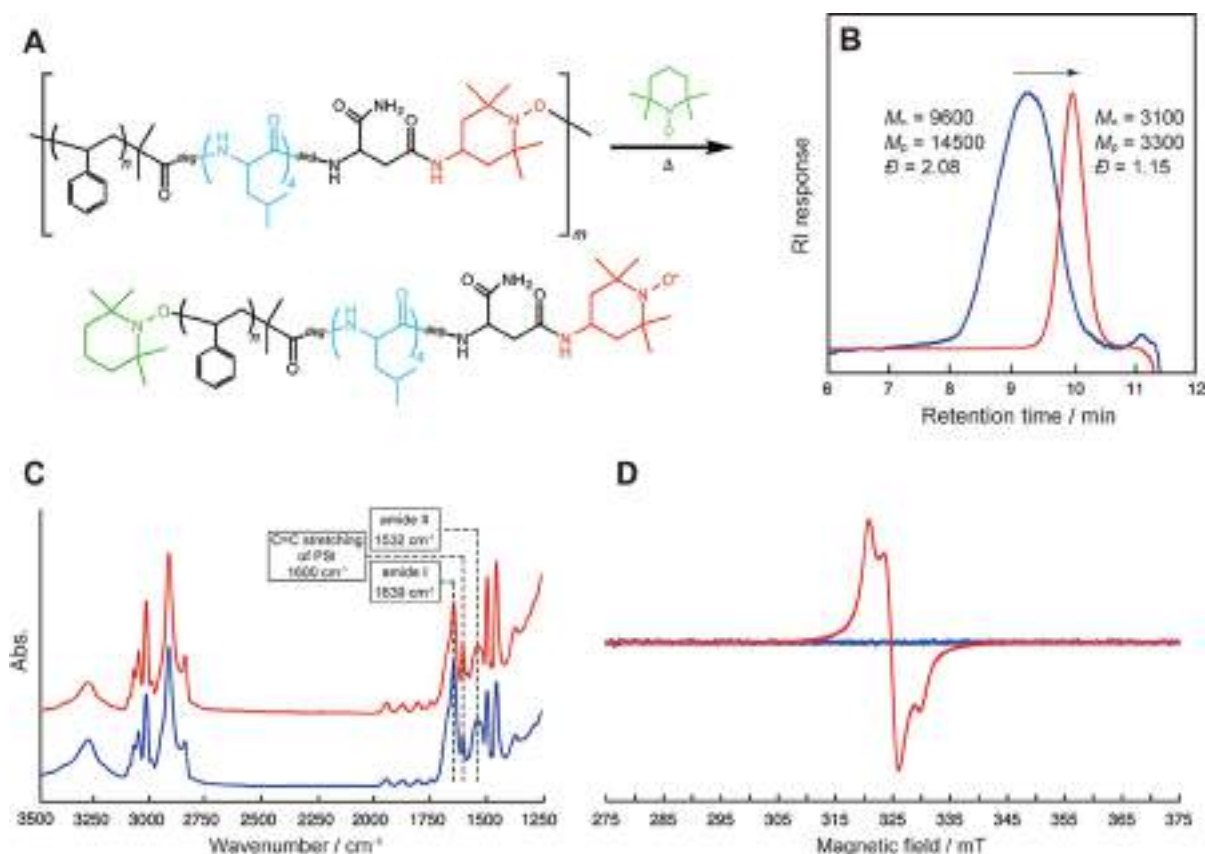


Figure 2. Fragmentation experiments of multiblock copolymer. A) Thermal treatment (110 °C, 6 h) of **P2** in the presence of excess TEMPO causes fragmentation from multi- to diblock architectures through a radical crossover reaction. B) SEC traces of multiblock **P2** obtained before (blue) and after (red) fragmentation in THF at 40 °C. RI = refractive index. C) Transmission FTIR spectra of **P2** (blue) and fragmented **P2** (red) cast from a solution in CHCl₃ onto a CaF₂ plate. D) Electron spin resonance (ESR) spectra of **P2** (blue) and fragmented **P2** (red) in CDCl₃ at –196 °C.

9600 g mol⁻¹, $M_{n,Theor} = 2640$ g mol⁻¹) and the polydispersities are relatively broad ($\mathcal{D} \approx 2.0$). Both FTIR and ¹H NMR spectroscopy results confirm the presence of the (Leu)₄ segment in the polystyrene (PSt)-based polymer. The FTIR spectrum (Figure 2C, blue line) shows strong bands at $\tilde{\nu} = 1639$ and 1532 cm⁻¹, which are characteristic of amide I and II, respectively, as well as the C=C stretching band of PSt at $\tilde{\nu} = 1600$ cm⁻¹. These results indicate that ring opening of initiator **1** and subsequent NMP form the multiblock structure.

Fragmentation experiments by using radical crossover reactions^[13] provide more definitive evidence. If the obtained polymer has a multiblock structure, thermally labile alkoxyamine bonds are incorporated into the main chain at multiple points, reflecting the block number. In this case, thermal treatment in the presence of a stable free radical should cause fragmentation of the polymer chain by a radical exchange reaction, generating a diblock structure (Figure 2A). Fragmentation reactions of **P1–P4** were performed in the presence of excess TEMPO (>100 equiv) in *N*-methyl-2-pyrrolidone at 110 °C for 6 h, and the resultant polymers were isolated by a reprecipitation method. SEC analyses show that the molecular weights of the obtained polymers substantially decrease and the dispersities become narrower than those of the corresponding original polymers for **P1–P4** (Figure 2B, red lines, and Figure S7 in the Supporting Information). For example, the value of M_n of **P2** changes from 9600 to about 3000 g mol⁻¹ ($\mathcal{D} = 1.15$) after such treatment (Table 1). On the other hand, neither the FTIR nor ¹H NMR spectra change significantly before and after fragmentation (Figure 2C and Figure S8 in the Supporting Information), that is, the peak ratio of the signals derived from PSt to that from (Leu)₄ remains virtually unchanged in both analyses, which indicates cleavage of the polymer chain without a compositional change. Of course, such fragmentation does not

occur for homopolymer (PSt) prepared by using 2,2'-azobisisobutyronitrile (AIBN); M_n (≈ 22700 g mol⁻¹) and \mathcal{D} remain the same after treatment. These data strongly support the proposed multiblock structure and its fragmentation mechanism from multi- to diblock.

Further evidence is obtained from ESR analysis, which shows that the ESR signal is clearly observed for a fragmented polymer due to the stable TEMPO radical generated at the diblock polymer end (Figure 2D). Notably, the ESR signal cannot be detected for the original multiblock copolymer, that is, the concentration of the stable radical is below the detection limit. This may be attributed to the high molecular weight and/or partial capping of the end TEMPO group by slightly generated styrenyl radical, although the possibility of a macrocyclic multiblock architecture cannot be excluded.

Most importantly, these fragmentation experiments reveal the well-controlled structure of the PSt blocks. Figure 3A shows the SEC chromatograms of the fragmented diblock polymers obtained for **P1** (18 h of polymerization)–**P4** (140 h of polymerization). The SEC results of all polymers are unimodal, even after fragmentation. Furthermore, the shift in the RI peaks to a shorter retention time at different time periods demonstrates that the molecular weight increases with conversion (Table 1). Figure 3B plots M_n and \mathcal{D} of the fragmented polymers as a function of monomer conversion. The calculated values of $M_{n,Theor}$ are also included as a solid line. The linearity of the plot of M_n versus conversion clearly shows that NMP proceeds in a well-controlled living manner. In addition, the observed M_n values of the fragmented polymers agree well with those of $M_{n,Theor}$ and the dispersities are below 1.3 throughout the polymerization. Based on the ratio of the molecular weight of the original polymer to the corresponding fragmented one (Table 1), it seems that the multiblock copoly-

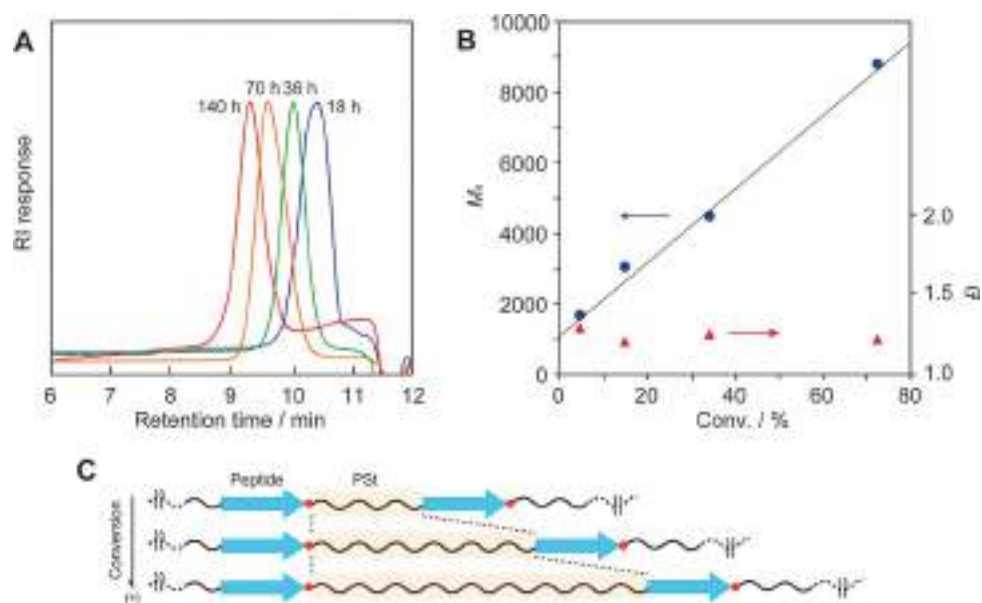


Figure 3. A) SEC traces (THF, 40 °C) of the fragmented block copolymers obtained for **P1–P4**. B) Plots of M_n (blue circles) and \mathcal{D} (red triangles) as a function of conversion. The solid line represents the theoretical M_n (see footnote [b] in Table 1). C) Schematic model of the multiblock architectures ((Leu)₄-b-PSt)_m. The PSt block length is precisely controlled by conversion, which enables a specific arrangement of peptide blocks in a single polymer chain.

mers, $[(\text{Leu})_4\text{-}b\text{-PSt}]_m$, contain approximately three repeats ($m \approx 3$) of the $(\text{Leu})_4\text{-}b\text{-PSt}$ diblock unit. Thus, it is concluded that this new method enables multiple peptide blocks to be incorporated directly into a well-defined PSt backbone with a specific arrangement in the course of solution polymerization.

We anticipate that this unique structural feature will facilitate single-chain folding of the polymer in a dilute organic solvent through both multiple hydrogen bonds among the oligopeptide blocks and the phase separation behavior of the component blocks. Herein, we chose multiblock **P4** with a long PSt block length of about 70–80-mer ($M_n(\text{fragment}) = 8800 \text{ g mol}^{-1}$, $D(\text{fragment}) = 1.18$) to study the folding behavior in toluene, which is a good solvent for the PSt block, but a poor solvent for the peptide. Dynamic light scattering (DLS) analysis of **P4** in toluene (0.1 wt%) at 20 °C reveals a hydrodynamic diameter of about 23 nm (Figure S9 in the Supporting Information). The tapping-mode AFM image of **P4** on mica deposited from a solution in toluene (0.1 wt%) clearly shows nanospheres with relatively uniform diameters of about 20 nm (Figure 4A). It should be noted that the height of the nanosphere (ca. 2–3 nm) observed by AFM cross-section analysis is quite small compared with the width (Figure S10 in the Supporting Infor-

mation). It is likely that the nanosphere collapses vertically during the drying process. To investigate the secondary structure of the peptide blocks in the nanosphere, the FTIR spectrum was measured in solution ($[\text{D}_8]\text{toluene}$, 0.1 wt%). We focused mainly on the band assigned to amide I of the peptide chain. Characteristic absorptions of the amide I bands are observed at $\tilde{\nu} = 1636$, 1678 (shoulder), and 1694 cm^{-1} (shoulder) (Figure 4B). These results demonstrate that the $(\text{Leu})_4$ blocks of **P4** form a primarily antiparallel β -sheet structure,^[14] although minor random-coil components (shoulder at $\tilde{\nu} = 1678 \text{ cm}^{-1}$) exist. Considering such a conformation and the molecular length of each block (that is, β -sheet $(\text{Leu})_4$ (1.4 nm) and average extended length of PSt (ca. 20 nm for 80-mer)), the observed nanosphere seems to be a flower-like unimer micelle with a β -sheet core and a PSt corona formed by folding through intramolecular hydrogen bonds among the peptide blocks specifically aligned in the polymer chain.

Variable-temperature ^1H NMR spectroscopy also confirms that the β -sheet peptide block is confined to the immobile core and the PSt corona is exposed to the solvent. The methine signal of the peptide main chain ($\delta \approx 3.9 \text{ ppm}$) is barely visible at 20–60 °C, but is clearly observed above 60 °C (Fig-

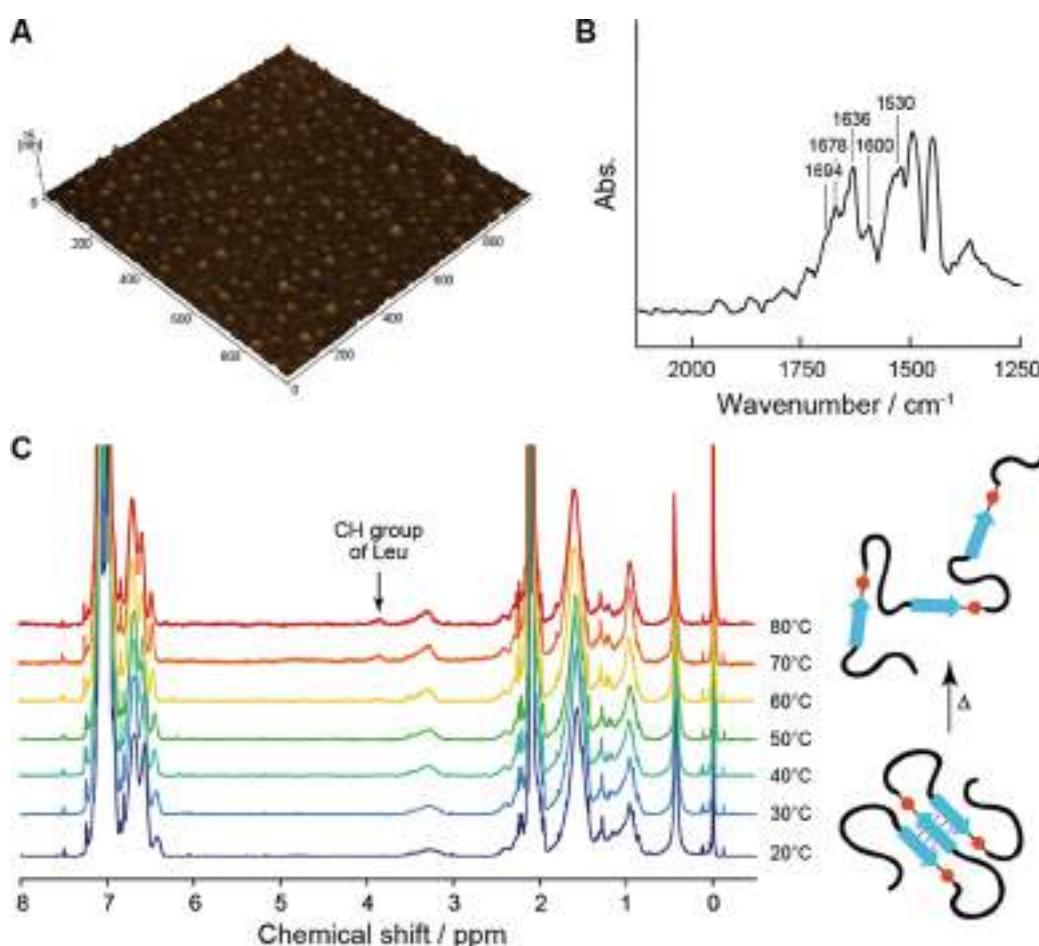


Figure 4. Folding behavior of multiblock **P4** in toluene. A) Tapping-mode AFM image of **P4** on mica deposited from a solution in toluene (0.1 wt%; $\approx 20^\circ\text{C}$). B) Transmission FTIR spectrum of **P4** in $[\text{D}_8]\text{toluene}$ (0.1 wt%) at room temperature ($\approx 20^\circ\text{C}$). C) Temperature dependence of the ^1H NMR spectra (500 MHz) of **P4** in $[\text{D}_8]\text{toluene}$ (0.1 wt%, 20–80 °C), showing folding into the unimer micelle with an immobile peptide core and the PSt corona exposed to a solvent below 60 °C (right).

ure 4C), which indicates increased core mobility upon increasing temperature. This observation is probably due to breaking of hydrogen bonds similar to the denaturation process of proteins. In addition, the ^1H NMR chemical shift from the methyl group of the Leu residues is sensitive to the concentration of **P4**; a downfield shift is observed for the methyl signal from $\delta = 0.5$ (0.1) to 1.1 ppm (1.0 wt%), together with a decrease in the integration (Figure S11 in the Supporting Information).

Because the chemical shifts of the protein methyl groups, such as Ala, Val, and Leu methyl groups, are strongly affected by the ring current, rotameric type, dihedral angles, and so forth,^[15] they provide useful information about the structure and dynamics of a protein. In our case, the self-assembly of **P4** seems to occur intermolecularly in a concentrated solution (1 wt%), rather than through intramolecular folding observed under dilute conditions, which causes a significant change in the local environments of the Leu residues, such as conformation and solvent accessibility. We previously reported a similar ^1H NMR chemical shift of Leu residues due to the self-assembly of the PSt-*b*-(Leu)₄-*b*-poly(ethylene glycol) triblock architecture in [D₈]toluene.^[79] To test the versatility of our synthetic approach, other multiblock copolymers that contain different sequential peptide and vinyl polymer blocks were targeted. We conducted polymerizations of St by using cyclic initiators **2** and **3** with (Leu-Gly)₂ and [Glu(OBzl)]₄ sequences, respectively. The resultant polymers (**P5** and **P6**) were characterized by SEC, FTIR, and NMR spectroscopy in the same manner as that described above (Table 1 and Figures S12 and S13 in the Supporting Information). In both cases, well-defined peptide/PSt multiblock copolymers of $M_n \approx 16\,000$ (**P5**) and $\approx 23\,000$ g mol⁻¹ (**P6**) are successfully obtained in a facile manner. These polymers are cleavable by a thermal treatment (under excess TEMPO), and the fragmented polymers exhibit M_n values close to those of the theoretical values as well as relatively low dispersities ($\mathcal{D} = 1.3\text{--}1.4$). Thus, this method can manipulate the desired peptide sequence to yield a functional multiblock copolymer. Moreover, the benzyl ester group of the Glu residues (used in this study as an example) can be cleaved easily into the carboxylic acid group and used for further site-specific modifications of the polymer chain.

To further demonstrate the enormous potential of this method, we also performed polymerization for three additional aromatic (co)monomers (*p*-ClSt, 4VP, and St/AN), and characterized the obtained polymers. In all cases, the synthesis of various multiblock copolymers (**P7**–**P9**) was successful (Table 1 and Figures S14–S16 in the Supporting Information). The dispersities of the three different vinyl polymer blocks remain satisfyingly low (i.e., between 1.13 and 1.23). Specifically, this cyclic peptide initiator is applicable to the copolymerization of St and AN. The St/AN copolymer is widely used as a general-purpose plastic with a high mechanical strength, chemical resistance, and rigidity. It is generally difficult to polymerize acrylates, including AN in a well-controlled living manner by conventional TEMPO-based NMP. However, it has been reported that their copolymerization with St (major component) proceeds in a living manner.^[16] In our system, the existence of the AN unit as a comonomer in vinyl polymer blocks is confirmed

by both FTIR and ^1H NMR spectroscopy; the characteristic C≡N stretching band at $\tilde{\nu} = 2240$ cm⁻¹ and the ^1H signal at $\delta \approx 3.3$ ppm (corresponding to $-\text{CH}(\text{C}\equiv\text{N})-$; Figure S16 in the Supporting Information). Fragmentation of **P9** yields a unimodal copolymer of $M_n = 9400$ g mol⁻¹ and $\mathcal{D} = 1.13$ ($F_{\text{St}} = 0.89$), which demonstrates the controlled copolymerization of St/AN.

Conclusion

NMP of various vinyl monomers by cyclic oligopeptides containing alkoxyamine bonds in the frames produce various types of well-defined multiblock peptide-polymer hybrids. To the best of our knowledge, this approach is the first example of a peptide-containing multiblock copolymer synthesis through a chain polymerization mechanism. This new method allows polymers with a complex primary structure to be readily synthesized without serious purification steps. However, a more important point is the versatility of this system, as demonstrated by the success of three examples, with easy manipulation of the peptide sequence, applicability to various monomers, and precise control over the block length with a narrow dispersity. We believe that the findings presented herein will open up a new avenue for the design of complex and functional macromolecular architectures with potential in various fields, such as nanostructured materials, degradable polymers,^[17] and single-chain folding.

Experimental Section

Full experimental details (synthesis and characterization of various compounds used herein) are available in the Supporting Information.

Materials

Solvents of analytical grade were used unless otherwise stated. DMF, *N*-methyl-2-pyrrolidone, methanol, TFA, THF, dichloromethane, toluene, diethyl ether, hexane, ethyl acetate, triethylamine (TEA), piperidine, St, sodium hydroxide, hydroquinone, AIBN, anhydrous sodium sulfate, [D₆]DMSO, CDCl₃, and [D₈]toluene were purchased from Nacalai Tesque. DMF was used after purification by distillation. Tetrakis(triphenylphosphine)palladium(0), phenylsilane, TIS, TEMPO, 4-amino-TEMPO, *tert*-butyl 2-bromoisobutyrate, copper(II) triflate, *p*-ClSt, 4VP, and AN were purchased from Tokyo Chemical Industry. LiBr, Cu⁰ (99.9%, $\phi = 75$ μm), *N,N,N',N',N''*-pentamethyldiethylenetriamine (PMDETA), *N,N'*-diisopropyl carbodiimide (DIPC), ethylenediaminetetraacetic acid disodium dihydrate (EDTA), and *N*-(9-fluorenylmethoxycarbonyloxy)succinimide (Fmoc-OSu) were purchased from Wako Pure Chemical. Fmoc-L-Leu, Fmoc-Gly, Fmoc-L-Glu-γ-benzyl ester (Fmoc-L-Glu(OBzl)), Fmoc-L-Asp-β-allyl ester (Fmoc-L-Asp(OAll)), Fmoc-NH-SAL MBHA resin (resin loading 0.67 mmol g⁻¹), and anhydrous 1-hydroxybenzotriazole (HOBt) were purchased from Watanabe Chemical Industries. 2,5-Dihydroxybenzoic acid (DHBA) was purchased from Sigma Aldrich. Fmoc-8-amino-3,6-dioxaoctanoic acid (Fmoc-deg-COOH) was purchased from Combi-Blocks. St was purified by being passed through activated alumina prior to use. 4VP, *p*-ClSt, and AN were distilled in the presence of hydroquinone to remove inhibitors prior to use; other compounds were used as received.

Measurements

^1H NMR spectra were acquired by using a JEOL JNM-ECA500 (JEOL Resonance) spectrometer (500 MHz). ESR spectra were obtained by using a JEOL JET-TE200 spectrometer. The values of M_n and \mathcal{D} of the block copolymers were determined by SEC on a JASCO LC-net II/AD instrument (JASCO Ltd.) equipped with a RI detector. Block copolymers **P1–P7** were analyzed in THF (flow rate: 1 mL min^{-1} , temperature: 40°C , column: GF-710F), and **P8** and **P9** were analyzed in DMF (containing 10 mM LiBr ; flow rate: 0.6 mL min^{-1} , temperature: 40°C , column: TSKgel α -4000). PSt was purchased from GL Sciences Inc. and used as the calibration standards. Direct analysis in real-time MS (DART MS) analysis was carried out on a DART-SVP spectrometer (Ionsense Inc.). MALDI-TOF MS analyses were carried out on an Autoflex speed instrument (Blaker Daltonics) by using DHBA as a matrix. Transmittance FTIR spectra were measured with a Nexus 470 (Thermo Nicolet Co.) spectrometer equipped with a mercury–cadmium–tellurium (MCT) detector (resolution: 4 cm^{-1} , number of scans: 256). AFM images were collected on a SPM9700 microscope (Shimadzu Co.) DLS measurements were performed on a DLS 7000 spectrometer (Otsuka Electric Ltd.) equipped with a He–Ne laser (632.8 nm). The sample was filtered through a Cosmonice filter (Nacalai Tesque, pore size: $0.45\text{ }\mu\text{m}$) to remove dust particles in solution prior to DLS measurements.

Synthesis of cyclic peptide NMP initiators

Cyclic peptide initiators (**1**, **2**, and **3**) used herein were prepared by SPPS by using Fmoc chemistry. The target sequences (linear peptides) were constructed on a Fmoc-NH-SAL MBHA resin by using Fmoc amino acid derivatives (Fmoc-L-Leu, Fmoc-Gly, Fmoc-L-Glu(OBzl), and Fmoc-L-Asp(OAll)), Fmoc-deg-COOH, Fmoc-NH-TEMPO-COOH (3 equiv), HOBT (3 equiv), and DIPC (3 equiv) in DMF for coupling, and piperidine (20 vol%)/DMF for Fmoc removal. De-protection of the allyl group of the Asp residue was carried out on resin through treatment with tetrakis(triphenylphosphine)palladium(0) (0.1 equiv) and phenylsilane (10 equiv) in CH_2Cl_2 for 3 h at room temperature under a N_2 atmosphere. Cyclization reactions were then carried out on the resin in DMF for 6 h together with HOBT (3 equiv) and DIPC (3 equiv). After cyclization, these peptides were cleaved from the resin by treatment with TFA/ CH_2Cl_2 /TIS (v/v/v 8.5/1/0.5) for 4 h. The obtained cyclic peptides were purified by repeated precipitation from a DMF/diethyl ether system, and subsequently identified by MALDI-TOF MS and ^1H NMR spectroscopy analyses.

General method to synthesize multiblock copolymers

In a typical multiblock copolymer synthesis, the vinyl monomer (St, *p*-ClSt, or 4VP; 1.0 mmol) and cyclic peptide initiator (**1**, **2**, or **3**; 0.010 mmol) were dissolved in DMF. The solutions were poured into a glass test tube at a constant monomer concentration of 6 M . The solutions were deoxygenated by three freeze–pump–thaw cycles under dry N_2 . Then the reaction mixtures were placed in a preheated oil bath at 110 or 120°C to initiate polymerization. After polymerization (18–140 h), the reaction tubes were removed from the oil bath, rapidly cooled in liquid N_2 , and exposed to ambient air to stop the polymerization. The resulting polymers were precipitated by dropping the polymer solutions into a large excess of methanol (or diethyl ether for **P8**). After centrifugation, the multiblock copolymers were further purified by a reprecipitation method from the DMF/methanol (or diethyl ether) system. The chemical structures and molecular weights of the multiblock co-

polymers were evaluated by ^1H NMR spectroscopy, FTIR, and SEC analyses.

Fragmentation of multiblock copolymers

In a typical fragmentation experiment, the multiblock copolymer **P2** (10.0 mg , $1.04\text{ }\mu\text{mol}$) and TEMPO (40.0 mg , $256\text{ }\mu\text{mol}$) were initially dissolved in *N*-methyl-2-pyrrolidone ($100\text{ }\mu\text{L}$), and the solution was poured into a glass test tube. The solution was deoxygenated by three freeze–pump–thaw cycles under dry N_2 . The fragmentation reaction was then performed in a preheated oil bath at 110°C for 6 h. The fragmented polymer was purified by repeated precipitation in methanol and dried to give a pale yellow powder. The molecular weights and \mathcal{D} values were evaluated by SEC, whereas the structures were analyzed by FTIR, ESR, and ^1H NMR spectroscopy. Fragmentations of other multiblock copolymers were conducted in a similar manner.

Characterization of the folding behavior

The folding behavior of the multiblock copolymer, $[(\text{Leu})_4\text{-b-PSt}]_m$, in toluene was characterized by a variety of techniques, including DLS, FTIR, ^1H NMR spectroscopy, and AFM analyses. DLS measurements of the multiblock copolymer were performed in toluene (0.1 wt%) at 20°C . Scattering light from the sample was analyzed at a 30° angle from the incident light. The non-negatively constrained least-squares (NNLS) method was used for the correlation analysis to obtain the diameter probability distribution functions. The transmittance FTIR spectra were measured in $[\text{D}_8]\text{toluene}$ (0.1 wt%) and obtained by subtracting the spectrum of the solvent ($[\text{D}_8]\text{toluene}$) from that measured. AFM images were collected at ambient temperature in tapping mode by using a silicon tip (tip radius $< 12\text{ nm}$). An aliquot (ca. $10\text{ }\mu\text{L}$) of the multiblock copolymer in toluene (0.1 wt%) was placed on freshly cleaved mica. After adsorption for 2 s, excess solution was removed by absorption onto filter paper. The scanning speed was at a line frequency of 1 Hz, and the original images were sampled at a resolution of 1024×1024 points.

Acknowledgements

This work was partly supported by Grants-in-Aid for Scientific Research (KAKENHI; nos. 17K04994 and 16K05800) from the Japan Society for the Promotion of Science (JSPS), and a MEXT-Supported Program for the Strategic Research Foundation at Private University.

Conflict of interest

The authors declare no conflict of interest.

Keywords: block copolymers · peptides · polymerization · self-assembly · synthesis design

- [1] a) L. Zhang, A. Eisenberg, *Science* **1995**, *268*, 1728–1731; b) S. I. Stupp, V. LeBonheur, K. Walker, L. S. Li, K. E. Huggins, M. Keser, A. Amstutz, *Science* **1997**, *276*, 384–389; c) J. J. L. M. Cornelissen, M. Fischer, N. A. J. M. Sommerdijk, R. J. M. Nolte, *Science* **1998**, *280*, 1427–1430; d) H.-A. Klok, S. Lecommandoux, *Adv. Mater.* **2001**, *13*, 1217–1229; e) H. Cui, Z. Chen, S. Zhong, K. L. Wooley, D. J. Pochan, *Science* **2007**, *317*, 647–650; f) F. H.

- Schacher, R. A. Rupar, I. Manners, *Angew. Chem. Int. Ed.* **2012**, *51*, 7898–7921; *Angew. Chem.* **2012**, *124*, 8020–8044.
- [2] a) M. Georges, R. P. N. Veregin, P. M. Kazmaier, G. K. Hamer, *Macromolecules* **1993**, *26*, 2987–2988; b) K. Matyjaszewski, J. Xia, *Chem. Rev.* **2001**, *101*, 2921–2990; c) M. Kamigaito, T. Ando, M. Sawamoto, *Chem. Rev.* **2001**, *101*, 3689–3746; d) G. Moad, E. Rizzardo, S. H. Thang, *Aust. J. Chem.* **2005**, *58*, 379–410.
- [3] a) N. Badi, J.-F. Lutz, *Chem. Soc. Rev.* **2009**, *38*, 3383–3390; b) A. H. Soeriyadi, C. Boyer, F. Nystrom, P. B. Zetterlund, M. R. Whittaker, *J. Am. Chem. Soc.* **2011**, *133*, 11128–11131; c) F. S. Bates, M. A. Hilmyer, T. P. Lodge, C. M. Bates, K. T. Delaney, G. H. Fredrickson, *Science* **2012**, *336*, 434–440; d) G. Gody, T. Maschmeyer, P. B. Zetterlund, S. Perrier, *Nat. Commun.* **2013**, *4*, 2505; e) N. G. Engalis, A. Anastasaki, G. Nurumbetov, N. P. Truong, V. Nikolaou, A. Shegiwal, M. R. Whittaker, T. P. Davis, D. M. Had-dleton, *Nat. Chem.* **2017**, *9*, 171–178.
- [4] a) M. T. Krejchi, E. D. Atkins, A. J. Waddon, M. J. Fournier, T. L. Mason, D. A. Tirrell, *Science* **1994**, *265*, 1427–1432; b) W. A. Petka, J. L. Harden, K. P. McGrath, D. Wirtz, D. A. Tirrell, *Science* **1998**, *281*, 389–392; c) T.-B. Yu, J. Z. Bai, Z. Guan, *Angew. Chem. Int. Ed.* **2009**, *48*, 1097–1101; *Angew. Chem.* **2009**, *121*, 1117–1121; d) H. T. More, K. S. Zhang, N. Srivastava, J. A. Frezzo, J. K. Montclare, *Biomacromolecules* **2015**, *16*, 1210–1217.
- [5] R. B. Merrifield, *J. Am. Chem. Soc.* **1963**, *85*, 2149–2154.
- [6] a) H. A. Lashuel, S. R. LaBrenz, L. Woo, L. C. Serpel, J. W. Kelly, *J. Am. Chem. Soc.* **2000**, *122*, 5262–5277; b) M. Reches, E. Gazit, *Science* **2003**, *300*, 625–627; c) M. D. Pierschbacher, E. Ruoslahti, *Nature* **1984**, *309*, 30–33.
- [7] a) B. Perly, A. Douy, B. Gallot, *Makromol. Chem.* **1976**, *177*, 2569–2589; b) S. Lecommandoux, M.-F. Achard, J. F. Langenwalter, H.-A. Klok, *Macromolecules* **2001**, *34*, 9100–9111; c) D. Eckhardt, M. Groenewolt, E. Krause, H. G. Börner, *Chem. Commun.* **2005**, 2814–2816; d) J. M. Smeenk, M. B. J. Otten, J. Thies, D. A. Tirrell, H. G. Stunnenberg, J. C. M. van Hest, *Angew. Chem. Int. Ed.* **2005**, *44*, 1968–1971; *Angew. Chem.* **2005**, *117*, 2004–2007; e) H. R. Marsden, A. V. Korobko, E. N. M. van Leeuwen, E. M. Pouget, S. J. Veen, N. A. J. M. Sommerdijk, A. Kros, *J. Am. Chem. Soc.* **2008**, *130*, 9386–9393; f) T. Koga, M. Koike, S. Kamiwatari, N. Higashi, *Chem. Lett.* **2011**, *40*, 1244–1246; g) T. Koga, S. Kamiwatari, N. Higashi, *Langmuir* **2013**, *29*, 15477–15484.
- [8] a) O. Rathore, D. Y. Sogah, *J. Am. Chem. Soc.* **2001**, *123*, 5231–5239; b) M. Bikram, C.-H. Ahn, S. Y. Chae, M. Lee, J. W. Yockman, S. W. Kim, *Macromolecules* **2004**, *37*, 1903–1916; c) C. Zhou, B. Leng, J. Yao, J. Qian, X. Chen, P. Zhou, D. P. Knight, Z. Shao, *Biomacromolecules* **2006**, *7*, 2415–2419.
- [9] a) S. E. Grieshaber, A. J. E. Farran, S. L. Gibson, K. L. Kiick, X. Jia, *Macromolecules* **2009**, *42*, 2532–2541; b) K. Luo, J. Yang, P. Kopečková, J. Kopeček, *Macromolecules* **2011**, *44*, 2481–2488.
- [10] a) T. Terashima, T. Mes, T. F. A. De Greef, A. J. Gillissen, P. Besenius, A. R. A. Palmans, E. W. Meijer, *J. Am. Chem. Soc.* **2011**, *133*, 4742–4745; b) M. Ouchi, N. Badi, J.-F. Lutz, M. Sawamoto, *Nat. Chem.* **2011**, *3*, 917–924; c) B. V. K. J. Schmidt, N. Fechner, J. Falkenhagen, J.-F. Lutz, *Nat. Chem.* **2011**, *3*, 234–238.
- [11] a) C. J. Hawker, *J. Am. Chem. Soc.* **1994**, *116*, 11185–11186; b) D. Benoit, V. Chaplinski, R. Braslau, C. J. Hawker, *J. Am. Chem. Soc.* **1999**, *121*, 3904–3920.
- [12] K. Matyjaszewski, B. E. Woodworth, X. Zhang, S. G. Gaynor, Z. Metzner, *Macromolecules* **1998**, *31*, 5955–5957.
- [13] H. Otsuka, K. Aotani, Y. Higaki, A. Takahara, *Chem. Commun.* **2002**, 2838–2839.
- [14] T. Miyazawa, E. R. Blout, *J. Am. Chem. Soc.* **1961**, *83*, 712–719.
- [15] A. B. Sahakyan, W. F. Vranke, A. Cavalli, M. Vendruscolo, *J. Biomol. NMR* **2011**, *50*, 331–346.
- [16] T. Fukuda, T. Terauchi, A. Goto, Y. Tsujii, T. Miyamoto, *Macromolecules* **1996**, *29*, 3050–3052.
- [17] V. Delplace, J. Nicolas, *Nat. Chem.* **2015**, *7*, 771–784.

Manuscript received: August 4, 2017

Accepted manuscript online: August 10, 2017

Version of record online: September 25, 2017



CrossMark
click for updates

Cite this: *RSC Adv.*, 2015, 5, 67652

Thermo-responsive amino acid-based vinyl polymers showing widely tunable LCST/UCST behavior in water†

Nobuyuki Higashi,* Ryo Sonoda and Tomoyuki Koga*

We report a thermo-responsive polymer system showing widely tunable UCST/LCST behaviors based on amino acid-derived vinyl polymers. Four amino acids of Gly, Ala, Phe and Val and their methyl esters were employed for preparation of vinyl polymers, by considering hydrophobicity of the side chain group. The water solubility of these polymers was first examined, and as a result most of the polymers were soluble in water at a neutral pH, except the methylated Phe-based polymer and the Val-based polymers. The COOH-carrying Ala-based polymer displayed an upper critical solution temperature (UCST) behavior in water below pH 2.0 due to thermo-reversible hydrogen bonding of the pendent COOH groups, while the Gly-based polymer did not show any phase separation. The methylation of such COOH groups induced a lower critical solution temperature (LCST) behavior. Widely tunable UCST/LCST behaviors were achieved between 18 °C and 73 °C by using copolymers from different monomer combinations. Cross-linking of methylated Ala-based polymers gave a thermo-reversible hydrogel, which exhibited swelling and deswelling transitions at around the same temperature as the LCST of the corresponding homopolymer.

Received 4th July 2015
Accepted 3rd August 2015

DOI: 10.1039/c5ra13009c

www.rsc.org/advances

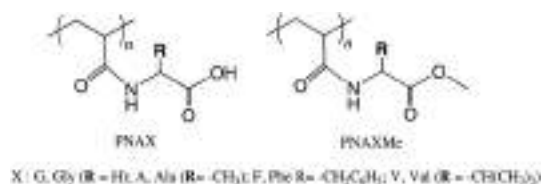
Introduction

Stimuli-responsive polymers exhibit a drastic change in properties upon only small changes in the environment such as temperature, pH, ionic strength, light irradiation, and mechanical stimuli.¹ These changes can result in phase separation from aqueous solutions. One of the representatives of stimuli-responsive polymers is a thermo-responsive polymer, the typical example being poly(*N*-isopropylacrylamide) (PNIPAM) which shows a lower critical solution temperature (LCST). It undergoes phase separation from dilute aqueous solution at about 33 °C.² Above this temperature the dissolved polymer changes from coil to the globule conformation.³ PNIPAM and its related polymers have been well characterized and widely used to design smart polymer materials, their current application being drug delivery system, actuators, and switchable surfaces with hydrophilic and hydrophobic properties.^{1,4-6} To mimic PNIPAM as a smart material, several attempts have been made to achieve thermo-responsive functions from synthetic polypeptides that were basically prepared by α -amino acid *N*-carboxylic acid anhydride (NCA) polymerization.⁷ There exists such a thermo-responsive polymer in naturally-occurred biopolymers. *Elastin*-like peptides (ELP), typical thermo-

responsive polypeptides, that consist of unique repeats of the pentapeptide sequence VPGXG (X is any amino acid except Pro) and undergo LCST transition depending on the kind of X.⁸⁻¹⁰ The LCST of ELPs can be precisely tuned between 0 and 100 °C by the replacement of X with other more than 20 kinds of amino acids.⁸ The high bio-compatibility of ELPs is also attractive for application to biomaterials such as scaffolds for cellular adhesion and bio-devices.¹¹ In spite of these fascinating properties of ELPs, their utilization seems to be limited because the preparation processes must take much time, compared with such convenient procedures as conventional radical polymerization, due to step-by-step reactions by a solid phase synthesis method and also this method is unsuitable for mass production of polymers. So then it occurred to us to prepare amino acid-based vinyl monomers and their polymers that would be expected to show thermo-responsiveness and good bio-compatibility. Taking account into hydrophobicity of the side group of amino acid that will certainly play an important role for thermal behaviors, we employed four types of amino acids: Gly (G), Ala (A), Phe (F) and Val (V), and also their corresponding methyl esters as shown in Scheme 1. In spite of the high potential of such an amino acid-based vinyl polymer system, research had been limited to a few scattered publications^{12,13} that had dealt with only a couple of amino acid-based vinyl polymers. The pioneer work on amino acid-based vinyl polymers by Mori *et al.* have focused on polyacrylamides containing proline and hydroxyproline as a collagen model prepared by reversible addition-fragmentation chain transfer polymerization and elucidated their thermal properties in water.¹² Agarwal *et al.*

Department of Molecular Chemistry & Biochemistry, Faculty of Science & Engineering, Doshisha University, Kyotanabe, Kyoto 610-0321, Japan. E-mail: nhigashi@mail.doshisha.ac.jp; tkoga@mail.doshisha.ac.jp; Tel: +81-774-65-6622/+81-774-65-6621

† Electronic supplementary information (ESI) available: ¹H NMR analyses, Table S1 and Fig. S1. See DOI: 10.1039/c5ra13009c



Scheme 1 Chemical structures for amino acid-based vinyl polymers employed in this study.

demonstrated the upper critical solution temperature (UCST) behavior of poly(*N*-acryloyl glycinamide) based on thermally reversible hydrogen bonding of the side chain amide groups.¹³ A series of our polymers are also expected to show LCST/UCST transitions on the basis of the same mechanism as previously reported,^{2,3,13} that is, LCST is derived from thermally reversible coil-to-globule conformational transition of the polymer chains due to hydrophobic dehydration and UCST is due to thermal formation–deformation of hydrogen bonding between the side chain groups.

In the present study, we report on thermal (LCST/UCST) behavior of aqueous solutions of PNAX and PNAXMe homopolymers prepared from the corresponding monomers, *N*-acryloyl amino acids (NAX) and *N*-acryloyl amino acid methyl esters (NAXMe), respectively and their copolymers. Network polymers (hydrogels) from these amino acid-based polymers have been prepared by polymerization in the presence of a cross-linker, and their thermo-responsive swelling behavior is additionally demonstrated.

Experimental section

Materials and methods

Solvents of analytical grade were used unless otherwise stated. Amino acids (Gly, *L*-Ala, *L*-Phe, and *L*-Val) and their corresponding methyl esters were purchased from Peptide Institute Inc., (Osaka, Japan, >99%) and from Watanabe Chemical Industries, Ltd (Hiroshima, Japan, >99%), respectively. Acryloyl chloride (EP grade), *N,N*-dimethyl-formamide (DMF), DMSO-*d*₆, MeOH-*d*₄, 2,2'-azobisisobutyronitrile (AIBN, 98%), diethyl ether, and tetrahydrofuran (THF) were purchased from Nacalai tesque Inc. (Kyoto, Japan). Ethylacetate, dichloromethane, triethylamine, and *N,N*-methylene-bisacrylamine (MBA, 99%) were purchased from Wako Pure Chemical Industries, Ltd (Osaka, Japan). Ammonium persulfate (APS, >99%) and *N,N,N',N'*-tetraethylmethylenediamine (TEMED, >98%) were purchased from Tokyo Chemical Industry (Tokyo, Japan). DMF was used after purification with distillation. ¹H NMR spectra were acquired using a JEOL JNM-AL400 (JEOL Resonance, Tokyo, Japan) spectrometer (400 MHz). The number-average molecular weight (*M*_n) and the polydispersity index (*M*_w/*M*_n) of each polymer were determined by size exclusion chromatography (SEC) using a JASCO LC-net II/AD (JASCO Ltd, Tokyo, Japan) equipped with a refractive index (RI) detector (eluent, DMF or THF; flow rate, 1 mL min⁻¹; temperature, 40 °C). Poly(methylmethacrylate)s were purchased from GL Sciences Inc. (Tokyo, Japan) and used as the

calibration standard. Transmittance of aqueous polymer solutions was recorded at 600 nm on a V-650 spectrophotometer (JASCO Ltd, Tokyo, Japan) equipped with a Peltier type thermostatic cell holder coupled with a controller PTC-423L (JASCO Ltd, Tokyo, Japan).

Preparation of amino acid-based monomer NAX

NAG was prepared as follows. Glycine (2.0 g, 27 mmol) was dissolved in 3 M NaOH aqueous solution (20 mL) at 4 °C, to which acryloyl chloride (2.9 g, 32 mmol) was added dropwise. After stirring the solution for 3 h with ice cooling, 1 M HCl aqueous solution was added so as to acidify the solution to pH 2.0. To extract the objective, the aqueous solution was washed with ethylacetate several times. The collected organic phase was dried with anhydrous MgSO₄, and after evaporation of the solvent the objective was obtained as a white solid in 61% (2.1 g) yield. ¹H NMR (DMSO-*d*₆, δ in ppm): 3.9 (2H, -COCH₂NH-), 5.6–5.7 (1H, CH₂CH-: vinyl (*cis*)), 6.1–6.2 (1H, CH₂CH-: vinyl (*trans*)), 6.3–6.4 (1H, CH₂CH-: vinyl), 8.4–8.5 (1H, -CH₂NHCO-: amide), 12.5–12.8 (1H, -COOH, carboxy). NAA, NAF and NAV were also prepared with the same procedure as that of NAG, and were obtained in 72, 54 and 58% yield, respectively. The chemical structures were confirmed by ¹H NMR spectroscopy.†

Preparation of amino acid-based monomer NAXMe

NAGMe was prepared by condensation reaction of glycine methyl ester (Gly-OMe) with acryloyl chloride. Gly-OMe-HCl (2.0 g, 16 mmol) was dissolved in dichloromethane (100 mL) together with triethylamine (5 mL, 50 mmol) at 4 °C. To this solution, dichloromethane solution (20 mL) of acryloyl chloride (1.7 g, 19 mmol) was added dropwise and then stirred under ice-cooling over night. After removal of the solvent, ethylacetate (100 mL) was added to the residue and the precipitated triethylamine hydrochloride was filtered off. The filtrate was washed with 1 M NaHCO₃ aq. (100 mL) several times to remove excess acrylic acid in the presence of 1 M MgSO₄ aq. due to salting-out effect and then the organic phase was dried. Finally, the residue after removal of the solvent was purified by using silica-gel column chromatography with diethyl ether as an eluent. Yield 48%, TLC (diethyl ether) *R*_f = 0.35 single spot. ¹H NMR (DMSO-*d*₆, δ in ppm): 3.6–3.7 (3H, -COOCH₃), 3.9–4.0 (2H, -COCH₂NH-), 5.6–5.7 (1H, CH₂CH-: vinyl (*cis*)), 6.1–6.2 (1H, CH₂CH-: vinyl (*trans*)), 6.3–6.4 (1H, CH₂CH-: vinyl), 8.5–8.6 (1H, -CH₂NHCO-: amide). NAAME, NAFMe and NAVMe were synthesized with the same procedure as that of NAGMe, and were obtained in 48, 58 and 61% yields, respectively. The chemical structures were confirmed by ¹H NMR spectroscopy.†

Polymerization of monomers

All polymers from the corresponding monomers, NAX and NAXMe, were prepared in almost the same manner, and thus only a typical example of NAGMe is described below. The polymerization of NAGMe (1.0 g, 8.7 mmol) was carried out in the presence of AIBN (0.01 g, 0.07 mmol) as an initiator in distilled DMF (3.5 mL) at 70 °C under nitrogen atmosphere. After 12 h, the content was condensed by evaporation of the

solvent and the residue was then washed with diethyl ether several times and dried to give a white powder. Copolymerizations were performed for two different combination of monomers, NAG–NAA and NAGMe–NAAME. The mixtures of such monomer combination (total monomer concentration = 2.0 M) having various compositions were copolymerized initiated with AIBN (1.0 wt% to monomers) in DMF at 70 °C for 12 h under nitrogen atmosphere. The copolymers thus obtained were purified in the same manner as described above. Molecular weight and PDI were measured by SEC, and the copolymer compositions were evaluated by ¹H NMR spectroscopy.

Preparation of hydrogels and their swelling properties

The PNAAME-derived network polymer was prepared by using a redox polymerization system (TEMED/APS) as follows. NAAME (10 mg) as monomer, MBA (1 mg) as cross-linker, and APS (5 mg) were dissolved in water (2 mL), and to this solution 3 μL of TEMED was added and stirred gently at 5 °C. This aqueous solution was poured into the silicon sheet (as a spacer with 0.5 mm thickness)-attached glass plate, and then sandwiched with the another hydrophobized glass plate and was kept at a constant temperature of 5 °C for 12 h. The crude product was purified by immersing it in pure water that was replaced with fresh water several times for three days so as to remove unreacted monomers and initiators. Swelling ratio of the gel thus obtained was evaluated as follows. The gel with about 0.5 mm thickness was swelled over night at 5 °C to reach an equilibrium in swelling, and then was weighed (W_s). From the weight of the polymer before swelling (W_d) and W_s , the swelling ratio (SR) can be calculated according to the following equation,

$$\text{SR (\%)} = \{(W_s - W_d)/W_d\} \times 100$$

The SRs were evaluated after 30 min-incubation at each temperature for swelling and deswelling cycling experiment.

Results and discussion

Preparation of amino acid-based monomers and polymers

Four amino acids of Gly, Ala, Phe and Val were employed for preparation of their vinyl monomers and polymers, by considering hydrophobicity of the side chain groups. The vinyl monomers of NAX and NAXMe were first synthesized by condensation reaction of acryloyl chloride with the corresponding amino acids and their methyl esters, respectively, with rather good yields of 60–80%. Polymers and copolymers of these amino acid-based vinyl monomers were then prepared by conventional radical polymerization initiated with AIBN in DMF ([monomer] = 2.0 M) at 60 °C for 12 h. The homopolymers thus obtained were characterized by means of SEC. The results of evaluated molecular weight (M_n) and polydispersity index (PDI) were summarized in Table 1, together with the conversion. The polymerization of all six monomers was found to proceed smoothly and reach above 90% conversion after 12 h.

First of all, water solubility of these polymers was examined at a polymer concentration of 0.5 wt% between 4 and 80 °C. For

Table 1 Results of polymerization of NAX and NAME in DMF at 70 °C for 12 h^a

Polymer	Conversion (%)	$M_n^b \times 10^{-4}$	M_w/M_n^b	Water solubility ^c
PNAG	91	6.5	2.1	+ ^d
PNAA	96	5.4	2.3	+ ^d
PNAF	91	3.8	1.4	+ ^d
PNAV	92	1.6	3.2	–
PNAGMe	95	3.9	1.6	+ ^e
PNAAME	94	1.5	1.5	+ ^e
PNAFMe	95	4.0	1.3	–
PNAVMe	95	5.6	1.4	–

^a [Monomer] = 2.0 M; [AIBN] = 1.0 wt% to monomer. ^b Determined by SEC measurements in THF relative to poly(methylmethacrylate). ^c Polymer concentration: 0.5 wt%. ^d At neutral pH. ^e At lower temperature (4 °C). + Good solubility. – Poor solubility.

the polymers of a series of PNAX, pH dependence was also checked because of the existence of COOH group at the side chains that would be ionizable upon pH change. As a result, PNAG, PNAA and PNAF were soluble in water at neutral pH, and their methyl esters, except PNAFMe, were also soluble in water at lower temperatures. However, Val-based polymers (PNAV, PNAVMe) did not show any solubility to water under the prescribed conditions probably due to higher hydrophobicity of their side chain group (i-propyl group) than others.¹⁴

Thermal phase transition in aqueous solutions

Thermo-responsive behaviors of COOH-containing PNAG, PNAA and PNAF were studied by measuring turbidity at 600 nm of their aqueous solutions. Gly-based PNAG provided transparent solutions from 4 to 80 °C even when the solution pH and the polymer concentration were varied from pH 2.0 to 12.0 and from 0.5 to 3.0 wt%, respectively. To the contrary, Ala-based PNAA showed UCST-type transition. Fig. 1(a) displays turbidity curves of PNAA solutions with various polymer concentrations at pH 2.0, at which the pendent COOH groups are protonated. The transmittance of each polymer solution was measured continuously from 80 °C to 35 °C with a constant cooling rate of 1.0 °C min⁻¹. It is obvious from the figure that the transmittance decreases upon cooling the solution and the steepness in transmittance decrement is enhanced with the polymer concentration. The observed temperature-dependence of turbidity means clearly the UCST behavior with transition temperature of 54 °C since above 1.0 wt% concentration the same turbidity curves were obtained. Furthermore, a reversible UCST behavior was observed for PNAA when returning the sample to 80 °C. Difference in the molecular structure between PNAG and PNAA exists only in the side chain group (–H and –CH₃, respectively) and so their hydrophobicity seemed to be important factor to cause such a UCST behavior. The UCST behavior thus observed for PNAA solutions can be considered as follows. At pH 2.0 (below pK_a value of the side chain COOH group) the side chain carboxylic acid group are protonated and the PNAA molecules allow to aggregate due to hydrogen bonding among COOH groups and/or between COOH and

amide bond, induced with hydrophobic interaction of the side chain methyl groups. Upon elevating temperature, such polymer aggregates were dissolved because of weakening such hydrogen bonds. To clarify the importance of hydrogen bonding that triggered off such polymer aggregation, the same turbidity experiments were performed for PNAA solutions at higher pH (>3.0), at which the COOH groups are deprotonated and behave as anions, and in the presence of urea that is a well-known hydrogen bonding inhibitor. In such higher pH region, the polymer solutions showed no turbidity probably because hydrogen bonding became weak and hydrophilicity of the whole polymer chain was enhanced due to deprotonation of COOH groups (Fig. S1a†). No phase transition was also observed when the same experiment was performed in the presence of urea (8 M) (Fig. S1b†). These results strongly suggest that hydrogen bonding of the side chain COOH groups was of critical importance to cause the UCST behavior. Agarwal and coworkers have also suggested the importance of hydrogen bonding of the pendent group to cause UCST-type thermo-responsiveness.¹³ Phe-based PNAF provided transparent solutions from 4 °C to 80 °C at pH > 4, and lowering pH to 3.1 did not lead such a clear phase transition (UCST) as was observed for PNAA but a turbid suspension and a precipitate with huge aggregates, probably due to more hydrophobic phenyl group compared to methyl group of PNAA. Effects of the methylation of COOH groups on thermal behaviors were subsequently examined. The turbidity measurements for methylated PNAGMe and PNAAME were performed in the same manner described above and their temperature dependences were displayed in Fig. 2. The aqueous solution of PNAGMe provides a typical LCST profile while that of PNAG before methylation showed no transition even at pH < 2.0 where the pendent COOH group was protonated completely. This clearly means that methylation of PNAG would increase significantly hydrophobicity of the polymer molecule and as a result induced such an LCST-type phase separation. PNAAME is of interest to show a reverse trend (LCST) to that of COOH-carrying PNAA (UCST) due to lack of hydrogen bonding of the COOH group. The phase transition temperatures (LCST) for PNAGMe and PNAAME are evaluated at high polymer concentrations in Fig. 2 to be 73 °C and 18 °C, respectively, and the observed difference in transition temperature can be assigned to the presence and the absence of methyl group on α -carbon of the amino acid residue. More hydrophobic PNAAME would enhance aggregation of polymer molecules at a lower temperature, compared to PNAGMe.

In order to tune LCST and UCST in wide range, the copolymers with various compositions were prepared for combinations of NAAME–NAGMe and NAA–NAG. Jones reported that the LCST of PNIPAM shifted to higher temperatures by copolymerization with more hydrophilic acrylic acid.¹⁵ Agarwal *et al.* demonstrated the lower temperature shift of UCST by copolymerization of *N*-acryloyl glycinamide with hydrophobic styrene.¹³ Copolymerizations for the combination of NAAME–NAGMe and NAA–NAG were carried out through conventional radical polymerization initiated with AIBN. Polymerization conditions and characterization of the resultant copolymers were summarized in Table S1.† Fig. 3 shows temperature dependent turbidity change and relationship

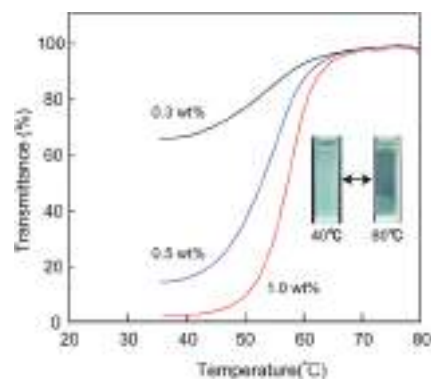


Fig. 1 Temperature dependence of the transmittance at 600 nm of aqueous solutions of PNAA with various concentration at pH 2.0.

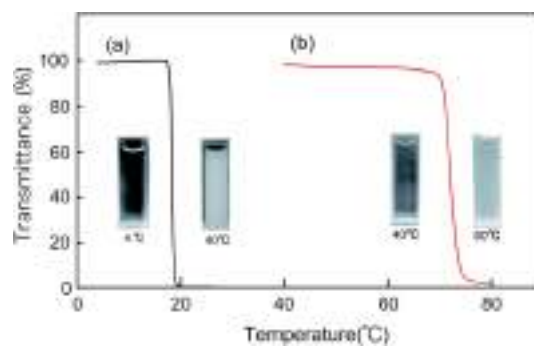


Fig. 2 Comparison of turbidity curves between PNAAME (a) and PNAGMe (b) aqueous solutions (1.0 wt%).

between LCST or UCST and the copolymer composition for the copolymers of poly(NAGMe-*co*-NAAME) and poly(NAG-*co*-NAA). In UCST-type phase transition (Fig. 3(b)), the incorporation of NAG unit into the NAA copolymer gradually lowers the phase separation temperature from 54 °C to 43 °C and above 15% of NAG unit there appears no UCST behavior due to critical increment in hydrophilicity of the copolymer. On the other hand, for the copolymers (poly(NAGMe-*co*-NAAME)) that appear LCST-type phase separation (Fig. 3(c)), they are found to show LCST behavior over whole copolymer composition (0–100% of NAAME), as was expected since each homopolymer provided an intrinsic phase transition temperature. In Fig. 3(d), the LCST is found to increase systematically with increasing the content of relatively hydrophilic NAGMe unit. It should be noted that the copolymers prepared from combination of only two kinds of amino acids (Gly and Ala) and their minor derivatives can lead to both UCST- and LCST-type phase separation and also make it possible to manipulate the phase transition temperature widely. These results must provide important insights into designing thermo-responsive polymers for objective purposes in aqueous media.

Hydrogels from PNAAME and its thermo-responsive properties

Finally we prepared a hydrogel from the LCST-type PNAAME and examined its thermo-responsive property on swelling.

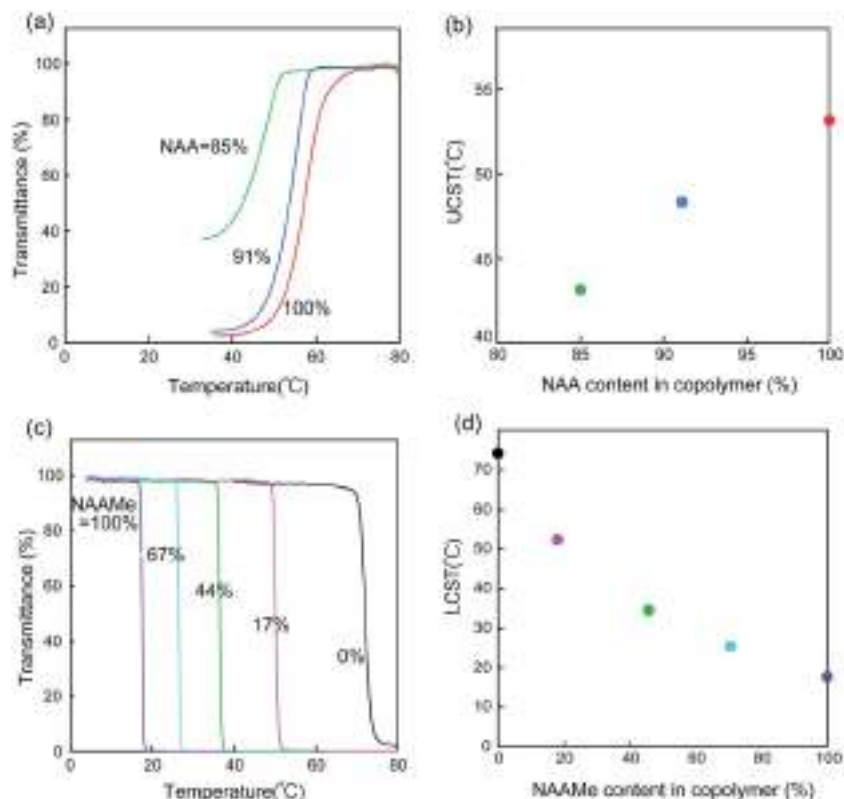


Fig. 3 Turbidity curves (a and c) and relationships between phase transition temperature (UCST or LCST) and copolymer composition (b and d) for poly(NAG-co-NAA) aqueous solution (pH 2.0) (a and b) and poly(NAGMe-co-NAAMe) aqueous solution (c and d). The copolymer concentration is 1.0 wt% for each solution.

A redox polymerization was utilized for preparing the network polymer of NAAMe because it is available under a lower temperature inhibiting LCST-type phase separation of the produced polymer chains. The polymerization of NAAMe was carried out in the presence of MBA as a cross-linker initiated with a redox system of TEMED/APS in water at 5 °C that is enough below the LCST of PNAAMe. After removal of unreacted monomers and initiators by washing with water several times, a water-swollen network polymer was obtained, in which the cross-kinking ratio was adjusted to be 1.0 wt%.

Thermo-responsiveness in swelling of the PNAAMe hydrogel thus obtained was examined. Fig. 4(a) shows temperature-dependent change of swelling ratio. It is found to steeply decrease from *ca.* 2500–500% in a narrow temperature range between 14 and 15 °C, meaning transition of the hydrogel from swelling to deswelling. Such transition was also observed visually (see photos in Fig. 4(a)). It should be noted that the temperature range of transition is close to the LCST of PNAAMe homopolymer (18 °C). Therefore the observed transition from swelling to deswelling must be correlated to hydration state of the PNAAMe homopolymer in water. Fig. 4(b) displays the thermo-responsive change in swelling ratio when the PNAAMe hydrogel was alternately immersed in water at 10 °C and 40 °C, at which the hydrogel was incubated for 30 min. Cooling from 40 °C to 10 °C leads to the increment in swelling ratio and heating returns it to the original one. These changes in swelling ratio were almost reversible although the values of swelling

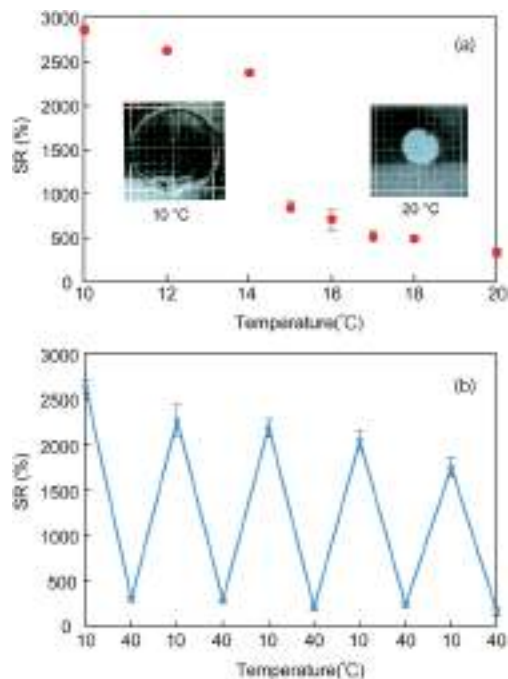


Fig. 4 Temperature dependence of the swelling ratio (SR, %) for PNAAMe hydrogel (a). Reversible changes between swelling (10 °C) and deswelling (40 °C) for PNAAMe hydrogel (b). Measurements of the swelling ratio were performed after 30 min-incubation at the prescribed temperatures. Each point is the mean of three independent measurements, and bars represent standard deviation of means.

ratio had a tendency to somewhat decrease in whole repeating process.

Conclusions

In this study, we demonstrated the tunable UCST/LCST behavior by using amino acid-based vinyl polymers, which were prepared through conventional radical polymerization of the corresponding monomers. In particular, we focused mainly on Gly- and Ala-based vinyl polymers, PNAG and PNAA, and PNAGMe and PNAAME, which contain COOH group and COOMe group, at the side chain, respectively. The COOH-carrying PNAA showed UCST behavior in water below pH 2 due to thermo-reversible hydrogen bonding of the pendent COOH groups while PNAG did not show any aggregation. The methylation of such COOH groups (PNAGMe and PNAAME) brought about LCST behavior because the side chains became more hydrophobic although transition temperatures were quite different between PNAGMe (73 °C) and PNAAME (18 °C) depending on hydrophobicity of the whole polymer molecule. The widely tunable UCST and LCST were achieved *via* copolymerization of different monomer combination of NAG–NAA and NAAME–NAGMe at varied ratio. The cross-linking of PNAAME in water provided a thermo-reversible hydrogel that exhibited swelling and deswelling transition at around the same temperature as the LCST of PNAAME homopolymer. These thermo-responsive amino acid-based polymers and hydrogels with tunable UCST and LCST will have great promising to construct new intelligent materials and in particular biomaterials for biomedical applications. We are currently extending this procedure to the design and synthesis of amino acid-based polymers having various architectures such as block and graft copolymers, whose segments have different thermal properties, that would show thermally-controllable self-organization behaviors.

Acknowledgements

This work was partly supported by a Grant-in-Aid for Scientific Research (KAKENHI) (No. 25410132 and No. 26390022) from

Japan Society for the Promotion of Science (JSPS) and a MEXT-Supported Program for the Strategic Research Foundation at Private Universities.

References

- 1 A. Cameron and K. M. Shakesheff, *Adv. Mater.*, 2006, **18**, 3321–3328.
- 2 H. G. Schild, *Prog. Polym. Sci.*, 2007, **208**, 245–253.
- 3 Y. Maeda, T. Higuchi and I. Ikeda, *Langmuir*, 2000, **16**, 7503–7509.
- 4 L. Jun, W. Bochu and W. Yazhou, *Int. J. Pharm.*, 2006, **2**, 513–519.
- 5 J. Hoffmann, M. Plotner, D. Kuckling and W. J. Fischer, *Sens. Actuators*, 1999, **77**, 139–144.
- 6 T. Okano, N. Yamada and H. Sakai, *Biomaterials*, 1995, **16**, 297–303.
- 7 (a) C. Chen, Z. Wang and Z. Li, *Biomacromolecules*, 2011, **12**, 2859–2863; (b) J. Shen, C. Chen, W. Fu, L. Shi and Z. Li, *Langmuir*, 2013, **29**, 6271–6278.
- 7c H. Liu, Y. Xiao, Y. Guan, J. Zhang and M. Lang, *Chem. Commun.*, 2015, **51**, 10174–10177;
- 8 D. W. Urry, *Angew. Chem., Int. Ed.*, 1993, **32**, 819–841.
- 9 D. W. Urry, *Prog. Biophys. Mol. Biol.*, 1992, **57**, 23–57.
- 10 D. E. Meyer and A. Chilkoti, *Biomacromolecules*, 2004, **5**, 846–851.
- 11 T. Koga, K. Nakamoto, K. Odawara, T. Matsuoka and N. Higashi, *Polymers*, 2015, **7**, 134–146.
- 12 (a) H. Mori, K. Sutoh and T. Endo, *Macromolecules*, 2005, **38**, 9055–9065; (b) H. Mori, H. Iwaya, A. Nagai and T. Endo, *Chem. Commun.*, 2005, 4872–4874; (c) H. Mori, I. Kato, M. Matsuyama and T. Endo, *Macromolecules*, 2008, **41**, 5604–5615.
- 13 (a) J. Seuring and S. Agarwal, *Macromol. Chem. Phys.*, 2010, **211**, 2109–2117; (b) J. Seuring, F. M. Bayer, K. Huber and S. Agarwal, *Macromolecules*, 2012, **45**, 374–384.
- 14 G. D. Rose, A. R. Geselowitz, G. J. Lesser, R. H. Lee and M. H. Zehfus, *Science*, 1985, **229**, 834–838.
- 15 M. S. Jones, *Eur. Polym. J.*, 1999, **35**, 795–801.